



UNIVERSITAT^{DE}
BARCELONA

Thermal and chemical imaging of the upper mantle anomalies: application to Western Mediterranean

Ajay Kumar



Aquesta tesi doctoral està subjecta a la llicència **Reconeixement 4.0. Espanya de Creative Commons.**

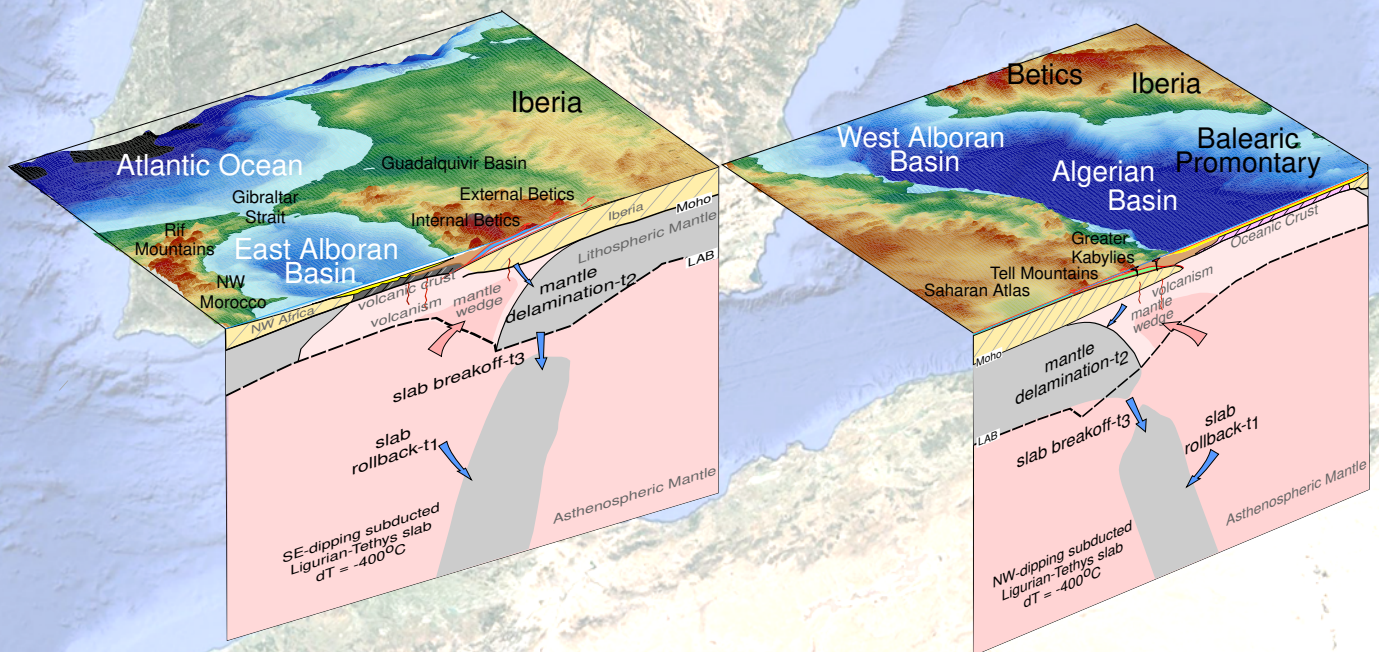
Esta tesis doctoral está sujeta a la licencia **Reconocimiento 4.0. España de Creative Commons.**

This doctoral thesis is licensed under the **Creative Commons Attribution 4.0. Spain License.**

THERMAL AND CHEMICAL IMAGING OF THE UPPER MANTLE ANOMALIES: APPLICATION TO WESTERN MEDITERRANEAN

Ajay Kumar

Ph.D. Thesis
Barcelona, October 2020



Director

Prof. Dr. Manel Fernàndez Ortiga
Prof. Dr. Jaume Vergés Masip

Departament de Dinàmica de la Terra i de l'Oceà
Facultat de Ciències de la Terra
Universitat de Barcelona

THERMAL AND CHEMICAL IMAGING OF THE UPPER MANTLE ANOMALIES: APPLICATION TO WESTERN MEDITERRANEAN

Tesi doctoral presentada per Ajay Kumar en el Departament de Dinàmica de la Terra i de l'Oceà de la Universitat de Barcelona per optar al grau de Doctor en Ciències de la Terra

Group of Dynamics of the Lithosphere (GDL)
Geosciences Barcelona (GEO3BCN)
Consejo Superior de Investigaciones Científicas (CSIC)

Directors

Prof. Dr. Manel Fernàndez Ortiga

Prof. Dr. Jaume Vergés Masip

Tutor

Prof. Dr. Juan José Ledo Fernández

Barcelona, Octubre 2020



To my parents and brother

Acknowledgements

It is my pleasure to be indebted to various people, who directly or indirectly contributed in the development of this thesis and who influenced my thinking, behaviour and acts during the course of this thesis.

First and foremost are my thesis supervisors Prof. Dr. Manel Fernàndez Ortega and Prof. Dr. Jaume Vergés Masip at ICTJA-CSIC (now Geo3Bcn), Barcelona. Manel has been an absolute source of motivation, support and fine tuned supervision. I still remember the first day I met him in his office in 2016 and till date the temperament of the meetings stayed same. Manel allowed me to explore things at my own pace and in case of dead end always brought me back on track. I am immensely thankful and grateful to him for tolerating my mistakes along the way and devoting time during the last stages of this thesis even after his retirement. Jaume has been another absolute source of motivation, support and supervision especially in the geological aspects of the complex Western Mediterranean and its implications for regional geodynamics. Greeting every day in the mornings complimented with a hand shake added an element of care to my day-to-day life at ICTJA. I am also grateful to Jaume for his good eye for aesthetics and presentation of the scientific data and making it much more appealing. I have tried to dig out every bit of an artist in me (though I am really bad in art) during this thesis. Huge thanks to Jaume. I am also thankful to both, Manel and Jaume, for the open-discussions in our meetings and laughs we shared. I also would like to thank Dr. Montserrat Torné Escasany, Dr. Ivone Jiménez Munt, and Dr. Daniel García-Castellanos for support and supervision on various research projects I have been involved at Geo3Bcn.

I also thank Prof. Dr. Juan José Ledo Fernández for accepting the tutoring of this thesis and the commission of doctorate from the UB (University of Barcelona) for the progress follow-up carried out during these years.

I also would like to thank friends, I made at ICTJA Geo3Bcn and Barcelona, Mireia, Encarni, Lavinia, Jonas, Angel, Max, Jordi, Luis, Pili, Mari, Marc, Ana, Milton, Hanneke, Erik, Enric, Cris, for their support and my Spanish name “Pepe”. Big thanks to Kittiphon (KB) for being an excellent friend, officemate, and shared interest in FOOD! A big hug and thanks to SUBITOP friends with whom I shared wonderful 3 years of my life. I am also thankful to Ranjana for being there and supporting me at long-distances (inter-state and trans-continental) for 10 years now.

I also thank the administrative and computing staff at Geo3Bcn (Chelo, Leonor, Montse, Nuria, Xavi, Esmeralda, Oscar, and Marc) for handling my affairs and “a curious case of an Indian without a surname”.

Lastly, I would like to thank my parents for their unconditionally support (whenever, wherever) and my brother for staying with them and handling the family matters for all these years for which I was too busy to care.

Funding

This thesis is funded by the EU Marie Curie Initial Training Network ‘SUBITOP’ (674899-SUBITOP-H2020-MSCA-ITN-2015) and partly by SUBTETIS (PIE-CSIC-201830E039, CSIC), GeoCAM (PGC2018-095154-B-I00, Spanish Government), and Equinor R&T Fornebu (Norway) projects. This thesis has been developed using the facilities of the Laboratory of Geodynamic Modelling from Geo3Bcn-CSIC.

Table of Contents

Table of Contents.....	vii
Summary.....	1
Chapter 1	9
Introduction	9
1.1. Objectives	18
1.2. Thesis outline	19
Chapter 2	25
Fundamentals	25
2.1. Lithosphere	25
2.2. Sublithospheric mantle.....	27
2.3. Gravitational field	28
2.3.1. Gravity anomaly	29
2.3.2. Geoid anomaly.....	30
2.4. Temperature field.....	32
2.5. Mineral physics	34
2.6. Physical properties.....	38
2.6.1. Density	38
2.6.2. Thermal conductivity	38
2.6.3. Mantle seismic velocities	39
2.7. Isostasy and elevation	41
2.8. Mantle melting and volcanism.....	42
Chapter 3	47
Integrated geophysical-petrological modelling of the upper mantle anomalies.....	47
3.1. General modelling workflow	48
3.2. Anelasticity	50
3.3. Sublithospheric mantle composition	55
3.4. Recalibration of elevation.....	57
3.5. Reference model for synthetic seismic tomography	58
3.6. Sublithospheric mantle anomalies	60
3.6.1. Thermal anomalies	61

3.6.2. Chemical composition anomalies	62
3.6.3. Seismic velocity anomalies.....	64
3.7. Open source graphic user interface (GUI) and input/output data	66
3.8. Application to a synthetic subduction zone.....	67
3.8.1. Input data, model geometry, and physical properties.....	67
3.9. Post-processing toolbox	70
3.9.1. Seismic velocities post-processing example	71
3.9.2. Depth distribution of stable mineral-assemblages.....	74
Chapter 4.....	77
Present-day crust and upper mantle structure of the Alboran and Algerian basins and their margins.....	77
4.1. Data	78
4.1.1. Regional geophysical data	78
4.1.2. Crustal data	81
4.1.3. Mantle structure and chemical composition	83
4.2. Alboran Basin geo-transect: structure, temperature, and density	85
4.2.1. Crustal and upper mantle structure	85
4.2.2. Temperature and density distribution	92
4.3. Algerian Basin geo-transect: structure, temperature, and density.....	94
4.3.1. Crustal and upper mantle structure	94
4.3.2. Temperature and density distribution	98
4.4. Mantle seismic velocities and comparison with passive seismological data	100
4.4.1. Alboran Basin geo-transect	100
4.4.2. Algerian Basin geo-transect	106
Chapter 5.....	113
Discussion	113
5.1. LitMod2D_2.0	114
5.2. Present-day crust and upper mantle structure of the Alboran and Algerian basins and their margins.....	115
5.2.1. Crustal and lithospheric structure	115
5.2.2. Mantle composition.....	118
5.2.3. Subducted Ligurian-Tethys slabs	128

5.2.4. Geodynamic implications	129
Chapter 6	139
Conclusions	139
6.1. LitMod2D_2.0: An improved tool for the integrated geophysical-petrological interpretation of upper mantle anomalies.....	140
6.2. Present-day crust and upper mantle structure in the Alboran and Algerian basins and their margins	142
List of Figures and Tables.....	145
References.....	154
Appendix	171

Summary

Summary

The closure of the Ligurian-Tethys Ocean, opened during Jurassic and consisting of highly segmented margins in between Africa and Iberia, has produced the Alboran and Algerian basins in the Western Mediterranean through subduction and slab roll-back processes during the Cenozoic. Towards the end of the slab roll back, collision with the continental margins led to the formation of the Betic-Rif orogen in south Iberia and the Tell-Kabylies in north Algeria. Both, the Betics-Rif and Tell-Kabylies, shows the high-pressure and low-temperature (HP-LT) rocks exhumed from the subduction channel but with opposite tectonic vergence, to the NW in Betics and to the SE in Kabylies. While the Cenozoic evolution of the back-arc basins in the Central and Eastern Mediterranean (i.e., Liguro-Provenca, Tyrrehenian and Aegean) are well understood, the evolution of the Alboran and Algerian basins in the Western Mediterranean is under debate, leading to the proposal of different geodynamic evolution models. All the models agree on that the subduction and subsequent slab-rollback was operating but argues for the direction of subduction trench and slab-rollback. At present, positive seismic velocity anomalies in the upper mantle are observed in the tomography models around the Alboran Basin and beneath the North-Algeria margin. These high velocity anomalies are qualitatively interpreted to be cold, hence, remnant of the subducted Ligurian-Tethys lithosphere in order to explain geodynamic evolution of the Alboran and Algerian basins.

Subduction processes must have left its imprint on the crust and upper mantle structure, temperature and chemical composition, which dictate the present-day physical state. Physical state inside the Earth controls the physical properties (i.e., density, seismic velocities, and thermal conductivity) which in turn control the geophysical observables at the surface (i.e., elevation, gravity anomaly, geoid height, and surface heat flow). Integrated geophysical-petrological modelling of these surface observables allows exploring and reconciling observations from different datasets and methods. However, thermal and/or chemical nature of the imaged seismic velocity anomalies (e.g., subducted Ligurian-Tethys) needs to be incorporated in such models. In general, seismic tomography models reports relative positive or negative velocities with respect to a reference model which are further inferred qualitatively as cold or hot regions in the upper mantle, respectively. Quantitative interpretation of the seismic velocity anomalies in terms of temperature and/or chemical composition is challenging and is at the forefronts of the modern day geophysics.

Hence, the objectives of this thesis is twofold: 1) to develop a methodological framework to incorporate the sublithospheric anomalies observed in seismic tomography in the integrated geophysical-petrological modelling of the geophysical surface observables, and 2) its application to the Alboran and Algerian basins and their margins to model the present-day crust and upper mantle thermo-chemical structure yielding temperature, density (i.e., chemical composition) and seismic velocities to put constraints on their geodynamic evolution.

In the first part, an already existing tool, LitMod2D_1.0, is improved into a new LitMod2D_2.0 version which allows to model the sublithospheric anomalies and to be available for the scientific community. Various synthetic tests of the upper mantle anomalies have been performed to understand the sensitivity of temperature and chemical composition to the density and seismic velocities. Results show nonlinearity between the sign of thermal and seismic velocity anomalies, and that S-wave velocities are more sensitive to temperature whereas P-wave velocities are to composition. A synthetic example of subduction is made to understand the sensitivity of sublithospheric mantle anomalies associated with the slab and the corner flow, on surface observables (elevation, geoid height, and gravity anomalies). A new open-source graphic user interface is incorporated in the new version for ease of application. The output of the code is simplified by writing only the relevant physical parameters (temperature, pressure, material type, density, and seismic velocities) to allow the user to utilize predefined post-processing codes from a toolbox (flexure, mineral assemblages, synthetic passive seismological data, and tomography) or designing new ones. A post-processing example is demonstrated by calculating synthetic seismic tomography, Rayleigh-surface-wave dispersion curves, P-wave receiver functions and stable minerals distribution from the output file of LitMod2D_2.0.

In the second part of this thesis, I apply improved LitMod2D_2.0 to define the present day crustal and lithospheric structure along two 2D geo-transects beneath the Betics-Alboran and Greater Kabylies-Tell-Algerian orogenic systems to discuss the highly debated and contrasting existing models. Results show a thick crust (37 km and 30 km) and a relative deep LAB (130 km and 150 km) underneath the HP-LT metamorphic units of the Internal Betics and Greater Kabylies that contrast with the ~16 km thick magmatic crust of the Alboran Basin and the ~10 km thick oceanic crust of the Algerian Basin, respectively. This sharp change in crustal thickness, from the orogenic wedge to the back-arc basins, contrasts with the gentler crustal thickening towards the respective opposed margins. Despite the similar LAB depth (~60 km) in both basins, the chemical composition of the lithospheric mantle beneath the Alboran

Basin is slightly more fertile than beneath the Algerian Basin. At sublithospheric levels, results show that both the Alboran slab beneath the Betics and Algerian slab beneath the Kabylies, are about -400 °C colder than the ambient mantle but have different chemical composition. Alboran slab is slightly fertile compared to the typical oceanic lithospheric of the Algerian slab. Both slabs are detached from the respective continental lithospheric mantle of Iberia and Africa, since their weight is not transmitted isostatically to the surface. Results show that the uplift related to the slab break-off is ~700–1000 m in the Betics and is ~600–1200 m in north Algeria.

The Ligurian-Tethys slab beneath the SE Iberia shows an apparent dip to the SSE whereas the slab below Algeria dips to the NNW, matching the NW- and SE-tectonic transport direction of the fold and thrust belts of the Betics and Greater Kabylies-Tell-Atlas subduction-related orogens, respectively. The large-scale configuration of present-day SE Iberia and Algerian margins as well as their mantle compositions in the Alboran and Algerian geo-transects is consistent with opposite dipping subduction of two segments of the Jurassic Ligurian-Tethys domain. Their present configurations agree with Neogene slab roll-back process triggering mantle delamination followed by slab break-off in both opposite subductions.

CHAPTER 1

Introduction

“Necessity is the mother of invention”

-Unknown

Chapter 1

Introduction

The closure of the Tethys Ocean, located along the northern margin of the paleo-continent Gondwana, associated with the northward displacement of India, Arabia, and Africa lead to the subduction of its different segments and has produced the ~12000 km long Alpine-Himalayan collision zone (Figure 1.1). The convergence velocity with respect to Eurasia was decreasing from east to west, such that India was moving ~120 mm/yr to NNE, Arabia was moving ~32 mm/yr to NNE-N, and Africa was moving 4 mm/yr -10 mm/yr to N-NNW (e.g., Hatzfeld and Molnar, 2010). To the east, after the consumption of the Tethys lithosphere, which at present is sitting in the underlying mantle, the Indian (at ~50 Ma) and Arabian (at ~35 Ma) continental lithosphere collided with Eurasia and has generated the Tibetan Plateau and the Zagros Mountains (e.g., Hatzfeld and Molnar, 2010). In the Mediterranean region, collision between Eurasia and Africa is not achieved yet and represents an early stage of continent-continent collision where a mixture of oceanic and transitional lithosphere is still present (Royden and Faccenna, 2018). The subduction of the different segments of the Tethys and subsequent slab rollback, in an overall slow convergent setting with Africa, generated different back-arc basins (e.g., Aegean Basin, Tyrrhenian Basin, Alboran Basin, Algerian Basin) in overriding plates leading to the formation of highly extended continental crust or new ocean floor, and several narrow arcuate orogens (e.g., Hellenic Arc, Calabrian Arc, Betic-Rif Arc) which are characteristic of the Alpine-Mediterranean system (e.g., Faccenna et al., 2014; Royden and Faccenna, 2018; van Hinsbergen et al., 2020).

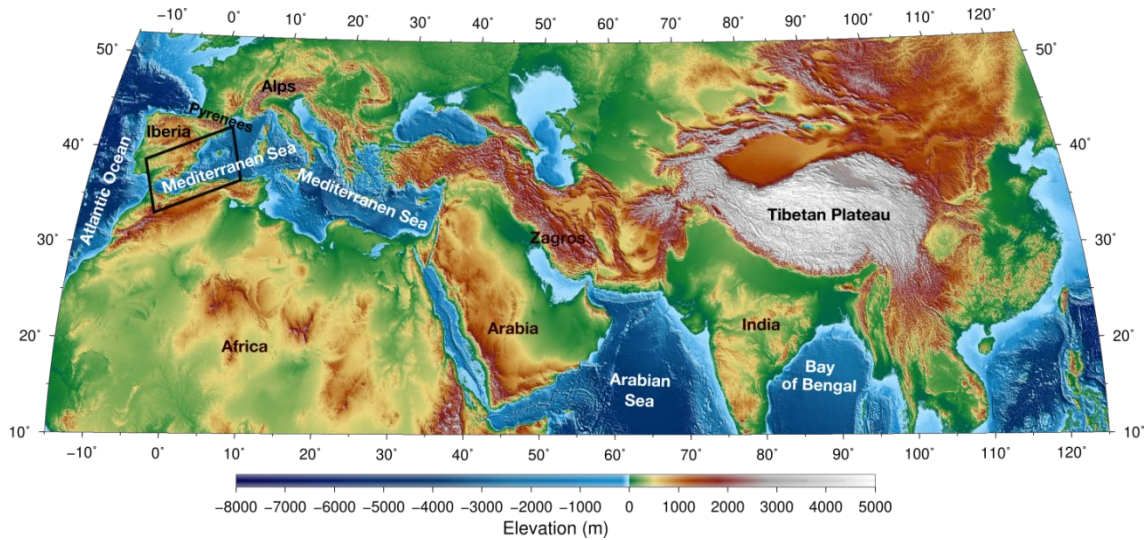


Figure 1.1 Topography map of the Alpine-Himalayan collision zone. The area inside the black box is the focus of this thesis.

The North Balearic Transform Zone is recognized as a major transform fault separating the Liguro-Provençal and the Tyrrhenian realm from the Alboran-Algerian realm (Figure 1.2). The Alboran and Algerian basins lie in the western end of the Alpine-Himalayan collision zone and constitute the Western Mediterranean in between Iberia and Africa (Figure 1.2). The origin of these basins, like other Mediterranean basins, has been attributed to the roll-back of the subducted Ligurian-Tethys lithosphere at the western end of the Tethys Ocean (Faccenna et al., 2004). The Ligurian-Tethys was generated by the propagation of the Central Atlantic ridge during the Early Jurassic in between Africa, Iberia and Adria, and was composed of several transtensive and highly extended continental segments transitioning to oceanic lithosphere to the east (Schettino and Turco, 2011; Stampfli and Borel, 2002). Trans-tension ceased in the Early Cretaceous as the mid-Atlantic ridge propagated northwards along the Newfoundland-Iberia margin and triggered the eastward motion of the Iberia plate together with the African plate (Nirrengarten et al., 2018). The protracted N-NNW displacement of Africa relative to Eurasia, varying from several millimetres per year across the Western Mediterranean to approximately 10 mm/yr across the eastern Mediterranean (e.g., Dewey et al. 1989, McClusky et al. 2003), since the Late Cretaceous is accommodated by the consumption of the highly segmented Ligurian-Tethys, a significant intra-plate deformation in the Iberian plate and the formation of the Pyrenees in the northern Iberian margin (Vergés and Fernández 2006; Macchiavelli et al., 2017). Subduction of the highly segmented Ligurian-Tethys and subsequent extension from the slab roll-back in an overall slow

convergence setting produced the Alboran and Algerian basins, and the consequent collision with the passive margins producing the Betic-Rif orogen in south Iberia and the Tell-Kabylies orogen in north Algeria (Figure 1.2).

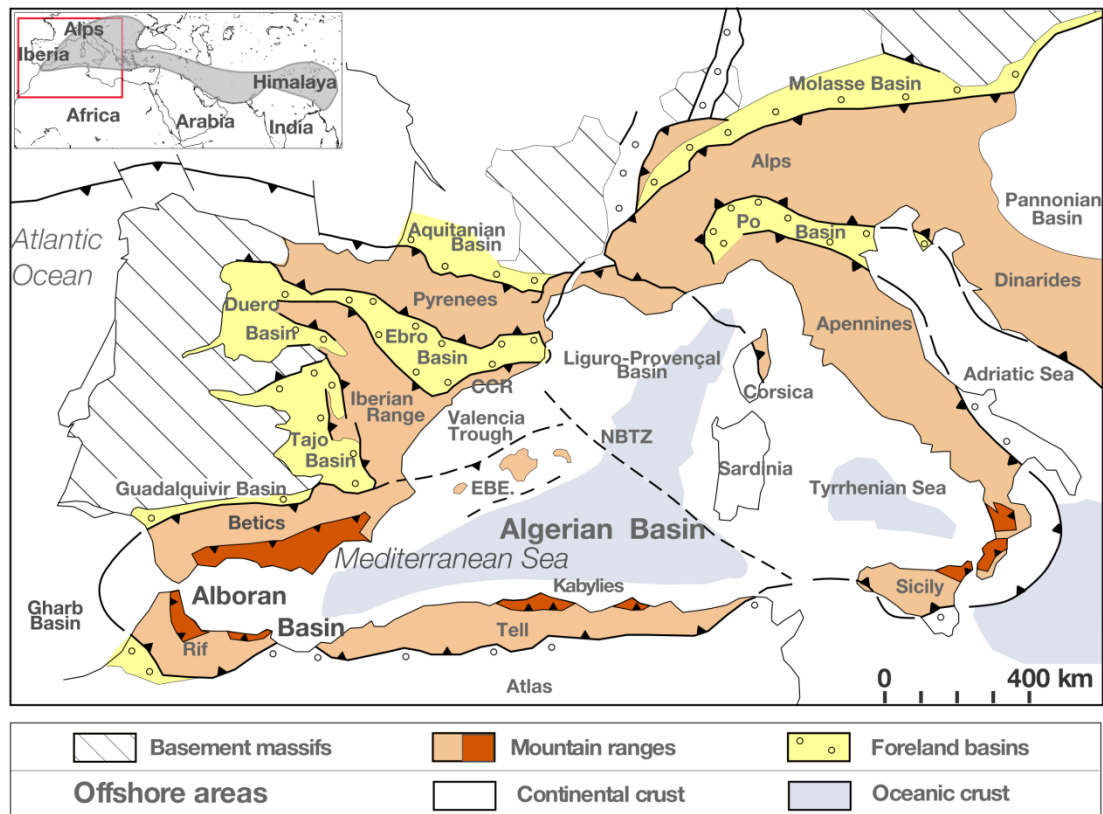


Figure 1.2 Geological map of the Western Mediterranean showing the main orogenic belts and basins (Modified from Vergés and Sàbat, 1999). NBTZ, North Balearic Transform Zone; EB, Emile-Baudot Escarpment.

Exhumation of high-pressure and low-temperature (HP/LT) metamorphic rocks is a typical process of roll-back subduction systems (e.g., Agard et al., 2018). Such metamorphic rocks, referred to as Internal Units in the literature, are found in the Betics-Rif orogen in the southern margin of Iberia and along the northern margin of Africa in Algeria (Figure 1.3). The Betic-Rif orogenic system consists of a typical subduction-related fold and thrust belt, which from the External to Internal Units is formed by the Guadalquivir and Rharb flexural foreland basins, the External Betics, the Flysch units, the Internal Betics, and the extensional back-arc Alboran Basin (see the structural style of these units in Michard et al., 2002; Vergés and Fernández, 2012). The HP/LT metamorphic rocks of the Betics Internal Units from bottom to top are the Nevado-Filabride, the Alpujarride and the Malaguide (Figure 1.3). The Rif fold and

thrust belt shows a similar tectonic architecture except for its N-S direction and for the lack of the equivalent Nevado-Filabride unit. The northern margin of Algeria shows similar characteristics but opposite spatial association compared to the Betic-Rif orogen (Figure 1.3). The main tectonic units, from the Internal to External units, are the extensional back-arc Algerian Basin, the HP/LT rocks in the Kabylies in the Internal Units followed by the thrusting of the Flysch Units over the External Units, and farther to the SSE, the fold and thrust belt in the Tell-Atlas Mountains (see the structural style in Khomsi et al., 2019).

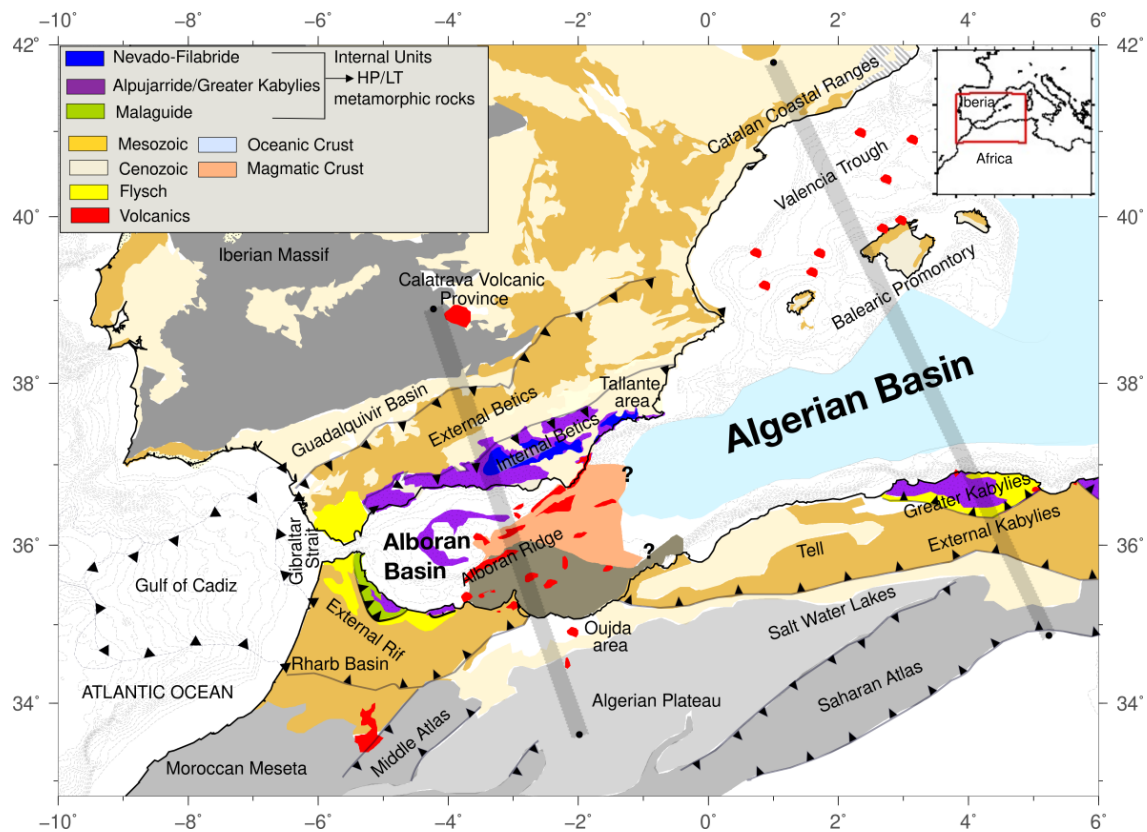


Figure 1.3 Detailed geological map of the Western Mediterranean showing main geologic units in the Alboran and Algerian basins, and the Betics-Rif and Kabylies-Tell-Atlas Mountains. Locations of the two geo-transects modelled in this thesis are shown by grey shadowed strips.

The basement in the Alboran Basin changes from the west to the east (Figure 1.3). The Western Alboran basin is floored by thin continental crust, including the HP Alpujarride metamorphic basement units (Soto and Platt, 1999), and numerous volcanic intrusions (Gómez de la Peña et al., 2018), whereas the Eastern Alboran basin is mostly floored by magmatic crust (Booth-Rea et al., 2007). South of the Alboran Ridge, situated in the middle of the Alboran Basin, the basin is floored by an

African continental crust with magmatic intrusions (Gómez de la Peña et al., 2018). The magmatic crustal domain of the Eastern Alboran basin transitions eastward to the oceanic crust of the Algerian Basin (Booth-Rea et al., 2007; Pascal et al., 1993). The Valencia Trough, situated NW of the Algerian Basin, in between the Catalan Coastal Ranges and the Balearic Promontory, has a very thin continental basement (Torné et al., 1992; Pascal et al., 1992), which experienced a huge extension during Mesozoic (Roca, 2001; Etheve et al., 2018). The trough underwent compression in late Paleogene during the convergence between Africa and Iberia, and renewed extension from Late Oligocene to Langhian period (Morgan and Fernández, 1992; Fernández et al., 1995; Roca, 1996; Torné et al., 1996; Sàbat et al., 1997; Gaspar-Escribano et al., 2004). The basement of the Balearic Promontory is continental, similar to the Iberian basement beneath the Catalan Coastal Ranges (Torné et al., 1992; Pascal et al., 1992; Vidal et al. 1998).

Volcanism in the Western Mediterranean has been a focus of numerous studies (Melchiorre et al., 2017; Lustrino et al., 2011; Lustrino and Wilson, 2007; Duggen et al., 2005, 2008; Martí et al., 1992). In the Alboran Basin volcanism is mainly orogenic with wide geochemical variation (Lustrino et al., 2011) showing tholeiitic Miocene affinity in the centre surrounded by calc-alkaline volcanism (Duggen et al., 2008). The southern Iberian (e.g., Tallante area) and north-western African (e.g., Oujda area) continental margins show Lower Pliocene to Upper Miocene Si-K-rich (i.e., orogenic) and Upper Miocene to Pleistocene Si-poor (i.e., anorogenic or intra-plate volcanism) magmatism (Duggen et al., 2005). The northern coast of Algeria, along the Algerian basin, experienced K-rich (and minor medium-K) calc-alkaline volcanic activity (i.e., orogenic) along a ~450 km long E-W trending zone during Miocene (17 to 11 Ma) (Maury et al., 2000; Fourcade et al., 2001; Laouar et al., 2005). The younger anorogenic volcanism (alkaline) is observed in the eastern and western end of the Tell Mountains (Coulon et al. 2002; Maury et al., 2000; Wilson and Bianchini, 1999). The Valencia Trough experienced calc-alkaline volcanism (i.e., orogenic) in the Early-Middle Miocene and alkaline volcanic activity (i.e., anorogenic) from Middle Miocene to Recent (Martí et al., 1992).

The upper mantle structure in the Western Mediterranean has been studied by various global, regional and local seismic tomography studies. A high-velocity anomaly around the Alboran Basin (Figure 1.4a) has been reported in global to local seismic tomography models (Palomeras et al., 2017; Villaseñor et al., 2015; Bezada et al., 2013; Spakman and Wortel, 2004). This anomaly shows an arcuate shape and lies in the mantle roughly beneath the Betics-Rif Mountains and is interpreted as a subducted

slab from the Ligurian-Tethys (i.e., Alboran slab). Imaging the mantle in the northern margin of Africa is limited by the absence of passive seismic data and hence, by intermediate to poor resolution in the standard travel-time seismic tomography models. Recently, Fichtner and Villaseñor (2015), using state of the art full-waveform inversion seismic tomography reported high-velocity anomalies beneath the North-Africa margin (Figure 1.4b). Full waveform tomography leverages the station coverage by using earthquake source and recording station in pairs and utilizing the complete recorded waveform instead of a part of the seismic waveform. These high-velocity anomalies are also interpreted as the subducted slabs from the Ligurian-Tethys and are detached from the African lithosphere.

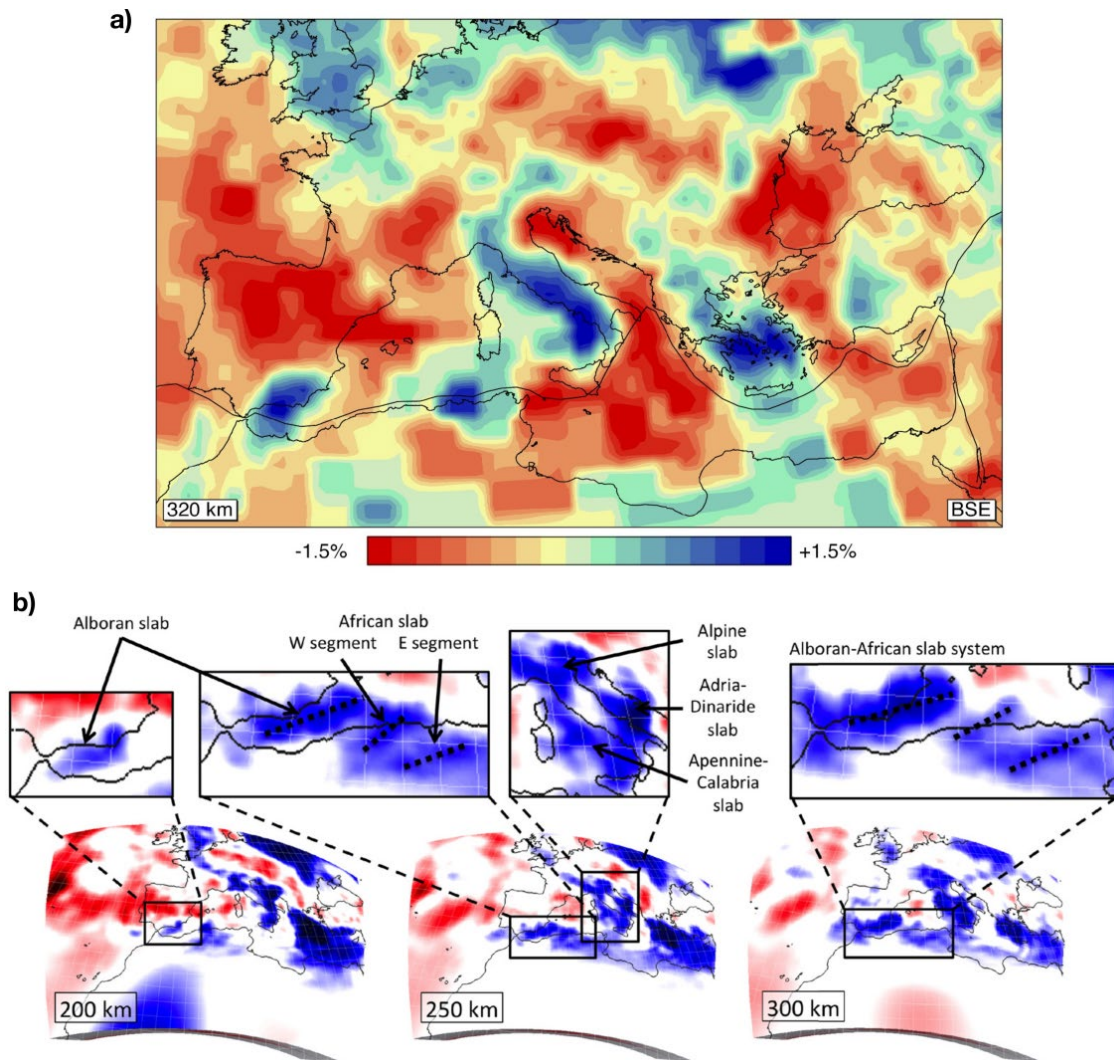


Figure 1.4 Upper mantle seismic tomography models in the Alboran and Algerian basins.(a) P-wave travel time tomography model slice at 320 km depth (Villaseñor et al.,2013) and (b) Full-waveform inversion seismic tomography model at different depths (Fichtner and Villaseñor, 2015).

While the Cenozoic evolution of the Liguro-Provençal, Tyrrhenian, and Aegean back-arc basins are well understood (Faccenna et al., 2004), the evolution of the Alboran and Algerian basins in the Western Mediterranean is still debated (Casciello et al., 2015; Faccenna et al., 2004; Jolivet et al., 2009; Spakman and Wortel, 2004; van Hinsbergen et al., 2014; Vergés and Fernández 2012). The opening of both basins for the last 35 My, is being explained by three different geodynamic scenarios, each based on slab roll-back as the driving mechanism (Figure 1.5). There is consensus that the Algerian Basin is an oceanic basin opened in the upper plate during the NW-dipping Tethys slab retreat, in agreement with the SSE-polarity of the Kabylies-Tell-Atlas orogenic system; however no agreement has been reached so far on the origin and evolution of the Alboran Basin and related Betic-Rif orogenic system. Main disagreements are on the original disposition of the tectono-sedimentary domains involved in the Betic-Rif subduction-related orogenic system and on the geodynamic interpretation used to build-up this orogenic system. The pros and cons of the three scenarios are discussed in detail by Chertova et al. (2014) using numerical modelling and concluding that both Scenario 1 and Scenario 3 are plausible despite the authors favour Scenario 1.

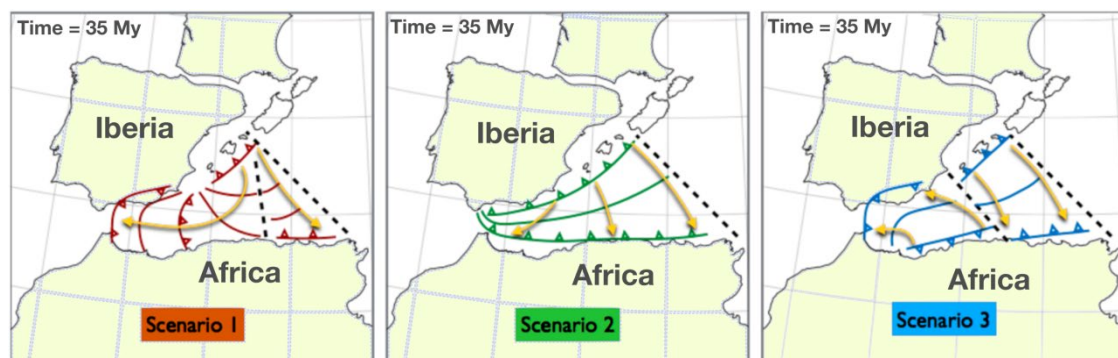


Figure 1.5 Models purposed for the geodynamic evolution of the Western Mediterranean. Scenario 1 after Van Hinsbergen et al. (2014) involves a single short subduction zone initially dipping to NW starting near the Balearic Promontory and then retreats to the SE before it separates into two different segment. One of the segments continue retreating to SE before it collides with North Africa and other continue retreating to the west and collides with Iberia resulting in 180° clock-wise rotation. Scenario 2 involves a long initial subduction dipping to the N-NW along the entire Gibraltar-Balearic Promontory margin (e.g., Gueguen et al., 1998; Faccenna et al., 2004; Jolivet et al., 2009). Scenario 3 after Vergés and Fernández (2012) involves two separate subduction segments with opposite subduction direction for the Alboran (subduction dipping to the SE and retreating to the NW) and Algerian (subduction dipping to the NW and retreating to the SE) basins. Direction of rollback is shown by the yellow arrows. Black dashed lines represent the proposed transform faults separating the different subduction segments (Figure modified after Chertova et al., 2014).

Presence of subduction in the Western Mediterranean during the Cenozoic is evident from the geological and geophysical observations (previous paragraphs). Although purposed models differ in the paleo-geographic setting of subduction, they all have subduction processes common to them (e.g., slab rollback, back-arc extension, slab tear). Irrespective of the model applicable to the Western Mediterranean, the subduction process must have left imprints on the present-day crust and mantle structure. A typical subduction system involves compression and the orogenic volcanism near the arc. In settings dominated by slab rollback, the upper plate undergoes extension and thins, producing anorogenic volcanism by mantle decompression. Sufficient decompressional melting can produce a new oceanic lithosphere as is observed in the Western Mediterranean basins (e.g., Algerian and Tyrrhenian basins). During the final stages of slab roll-back subduction system, collision with the continental lithosphere leads to the stacking and exhumation of the metamorphic slices of the subducted thinned continental crust of the former extended margins (Brun and Faccenna, 2008). Involvement of the passive margin also introduces mechanical weakness and the dense slabs can break-off/tear/detach (Fernández-García et al., 2019). Hence, the compression near the subduction front and extension in the back-arc must have affected the present-day lithospheric thickness. Further, the chemical composition of the lithospheric mantle must also be affected. Therefore, precise knowledge of the present-day lithospheric structure and chemical composition of the upper mantle are crucial constraints to decipher the geodynamic evolution of the Western Mediterranean.

The characterization of the present-day physical state (pressure, temperature, density, i.e. chemical composition, and seismic velocities) of the lithosphere and sublithospheric upper mantle and its architecture are fundamental for understanding their evolution through geological time scale and is a primary goal of modern geophysics (Afonso et al., 2016a; Hoggard et al., 2020). In this context a great deal of information comes from modelling, standalone or in pairs, of surface observables sensitive to temperature (surface heat flow), density (gravity, geoid, elevation), seismic velocities (passive and active seismic data), and chemical composition derived from mantle xenocrysts and xenoliths (e.g., Lachenbruch and Morgan, 1990; Griffin et al., 1999; Deen et al., 2006; Goes et al., 2000; Ritzwoller et al., 2004; Zeyen et al., 2005; Priestley and McKenzie, 2006; Fullea et al., 2007). However, significant discrepancies in the predictions from these methods are rather common in the literature (Afonso et al., 2008 and references therein)

Integrated geophysical-petrological modelling of these observables (i.e., elevation, gravity anomalies, geoid height, surface heat-flow, seismic velocities, mantle xenoliths and xenocrysts data) is a particular approach that allows exploring and reconciling observations from different datasets and methods. In particular, LitMod2D_1.0 (Afonso et al., 2008) is a tool developed to study the thermal, compositional, density, and seismological structure of the crust and the lithospheric and sublithospheric mantle by combining information from petrology, mineral physics, and geophysical observables within a self-consistent thermodynamic framework. As such, this approach is well suited to i) handle the intrinsic non-uniqueness problem associated with the modelling of single observables and ii) distinguish thermal from compositional effects in geophysical signatures.

LitMod2D_1.0 has been successfully applied in various tectonic settings including continental margins (e.g., Fernández et al., 2010; Pedreira et al., 2015) and continental collision regions (e.g., Carballo et al., 2015a; Tunini et al., 2015). It allows considering different chemical compositional domains within the lithospheric mantle, but assumes a homogeneous sublithospheric mantle with a theoretically determined primitive upper mantle (PUM) chemical composition (McDonough and Sun, 1995). The latter assumption limits the use of LitMod2D_1.0 to regions affected by mantle upwelling, subduction, and/or delamination (e.g., Western Mediterranean). These regions are often characterized by changes in temperature and/or chemical composition in the sublithospheric mantle, as suggested by tomography models and are imaged in terms of seismic velocities variation (e.g., Koulakov et al., 2016; Cammarano et al., 2009). Seismic tomography models usually report positive and negative velocity anomalies with respect to global average reference seismic velocity models (e.g., ak135) in the mantle and are qualitatively interpreted. Positive seismic velocity anomalies are commonly interpreted, as in the case of the Western Mediterranean, as colder than average subducted slabs. The prompt question one could ask is: how much cold are these slabs with respect to the ambient mantle? And further to be comprehensive: what is the chemical composition of these slabs? For such a quantitative interpretation, one needs to decouple the temperature and chemical composition signal from the observed seismic velocities, which is not a straightforward task (Cammarano et al., 2009). Challenges in doing so come from the highly non-linear nature of the problem, computation of the temperature field in regions with subducted slabs, and temperature-pressure dependent anelastic attenuation correction of mineral physics derived anharmonic seismic velocities in the mantle.

1.1. Objectives

The generic objective of this thesis is twofold:

- To develop a methodology to decipher temperature and chemical composition of upper mantle anomalies observed in seismic tomography models.
- Using the developed methodology to model the present-day crust to upper mantle (~400 km) structure across the Alboran and Algerian basins in the Western Mediterranean and to interpret the results in terms of the geodynamic evolution of the region.

Hence, this thesis is divided into two main parts (Figure 1.6). In the first part, the LitMod2D_1.0 software package (Afonso et al., 2008) has been improved to incorporate sublithospheric mantle anomalies in the modelling along with other improvements into a new LitMod2D_2.0 version. The specific objectives of this part are:

- Use of a depleted chemical composition of the sublithospheric mantle determined from geochemical data as opposed to the theoretical primitive upper mantle (PUM; McDonough and Sun, 1995) used in LitMod2D_1.0.
- Incorporation of anelasticity calculations in the GENERATOR module to allow the conversion of seismic velocities to temperature anomalies and vice versa using the latest experimentally determined anelastic attenuation parameters on the anharmonic seismic velocities calculated from stable mineral assemblages.
- Defining a reference chemical compositional model of the upper mantle to compare the seismic velocity anomalies obtained in LitMod2D_2.0 with seismic tomography models.
- Development of a new open-source graphic user interface (GUI) with improved functionalities to facilitate its updating and cross-platform use.
- To simplify the input and output data in the LitMod2D_2.0 to facilitate the use of a central post-processing tool-box. The post-processing tool-box will help the users to use provided codes/scripts according to specific modelling needs.

In the second part of the thesis, the new LitMod2D_2.0 package is employed to model the present-day crust to upper mantle (~400 km) scale temperature, density and seismic velocity structure along two NNW-SSE oriented cross-sections (from now on

referred as geo-transects) across the Alboran and Algerian basins and the respective Iberian and African margins (Figure 1.3). Orientation and location of the geo-transects are chosen based on: i) the regional vergence of the major tectonic units (Figure 1.3), ii) available recent geophysical data (e.g., seismic tomography, active seismic lines and geological cross-sections), and iii) the different tectonic style, crustal nature, and lithospheric geometry of both basins. These two geo-transects are also chosen to see the possible opposite symmetry in the crust and upper mantle structure related to the opposite subduction polarity proposed for the geodynamic evolution of the Alboran and Algerian basins (Scenario 3, Figure 1.5; Vergés and Fernández, 2012). The specific objectives of this part are:

- To develop a detailed crustal cross-section along the geo-transects incorporating surface geology, geological data, seismic tomography and active seismic lines.
- To identify different lithospheric mantle domains along the geo-transects based on surface geology and mantle xenoliths. In regions dominated by extensive magmatism the mantle chemical composition must be compatible with melting models.
- To determine the composition and temperature of the subducted slabs inferred from the seismic tomography models, and their control on the elevation.
- Finally, to compare the obtained results along the geo-transects and to discuss their tectonic significance in terms of the geodynamic evolution of the Western Mediterranean.

1.2. Thesis outline

This thesis is divided into six chapters which are organised as follows:

Chapter 2 focuses on basic concepts. The general definition of the lithosphere and sublithosphere are described. Mathematical formulation of the physical properties (i.e., density, seismic velocities and thermal conductivity) and how they are sensitive to the surface observables (e.g., the gravitational field of the Earth, surface heat-flow, and elevation) are described.

Chapter 3 is dedicated to methodological improvements to the previous LitMod2D_1.0 version incorporated into a new LitMod2D_2.0 version. In this chapter, I present the numerical implementation of the new improvements, which are directed to provide a modelling tool for the scientific community to be used in regions affected by

geodynamic processes that can affect temperature and chemical composition in the sublithospheric mantle. The dependence of relevant physical properties of the upper mantle (i.e., seismic velocities and density) on the temperature and chemical composition is analyzed through synthetic models. The new graphic user interface (GUI) is used to perform synthetic model of a subduction zone to demonstrate full capability of LitMod2D_2.0. Post-processing tool-box is used to calculate synthetic receiver functions and surface-wave dispersion curves using the seismic velocities from the synthetic subduction zone model, and the stable minerals in the mantle.

The results presented in Chapter 3 are published in the scientific journal *Geochemistry, Geophysics, Geosystems* (American Geophysical Union):

Kumar, A., Fernández, M., Jiménez-Munt, I., Torne, M., Vergés, J., & Afonso, J. C. (2020). *LitMod2D_2.0: An improved integrated geophysical-petrological modelling tool for the physical interpretation of upper mantle anomalies*. *Geochemistry, Geophysics, Geosystems*, 21, <https://doi.org/10.1029/2019GC008777>.

A version of the LitMod2D_2.0 has been used in a collaborative study along a geo-transect running from South Iberia to North Africa crossing the western Gibraltar Arc and published in the scientific journal:

Jiménez-Munt, I., Torne, M., Fernández, M., Vergés, J., Kumar, A., Carballo, A., & García-Castellanos, D. (2019). *Deep seated density anomalies across the Iberia-Africa plate boundary and its topographic response*. *Journal of Geophysical Research: Solid Earth*, 124, <https://doi.org/10.1029/2019JB018445>.

Chapter 4 presents the results of the present-day structure along two selected geo-transects in the Alboran and Algerian basins. Previously published geological cross-sections, active seismic lines, Moho depths active and passive seismic data and surface geology along the geo-transects are used to constrain crustal-scale cross-sections. The lithospheric mantle is incorporated to the model based on published LAB depths, and chemical compositional domains are added based on available mantle xenoliths and surface geology data. Predictions of the surface observables from the lithospheric scale models are compared with the observed data, and finally, sublithospheric mantle anomalies observed in seismic tomography are added to the model. A range of possible chemical compositions of the subducted slabs are tested in order to fit the surface observables. Computed seismic velocities are also compared with the available passive seismological data.

A manuscript showing the results presented in Chapter 4 is in preparation to be submitted in a scientific journal.

Chapter 5 presents the general discussion on the new LitMod2D_2.0 software package and its application to model the present-day crust to upper mantle structure in the Western Mediterranean. The discussion on LitMod2D_2.0 is focused on the assumptions made and the potential future developments. The obtained results along the two modelled geo-transects are compared and discussed in terms of their tectonic significance.

Finally, Chapter 6 presents the final conclusions of this thesis.

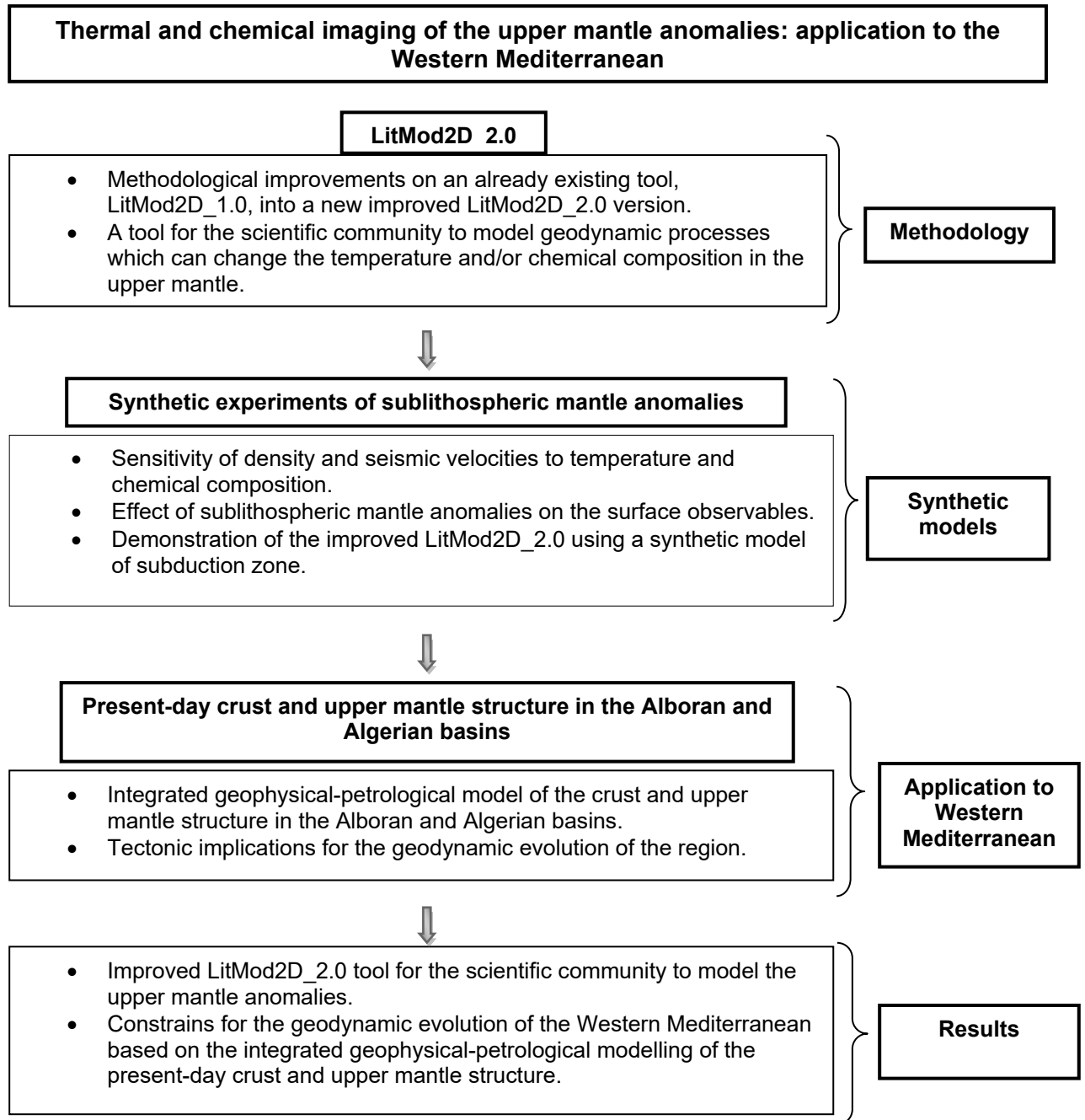


Figure 1.6 Flow chart showing the work-flow and the steps followed to achieve the objectives of this thesis.

CHAPTER 2

Fundamentals

“If you want to find the secrets of the universe, think in terms of energy, frequency and vibration”

-Nikola Tesla

Chapter 2

Fundamentals

This thesis is based on integrating the surface observables (i.e., gravity anomaly, geoid height, and surface heat flow, elevation, and mantle xenoliths and xenocrysts) and the physical properties sensitive to them (i.e., temperature, density, and seismic velocities) in a self-consistent thermodynamic manner to model the thermal, chemical and physical architecture of the lithosphere and upper mantle. Hence, it is necessary to state the basic principles and definitions adopted and the physical laws used in this thesis. In this chapter, I describe the basic definitions of the lithosphere, sublithosphere, surface observables (i.e., data) and their dependence on the physical properties.

2.1. Lithosphere

The lithosphere is the long-term rigid outer shell of the Earth and it is subdivided into tectonic plates, fundamental units of plate tectonics. However, depending on the timescale of applied stresses and the amount of strain rate, rocks in the Earth can show distinct behaviour (elastic, viscous, plastic). The lithosphere is a chemical, mechanical, and thermal boundary layer that overtops a hotter and rheological weak material. Chemically, the lithosphere is divided into the crust (usually silica rich) and the uppermost mantle (lithospheric mantle) where the conductive mode of heat transfer prevails.

The crust is the outermost layer of the Earth consisting mainly of sediments, granite, gneisses, granodiorite, gabbro, amphibolite, granulite and volcanic material for the continental crust, and of sediments, basalts, gabbros and some serpentinites for the oceanic crust. From a chemical point of view five oxides: SiO_2 , Al_2O_3 , FeO , MgO , CaO , and Na_2O dominate in the crust (Table 2.1). The continental crust contains higher silica and aluminium than the basaltic oceanic crust, hence is less dense than basalt. The Mohorovičić discontinuity (Moho) separates the crust from the relatively ductile mantle and represents a major chemical discontinuity from felsic crust to mafic upper mantle resulting in a major seismic velocity and density contrast. This major velocity contrast is imaged using earthquake waveforms or active seismic sources to map the depth of this discontinuity. The continental crust is usually divided

into three layers: an upper crust with densities between 2650 kg/m³ and 2710 kg/m³, a middle crust with densities from 2710 kg/m³ to 2860 kg/m³, and a lower crust ranging from 2860 kg/m³ to 2960 kg/m³ (Christensen and Mooney, 1995). The oceanic crust is composed by a gabbroic layer, overlain by basaltic pillow lavas and sheeted dykes. A low velocity and density sedimentary layer is usually present in the crust regardless of continental or oceanic showing a wide variety of density values (2000-2650 kg/m³).

Table 2.1 Major oxide compositions (weight %) of the crust.

Name	SiO ₂	Al ₂ O ₃	FeO	MgO	CaO	Na ₂ O
Continental upper crust ^a	66.60	15.40	5.00	2.50	3.59	3.27
Continental middle crust ^a	63.50	15.00	6.02	3.60	5.25	3.39
Continental lower crust ^a	53.40	16.90	8.57	7.20	9.59	2.65
Oceanic upper crust ^b	48.99	14.89	9.86	7.56	11.26	2.70
Oceanic lower crust ^c	52.58	13.83	6.74	12.48	10.52	1.20

^a Rudnick and Gao (2003); ^b Schilling et al. (1983); ^c Behn and Kelemen (2003)

The lithospheric mantle is a chemically distinct layer spanning from the Moho to the top of the asthenosphere. The base of the lithospheric mantle is also denoted as the lithosphere-asthenosphere boundary (LAB) whose depth and physical characteristics depend on the way it is observed. The seismological lithosphere is defined as the high velocity lid that overlies the upper mantle Low Velocity Zone (LVZ), although this definition is more appropriate for oceanic rather than for continental lithospheres (Anderson, 1989; Carlson et al., 2005). Thermally, the lithosphere is defined as the thermal boundary layer in which the heat transfer by conduction predominates over convective processes. The base of the lithospheric mantle or LAB is commonly defined as a particular isotherm (usually 1200 °C - 1350 °C) determined by the intersection between a conductive geotherm and a mantle adiabat (Schubert et al., 2001). From a geochemical point of view the LAB would be the maximum depth from which low-Y (< 10 ppm) garnets, characteristic of depleted lithosphere, are derived (Griffin et al., 1999). This definition matches pretty well with the thermal definition of the LAB being at the 1200 °C - 1300 °C isotherm. The mechanical lithosphere can be defined as a layer not affected by the convection beneath it, at geological time scales. The boundary between mechanical lithosphere and convective mantle is typically around 800 °C - 900 °C, based on the deformation of the olivine-rich rocks (Schubert et al., 2001). Hence, the thermal lithosphere includes the mechanical lithosphere. Accordingly, there is an upper layer that takes no active part in

convection, underlain by the lower part of the thermal boundary layer which, under some circumstances, can become unstable and convect. Hence, depending on the considered physical property in observing or modelling the lithosphere its definition can change. In this thesis, LAB is referred to as a thermal and a chemical boundary unless specified otherwise.

2.2. Sublithospheric mantle

The Earth's mantle beneath the LAB spans until the core-mantle boundary, which is roughly at ~2900 km. The mantle is further divided into upper and lower mantle separated by the mantle transition zone (MTZ). The MTZ starts at 410 km, which is marked by the exothermic phase transition of olivine to its high-pressure polymorph, wadsleyite. The bottom of the MTZ lies at 660 km depth involving the endothermic phase transition of wadsleyite to its high-pressure polymorph called ringwoodite. The thickness and depth of the mantle transition zone can vary locally since it is defined by endothermic and exothermic phase transition (e.g., if a cold subducting slab penetrates the MTZ its thickness increases whereas if a hot plume rises through MTZ its thickness decreases). In this thesis, I only focus up to the upper mantle (400 km depth) and refer to it as sublithospheric mantle (i.e., asthenosphere). Hence, the base of the sublithospheric mantle is fixed at 400 km depth, and the temperature at this depth is taken to be 1520 °C (Afonso et al., 2008) which is consistent with the experiments at high-pressure and high-temperature on phase equilibria of olivine-wadsleyite (Ito and Katsura, 1989; Katsura et al., 2004) giving a temperature of $1487 \pm 45^\circ\text{C}$ at the 410km discontinuity.

The sublithospheric mantle is the hotter layer beneath the LAB in which convection prevails, implying a more ductile behaviour than the lithosphere at geologic time scale. Heat transport in the sublithospheric mantle is carried out by convection and is parameterized with an adiabatic thermal gradient.

Chemically, the sublithospheric mantle is homogenous but distinct than the lithospheric mantle. One basis on which composition in the mantle is compared is the fertility, which simply means enrichment in compatible elements concentration and depletion in incompatible elements. The compatible/incompatible nature of elements depends on the bulk distribution coefficient during solid to liquid phase transition called chemical differentiation. The bulk distribution coefficient is the ratio of the element concentration in the solid phase over the liquid phase. In Figure 2.1, it can be seen that MgO is highly compatible and Al_2O_3 , CaO, and Na_2O are incompatible whereas

FeO and SiO₂ are slightly incompatible. The sublithospheric mantle is a chemical reservoir source to Mid-Oceanic-Ridge-Basalts (MORB) since the onset of plate-tectonics and is depleted in incompatible elements (i.e., Ca, Al, Fe) and enriched in compatible elements (Mg) and hence, is more fertile than the lithospheric mantle.

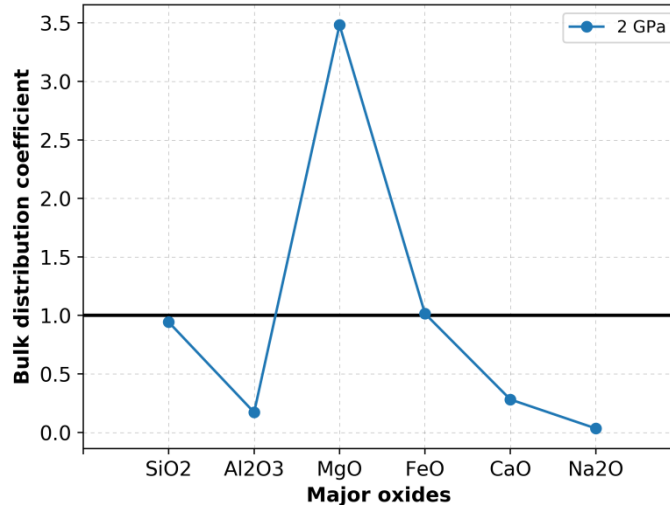


Figure 2.1 Bulk distribution coefficients of major oxides during melting at the mid-oceanic-ridge calculated using empirical relations from Niu (1997). A black horizontal line with bulk distribution coefficient of 1 separates compatible elements above it from the incompatible elements below it.

2.3. Gravitational field

The Earth's gravitational field is a direct manifestation of the density distribution in the Earth's interior and hence, complements other geophysical observables (i.e., elevation and passive and active seismic data). The real equipotential surface of the Earth, called geoid, follows the mean sea level in the oceanic areas and referenced sea level surface over the continents. As a good approximation, the geoid can be described by an equipotential revolution ellipsoid and is called the normal or theoretical field, or the reference geoid.

Mathematically, the gravity potential of the Earth can be adequately described using a global geopotential model, i.e., a spherical harmonic expansion, to degree and order N , plus a centrifugal term:

$$W(r, \phi, \lambda) = \frac{GM_T}{r} \left(\sum_{n=2}^N \left(\frac{a}{r} \right)^n \sum_{m=0}^n [\overline{C_{nm}} \cos(m\lambda) + \overline{S_{nm}} \sin(m\lambda)] \overline{P_{nm}}(\sin \phi) \right) + \frac{1}{2} \omega^2 (x^2 + y^2) \quad (2.1)$$

where G is the universal gravitational constant ($6.674 \times 10^{-11} \text{ m}^3/\text{kg.s}^2$), M_T the total mass of the Earth, r , ϕ , λ , x and y the geocentric coordinates of the observation point, $\overline{C_{nm}}$, $\overline{S_{nm}}$ a set of fully normalized coefficients, $\overline{P_{nm}}$ the fully normalized associated Legendre functions, and ω is the angular rotation velocity of the Earth.

The actual gravity potential of the Earth, W , can be written as sum of the potential from the reference ellipsoid, U , and the difference between W and U called anomalous potential:

$$W = U + T \quad (2.2)$$

Such partition of the Earth's gravity field simplifies the mathematical formulation of the normal potential (U) as the ellipsoidal field and its deviation with respect to the real field. Both, the gravity (free air and Bouguer) and the geoid anomalies, are referred to the normal field produced by the reference ellipsoid.

2.3.1. Gravity anomaly

The gravity anomaly (δg) is the difference between the measured gravity over or reduced to the geoid, g , and the normal (theoretical) gravity at a point projected along a normal to the reference ellipsoid from the measurement point, λ . Both, the measured and the normal gravity, can be derived from the Earth and ellipsoidal potentials:

$$g = \nabla W \quad (2.3)$$

$$\lambda = \nabla U \quad (2.4)$$

Since gravity anomaly follows the inverse square law, it is mainly sensitive to lateral density variations at crustal depths. Measured gravity data contain the effects of latitude, Earth tides, instrumental drift, distance from the reference ellipsoid and masses between the actual topography and the reference ellipsoid. Hence, in order to obtain anomalies comparable over large areas, corrections must be applied for the above mentioned effects. Corrections for Earth tides, instrumental drift, latitude, and free air to the measured gravity gives us the free air gravity anomaly (Δg_{FA}), which at short wavelengths correlates strongly with topography. The free air correction takes into account whether the measuring point is above or below the reference ellipsoid, considering the vertical gravity gradient. Once the correction for the topography masses are applied to the free-air gravity anomaly, called terrain correction, the Bouguer anomaly (Δg_B) is obtained. The primary objective of the complete Bouguer

correction is to remove all non-geological components of the gravity anomalies enhancing subsurface mass variations by correcting for the gravitational attraction of topography to the free-air anomaly. Hence, Bouguer anomaly correlates mainly with lateral variations of the density and thickness of the crust.

2.3.2. Geoid anomaly

The geoid is the equipotential surface of the Earth and coincides with the average sea level and contains, ideally, all the mass of the Earth. However, this is not a rigorous definition, since the average sea level is not completely equipotential (dynamic ocean processes) and, in addition, onshore topographical masses can lie above the geoid. The geoid anomaly is then the distance between the geoid surface and the reference ellipsoid model. The geoid anomaly, N , and the anomalous potential, T , in equation 2.2, are related by the Brun's formula:

$$N = \frac{T}{\gamma} \quad (2.5)$$

where γ is the normal gravity field. In equation 2.5 it is assumed that the potential of the geoid and the reference ellipsoid are equal. In addition, the geoid anomaly, the gravity anomaly and the anomalous potential are related by the fundamental equation of the physical geodesy (Heiskanen and Moritz, 1967):

$$\nabla g = -\frac{\partial T}{\partial E} + N \frac{\partial \gamma}{\partial E} \quad (2.6)$$

where E is the elevation or orthometric height along the plumb line (positive upwards, negative towards the Earth's interior). Although equation 2.6 has the form of a partial differential equation, it must be considered as a boundary condition, as the gravity anomaly, i , is only known over a surface (the geoid). If we assume that the mass distribution outside the geoid is null, T becomes a harmonic function and:

$$\nabla^2 T = 0 \quad (2.7)$$

Equation 2.7, in conjunction with the boundary condition expressed by equation 2.6, is a genuine partial differential equation. The knowledge of the anomalous potential using gravity measurements (Equations 2.6 and 2.7) allows us to determine the geoid anomaly through equation 2.5. The spherical approximation considers the reference ellipsoid as a sphere and it is interesting for practical purposes. In the spherical approximation, equation 2.6 has the following form:

$$\nabla g + \frac{\partial T}{\partial r} + 2 \frac{T}{R_T} = 0 \quad (2.8)$$

where r is the radial distance and R_T is the radius of the Earth. Offshore, geoid variations can be determined straightforward via satellite altimetry. Onshore, the geoid anomaly must be determined by indirect methods. The Stokes formula gives us the geoid anomaly as a function of the gravity anomalies in the spherical approximation:

$$N = \frac{R_T}{4\pi g_0} \iint \nabla g S(\psi) d\sigma \quad (2.9)$$

where ψ is the spherical distance between the calculation point and the mass distribution, g_0 is an average value of the gravity attraction over the surface of the Earth, $d\sigma$ is the differential element of surface, and $S(\psi)$ is the Stokes function, defined as:

$$S(\psi) = \frac{1}{\sin\left(\frac{\psi}{2}\right)} - 6 \sin\left(\frac{\psi}{2}\right) + 1 - 5 \cos(\psi) - 3 \cos(\psi) L \left[\sin\left(\frac{\psi}{2}\right) + \sin^2\left(\frac{\psi}{2}\right) \right] \quad (2.10)$$

The surface integral of equation 2.9 spans the whole surface of the Earth, and assumes the following assumptions:

- The mass within the reference ellipsoid is equal to the mass of the Earth.
- The potential of the geoid and the reference ellipsoid are equal.
- The centre of the reference ellipsoid is coincident with the centre of the Earth.
- There are no masses outside the geoid (equation 2.7).
- Spherical approximation.

The assumption that no masses lie outside the geoid is not valid over the continents, since the geoid surface is located beneath the topography. In such cases, topography outside the geoid must be removed by some procedure (e.g., Helmert condensation) taking into account the indirect effect that such procedure introduces in the geoid determination.

Since the geoid anomaly is the difference between two potential surfaces, it depends on the inverse of the distance to density anomalies and is affected by lateral density variations located in a wide range of depths ranging from the core-mantle boundary up to crustal levels. As a general rule of thumb, an excess of mass produces positive geoid anomalies and vice versa. Unfortunately, it is not possible to determine univocally the depth of the density anomaly, i.e., to decompose the potential field of

the Earth into its causative sources (Bowin, 2000). However, global studies show that the geoid anomalies with wavelengths greater than 4000 km are produced by density variations at sublithospheric depths (Bowin, 1983). As consequence, to study the upper mantle structure, we must retain only geoid signal with wavelengths smaller than 4000 km. The relation between the degree, n , and the associated wavelength of the spherical harmonics, λ , is (Strang van Hees, 2000):

$$\lambda = \frac{4\sqrt{\pi}R_T}{n+1} \quad (2.11)$$

According to equation 2.11, for the degree 10 harmonic, the associated wavelength is about 4106 km. Therefore, degrees $n \leq 10$ must be removed in order to keep the more likely “upper mantle” contribution to the geoid anomaly. For a punctual mass, m_p , we can obtain an equation that relates the gravity anomaly and the geoid anomaly in spherical coordinates. The anomalous potential produced by a punctual mass anomaly at a depth z is:

$$T = G \frac{m_p}{z} \quad (2.12)$$

The gravity anomaly produced by the same punctual mass anomaly reads:

$$\Delta g = G \frac{m_p}{z^2} \quad (2.13)$$

Combining equations 2.12 and 2.13 with equation 2.5, the following expression is obtained for the depth at which the punctual mass anomaly is located:

$$z = \frac{N\gamma}{\Delta g} \quad (2.14)$$

According to equation 2.14, a punctual mass anomaly that produces a gravity anomaly of 50 mGal, and a geoid anomaly of 1 m, would be located at a depth of about 20 km.

2.4. Temperature field

Dynamics of the Earth is essentially related with dissipation of the primordial heat (i.e., the heat generated during formation of the Earth) and the heat generated from the decay of radioactive elements. Inside the Earth heat can be transferred in four different ways: advection, convection, conduction, and radiation. The advection heat transfer occurs due to forced motion of mass and, in geological processes, via

erosion/sedimentation, isostatic uplift, magmatic ascent, and tectonic deformation. Convection is a special form of advection in which the motion is related to the grain level boundaries of the material, and is important in fluids and gases. Conduction of heat implies the transmission of the kinetic energy between adjacent atoms in the crystalline lattice or between neighbourhood molecules. Radiation involves the direct transfer of heat by electromagnetic radiation.

Although convection is not applicable to the rigid solids, over geological times the mantle behaves as a very high viscosity fluid and, therefore, slow convection is possible in the mantle. The lithosphere acts as a thermal boundary layer where the primary mode of heat transfer is conductive.

The heat transport inside the Earth can be expressed by the general equation (e.g., Schubert et al., 2001):

$$\rho C_p \frac{dT}{dt} = \nabla \cdot (k \nabla T) + H - \rho C_p \vec{u} \cdot \nabla T \quad (2.17)$$

where, T is the temperature, t is the time, k is the thermal conductivity (W/K.m), ρ is the density (kg/m³), C_p is the specific heat at constant pressure (J/K.kg), u is the vector of velocity (m/s), and H is the radiogenic heat production per unit volume (μ .W/m³). The first term of the right-hand side of equation 2.17 corresponds to diffusion of heat by conduction, the second one reflects the presence of heat sources, and the third one is the advective/convective transfer of heat.

Under steady-state conditions and in the absence of advection, equation 2.17 can be written as:

$$\nabla \cdot (k \nabla T) = -H \quad (2.18)$$

In absence of advection/convection, the main contribution to the heat source term, H , comes from the radiogenic heat production from the radioactive decay of isotopes U²³⁸, Th²³² and K⁴⁰. On average, uranium and thorium contribute more to the heat production than potassium. In general, granite has a more important internal heat generation ($2 - 4 \mu$.W/m³) than mafic igneous rocks ($0.2 - 0.4 \mu$.W/m³) (e.g., Vilà et al., 2010). The undepleted mantle contribution to the heat source term is very low ($0.01 - 0.02 \mu$.W/m³).

Numerically computed temperature field yields forward prediction of the surface heat flow (SHF), which is a measure of the energy released from the Earth per unit area and per unit time, and can be compared with measurements at the surface.

However, SHF measurements are expensive (particularly for continental areas) and, therefore, are sparse. Further, SHF data are submitted to various perturbation processes like water circulation, faults, paleoclimate variations or data acquisition. In continents (including arcs and continental margins), the average SHF (64.7 m.W/m²) is low compared to the average value for the oceans (95.9 m.W /m²; Davis, 2013). In the absence of advection due to tectonic activity, SHF is mainly controlled by the radiogenic heat production in the crust and the heat flow from the underlying mantle. SHF values tend to be higher in the areas with recent tectonic activity.

2.5. Mineral physics

For any given thermodynamic system (e.g., a mineral) with its chemical composition and components, the equilibrium state in terms of state variables (i.e. pressure and temperature) can be calculated by minimizing the Gibb's free energy. This equilibrium state consists of thermodynamically stable components at a given pressure and temperature and allows calculating the physical properties. Recalling the first law of thermodynamics, the total energy of a system is conserved or, in other words, the internal energy, U of a mineral structure, considered as a thermodynamic system, is constant. The internal energy is the sum of the potential energy stored in the interatomic chemical bonds and the kinetic energy related to atomic vibrations. If any heat is supplied to the system, the kinetic energy through the vibrations of chemical bonds will increase, leading to an increase in the temperature and, ultimately, in the internal energy. If any work is done on a mineral structure or if it is allowed to expand, it will do some work on the surrounding and its internal energy will change. The change in the internal energy can be expressed as

$$dU = dQ - PdV \quad (2.19)$$

where dQ is the exchanged heat, and PdV is the work done during expansion, P being the pressure and dV the change in volume (V) due to the expansion. Since temperature is a state variable, any property changing it, is a fundamental property of a material and hence, heat capacity C is defined as the amount of heat dQ required to raise the temperature of a mole of material by dT . Expressing dQ in the equation 2.19 in terms of C gives the following expression:

$$C = \frac{dU}{dT} + \frac{PdV}{dT} \quad (2.20)$$

If the volume is constant then C in equation 2.20 becomes the heat capacity at constant volume that is C_v , which then becomes the direct measure of change in the internal energy. In experiments involving solids, it is easier to maintain constant pressure than constant volume, so we need to define another energy function called enthalpy, H as

$$H = U + PV \quad (2.21)$$

Since we are interested in changes of these energy functions, let us differentiate it

$$dH = dU + PdV + VdP \quad (2.22)$$

Substituting for dU from equation 2.19 and for heat capacity and rearranging we get

$$C = \frac{dH}{dT} + \frac{VdP}{dT} \quad (2.23)$$

Now if pressure is constant, the above equation becomes the heat capacity at constant pressure, C_p , which is the heat change, dQ , required to change the temperature by dT at constant pressure and is equal to the enthalpy change and can be easily measured in the laboratory experiments. Hence, enthalpy becomes analogous to internal energy. The difference between C_p and C_v is expressed as

$$C_p - C_v = TV \frac{\alpha^2}{\beta} \quad (2.24)$$

where α is the thermal expansion coefficient and β is the compressibility which are again properties of a system. α and β can be experimentally measured for individual minerals, hence C_v can be calculated using equation 2.24 and the change in the internal energy can be calculated.

During the change in internal energy of a mineral, heat is exchanged with the surrounding and the state of order, a measure of entropy (S), changes. Now, recalling the second law of thermodynamics, for any reaction in nature entropy always increases and the entropy change is defined as

$$dS > \frac{dQ}{T} \quad (2.25)$$

Since the exchange of heat is related to enthalpy, the final criteria for feasibility of reactions become

$$dH - TdS < 0 \quad (2.26)$$

The left-hand side of equation 2.26 is defined as the Gibbs free energy (Equation 2.27) of the reaction, and its change should be negative for a reaction to proceed or, in other words, the components assemblages that have the minimum Gibbs free energy change will be stable for a given temperature and pressure.

$$G = H - TS \quad (2.27)$$

Hence, to determine thermodynamically stable minerals assemblages inside the Earth, a thermodynamic database is needed which consists of V , α , β , H , S , $C_p(T, P)$ values for the possible mantle minerals to determine the Gibbs free energy for a given geotherm.

The chemical composition of the mantle can be described by the bulk rock major element oxides (in weight %), within the $\text{Na}_2\text{O}-\text{CaO}-\text{FeO}-\text{MgO}-\text{Al}_2\text{O}_3-\text{SiO}_2$ (NCFMAS) system since they account for the ~99% of the Earth's mantle (Palme and O'Neill, 2013). Since observational data (i.e., gravity field, SHF, seismograms, elevation) depends on bulk rock physical properties (density, bulk and shear modulus, and thermal conductivity), the major oxides chemical composition needs to be converted to pressure-temperature dependent stable phases called P-T phase diagrams for the mantle (Figure 2.2). Phases include the stable mineral assemblages found in the mantle, which allows calculating their physical properties. Minerals in the mantle exist in the form of solid solutions (Table 2.2) and have thermodynamically stable equilibrium assemblages as a function of pressure-temperature and composition. The upper mantle down to 400 km depth is mainly composed of olivine, garnet, orthopyroxene, and clinopyroxene (Figure 2.2). In the lithospheric mantle, at shallower depths, two other Al bearing minerals, plagioclase and spinel, are present depending on the depth (plagioclase is stable at shallow depths which converts to spinel at relatively higher depths and ultimately to garnet at greater depths).

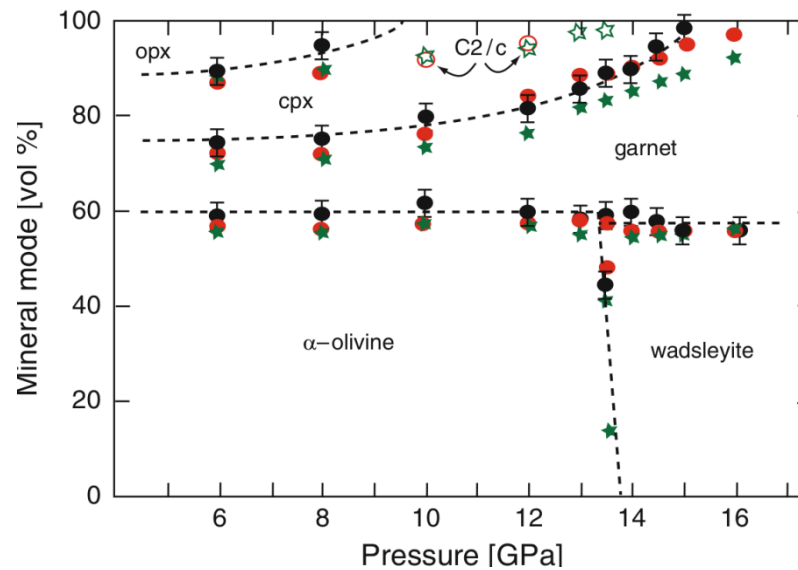


Figure 2.2 Mineral proportions for a pyrolitic composition as function of pressure and temperature range in the mantle. Black circles with error bars shows the experimentally determined phase proportions in dry pyrolite from Irifune and Isshiki (1998) based on high-T-P experiments. Red circles are predictions from Afonso and Zlotnik (2011) thermodynamic database and stars are predictions from the dataset of Xu et al. (2008). Figure is taken from Afonso and Zlotnik (2011).

Stable phase and mineral assemblages can be computed numerically using a Gibbs free-energy minimization algorithm (e.g., Connolly, 2005, 2009), which requires a thermodynamic database as explained above. A thermodynamic database contains experimentally determined thermodynamic parameters of end-member minerals contribution to the phase solution and their pressure-temperature dependent physical properties (e.g., density, bulk and shear modulus, thermal conductivity).

Table 2.2 Mineral solid solution notation and formulae.

Symbol	Solution	Chemical formula
Ol	Olivine	$[\text{Mg}_x\text{Fe}_{1-x}]_2\text{SiO}_4$
Gt	Garnet	$\text{Fe}_{3x}\text{Ca}_{3y}\text{Mg}_{3(1-x+y+z/3)}\text{Al}_{2-2z}\text{Si}_{3+z}\text{O}_{12}$; $x+y+4z/3 \leq 1$
Opx	Orthopyroxene	$[\text{Mg}_x\text{Fe}_{1-x}]_{2-y}\text{Al}_y\text{Si}_{2-y}\text{O}_6$
Cpx	Clinopyroxene	$\text{Ca}_{1-y}[\text{Mg}_x\text{Fe}_{1-x}]_{1+y}\text{Si}_2\text{O}_6$
C2/c	Pyroxene	$[\text{Mg}_x\text{Fe}_{1-x}]_4\text{Si}_4\text{O}_{12}$
Sp	Spinel	$\text{Mg}_x\text{Fe}_{1-x}\text{Al}_2\text{O}_4$
Pl	Plagioclase	$\text{Na}_x\text{Ca}_{1-x}\text{Al}_{2-x}\text{Si}_{2+x}\text{O}_8$
Wad	Wadsleyite	$[\text{Mg}_x\text{Fe}_{1-x}]_2\text{SiO}_4$

2.6. Physical properties

The equilibrium compositions of the phases using Gibb's free energy minimization allow estimating the amount of end-member minerals present in each phase. The relative amount of end-member minerals present in each phase allows calculating the bulk rock physical properties using rules of mixtures.

2.6.1. Density

In general, the mineral equilibria within the crust are not solved due to the large variety of mineral phases and then, the density can be calculated using

$$\rho(T, P) = \rho_0 - \rho_0 \alpha (T - T_0) + \rho_0 \beta (P - P_0) \quad (2.28)$$

where ρ_0 is the reference density at temperature (T_0) and pressure (P_0), α is the thermal expansion coefficient and β is the compressibility.

In the mantle, the fourth-order Birch-Murnaghan equation of state (EoS) allows to calculate the density of end-member minerals. Density of phases is computed using experimental models (e.g., Brey et al., 1999; Lee, 2003) where densities of each end-member are weighted by their mole fraction in each stable phase. Finally, the bulk rock density as a function of temperature and pressure for a given composition, including phase changes as well, can be calculated using a rule of mixture as:

$$\rho = \sum_{i=1}^{i=n} \rho_i v_i \quad (2.29)$$

where n is the number of stable phases, ρ_i and v_i are the density and volumetric fraction of the i th phase, respectively.

2.6.2. Thermal conductivity

Thermal conductivity, which controls the heat transport, depends on pressure, temperature and chemical composition. Conductive heat transport occurs by two processes: 1) lattice vibrations and 2) diffusive radiation. Lattice vibrations mainly involve vibration of the chemical bonds upon transfer of heat from neighboring molecules and dissipating it. Diffusive radiation involves electromagnetic radiation from the molecules upon receiving the heat from neighbouring molecules and, in turn, affecting them. Since these processes occur simultaneously, the total thermal conductivity is the sum of the lattice vibrations and the radiative transfer.

Thermal conductivity, k , is related to the thermal diffusivity, D , by:

$$D = \frac{k}{\rho C_p} \quad (2.30)$$

where ρ is the density and C_p is the heat capacity at constant pressure. Equation 2.30 suggests strong dependence of thermal conductivity on the chemical composition since density and heat capacity are specific for each mineral.

Thermal diffusivity for each mineral can be expressed as (Grose and Afonso, 2013):

$$D(T) = a + b \cdot \exp^{-cT} + d \cdot \exp^{-eT} \quad (2.31)$$

where T is temperature and a, b, c, d, e are the coefficients corresponding to each mineral derived from laboratory measurements.

The radiative contribution to the thermal conductivity is calculated as a function of the temperature, composition, grain size, and optical properties of crystals (Hofmeister, 2005), using:

$$k_{rad}(T, d) = A \exp\left(\frac{(T - T_A)^2}{2x_A^2}\right) + B \left(\frac{(T - T_B)^2}{2x_B^2}\right) \quad (2.32)$$

where A, B, T_A, T_B, x_A, x_B are all a function of grain size d (further details in Grose and Afonso, 2013; Tunini, 2015).

Then thermal conductivity for each mineral is calculated using equation 2.30 including thermal diffusivity (Equation 2.31), and radiative contribution is added using equation 2.32.

2.6.3. Mantle seismic velocities

Mantle seismic velocities depend on composition, pressure and temperature. The calculation requires knowledge of the elastic moduli (K : bulk modulus and G : shear modulus) of each end-member mineral and the bulk rock density at the pressures and temperatures of interest. In this manner, isotropic anharmonic seismic compressional (V_p) and shear (V_s) wave velocities can be calculated using the following equations:

$$V_p^2 \rho = K + \frac{4}{3} G \quad (2.33)$$

$$V_s^2 \rho = G \quad (2.34)$$

where ρ is the temperature-, pressure- and composition-dependent bulk rock density, K is the bulk modulus, and G is the shear modulus of each end-member mineral determined experimentally and are included in the thermodynamic database. Bulk rock density is calculated as mentioned in section 2.6.1.

To calculate the bulk rock elastic moduli used in equations 2.33 and 2.34, first the elastic moduli of each phase is calculated using the molar proportions weighted arithmetic mean of the elastic moduli of each end-member mineral. These elastic moduli are pressure and temperature dependent, and are calculated when constructing the thermodynamic database (e.g., Connolly and Kerrick, 2002). Then, bulk rock elastic moduli are computed from volumetrically weighted elastic moduli of each phase using a Voigt-Reuss-Hill (VRH) averaging scheme (Hill, 1952) as:

$$M_B = \left[\left(\sum_{i=1}^{i=n} \frac{w_i}{M_i} \right)^{-1} + \sum_{i=1}^{i=n} w_i M_i \right] \quad (2.35)$$

where n is the total number of phases, M_i and w_i are the moduli of the phases calculated in the first step and their volumetric fractions, respectively.

Seismic velocities calculated from elastic moduli of stable mineral and phase assemblages represent the unrelaxed oscillation of the chemical bonds in response to the elastic stresses produced by the propagation of high-frequency waves. In nature, rocks are not perfect solids or simple oscillators and the presence of defects in the crystalline structure, melt, and viscous nature at high temperatures can lead to dissipation of the energy imparted by elastic stresses, leading to relaxation of chemical bonds. This dissipation, called anelastic attenuation, results in loss of energy or relaxation of the elastic modulus leading to dispersion and change in the seismic velocities. Hence, in order to be able to compare calculated seismic velocities with the modelled seismic velocities using passive seismological data, anelastic effects must be accounted in the calculated seismic velocities (Chapter 3).

2.7. Isostasy and elevation

Under the assumption of isostatic equilibrium, local isostasy implies that a series of rigid vertical columns (the lithosphere) float freely on an inviscid liquid (the sublithospheric mantle) such that the pressure does not vary laterally below a certain compensation level. Alternatively, this implies that the lithosphere does not support vertical shear stresses. Local isostasy is an alternative statement of Archimedes' principle of hydrostatic equilibrium. Local isostasy has been proven to be an apt approximation in the absence of short-wavelength, elastically supported, features such as topographic and/or buried loads (Turcotte and Schubert, 1982). The principle of isostasy implies that all regions of the Earth with the same elevation must have the same buoyancy when referenced to a common compensation level. For the lithosphere and sublithosphere mantle, it can be assumed that the compensation level is located at 400 km depth (Afonso et al., 2008). The choice of a global compensation level at this depth has two advantages: (1) it covers the whole range of estimated lithospheric thicknesses, and (2) there is no need to change the calibration constants for different regions.

To calculate the absolute elevation, a calibration with respect to a reference column is needed. This reference column can be taken at a mid-oceanic ridge (MOR), where the mean elevation and the density-depth distribution are assumed to be known (Afonso et al., 2008). The absolute elevation is calculated using the following equations:

$$E_a = \int_{L_{top}}^{L_{bottom}} \frac{\rho_b - \rho_l(z)}{\rho_b} dz - \Pi_o \quad (2.36)$$

$$E_b = E_a \frac{\rho_b}{\rho_b - \rho_w} \quad (2.37)$$

where E_a and E_b are the elevations above and below the sea level, respectively. L_{top} is top of the column and L_{bottom} is the bottom of the column, ρ_b is the density of the mantle at 400 km depth and ρ_l is the depth-dependent density of the column, and ρ_w is the density of seawater. Π_o is a calibration constant which depends on the average density, structure, and the elevation of the reference column (see Afonso et al., 2008).

Due to the long-term rigid nature of the lithosphere, it flexes under vertical loading and can be considered as an elastic plate with an effective elastic thickness, T_e , resting on an inviscid or on a viscous fluid. Local isostasy ignores the short-

wavelength loads, and such loads can partly be supported elastically resulting in lithospheric deflection. The flexural response of a thin elastic plate is (e.g., Turcotte and Schubert, 1982):

$$q(x) = D \frac{d^4 w(x)}{dx^4} + N \frac{d^2 w(x)}{dx^2} + q_d(x) \quad (2.38)$$

$$D = \frac{E_y T_e^3}{12(1 - \nu^2)} \quad (2.39)$$

where D is the flexural rigidity, q the vertical load, q_d the restoring force, w is the deflection, N is the horizontal force per unit length, E_y is the Young's modulus, ν is the Poisson's ratio, and T_e is the elastic thickness of the plate. Solving for the surface deflections using equation 2.38 allows integrating the elastic nature of the lithosphere along with its thermal and chemical nature in order to reconcile the short wavelength variations of elevation.

2.8. Mantle melting and volcanism

Melting of rocks inside the Earth requires either its temperature to increase, such that it surpasses the solidus, or changes in the composition (e.g., the addition of volatiles), which lowers the solidus temperature. One other process which leads to melting at the Mid-Oceanic-Ridge is the adiabatic decompression. In thermodynamics, adiabatic processes occur without transfer of heat to the surroundings, hence when decompression occurs and the mantle is brought up with an almost constant temperature that surpasses the solidus temperature, melting occurs.

Volatiles (e.g., water in sediments) brought into the subduction channel leads to melting along the fore-arc in the subduction zones. The volcanic rocks produced in these settings inherit a crustal geo-chemical imprint and the associated volcanism is called orogenic volcanism. In contrast, melting in the intra-plate regions that does not have this crustal imprint is called anorogenic volcanism. However, the interaction of the ascending melts with the crust can change the geochemical signature of the emplaced volcanic rocks. Likewise, sediments brought into the mantle by subduction can change the mantle composition locally and influence the composition of volcanic rocks upon its melting.

Partial melting experiments on natural mantle peridotites have put important constraints on the total amount of partial melting (Kushiro, 2001). Combining information from laboratory melting experiments with the formal thermodynamic relations, we can calculate the total amount of partial melting necessary to generate a “standard” oceanic crust ~6–7 km thick (e.g., Klein and Langmuir, 1987; McKenzie and Bickle, 1988; Asimow et al., 2001, 2004; Kushiro, 2001; Presnall et al., 2002). Klein and Langmuir (1987) first proposed such formalism for the relationship between fraction melting, F , and the thickness of oceanic crust, h_c , at the ridge. The total amount of F can be calculated from a path integral of pressure from the pressure at which melting starts, P_0 , to the pressure at which melting stops, P_f , as follows:

$$F = \int_{P_0}^{P_f} F(P) dP \quad (2.40)$$

The mean fractional melting, \bar{F} can be calculated as

$$\bar{F} = \frac{\int_{P_0}^{P_f} F(P) dP}{(P_0 - P_f)} \quad (2.41)$$

The function $F(P)$ is a complex function of P (depth); however, it can be approximated within a finite pressure interval, n , by a constant slope, γ_n called the productivity function as (Langmuir et al., 1992; Phipps Morgan, 2001)

$$\gamma_n = \left(\frac{dF}{dP} \right)_s = \frac{\frac{\alpha T}{\rho c_p} - \left(\frac{dT_s}{dP} \right)_F}{\frac{H_m}{c_p} + \left(\frac{dT_s}{dF} \right)_P} \quad (2.42)$$

where T_s is the solidus temperature, α the coefficient of thermal expansion (CET), c_p the heat capacity, and H_m the latent heat of melting. For commonly accepted values of these variables, average γ values range between 10%- 20% per GPa of pressure release (e.g., Langmuir et al., 1992). The amount of melt present at any pressure P_x is given by the sum of $\gamma_n(P_{n-1} - P_n)$ for all relevant n (i.e., pressure intervals), where P_n becomes P_f in the last pressure interval and P_{n-1} is P_0 in the first pressure interval. Thus, equation 2.42 becomes

$$\rho_c g h_c = \bar{F} (P_0 - P_f) \quad (2.43)$$

Rearranging equation 2.43 and taking pressure in GPa, densities in kg/m³, and \bar{F} in % crustal thickness, h_c , can be approximated as

$$h_c = \bar{F}(P_0 - P_f) \frac{10^4}{\rho_c g} \quad (2.44)$$

For example, for typical values of $\bar{F} = \sim 7.2\%$, $P_0 = 2.75$ GPa, $P_f = 0.2$ GPa, and $\rho_c = 2880$ kg/m³, gives $h_c = 6.5$ km (Asimow et al., 2001).

Once melt is produced and segregated from the source, the chemical composition of the residue changes. The composition of the residue can be calculated from mass-balance using the initial concentration of element or component in the system (e.g., major oxides), the bulk distribution coefficient D , and the fraction of liquid F . As a first-order approximation the composition of the solid residue can be estimated as (Langmuir et al., 1992)

$$x_i^s = \frac{x_i^o}{\frac{F}{D_i} (1 - F)} \quad (2.45)$$

where x_i^o and x_i^s is the concentration of the i^{th} oxide in the original source and in the residue, respectively. D_i is the bulk distribution coefficient of the i^{th} oxide. The bulk distribution coefficients are function of pressure and amount of the melting (Niu, 1997). Therefore if the mean fractional melting, F , is known then equation 2.45 allows calculating the amount of each oxide in the solid residue after melting.

CHAPTER 3

Integrated geophysical-petrological modelling of the upper mantle anomalies

Chapter 3

Integrated geophysical-petrological modelling of the upper mantle anomalies

Integrated geophysical-petrological modelling of surface observables (i.e., gravity anomalies, geoid height, SHF, seismic velocities, xenolith data, and elevation) is a comprehensive approach and allows reconciling observations made by different datasets and methods. Each one of these observables is sensitive to the thermophysical properties of the materials under study, which in turn depend on temperature, pressure, and composition (Chapter 2). Therefore, a simultaneous fit to the surface observables reduces the uncertainties associated with the modelling of each of them alone or in pairs, as commonly found in the literature. Moreover, since these observables have a distinctive sensitivity to shallow/deep, thermal/compositional density anomalies (Chapter 2), this approach allows having improved control of thermal and density (i.e., composition) variations at different depths.

In this chapter, I present the new LitMod2D_2.0 software package, an updated version of the original 2D software by Afonso et al. (2008). In order to make physical inferences on seismic velocities, results on anelastic attenuation from recent laboratory-based measurements are incorporated in the anharmonic seismic velocities obtained from stable mineral assemblages that were considered externally in the previous version, LitMod2D_1.0. I test different available depleted chemical compositions in the sublithospheric mantle in order to be consistent with geochemical data. The numerical implementation of sublithospheric mantle anomalies is illustrated with the help of synthetic models. The nature of these anomalies can be i) chemical composition, ii) thermal, iii) seismic velocities (relative or absolute), and a combination of chemical composition with the latter two. LitMod2D_2.0 works under a forward modelling scheme and needs interactive input based on the assessment of the fit to the geophysical observables within uncertainty bounds. A new open-source graphic user interface (GUI) has been developed under Python programming language (Hunter 2007; Rossum, 1995), with improved functionalities, ease of use, and cross-platform dependence. Further, I make a synthetic model of a subduction zone setting to illustrate the sensitivity of sublithospheric mantle anomalies to the surface

observables. Finally, I discuss the post-processing capabilities of the LitMod2D_2.0 outputs to incorporate additional datasets in the modelling. As an example of post-processing, I compute Rayleigh-surface-wave dispersion curves, synthetic P-wave receiver-functions, and stable minerals distribution with depth in the mantle. Dispersion curves and receiver functions are calculated to demonstrate the possibility of comparing the resultant seismic velocities from LitMod2D_2.0 with passive seismological data.

3.1. General modelling workflow

LitMod2D is a software package based on the finite-element forward modelling approach of the CAGES code (Zeyen and Fernández 1994). LitMod2D_1.0 incorporated an external GENERATOR module based on Perple_X subroutines (Connolly, 2005), later upgraded (Connolly, 2009), to calculate the mineral assemblages and their physical properties as functions of the bulk composition of mantle domains. It also incorporates a MATLAB-based GUI. For a detailed description of LitMod2D_1.0 the reader is referred to Afonso et al. (2008). Here, I provide a brief summary of the critical aspects of the method and focus on the implementation of the new features/improvements in LitMod2D_2.0.

The general work-flow (Figure 3.1) in both versions is similar, except for the simplified input/output files, new improvements, and the new post-processing toolbox module. The numerical domain extends from the surface to 400 km depth and comprises different crustal and mantle bodies characterized by their individual thermo-physical properties and chemical composition. Crustal bodies are characterized by user-defined thermo-physical properties (e.g., thermal conductivity, volumetric heat production rate, coefficient of thermal expansion, and compressibility), with an option of depth and/or temperature dependence. The composition of upper mantle bodies is assigned within the $\text{Na}_2\text{O-CaO-FeO-MgO-Al}_2\text{O}_3\text{-SiO}_2$ (NCFMAS). Stable mineral assemblages are calculated by the external module GENERATOR using a Gibbs free-energy minimization algorithm (Connolly, 2005; 2009; Chapter 2 section 2.5) for pressure and temperature ranges in the upper mantle (Chapter 2, Table 2.2). Here, I use an augmented-modified version of Holland and Powell (1998) thermodynamic database (Afonso and Zlotnik, 2011). Relevant physical properties (density, thermal conductivity, and bulk and shear modulus) are calculated for each mineral and averaged according to Voigt-Reuss-Hill procedure (Hill, 1952) producing look-up tables as function of P and T (Chapter 2, section 2.6). In this way, the user can produce its own library of look-up tables for different mantle compositions beforehand.

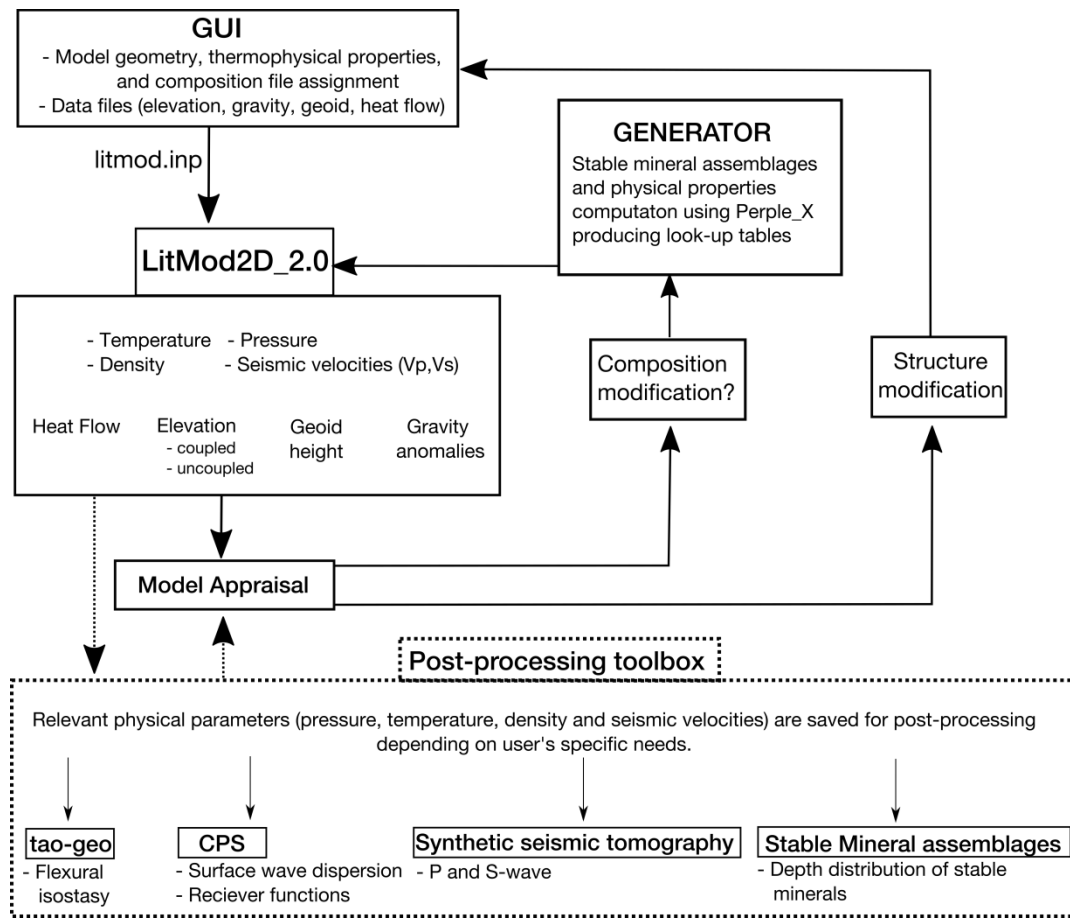


Figure 3.1 Flow chart diagram showing the workflow of LitMod2D_2.0. The new LitMod2D version may account for sublithospheric mantle anomalies in which case coupled elevation is calculated. It also has an option for post-processing of relevant physical properties (temperature, pressure, density and seismic velocities) to compare with additional datasets. Flexural isostasy is included by coupling ‘tao-geo’ software (Garcia-Castellanos et al., 2002). “Computer Programs in Seismology” (CPS, Herrmann, 2013) is also coupled to work with passive seismological datasets. Stable mineral-assemblages are extracted from the material files produced by the GENERATOR subprogram.

The heat transport equation 2.18, Chapter 2, is solved with finite elements using Galerkin’s ponderation method (Zienkiewicz, 1977) under steady-state, subjected to prescribed boundary conditions at the surface (e.g., 0 °C), at the LAB (e.g., 1320 °C) , and no heat flow across the lateral boundaries of the model. Thermal conductivities for crustal bodies are taken from literature, whereas for the lithospheric mantle are calculated by GENERATOR (Chapter 2, section 2.6.2), and are temperature, pressure, and composition dependent and read from the look-up tables. Below the LAB, the algorithm considers a 40 km thick thermal buffer with a temperature of 1400 °C at its base to avoid unrealistic discontinuities between a conductive thermal gradient within the lithospheric mantle and an adiabatic thermal

gradient within the sublithospheric mantle. The temperature gradient below the thermal buffer layer is restricted to $0.35 \leq dT/dz \leq 0.50$ °C/km.

The density distribution is obtained with an iterative scheme to include the effect of pressure, temperature and composition. Pressure is calculated at every node as a function of the overburden lithostatic pressure and it is then used to obtain the P-T-composition dependent density at the node. In case of bodies with assigned composition (e.g., in the mantle), density is read from the look-up tables produced by GENERATOR. This density then is used in the next iteration to update the overburden pressure and to solve for an updated density.

Once the final density distribution is obtained, the gravity potential field is calculated. Gravity anomalies are calculated by applying the Talwani's algorithm for polygonal bodies (Talwani et al., 1959) to the elements of the mesh, therefore considering both horizontal and vertical density variations. The gravity effect of all the elements is finally added and calculated either at the top of the model or at the sea level, depending on if the elevation is above or below sea level, respectively. .

Geoid height is calculated converting the adjacent elements of the numerical mesh into rectangular prisms, then solving the integral of the gravity potential and substituting the result into the Brun's formula (Equation 2.5) and is expressed as:

$$N = \frac{G \rho}{g_0} \iiint_{x_1, y_1, z_1}^{x_2, y_2, z_2} \frac{1}{\sqrt{x^2 + y^2 + z^2}} dx dy dz \quad (3.1)$$

where G is the universal gravitational constant, g_0 the normal gravity acceleration, ρ the rectangular prism density, and x, y, z the prism boundary coordinates. LitMod2D uses the method by Zeyen et al. (2005), based on an analytical solution of equation 3.1, to obtain 2.5-D geoid heights along the model. In calculating both gravity and geoid anomalies, the models are extended horizontally 1×10^5 km beyond the profile limits to avoid boundary effects.

3.2. Anelasticity

A physical interpretation of seismic velocities in terms of temperature and/or chemical composition requires anelastic effects to be incorporated in the anharmonic seismic velocities from stable mineral assemblages (Lau and Faul, 2019; Takei, 2017; Abers et al., 2014; Afonso et al., 2008; Cammarano et al., 2008; Goes et al., 2000;

Sobolev et al., 1996). Understanding of anelasticity mainly comes from two approaches: 1) attenuation tomography using passive seismological data, and 2) laboratory experiments on materials representative of the mantle (e.g., olivine). Attenuation tomography using passive seismological data is often low resolution and has large uncertainties. Controlled laboratory experiments on the polycrystalline olivine help understanding the fundamental physical processes involved and then extrapolation of observations to the physical conditions (mainly for grain size and pressure) inside the Earth.

Experiments at mantle temperatures and seismic wave frequencies show that grain boundary sliding is the main process of energy dissipation (attenuation). Grain boundaries have a finite width and viscosity and, under the application of shear stress, result in relative motion on either side. Motion is resisted by the viscosity of the grain boundary resulting in dissipation of energy, which is termed as elastically accommodated grain boundary sliding. In case the shear stresses are continued to high temperatures, the normal stresses concentrated at the grain corners resulting from the grain boundary sliding drive diffusion (Raj, 1975), and these normal stresses act as a restoring force upon removal of shear stresses. Redistribution of the stresses from diffusion results in transient creep, termed as diffusion assisted grain boundary sliding (Morris and Hackson, 2009) resulting in continuously increasing dissipation with increasing timescale and causing the high-temperature background or absorption band (Anderson and Minster 1979; Gribb and Cooper 1998). This transient phase ends when the stress distribution matches the steady-state diffusion creep stress distribution. This type of diffusion occurs on the scale of the grain size because of a constant grain boundary normal stress, and the resulting strain is not recoverable. The transition from diffusion assisted grain boundary sliding to steady-state diffusion creep is a function of timescale as it is evident that at earthquake time scale mantle behaves as elastic solid, but at geological time scales it behaves as a fluid.

A consistent and robust feature of the experimental studies on melt-free polycrystalline aggregates is an absorption band with mild frequency dependence between 900 °C - 1100 °C temperature range prevalent in the lithospheric mantle (Jackson and Faul, 2010; Faul and Jackson, 2015). Jackson and Faul (2010) showed that the experimental data on dissipation for this absorption band are consistent with power-law variation of dissipation, however, they propose more complex models (e.g., extended Burgers model) mainly to explain the dissipation peak at temperatures < 900 °C representing elastically accommodated grain boundary sliding. This peak occurs at the experimental resolution limit and is less constrained (Faul and Jackson, 2015);

therefore I use the power-law attenuation model to correct for anelastic attenuation (Jackson and Faul, 2010). Further, the power law formulation reproduces the seismological determined global average attenuation (Figure 3.2).

In the previous LitMod2D_1.0 version, the anelastic attenuation correction was incorporated a posteriori using an external code. The new LitMod2D_2.0 package incorporates the anelastic effects according to stable mineral assemblages at the corresponding P-T conditions in the look-up tables produced by the GENERATOR module, using equations 3.2 to 3.4 and the empirical parameters proposed by Jackson and Faul (2010).

$$V_P = V_{Po}(T, P) \left[1 - \frac{2}{9} \cot\left(\pi \frac{\alpha}{2}\right) Q_S^{-1} \right] \quad (3.2)$$

$$V_S = V_{So}(T, P) \left[1 - \frac{1}{2} \cot\left(\pi \frac{\alpha}{2}\right) Q_S^{-1} \right] \quad (3.3)$$

$$Q_S^{-1} = A \left[T_o d^{-1} \exp\left(\frac{(-E + VP)}{RT}\right) \right]^\alpha \quad (3.4)$$

where $Q_P = (9/4)Q_S$ is assumed. $V_{Po}(T, P)$ and $V_{So}(T, P)$ are the anharmonic seismic velocities at a given temperature and pressure for a given chemical composition, and $A = 816 \text{ s}^{-\alpha} \mu\text{m}^{-\alpha}$, $\alpha = 0.36$ is the frequency dependence factor, $E = 293 \text{ kJ/mol}$ is the activation energy, $V = 1.2 \times 10^{-5} \text{ m}^3/\text{mol}$ is the activation volume, and R the universal gas constant. Here, I use a grain size of $d = 10 \text{ mm}$ in the mantle and an oscillation period of $T_o = 75 \text{ s}$, since this combination produces Q_P and Q_S values in the range of global average attenuation models, particularly close to the LAB where anelastic attenuation is believed to be high (Figure 3.2). Both grain size and oscillation period are input parameters that can be modified. Moreover, the user can incorporate her/his preferred attenuation model into the GENERATOR module by changing the provided source code. Hereinafter, I use seismic velocities corrected for anelastic attenuation unless specified otherwise.

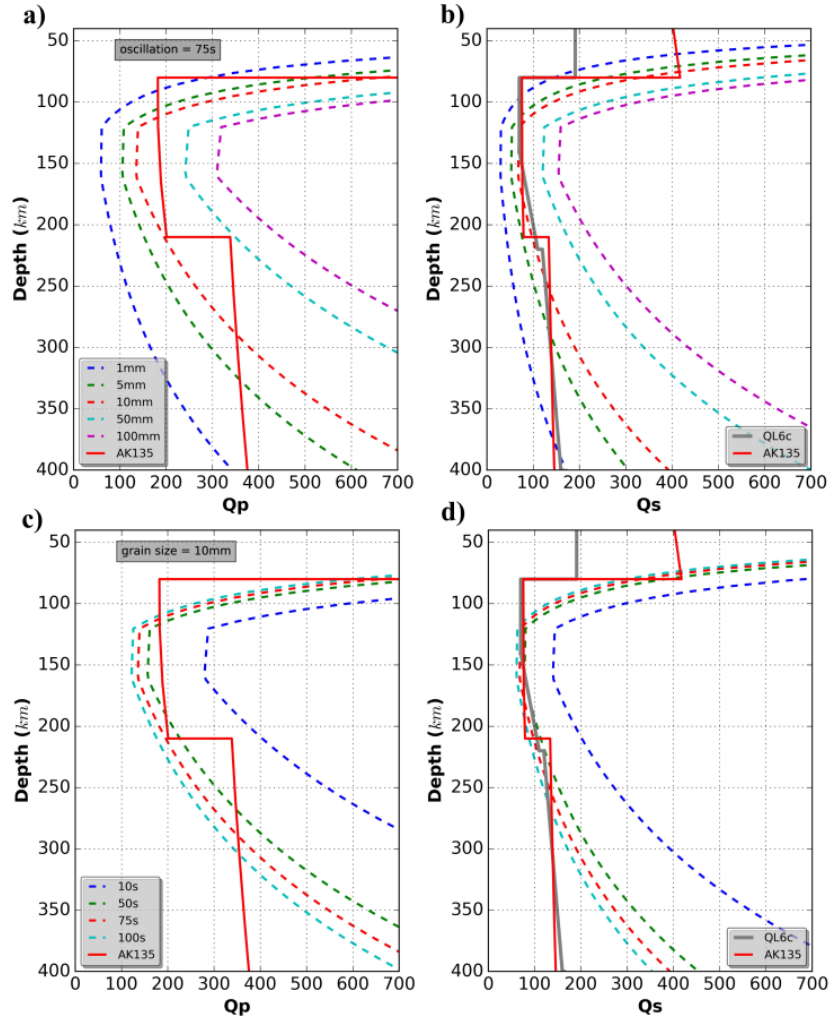


Figure 3.2 Depth distribution of anelastic attenuation parameter (Q , quality factor) for a range of grain sizes (1-100 mm) and oscillation periods (10-100s) compared with global average Q_P and Q_S models. (a) and (b) shows the depth distribution of Q_P and Q_S for varied grain size and constant oscillation period of $T_0 = 75$ s, respectively. (c) and (d) shows depth distribution of Q_P and Q_S for varied oscillation period (10-100 s) and constant grain size of $d = 10$ mm, respectively. Q_P and Q_S from ak135 global average model (continuous red solid line, Kennett et al., 1995), and Q_S from QL6c (continuous grey line, Durek and Ekström, 1996), are also plotted for comparison.

Anelastic attenuation parameters derived from laboratory measurements on dry polycrystalline olivine often need to be extrapolated to conditions pertaining to the upper mantle, as explained above, thus introducing unquantifiable uncertainties (Priestley and McKenzie, 2013; Faul and Jackson, 2015). While it is hard to put quantifiable uncertainty values on these parameters, here I assume 10 % error and explore how these errors propagate to the calculated seismic velocities. Uncertainties in computed seismic velocities (V_P and V_S) are calculated using:

$$\delta V_{P/S} = \sqrt{\left(\frac{\partial V_{P/S}}{\partial \alpha} \delta \alpha\right)^2 + \left(\frac{\partial V_{P/S}}{\partial E} \delta E\right)^2 + \left(\frac{\partial V_{P/S}}{\partial V} \delta V\right)^2} \quad (3.5)$$

where $\frac{\partial V_{P/S}}{\partial \alpha}$ is the partial derivative of the P- or S-wave velocities (Equations 3.2 and 3.3) with respect to α , and $\delta \alpha$ is the assumed error in α ; similar terms apply for E and V .

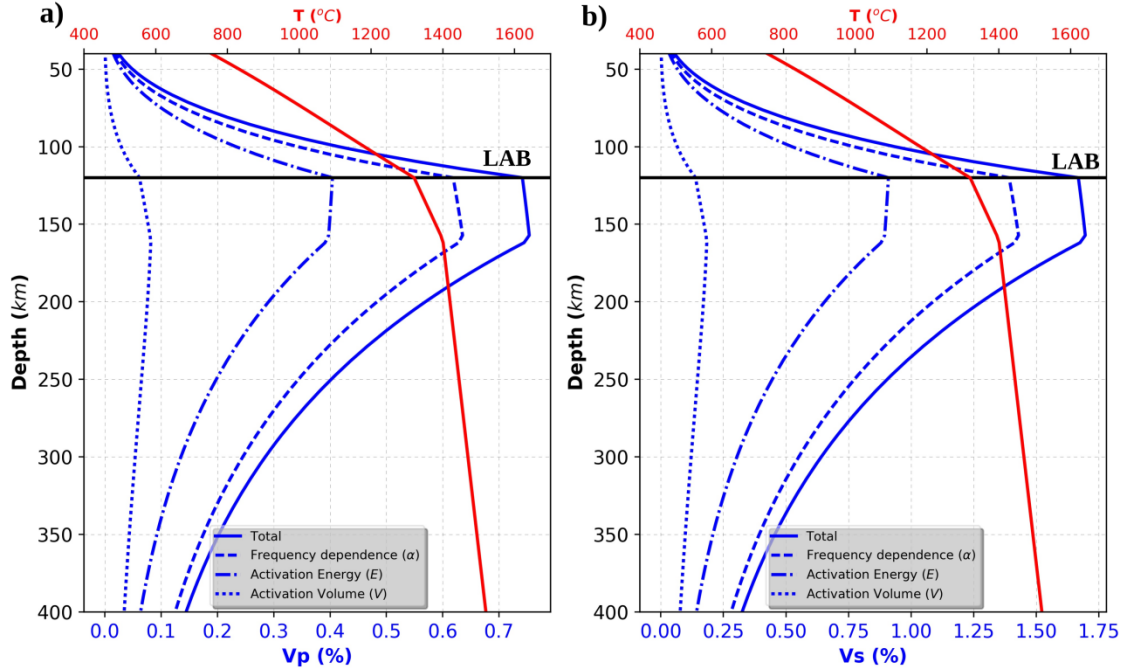


Figure 3.3 Percentage error introduced in the (a) P-wave velocities and (b) S-wave velocities considering 10% error in α (dashed blue line), E (dotted-dashed blue line), and V (dotted blue line). The total error is plotted in solid blue line and temperature distribution is plotted in solid-red line.

Figure 3.3 shows the resulting errors in V_P and V_S . These errors have the largest effect on seismic velocities around the LAB, being the frequency, α , the dominant source of uncertainty affects the seismic velocities the most and V , the activation volume, the least influential. Note that the error in velocity (Equation 3.5) is directly proportional to the error in anelastic parameters and therefore increasing uncertainty in any individual parameter will scale the uncertainty in the velocity in a quasi-linear fashion. The effects of melt or water content on seismic velocities are not included here. If melt is present, an additional correction needs to be applied to the computed seismic velocities (e.g., Afonso et al., 2016b) which can easily be included into the GENERATOR module by changing the provided codes.

3.3. Sublithospheric mantle composition

The chemical composition of the lithospheric mantle may be estimated from available mantle xenoliths and xenocrysts and/or exposed massifs in mobile belts. Although sublithospheric mantle rocks are less represented in these suites, compositional estimates can sometimes be obtained by analyzing the chemistry of primitive basaltic melts when available (e.g., Shorttle and MacLennan, 2011; Brown et al., 2020). As mentioned in the Chapter 1, LitMod2D_1.0 uses a fixed chemical composition for the sublithospheric mantle, corresponding to the primitive upper mantle (PUM) of McDonough and Sun (1995). The upper mantle however, has been a source for oceanic and continental crust since the onset of plate tectonics and should be less fertile than PUM (Van Keken et al., 2002). Here, I test the most common sublithospheric mantle compositions proposed so far (Table 3.1), and compare their relevant physical properties with that of PUM. The depleted MORB mantle (DMM) is a source reservoir to mid-ocean-ridge basalts (MORBs) and has been computed using a robust geochemical dataset (trace elements) on abyssal peridotites (Workman and Hart, 2005). Other commonly used sublithospheric mantle compositions are PUM-3%_N_MORB (Workman and Hart, 2005) and pyrolite (Ringwood, 1977). PUM-3%_N_MORB is computed by extracting 3% of normal MORB from PUM composition, whereas pyrolite is calculated by mixing appropriate fractions of basalts (partial melts from the mantle) and peridotites (the presumed residues from partial melting).

Table 3.1 Major oxide compositions (weight %) in the mantle.

Name	SiO ₂	Al ₂ O ₃	FeO	MgO	CaO	Na ₂ O	Mg# ^a
Lithospheric mantle							
Average Garnet Tecton ^b	44.50	3.50	8.00	39.80	3.10	0.240	89.8
Oceanic lithosphere	44.43	2.97	8.23	40.78	2.70	0.045	89.7
Sublithospheric mantle							
PUM	45.00	4.50	8.10	37.80	3.60	0.360	89.3
DMM ^c	44.70	3.98	8.18	38.73	3.17	0.130	89.4
PUM - 3% N_MORB	44.90	4.07	8.05	38.68	3.27	0.300	89.5
Pyrolite	45.10	4.60	7.60	38.10	3.10	0.400	89.9

^aMg# = 100xMgO/[MgO + FeO], ^bAfter (Griffin et al., 2009), ^cWater 100 ppm (Workman and Hart, 2005), PUM- Primitive upper mantle (McDonough and Sun, 1995), DMM- depleted mid-oceanic ridge basalt mantle (Workman and Hart, 2005), PUM-3% N_MORB- Primitive upper mantle after 3% extraction of normal mid-oceanic ridge basalt (Workman and Hart, 2005).

All tested compositions are less dense than PUM at sublithospheric mantle depths (Fig 3.4a), which is consistent with their higher Mg# ($100 \times \text{MgO} / [\text{MgO} + \text{FeO}]$) and depleted reservoirs. DMM shows a small density change of -0.18% relative to PUM between 120 km and 340 km depth and an increase of $\sim 0.1\%$ below ~ 340 km, whereas pyrolite shows a maximum change of $\sim -0.6\%$. PUM-3%_N_MORB exhibits variations in between those associated with DMM and pyrolite. In terms of anharmonic P- and S-wave velocities (Figures 3.4b and 3.4c), pyrolite is the slowest, DMM is slightly faster in comparison to PUM, and PUM-3%_N_MORB is intermediate. A water content of 100 ppm (70-160 ppm; Workman and Hart, 2005) in DMM slightly decreases the density compared to its dry counterpart and produces a decrease in P-waves velocities higher than in S-wave velocities because of its lower bulk modulus (Watanabe, 1993).

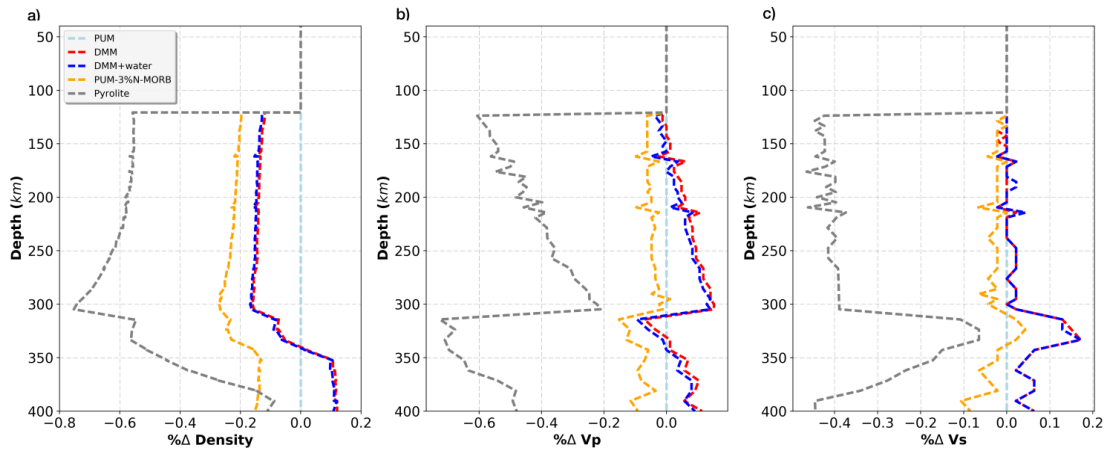


Figure 3.4 Comparison of different compositions tested in the sublithospheric mantle (Table 3.1). Resulting density (a), P-wave velocities (b) and S-wave velocities (c) are compared with that to PUM.

Although PUM-3%_N_MORB and pyrolite attest to be depleted with respect to PUM, they still are theoretically computed. Furthermore, the pyrolite composition has been reported not to satisfy trace elements or isotopic data on basalts, violating the chondritic abundances (Anderson, 1989). DMM composition is consistent with trace elements data and with $\sim 6\%$ aggregated fractional melting to produce an average 6 km thick oceanic crust at the mid-oceanic-ridge (Workman and Hart, 2005; Klein and Langmuir, 1987). In addition, DMM has also been shown to be balanced by continental crust, ocean-island-basalt (OIB) source, and oceanic crust, which are the products of mantle melting (Workman and Hart, 2005). Although the differences in physical

properties are small, in the new LitMod2D_2.0 version I fix the sublithospheric mantle chemical composition corresponding to DMM for geochemical consistency.

3.4. Recalibration of elevation

Changing the chemical composition of the sublithospheric mantle requires a recalibration of the calculated absolute elevations since the total load of the sublithospheric mantle will vary according to the adopted composition. In contrast to LitMod2D_1.0, that considers a reference column at mid-oceanic-ridge (MOR) down to 400 km depth, in LitMod2D_2.0I consider a reference column corresponding to a thermally stable oceanic lithosphere and the underlying sublithospheric mantle. A thermally stable oceanic lithosphere is chosen because the depth-dependent T-P-composition is arguably less complicated than at actively spreading MOR, where melt content and short-lived buoyancy sources can complicate its characterization. Four compositional layers have been considered in the lithosphere and their bulk composition is calculated according to the depth-dependent melt fraction for a standard MOR model (Turcotte and Morgan, 2013; Niu, 1997) as used in Fernández et al. (2010) (Table 3.2). Calibration is done using the formulation described in Afonso et al. (2008) and Fullea et al. (2009), where I solve for a calibration parameter Π_0 , the thermal and lithostatic equations on a given reference column (Equations 2.36 and 2.37; Chapter 2). This reference column, corresponding to a stable oceanic lithosphere, consists of a 5.37 km water layer with a density of 1030 kg/m³, 6.8 km crustal thickness including sediments, with an average density of 2858 kg/m³, and a LAB depth of ~122 km with an average density resulting from the mineral compositions and assemblages mentioned previously (Table 3.2).

Table 3.2 Physical properties and major oxides composition in the mantle of a column at an old oceanic lithosphere used to compute calibration parameters for elevation.

Layer	Thickness (km)	Density (kg/m³)					
Crust							
Water	5.37	1030					
Sediments	0.80	2200					
Oceanic crust	6.140	2930					
Lithospheric Mantle							
Mantle layer	Thickness (km)	SiO ₂	Al ₂ O ₃	FeO	MgO	CaO	Na ₂ O
Layer 1	17.4	44.00	1.50	8.23	43.40	1.90	0.010
Layer 2	20.0	44.60	2.77	8.14	40.70	2.75	0.035
Layer 3	25.0	44.90	3.60	8.08	39.20	3.30	0.170
Layer 4	48.0	44.95	4.00	8.06	38.50	3.48	0.235
Sublithospheric Mantle (DMM)	278.0	44.70	3.98	8.18	38.73	3.17	0.130

3.5. Reference model for synthetic seismic tomography

The calculated seismic velocities in the sublithospheric mantle also depend on chemical composition. Seismic tomography models are usually reported as deviations from global reference velocity models, ak135 being one of the most widely used reference models (Kennett et al., 1995). To compare the seismic velocities obtained from LitMod2D_2.0 with those from ak135, I consider a model with i) a 35-km thick continental crust, and ii) a 85-km thick lithospheric mantle, similar to ak135 model, with Average Garnet Tecton composition (Tc_1 in Griffin et al., 2009), resulting in a LAB depth of 120 km. The composition of the sublithospheric mantle corresponds to DMM. The thermo-physical parameters used in the crust and the composition used in the lithospheric mantle are listed in Table 3.3 and Table 3.1, respectively.

The ak135 model was designed to predict arrival times for seismic phases in observational seismology by inverting smoothed empirical travel times (Kennett et al., 1995; Kennett, 2006). P-wave velocities are better constrained than S-wave velocities since P-waves are first arrivals, whereas S-waves have low frequency and can be interfered by the CODA of P-waves. Considering this and the inherent uncertainties in earthquake hypocentres, I assign uncertainties of 0.5% and 1% to P- and S-wave velocities, respectively.

Table 3.3 Thermophysical parameters used in the crust to compare calculated seismic velocities with those from ak135 model.

Body name	Density (kg/m ³)	Heat Production (μ W/m ³)	Thermal conductivity (W/K.m)
Continental crust	2800	1.00	2.5
Oceanic crust	2950	0.30	2.2

Different thermodynamic databases produce noticeably different seismic velocities, particularly in the sublithospheric mantle (Figure 3.5), resulting in a dispersion of $\sim 1\%$. Formal errors resulting from each thermodynamic database can be calculated from the uncertainties in the elastic moduli of individual minerals. Both Stixrude and Lithgow-Bertelloni (2005) and Holland and Powell (1998) modified by Afonso and Zlotnik (2011) databases reasonably reproduce the ak135 model for depths between 35 km and 250 km, whereas Xu et al. (2008) database results in very slow P-wave velocities (Figure 3.5a). Below 250 km depth, only Stixrude and Lithgow-Bertelloni (2005) database shows good agreements with ak135 model, both in P- and S-velocities, whereas Holland and Powell (1998) modified by Afonso and Zlotnik (2011) and Xu et al. (2008) databases are significantly slower ($\sim 1\text{--}2\%$). Slow velocities below 250 km depth are also observed in Cammarano et al. (2005). Fitting the ak135 velocities below 250 km with these thermodynamic databases would require either a lower temperature than that predicted by the assumed adiabatic thermal gradient, or a change in the chemical composition at these depths (Cammarano et al., 2009). Another possible contribution to the discrepancies between predicted and reference velocities could be that the temperature and pressure derivatives of elastic moduli in Afonso and Zlotnik (2011) need to be updated. In contrast to the other two databases/formalisms, that of Afonso and Zlotnik (2011) supplements equilibrium phase diagrams with an independent database of velocity derivatives. Small corrections to these derivatives can produce changes in the velocities of the same order as the discrepancies in Figure 3.5. Despite this, the phase equilibria predictions show excellent agreement with experimental data (Figure 2.2, Chapter 2; Afonso and Zlotnik, 2011).

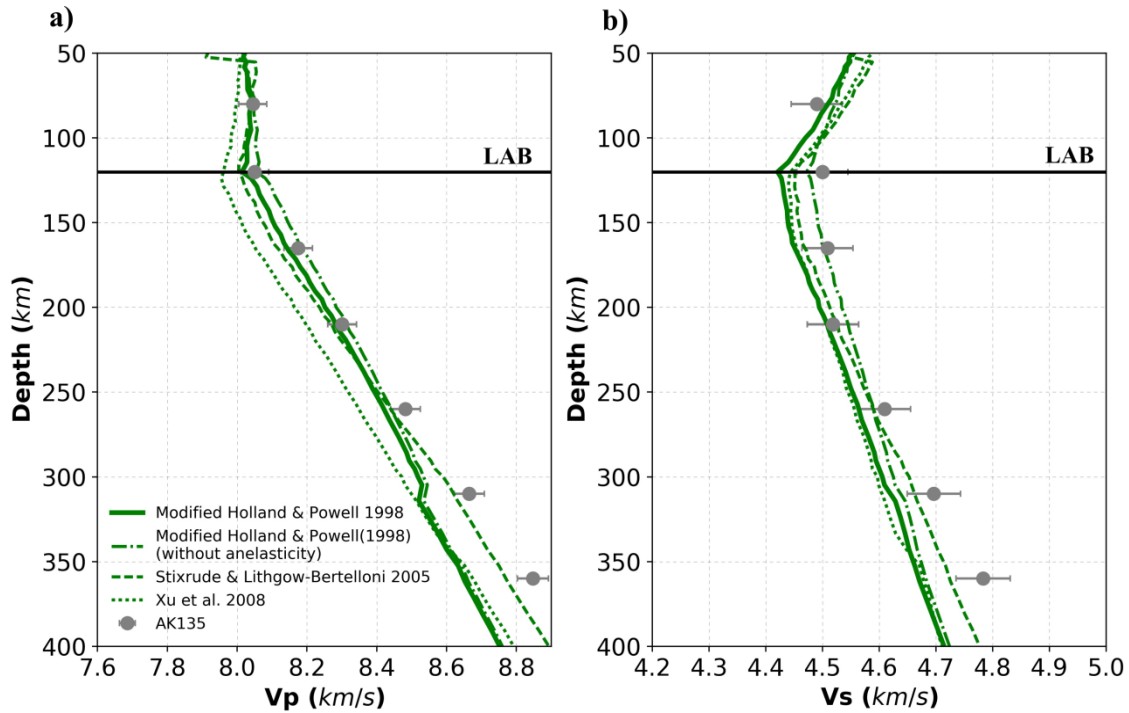


Figure 3.5 Depth distributions of seismic velocities, (a) P-wave and (b) S-wave assuming an Average Garnet Tecton composition in the lithosphere mantle and a DMM composition in the sublithospheric mantle. Seismic velocities are calculated using Afonso and Zlotnik (2011) (solid, modified Holland and Powell, 1998), Stixrude and Lithgow-Bertelloni (2005) (thick dashed) and Xu et al. (2008) (thin dashed) thermodynamic databases. Resulting seismic velocities are corrected for anelastic attenuation using a constant grain size of 10 mm and oscillation period of 75 s. Global average seismic velocities from ak135 (Kennett et al., 1995), in solid grey circles, with an error of 0.5% in P-wave velocities and 1% in S-wave velocities are plotted for comparison.

Here, I choose the Holland and Powell (1998) modified by Afonso and Zlotnik (2011) database in LitMod2D_2.0 to calculate the physical properties in the upper mantle given its performance in reproducing experimental data, but I note that a future reassessment of the elastic moduli derivatives is necessary. Since deviations with respect to the ak135 model are always negative below ~250 km (in the absence of thermal or compositional perturbations at these depths), I use the aforementioned reference model (35 km thick crust and 120 km LAB depth; Figure 3.5) to avoid this systematic misfit when calculating synthetic tomography from LitMod2D_2.0.

3.6. Sublithospheric mantle anomalies

A major contribution of LitMod2D_2.0 is the possibility to incorporate sublithospheric mantle anomalies into the modelling workflow, thus opening up the possibility of modelling complex geodynamic processes, such as mantle upwelling,

subduction, delamination, and metasomatism (i.e., processes that can easily modify the temperature and/or the chemical composition beneath the LAB). Since seismic tomography has the potential to detect such perturbations in terms of fast/slow velocities, I added in LitMod2D_2.0 a functionality to incorporate i) thermal anomalies, ii) compositional anomalies, and iii) seismic velocity (V_P, V_S) anomalies, in the sublithospheric mantle.

In this section I discuss the numerical implementation of sublithospheric mantle anomalies and its applicability to various geological settings considering the reference model defined in the previous section to calculate synthetic tomography. I consider an anomalous region in the depth range of 200–325 km and change systematically its nature to i) thermal, ii) chemical composition, and iii) seismic velocities (V_P and V_S).

3.6.1. Thermal anomalies

Mantle flow can change the temperature in the sublithospheric mantle producing colder and hotter domains, which can be represented as thermal anomalies in LitMod2D_2.0. To account for these thermal perturbations, I modify the constant adiabatic thermal gradient such that the imposed temperature perturbation (ΔT) is added to the steady state temperature distribution. Then, LitMod2D_2.0 recalculates the relevant physical properties (density, seismic velocities, phase changes, and thermal conductivity) at $T+\Delta T$ and P conditions, where T and P , are pressure and temperature at a given depth below the LAB.

To illustrate the effect of hot and cold thermal anomalies on the sublithospheric mantle with a DMM composition, I consider a thermal anomaly ranging from $-400\text{ }^{\circ}\text{C}$ to $+400\text{ }^{\circ}\text{C}$ in steps of $100\text{ }^{\circ}\text{C}$ (Figure 3.6). As expected, cold thermal anomalies increase density, P - and S -wave velocities, while hot anomalies have the opposite effect. The amplitude of the resulting anomalies varies such that density has the least relative change, whereas S -waves have the highest change due to the high sensitivity of S -wave velocities to temperature. To first order, the absolute density change depends linearly on the sign of the thermal anomaly, thus similar perturbations (in magnitude) can be seen at both sides of the 0% anomaly in Figure 3.6b. In contrast, seismic velocities show higher relative changes for positive temperature perturbations than for the equivalent negative ones (Figures 3.6c and 3.6d). This is because of the enhanced anelastic attenuation at higher temperatures. Moreover, the amplitude of seismic velocity anomalies decreases with depth due to the decreasing attenuation of seismic waves (low Q factor, Figure 3.2) at lithosphere-sublithosphere transition depths. This

non-linear dependence of seismic velocities on temperature has strong implications for qualitative interpretation of seismic tomography models (Cammarano et al., 2003). A second order variation in density and seismic velocities occurs around 310 km depth (Figure 3.6, inset) coinciding with the orthopyroxene-clinopyroxene (Figure 3.12) phase transition and could be the reason for the X-discontinuity imaged in seismic data (Revenaugh et al., 2008).

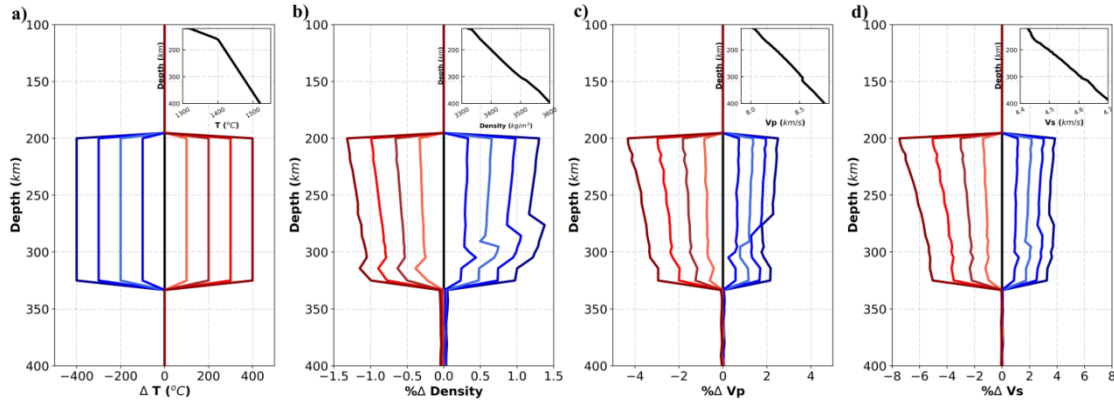


Figure 3.6 Synthetic examples of thermal anomalies in the sublithospheric mantle. Input thermal anomalies are plotted in (a). Resultant change in (b) density, (c) P-wave velocities, and (d) S-wave velocities are plotted with same colour code as input. All anomalies are referred to a reference model, shown as inset in the upper right corner.

3.6.2. Chemical composition anomalies

Understanding of chemical heterogeneity in the upper mantle is crucial for the geochemical evolution of the Earth governed by lithosphere recycling, mineral phase changes and mantle mixing models (Van Keken et al., 2002). Chemical heterogeneity in the upper mantle can be a result of metasomatic processes changing the chemical composition in the sublithospheric mantle by enrichment or depletion of the major elements. In turn, delamination, slab break-off, and slab tear processes can induce the sinking of pieces of cold lithosphere, with different chemical composition, into the sublithospheric mantle. LitMod2D_2.0 allows considering such types of anomalies of chemical origin, or a combination of chemical composition and temperature. For the case of chemical compositional anomalies, LitMod2D_2.0 recalculates the relevant physical parameters at the corresponding P-T conditions according to the prescribed composition in a given region beneath the LAB. For the case of combined thermal and compositional anomalies, the relevant parameters are recalculated at $T+\Delta T$ and P conditions from the prescribed chemical composition.

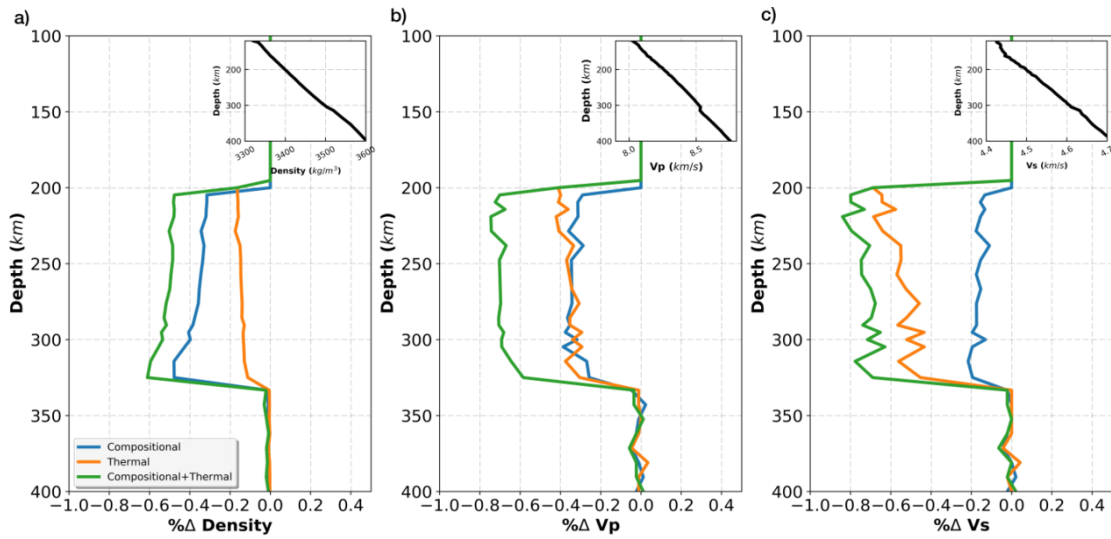


Figure 3.7 Synthetic example illustrating the contribution of compositional (Average Garnet Tecton, blue), thermal (+50 °C, orange), and combination of both (green) anomalies to (a) density, (b) P-wave velocities, and (c) S-wave velocities, with respect to the reference model shown as inset in the upper right corner.

Figure 3.7 shows a synthetic example of a compositional and a combination of thermal and compositional anomalies, where the separate effect of temperature is also shown. In the case of compositional anomaly, I have considered an Average Garnet Tecton chemical composition, which is depleted with respect to DMM (Table 3.1). Results show that density reduces by ~0.4% (Figure 3.7a), which is almost equal to the average change in P-wave velocities (~0.4%, Figure 3.7b) and higher than the change in S-wave velocities (~0.2%, Figure 3.7c). A combination of compositional and thermal anomalies ($\Delta T = +50$ °C) results in a maximum decrease in density and seismic velocities (Figure 3.7) because increasing temperature also tends to decrease density and seismic velocities. Indeed, P-wave velocities are more sensitive to composition than S-wave velocities. By studying the effect of melt removal from a fertile composition (i.e., range of Mg#) on S-wave velocities, Priestley and McKenzie (2006) have also reported low sensitivity of S-waves to composition. Note that depending on the chemical composition of the anomaly (degree of depletion) and the temperature perturbation, the sublithospheric anomalies can have competing effects on density and seismic velocities.

3.6.3. Seismic velocity anomalies

LitMod2D_2.0 allows for implementing seismic velocity anomalies by providing the absolute velocity values or the velocity variation, in percentage, relative to a reference model. The anomalies are incorporated in two ways: 1) giving the average absolute or relative value of the anomaly over a predefined region beneath the LAB; and 2) varying the absolute or relative magnitude of the anomaly along up to five depth levels beneath the LAB. In the first case, a chemical compositional anomaly can also be assigned to the anomalous region. In the second case, a separate input file including horizontal distances and depth levels together with the anomalous values must be specified. Seismic velocities are non-linear function of temperature because of the non-linear dependence of the anelastic attenuation on temperature (Eqns. 3.2-3.4) and stability of stable mineral phase-assemblages (Chapter 3, Section 2.5). Hence, in order to convert input seismic velocity anomaly (relative or absolute) to temperature, LitMod2D_2.0 looks up for the temperature at the prevailing pressure and adjusted seismic velocities for the input anomaly from the assigned chemical composition material file for the anomalous region. Once seismic velocity anomalies are converted to temperature, they are treated as thermal anomalies (section 3.6.1) and, in case of assigned chemical composition, as a combination of thermal and compositional anomalies (section 3.6.2).

Figure 3.8 shows an example of seismic velocities anomalies at different depth levels below LAB along the profile using a separate input file. This is applicable in regions where seismic tomography depth slices are available. Figure 3.8a show an input file with a relative P-wave seismic velocity anomaly with varying magnitude along the profile at five depths levels, namely 160 km, 250 km, 300km, 350 km and 400 km. In every input file, the level at 400 km, base of the model, must be specified. Lines below the specified depth of each level indicate the anomaly magnitude at each node (distance) along the profile. This allows the user to define a varying magnitude of anomaly along the profile as well in depth by specifying different depth levels. Figure 3.8b shows the resultant variation in temperature, density and absolute seismic velocities (P- and S-wave).

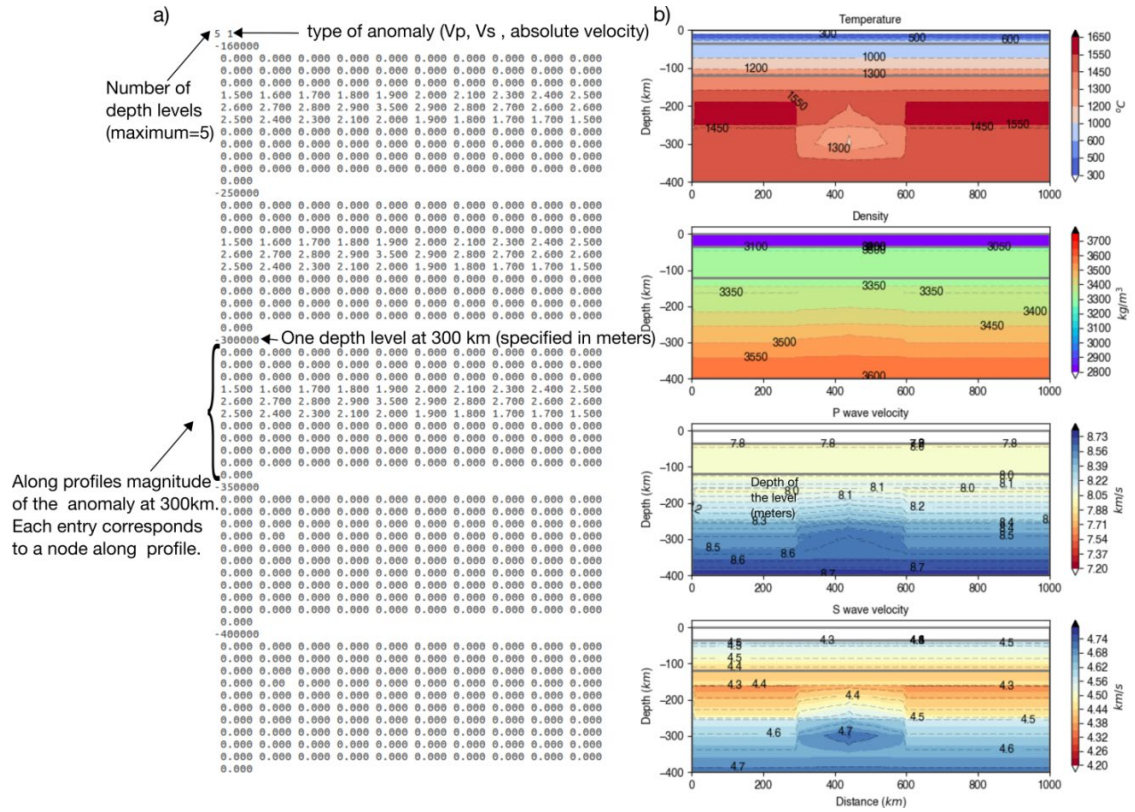


Figure 3.8 Example of a varying magnitude (along the profile) relative P-wave seismic velocity anomaly. (a) Screenshot of the input file used in this synthetic example. (b) Resultant temperature, density and seismic velocities.

Here, I focus on anomalous seismic velocities (V_P and V_S) assigned to a predefined region beneath the LAB and their translation into temperature and densities. I consider relative anomalies of $\pm 1.5\%$ in P- and S-wave velocities below the LAB and discuss the equivalent thermal and density recovery (Figure 3.9). Results show that for a given magnitude of seismic anomaly, 1.5% in the presented example, P-wave translates into a higher temperature anomaly of $\sim 250^\circ\text{C}$ than that from S-wave ($\sim 150^\circ\text{C}$) (Figure 3.9a) which is consistent with the higher sensitivity of S-waves to temperature. In other words, a given temperature change requires a higher percentage variation in the S-wave velocities than in the P-wave velocities as shown in Figure 3.6. Subsequently, density change (Figure 3.9b) is higher ($\sim 0.75\%$) in case of P-wave velocity input than S-wave input ($\sim 0.45\%$). Note that density and temperature changes are not symmetric for positive and negative velocity anomalies. Changes in density depend on the P-T conditions, which control stable phase and mineral assemblages.

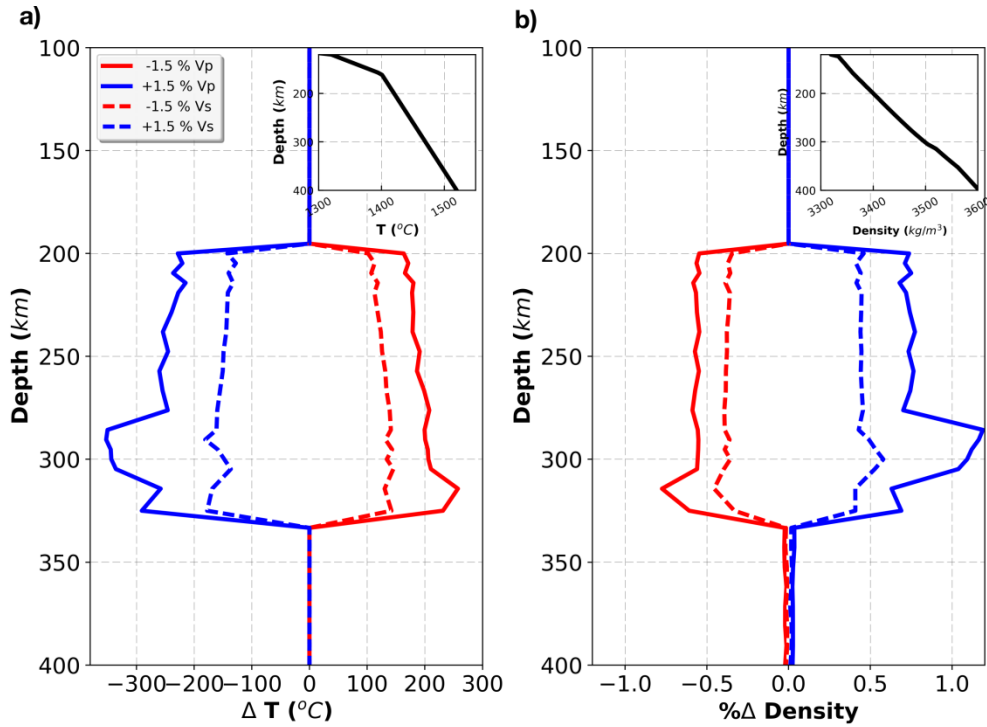


Figure 3.9 Synthetic examples of input P- and S-wave anomalies of $\pm 1.5\%$ in the sublithospheric mantle. Recovered temperature (a) and density (b) from the input seismic velocity anomalies are plotted with respect to the reference model shown in the upper right corner.

3.7. Open source graphic user interface (GUI) and input/output data

To make LitMod2D_2.0 more accessible to users, I have developed an open source GUI in Python, which is not platform depending and can be easily updated/modified by the user. A detailed manual (Appendix A) is provided with the new LitMod2D_2.0 version distributed through online GitHub repository (https://github.com/ajay6763/LitMod2D_2.0_package_dist_users). Here, I briefly discuss the main features. The new GUI allows the organization of different projects in separate folders containing the relevant surface geophysical observables (e.g., elevation, Bouguer and free-air gravity anomaly, geoid height, and SHF) and the material files with thermo-physical properties for each project. Mantle material files are lookup tables of all relevant physical properties (density, thermal conductivities and seismic velocities) as functions of pressure, temperature, and chemical composition. These are computed by the GENERATOR module (Section 3.1) using components of the software Perple_X (Connolly, 2005; 2009). An option to plot previously digitized data on the background (e.g., Moho depths, LAB depths, interpretation from active seismic lines) is also provided.

The GUI main window allows defining the geometry of the model made up of different bodies, each one with its physical properties. Different buttons are provided in the top and bottom of the main window to add and delete bodies, edit properties and shape of bodies, and to run the model (Figure 3.10a). After the run finishes, a window shows up with the geometry of the model and the fit between surface observables and the calculated values (Figure 3.10b, left panel), and the calculated temperature, density, and seismic velocities distributions (Figure 3.10b, right panel). Results are plotted in an interactive Matplotlib environment and can be modified for publication purposes. All the surface observables (elevation, Bouguer and free-air gravity anomalies, geoid height, and surface heat-flow) are saved, and can be used for customized visualization and further processing of the model output. Likewise, a master output file containing the Cartesian coordinates of the grid nodes and the corresponding temperature, pressure, seismic velocities, density, and material file code are saved to be used in the post-processing toolbox according to the particular needs of the user (Section 3.9).

3.8. Application to a synthetic subduction zone

To illustrate the applicability of the new LitMod2D_2.0 package, I performed a synthetic model representing a simplified active margin with a subducting slab and the associated mantle wedge. The objective of this section is to show the functionalities and practicalities of LitMod2D_2.0, as well as the possibilities of the post-processing tool-box rather than studying specific aspects of a real subduction setting.

3.8.1. Input data, model geometry, and physical properties

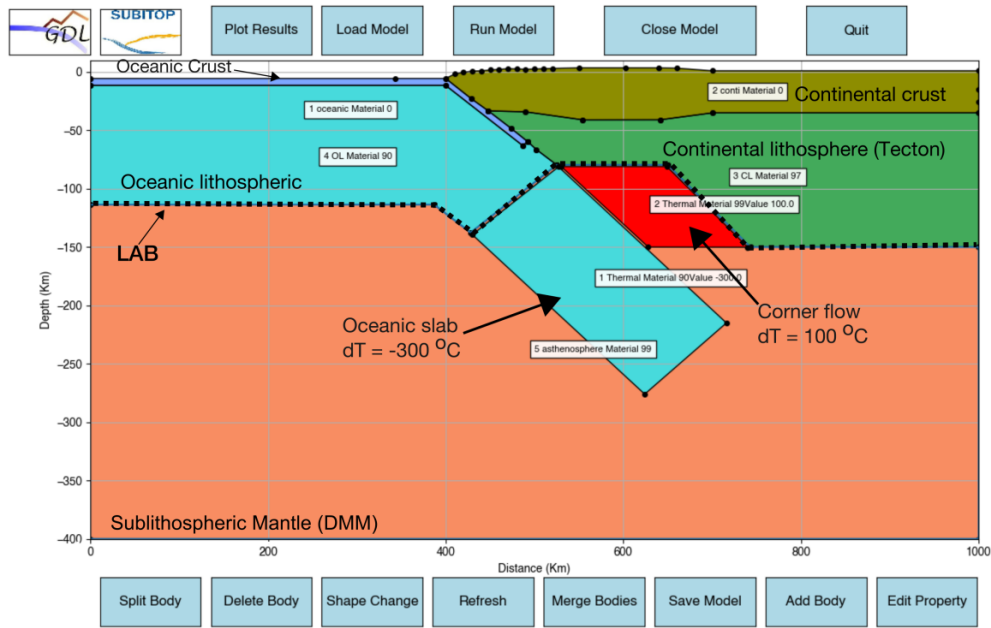
The synthetic model is 1000 km long, and comprises three regions: the oceanic domain, the active subduction zone, and the continental domain (Fig 3.10a). The oceanic domain is characterized by a bathymetry of 5.5 km, and a 6 km thick crust without sediments, and a 100 km thick lithospheric mantle with a composition calculated by 7% fractional melting considering DMM as source. Active subduction zones are characterized by inverted isotherms such that the 1300 °C can be found at three different depths for the same horizontal position, resulting in a triple LAB. This boundary condition cannot be solved by the 2D heat transport equation under steady-state incorporated in the LitMod2D_2.0 code and hence, the subducted oceanic lithosphere is modelled as a sublithospheric thermo-compositional anomaly, with $\Delta T =$

-300 °C and with an oceanic lithosphere chemical composition. Similarly, the mantle wedge is modelled as a sublithospheric thermal anomaly with $\Delta T = +100$ °C. This simple treatment of the active subduction zone allows calculating the average physical properties of the anomalous bodies and their effects on elevation, seismic velocities, and gravity potential field. The stable continental domain consists of a 35 km thick crust and a 115 km thick lithospheric mantle with Average Garnet Tecton composition. Near the subduction zone the crust thickens up to 40 km whereas the lithospheric mantle thins to minimum values of 78 km. For simplicity, I have considered a single crustal layer but the user can add as many layers and bodies as needed through the GUI. Thermo-physical parameters in the crust and chemical composition in the lithosphere mantle are incorporated via GUI and correspond to those listed in Table 3.3 and Table 3.1, respectively.

Figure 3.10b shows a screenshot of the main results window, which includes the calculated and measured surface observables together with the model geometry and the calculated temperature, density and P- and S-wave velocities distribution. The anomalous sublithospheric bodies have a clear signature on the temperature distribution, as they have been defined as thermal anomalies, but also on the calculated density and seismic velocities. In the case of the subducting slab, the combined thermal and compositional anomalies increase density and P- and S-wave seismic velocities, whereas along the mantle wedge, the temperature increase of 100 °C results in a decrease of the three observables.

As the modelled profile is a synthetic model, I have considered that the observed elevation, gravity, geoid and heat flow coincide exactly with the calculated values and an additional run of the model is made without sublithospheric anomalies, all the other parameters unmodified. In this way, I highlight the effect of the sublithospheric anomalies on the surface observables (Figure 3.10b).

a) GUI input window



b) GUI output windows

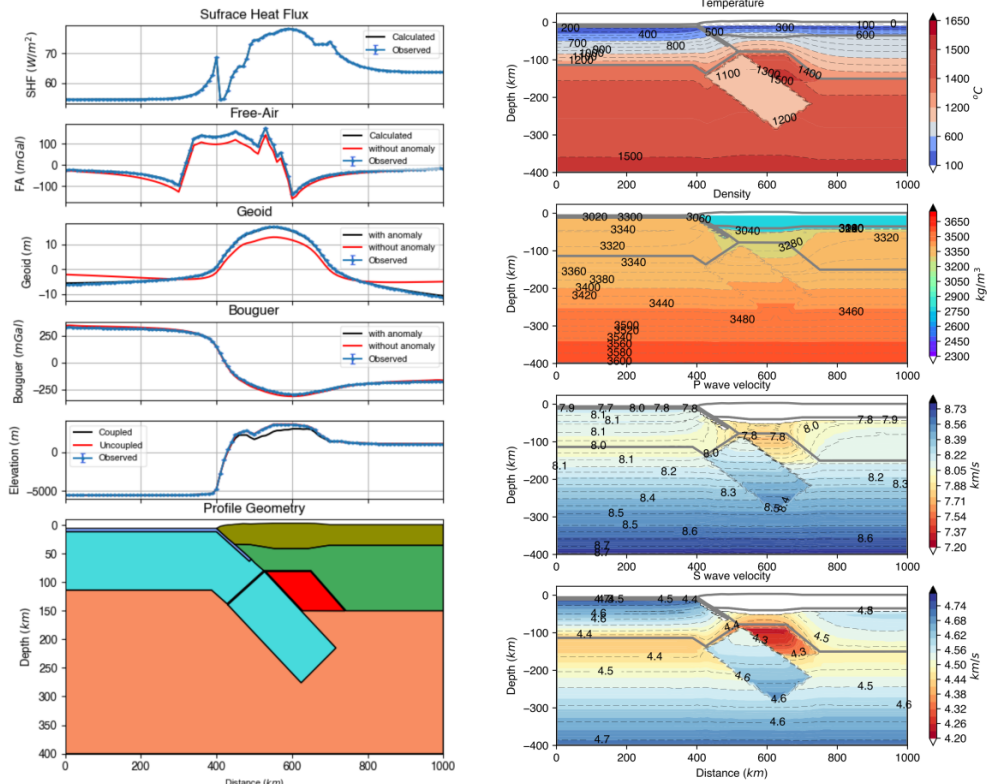


Figure 3.10 Screen shots from the new open-source GUI, provided with LitMod2D_2.0, (a) Graphic user interface input window showing the geometry of the modelled profile and various functions to interact and work with the model. (b) Screenshots of model outputs from the model, in the left panel forward prediction of surface observables, observed (blue) and calculated (red and black) and the model geometry at the bottom. Surface observables without the sublithospheric mantle anomalies are plotted in red to highlight their effect. Right panel in (b) shows the temperature, density and seismic velocity distribution (P-wave and S-wave) from the model.

LitMod2D_2.0 calculates the absolute elevation from the final density distribution, under the assumption of local isostatic equilibrium with a compensation depth at the base of the model (400 km). Lateral density variations beneath the LAB will tend to generate dynamic Stokes flow in the underlying less viscous mantle which can be enhanced by sublithospheric mantle anomalies. Vertical stresses associated with this dynamic flow can be transmitted to the surface topography depending on the viscosity distribution with depth. By default, LitMod2D_2.0 estimates the influence of sublithospheric mantle anomalies on the calculated elevation by considering two end member conditions representing the upper and lower bounds of the dynamic topography contribution (Carballo et al., 2015b; Tunini et al., 2016; Jiménez-Munt et al., 2019): 1) coupled elevation, when the vertical stresses induced by the buoyancy of sublithospheric mantle anomalies are completely transmitted to the surface; and 2) uncoupled elevation, when sublithospheric mantle anomalies have no effect on topography. In the synthetic model presented here, the net effect of the sublithospheric anomalies on elevation is of ≤ 1000 m (Fig 3.10b). In the case of coupled anomalies, the cold slab near the subduction zone pushes down the elevation because of its higher density. The relatively lower density of the mantle wedge does not suffice to cancel the negative slab buoyancy. Density perturbations from the cold subducted slab and the hot corner flow primarily affect the geoid height and free-air gravity anomaly across the model whereas Bouguer anomaly is slightly affected. This is because geoid is sensitive to the density moment which in the modelled synthetic profile is mainly related to the topography and the sublithospheric anomalies. Free-air is very sensitive to topography and in a less extent to sublithospheric anomalies due to the inverse square law dependence; whereas Bouguer anomaly is also depending on the inverse square law but corrected for topography effects and then, is essentially sensitive to lateral crustal density variations.

3.9. Post-processing toolbox

The main idea of the post-processing toolbox is that from the obtained parameters characterizing the physical state of the crust and upper mantle (pressure, temperature, density, P- and S-wave seismic velocities, and material type) at each node, the user can further process these data to do a variety of additional calculations, such as strength envelopes, flexural effects on elevation, Stokes flow, distribution of stable mineral-assemblages, synthetic passive seismological data, etc. The post-processing toolbox is a set of independent scripts/codes linking the LitMod2D_2.0 master output with other software (Figure 3.1). The user can use, adapt or create new

scripts or codes according to her/his own interest and needs and can add them to the GitHub (https://github.com/ajay6763/LitMod2D_2.0_package_dist_users) for the community to use.

3.9.1. Seismic velocities post-processing example

The following example illustrates the potential of the post-processing toolbox focused, in this case, on the calculation of synthetic seismic tomography and synthetic passive seismological data. Post-processing of seismic velocities is done in the light of non-uniqueness and variability in the tomography models, as discussed in Foulger et al. (2013).

I provide shell scripts to compute synthetic tomography from the LitMod2D_2.0 seismic velocities, using the reference model defined in section 3.5. For the presented synthetic example, maximum positive anomalies are observed along the oceanic lithosphere, whereas the thinned continental lithosphere above the subducted slab results in negative velocity anomaly (Figure 3.11a). Thick continental lithosphere results in positive velocity anomaly but with smaller magnitude relative to the oceanic lithosphere. In the sublithospheric mantle, the subducted slab and corner flow regions result in positive and negative velocity anomalies, respectively, and the rest of the sublithospheric mantle show no deviation from the reference model.

Joint inversion of receiver-functions and surface-wave dispersion has been widely used to image major velocities discontinuities and absolute seismic velocity distributions with depth (e.g., Julià et al., 2000; Langston, 1979; Vinnik, 1977). P-wave receiver functions are sensitive to the S-wave velocity discontinuities where P-to-S converted waves sample the subsurface discontinuities, whereas surface-waves are sensitive to the average S-wave velocities distribution.

LitMod2D_2.0 gives the depth distribution of absolute P- and S-wave velocities from a structural (e.g., Moho and LAB geometries), thermal and chemical composition model. Hence, comparing observed surface-wave dispersions and P-wave receiver functions with those inferred from LitMod2_2.0 can further constrain the obtained models. This is done by coupling the calculated P- and S-wave seismic velocities from LitMod2D_2.0 with the 'Computer Programs in Seismology' tool by Herrmann (2013) through Shell and Python scripts to calculate synthetic Rayleigh-surface-wave dispersion curves and P-wave receiver functions. Within the crust, P-wave velocities are calculated using empirical V_P -density relationships from Brocher (2005), whereas S-wave velocities are calculated assuming a constant input of $V_P/V_S = 1.73$ (Fig 3.11b).

Indeed, an option including crustal material files is kept for future or if user have a thermodynamic database for the crustal chemical composition (e.g., Diaferia and Cammarano, 2017). Below 400 km depth (base of the model), velocities from ak135 model are used.

The depth distributions of the resulting S-wave velocity at three locations along the synthetic profile are shown in Figure 3.11b corresponding to: a) ocean (300 km), b) subduction zone (500 km), and c) continent (950 km). Synthetic P-wave receiver functions (Figure 3.11c) show a clear positive converted phase (P_s , black) at Moho discontinuity, which arrives earlier for oceanic domain because of the lower crustal thickness, and is delayed for thick continental crust. Each of the converted phase at Moho (P_s) has a positive phase (P_{pps}) and a negative phase (P_{pss}) multiples which are helpful in determining whether the P_s phase corresponds to a velocity discontinuity. Rayleigh group and phase velocities (Figure 3.11d) are faster for the oceanic domain than for the continental domain because of the high S-wave velocities of the oceanic lithosphere at lithospheric depths (Figures 3.11b and 3.10b). At short periods, velocities are lower than at higher periods because shallow structures (slow velocities) are more sensitive to surface waves at short time periods. Group velocities show an absolute maximum, whereas phase velocities show relative maxima increasing for higher periods. This behaviour is because of the differential depth sensitivity of group and phase velocities. For the oceanic domain the maxima of group velocities is at ~ 25 s, whereas for the subduction zone and the continental domains maxima is reached at ~ 75 s. Phase velocities show a local maxima which is shifted towards lower periods relative to the maximum of group velocities. The effect of lithosphere thickness is observed in the continental domain showing higher velocities (both group and phase) in regions with thick lithosphere than in the thin lithosphere near the subduction zone. The effect of the cold subducted slab is clearly visible in both group and phase velocities (black dashed line), where maxima for group velocities (local maxima in case of phase velocities) has been shifted towards high periods and velocities are increased in comparison to dispersion curves without slab.

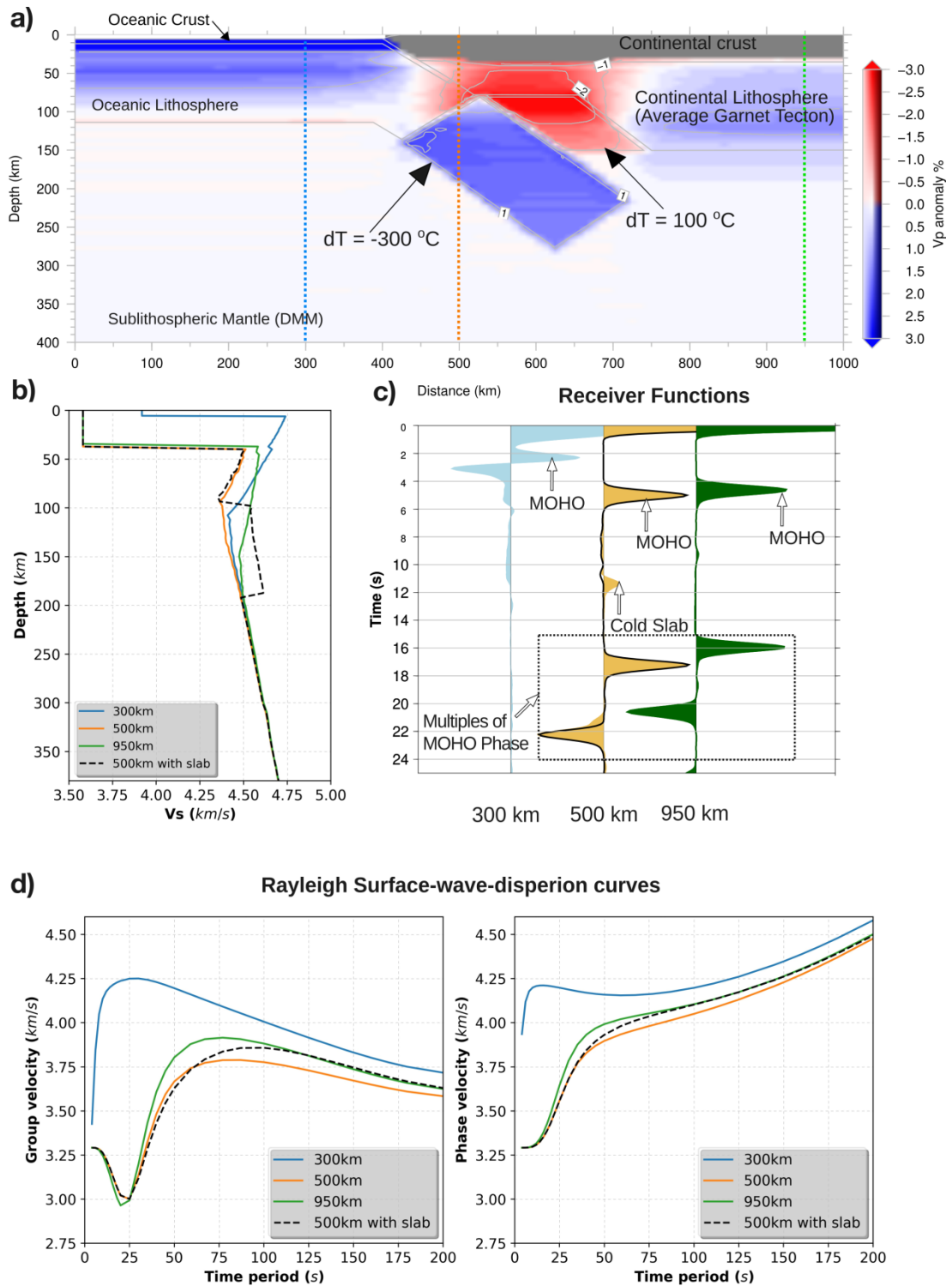


Figure 3.11 Example of seismic velocities post-processing. (a) Synthetic P-wave tomography along the modelled synthetic profile. (b) Depth distribution of S-wave velocities at three locations along the profile with colour coded and marked in (a). (c) Synthetic P-wave receiver functions at the three locations marked in (a). At the subduction zone two receiver functions with (filled orange) and without (black line) the subducted slab, are plotted for comparison. (d) Synthetic Rayleigh-surface-wave group (left) and phase (right) velocities. At the subduction zone orange dispersion curves corresponds to the model without the slab and dashed-black line to the model with the slab.

3.9.2. Depth distribution of stable mineral-assemblages

I provide a collection of Python and bash-shell scripts to plot the depth distribution of volume fraction, weight%, density, and seismic velocities of stable mineral-assemblage in LitMod2D_2.0. These scripts look for the stable mineral assemblages, at the pressure and temperature conditions along the profile, in the extended material files. Extended material files are produced by opting for the full property and system option in the GENERATOR module (Appendix A). Options for depth distribution of all minerals at a distance point (Figure 3.12), or depth distribution of individual mineral along the profile (Figure 3.13), are provided. Figure 3.12 shows an example of stable mineral distribution with depth for the reference model defined in section 3.5. Major discontinuities in the upper mantle (Moho and LAB) are manifested by changes in stable mineral weight percentages. Plagioclase and spinel are stable in the shallow part of the lithosphere and constitute few weight percentage of the total. Olivine constitutes most of the upper mantle, about ~60 weight%. The weight% increases with depth for garnet, whereas it decreases for orthopyroxene which almost disappears at around 310 km. Clinopyroxene weight% varies from around 13–10% in the upper mantle.

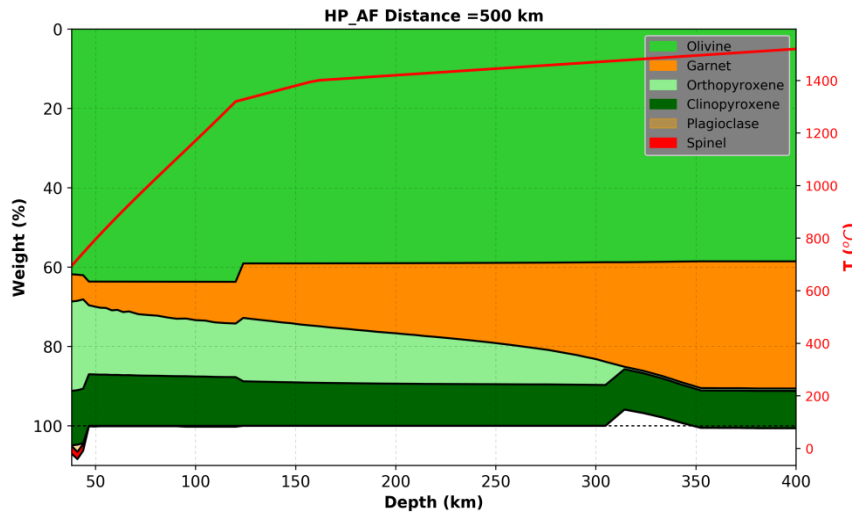


Figure 3.12 Weight% of different stable minerals with depth for the reference model defined in LitMod2D_2.0 (section 3.5). Note that total weight% does not add to 100% in the shallow lithosphere (< 50 km) and around 300 km; this could be because of the failed numerical energy minimizations during the computation of stable mineral assemblage, although difference is only about <5%.

CHAPTER 4

Present-day crust and upper mantle structure of the Alboran and Algerian basins and their margins

Chapter 4

Present-day crust and upper mantle structure of the Alboran and Algerian basins and their margins

In this chapter, I present the modelling results of the present-day crust to upper mantle (~400 km depth) structure along two NNW-SSE oriented geo-transects in the Alboran and Algerian basins (Figure 4.1a). Improved LitMod2D_2.0 presented in Chapter 3 (Kumar et al., 2020) is used to model the temperature, density (i.e., chemical composition) and seismic velocity distribution by combining surface geology, elevation, Bouguer anomaly, geoid height, SHF and mantle xenoliths data in a self-consistent thermodynamic framework.

The Alboran Basin geo-transect is presented for the first time while the Algerian Basin geo-transect follows the TRANSMED-II profile, that was modelled using a thermal approach (Roca et al., 2004), and later refined in Carballo et al. (2015a) using integrated geophysical-petrological modelling. Although the regional structure of the lithosphere across the region has already been studied by Carballo et al. (2015a,b) and Fullea et al. (2010), I focus here on more detailed structure of the Betics and Greater Kabylies belts and offshore regions (i.e. Alboran and Algerian basins) using the new LitMod2D_2.0 version. LitMod2D_2.0 allows to model thermal/seismic/compositional sublithospheric mantle anomalies (Chapter 3), thus allowing to incorporate the well imaged positive seismic velocity anomalies in the high resolution tomography, beneath the Betics (Figure 4.1b; Palomeras et al., 2017; Villaseñor et al., 2015; Bezada et al., 2013; Spakman and Wortel, 2004), and the Kabylies (Figure 4.1; Fichtner and Villaseñor, 2015). The models presented here also integrate the latest geophysical results along the Algerian margin of NW Africa, mainly new active seismic data (e.g., SPIRAL, Aïdi et al., 2018), and the Moroccan margin (Gómez de la Peña et al., 2018).

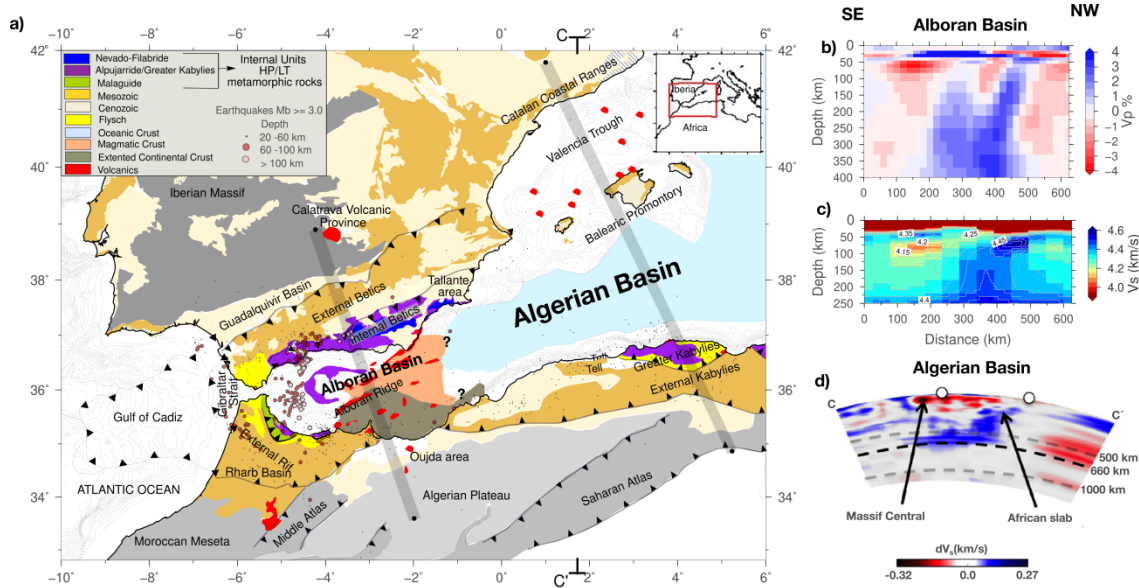


Figure 4.1 (a) Simplified geological map of the study region showing the location of the Alboran and Algerian basin geo-transects in shaded grey line. Earthquakes location colour coded for depth from 1964-2016 taken from International Seismological Centre (ISC, <https://doi.org/10.31905/D808B830>) catalogue are also plotted. (b) P-wave travel-time tomography along the Alboran Basin geo-transect from Bezada et al. (2013). (c) Absolute S-wave velocity model from Rayleigh surface-wave dispersion tomography (Palomeras et al. 2014) along the Alboran Basin geo-transect. (d) S-wave tomography using full-waveform inversion (modified after Figure 8 of Fichtner and Villaseñor, 2015) along the direction of cross-section C-C' marked in (a).

4.1. Data

4.1.1. Regional geophysical data

Elevation data from ETOPO1 (Amante and Eakins, 2009), a global elevation model of the Earth surface with 1x1-min arc resolution available on the NOAA website (National Oceanic and Atmospheric Administration, <http://www.ngdc.noaa.gov/mgg/global/global.html>) is used (Figure 4.2a). The Bouguer gravity anomaly data comes from a recent compilation of gravity data in Iberia (Ayala, et al., 2016) (Figure 4.2b). For the rest of Africa and offshore regions, it is calculated by applying the complete Bouguer correction to free air satellite data (Sandwell and Smith, 1997), updated 2007) using the software FA2BOUG (Fullea et al., 2008) with a density reduction of 2670 kg/m³. Geoid height data come from ICGEM (Ince et al., 2019; <http://icgem.gfz-potsdam.de>) where GECO model (Gilardoni et al., 2016) is used (Figure 4.2c). Geoid data is filtered up to degree and order 10, to retain geoid anomalies coming from lateral density variations within the crust and upper mantle to ~400 km depth (Chapter 2, Section 2.3.2). SHF measurements have been compiled

from Poort et al. (2020) in the Algerian Basin, Rimi et al. (2005) in Morocco, Marzán (2000) and Fernández et al. (1998a) in Iberia, Polyak et al. (1996) in the Alboran Basin, Foucher et al. (1992) in the Valencia Trough, and the International Heat Flow Commission global data set for Algeria (<http://www.heatflow.und.edu/index2.html>) (Figure 4.2a).

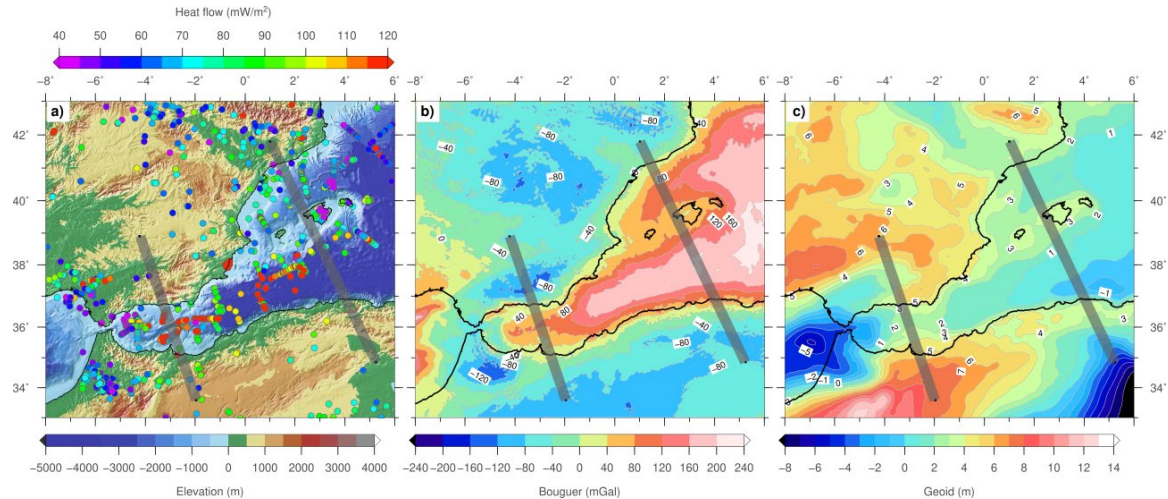


Figure 4.2 Geophysical observables in the region. (a) Shaded elevation and surface heat flow (dots), (b) Bouguer anomaly, (c) geoid filtered up to degree and order 10. Grey thick lines show the locations of the modelled NNW-SSE oriented geo-transects.

Alboran Basin geo-transect

In onshore Iberia, elevation increases from 500 m in the Iberia Massif to as much as ~2500 m in the eastern Internal Betics, coinciding with a decrease of the Bouguer anomaly to values of -120 mGal. Geoid height also decreases from 6–7 m in the SW Iberian Massif to 3–0 m in the western Betics and the Guadalquivir Basin, respectively. A local geoid high of 6 m is observed in the eastern Internal Betics where elevation attains its maximum values (Figure 4.2). The Alboran Basin shows positive Bouguer anomalies, except in its westernmost end where large accumulations (up to 8–9 km) of Oligocene to Recent sediments are recorded. An ENE-WSW relative high delineates the central region of the basin, attaining values of up to 160 mGal in its easternmost end, in the transition to the oceanic crust of the Algerian Basin. Along the geo-transect, Bouguer anomalies decrease asymmetrically from the axis of the basin to the onshore regions. While to the Iberian margin there is a rapid decrease of the anomalies, towards the African margin there is a gentler decrease towards the Algerian Plateau where values of -90 mGal are achieved (Figure 4.2b). The Alboran

Basin shows a geoid high (~ 3 m) in its central region that asymmetrically decreases to the east and west, increasing in an N-S direction, with values of 5–6 m in onshore Iberia and >7 m in the Algerian Plateau (Figure 4.2c). The N-S geoid high delineates the magmatic arc region and the North African continental margin block and separates the prominent geoid low associated with the Gulf of Cadiz accretionary wedge and the fore-arc West Alboran Basin from the Algerian oceanic back-arc basin. Interestingly along the geo-transect, geoid height and elevation follow a similar regional trend, characterized by a rapid increase from the centre of the basin to the Internal Betics with local highs of 6 m and >2000 m, respectively, and a smoother increase towards the Algerian Plateau, where geoid and elevation attain values of up to 8 m and 1000 m, respectively. On the contrary, the Bouguer anomaly does not record a similar local high and instead there is a rapid decrease from the gravity high of central Alboran Basin to the gravity low of the Internal Betics. SHF data, though sparse, shows relatively higher values in the Alboran Basin increasing from west to east into the Algerian Basin (Figure 4.2a). Onshore Iberia shows lower SHF (~ 48 mW/m²) than the onshore north Africa (~ 100 mW/m²).

Algerian Basin geo-transect

In the interior regions of the Tell Mountains and Salt Waters Lakes, elevation ranges from 500 m to 1000 m, with a local low located at the SSE end of the geo-transect, whereas Bouguer anomalies are in the range of -40 mGal to -80 mGal decreasing towards the Saharan Atlas. Geoid shows values of ~ 3 –4 m in the Tell Mountains that rapidly decrease to the SE where a prominent regional geoid low is located (Figure 4.2c). Along the geo-transect, local highs of elevation and Bouguer anomaly are observed in the Greater Kabylies and Tell Mountains, which coincide with a geoid regional high. The Bouguer anomaly increases abruptly from 60–80 mGal close to the shoreline, to above 160 mGal in the central regions of the Algerian Basin indicating the pronounced crustal thinning along the continental slope and slope break, and the oceanic nature of the crust in the central Algerian Basin. Elevation and geoid abruptly decrease to reach values of < -3000 m and 0–1 m, respectively, in the slope break, values that characterize the central regions of the basin.

A very abrupt increase of elevation is observed along the Emile-Baudot escarpment that marks the southeast side of the Balearic Promontory, a ~ 350 km long and 105–155 km wide topographic feature with an average elevation of 500 m that separates the Valencia Trough to the northwest, from the Algerian Basin to the southeast. The Promontory is characterized by a smooth decrease of the Bouguer

anomaly and an increase of geoid heights (Figure 4.2b and c). Elevation and geoid decrease towards the central region of the Valencia Trough coinciding with an increase of the gravity anomalies indicating the presence of a thinned continental crust. SHF data exhibit a wide scatter around a mean value of 65 mW/m² onshore eastern Iberia, increasing to 70–90 mW/m² in the Valencia Trough, and decreasing again to the Balearic Promontory, where measurements are strongly affected by shallow groundwater circulation (Fernández and Cabal, 1992). SHF data show a very poor coverage in the Algerian Basin and onshore Africa along the geo-transect. Nevertheless, seafloor heat flow measurements carried out in the western Algeria Basin show values ranging from 90–120 mW/m² (Marzán Blas, 2000) (Figure 4.2a). In summary both basins show a rather similar regional pattern of the surface observables, the main difference being their amplitude that reflects the different stages of their evolution. While back-arc extension in the Algerian Basin progressed to the onset of new oceanic crust, in the Valencia Trough extension resulted in noticeable crustal thinning that progresses in a SW-NE direction towards the Ligurian-Provencal Basin.

4.1.2. Crustal data

Thermo-physical properties in the crust are taken from the previous studies and are listed in Table 4.1. The initial crustal geometry along the geo-transects is based on geological maps and cross-sections, and active and passive seismology experiments. Along the Alboran Basin geo-transect, the crustal structure in the Iberian Massif is mainly based on the ALCUDIA2 Wide-Angle Seismic Reflection Transect (Ehsan et al., 2015). In the Guadalquivir Basin and Betics (Internal and External), seismic data come from different experiments (e.g., Banda et al., 1993; Carbonell et al., 1997; Comas et al., 1995; Gallart et al., 1995) and geological cross-sections (e.g., Ruiz-Constan et al., 2012; Frizon de Lamotte et al., 2004; Platt et al., 2003; Michard et al., 2002; Berástegui et al., 1998; Banks and Warburton, 1991). Crustal data in the Alboran Basin and the North Africa margin come from active seismic lines processed and interpreted in Gómez de la Peña et al. (2018). In addition to these data, the Moho depth along the geo-transect is also constrained by the active and passive seismic data compilation (Diaz et al., 2016), joint inversion of elevation and gravity (Globig et al., 2016; Torne et al., 2015), surface wave dispersion tomography (Palomeras et al., 2017) and previous integrated geophysical-petrological modelling (Carballo et al., 2015a, b; Fullea et al., 2010) (Figure 4.3a).

Table 4.1 Thermo-physical properties of the different tectonic units in the crust along the geo-transects.

Tectonic units		Density (kg/m ³)	Thermal Conductivity (W/K·m)	Radiogenic Heat Production (μW/m ³)
Sediments	Neogene	2400	2.2	1.00
	Neogene/Mesozoic	2600	2.4	1.00
	Mesozoic sediments	2650	2.5	1.00
Betics	Nevado-Filabride	2900	2.5	1.00
	Alpujarride	2850*	2.5	1.00
	External Units	2600*	2.5	1.20
Greater Kabylies	Internal Units	2900*	2.5	1.00
	External Units	2600*	2.5	1.20
Continental crust	Upper crust	2750	2.4	1.65
	Middle crust	2850	2.1	0.50
	Lower crust	2950	2.0	0.20
Volcanic crust		2820	2.1	0.20
Oceanic crust		2950	2.5	0.30

*Calculated as a function of depth to incorporate pressure dependence. Densities are assigned according to previous studies (e.g., Carballo et al., 2015a, b) and using velocity-density envelopes defined in Brocher (2005). The densities of the HP/LT units result from modelling (Figure 4.4). Thermal conductivities are taken from previous studies (e.g., Carballo et al., 2015a,b; Torne et al., 2000, 2015; Teixell et al., 2005; Zeyen et al., 2005), and radiogenic heat production comes from direct measurements in the Iberian Massif and Betics (Fernández et al., 1998b) and a global compilation of relevant crustal rocks (Vilà et al., 2010).

The crustal geometry along the Algerian Basin geo-transect, except for the onshore northern Africa margin, is well known from the numerous deep seismic reflection and wide-angle/refraction geo-transects collected during the last decades (Figure 4.3b). Moho depths for the Valencia Trough and Balearic Promontory are taken from Torne et al. (1992) and Pascal et al. (1992), while the crustal structure is summarized in TRANSMED-II transect (Roca et al., 2004) and Carballo et al. (2015a). For the sake of completeness, original seismic data come from VALSIS-II (Torne et al., 1992), ESCI-Valencia (Vidal et al., 1998), Hinz (1972), and ALE-4 (an industry transect) in the Algerian Basin. In the North Africa margin, crustal structure is taken from the SPIRAL active seismic experiment (Aïdi et al., 2018) and further south from the geological cross-section by Frizon de Lamotte et al. (2011). Onshore, in the

Catalan Coastal Ranges, receiver function and deep seismic sounding Moho depths are taken from Diaz et al. (2016).

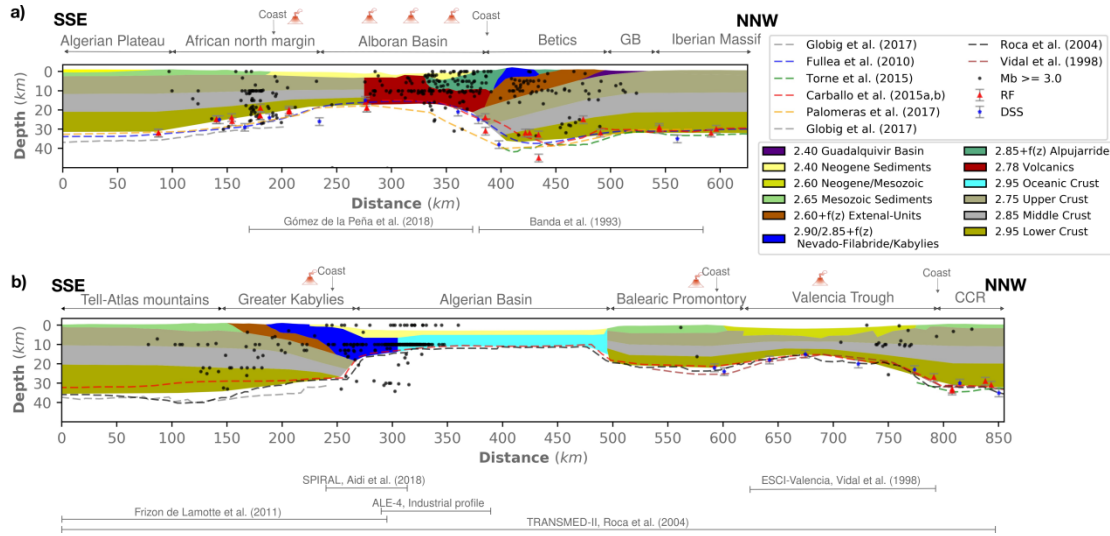


Figure 4.3 Crustal structure corresponding to the best fitting model for the (a) Alboran Basin and (b) Algerian Basin geo-transects. Densities used in each body are colour-coded (see the legend). Moho depths from previous studies (including active seismic, receiver functions, surface wave dispersion and joint modelling of gravity and elevation) are also plotted for comparison. Earthquakes ($M_b \geq 3.0$; 1964-2016, ISC catalogue) projected 50 km across the geo-transects are plotted with black circles. Note that the y-axis is exaggerated by two times the x-axis for better visualization. GB, Guadalquivir Basin; CCR, Catalan Coastal Ranges; RF, Receiver functions; DSS, Deep seismic sounding.

4.1.3. Mantle structure and chemical composition

The depth to the base of the lithosphere (LAB), the chemical composition of the defined lithospheric domains, and the sublithospheric mantle anomalies are constrained by available tomography studies, geochemical analyses from mantle xenoliths and exhumed rocks, and previous modelling results. Initial LAB depths along the geo-transects come from previous 2D and 3D lithospheric models using elevation, gravity and geoid height, based on pure thermal and geophysical-petrological approaches (e.g., Carballo et al., 2015a, b; Fulla et al., 2010; Globig et al., 2016; Torne et al., 2015) and, in the case of the Alboran Basin geo-transect, also from the regional seismic tomography model by Palomeras et al. (2017).

Table 4.2 Major elements composition (weight %) in the NCFMAS system for the lithospheric mantle and sublithospheric domains used in the modelling and corresponding relevant physical properties at lithosphere and sublithospheric mantle pressure and temperature.

Name	SiO ₂	Al ₂ O ₃	FeO	MgO	CaO	Na ₂ O	#Mg	ρ (kg/m ³)		V _P & V _S (km/s)	
								P=3GPa (~100km) T=1300 °C	P=6GPa (~200km)T =1400°C	P=3GPa (~100km)T =1300 °C	P=6GPa (~200km) T=1400°C
PUM	45.00	4.50	8.10	37.80	3.60	0.360	89.3	3310	3396	7.986 4.441	8.254 4.523
DMM	44.70	3.98	8.18	38.73	3.17	0.130	89.4	3307	3391	7.950 4.396	8.232 4.491
DMM - 3%*	44.59	3.51	8.21	39.63	3.02	0.007	89.6	3300	3385	7.936 4.390	8.222 4.488
DMM - 6%*	44.47	3.08	8.23	40.54	2.78	0.051	89.7	3294	3378	7.929 4.388	8.211 4.484
DMM - 7% *	44.43	2.97	8.23	40.78	2.70	0.045	89.8	3293	3376	7.927 4.388	8.209 4.484
Tc_1	44.50	3.50	8.00	39.79	3.10	0.240	89.8	3296	3381	7.934 4.391	8.213 4.488
Pr_6	45.40	3.70	8.30	39.90	3.20	0.260	90.6	3299	3385	7.931 4.388	8.213 4.486
CVP	44.51	3.76	8.75	37.89	3.28	0.360	91.0	3309	3395	7.909 4.374	8.194 4.473

*Calculated using melting model described in Chapter 2, Section 2.8. PUM, Primitive Upper mantle (McDonough and Sun, 1995); DMM, Depleted mid-oceanic-ridge-basalt Mantle (Workman and Hart, 2005); Tc_1, Average Garnet Tecton (Griffin et al., 2009); Pr_6, Average Proton Lherzolite (Griffin et al., 2009; Le Roux et al., 2007); CVP, Calatrava Volcanic Province (Villasaca et al., 2010)

In the onshore regions (Iberia and north Africa) lithospheric mantle compositional domains are taken from the previous studies in the same zone, which are based on mantle xenoliths, exhumed mantle rocks or tectono-thermal age of the crust (e.g., Jiménez-Munt et al., 2019; Carballo et al., 2015a,b; Fullea et al., 2010; Griffin et al., 2009). In the Algerian and Alboran basins, the Valencia Trough, and the Kabylies and Betics, mantle chemical composition is calculated from the major oxides partition as a function of aggregate melting using the empirical formulation of Niu (1997), as discussed in Chapter 2.

4.2. Alboran Basin geo-transect: structure, temperature, and density

4.2.1. Crustal and upper mantle structure

The crust of the Iberian and African mainland and their margins has been modelled using a three-layer crustal model; upper, middle and lower crust (Table 4.1 and Figure 4.3a). In the Iberian Massif the crust is ~32 km thick which is consistent with previous studies and thickens up to ~37 km below the Internal Betics over a distance of 100 km. The Guadalquivir foreland basin, reaches a maximum depth of 4 km close to the Betic fold belt front. The structure of the External Betics is constrained by low seismic velocity anomalies at crustal levels as observed in tomography models (Moudnib et al., 2015; Carbonell et al., 1998), while the structure of the Nevado-Filabride and Alpujarride Internal Units are mainly defined from geological observations (Figure 4.3a). These two tectonically stacked HP/LT Betics Internal Units are defined as high density tectonic nappes according to P-T conditions of their metamorphic facies and densities of their basement and cover protoliths after metamorphic peaks (e.g., Gómez-Pugnaire et al., 2019) (Figure 4.4). The Nevado-Filabride, at the base of the thrust sheet pile, forms an open and elongated dome that is overlaid to the N by the Alpujarride thrusts. To the SSE, the Alpujarride Unit is slightly dipping towards the Alboran Basin and thus forming the basement of the Neogene sedimentary infill in the proximal Iberian margin. The crust of the Alboran Basin is modelled as a highly intruded volcanic domain cropping out near the Alboran Ridge (Gómez de la Peña et al., 2018). The thinnest crust along the whole geo-transect is found in the Alboran Basin with Moho depths of 16–17 km being consistent with previous estimates (Figure 4.3a). Southeast of the Alboran Ridge, the crust is interpreted as African continental crust of about 18 km thickness, with thinning localized mainly at mid- and lower-crustal levels (Gómez de la Peña et al., 2018). Moho depth increases gradually southwards from 17 km to 31 km across the North Africa margin (Figure 4.3a).

Present-day crust and upper mantle structure of the Alboran and Algerian basins

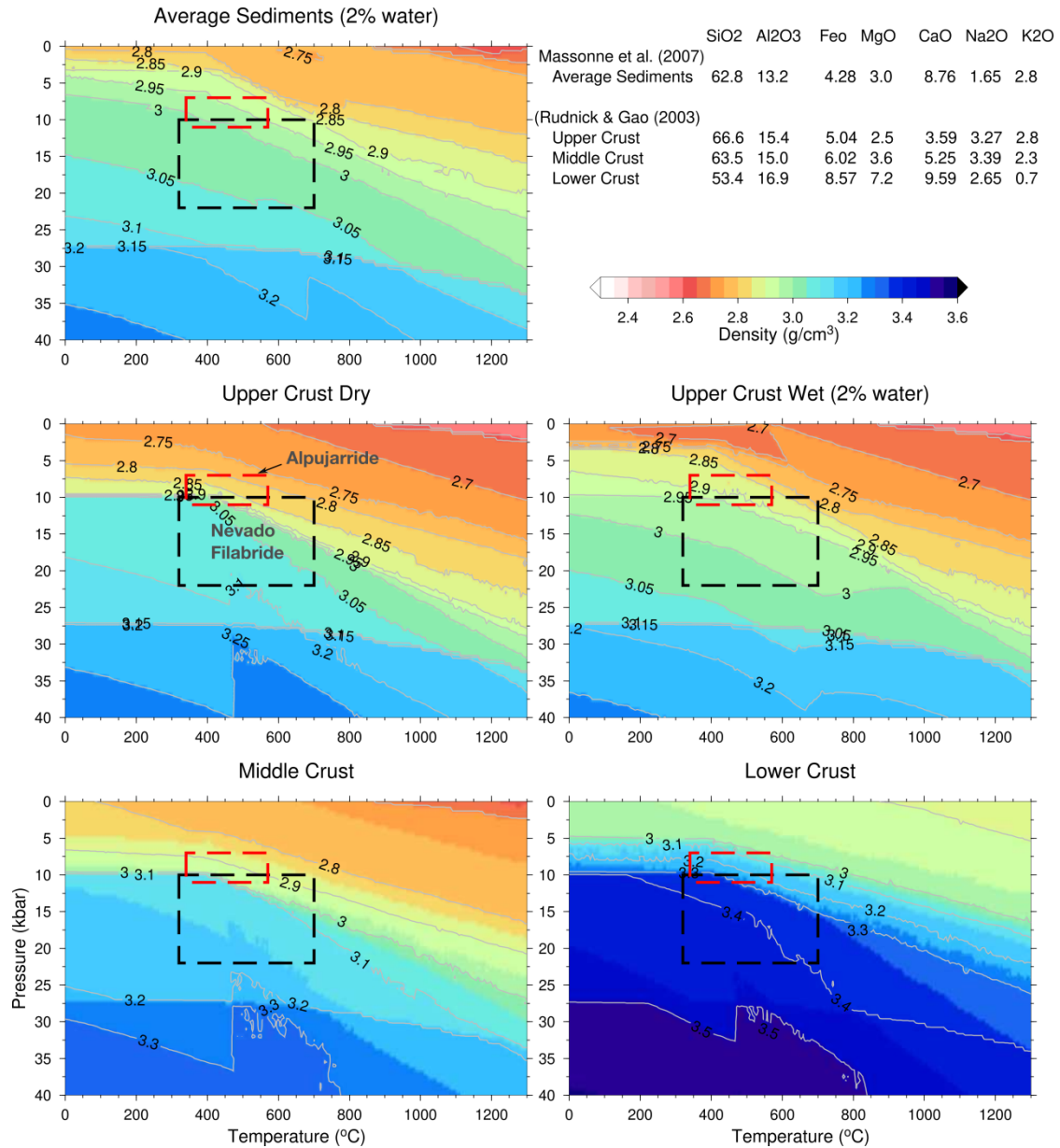


Figure 4.4 Pressure and temperature dependent density distribution for average sediments, upper crust, middle crust and lower crust compositions (see legend), computed from stable phases and mineral assemblages using the Gibbs free-energy minimization algorithm (Connolly, 2005, 2009). Red and black dashed line boxes mark the range of high pressure metamorphic peaks for Alpujarride and Nevado-Filabride HP/LT metamorphic units, respectively, determined from thermo-barometry (Augier et al., 2005; López Sánchez- Vizcaíno et al., 2001; Puga et al., 2000; Azañón and Crespo-Blanc, 2000).

Three different chemical composition domains are deemed within the lithospheric mantle along the Alboran Basin geo-transect (Table 4.2 and Figure 4.5). For the Iberian lithosphere, a depleted composition is considered which is taken from mantle xenoliths sampled in the Calatrava Volcanic Province (CVP, Villaseca et al., 2010) as in Jiménez-Munt et al. (2019). In the Alboran Basin, the lithospheric mantle

composition corresponds to the residual of 6% aggregate decompressional melting of DMM based on the pervasive magmatic intrusion related to the retreat of the Alboran slab. This chemical domain extends also beneath the Betics as a result of the NNW directed slab roll-back and associated mantle delamination (Figure 4.5). In the North African margin and the Algerian Plateau, the composition of the lithospheric mantle corresponds to Average-Garnet-Tecton, an average Phanerozoic mantle composition (Tc_1; Griffin et al., 2009), in agreement with previous models on the region (e.g., Carballo et al., 2015a; Fullea et al., 2010). The LAB depth is ~110 km beneath the stable Iberian Massif increasing to ~130 km beneath the Betics and decreasing abruptly to ~64 km towards the Alboran Basin from where the LAB deepens gently beneath the North African margin down to ~112 km below the Algerian Plateau (Figure 4.5e).

Seismic tomography models show a positive velocity anomaly beneath the Betics that amounts ~2–3 % in P-wave relative to the ak135 global velocity model (e.g., Garcia-Castellanos and Villaseñor, 2011; Bezada et al., 2013; Villaseñor et al., 2015) and an excess of 0.15-0.3 km/s in S-wave (e.g., Palomeras et al., 2014,2017; Civiero et al., 2018). This anomaly extends down to 670 km depth and has been interpreted as the Tethyan subducted lithosphere that is detached from the Iberian lithosphere along a lateral tear affecting the region crossed by the geo-transect (e.g., Spakman and Wortel, 2004; Garcia-Castellanos and Villaseñor, 2011; Bezada et al., 2013; Palomeras et al., 2017) (Figures 1.4, 4.1b and 4.1c). Consequently, I have considered a sublithospheric mantle anomaly situated below 140 km depth simulating the detached Alboran slab characterized by a P-wave velocity anomaly of $\Delta V_P = +2\%$ and using the residual composition after 3% aggregate melting from DMM (DMM-3%; Figure 4.5). I have tested different possible chemical compositions for the Alboran slab ranging from pure oceanic lithosphere to CVP (Table 4.3 and Figure 4.6), DMM-3% being the one with the best-fitting

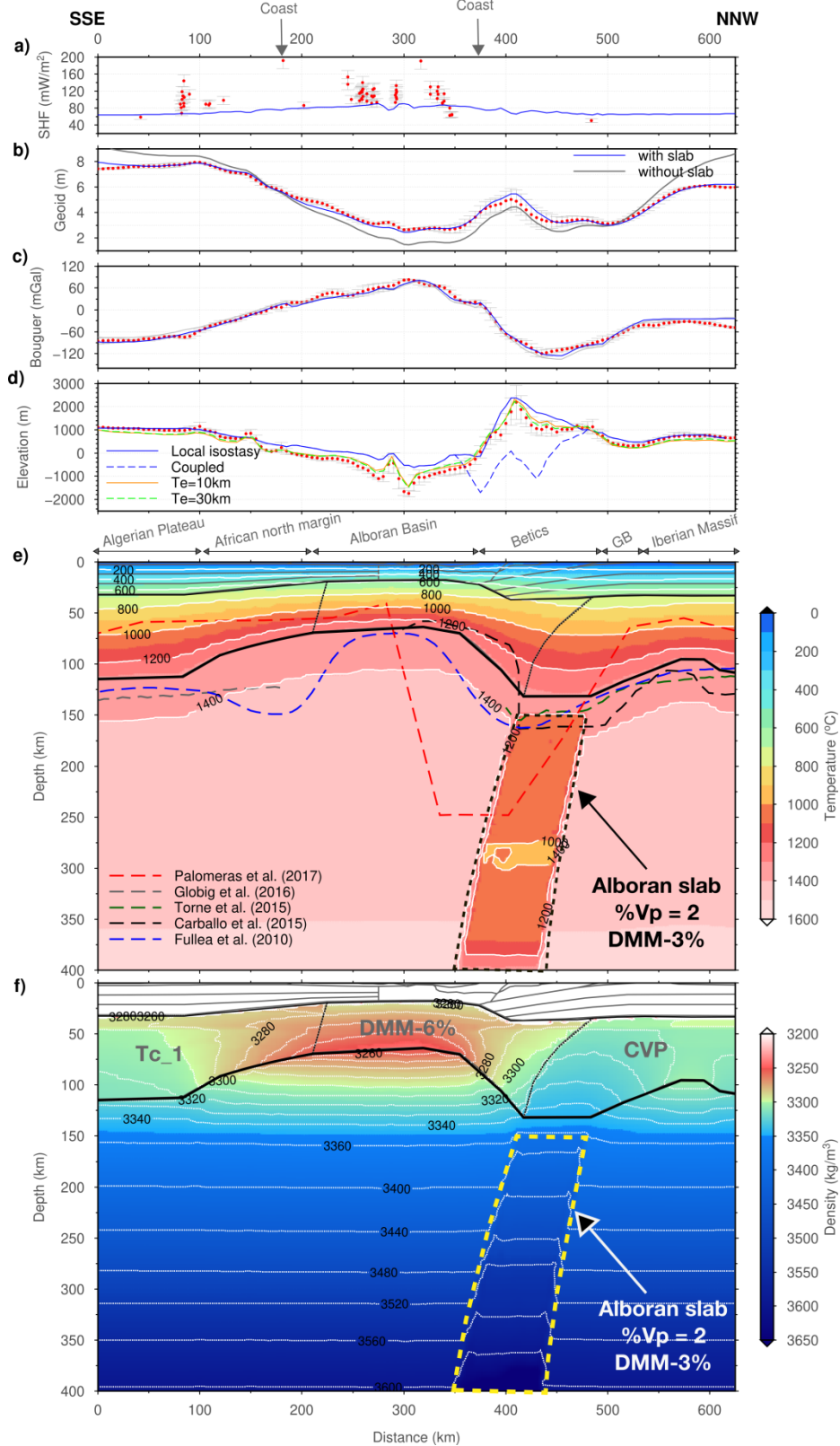


Figure 4.5 Best fitting model along the Alboran Basin geo-transect. (a) Surface heat flow. (b) Geoid height. (c) Bouguer anomaly. (d) Elevation. Blue line represents the calculated values from the model. Red dots denote measured data, and vertical bars denote the standard deviation calculated across a strip of 25 km half width. In (b) geoid height with no slab anomaly is plotted in grey for comparison. In (d) isostatic elevation is plotted in solid blue while the effect of slab on elevation (coupled elevation) is plotted

in dashed blue line. Elevation assuming flexural isostasy for elastic thickness of 10 km and 30 km are plotted in orange and light-green, respectively. (e) Temperature distribution along the geo-transect. Continuous black lines highlight the Moho and LAB depth from our model. LAB depths from previous studies (dashed colour lines) are overlay plotted for comparison. (f) Density distribution in the mantle. The different composition domains in the lithospheric mantle are separated by thin black lines. The bold text in grey colour denotes chemical composition used in the different lithospheric mantle domains listed in Table 4.2.

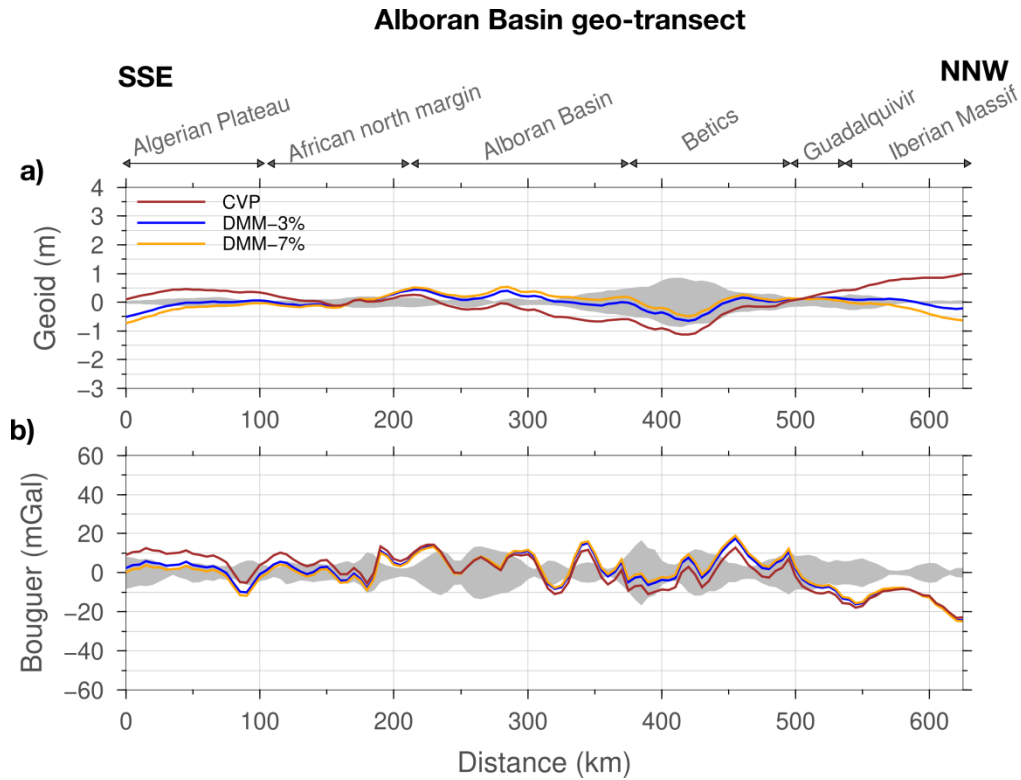


Figure 4.6 Alboran slab chemical composition sensitivity to the (a) geoid height and (b) Bouguer anomaly. Chemical composition has minuscule effect on the Bouguer anomaly and has noticeable effect on the geoid height. Variation in the Alboran slab composition, situated at depths >140 km, changes the mass distribution in the slab region and consequently affects the geoid at longer wavelengths along the geo-transect. DMM-3% chemical composition fits the geoid better along the Alboran Basin geo-transect.

The geophysical observables and the calculated values obtained with the proposed model are shown in the upper panels of Figure 4.5. The calculated SHF falls within the available measurements though these are sparse and uncorrected for surface perturbations and transient effects (Figure 4.5a). Deep groundwater circulation in the Tell Mountains can result in anomalously high heat flow in the Algerian Plateau. Similarly, recent mantle upwelling and volcanism can be responsible for the high heat flow measured in the Alboran Basin. The calculated geoid height and the Bouguer gravity anomaly match satisfactorily the observations (Figures 4.5b and 4.5c), whereas

local isostatic elevation shows remarkable misfits of ~100 m in the Guadalquivir Basin, and ~500 m in the Betics and the Alboran Basin (Figure 4.5d). However, when flexural rigidity of the lithosphere is considered and vertical loads associated with the topography misfits are applied, the calculated elevation fits well with the observations (Figure 4.5d). An effective elastic thickness (T_e) of 10 km is enough to fit the elevation over most of the geo-transect. This value agrees with the elastic thickness obtained in the same region from other methodologies (e.g. Kaban et al., 2018). It is worth noting that elevation is well reproduced when considering that the sublithospheric anomaly related to the detached slab does not transfer any traction stress on the overlying lithosphere. In the case that the slab would transfer all the gravitational potential to the surface, i.e. when the sublithospheric anomaly is fully coupled to the lithosphere, the resulting isostatic elevation would decrease by ~1000–2000 m in the Betic region and increase by few 100 m in the Alboran Basin depending on the considered equivalent elastic thickness (dashed lines in Figure 4.7a).

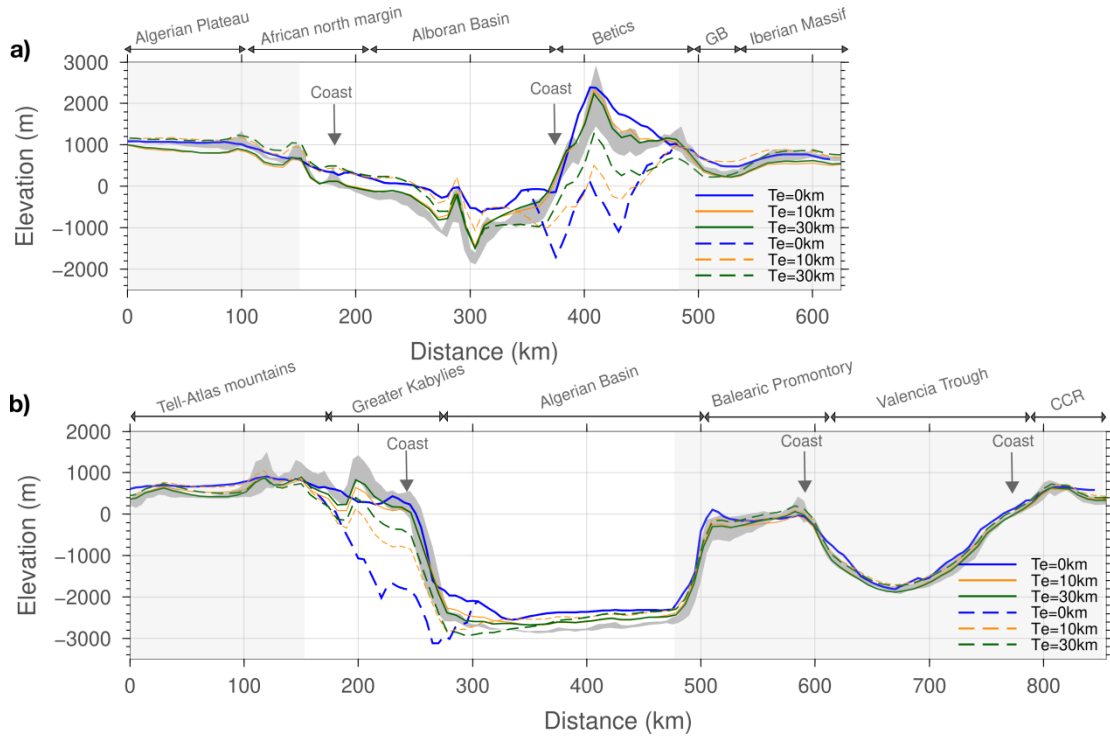


Figure 4.7 Observed and modelled elevation across (a) Alboran Basin geo-transect and (b) Algerian basin geo-transect. Region highlighted in white shows extend along the geo-transect to which the slabs would affect the elevation. Dark-grey shaded strip shows the observed elevation across 50 km wide swath along the geo-transects. Solid coloured lines represent elevation with no slab anomaly (uncoupled), while dashed colour lines show calculated elevation considering the slab (coupled elevation). Blue lines shows isostatic elevation (i.e. $T_e = 0$ km). Orange and green lines show elevation considering flexural isostasy, $T_e = 10$ km, and 30 km, respectively.

Table 4.3 Root mean square error (RMSE) associated with the tested models. RMSE is calculated by considering the lateral variability of the observables through the assigned error bars (see text for explanation).

Geo-transect	Model	Model fit (RMSE)				
		Geoid (m)	Bouguer anomaly (mGal)	Topography (m)		
				Te=0 km	Te=10 km	Te=30 km
Alboran Basin	homogenous lithospheric mantle composition (Tc_1)	0.96	12.41	332	96	73
	without the slab	0.85	7.41	256	62	42
	Alboran slab with CVP composition	0.31	5.55	256	500	339
	Alboran slab with DMM-7% Composition	0.20	5.42	256	197	113
	Alboran slab with DMM-3% composition (Figure 4.5)	0.10	5.26	256	266	164
Algerian Basin	homogenous lithospheric mantle composition (Tc_1)	0.78	15.17	226	48	31
	without the slab	0.56	14.80	202	52	30
	Algerian slab with DMM-7% composition (Figure 4.9)	0.25	13.14	202	212	153

Table 4.3 displays the root mean square error (RMSE) associated with different tested models including no slab with homogenous and non-homogeneous lithosphere, detached slab of different compositions (CVP, DMM-3% and DMM-7%; Table 4.2), and different elastic thickness ($T_e = 0$ km, 10 km and 30 km). To calculate the RMSE related to geoid, gravity and elevation, I have considered the absolute difference between the calculated and observed values and its associated standard deviation. Therefore, $RSME = 0$, for $|calc - obs| \leq std$, and $RMSE = |calc - obs| - std$, for $|calc - obs| > std$; where *calc*, *obs*, and *std* are the calculated and observed values, and the standard deviation, respectively. Variations in the composition of the detached slab decrease noticeably the RMSE of the geoid height and in a lesser extent the RSME of the Bouguer gravity anomaly. If the sublithospheric anomaly is ignored the RMSE related to the geoid height is eight times higher than the best fitting model and then is unacceptable as shown in Figure 4.5b. Note that the RMSE of elevation for $T_e = 0$ km

does not vary with the composition of the slab because in all the cases I am considering that it acts as an uncoupled sublithospheric anomaly and then it is irrelevant for the calculated elevation. Whereas, for $T_e = 10$ km and $T_e = 30$ km, RMSE for elevation varies because of density variations associated with slab composition and resulting pressure variations related to topography loads at the base of the model.

4.2.2. Temperature and density distribution

The temperature distribution along the entire geo-transect is shown in Figure 4.5e. The Iberian Massif is characterized by flat isotherms in the crust with a Moho temperature of ~ 650 °C, and a slight upward deflection at deep lithospheric mantle levels related to the thinning of the lithosphere beneath the Calatrava Volcanic Province. In the Betics, the slab break-off produces the deepening of the LAB and the consequent downward deflection of the isotherms. The maximum Moho temperature along the geo-transect is reached in the Betics (800 °C) as a combined effect of crustal thickening and the sharp lithospheric thinning towards the adjacent Alboran Basin, where Moho temperatures are around 550 °C. Towards the stable Algerian Plateau the isotherms become roughly horizontal with a Moho temperature similar to the Iberian Massif (~ 650 °C). The temperature distribution within the sublithospheric mantle results from the combined effect of lithospheric thickness variations and the imposed adiabatic thermal gradient except within the detached lithospheric slab where the P-wave velocity anomaly of $\Delta V_P = +2\%$ translates into a depth average temperature anomaly of $\Delta T \approx -430$ °C. Note that the temperature variation with depth within the slab is not constant because of the non-linear relationship between temperature and seismic velocities. The calculated density variations in the lithospheric mantle are due to the different chemical compositions and the P-T conditions resulting from laterally varying the lithospheric thickness (Figure 4.5f). In the Iberian Massif density is almost constant in the Calatrava Volcanic Province (3300–3310 kg/m³) increasing rapidly towards the Betics where density increases with depth from 3300 kg/m³ beneath the Moho to ~ 3350 kg/m³ near the LAB. This lateral change in the density distribution is mainly related to the variations in the LAB depth and its effect on pressure and temperature distribution. The pronounced lithospheric thinning affecting the Alboran Basin results in high temperature and low pressure conditions that decrease the density in the lithospheric mantle. This effect adds to the density decrease associated with the compositional change between the Iberian lithospheric mantle (CVP) to the oceanic-like lithospheric mantle of the Alboran Basin (DMM-6%), which may amount

10 - 15 kg/m³ (Table 4.2). As a result, the lithospheric mantle density in the central part of the Alboran Basin shows the lowest values along the geo-transect with a depth-dependent decrease from 3290 kg/m³ beneath the Moho to 3250 kg/m³ near the LAB. Towards the Iberian and African margins density increases laterally and keeps almost constant with depth due to strong variations in the LAB depth indicating that in these regions pressure and temperature effects tend to counterbalance each other. Beneath the stable Algerian Plateau density in the lithospheric mantle increases with depth from 3270 kg/m³ beneath the Moho to 3320 kg/m³ near the LAB.

At shallow sublithospheric mantle levels, the lateral density variations are related to the changes in the lithospheric thickness such that the thinner the lithosphere the lower the density, with values ranging from 3345 kg/m³ beneath the Betics to 3260 kg/m³ beneath the Alboran Basin. At deeper sublithospheric mantle depths (>150 km) density increases with depth almost linearly and lateral variations are negligible, except for the cold and detached Alboran slab region, where the associated depth averaged density anomaly amounts ~50 kg/m³ (Figure 4.8) and increases as much as ~125 kg/m³ at the base of the model (400 km) due to the depth decrease of the olivine-wadsleyite phase transition resulting from the colder temperatures within the slab.

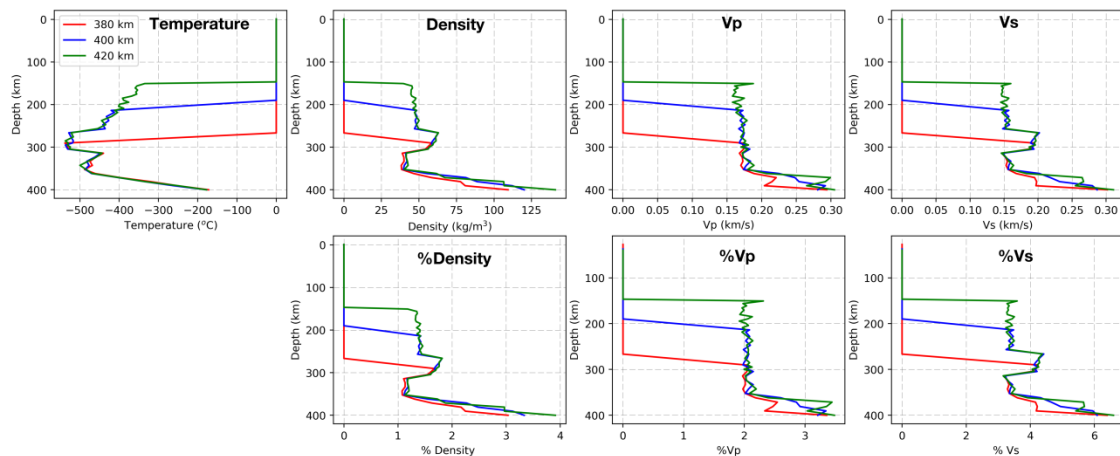


Figure 4.8 Temperature, density, and P- and S-wave velocity depth distribution in the Alboran slab at three locations spanning the slab region along the Alboran Basin geo-transect (see the legend). Upper panel shows the absolute deviation with respect to the LitMod reference column (Chapter 3) and lower panel shows the percentage change.

4.3. Algerian Basin geo-transect: structure, temperature, and density

4.3.1. Crustal and upper mantle structure

The crustal structure roughly coincides with that proposed by Carballo et al. (2015a) except for the three-layered continental crust and the internal structure of the Greater Kabylies (Figure 4.3b). The crust is ~36 km thick beneath the Tell-Atlas Mountains gently thinning towards the margin up to ~30 km with the basement deepening smoothly beneath the Greater Kabylies. The Greater Kabylies are characterized by high density metamorphic slices (Internal Units) thrusting onto the folded non-metamorphic Mesozoic External Units overlying the African crust showing an architecture similar to the Betics (Figure 4.3a). Further to the NNW, the crust thins abruptly towards the Algerian Basin where the Moho is found at 10–12 km depth. The crust of the Algerian Basin is composed of a ~6 km thick oceanic layer overlaid by a ~3 km thick Neogene sedimentary layer. The Balearic Promontory, the Valencia Trough and the Catalan Coastal Ranges are characterized by a thinned continental crust and a Mesozoic to Neogene sedimentary cover of variable thickness. Our results are consistent with previous findings derived from active seismic experiments (e.g., Torne et al., 1992; Vidal et al., 1996), which proposed a clear crustal asymmetry between the Catalan Coastal Ranges, with a thickness of ~32 km, and the thinner crust (~22 km) below the Balearic Promontory. In the axis of the Valencia Trough, the Moho is found at ~18 km along the modelled transect, in agreement with the aforementioned works (Figure 4.3b).

In the mantle along the Algerian Basin geo-transect, I have considered five lithospheric mantle domains (Figure 4.9 and Table 4.2) following the structure from Carballo et al. (2015a) and the different tectonic domains. In the Catalan Coastal Ranges and the Balearic Promontory I use an Average Proton Lherzolite (Pr_6; Griffin et al., 2009; Le Roux et al., 2007) as in Carballo et al. (2015a), except for the Balearic Promontory where they used a primitive upper mantle composition. In the Valencia Trough I use a residual composition corresponding to DMM-6% based on the inferred high degree of decompression melting driven by lithospheric extension and mantle upwelling (Martí et al., 1992). Since the Algerian Basin is a back-arc oceanic basin with a ~6 km thick oceanic magmatic layer (Booth-Rea et al., 2007), I have increased the amount of melting to ~7% (Klein and Langmuir, 1987), while beneath the Greater Kabylies this percentage is reduced to 3% to account for the melting of the depleted asthenosphere (DMM) following delamination and slab detachment (Chazot et al.,

2017). In the North Africa margin, beneath the Tell-Atlas Mountains, I have considered a lithospheric mantle with a Phanerozoic Tc_1 composition according to Carballo et al. (2015a), which is similar to the North Africa margin mantle to the west along the Alboran Basin geo-transect. The LAB depth varies from ~135 km over a flat region beneath the Tell-Atlas Mountains to ~150 km below the Greater Kabylies and decreases rapidly to ~60 km in the Algerian Basin. Towards the Balearic Promontory the LAB deepens abruptly to ~84 km shallowing slightly towards the centre of the Valencia Trough (~80 km) and increases gradually to ~120 km onshore Iberia.

The positive seismic velocity anomaly beneath the North Africa margin (Figures 1.4b and 4.1d; after Fichtner and Villaseñor, 2015) is modelled as a sublithospheric mantle body situated below 200 km depth with an anomalous S-wave velocity of $\Delta V_s = +3.5\%$ and a chemical composition similar to that of the current Algerian Basin lithospheric mantle (DMM-7%). This composition fits better the geoid height than the African lithospheric mantle composition (i.e., Tc_1) and the more enriched DMM-3% considered for the delaminated mantle beneath the Greater Kabylies (Table 4.3 and Figure 4.10).

Present-day crust and upper mantle structure of the Alboran and Algerian basins

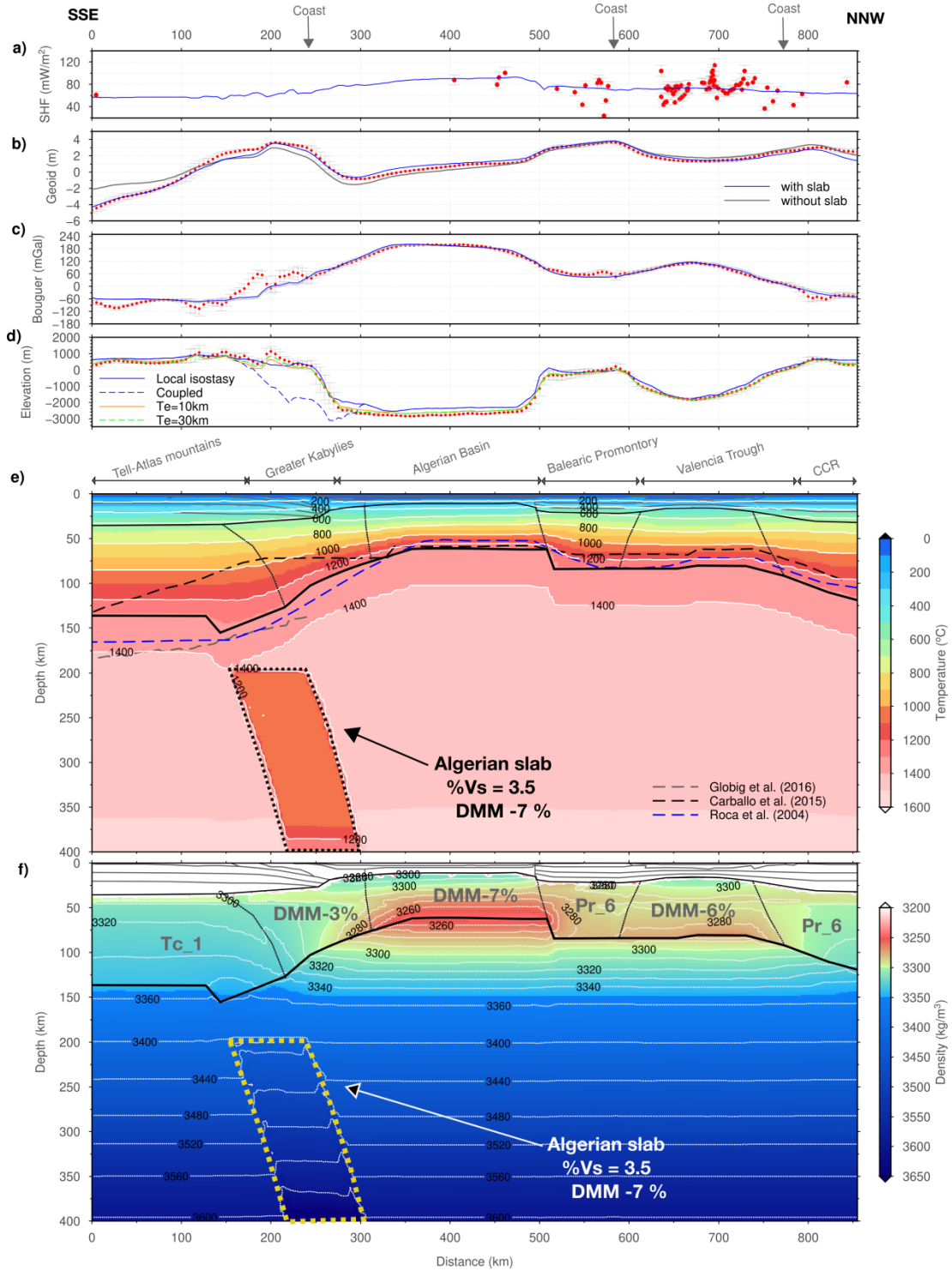


Figure 4.9 Best fitting model along the Algerian Basin geo-transect, rest of the caption as in Figure 4.5.

Figure 4.9 shows the fitting of the geophysical observables from the proposed model. The calculated SHF falls within the range of measured values though these are unevenly distributed and show a high scatter (Figure 4.9a). The calculated geoid height shows a very good fit with observations all along the geo-transect (Figure 4.9b),

with minor misfits ($< 1\text{ m}$) in the Greater Kabylies. The calculated Bouguer anomaly matches the regional trend (Figure 4.9c) with significant misfits all along the Greater Kabylies, where the calculated values are clearly underestimated though the low quality of available gravity data in the region does not allow for firm conclusions. This model shows the minimum RMSE values for geoid height and Bouguer anomaly, 0.25 m and 13.14 mGal, respectively when compared to a no slab model or to model with DMM-3% and Tc_1 slab composition (Table 4.3 and Figure 4.10).

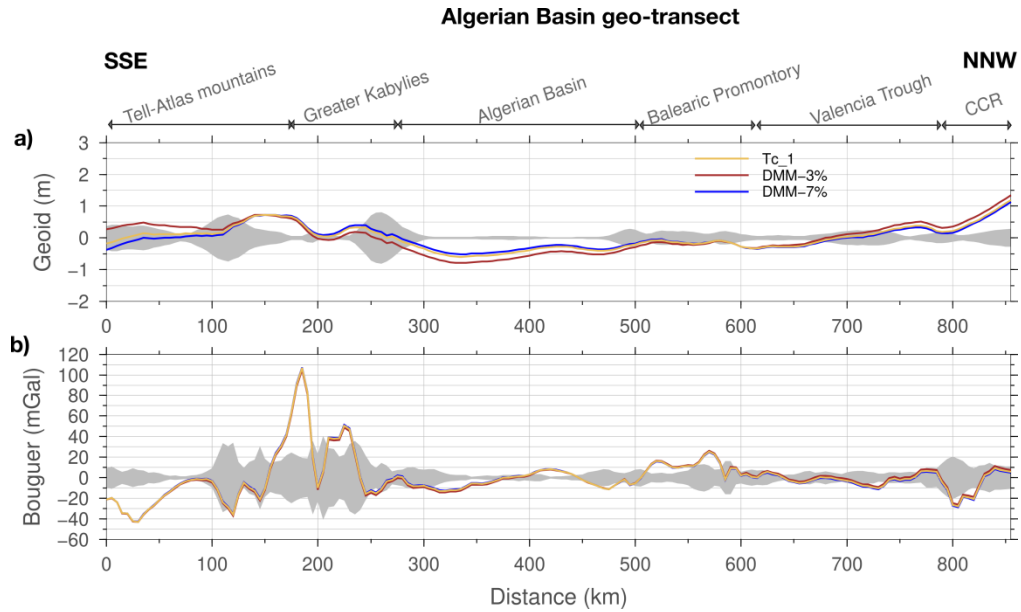


Figure 4.10 Algerian slab chemical composition sensitivity to the (a) geoid height and (b) Bouguer anomaly. DMM-7% chemical composition, resulting from 7%melting of DMM, fits better the geoid height along the Algerian Basin geo-transect.

The calculated isostatic elevation also matches the regional trend but shows a long wavelength misfit of $\sim 400\text{ m}$ in the Algerian Basin and $\sim 250\text{ m}$ in the Tell-Atlas Mountains, with local misfits of $\sim 700\text{ m}$ in the Greater Kabylies (Figure 4.9d). However, when I consider the flexural rigidity of the lithosphere, the fit between calculated and observed elevation is largely improved (Figure 4.7b). Along most of the profile, an effective elastic thickness of $T_e = 10\text{ km}$ reduces the RMSE from 202 m to 52 m (Table 3), although a higher elastic thickness ($T_e = 30\text{ km}$) is required for the Africa mainland resulting in $\text{RMSE} = 30\text{ m}$ (Figure 4.7b and Table 4.3). These elastic thickness values are in agreement with those predicted by coherence analysis of topography and gravity (e.g. Pérez-Gussinyé et al., 2009; Kaban et al, 2018). The estimated coupled elevation, which includes the isostatic effect of the cold and denser slab, would decrease the elevation by 500–2000 m in the Greater Kabylies. Near the

coast, elevation decreases because of the fore-deep and increases in the Algerian Basin because of the fore-bulge associated with the assumed Algerian slab attached to the lithosphere (Figure 4.7b). These variations in elevation amount few hundred meters depending on the considered elastic thickness.

4.3.2. Temperature and density distribution

The temperature distribution along the Algerian Basin geo-transect is shown in Figure 4.9e. At deep lithospheric levels, isotherms mimic the depth variations of the LAB showing a step-like shape. In the Tell-Atlas Mountains region isotherms are roughly flat showing an upward deflection beneath the Great Kabylies and the Africa margin, and become flat again in the Algerian Basin. Further to the NNW, isotherms deepen slightly below the Balearic Promontory flattening beneath the Valencia Trough and deepening gently towards the Catalan Coastal Ranges. The calculated temperature at the Moho varies from ~630 °C in the Tell-Atlas Mountains, decreasing rapidly beneath the Greater Kabylies (600–400 °C) and reaching the minimum value of ~250 °C in the Algerian Basin. Towards the Iberia Margin, the Moho temperature shows noticeable variations reaching ~600 °C in the Balearic Promontory, ~400 °C in the Valencia Trough and ~700 °C in the Catalan Coastal Ranges. At sublithospheric mantle levels, below 200 km depth, the temperature distribution responds to the imposed adiabatic thermal gradient except within the detached slab where the seismic anomaly of $\Delta V_s = 3.5\%$ translates into a depth average temperature anomaly of $\Delta T \approx -400$ °C (Figure 4.11).

The calculated density distribution along the Algerian Basin geo-transect is shown in Figure 4.9f, reflecting the different chemical compositions and P-T conditions in the upper mantle. The lithospheric mantle in the Tell-Atlas Mountains, with the same composition than in the Algerian Plateau (i.e., Tc_1, Table 4.2) shows a density increase with depth from ~3280 kg/m³ at the Moho to ~3340 kg/m³ at the LAB being slightly higher than in the Algerian Plateau lithosphere of the parallel Alboran Basin geo-transect (3270kg/m³-3320 kg/m³, Figure 4.5f) due to the higher lithospheric thickness. Density decreases laterally across the margin, beneath the Greater Kabylies, and towards the Algerian Basin from 3320 kg/m³ to less than 3290 kg/m³ being almost constant with depth. These density changes are the combined effect of varying the chemical composition from Tc_1 to DMM-3% (Table 4.2) and the lithospheric thinning which counterbalance the depth-dependent pressure and temperature effects. The oceanic lithospheric mantle in the Algerian Basin, with a DMM-7% composition (Table 4.2), shows a density exceeding 3300 kg/m³ at the

uppermost mantle levels until a depth of ~20 km related to the plagioclase-spinel phase transition. Below this depth, density decreases with depth to 3250 kg/m³ at the LAB, which is the lowest mantle density along the geo-transect. To the NNW, the transition to a Proterozoic composition (Pr-6, Table 4.2) beneath the Balearic Promontory together with the lithosphere thickening, results in a lateral increase of densities to an average value of ~3285 kg/m³ which keeps almost constant with depth. The lithospheric mantle beneath the Valencia Trough, with DMM-6% composition, shows a density of ~3300 kg/m³ at the Moho depth decreasing to 3280 kg/m³ at the LAB demonstrating some oscillations in the pressure gradient related to the plagioclase-spinel (25–35 km depth) and spinel-garnet (60–90 km depth) phase transitions. Density increases again laterally towards the Catalan Coastal Ranges as a combined effect of composition and P-T conditions.

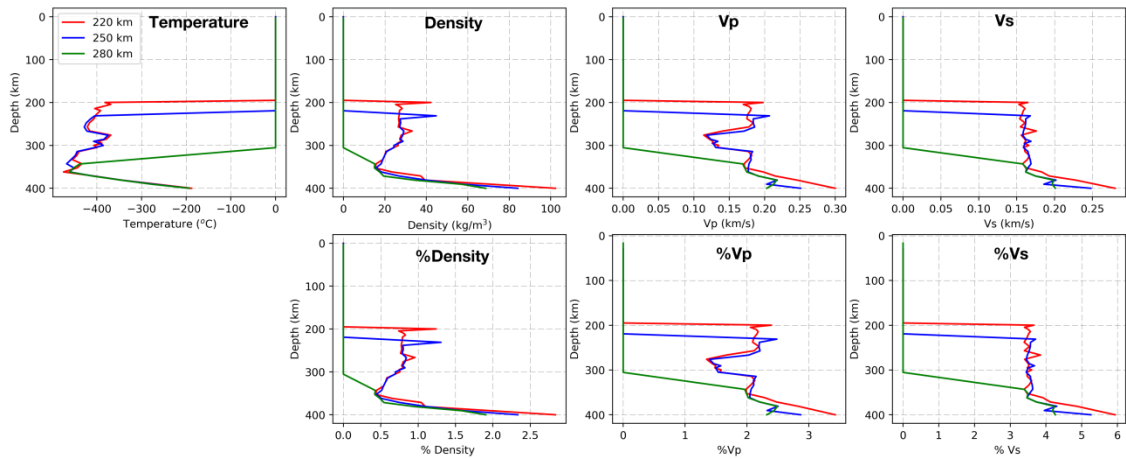


Figure 4.11 Temperature, density, P-wave velocity and S-wave velocity depth distribution in the Algerian slab at three locations (see the legend) spanning the slab region along the Algerian Basin geo-transect. Rest of the caption is same as in Figure 4.8.

Similar to the Alboran Basin geo-transect, at shallow sublithospheric mantle levels, density variations are related to LAB depth variations affecting especially the Algerian Basin, the Balearic Promontory and the Valencia Trough regions. At deeper sublithospheric mantle levels (> 150 km), lateral variations are negligible, except for the detached Algerian slab region where above 300 km depth, density increases by ~30 kg/m³ and decreases to < 20 kg/m³ at 350 km depth, as composition effects competes with those of the temperature (Figure 4.11). Close to the base of the model, density increases by as much as ~100 kg/m³ in the slab region due to the olivine-wadsleyite phase transition alike to the Alboran slab at these depths (Figures 4.8 and

4.11). It is interesting to note that the density change in case of the Alboran slab at 400 km is higher than that for the Algerian slab. The temperature change at these depths is similar for both slabs at these depths; hence, the difference in the density change can be attributed to the composition which is relatively more fertile in the Alboran slab (DMM-3%, Table 4.2) than in the Algerian slab (DMM-7%, Table 4.1).

4.4. Mantle seismic velocities and comparison with passive seismological data

In this section, I show the calculated seismic velocities in the upper mantle according to the mineral aggregates resulting from the ascribed chemical composition, and the prevailing pressure and temperature conditions. The results are compared with the available seismic data and tomography models.

As discussed in Chapter 3, absolute seismic velocities obtained in LitMod2D_2.0 can be used to compute passive seismological data (e.g., receiver functions and surface wave dispersion curves). Forward prediction of P-wave receiver functions and dispersion curves of Rayleigh surface-wave phase velocities dispersion curves are computed using the post-processing toolbox in LitMod2D_2.0 and are also compared with the available observed data.

4.4.1. Alboran Basin geo-transect

Figure 4.12a shows the P-wave velocity distribution along the Alboran Basin geo-transect. As shown in Table 4.2, seismic velocities depend to a larger extent on temperature and pressure than on composition. The lower V_P values within the lithospheric mantle are found close to the LAB in regions affected by lithospheric thinning, as the Calatrava Volcanic Province in the Iberian Massif ($V_P < 8.0$ km/s), and the Alboran Basin and its margins ($V_P < 7.85$ km/s). In these regions, V_P decreases with depth indicating that the temperature effect prevails on the pressure effect. In contrast, P-wave velocities beneath the Betics, in the thicker lithosphere region, increase from ~ 8.05 km/s in the uppermost mantle, consistent with the observed P_n velocities of 8.0 km/s - 8.2 km/s (Diaz et al., 2008, 2013), to 8.1 km/s at LAB depths. Beneath the Algerian Plateau, P-wave velocities keep almost constant with depth ($V_P \approx 8.0$ km/s) showing a lateral decrease towards the Africa margin.

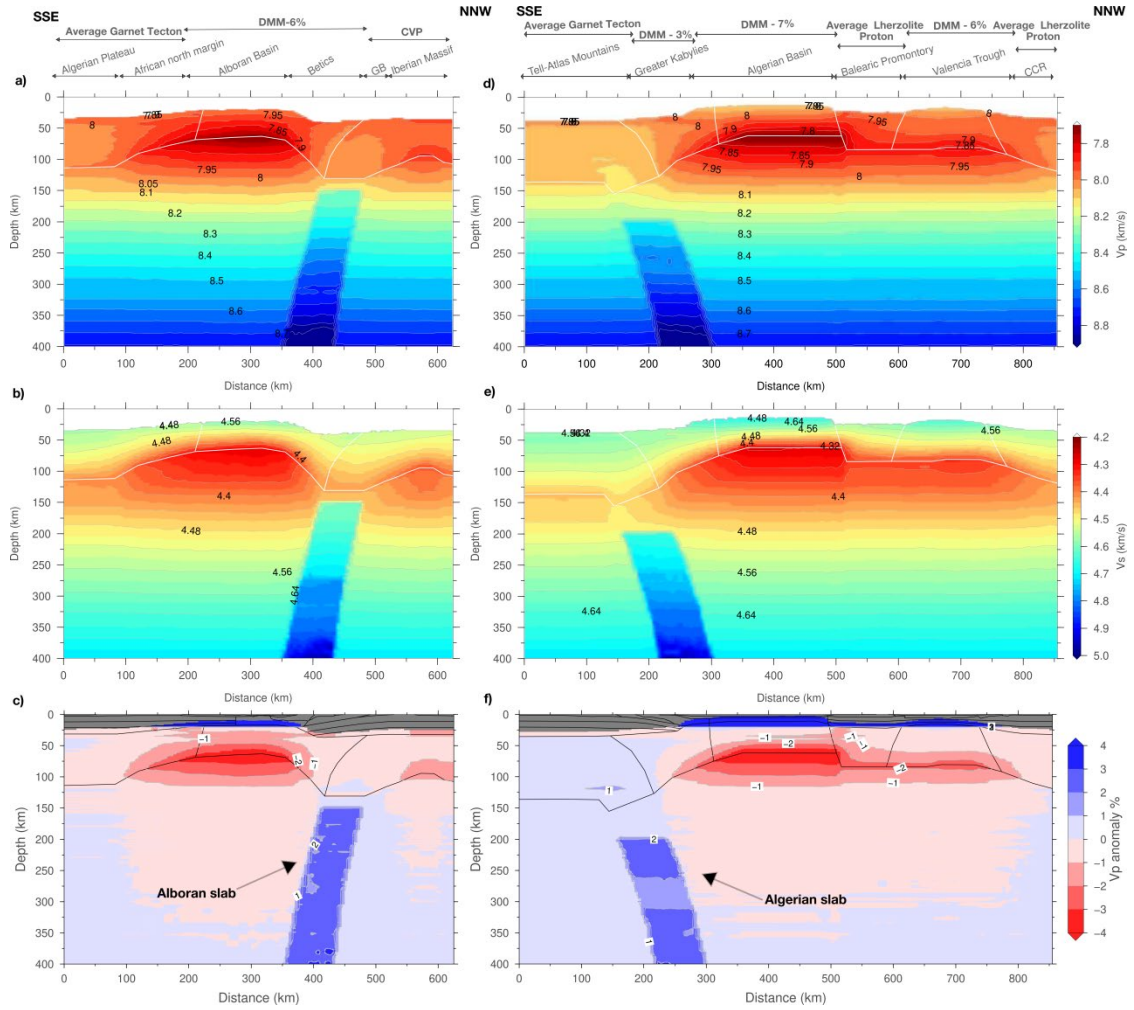


Figure 4.12 Seismic velocities and synthetic seismic tomography along the geo-transects. (a) and (b) shows the absolute P-wave and S-wave velocities, respectively and (c) synthetic P-wave anomalies for the Alboran Basin geo-transect. Similarly (d) and (e) shows the absolute P- and S-wave velocities, respectively, and (f) synthetic P-wave anomalies along the Algerian Basin geo-transect.

The relatively fertile (DMM-6%) composition of the central segment of the geo-transect, close to primitive upper mantle (PUM; McDonough and Sun, 1995), produces shallow mantle P-wave velocities of 7.97 km/s in the Alboran Basin as found by Fullea et al. (2010). These low P-wave velocities can be further reduced by the presence of partial melts, as the geotherm intersects the dry peridotite solidus (Figure 4.13a), and anisotropy (not considered here) becoming close to the observed low Pn velocities (7.5–8.1 km/s, Hatzfeld et al., 1978; Calvert et al., 2000b). At sublithospheric mantle depths down to 150 km, lateral variations of seismic velocities result solely from the P-T conditions imposed by the lateral lithospheric thickness variations since the entire sublithospheric mantle has the same composition, except in the slab region. Below 150 km, P-wave velocities increase almost linearly with depth up to >8.7 km/s at 400

km depth. In the region of the detached Alboran slab, P-wave velocities increase by ~ 0.18 km/s as imposed from tomography models ($\Delta V_P = 2\%$) with a highest increase of ~ 0.3 km/s just above 400 km depth related to the olivine-wadsleyite phase transition (Figure 4.8).

Calculated S-wave velocities (Figure 4.12b) show a similar pattern than P-wave velocities but with a lesser influence of pressure such that, V_S decreases with depth from Moho to LAB all along the geo-transect. Likewise, changes in the composition domain show smaller effects on V_S than on V_P due to the lesser sensitivity of S-wave to composition (e.g., Kumar et al., 2020; Priestley and McKenzie, 2006). Below the LAB, V_S increases with depth delineating a low-velocity zone down to 200–250 km which is enhanced in magnitude in those regions affected by lithospheric thinning.

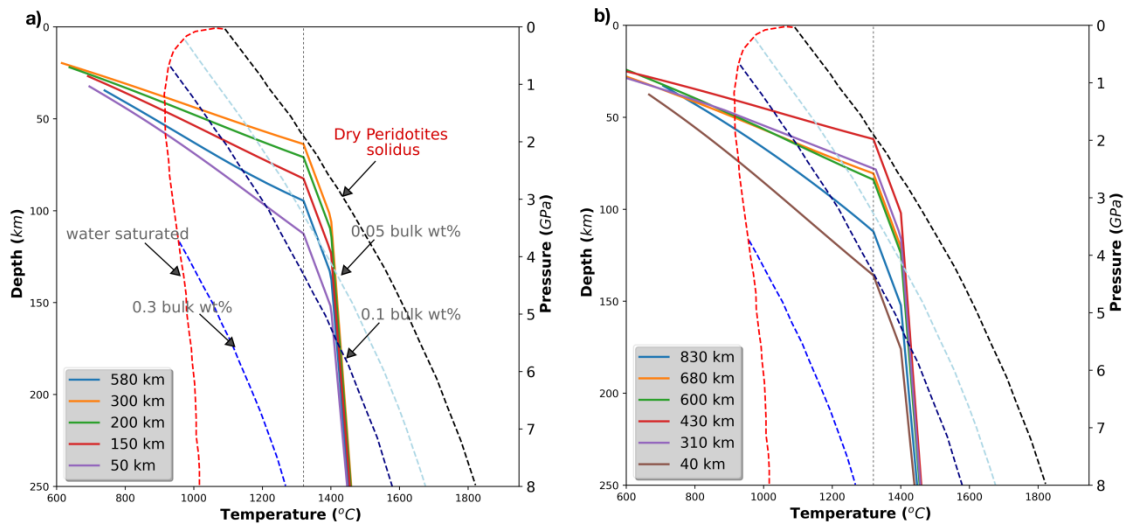


Figure 4.13 Geotherms (solid lines) at selected locations along the (a) Alboran Basin and (b) Algerian Basin geo-transects. Dry and wet peridotites solidus for different amount of bulk water from Katz and Spiegelman (2003) are also plotted. Presence of water in the mantle brings down the solidus resulting in presence of partial melts.

The Alboran slab shows an S-wave velocity increase of ~ 0.15 km/s (+3.5%) up to ~ 270 km resulting from the prescribed 2% P-wave anomaly. The resulting variation in the S-wave velocities below ~ 270 km is related to the implied temperature in the slab and increases to a maximum value ~ 0.30 km/s (+7%) at 400 km depth which is related to the olivine-wadsleyite phase transition (Figure 4.8). The calculated S-wave velocity pattern compares well with the regional S-wave tomography model projected onto the transect (Figure 4.1c) obtained by Palomeras et al. (2017) from Rayleigh surface-wave dispersion tomography.

In order to compare the computed mantle velocities with the P-wave travel-time tomography models, the lateral variations of P-wave in % (Figure 4.12c) are calculated relative to the reference column defined in LitMod2D_2.0 (Chapter 3; Kumar et al., 2020). The computed synthetic tomography reproduces the main pattern of slow and fast velocity regions observed in the global/regional P-wave tomography models (Bezada et al., 2013, Figure 4.1b) with minor discrepancies in the amplitudes. Note that the colour scale of the calculated tomography saturates in the regions of Moho depth < 35 km because of the used reference model, which consists of a 35 km crust (Kumar et al., 2020) and, highlights the crustal thinning as observed in the tomography model of Bezada et al. (2013) (Figure 4.1b).

Comparison with the passive seismological data

Broadband teleseismic earthquake waveform data recorded at stations shown in Figure 4.14 are downloaded from the IRIS-DMC (<https://ds.iris.edu/ds/nodes/dmc/>). Earthquakes in the epicentral distance range of 30° to 90° are used for P-wave receiver function calculations.

I use the following processing steps to calculate P-receiver functions:

- The three-component broadband earthquake waveform data are pre-processed by rotating the horizontal (north-south and east-west) components into radial and tangential directions to separate P-SV energy.
- Waveforms are cut 20s before and 60 s after the hand-picked arrival of P-wave on the vertical component.
- Waveforms are filtered using a low-pass Gaussian filter of width 2.5 with a corner frequency of ~ 1.2 Hz.
- Iterative time-domain deconvolution algorithm (Ligorria and Ammon, 1999) is applied to construct a spike train by cross-correlating the radial waveforms with the vertical waveforms. The spike train is then convolved with the observed vertical component waveform to produce synthetic radial component and is compared with the observed radial component in a least square manner. This step is repeated until a threshold least square fit is reached (chosen 0.001) or the maximum numbers of iterations are reached (200).
- The final P-wave receiver functions are assessed for quality by % fit of the calculated radian component to the observed radial component. I use waveforms with fit $> 80\%$ for further analysis.

This procedure is repeated for all stations along the Alboran Basin geo-transect (Figure 4.14). Then, I calculate the piercing point for all the calculated P-wave receiver functions at 35 km depth by back-projecting the traces using the ak135 velocity model and obtain a latitude and longitude for each receiver function at 35 km depth. Then, I stack all the receiver functions along the geo-transect within a 10 km distance bin along the profile and 25 km half-width window across the profile.

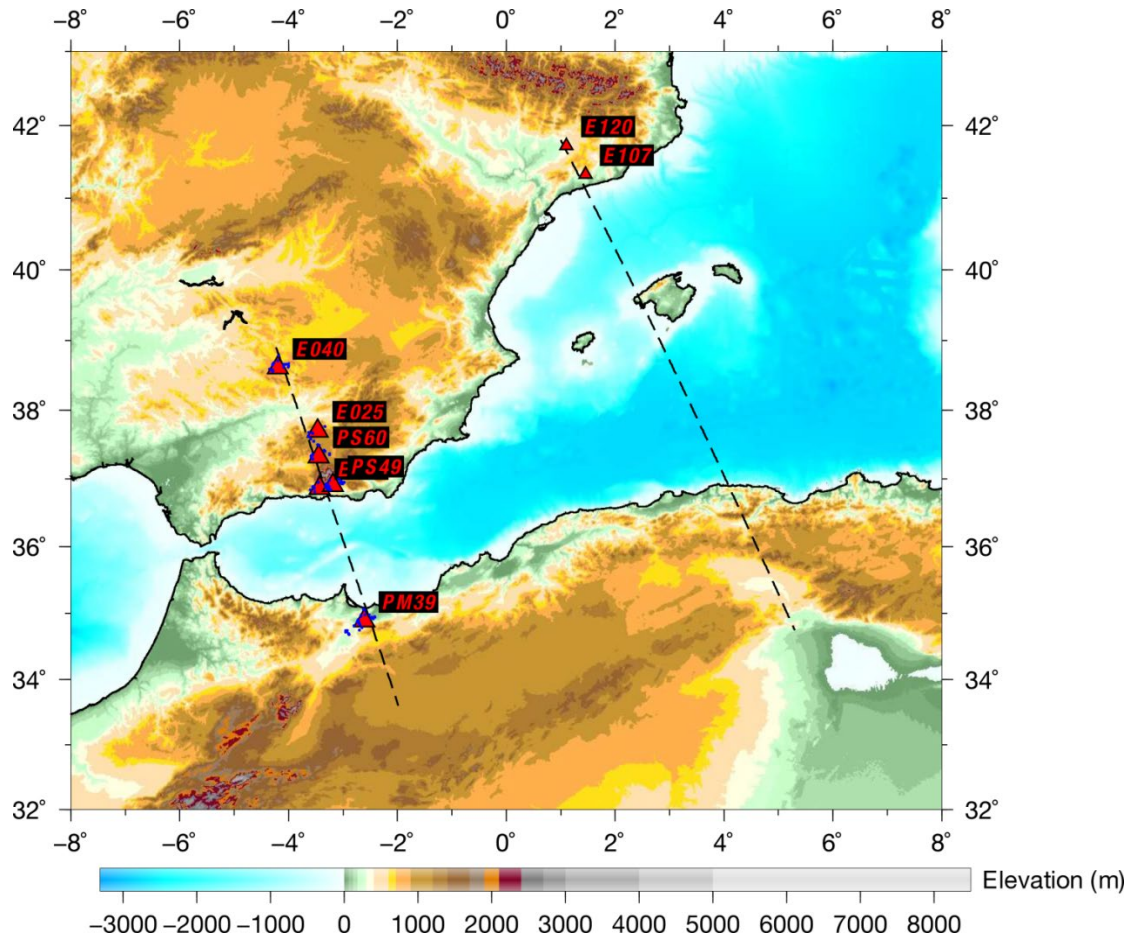


Figure 4.14 Location of the seismic stations along the geo-transects used to calculate P-wave receiver functions. Blue points show the location of piercing point at a depth 35 km along the Alboran Basin geo-transect.

Fundamental mode Rayleigh-surface-wave phase velocity tomography model from Palomeras et al. (2017) is used to extract dispersion curves along the Alboran Basin geo-transect. This tomography model uses data from 368 broadband seismic stations of permanent and temporary arrays in Morocco, Spain, Portugal, IberArray (2007-2013, Spain), and PICASSO (2009-2012) experiments. The model includes Ambient Noise Tomography between 4 s - 50 s periods to enhance the shallow depth structure

together with natural earthquake data in 20–167 s periods for deep structure until ~200 km. Note that the North Africa margin along the Alboran Basin geo-transect falls outside the good-ray-coverage/less-resolved region of Palomeras et al. (2017) (see their Figure 2)

Post-processing tool-box in the LitMod2D_2.0 (Chapter 3) is used to calculate synthetic the P-receiver functions and fundamental mode Rayleigh-surface-wave phase velocities from the S-wave velocity along the Alboran Basin geo-transect (Figure 4.12b). As I do not solve for phase equilibrium in the crust, the P- and S-wave velocities are calculated using empirical V_P -density relationships from Brocher (2005), and S-wave velocities in the crust are calculated assuming a constant $V_P/V_S = 1.73$ ratio (Figure 4.15a). In the lithospheric and sublithospheric mantle, seismic velocities from LitMod2D_2.0 are used (Figure 4.12b). Below 400 km depth (base of the model), velocities from the ak135 model are used.

Forward calculated P-wave receiver functions (Figure 4.15b, green) matches reasonably well with the observed P-wave receiver functions (wherever available, Figure 4.15b, grey). Some misfit can be seen, delay or advance of phases which can be attributed to the assumption of constant V_P/V_S ratio used here. V_P/V_S ratio should vary with depth at least in the Alboran Basin and Betics because of the HP/LT metamorphic and volcanic rocks (Figure 4.3a).

In case of Rayleigh-surface-wave phase velocity dispersion, forward predictions fit very well at long-periods (> 30 s), which are sensitive to the mantle velocity structure, for the Alboran Basin, Betics, and Iberian Massif regions (Figure 4.15c). For the North Africa margin (distance along profile < 225 km) synthetic phase velocities are consistently higher than observed ones (period 30–100 s) which can be attributed to less resolution for this region in the observed phase velocities, as mentioned before. Hence, S-wave velocities for the Alboran Basin geo-transect model are consistent with the available surface wave dispersion data in the upper mantle. Predicted higher phase velocities at the short-period (< 30 s) could be again explained by using a constant V_P/V_S ratio.

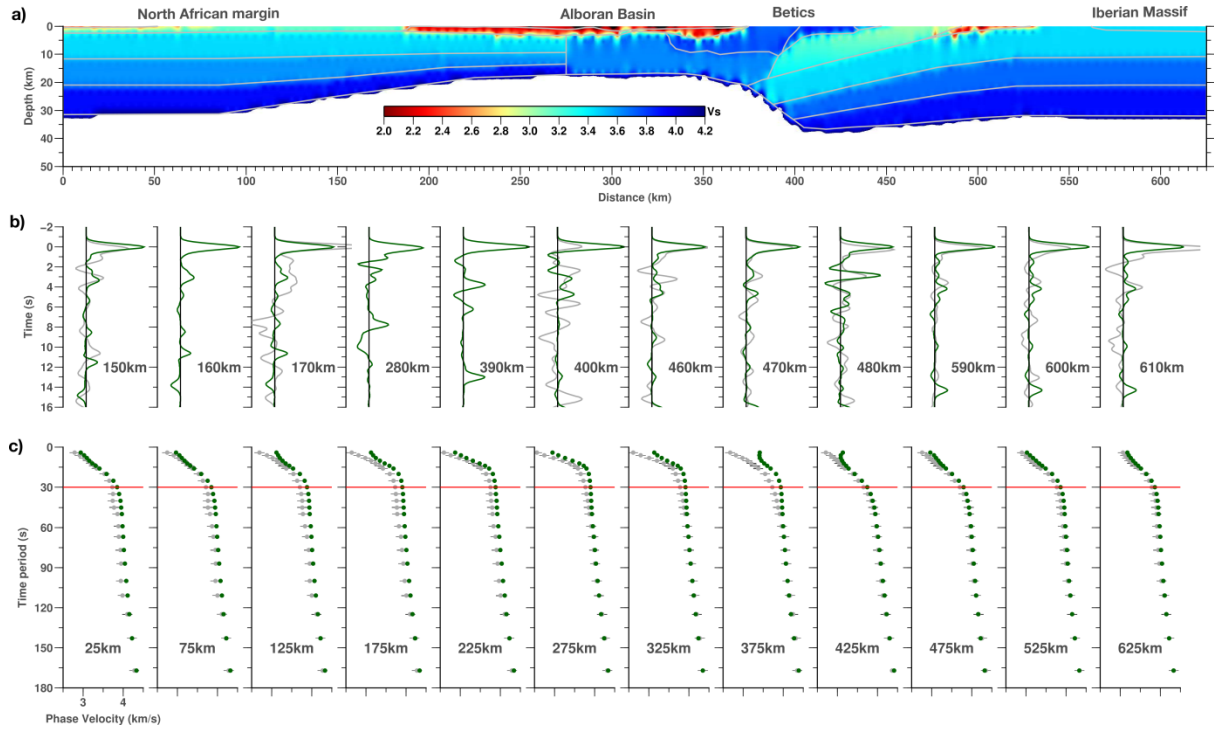


Figure 4.15 Plot showing the forward calculation of passive seismological data from the velocities obtained along Alboran Basin geo-transect. (a) Crustal S-wave velocities calculated using empirical relations (see text for details). (b) P-wave receiver function at distance, labelled in each plot, along the geo-transect. Solid green represent forward calculation and grey is observed P-wave receiver function (where available). (c) Rayleigh surface-wave fundamental mode phase velocity dispersion curves along the Alboran Basin geo-transect at distance along the geo-transect labelled in each plot. Grey circles represent the observed phase velocities and bars represent corresponding error. Green circles represent the forward calculation from the seismic velocity model obtained from LitMod2D_2.0.

Receiver functions are sensitive to depths of impedance contrasts (i.e., seismic velocity discontinuities), while surface wave dispersion curves are sensitive to the vertical averages of shear wave velocity. Joint inversion of the two data sets complements each other and provides better constrained S-wave velocity structure of the crust. S-wave velocities from integrated geophysical-petrological modelling can serve as the starting model, and joint inversion will allow better imaging of the crustal S-wave velocity structure. I note it to be one of the future directions to perform such joint inversion.

4.4.2. Algerian Basin geo-transect

Figure 4.12d shows the calculated P-wave mantle velocities along the Algerian Basin geo-transect. As in the Alboran Basin geo-transect, the lower velocities are found at LAB levels in regions affected by lithospheric thinning including the Algerian

Basin, the Balearic Promontory and the Valencia Trough. In these regions, V_P decreases from 7.90–7.95 km/s beneath the Moho to < 7.9 km/s at LAB depths with the lowest value along the whole geo-transect (< 7.8 km/s) being at the Algerian Basin. The calculated uppermost mantle velocities are slightly higher than the reported P_n velocities in the Valencia Trough and the Algerian Basin, ranging from 7.7 km/s to 7.95 km/s (Torne et al., 1992; Dañobeitia et al., 1992; Vidal et al., 1998). Note that I do not include the effects of melt; hence, calculated velocity will further decrease as the geotherm in Algerian Basin is intersecting the mantle solidus (Figure 4.13b). Towards the Iberian and African margins (Catalan Coastal Ranges and Greater Kabylies, respectively), P-wave velocities increase laterally showing almost constant values with depth. Beneath the thicker lithosphere of the Tell-Atlas Mountains, P-wave velocities increase with depth from 7.9 km/s at the Moho to 8.1 km/s at the LAB, being slightly higher than in the Algerian Plateau lithosphere (Figure 4.12a). Down to ~ 150 km depth, the effect of lithosphere thickness is reflected in P-wave velocities where the thin lithosphere of the Algerian Basin results in a low velocity zone, similar to that in the Alboran Basin, extending towards the Balearic Promontory and the Valencia Trough. Below this depth, P-wave velocities are essentially depending on pressure increasing mostly linearly with depth up to > 8.7 km/s at 400 km depth. In the region of the detached Algerian slab, P-wave velocities are increased by ~ 0.18 km/s ($\sim 2\%$) and near the base of the slab (400 km) increase to as high as 0.30 km/s ($> \sim 3\%$) because of the olivine-wadsleyite phase transition (Figure 4.14).

S-wave velocities also show a low velocity zone extending from mid-lithospheric mantle levels to 200–250 km depth being more pronounced beneath the Algerian Basin, the Balearic Promontory and the Valencia Trough due to the prevalence of temperature effects on pressure effects in these regions (Figure 4.9e). Minimum values of S-wave velocities (≤ 4.35 km/s) are obtained at the base of the lithosphere along the thinned lithosphere regions, whereas beneath the Africa and Iberia mainland, minimum S-wave velocities exceed 4.45 km/s. The region corresponding to the detached Algerian slab, is characterized by an average increase of S-wave velocity of ~ 0.16 km/s in agreement with the prescribed anomaly of $\Delta V_S = 3.5\%$. The computed synthetic P-wave tomography (Figure 4.12f) shows negative V_P anomalies of less than -2% beneath the Algerian Basin and the Valencia Trough, in agreement to regional and global P-wave tomography models (e.g., Amaru, 2007; Piromallo and Morelli, 2003; Spakman and Wortel, 2004). The detached Algerian slab is characterized by a positive V_P anomaly of $\sim 2\%$ resulting from the prescribed V_S anomaly ($\Delta V_S = 3.5\%$; Fichtner and Villaseñor, 2015).

Comparison with the passive seismological data

There is a lack of passive seismic data along most of the Algerian Basin geo-transect (Figure 4.14); hence in this section, I compare the synthetic receiver functions and Rayleigh surface-wave dispersion curves in the Algerian and Alboran basins, and in the regions of subducted slabs (Figure 4.16).

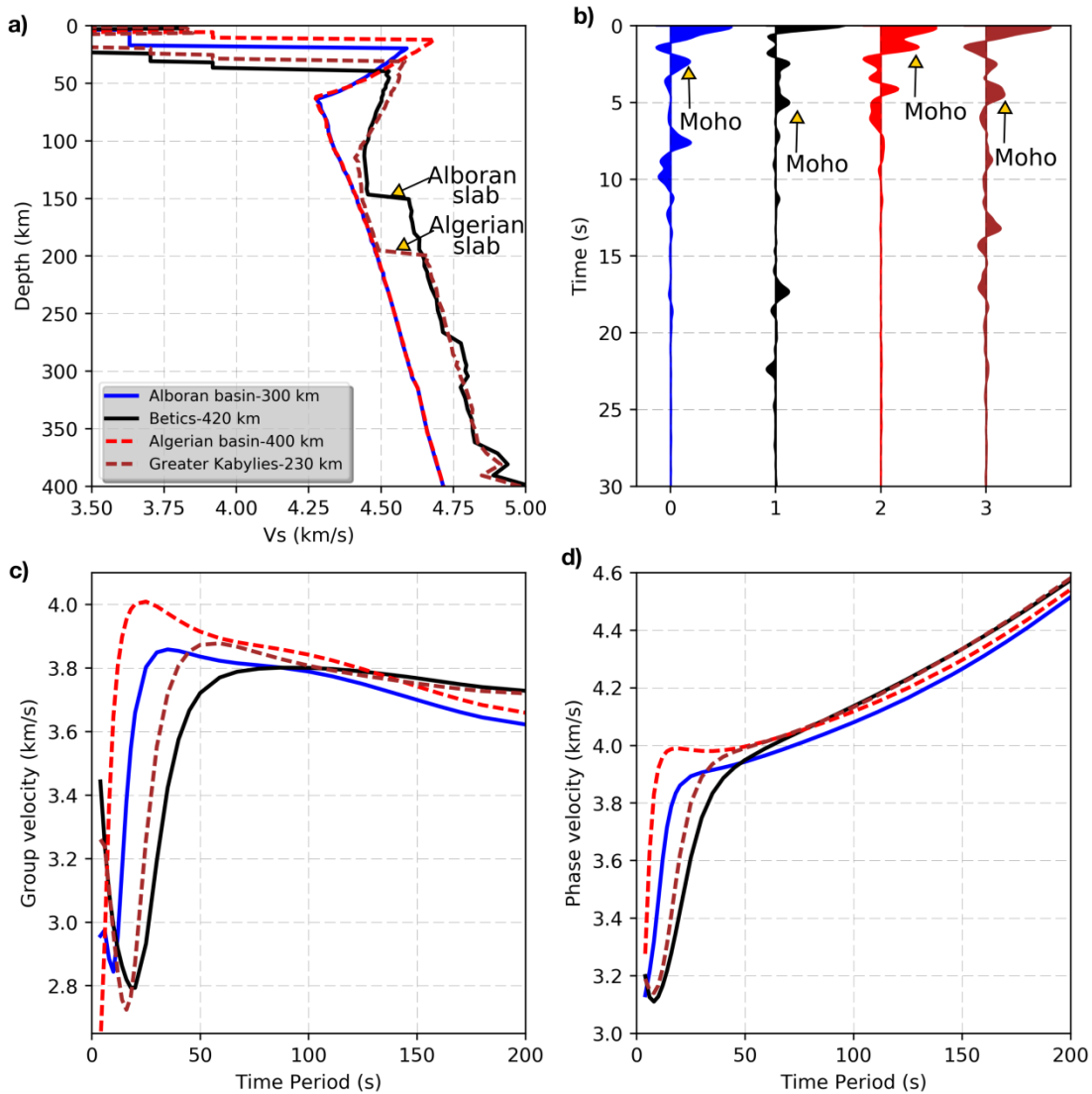


Figure 4.16 Plot showing the comparison between forward prediction of receiver functions and Rayleigh surface-wave dispersion curves at selected locations. (a) Shows the depth distribution of S-wave velocities colour coded for location (see the legend). (b) P-wave receiver function, (c) group velocities, and (d) phase velocities colour coded for location (see legend in a).

Both the P-wave receiver functions and Rayleigh surface-wave dispersion curves show distinctive features at the selected locations (Figure 4.16). The effect of

thin crust and higher seismic velocities in the Algerian Basin is clearly reflected by the early arrival of Moho converted phase (Ps) compared to the delayed arrival in the thicker Alboran Basin (Figure 4.16b). The P-wave receiver functions for the Betics and Greater Kabylies show much delayed Moho converted phase in comparison to the Algerian and the Alboran basins, though that of the Betics is slightly more delayed than that of the Greater Kabylies because of the thicker crust in the Betics. Phases before the Moho phase reflect the three-layered continental crust considered beneath the Betics and the Greater Kabylies. Rayleigh surface-wave dispersion curves at low periods (< 50 s) show a distinct pattern, being highest in the Algerian Basin and lowest in the Betics reflecting the highest and lowest S-wave velocities pattern at crustal depths, respectively (Figure 4.16a). Both, the group and phase velocities, shows higher values at longer periods (> 100 s) reflecting the increased S-wave velocities in the sublithospheric mantle because of the Alboran and Algerian slabs.

CHAPTER 5

Discussion

Chapter 5

Discussion

The observed sublithospheric mantle positive seismic velocity anomalies beneath the Betics-Rif and the north-Algeria margin in the Western Mediterranean motivated this thesis. These anomalies are qualitatively interpreted as the subducted Ligurian-Tethys lithosphere, which is one of the constraining basis for the geodynamic evolution models of the Western Mediterranean. In general, such anomalies are understood qualitatively as colder than average mantle in case of positive seismic velocity anomalies, or as hotter in case of negative seismic velocity anomalies. A quantitative physical interpretation (thermal and/or compositional) of sublithospheric mantle anomalies is challenging and is required to understand the geodynamic and geological processes. In the first part of this thesis, I improved an already existing tool, LitMod2D_1.0, to LitMod2D_2.0 to model such seismic velocity anomalies to quantitatively infer them in terms of temperature and/or composition using thermodynamically self-consistent integrated geophysical-petrological modelling approach. In the second part of the thesis, I applied the improved LitMod2D_2.0 to model the present-day crust and upper mantle (up to 400 km depth) structure of the Betics-Rif and Kabylies-Tell-Atlas orogenic systems along two geo-transects crossing the Alboran and Algerian back-arc basins and their opposed margins of North Africa and Iberia, respectively.

In this chapter, I first present the discussion on the methodological developments in the improved LitMod2D_2.0. Then, I compare and discuss the results of present-day crust and upper mantle structure derived using improved LitMod2D_2.0 in the Alboran and Algerian Basin geo-transects. The results are discussed in terms of the geodynamic implications for the closure of the Jurassic Ligurian-Tethys Ocean and the opening of the new oceanic and thinned continental domains of the Algerian and Alboran back-arc basins in an overall convergence regime that has lasted for the past 85 My involving the African and European plates.

5.1. LitMod2D_2.0

The improved LitMod2D_2.0 software has been presented in Chapter 3, which allows studying the temperature, density (i.e., chemical composition), and seismic velocities of the crust and upper mantle, including thermal, chemical, and seismic-velocities anomalies in the sublithospheric mantle. The discussion related to each improvement is already included in Chapter 3. In the following paragraphs, I will mainly discuss the assumptions made in LitMod2D_2.0 and how they can be relaxed in future.

The integrated geophysical-petrological modelling in LitMod2D_2.0 assumes thermal steady-state regime without advection. Although this assumption is valid for old tectono-thermal regions (>100 Ma) it is less valid in regions with recent tectonic deformation (e.g., in Western Mediterranean where tectonic deformation is Cenozoic). Despite this, the modelling results are constrained by the simultaneous fitting of a set of “instantaneous” density-dependent observables such as gravity, geoid and elevation. Hence, the results must be considered as a snapshot of the present-day density distribution related to active tectonic processes. In regions affected by thermal relaxation after lithospheric thinning, the actual temperature at Moho depth levels is higher than the calculated assuming thermal steady-state because the mass deficit associated with the transient thermal perturbation must be compensated by a larger lithospheric thickness to keep elevation. Therefore, steady-state modelling tends to underestimate the Moho temperature and overestimate the actual lithospheric thickness in regions of lithospheric thinning, showing the opposite effects where the lithosphere is thickened (Fullea et al., 2007). Temperature and density distribution could be improved using a transient thermal model but this requires a more sophisticated numerical approach (i.e., solving the diffusion and advection terms in heat flow equation with time) and, more importantly, an in-depth knowledge of the past and ongoing geodynamic processes and particularly their evolution through time.

LitMod2D_2.0 integrates data across disciplines to put integrated constraints on the present-day structure but makes it challenging to put uncertainties introduced from the errors in the used parameters (e.g., thermodynamic database, Moho depths, and LAB depths). A formal solution to put uncertainties on the final results, noted to be one of the future directions, would be to formulate the modelling in an inversion scheme as recently done in the 3D versions of LitMod (LitMod_4INV; Afonso et al., 2013a, b and 2016b) at the cost of computation resources. Although, inversion algorithms allow an exhaustive sampling of the parameter space, they still need an

initial model and appraisal of the inversion results, requiring additional information (e.g., geology of the study area). However, an ad-hoc procedure can be applied by iteratively changing the parameters of interest to study their sensitivity as done in composition of subducted slabs and lithospheric mantle in Chapter 4.

Surface topography has contributions from three fundamental processes: isostasy, flexure and dynamic flow in the mantle. Decoupling the individual contribution of these three processes to the surface topography is fundamental to understand landscape evolution and facilitates linking deep Earth processes to surface processes. LitMod2D_2.0 does model the isostatic and flexural component of the topography but does not model the dynamic component (also known as dynamic topography) explicitly, which is most likely to be present in tectonically active areas (e.g., subduction zones). In cases where upper mantle anomalies are detached from the overlying lithosphere, LitMod2D_2.0 calculates coupled elevation by accounting for the density variations from anomalous regions, which together with the uncoupled elevation (i.e., isostatic elevation) can serve as lower and upper bound for the dynamic topography, respectively. A more complete treatment of the problem would require using the density and viscosity distribution, calculated as a function of pressure, temperature and composition from LitMod2D_2.0 to solve the Stokes flow equation for the whole modelling domain. The resulting normal stresses at the surface or at the base of the lithosphere will allow calculating a more realistic dynamic topography contribution (e.g., Afonso et al., 2016b). Integrating a Stokes flow solver in the post-processing LitMod2D_2.0 tool-box is one of the future directions.

5.2. Present-day crust and upper mantle structure of the Alboran and Algerian basins and their margins

5.2.1. Crustal and lithospheric structure

The multiple seismic surveys carried out in the study region allowed me to have a good constraint on the Moho depth along most of the sections of both the Alboran and Algerian basins geo-transects (Figure 4.3). The sections that are less constrained are the Algerian Plateau, the Tell-Atlas Mountains and the Greater Kabylies where deep seismic data are not available.

To overcome the uncertainties associated with seismic data and its uneven coverage, I have considered that the crust of the Iberia and Africa mainland consists of three layers, namely upper, middle and lower crust, plus a sedimentary cover. The geometry of these crustal layers responds to the density variations required to fit the observables (Bouguer anomaly, geoid, and elevation) and to tectonic criteria. The structure of the Betics and Greater Kabylies is more complex and differs noticeably from previous lithospheric cross-sections (e.g., Frizon de Lamotte et al., 2004; Roca et al., 2004; Carballo et al., 2015a, b). In these regions, I have included exhumed high-density metamorphic rocks of the Internal Units overthrusting the folded External Units that belonged to the former passive margins (see latter in Geodynamic implications section). Across the Alboran Basin, main differences with previous sections are due to the incorporation of recent interpretations of seismic data (Gómez de la Peña et al., 2018) that led me to consider a thin and highly intruded continental crust in the north Alboran margin transitioning to a magmatic crust in the central part of the Alboran Basin. Seismic data suggest a sharp transition in the centre of the basin (Alboran Ridge), separating the magmatic crust domain from the thinned north-Africa continental crust domain, which continues towards the Africa mainland.

After incorporating these changes, the Moho depth obtained from the models is generally within the uncertainty bounds of seismic data and follows similar trends of previous studies with some localized differences in the margins of the Alboran and Algerian basins and the Valencia Trough (Figure 4.3). Moho depth is a major physical and chemical discontinuity which is imaged by modelling the data sensitive to physical properties, i.e., seismic velocities and density. P-wave receiver functions are routinely used to determine the depth of this contrast using standard H-k stacking method (Zhu and Kanamori, 2000). In H-k stacking, depth of the Moho (H) is determined by assuming an average $V_P/V_S(k)$ for the crust and fitting the arrival time of the Moho converted phase and associated reverberations valid for the isotropic velocity structure. Note that P-wave receiver functions are also sensitive to the intra-crustal structure (e.g., dipping layers) and anisotropy which is not considered in H-k stacking method. Indeed, noticeable discrepancies on Moho depths derived from receiver functions (Diaz et al., 2016) are observed beneath the Betics, which can be attributed to the presence of intra-crustal dipping layers with varying V_P/V_S ratio with depth, and to a heterogeneous crustal structure (Figure 4.3).

Figures 4.5e and 4.9e compare the calculated LAB depths to that reported from other modelling approaches and techniques showing that although there is coincidence with the main trends of lithospheric thickness variations, there are also

pronounced discrepancies in the LAB depth values. Along the Alboran Basin geo-transect, the LAB depth beneath the Iberian Massif, the Betics Mountains and the north Alboran margin is consistent with previous models based on potential field modelling and thermal analysis (Torne et al., 2015) and 2D geophysical-petrological modelling (Carballo et al., 2015b), though our LAB depth values are consistently shallower. These discrepancies in LAB depth ($< 15\%$) are related to the different modelling approach and the simplified crustal structure used in Torne et al. (2015), and differences in the geometry of intra crustal bodies beneath the Betics and the chemical composition of the upper mantle used in Carballo et al. (2015b).

Discrepancies with the LAB depth derived from the 3D geophysical-petrological model by Fullea et al. (2010) are noticeably larger (Figure 4.5e). The LAB proposed by Fullea et al. (2010) beneath the Betics and the north-African margin is much deeper in comparison, with a similar lithospheric thinning below the Alboran Basin affecting a narrower region. These discrepancies may be related to the simpler crustal structure considered by these authors, differences in crustal thickness and chemical compositional domains in the Alboran Basin lithosphere (PUM instead of DMM-6%) and sublithospheric mantle (PUM instead of DMM), and lack of the radiative contribution in calculating the mantle thermal conductivities. The LAB depth beneath the north African margin derived from combined elevation and geoid modelling by Globig et al. (2016) is also noticeably higher (Figure 4.5e) due to the different approach used by these authors, yielding a > 5 km thicker crust in this region (Figure 4.3a).

The LAB depth proposed by Palomeras et al. (2017) from surface wave tomography shows a similar lateral trend with consistently shallower depths that roughly follows the 1000 ± 50 °C isotherm, except beneath the Betics where the LAB is deeper coinciding with the high velocity anomaly related to the Alboran slab (Figure 4.5e). Seismically, the LAB is defined as a low-velocity layer and in Palomeras et al. (2017) it is derived from the depth of the negative S-wave velocity gradient and, therefore, is a proxy of the base of the high-velocity mantle lid. A major misfit occurs at the central part of the Alboran Basin, where the seismically derived LAB is at 250 km depth. Although the precise determination of the LAB depth depends on how it is measured (Eaton et al., 2009), the different definitions should show a similar trend as they all are imaging the rheological strong outer layer of the Earth.

Along the Algerian Basin geo-transect, the only previous works extending along the whole profile are from Roca et al. (2004), based on a pure-thermal

integrated geophysical approach with a temperature-dependent lithospheric mantle density; and Carballo et al. (2015a), based on an integrated geophysical-petrological methodology. Both works show similar results from the Catalan Coastal Ranges to the southern margin of the Algerian Basin, which are also roughly coincident with the model presented in this thesis, despite the methodological differences (Figure 4.8e). It is worth noting that beneath the Algerian margin and the Greater Kabylies region none of the previous works, including Globig et al. (2016) for Africa mainland, considered the presence of a detached Ligurian-Tethys slab segment (i.e., Algerian slab, Figure 4.1d). Despite of that, main discrepancies are found regarding to the work by Carballo et al. (2015a), who proposed a LAB depth up to 60 km shallower than that proposed in this thesis beneath the Greater Kabylies, whereas discrepancies with Roca et al. (2004) and Globig et al. (2016) amount less than 20–25 km. The method used in Carballo et al. (2015a) is similar to the approach used in this thesis; however, calculation of mantle thermal conductivity including the radiative contribution was still not included. Therefore, differences in the LAB-depth can be mainly attributed to small differences in the calculated mantle thermal conductivity, but also to the crustal structure differences (Figure 4.3b) and to the positive seismic velocity anomaly beneath north Algeria (Figure 4.1d) resulting in a deeper LAB in this part of the geo-transect.

5.2.2. Mantle composition

Identifying bulk mantle composition based on density and seismic velocities is not straightforward because of the highly non-linear nature of the problem and the lack of uniqueness. Based on a non-linear 3D multi-observable probabilistic (Bayesian) inversion, Afonso et al. (2013a, b) showed that a wide range of compositions can, equally well, explain multiple geophysical data. In consequence, the considered mantle chemical compositions compatible with the geophysical observables needs further appraisal based on the geological history of the study region.

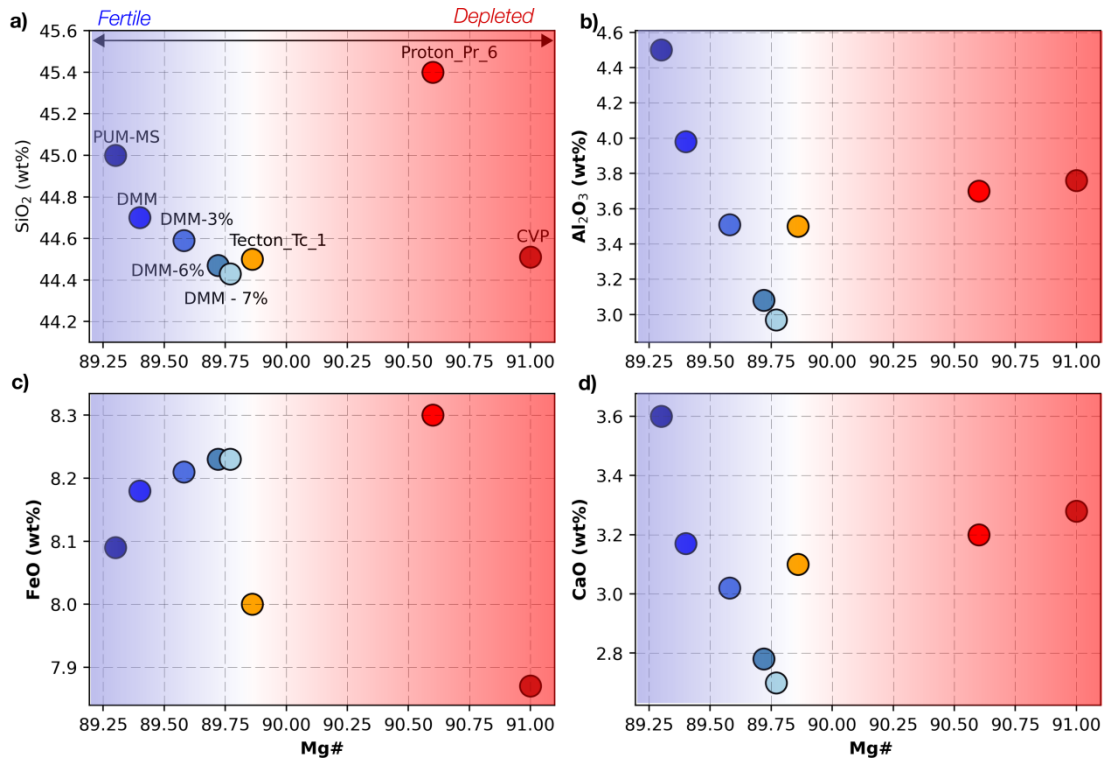


Figure 5.1 Major element oxide weight% of the upper mantle compositions (Table 4.2) are plotted as function of Mg#, a measure of the fertility of the mantle. PUM-MS is also plotted for comparison. Blue shaded region represents the oceanic lithospheres and red shaded area the continental lithospheres.

DMM composition and its derivatives (Table 4.2) show correlation between #Mg and major oxides as a function of the percentage of melting indicating progressive depletion (Figure 5.1). The mantle compositions used in the onshore lithospheres (i.e., continental lithospheres), though have higher #Mg, does not follow the depletion trend as the derivatives of DMM, suggesting that these compositions might have experienced refertilization through metasomatism events, as they are geologically much older than the oceanic lithosphere. CVP composition has been reported to be refertilized indicating mixing between asthenospheric mantle and deeply recycled enriched mantle from oceanic subduction (e.g., Bianchini et al., 2010; Villaseca et al., 2010). High CaO and Al₂O₃ content in the Average Proton Lherzolite (Pr_6) has been reported to be representative of Phanerozoic reworking of Proterozoic to Archean crust (Griffin et al., 2009). Interestingly Average Garnet Tecton (Tc_1) lies near the transition between DMM derivative compositions to continental composition suggesting its juvenile nature because of the moderate depletion from the primitive upper mantle (Griffin et al., 2009).

Although lithospheric mantle compositions in Table 4.2 show small variations in major oxides and #Mg space (Figure 5.1), the computed stable minerals in the models show noticeable differences in the mantle (Figures 5.2 and 5.3). Variation in weight% of each mineral is a function of pressure-temperature and elements these minerals can accommodate in their lattice structure, hence, the bulk mantle composition (Table 2.2).

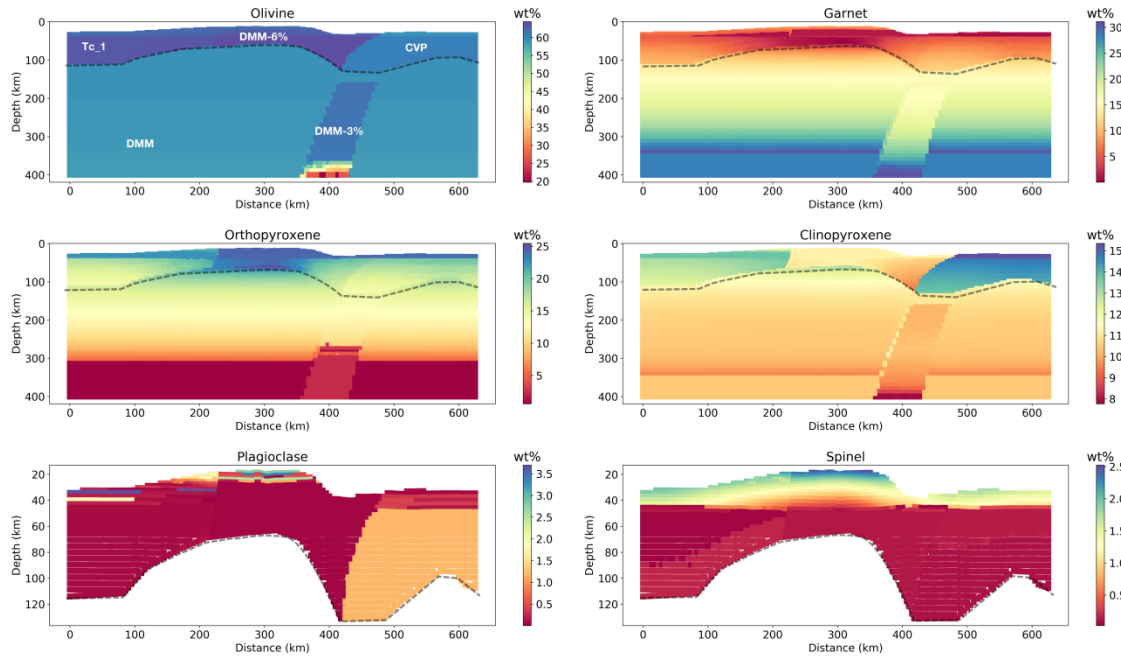


Figure 5.2 Depth distribution of weight% of the stable minerals (see the title of each subplot) along the Alboran Basin geo-transect computed from the Gibbs-free energy minimization. Dashed light black line indicates the LAB and text in white colour indicates the chemical composition listed in the Table 4.2.

In the lithospheric mantle, different compositional domains show variation in weight% of the minerals (Figures 5.2 and 5.3). Plagioclase and spinel are stable at shallow mantle depths and accommodates Al, Ca and Na, hence, there is low weight% of garnet at shallow depths. The regions with thin lithosphere (i.e., Alboran and Algerian basins, Valencia Trough, Balearic Promontory) shows higher weight% of plagioclase and spinel whereas regions corresponding to thick lithosphere (i.e., onshore Iberia and Africa) shows relatively higher weight% of garnet because of the resultant pressure-temperature conditions. Olivine, orthopyroxene, and clinopyroxene also show variations laterally, as well as, with depth. Lateral variations in the mineral weight% occur because of the different compositional domains defined in the lithospheric mantle. Depth-wise variations in the mineral weight% are stronger in the

regions of thin lithosphere in the Western Mediterranean in comparison to the thick lithosphere in the onshore regions.

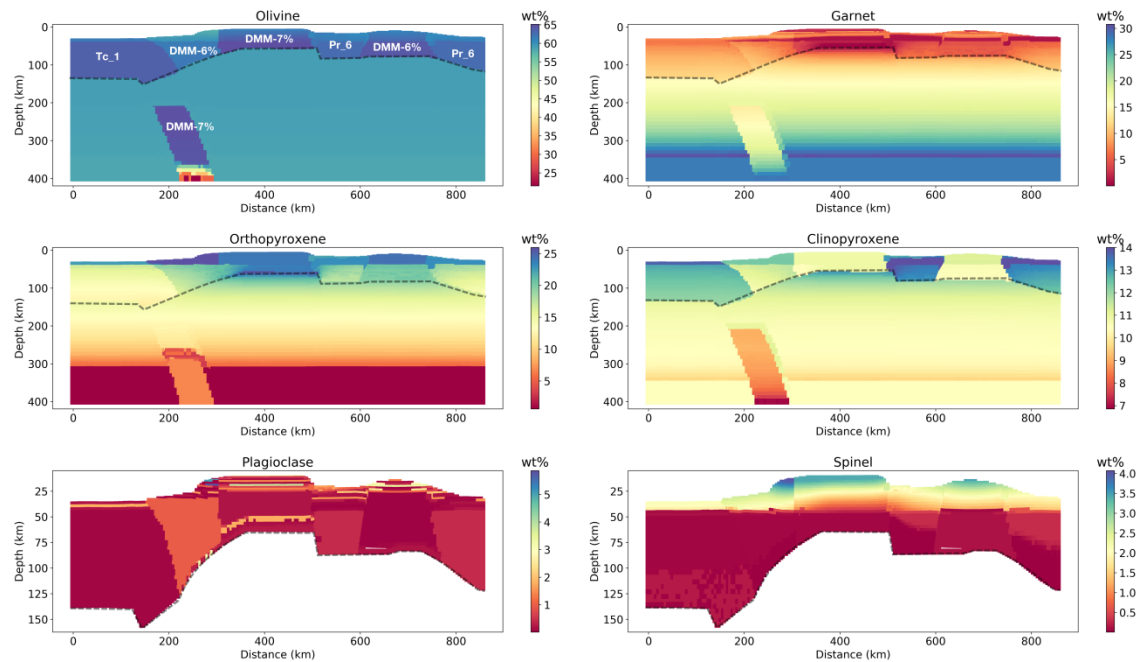


Figure 5.3 Depth distribution of weight% of the stable minerals (see the title of each subplot) along the Algerian Basin geo-transect computed from the Gibbs-free energy minimization chemical compositions used in the mantle. Rest of the caption as in Figure 5.2.

Sublithospheric mantle shows, except in the slab regions, a rather constant distribution of olivine and a varying distribution with depth of garnet, orthopyroxene, and clinopyroxene. A major change in the weight% of these minerals occurs at ~310 km depth, where garnet weight% increases while that of orthopyroxene decreases. This is because both the garnet and orthopyroxene can accommodate Al and increasing the stability of one of them results in decreasing the other (Table 2.2). The variation of minerals weight% in the slab regions is mainly related to the colder temperature and different chemical composition relative to that of the ambient sublithospheric mantle. A clear example of such variation is the decrease in the olivine weight% at ~400 km, indicating transformation to its denser polymorph, wadsleyite (Figure 2.2).

Al_2O_3 , FeO , and SiO_2 are three main oxides primarily controlling the physical properties (i.e., density, P-wave velocity, S-wave velocity) of the mantle. The amount of Al_2O_3 controls the amount of the high-density-velocity Al phases (i.e., spinel - shallow mantle, garnet - deep mantle), which in turn exerts a first-order control on the

physical properties of the bulk mantle. FeO controls the bulk physical properties of all dominant phases, olivine and pyroxene and their relative proportions are controlled by the SiO₂ content. Hence, the variations in weight% of individual minerals will affect the relevant bulk rock physical properties as they are calculated by taking in account the individual mineral abundance (Equations 2.29 and 2.35) and the physical properties are different for each mineral (Figure 5.4). Garnet shows highest density as well as both the P-and S-wave velocities in the upper mantle. Orthopyroxene shows the least density and increases progressively for: clinopyroxene, and olivine. For the seismic velocities, both the P-and S-wave, this trend breaks and clinopyroxene shows the least values and increases for olivine and orthopyroxene. Variation in the individual minerals weight% in the slab regions (Figures 5.2 and 5.3) causes the second order variations of density and P-and S-wave velocities (Figures 4.8 and 4.11). As pointed out in Chapter 4, Section 4.3.2, at 400 km depth the Alboran slab shows a higher density change than the Algerian slab, which is due to the higher amount of garnet in the case of the Alboran slab (Figures 5.2 and 5.3) as DMM-3% composition has higher amount of Al₂O₃ than DMM-7% (Figure 5.1).

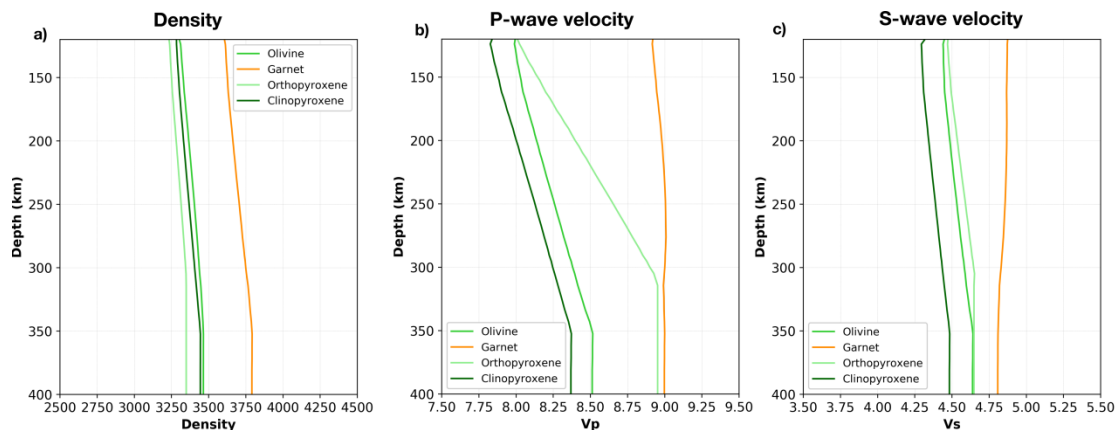


Figure 5.4 Plots showing depth variation of (a) density, (b) P-wave velocity, and (c) S-wave velocity for different minerals present in the mantle.

The bulk density of DMM derivative compositions (e.g., DMM-3%, DMM-6%, DMM-7%) decreases with depletion or in other words with increasing #Mg; however, this trend breaks for the continental lithospheric mantle compositions (Figure 5.5a). Interestingly, Al₂O₃ shows a positive correlation with density for all the compositions used here, since it controls the abundance of the high-density mineral garnet (Figure 5.4), serving as a metric for mantle fertility (Afonso et al., 2013a) (Figure 5.5b). Seismic velocities show a decreasing trend with increasing #Mg, though the

magnitude of its variation among the compositions used is within <0.1 km/s for the P-wave velocities and < 0.04 km/s for the S-wave velocities (Figures 5.5c and d), which is contrary to the positive correlation between #Mg and seismic velocities (Griffin et al., 2009). Note that the mantle compositions I used here are skewed to the lower #Mg values, so the dichotomy in density versus #Mg and decreasing seismic velocities with Mg# for DMM derivatives and continental compositions might not be representative of the mantle composition variability. Afonso et al. (2010), using global database of garnet and spinel peridotite xenoliths (#Mg range ~88 to 95), have shown negative correlation between density and #Mg whereas positive correlation between seismic velocities and #Mg.

Although there is no univocal relationship between mantle chemical composition and its density and elastic properties, the considered lithospheric mantle compositions can be related to major geodynamic processes operating in the Western Mediterranean, which are dominated by subduction of the Ligurian-Tethys Ocean. Subduction processes can modify the mantle chemical composition by incorporating fluids and sediments carried by the subducting slab resulting in chemical enrichment by metasomatism (Ringwood, 1974; Spandler and Pirard, 2013). At the same time, mantle flow generated during subduction can produce melting by adiabatic decompression which will deplete the sublithospheric mantle (Magni, 2019). Generally, volcanic rocks produced from mantle melting show the geochemical signatures similar to the environment in which they are produced. However, interactions of magmas with crustal rocks during ascent and emplacement can influence their geochemical signature. Melchiorre et al. (2017) using Principal Component Analysis (PCA) applied to the Western Mediterranean volcanism concluded that the subduction-related (i.e., orogenic) volcanism shows a greater compositional variability than the intraplate (i.e., anorogenic) volcanism. Compositional variation in orogenic volcanism is associated with the extensive recycling of geochemically different lithologies producing large heterogeneities in the lithospheric mantle (Melchiorre et al., 2017). The large variability of volcanic chemical composition in the Mediterranean region impedes to assign a unique genetic origin to the volcanism and it has been interpreted as the interaction of multiple processes as mentioned by many authors (e.g., Lustrino et al., 2011; Duggen et al., 2008; Melchiorre et al., 2017).

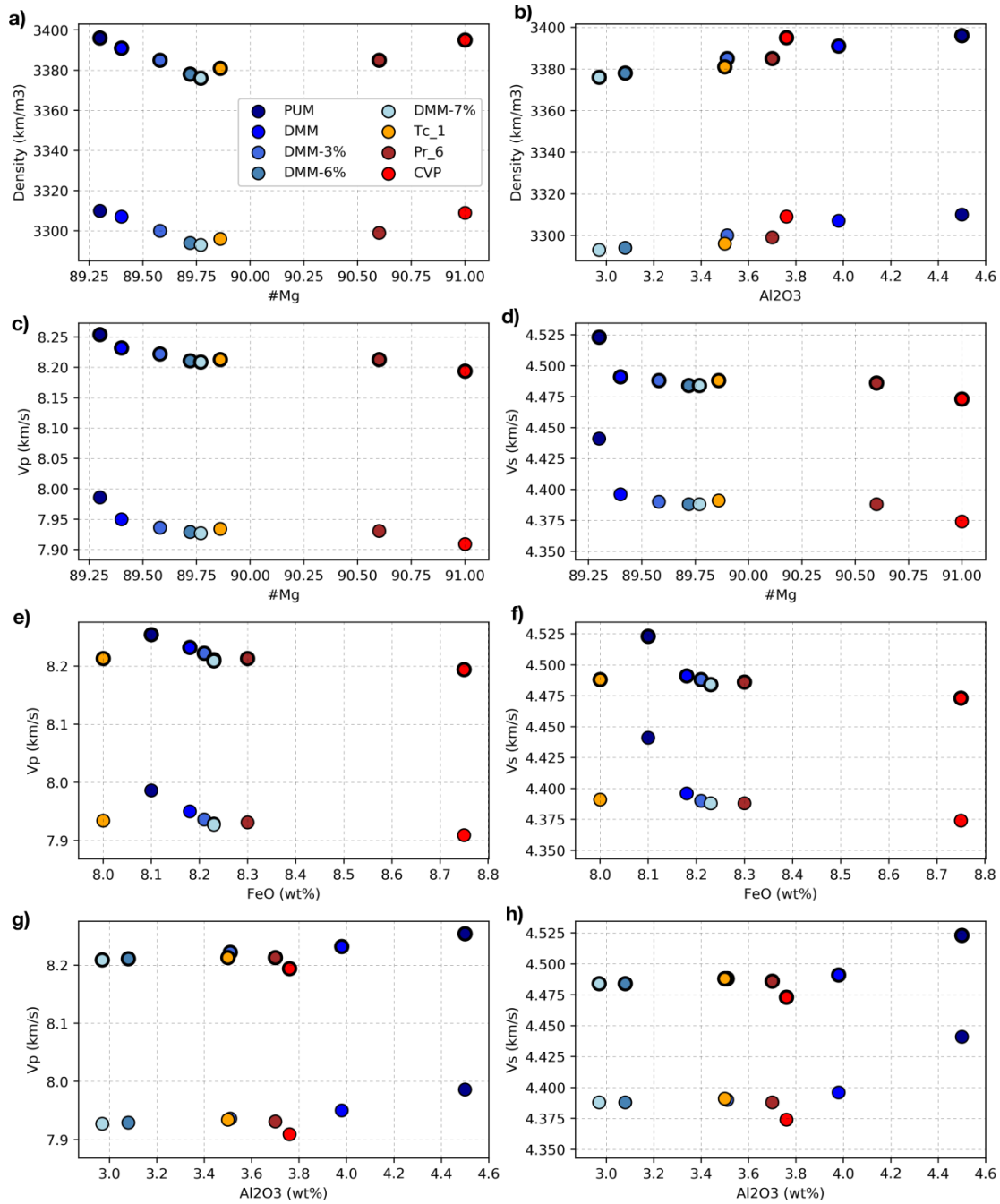


Figure 5.5 Plots showing variation of relevant physical properties with #Mg and major oxide weight percentages for the composition in Table 4.2, colour coded in (a). (a) Shows variation of density with #Mg and (b) with Al₂O₃. (c) - (h) show variation of P-wave and S-wave velocity with #Mg, FeO, Al₂O₃. Circles with thin-black outline corresponds to $P = 3$ GPa (~ 100 km) and $T = 1300$ °C, and circles with thick black outline corresponds to at $P = 6$ GPa (~ 200 km) and $T = 1400$ °C (listed in Table 4.2).

The lithospheric mantle composition of the offshore segments is related to their back-arc origin and the degree of partial melting expected from the nature and volume of magmatic events. During slab roll-back the space opened between the trench and the upper plate is replaced by fertile sublithospheric mantle with DMM composition that

will undergo partial melting by adiabatic decompression. The Algerian Basin shows a typical oceanic crust of 6 km thickness (Booth-Rea et al., 2007) which corresponds to a ~7% of sublithospheric mantle melting and hence to the DMM-7% composition (Klein and Langmuir, 1987; Workman and Hart, 2005). However, in the Valencia Trough and the Alboran Basin melting was less extensive producing large magmatic intrusions and volcanism, hence a DMM-6% composition is more likely. These subtle differences in the chemical composition of the lithospheric mantle respond to geodynamic criteria that require a depleted DMM composition and allow fitting the geophysical observables. Moreover, compositions in the offshore lithospheric mantle also reproduce the seismic velocities derived from seismic data (see Chapter 4, section 4.4).

In the models presented in this thesis, the lithospheric mantle beneath the Betics and Greater Kabylies is fertile compared to the Iberian and North African lithospheric mantle (Figures 4.5 and 4.9). This suggests that continental basement beneath the South Iberia and North Algeria is not attached to the continental lithospheric mantle and indicates the delamination of the continental lithospheric mantle during collision of the retreating slabs with the passive margins. The Alboran Basin geo-transect runs across the zone where the Iberian lithosphere has been interpreted to be delaminated, and the Alboran slab has broken off, whereas to the west delamination has not been achieved, and slab-tear is in progress (Mancilla et al., 2015), as is manifested by the lack of lithospheric mantle level earthquakes in the eastern Betics (depth 60–100 km) (Figures 4.1). A similar situation occurs in the Algerian Basin geo-transect beneath the Greater Kabylies.

In order to test the implied delamination and replacement by the relatively fertile sublithospheric mantle (DMM) beneath the Betics and Greater Kabylies, I run models where composition of the mantle beneath the Betics and Greater Kabylies is changed to as that of the continental lithosphere and LAB depths varies smoothly towards the back-arc basins (Figures 5.6 and 5.7). These models results in a noticeable misfit in geoid height in the Betics and Greater Kabylies.

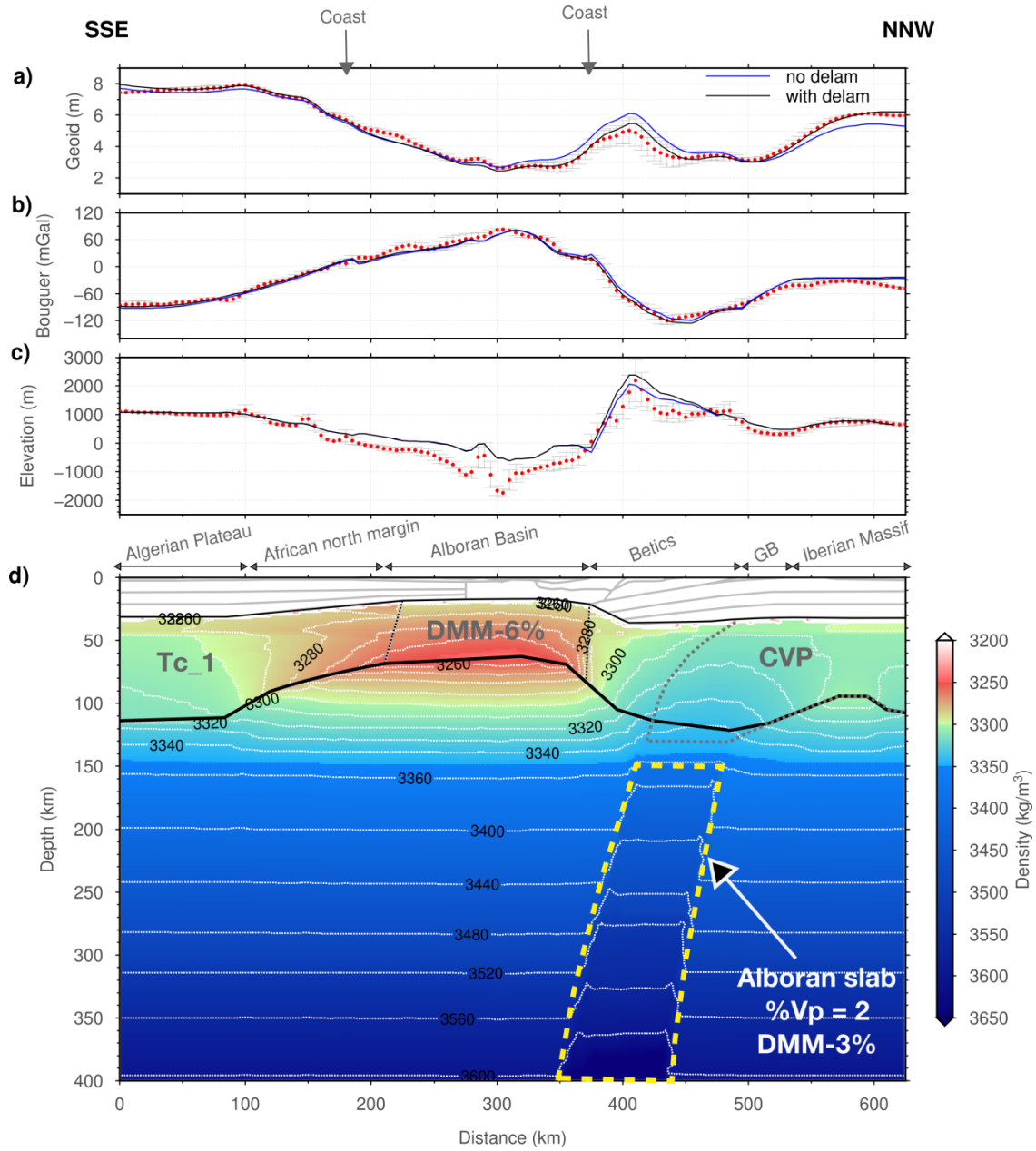


Figure 5.6 Model showing the effect of the delaminated Iberian lithospheric mantle on (a) geoid, (b) Bouguer anomaly, and (c) elevation. In (d) resulting density distribution in the mantle is plotted. Blue line represents the calculated values from the model. Red dots denote measured data, and vertical bars denote the standard deviation calculated across a strip of 25 km half width. Continuous black lines highlight the Moho and LAB depth. The different composition domains in the lithospheric mantle are separated by thin black lines. The bold grey text denotes different chemical composition listed in Table 4.2. Note the continuation of the Iberian lithospheric mantle (CVP) beneath the Betics to simulate no delamination and geometry of the delaminated lithosphere corresponding to the best fitting model is shown with thick dashed grey line.

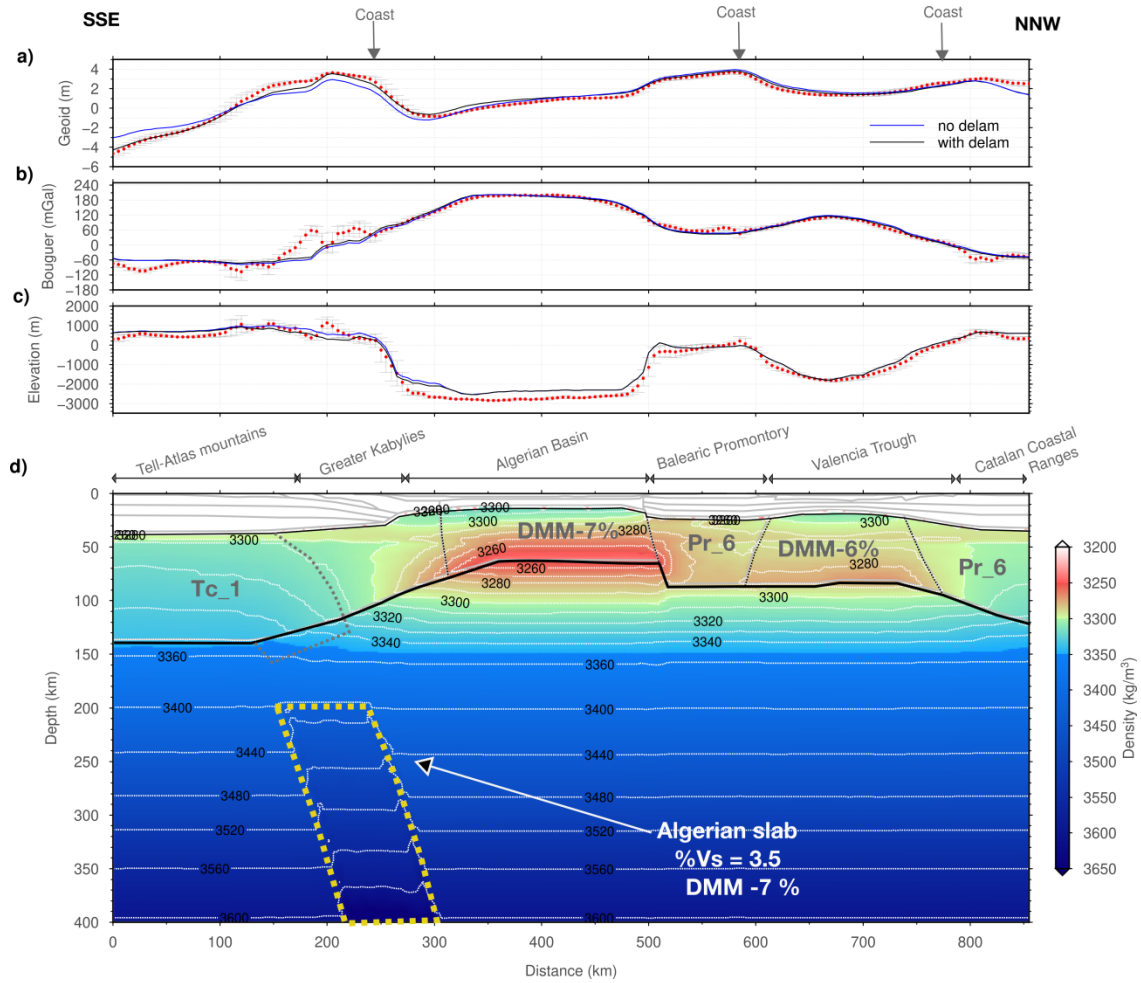


Figure 5.7 Model showing the effect of the delaminated African lithospheric mantle on (a) geoid, (b) Bouguer anomaly, and (c) elevation. In (d) resulting density distribution in the mantle is plotted. Note the continuation of the African lithospheric mantle (Tc_1) beneath the Greater Kabylies to simulate no delamination. Rest of the caption is same as in Figure 5.6.

As mentioned before, different compositional domains in the lithosphere are required in order to fit the geophysical data (Table 4.3) and have consistency with the geological and geodynamic constrains. Having said that, it does not mean that these compositional domains are homogeneous with depth and depth dependent variation in composition is plausible. For example, the oceanic lithosphere is known to have pressure dependent (i.e., depth dependent) degree of fraction melting and hence, depth varying composition (Chapter 2, Section 2.8). Also in the case of the continental lithosphere, mantle xenoliths from Slave, Siberian, and Kaapval cratons show depth dependent fertility where at depths >150 km, composition is more fertile (Lee et al., 2011). Hence, the composition considered in the different lithospheric mantle domains should be conceived as a depth averaged composition.

5.2.3. Subducted Ligurian-Tethys slabs

During subduction, the slab exchanges heat with the hotter ambient sublithospheric mantle and the temperature of the slab increases while the amplitude of the positive seismic velocity anomaly decreases through time (e.g., Boonma et al., 2019). The precise quantification of these transient effects needs additional data regarding the angle and velocity of subduction and other parameters that are poorly constrained (e.g., thermal diffusivity, mantle viscosity, volatile content etc.). The Cenozoic evolution of the Alboran and Algerian basins is related to the subduction of the Ligurian-Tethys Ocean which, according to paleo-geographic reconstructions, was composed of several transtensive and highly extended continental segments transitioning to oceanic lithosphere to the east (Fernández et al., 2019; Schettino and Turco, 2011; Stampfli and Borel, 2002).

Both the Alboran and Algerian slabs have been modelled as ~80 km thick bodies centred on the highest positive velocity anomaly and converted to temperature anomalies according to their chemical composition and P-T conditions, resulting in $\Delta T \approx -400$ °C in both cases (Figures 4.5 and 4.9). It is of interest to highlight the consistency of the seismic velocity anomalies depicted by two independent tomography models based on P-wave travel-time (Alboran slab) and S-wave full-waveform inversion (Algerian slab), which result in very similar temperature anomalies as corresponds to slabs of comparable ages. Further, DMM-3% composition in the Alboran slab is consistent with the paleo-geographic reconstructions purposing highly extended segments in west as compared to the fully developed oceanic lithosphere in the east (i.e. DMM-7% composition of the Algerian slab).

The weight of the cold and dense slabs is not transmitted isostatically to the surface because they have torn/broken off (Figure 4.7). If the slabs were attached, it would decrease the elevation in the Betics by 700–1000 m, and in the Greater Kabylies by 600–1200 m, and increase it by few 100 m in both the Alboran and Algerian basins for an effective elastic thickness of 30 km (Figure 4.7). The subsidence produced by the attached Alboran slab in the Betics compares well with the residual topography model of Civiero et al. (2020) indicating the magnitude of the isostatic rebound after slab tear which can be related to the closure of the connection between the Atlantic Ocean and the Mediterranean Sea through the Betics corridor before the Messinian salinity crisis (García-Castellanos and Villaseñor, 2011). The modelled unhooked slab below the Betics agrees with the reported slab tearing from tomography images (e.g. García-Castellanos and Villaseñor, 2011; Civiero et al.,

2020). Increased elevation in the Alboran and Algerian basins also hints towards the fact that slabs are not attached to the lithosphere, hence, does not contribute to the flexural isostasy. Further, the best fitting modelled elevation (i.e., isostasy + flexure for the uncoupled case) falls at the upper bound of the observed elevation in the Betics and the lower bound in the Greater Kabylies. This suggests that the potential dynamic pull associated with the dense slabs in the less viscous mantle, not modelled here, is higher in the Betics because the torn Alboran slab lies at shallow depths (Figure 4.5). The exact magnitude of the contribution of the dynamic slab pull to elevation will depend on the coupling in between the slabs and the ambient mantle, and requires computation of the induced mantle flow.

5.2.4. Geodynamic implications

The present-day structure of the crust and lithospheric mantle in the Western Mediterranean is the result of a long-lived tectonic evolution since the Jurassic stretching and ocean spreading of the Ligurian Tethys Ocean to the present-day configuration of Western Mediterranean. The analyzed geo-transects show the present-day crust mostly formed during the pervasive Cenozoic northern Africa convergence triggering the building of the Betics-Rif and Kabylies-Tell-Atlas subduction-related orogenic systems. On the contrary, the upper mantle structure shows its current state that is mostly post-tectonic, since it is the result of the lithosphere-asthenosphere interaction governed by the subduction of Ligurian-Tethys lithosphere.

The Alboran Basin has experienced different and partially coeval geodynamic processes. These are the subduction of the Ligurian-Tethys due to the convergence of Africa-Iberia and further roll-back, delamination and slab break-off processes related to the subducting slab. The high density Internal Betics, mostly characterized by Paleozoic and pre-Upper Triassic HP/LT metamorphic rocks, are interpreted to represent the highly extended Iberian distal margin (Vergés and Fernández, 2012; Figure 4.3a). This SE Iberian margin of the Ligurian-Tethys Ocean underwent partial subduction during Africa-Iberia convergence as evidenced from P-T-t paths and ages of HP/LT metamorphic peaks (summary in Gómez-Pugnaire et al., 2019). These HP/LT metamorphic units were later exhumed along the subduction interface forming a roughly NW-directed stack of relatively thin tectonic nappes, each nappe recording specific metamorphic histories. The low-density External Units in the Betics is constituted by a thick sedimentary sequence starting in the Upper Triassic evaporites

that constitute the main detachment level of the Betics orogenic system at the scale of the whole orogenic system as discussed in Vergés and Fernández (2012).

I also test the alternative scenario where the Internal Units are thicker and overlie the Iberian basement as proposed by Mancilla et al. (2015) from receiver function data (Figure 5.8). Increasing the thickness of the Internal Units significantly increases the geoid and the Bouguer anomaly because of the higher volume of the denser Nevado-Filabride units (2900 kg/m^3 ; Table 4.1). It can be argued that the density of the HP/LT units could be $< 2900 \text{ kg/m}^3$ improving the fit to the gravity data, however, as shown in Figure 4.4, the high density of Internal Units are highly plausible.

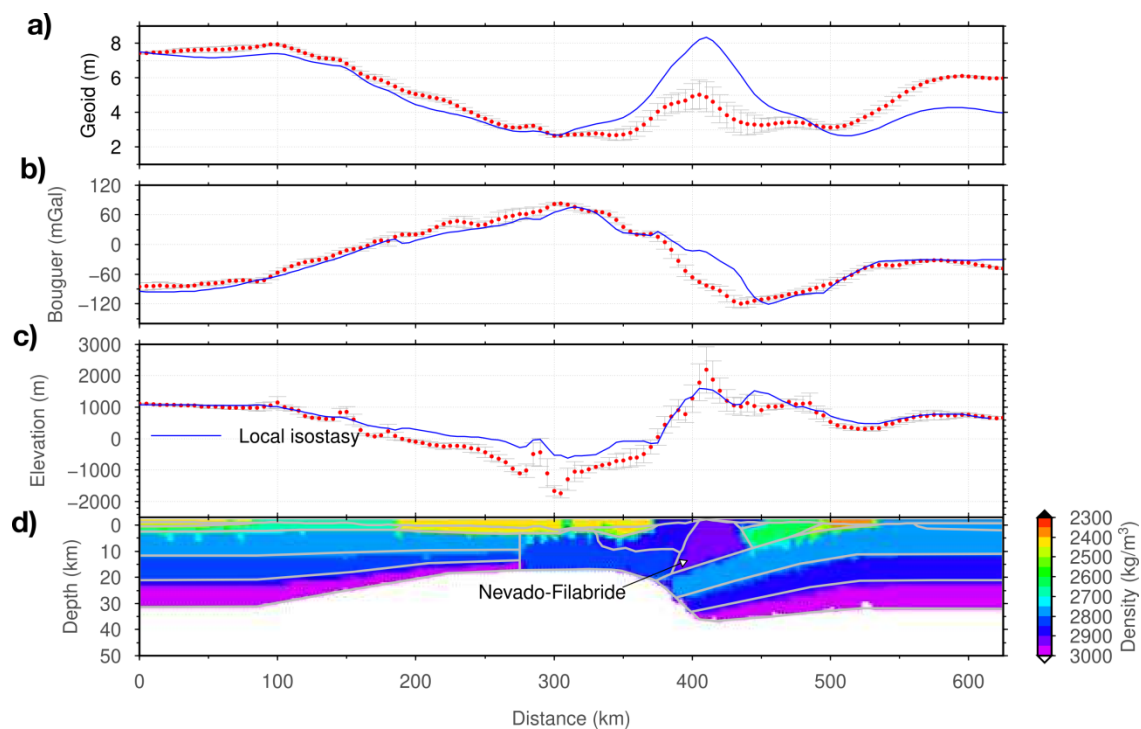


Figure 5.8 Model showing the effect of the thick Nevado-Filabride HP/LT Internal Units on (a) geoid, (b) Bouguer anomaly, and (c) elevation. In (d) resulting density distribution in the crust is plotted. Blue line represents the calculated values from the model. Red dots denote measured data, and vertical bars denote the standard deviation calculated across a strip of 25 km half width. Note that below the crust, the model is the same as that of the best fitting model in Figure 4.5.

The External Betics represents the Upper Triassic and post-Upper Triassic non-metamorphic sedimentary rocks. The External Units attain a similar density at mid-crustal depths as that of the upper crust because of the higher pressure and cannot be distinguished solely based on the gravity field, allowing for an alternative interpretation (Figure 5.9). However, underthrusting of the cover is conceptually

consistent with the NW retreat of the Alboran slab. Additionally, clustering of the seismicity in the External Betics, beneath the Internal Units, points to activated weaknesses (i.e., faults) developed during accretion of the cover. The Betic orogenic system is therefore formed by a system of thrusts that tectonically emplace the large Jurassic Ligurian-Tethys extensional domains that configured the SE Iberian margin on top of each other from the most distal margin (Internal Betics) in the hinterland to the proximal margin (External Betics) in the foreland (e.g., Vergés and Fernández, 2012; Pedrera et al., 2020).

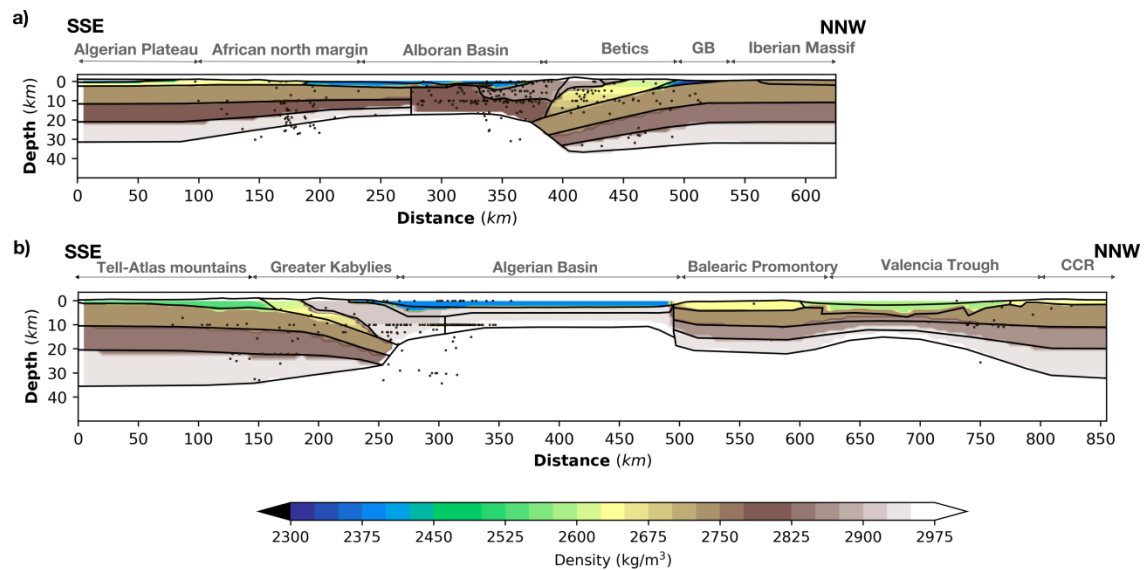


Figure 5.9 Crustal density distribution along the (a) Alboran Basin and (b) Algerian Basin geo-transects. Seismicity similar to the Figure 4.3 is also plotted. Note the increasing density with depth in the External units reaching values close to the upper crust.

The evolution of the Algerian Basin is triggered by the NW-dipping subduction of the Ligurian-Tethys oceanic segments existing between the Balearic Promontory and the Algerian domain of the NW Africa margin (Alvarez et al., 1974), and is widely accepted by most models (e.g., Frizon de Lamotte et al., 2000; Roure et al., 2012; Verges and Sabat, 1999; van Hinsbergen et al., 2014; Casciello et al., 2015; among others). The Kabylies form the HP/LT Internal Units with a relatively high density (Bruguier et al., 2017; Caby et al., 2014; Fernandez et al., 2016; Mahdjoub et al., 1997; Michard et al., 2006; Platt et al., 2013; Rossetti et al., 2010); the Flysch units represent the detached cover above the Ligurian-Tethys sea floor from Jurassic to Late Miocene (e.g., Guerrera and Martín-Martín, 2014, among others), while the Tell and the Atlas form the External Units corresponding to the Algerian margin of the

Ligurian-Tethys Ocean (Leprêtre et al., 2018; Roure et al., 2012). For the modelling purposes the Flysch and External Units are combined since they represent the sedimentary cover (Figure 4.3b). Similar to the Betics, the Internal Units of the Greater Kabylies Massif are thrusting on the Flysch units which are further thrust over the Tellian External Units. Seismicity beneath the Greater Kabylies is distributed in the African basement and the External and Internal Units, although it does not show clear clustering probably due to the lack of local seismic recording stations. Earthquakes below Moho near the present-day passive margin of Algeria could represent the proposed initiation of a new subduction zone (e.g., Déverchère et al., 2005; Hamai et al., 2018).

In a slab roll-back subduction system the crust thickens in the arc region and thins/stretches in the back-arc. Sufficient stretching in the back-arc can lead to the decompressional melting of the fertile mantle producing new oceanic lithosphere. In the models for the Alboran and Algerian basin geo-transects, Crust is thicker in the regions of HP/LT exhumed metamorphic rocks and thins drastically over short distance to the oceanic/magmatic crust of the back-arc regions in comparison to the gradual thickening in the opposed margins (Figure 5.10). Along the Alboran Basin geo-transect, ~37 km thick crust beneath the Betics thins drastically to ~16 km magmatic and volcanism intruded crust of the East Alboran Basin before it transitions to the thinned continental crust south of the Alboran Ridge and thickens gradually further to the SSE in the NW African margin (e.g., Booth-Rea et al., 2007; Gómez de la Peña et al., 2020). Along the Algerian basin geo-transect a relatively thick crust of ~30 km beneath northern Algeria (Greater Kabylies) transitions abruptly to ~10 km thick oceanic crust of the Algerian Basin to the NNW (Figure 5.10). Similarly, thicker lithospheres beneath the Betics and northern Algeria transitions abruptly to only ~60 km thick and fertile lithosphere (i.e., oceanic lithosphere) of both the Alboran and Algerian back-arc basins (Figure 5.10).

The lithospheric structures beneath Algeria and SE Iberia margins, though comparable, are different in width and thickness. The Algerian margin is ~200 km wide while that of Alboran is only 80 km wide. The maximum lithospheric thickness is ~150 km below Algeria and ~130 km below Iberia, although the regional lithospheric thickness of Africa is thicker than in Iberia (Figure 5.10). The existence of quasi-vertical detached Ligurian-Tethys lithospheric slabs under the north Algeria and SE Iberian margins is another feature of resemblance although with opposite apparent dip, to the SSE under Iberia and to the NNW beneath Algeria (Figure 5.10). The two lithospheric slabs are located ~80 km inland from the current shoreline because of the

post slab roll-back mantle delamination and subsequent slab tear, detachment or break-off, of subduction and collision with the margins Iberia and Algeria. Mantle delamination could have promoted the inflow of the fertile sublithospheric mantle beneath the Iberian and Algerian crusts underlying the allochthonous HP/LT metamorphic nappes of the Internal Betics and Greater Kabylies explaining their relatively fertile lithospheric mantle compared to the depleted continental lithospheres of foreland regions in Iberia and Saharan Atlas (Figure 5.10).

Interestingly, the crustal and upper mantle structures in the Betics and the Kabylies-Tell-Atlas are roughly similar, but with opposite tectonic vergence, which could be conceived as having been moulded by similar lithospheric and sublithospheric processes (Figure 5.10). According to our models, the South Iberia margin acted as active margin where the HP/LT slices are stacked leaving the NW Africa margin, in between Rif and Tell-Atlas, as a passive margin influenced by the extension during the slab retreat. An opposite situation occurs in the Algerian Basin where north Algeria acted as an active margin and the Balearic Promontory and Valencia Trough acted as passive margins experiencing extension from the slab retreat (Figure 5.10).

The present-day lithospheric scale thickening beneath the Greater Kabylies and extensional back-arc oceanic Algerian Basin is consistent with SSE retreating subduction kinematics, hence can be explained by all the three geodynamic scenarios proposed for the Western Mediterranean evolution (Figures 1.5 and 5.10). However, each of these models imply different lithospheric structure along the Alboran Basin geo-transect. The geodynamic model with a single long subduction, scenario 2, covering both the Alboran and Algerian basins, retreating to the south cannot explain the NW vergence of the Internal and External Units of the Betics nor their age of tectonic emplacement, the lithospheric structure, and the position of the Alboran slab beneath the Betics (Figure 1.5, scenario 2). Whereas the other two models, scenario 1 and scenario 3 are consistent with the structure beneath the Betics but implying contrary lithospheric structure along the NW Africa margin. According to the scenario 1 model (Figure 1.5, van Hinsbergen et al., 2014), the Alboran slab segment retreated to the west, before colliding with the Iberian margin and rotating by $\sim 180^\circ$, along the purposed North Africa transform fault (i.e. Subduction-Transform Edge Propagator, or STEP fault; Govers and Wortel, 2005) and should produce a significant step in the lithospheric structure of NW Africa, in between Rif and Tell-Atlas Mountains, which is contrary to the observed gradual lithospheric thinning in our lithospheric structure model (Figure 5.10).

The opposite direction of slab retreat in the adjacent segments according to the scenario 3 (Figure 1.5, Vergés and Fernández, 2012) implies opposite symmetry in the crust and upper mantle structure as observed in our models (Figure 5.10). This scenario 3 is based on the pre-convergence geometry of the Iberia-Africa Ligurian Tethys segmented margin configuration (Frizon de Lamotte et al., 2011; Schettino & Turco, 2011; Vergés & Fernández, 2012; Fernández et al., 2019; Fernandez, 2019; Ramos et al., 2020; Martín-Chivelet et al., 2019) that exerted a strong control on further evolution during Africa northern convergence since the Late Cretaceous (e.g., Macchiavelli et al., 2017). The dynamics of such subduction system has been studied using analogue and numerical experiments by Peral et al. (2018) and Peral et al. (2020a and b). The observed lithospheric scale thickening beneath the HP/LT metamorphic rocks of the Betics followed by extension driven thinning and abundant volcanism in the Alboran Basin is consistent with a NW retreating subduction. It must be noted that, to the west of NW Africa margin, in the Rif mountains, lithosphere is thick, which is related to NW-W retreat of the Alboran slab and the trench curvature produced by the higher resistance to slab retreat in the western end of the segment and the further tightening due to the protracted Iberia–Africa convergence (Fernández et al., 2019; Kumar et al., 2018; Peral et al., 2020a, b).

The amount of isostatic rebound in both margins after slab tearing/detachment could reach 500 m - 1200 m when considering T_e values between 10 and 30 km or up to 1500m - 2000 m in the absence of flexural rigidity, as calculated indirectly in the region of Gibraltar (Jiménez-Munt et al., 2019). The slab is still attached under the western Betics (e.g., Civiero et al., 2020; Mancilla et al., 2015). Slab break-off, that along strike, is defined as slab tear with a large gap in the east decreasing towards the west where the slab is continuous at depth below the Gibraltar arc (Mancilla et al., 2018; Negredo et al., 2020).

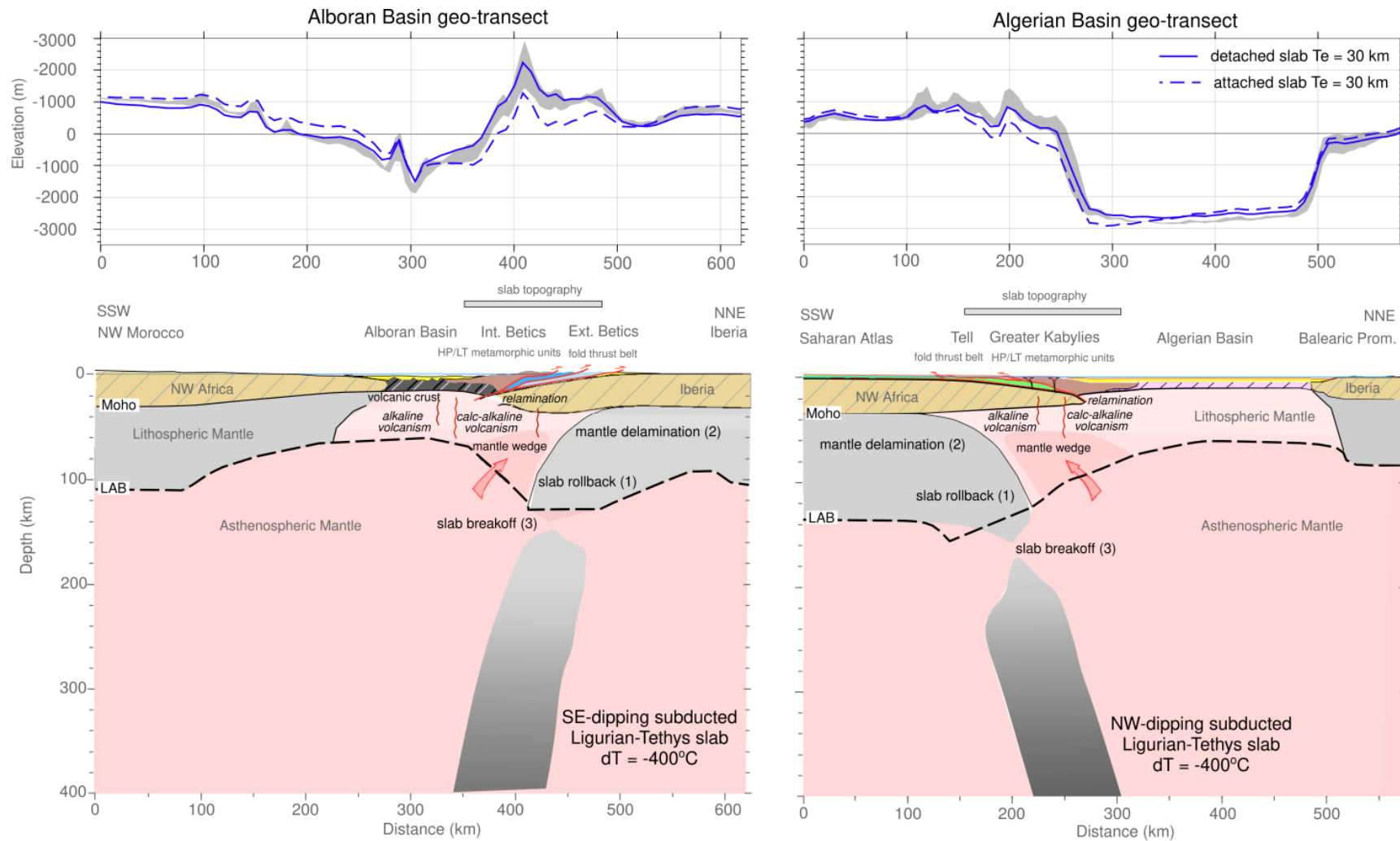


Figure 5.10 Crustal and lithospheric cross-sections at scale along modelled Algerian Basin-Kabylies-Tell-Atlas and Alboran Basin-Internal Betics-External Betics-foreland geo-transects. The structure of both the margins is similar and comparable implying that the underlying geodynamic processes are same for both the margins.

CHAPTER 6

Conclusions

Chapter 6

Conclusions

In this thesis, I have presented an improved LitMod2D_2.0 software package, which allows studying the thermal, density (i.e., composition), and seismic velocity structure of the non-homogeneous lithosphere and sublithospheric mantle by integrating geophysical and geochemical datasets in a self-consistent thermodynamic way. The most exciting improvement in LitMod2D_2.0 is to infer the thermal and/or chemical nature of the sublithospheric mantle anomalies observed in seismic tomography models and their effect on the elevation. The main motivation for this improvement came from the Western Mediterranean, which has experienced subduction during Cenozoic, resulting in subducted slabs in the sublithospheric mantle. Hence, it became the first part of the thesis. In general, this improvement allows the application of LitMod2D_2.0 to regions affected by complex geodynamic processes, such as mantle upwelling, subduction, delamination, and metasomatism (i.e., processes that can easily modify the temperature and/or chemical composition beneath the LAB). In the second part of the thesis, the improved LitMod2D_2.0 is applied to study the present-day thermal, density and seismic velocity structure along two geo-transects in the Alboran and the Algerian basins and their corresponding margins in Iberian and North Africa. The main novelty relative to previous studies is the incorporation of the positive seismic velocity anomalies observed in the seismic tomography models as subducted slabs of the Liguria-Tethys lithosphere. Knowledge of the present-day deep structure and composition of the lithosphere and uppermost sublithospheric mantle may help to discriminate among the proposed models and therefore in constraining the geodynamic evolution of the region. In the following, I report the conclusion from the two parts separately.

6.1. LitMod2D_2.0: An improved tool for the integrated geophysical-petrological interpretation of upper mantle anomalies

In Chapter 3, I have presented an improved version of the LitMod2D_2.0. The new improvements have been demonstrated with the help of synthetic examples. Based on the synthetic experiment, I draw the following conclusions and list the main improvements included in the new LitMod2D_2.0 software package:

- All the purposed depleted chemical compositions for the sublithospheric mantle shows $< 1\%$ of variations in physical properties (i.e., density and seismic velocities) with respect to the Primitive Upper Mantle composition (PUM).
- DMM (depleted MORB mantle) instead of PUM (primitive upper mantle) chemical composition is used in the sublithospheric mantle for geochemical consistency. Nevertheless, the relative differences with respect to PUM in the calculated density and P- and S-wave seismic velocities are less than 0.2% .
- Anelasticity is now calculated in the GENERATOR thermodynamic module using updated parameters in the power-law attenuation model allowing for the physical (temperature, composition) characterization of sublithospheric mantle anomalies. Both oscillation period and grain size remain as input parameters. Assuming the same errors in anelastic attenuation parameters, the frequency dependence of anelastic attenuation and activation energy contributes more to the errors in the final seismic velocities than the activation volume.
- Sublithospheric mantle anomalies may have a thermal, seismic or compositional origin, or a combination of them, allowing for estimating the response of geodynamic processes such as mantle upwelling, subduction, delamination, and metasomatism on the surface observables (elevation, gravity, and geoid).
- Synthetic experiments on thermal anomalies in the sublithospheric mantle show a non-linear dependence between the sign of the thermal anomaly and the resulting magnitude of seismic velocities. Depending on the sign (decreasing/increasing), thermal anomalies produce different magnitude of seismic velocity anomalies. This non-linearity has an important implication for the qualitative interpretation of seismic velocity anomalies observed in tomography models.
- Synthetic experiments show that shear wave velocities are more sensitive to temperature, whereas P-wave velocities are to composition. Hence, modelling

both P-and S-wave velocities together with geoid height, which is sensitive to deep mantle level density variations, holds a potential to infer the thermal and/or chemical heterogeneity in the mantle.

- To compute synthetic V_P and V_S tomography models, an upper mantle model is made, which consists of Average Garnet Tecton composition in the lithospheric mantle, with $Z_{\text{Moho}} = 35$ km and $Z_{\text{LAB}} = 120$ km, and a DMM composition in the sublithospheric mantle down to 400 km depth. This model reproduces the P-wave seismic velocities of the global average reference model ak135 in the depth range of 35 – 250 km and avoids the unsolved mismatch between the thermodynamically calculated seismic velocities and those from ak135 model below 250 km depth.
- A new open-source graphic user interface is developed under Python programming language simplifying the input/output data files to obtain across platforms versatility, to gain ease of use, and allow future user developments.
- A post-processing toolbox is incorporated allowing the user to apply predefined/customized codes and scripts linking with the LitMod2D_2.0 output file to calculate additional observables according to specific needs (synthetic tomography, regional isostasy, stable mineral assemblages, surface wave dispersion curves and receiver functions, etc.). The user can customize the provided codes/scripts or develop new ones to be shared with the scientific community.

6.2. Present-day crust and upper mantle structure in the Alboran and Algerian basins and their margins

In the second part of the thesis, Chapter 4, I presented an integrated geophysical-petrological models of the crust and upper mantle structure of the Western Mediterranean along two geo-transects crossing the Alboran and Algerian basins, and the active/orogenic margins of the Betics and Kabylies-Tell-Atlas Mountains, and the passive/conjugate margins of NW Africa and Eastern Iberia (i.e., Balearic Promontory and Valencia Trough), respectively. At the crust level models presented in this thesis differ from previous crustal-scale models highlighting the use of relatively thin Internal Units above sediments of the External Units in the Betics and Greater Kabylies. The resulting models are constrained by geological and geophysical data and are consistent with the surface observables (elevation, gravity, geoid and surface heat flow) and seismic tomography models. Different lithospheric mantle compositional domains in accordance with geological domains are required to fit the surface observables. Modelling results show an active interaction between the lithosphere and the underlying sublithospheric mantle which was governed by the Alpine subduction dynamics in addition to the NW-SE Africa-Eurasia convergence acting since Late Cretaceous. From the results presented in Chapter 4, I draw following conclusions:

- The thick crust beneath the Betics (~37 km) thins abruptly to 16 km below the Eastern Alboran Basin, which is modelled as a mostly magmatic crust largely intruded by volcanic rocks, and thickens gradually to ~31 km further to the SE in NW Morocco. The thick crust beneath the Greater Kabylies (~30 km) is thinning more abruptly to the northwest reaching ~10 km below the Algerian Basin, modelled as oceanic crust.
- The lithospheres beneath the Internal Betics and the Greater Kabylies are thick and structures are comparable but showing an opposite symmetry, though the lithospheric thickness is larger below the Greater Kabylies. In SE Iberia, the lithosphere beneath the Betics is ~130 km thick thinning sharply to the SSE to ~60 km under the Alboran Basin and thickens again, but gradually, towards NW Africa to ~112 km. The lithosphere beneath the Greater Kabylies is of ~150 km thickness and thins to the NNW to ~60 km thick oceanic lithosphere of the Algerian Basin.

- The present-day lithospheric mantle composition of the Alboran and Algerian basins are modelled as depleted residue from 6–7% aggregate decompressional melting of the relatively fertile sublithospheric mantle composition. This is consistent with the back-arc setting of both the Alboran and Algeria basins related to the retreating of the Ligurian-Tethys lithosphere. Slab retreat triggered the melting of the underlying fertile sublithospheric mantle generating oceanic crust in the Algerian Basin and extensive magmatic and volcanic crust in the Alboran Basin.
- The modelled lithospheric mantle composition beneath the Internal Betics and Greater Kabylies HP/LT metamorphic domains is fertile compared to the corresponding continental lithosphere of the External Betics and Saharan Atlas, respectively. This fertile composition beneath the internal domains of the orogenic systems is related to mantle delamination and inland displacement of the slabs during the later stages of subduction and collision, which promoted the inflow of the fertile sublithospheric mantle material.
- Two detached sub-vertical Ligurian-Tethys lithospheric slabs, with an anomalous temperature of about -400 °C, constrained using the seismic tomography models, about 80 km onshore from the present-day coastlines and restricted to beneath SE Iberia and Algeria. Their most suitable composition is relatively fertile (alike to an oceanic lithosphere), than those below the continental lithospheres of Iberia and North Africa.
- The Ligurian-Tethys slab beneath the SE Iberia shows an apparent dip to the SE whereas the slab below Algeria dips to the NNW, matching the NW- and SE-tectonic transport direction of the fold and thrust belts of the Betics and Greater Kabylies-Tell-Atlas subduction-related orogens, respectively.
- The large-scale configuration of present-day SE Iberia and Algerian margins as well as their mantle compositions in the Alboran and Algerian geo-transects is consistent with opposite dipping subduction of two segments of the Jurassic Ligurian-Tethys domain. Their present configurations agree with Neogene slab roll-back process triggering mantle delamination followed by slab break-off in both opposite subduction segments.
- Uplift related to the slab break-off, considering local and regional isostasy, is ~700–1000 m in SE Iberia and ~600–1200 m in Algeria. These detached Ligurian-Tethys slabs might exert a vertical pull down related to the induced dynamic mantle flow.

List of Figures and Tables

Figure 1.1 Topography map of the Alpine-Himalayan collision zone. The area inside the black box is the focus of this thesis.....	10
Figure 1.2 Geological map of the Western Mediterranean showing the main orogenic belts and basins (Modified from Vergés and Sàbat, 1999). NBTZ, North Balearic Transform Zone; EB, Emile-Baudot Escarpment.	11
Figure 1.3 Detailed geological map of the Western Mediterranean showing main geologic units in the Alboran and Algerian basins, and the Betics-Rif and Kabylies-Tell-Atlas Mountains. Locations of the two geo-transects modelled in this thesis are shown by grey shadowed strips.	12
Figure 1.4 Upper mantle seismic tomography models in the Alboran and Algerian basins.(a) P-wave travel time tomography model slice at 320 km depth (Villaseñor et al.,2013) and (b) Full-waveform inversion seismic tomography model at different depths (Fichtner and Villaseñor, 2015).	14
Figure 1.5 Models purposed for the geodynamic evolution of the Western Mediterranean. Scenario 1 after Van Hinsbergen et al. (2014) involves a single short subduction zone initially dipping to NW starting near the Balearic Promontory and then retreats to the SE before it separates into two different segment. One of the segments continue retreating to SE before it collides with North Africa and other continue retreating to the west and collides with Iberia resulting in 180° clock-wise rotation.Scenario 2 involves a long initial subduction dipping to the N-NW along the entire Gibraltar-Balearic Promontory margin (e.g., Gueguen et al., 1998; Faccenna et al., 2004; Jolivet et al.,2009). Scenario 3 after Vergés and Fernàndez (2012) involves two separate subduction segments with opposite subduction direction for the Alboran (subduction dipping to the SE and retreating to the NW) and Algerian (subduction dipping to the NW and retreating to the SE) basins. Direction of rollback is shown by the yellow arrows. Black dashed lines represent the proposed transform faults separating the different subduction segments (Figure modified after Chertova et al., 2014).....	15
Figure 1.6 Flow chart showing the work-flow and the steps followed to achieve the objectives of this thesis.	22

Figure 2.1 Bulk distribution coefficients of major oxides during melting at the mid-oceanic-ridge calculated using empirical relations from Niu (1997). A black horizontal

line with bulk distribution coefficient of 1 separates compatible elements above it from the incompatible elements below it..... 28

Figure 2.2 Mineral proportions for a pyrolitic composition as function of pressure and temperature range in the mantle. Black circles with error bars shows the experimentally determined phase proportions in dry pyrolite from Irifune and Isshiki (1998) based on high-T-P experiments. Red circles are predictions from Afonso and Zlotnik (2011) thermodynamic database and stars are predictions from the dataset of Xu et al. (2008). Figure is taken from Afonso and Zlotnik (2011). 37

Figure 3.1 Flow chart diagram showing the workflow of LitMod2D_2.0. The new LitMod2D version may account for sublithospheric mantle anomalies in which case coupled elevation is calculated. It also has an option for post-processing of relevant physical properties (temperature, pressure, density and seismic velocities) to compare with additional datasets. Flexural isostasy is included by coupling 'tao-geo' software (Garcia-Castellanos et al., 2002). "Computer Programs in Seismology" (CPS, Herrmann, 2013) is also coupled to work with passive seismological datasets. Stable mineral-assemblages are extracted from the material files produced by the GENERATOR subprogram..... 49

Figure 3.2 Depth distribution of anelastic attenuation parameter (Q , quality factor) for a range of grain sizes (1-100 mm) and oscillation periods (10-100s) compared with global average Q_P and Q_S models. (a) and (b) shows the depth distribution of Q_P and Q_S for varied grain size and constant oscillation period of $T_0 = 75$ s, respectively. (c) and (d) shows depth distribution of Q_P and Q_S for varied oscillation period (10-100 s) and constant grain size of $d = 10$ mm, respectively. Q_P and Q_S from ak135 global average model (continuous red solid line, Kennett et al., 1995), and Q_S from QL6c (continuous grey line, Durek and Ekström, 1996), are also plotted for comparison. 53

Figure 3.3 Percentage error introduced in the (a) P-wave velocities and (b) S-wave velocities considering 10% error in α (dashed blue line), E (dotted-dashed blue line), and V (dotted blue line). The total error is plotted in solid blue line and temperature distribution is plotted in solid-red line..... 54

Figure 3.4 Comparison of different compositions tested in the sublithospheric mantle (Table 3.1). Resulting density (a), P-wave velocities (b) and S-wave velocities (c) are compared with that to PUM. 56

Figure 3.5 Depth distributions of seismic velocities, (a) P-wave and (b) S-wave assuming an Average Garnet Tecton composition in the lithosphere mantle and a DMM composition in the sublithospheric mantle. Seismic velocities are calculated using Afonso and Zlotnik (2011) (solid, modified Holland and Powell, 1998), Stixrude and Lithgow-Bertelloni (2005) (thick dashed) and Xu et al. (2008) (thin dashed) thermodynamic databases. Resulting seismic velocities are corrected for anelastic attenuation using a constant grain size of 10 mm and oscillation period of 75 s. Global average seismic velocities from ak135 (Kennett et al., 1995), in solid grey circles, with an error of 0.5% in P-wave velocities and 1% in S-wave velocities are plotted for comparison.	60
Figure 3.6 Synthetic examples of thermal anomalies in the sublithospheric mantle. Input thermal anomalies are plotted in (a). Resultant change in (b) density, (c) P-wave velocities, and (d) S-wave velocities are plotted with same colour code as input. All anomalies are referred to a reference model, shown as inset in the upper right corner.	62
Figure 3.7 Synthetic example illustrating the contribution of compositional (Average Garnet Tecton, blue), thermal (+50 °C, orange), and combination of both (green) anomalies to (a) density, (b) P-wave velocities, and (c) S-wave velocities, with respect to the reference model shown as inset in the upper right corner.	63
Figure 3.8 Example of a varying magnitude (along the profile) relative P-wave seismic velocity anomaly. (a) Screenshot of the input file used in this synthetic example. (b) Resultant temperature, density and seismic velocities.	65
Figure 3.9 Synthetic examples of input P- and S-wave anomalies of $\pm 1.5\%$ in the sublithospheric mantle. Recovered temperature (a) and density (b) from the input seismic velocity anomalies are plotted with respect to the reference model shown in the upper right corner.	66
Figure 3.10 Screen shots from the new open-source GUI, provided with LitMod2D_2.0, (a) Graphic user interface input window showing the geometry of the modelled profile and various functions to interact and work with the model. (b) Screenshots of model outputs from the model, in the left panel forward prediction of surface observables, observed (blue) and calculated (red and black) and the model geometry at the bottom. Surface observables without the sublithospheric mantle anomalies are plotted in red to highlight their effect. Right panel in (b) shows the temperature, density and seismic velocity distribution (P-wave and S-wave) from the model.	69
Figure 3.11 Example of seismic velocities post-processing. (a) Synthetic P-wave tomography along the modelled synthetic profile. (b) Depth distribution of S-wave	

velocities at three locations along the profile with colour coded and marked in (a). (c) Synthetic P-wave receiver functions at the three locations marked in (a). At the subduction zone two receiver functions with (filled orange) and without (black line) the subducted slab, are plotted for comparison. (d) Synthetic Rayleigh-surface-wave group (left) and phase (right) velocities. At the subduction zone orange dispersion curves corresponds to the model without the slab and dashed-black line to the model with the slab. 73

Figure 3.12 Weight% of different stable minerals with depth for the reference model defined in LitMod2D_2.0 (section 3.5). Note that total weight% does not add to 100% in the shallow lithosphere (< 50 km) and around 300 km; this could be because of the failed numerical energy minimizations during the computation of stable mineral assemblage, although difference is only about <5%. 74

Figure 4.1 (a) Simplified geological map of the study region showing the location of the Alboran and Algerian basin geo-transects in shaded grey line. Earthquakes location colour coded for depth from 1964-2016 taken from International Seismological Centre (ISC, <https://doi.org/10.31905/D808B830>) catalogue are also plotted. (b) P-wave travel-time tomography along the Alboran Basin geo-transect from Bezada et al. (2013). (c) Absolute S-wave velocity model from Rayleigh surface-wave dispersion tomography (Palomeras et al. 2014) along the Alboran Basin geo-transect. (d) S-wave tomography using full-waveform inversion (modified after Figure 8 of Fichtner and Villaseñor, 2015) along the direction of cross-section C-C' marked in (a). 78

Figure 4.2 Geophysical observables in the region. (a) Shaded elevation and surface heat flow (dots), (b) Bouguer anomaly, (c) geoid filtered up to degree and order 10. Grey thick lines show the locations of the modelled NNW-SSE oriented geo-transects. 79

Figure 4.3 Crustal structure corresponding to the best fitting model for the (a) Alboran Basin and (b) Algerian Basin geo-transects. Densities used in each body are colour-coded (see the legend). Moho depths from previous studies (including active seismic, receiver functions, surface wave dispersion and joint modelling of gravity and elevation) are also plotted for comparison. Earthquakes ($M_b \geq 3.0$; 1964-2016, ISC catalogue) projected 50 km across the geo-transects are plotted with black circles. Note that the y-axis is exaggerated by two times the x-axis for better visualization. GB,

Guadalquivir Basin; CCR, Catalan Coastal Ranges; RF, Receiver functions; DSS, Deep seismic sounding.....	83
--	----

Figure 4.4 Pressure and temperature dependent density distribution for average sediments, upper crust, middle crust and lower crust compositions (see legend), computed from stable phases and mineral assemblages using the Gibbs free-energy minimization algorithm (Connolly, 2005, 2009). Red and black dashed line boxes mark the range of high pressure metamorphic peaks for Alpujarride and Nevado-Filabride HP/LT metamorphic units, respectively, determined from thermo-barometry (Augier et al., 2005; López Sánchez- Vizcaíno et al., 2001; Puga et al., 2000; Azañón and Crespo-Blanc, 2000).	86
--	----

Figure 4.5 Best fitting model along the Alboran Basin geo-transect. (a) Surface heat flow. (b) Geoid height. (c) Bouguer anomaly. (d) Elevation. Blue line represents the calculated values from the model. Red dots denote measured data, and vertical bars denote the standard deviation calculated across a strip of 25 km half width. In (b) geoid height with no slab anomaly is plotted in grey for comparison. In (d) isostatic elevation is plotted in solid blue while the effect of slab on elevation (coupled elevation) is plotted in dashed blue line. Elevation assuming flexural isostasy for elastic thickness of 10 km and 30 km are plotted in orange and light-green, respectively. (e) Temperature distribution along the geo-transect. Continuous black lines highlight the Moho and LAB depth from our model. LAB depths from previous studies (dashed colour lines) are overlay plotted for comparison. (f) Density distribution in the mantle. The different composition domains in the lithospheric mantle are separated by thin black lines. The bold text in grey colour denotes chemical composition used in the different lithospheric mantle domains listed in Table 4.2.....	88
--	----

Figure 4.6 Alboran slab chemical composition sensitivity to the (a) geoid height and (b) Bouguer anomaly. Chemical composition has minuscule effect on the Bouguer anomaly and has noticeable effect on the geoid height. Variation in the Alboran slab composition, situated at depths >140 km, changes the mass distribution in the slab region and consequently affects the geoid at longer wavelengths along the geo-transect. DMM-3% chemical composition fits the geoid better along the Alboran Basin geo-transect.	89
--	----

Figure 4.7 Observed and modelled elevation across (a) Alboran Basin geo-transect and (b) Algerian basin geo-transect. Region highlighted in white shows extend along the geo-transect to which the slabs would affect the elevation. Dark-grey shaded strip shows the observed elevation across 50 km wide swath along the geo-transects. Solid coloured lines represent elevation with no slab anomaly (uncoupled), while dashed colour lines show calculated elevation considering the slab (coupled elevation). Blue	
--	--

lines shows isostatic elevation (i.e. $T_e = 0$ km). Orange and green lines show elevation considering flexural isostasy, $T_e = 10$ km, and 30 km, respectively.....	90
Figure 4.8 Temperature, density, and P- and S-wave velocity depth distribution in the Alboran slab at three locations spanning the slab region along the Alboran Basin geo-transect (see the legend). Upper panel shows the absolute deviation with respect to the LitMod reference column (Chapter 3) and lower panel shows the percentage change.....	93
Figure 4.9 Best fitting model along the Algerian Basin geo-transect, rest of the caption as in Figure 4.5.....	96
Figure 4.10 Algerian slab chemical composition sensitivity to the (a) geoid height and (b) Bouguer anomaly. DMM-7% chemical composition, resulting from 7%melting of DMM, fits better the geoid height along the Algerian Basin geo-transect.....	97
Figure 4.11 Temperature, density, P-wave velocity and S-wave velocity depth distribution in the Algerian slab at three locations (see the legend) spanning the slab region along the Algerian Basin geo-transect. Rest of the caption is same as in Figure 4.8.	99
Figure 4.12 Seismic velocities and synthetic seismic tomography along the geo-transects. (a) and (b) shows the absolute P-wave and S-wave velocities, respectively and (c) synthetic P-wave anomalies for the Alboran Basin geo-transect. Similarly (d) and (e) shows the absolute P- and S-wave velocities, respectively, and (f) synthetic P-wave anomalies along the Algerian Basin geo-transect.....	101
Figure 4.13 Geotherms (solid lines) at selected locations along the (a) Alboran Basin and (b) Algerian Basin geo-transects. Dry and wet peridotites solidus for different amount of bulk water from Katz and Spiegelman (2003) are also plotted. Presence of water in the mantle brings down the solidus resulting in presence of partial melts...	102
Figure 4.14 Location of the seismic stations along the geo-transects used to calculate P-wave receiver functions. Blue points show the location of piercing point at a depth 35 km along the Alboran Basin geo-transect.....	104
Figure 4.15 Plot showing the forward calculation of passive seismological data from the velocities obtained along Alboran Basin geo-transect. (a) Crustal S-wave velocities calculated using empirical relations (see text for details). (b) P-wave receiver function at distance, labelled in each plot, along the geo-transect. Solid green represent forward calculation and grey is observed P-wave receiver function (where available). (c) Rayleigh surface-wave fundamental mode phase velocity dispersion curves along	

the Alboran Basin geo-transect at distance along the geo-transect labelled in each plot. Grey circles represent the observed phase velocities and bars represent corresponding error. Green circles represent the forward calculation from the seismic velocity model obtained from LitMod2D_2.0. 106

Figure 4.16 Plot showing the comparison between forward prediction of receiver functions and Rayleigh surface-wave dispersion curves at selected locations. (a) Shows the depth distribution of S-wave velocities colour coded for location (see the legend). (b) P-wave receiver function, (c) group velocities, and (d) phase velocities colour coded for location (see legend in a). 108

Figure 5.1 Major element oxide weight% of the upper mantle compositions (Table 4.2) are plotted as function of Mg#, a measure of the fertility of the mantle. PUM-MS is also plotted for comparison. Blue shaded region represents the oceanic lithospheres and red shaded area the continental lithospheres. 119

Figure 5.2 Depth distribution of weight% of the stable minerals (see the title of each subplot) along the Alboran Basin geo-transect computed from the Gibbs-free energy minimization. Dashed light black line indicates the LAB and text in white colour indicates the chemical composition listed in the Table 4.2. 120

Figure 5.3 Depth distribution of weight% of the stable minerals (see the title of each subplot) along the Algerian Basin geo-transect computed from the Gibbs-free energy minimization chemical compositions used in the mantle. Rest of the caption as in Figure 5.2. 121

Figure 5.4 Plots showing depth variation of (a) density, (b) P-wave velocity, and (c) S-wave velocity for different minerals present in the mantle. 122

Figure 5.5 Plots showing variation of relevant physical properties with #Mg and major oxide weight percentages for the composition in Table 4.2, colour coded in (a). (a) Shows variation of density with #Mg and (b) with Al_2O_3 . (c) - (h) show variation of P-wave and S-wave velocity with #Mg, FeO, Al_2O_3 . Circles with thin-black outline corresponds to $P = 3 \text{ GPa}$ ($\sim 100 \text{ km}$) and $T = 1300 \text{ }^\circ\text{C}$, and circles with thick black outline corresponds to at $P = 6 \text{ GPa}$ ($\sim 200 \text{ km}$) and $T = 1400 \text{ }^\circ\text{C}$ (listed in Table 4.2). 124

Figure 5.6 Model showing the effect of the delaminated Iberian lithospheric mantle on (a) geoid, (b) Bouguer anomaly, and (c) elevation. In (d) resulting density distribution in the mantle is plotted. Blue line represents the calculated values from the model. Red dots denote measured data, and vertical bars denote the standard deviation calculated across a strip of 25 km half width. Continuous black lines highlight the Moho and LAB

depth. The different composition domains in the lithospheric mantle are separated by thin black lines. The bold grey text denotes different chemical composition listed in Table 4.2. Note the continuation of the Iberian lithospheric mantle (CVP) beneath the Betics to simulate no delamination and geometry of the delaminated lithosphere corresponding to the best fitting model is shown with thick dashed grey line. 126

Figure 5.7 Model showing the effect of the delaminated African lithospheric mantle on (a) geoid, (b) Bouguer anomaly, and (c) elevation. In (d) resulting density distribution in the mantle is plotted. Note the continuation of the African lithospheric mantle (Tc_1) beneath the Greater Kabylies to simulate no delamination. Rest of the caption is same as in Figure 5.6..... 127

Figure 5.8 Model showing the effect of the thick Nevado-Filabride HP/LT Internal Units on (a) geoid, (b) Bouguer anomaly, and (c) elevation. In (d) resulting density distribution in the crust is plotted. Blue line represents the calculated values from the model. Red dots denote measured data, and vertical bars denote the standard deviation calculated across a strip of 25 km half width. Note that below the crust, the model is the same as that of the best fitting model in Figure 4.5. 130

Figure 5.9 Crustal density distribution along the (a) Alboran Basin and (b) Algerian Basin geo-transects. Seismicity similar to the Figure 4.3 is also plotted. Note the increasing density with depth in the External units reaching values close to the upper crust..... 131

Figure 5.10 Crustal and lithospheric cross-sections at scale along modelled Algerian Basin-Kabylies-Tell-Atlas and Alboran Basin-Internal Betics-External Betics-foreland geo-transects. The structure of both the margins is similar and comparable implying that the underlying geodynamic processes are same for both the margins. 135

Table 2.1 Major oxide compositions (weight %) of the crust..... 26

Table 2.2 Mineral solid solution notation and formulae..... 37

Table 3.1 Major oxide compositions (weight %) in the mantle. 55

Table 3.2 Physical properties and major oxides composition in the mantle of a column at an old oceanic lithosphere used to compute calibration parameters for elevation. . 58

Table 3.3 Thermophysical parameters used in the crust to compare calculated seismic velocities with those from ak135 model..... 59

Table 4.1 Thermo-physical properties of the different tectonic units in the crust along the geo-transects.	82
Table 4.2 Major elements composition (weight %) in the NCFMAS system for the lithospheric mantle and sublithospheric domains used in the modelling and corresponding relevant physical properties at lithosphere and sublithospheric mantle pressure and temperature.....	84
Table 4.3 Root mean square error (RMSE) associated with the tested models. RMSE is calculated by considering the lateral variability of the observables through the assigned error bars (see text for explanation).	91

References

- Abers, G. A., K. M. Fischer, G. Hirth, D. A. Wiens, T. Plank, B. K. Holtzman, C. McCarthy, & E. Gazel (2014). Reconciling mantle attenuation-temperature relationships from seismology, petrology, and laboratory measurements, *Geochem. Geophys. Geosyst.*, 15, 3521–3542, doi:10.1002/2014GC005444.
- Afonso, J., Moorkamp, M., Fullea, J. (2016a). Imaging the lithosphere and upper mantle. *Geophysical Monograph Series*, pp. 191–218.
- Afonso, J. C., Fernández, M., Ranalli, G., Griffin, W. L., & Connolly, J. A. D. (2008). Integrated geophysical-petrological modeling of the lithosphere and sublithospheric upper mantle: Methodology and applications. *Geochemistry, Geophysics, Geosystems*, 9, Q05008.
- Afonso, J. C., Fullea, J., Griffin, W. L., Yang, Y., Jones, A. G., Connolly, J. A. D., & O'Reilly, S. Y. (2013a). 3-D multiobservable probabilistic inversion for the compositional and thermal structure of the lithosphere and upper mantle. I: A priori petrological information and geophysical observables. *Journal of Geophysical Research: Solid Earth*, 118, 2586–2617. <https://doi.org/10.1002/jgrb.50124>
- Afonso, J. C., Fullea, J., Yang, Y., Connolly, J. A. D., & Jones, A. G. (2013b). 3-D multi-observable probabilistic inversion for the compositional and thermal structure of the lithosphere and upper mantle. II: General methodology and resolution analysis. *Journal of Geophysical Research: Solid Earth*, 118, 1650–1676.
- Afonso, J.C., Ranalli, G., Fernández, M., Griffin, W.L., O'Reilly, S.Y. & Faul, U. (2010). On the Vp/Vs–Mg# correlation in mantle peridotites: Implications for the identification of thermal and compositional anomalies in the upper mantle. *Earth and Planetary Science Letters*, 289(3–4), pp.606–618.
- Afonso, J. C., Rawlinson, N., Yang, Y., Schutt, D., Jones, A. G., Fullea, J., & Griffin, W. L. (2016b). 3-D multiobservable probabilistic inversion for the compositional and thermal structure of the lithosphere and upper mantle: III. Thermochemical tomography in the Western-Central U.S. *Journal of Geophysical Research: Solid Earth*, 121, 7337–7370. <https://doi.org/10.1002/2016JB013049>
- Afonso, J. C., & Zlotnik, S. (2011). The subductability of the continental lithosphere: The before and after story. In D. Brown & P. D. Ryan (Eds.), *Arc-Continent Collision* (pp. 53–86). Berlin: *Frontiers in Earth Sciences*, Springer.
- Agard, P., Plunder, A., Angiboust, S., Bonnet, G., & Ruh, J. (2018). The subduction plate interface: rock record and mechanical coupling (from long to short timescales). *Lithos*, 320–321, 537–566.
- Aïdi, C., Beslier, M. O., Yelles-Chaouche, A. K., Klingelhoefer, F., Bracene, R., Galve, A., Bounif, A., Schenini, L., Hamai, L., Schnurle, P., Djellit, H., Sage, F., Charbis, P., & Déverchère, J., (2018). Deep structure of the continental margin and basin off Greater Kabylia, Algeria—New insights from wide-angle seismic data modeling and multichannel seismic interpretation. *Tectonophysics*, 728, 1–22.
- Alvarez, W., Coccozza, T., & Wezel, F. C. (1974). Fragmentation of the Alpine orogenic belt by microplate dispersal. *Nature*, 248(5446), 309–314.
- Amante, C., & Eakins, B. W. (2009). ETOPO1 1 Arc-minute global relief model: Procedures, data sources and analysis. NOAA Technical Memorandum NESDIS NGDC-24, <http://www.ngdc.noaa.gov/mgg/global/global.html>

- Amaru, M. L. (2007). Global travel time tomography with 3-D reference models (Vol. 274). Utrecht University.
- Anderson, D.L. & Minster, J.B. (1979). The frequency dependence of Q in the Earth and implications for mantle rheology and Chandler wobble. *Geophys. J. R. Astron. Soc.* 58:431–40
- Anderson, D. (1989). Appendix "Theory of the Earth". *Theory of the Earth*, 52 (1354), 569–569.
- Asimow, P.D., Hirschmann, M.M. & Stolper, E.M. (2001). Calculation of peridotite partial melting from thermodynamic models of minerals and melts, IV. Adiabatic decompression and the composition and mean properties of mid-ocean ridge basalts. *Journal of Petrology*, 42(5), pp.963–998.
- Asimow, P. D., M. M. Hirschmann, & L. M. Stolper (2001), Calculation of peridotite partial melting from thermodynamic model of minerals and melts, IV. Adiabatic decompression and the composition and mean properties of mid-ocean basalts, *J. Petrol.*, 42, 963–998.
- Asimow, P. D., Dixon, J. E. & Langmuir, C. H. (2004), A hydrous melting and fractionation model for mid-ocean ridge basalts: Application to the Mid-Atlantic Ridge near the Azores, *Geochem. Geophys. Geosyst.*, 5, Q01E16, doi:10.1029/2003GC000568.
- Augier, R., Agard, P., Monié, P., Jolivet, L., Robin, C., Booth-Rea, G., (2005). Exhumation, doming and slab retreat in the Betic Cordillera (SE Spain): in situ $^{40}\text{Ar}/^{39}\text{Ar}$ ages and P–T–d–t paths for the Nevado-Filabride complex. *Journal of Metamorphic Geology* 23, 357–381.
- Ayala, C., Bohoyo, F., Maestro, A., Reguera, M. I., Rubio, F. M., Torne, M., et al. (2016). Updated Bouguer anomaly map of the Iberian Peninsula: A new perspective to interpret the regional geology. *Journal of Maps*. <https://doi.org/10.1080/17445647.2015.1126538>
- Azañón, J.M., Crespo-Blanc, A. (2000). Exhumation during a continental collision inferred from the tectonometamorphic evolution of the Alpujarride Complex in the central Betics (Alboran Domain, SE Spain). *Tectonics* 19, 549–565.
- Banda, E., Gallart, J., Garcia-Duenas, V., Danobeitia, J.J., Makris, J. (1993). Lateral variation of the crust in the Iberian Peninsula. New evidence from the Betic Cordillera. *Tectonophysics* 221, 53–66
- Banks, C.J., Warburton, J. (1991). Mid-crustal detachment in the Betic system of southeast Spain. *Tectonophysics* 191, 275–289.
- Behn, M., & Kelemen, P. (2003). The relationship between seismic P-wave velocity and the composition of anhydrous igneous and meta-igneous rocks. *Geochem Geophys Geosyst* 4:1041. doi:10.1029/2002GC000393
- Berástegui, X., Banks, C.J., Puig, C., Taberner, C., Waltham, D., Fernandez, M. (1998). Lateral diapiric emplacement of Triassic evaporites at the southern margin of the Guadalquivir Basin, Spain. In: Mascle, A., Puigdefabregas, C., Luterbacher, H., Fernandez, M. (Eds.), *Cenozoic Foreland Basins of Western Europe*. Geological Society Special Publications 134, pp. 49–68.
- Bezada, M. J., Humphreys, E. D., Toomey, D. R., Harnafi, M., Dávila, J. M., & Gallart, J. (2013). Evidence for slab rollback in westernmost Mediterranean from improved mantle imaging. *Earth and Planetary Science Letters*, 368, 51–60. <https://doi.org/10.1016/j.epsl.2013.02.024>
- Boonma, K., Kumar, A., García-Castellanos, D., Jiménez-Munt, I., & Fernández, M. (2019). Lithospheric mantle buoyancy: the role of tectonic convergence and mantle composition. *Scientific reports*, 9(1), 1–8.

- Booth-Rea, G., Ranero, C. R., Martínez-Martínez, J. M., & Grevemeyer, I. (2007). Crustal types and Tertiary tectonic evolution of the Alborán sea, western Mediterranean. *Geochemistry, Geophysics, Geosystems*, 8(10).
- Bianchini, G., Beccaluva, L., Bonadiman, C., Nowell, G. M., Pearso, D. G., Siena, F., & Wilson, M. (2010). Mantle metasomatism by melts of HIMU piclogite components: New insights from Fe-Iherzolite xenoliths (Calatrava Volcanic District, central Spain). In M. Coltorti, H. Downes, M. Gregoire, & S. O'Renly (Eds.), *Petrological evolution of the European lithospheric mantle*, Special Publications (Vol. 337, pp. 107–124). London: Geological Society.
- Bowin, C., (1983). Depth of principal mass anomalies contributing to the Earth's Geoidal Undulations and gravity anomalies. *Marine Geodesy*, 7: 61-100.
- Bowin, C., (2000). Mass anomalies and the structure of the Earth. *Physics and Chemistry of the Earth*, 25 (4): 343-353.
- Brey, G. P., Doroshev, A. M., Giris, A. V. & Turkin, A. I. (1999), Garnet-spinel-olivine-orthopyroxene equilibria in the FeO-MgO-Al₂O₃-SiO₂-Cr₂O₃ system: I. Composition and molar volumes of minerals, *Eur. J. Mineral.*, 11, 599–617.
- Brocher, T. (2005). Empirical relations between elastic wavespeeds and density in the Earth's crust. *Bulletin of the Seismological Society of America*, 95 (6), 2081-2092.
- Brown, E. L., Petersen, K. D., & Leshner, C. E. (2020). Markov chain Monte Carlo inversion of mantle temperature and source composition, with application to Reykjanes Peninsula, Iceland. *Earth and Planetary Science Letters*. 2020. 532. <https://doi.org/10.1016/j.epsl.2019.116007>.
- Bruguier, O., Bosch, D., Caby, R., Vitale-Brovarone, A., Fernandez, L., Hammor, D., Laouar, R., Ouabadi, A., Abdallah, N., & Mechat, M. (2017). Age of UHP metamorphism in the Western Mediterranean: insight from rutile and minute zircon inclusions in a diamond-bearing garnet megacryst (Edough Massif, NE Algeria). *Earth and Planetary Science Letters*, 474, 215-225.
- Brun, J. P., & Faccenna, C. (2008). Exhumation of high-pressure rocks driven by slab rollback. *Earth and Planetary Science Letters*, 272(1-2), 1-7.
- Caby, R., Bruguier, O., Fernandez, L., Hammor, D., Bosch, D., Mechat, M., Laouar, R., Ouabadi, A., Abdallah, N., & Douchet, C. (2014). Metamorphic diamonds in a garnet megacryst from the Edough Massif (northeastern Algeria). *Recognition and geodynamic consequences. Tectonophysics*, 637, 341-353.
- Calvert, A., Sandvol, E., Seber, D., Barazangi, M., Roecker, S., Mourabit, T., Vidal, F., Alguacil, G., Jabour, N., (2000). Propagation of regional seismic phases (Lg and Sn) and Pn velocity structure along the Africa–Iberia plate boundary zone. *Geophysical Journal International* 142, 384–408.
- Cammarano, F., & Romanowicz, B. (2008). Radial profiles of seismic attenuation in the upper mantle based on physical models. *Geophysical Journal International*, 175 (1), 116-134.
- Cammarano, F., Deuss, A., Goes, S., & Giardini, D. (2005). One-dimensional physical reference models for the upper mantle and transition zone: Combining seismic and mineral physics constraints. *Journal of Geophysical Research: Solid Earth*, 110 (1), 1-17.
- Cammarano, F., Goes, S., Vacher, P., & Giardini, D. (2003). Inferring upper-mantle temperatures from seismic velocities. *Physics of the Earth and Planetary Interiors*, 138 (3-4), 197-222.
- Cammarano, F., Romanowicz, B., Stixrude, L., Lithgow-Bertelloni, C., & Xu, W. (2009). Inferring the thermochemical structure of the upper mantle from seismic data. *Geophysical Journal International*, 179 (2), 1169-1185.

- Carlson, R.W., Pearson, D.G. & James, D.E. (2005). Physical, chemical, and chronological characteristics of continental mantle. *Reviews of Geophysics*, 43:RG1001.
- Casciello, E., Fernández, M., Vergés, J., Cessarano, M., & Torne, M. (2015). The Alboran Domain in the Western Mediterranean evolution: The birth of a concept. *Bull. Soc. Géol.*, 186, 23–34.
- Carballo, A., Fernandez, M., Torne, M., Jiménez-Munt, I., & Villaseñor, A. (2015a). Thermal and petrophysical characterization of the lithospheric mantle along the northeastern Iberia geo-transect. *Gondwana Research*, 27, 1430-1445.
- Carballo, A., Fernandez, M., Jiménez-Munt, I., Torne, M., Vergés, J., Melchiorre, M., et al. (2015b). From the North-Iberian Margin to the Alboran Basin: A lithosphere geo-transect across the Iberian Plate. *Tectonophysics*, 399-418.
- Carbonell, R., Torne, M., García-Dueñas, V., Moya, R., & Banda, E., (1997). The ESCI-Béticas: a seismic reflection image of the Betics orogen. *Rev. Soc. Geol. Esp.* 8, 503–512.
- Carbonell, R., Sallarès, V., Pous, J., Dan, J. J., Queralt, P., Ledo, J. J., & Duen, V. G. (1998). A multidisciplinary geophysical study in the Betic chain (southern Iberia Peninsula). *Tectonophysics*, 288(1-4), 137-152.
- Chazot, G., Abbassene, F., Maury, R. C., Déverchère, J., Bellon, H., Ouabadi, A., & Bosch, D. (2017). An overview on the origin of post-collisional Miocene magmatism in the Kabylies (northern Algeria): evidence for crustal stacking, delamination and slab detachment. *Journal of African Earth Sciences*, 125, 27-41.
- Chertova, M.V.; Spakman, W.; Geenen, T.; van den Berg, A.P.; & van Hinsbergen, D.J.J. (2014). Underpinning tectonic reconstructions of the western Mediterranean region with dynamic slab evolution from 3-D numerical modeling. *J. Geophys. Res.: Solid Earth*, 119, 5876–5902.
- Christensen, N., Mooney, W. (1995). Seismic velocity structure and composition of the continental crust: a global view. *J. Geophys. Res.* 100 (B6), 9761–9788. <http://dx.doi.org/10.1029/95JB00259>
- Civiero, C., Strak, V., Custódio, S., Silveira, G., Rawlinson, N., Arroucau, P., & Corela, C. (2018). A common deep source for upper-mantle upwellings below the Ibero-western Maghreb region from teleseismic P-wave travel-time tomography. *Earth and Planetary Science Letters*, 499, 157-172.
- Civiero, C., Custódio, S., Duarte, J. C., Mendes, V. B., & Faccenna, C. (2020). Dynamics of the Gibraltar Arc System: A Complex Interaction Between Plate Convergence, Slab Pull, and Mantle Flow. *Journal of Geophysical Research: Solid Earth*, 125(7), e2019JB018873.
- Comas, M.C., Dañobeitia, J.J., Alvarez-Marrón, J., Soto, J.I., (1995). Crustal reflections and structure in the Alboran Basin: Preliminary Results of the SCI-Alboran Survey. In: Santanach, P. (Ed.) *Revista de la Sociedad Geológica de España* 8, pp. 75–88
- Connolly, J. (2005). Computation of phase equilibria by linear programming: A tool for geodynamic modeling and its application to subduction zone decarbonation. *Earth and Planetary Science Letters*, 236 (1-2), 524-541.
- Connolly, J. A. D. (2009). The geodynamic equation of state: What and how, *Geochem. Geophys. Geosyst.*, 10, Q10014, doi:10.1029/2009GC002540.
- Connolly, J. A. D., & Kerrick, D. M. (2002), Metamorphic controls on seismic velocity of subducted oceanic crust at 100–250 km depth, *Earth Planet. Sci. Lett.*, 204, 61–74.
- Coulon, C., Megartsi, M., Fourcade, S., Maury, R.C., Bellon, H., Louni-Hacini, A., Cotten, J., Coutelle, A., & Hermitte, D., (2002). Post-collisional transition from calc-alkaline to alkaline

- volcanism during the Neogene in Oranie (Algeria): magmatic expression of a slab breakoff. *Lithos* 62, 87–110.
- Dañobeitia, J.J., Arguedas, M., Gallart, F., Banda, E., & Makris, J., (1992). Deep crustal configuration of the Valencia trough and its Iberian and Balearic borders from extensive refraction and wide-angle reflection profiling. *Tectonophysics* 203, 37–55.
- Davies, J. H. (2013). Global map of solid Earth surface heat flow. *Geochemistry, Geophysics, Geosystems*, 14(10), 4608–4622.
- Deen, T. J., W. L. Griffin, G. Begg, S. Y. O'Reilly, L. M. Natapov, & J. Hronsky (2006), Thermal and compositional structure of the subcontinental lithospheric mantle: Derivation from shear wave seismic tomography. *Geochem. Geophys. Geosyst.*, 7, Q07003, doi:10.1029/2005GC001120.
- Déverchère, J., Yelles, K., Domzig, A., Mercier de Lépinay, B., Bouillin, J.P., Gaullier, V., Bracène, R., Calais, E., Savoye, B., Kherroubi, A. & Le Roy, P., 2005. Active thrust faulting offshore Boumerdes, Algeria, and its relations to the 2003 Mw 6.9 earthquake. *Geophysical research letters*, 32(4).
- Dewey, J.F., Helman, M.L., Turco, E., Hutton, D.H.W., Knott, S.D. (1989). Kinematics of the western Mediterranean. In *Alpine Tectonics*, ed. M.P. Coward, D. Dietrich, R.G. Park, pp. 265–83. *Geol. Soc. Spec. Publ.* 45. London: Geol. Soc. Lond.
- Diaferia, G., & Cammarano, F. (2017). Seismic Signature of the Continental Crust: What Thermodynamics Says. An Example From the Italian Peninsula. *Tectonics*, 36 (12), 3192–3208.
- Díaz, J., Gallart, J., & Carbonell, R. (2016). Moho topography beneath the Iberian-Western Mediterranean region mapped from controlled- source and natural seismicity surveys. *Tectonophysics*, 692, 74–85. <https://doi.org/10.1016/j.tecto.2016.08.023>
- Díaz, J., Gallart, J. (2009). Crustal structure beneath the Iberian Peninsula and surrounding waters: a new compilation of deep seismic sounding results. *Phys. Earth Planet. Sci. Lett.* 173, 181–190. <http://dx.doi.org/10.1016/j.pepi.2008.11.008>.
- Díaz, J., Gil, A., Gallart, J. (2013). Uppermost mantle seismic velocity and anisotropy in the Euro-Mediterranean region from Pn and Sn tomography. *Geophys. J. Int.* <http://dx.doi.org/10.1093/gji/ggs016>.
- Duggen, S., Hoernle, K., van den Bogaard, P., & Garbe-Schönberg, D. (2005). Post-collisional transition from subduction- to intraplate-type magmatism in the westernmost Mediterranean: Evidence for continental-edge delamination of subcontinental lithosphere. *Journal of Petrology*, 46, 1155–1201. <https://doi.org/10.1093/petrology/egi013>
- Duggen, S., Hoernle, K. A., Klugel, A., Geldmacher, J., Thirlwall, M. F., Hauff, F., et al. (2008). Geochemical zonation of the Miocene Alborán Basin volcanism (westernmost Mediterranean): Geodynamic implications. *Contributions to Mineralogy and Petrology*, 156, 577–593. <https://doi.org/10.1007/s00410-008-0302-4>
- Durek, J., & Ekström, G. (1996). A radial model of anelasticity consistent with long-period surface-wave attenuation. *Bulletin of the Seismological Society of America*, 86 (1 SUPPL. A), 144–158.
- Eaton, D. W., Darbyshire, F., Evans, R. L., Grütter, H., Jones, A., & Yuan, X. (2009). The elusive lithosphere-asthenosphere boundary (LAB) beneath cratons. *Lithos*, 109, 1–22. <https://doi.org/10.1016/j.lithos.2008.05.009>
- Ehsan, S. A., Carbonell, R., Ayarza, P., Martí, D., Jesús Martínez-Poyatos, D., Simancas, J., et al. (2015). Lithospheric velocity model across the Southern Central Iberian Zone (Variscan Iberian Massif): The ALCUDIA wide-angle seismic reflection transect. *Tectonics*, 34, 535–554. <https://doi.org/10.1002/2014TC003661>

- Etheve, N., Mohn, G., Frizon de Lamotte, D., Roca, E., Tugend, J., & Gómez-Romeu, J. (2018). Extreme Mesozoic crustal thinning in the eastern Iberia margin: the example of the Columbrets Basin (Valencia Trough). *Tectonics*, 37(2), 636-662.
- Faccenna, C., Becker, T. W., Auer, L., Billi, A., Boschi, L., Brun, J. P., & Piromallo, C. (2014). Mantle dynamics in the Mediterranean. *Reviews of Geophysics*, 52(3), 283-332.
- Faccenna, C., Piromallo, C., Crespo-Blanc, A., Jolivet, L., & Rossetti, F. (2004). Lateral slab deformation and the origin of the western Mediterranean arcs. *Tectonics*, 23(1).
- Faul, U. & Jackson, I. (2015). Transient Creep and Strain Energy Dissipation: An Experimental Perspective. *Annual Review of Earth and Planetary Sciences* 2015 43:1, 541-569.
- Fernandez, L., Bosch, D., Bruguier, O., Hammor, D., Caby, R., Monié, P., et al. (2016). Permo-carboniferous and early miocene geological evolution of the internal zones of the Maghrebides-new insights on the western Mediterranean evolution. *Journal of Geodynamics* 96: 146–173.
- Fernández-García, C., Guillaume, B., & Brun, J. P. (2019). 3D slab breakoff in laboratory experiments. *Tectonophysics*, 773, 228223.
- Fernàndez, M., & Cabal, J. (1992). Heat-flow data and shallow thermal regime on Mallorca and Menorca (western Mediterranean). *Tectonophysics*, 203(1-4), 133-143.
- Fernàndez, M., Afonso, J., & Ranalli, G. (2010). The deep lithospheric structure of the Namibian volcanic margin. *Tectonophysics*, 481 (1-4), 68-81.
- Fernàndez, M., Marzan, I., Correia, A., Ramalho, E., (1998a). Heat flow, heat production, and lithospheric thermal regime in the Iberian Peninsula. *Tectonophysics* 291, 29–53. [http://dx.doi.org/10.1016/S0040-1951\(98\)00029-8](http://dx.doi.org/10.1016/S0040-1951(98)00029-8).
- Fernàndez, M., Berástegui, X., Puig, C., García-Castellanos, D., Jurado, M.J., Torné, M., Banks, C., (1998b). Geophysical and geological constraints on the evolution of the Guadalquivir foreland basin, Spain. In: Mascle, A., Puigdefàbregas, C., Luterbacher, H.P., Fernàndez, M. (Eds.), *Cenozoic Foreland Basins of Western Europe: Geological Society Special Publications*, 134, pp. 29–48.
- Fernàndez, M., Foucher, J.P., & Jurado, M.J. (1995). Evidence for the multi-stage formation of the south- western Valencia Trough. *Marine and Petroleum Geology*, 12, 101-109.
- Fernàndez, M., Torne, M., Vergés, J., Casciello, E., & Macchiavelli, C. (2019). Evidence of Segmentation in the Iberia–Africa Plate Boundary: A Jurassic Heritage?. *Geosciences*, 9(8), 343.
- Fichtner, A., Villaseñor, A., (2015). Crust and upper mantle of the western Mediterranean - constraints from full-waveform inversion. *Earth Planet. Sci. Lett.* 428, 52–62.
- Foucher, J.E., Mauffret, A., Steckler, M., Brunet, M.E., Maillard, A., Rehanlt, J.E., Alonso, B., Desegaulx, E., Murillas, J., & Ouillon, G., (1992). Heat flow in the Valencia trough: geodynamic implications. *Tectonophysics* 203, 77–97.
- Foulger, G.R., Panza, G.F., Artemieva, I.M., Bastow, I.D., Cammarano, F., Evans, J.R., Hamilton, W.B., Julian, B.R., Lustrino, M., Thybo, H. & Yanovskaya, T.B., (2013). Caveats on tomographic images. *Terra Nova*, 25 (4), 259-281.
- Fourcade, S., Capdevila, R., Ouabadi, A., & Martineau, F. (2001). The origin and geodynamic significance of the Alpine cordierite-bearing granitoids of northern Algeria. A combined petrological, mineralogical, geochemical and isotopic (O, H, Sr, Nd) study. *Lithos*, 57(2-3), 187-216.
- Fullea, J., Fernàndez, M., Zeyen, H., & Vergés, J. (2007). A rapid method to map the crustal and lithospheric thickness using elevation, geoid anomaly and thermal analysis: Application

- to the Gibraltar Arc System, Atlas Mountains and adjacent zones. *Tectonophysics*, 430, 97–117.
- Fullea, J., Fernàndez, M., Afonso, J. C., Vergés, J., & Zeyen, H. (2010). The structure and evolution of the lithosphere–asthenosphere boundary beneath the Atlantic–Mediterranean Transition Region. *Lithos*, 120(1-2), 74-95.
- Fullea, J., Afonso, J., Connolly, J., Fernàndez, M., García-Castellanos, D., & Zeyen, H. (2009). LitMod3D: An interactive 3-D software to model the thermal, compositional, density, seismological, and rheological structure of the lithosphere and sublithospheric upper mantle. *Geochemistry, Geophysics, Geosystems*, 10 (8), 1-21.
- Fullea, J., Fernàndez, M., & Zeyen, H. (2008). FA2BOUG—A FORTRAN 90 code to compute Bouguer gravity anomalies from gridded free air anomalies: Application to the Atlantic–Mediterranean transition zone. *Computers & Geosciences*, 34, 1665–1681. <https://doi.org/10.1016/j.cageo.2008.02.018>
- Frizon de Lamotte, D., Crespo-Blanc, A., Saint-Bezar, B., Comas, M., Fernandez, M., Zeyen, H., Ayarza, P., Robert-Charreau, C., Chalouan, A., Zizi, M., Teixel, A., Arboleya, M.L., Alvarez-Lobato, F., Julivert, M., Michard, A., (2004). TRASNSMED-transect I (Betics, Alboran Sea, Rif, Moroccan Meseta, High Atlas, Jbel Saghro, Tindouf basin). In: Cavazza, W., Roure, F., Spakman, W., Stampfli, G.M., Ziegler, P.M. (Eds.), *The TRANSMED Atlas- the Mediterranean region from Crust to Mantle*. Springer, Berlin Heidelberg.
- Frizon de Lamotte, D., Saint Bezar, B., Bracène, R., & Mercier, E. (2000). The two main steps of the Atlas building and geodynamics of the western Mediterranean. *Tectonics*, 19(4), 740-761.
- Frizon de Lamotte, D., Raulin, C., Mouchot, N., Wrobel-Daveau, J.-C., Blanpied, C., Ringenbach, J.C., (2011). The southernmost margin of the Tethys realm during the Mesozoic and Cenozoic: initial geometry and timing of the inversion processes. *Tectonics* 30, TC3002. <http://dx.doi.org/10.1029/2010TC002691>.
- Gallart, J., Vidal, N., Dañobeitia, J.J., (1995). Multichannel seismic image of the crustal thinning at the NE Iberian margin combining normal and wide angle reflection data. *Geophys. Res. Lett.* 22, 489–492.
- Garcia-Castellanos, D., Fernandez, M., & Torne, M. (2002). Modeling the evolution of the Guadalquivir foreland basin (southern Spain). *Tectonics*, 21 (3).
- Garcia-Castellanos, D., & Villasenor, A. (2011). Messinian salinity crisis regulated by competing tectonics and erosion at the Gibraltar arc., *Nature*, 480(7377), 359–363. <https://doi.org/10.1038/nature10651>
- Gaspar-Escribano, J. M., Garcia-Castellanos, D., Roca, E., & Cloetingh, S. A. P. L. (2004). Cenozoic vertical motions of the Catalan Coastal Ranges (NE Spain): The role of tectonics, isostasy, and surface transport. *Tectonics*, 23(1).
- Gilardoni, M., Reguzzoni, M., & Sampietro, D. (2016). GECO: A global gravity model by locally combining GOCE data and EGM2008. *Studia Geophysica et Geodaetica*, 60, 228–247. <https://doi.org/10.1007/s11200-015-1114-4>
- Globig, J., Fernàndez, M., Torne, M., Vergés, J., Robert, A., & Faccenna, C. (2016). New insights into the crust and lithospheric mantle structure of Africa from elevation, geoid, and thermal analysis. *Journal of Geophysical Research - Solid Earth*, 121, 5389–5424. <https://doi.org/10.1002/2016JB012972>
- Goes, S., Govers, R., & Vacher, P. (2000). Shallow mantle temperatures under Europe from P and S wave tomography . *Journal of Geophysical Research: Solid Earth*, 105 (B5), 11153-11169.

- Gómez de la Peña, L., Ranero, C. R., & Gràcia, E. (2018). The crustal domains of the Alboran Basin (western Mediterranean). *Tectonics*, 37, 3352–3377. <https://doi.org/10.1029/2017TC004946>
- Govers, R., Wortel, M., 2005. Lithosphere tearing at STEP faults: response to edges of subduction zones. *Earth Planet. Sci. Lett.* 236, 505–523. doi:10.1016/j.epsl.2005.03.022
- Gribb, T.T. & Cooper, R.F. 1998. Low-frequency shear attenuation in polycrystalline olivine: Grain bound- ary diffusion and physical significance of the Andrade model for viscoelastic rheology. *J. Geophys. Res.* 103:27,267–79
- Griffin, W., O'Reilly, S. Y. & Ryan, C. G. (1999). The composition and origin of sub-continental lithospheric man- tle, in *Mantle Petrology: Field Observations and High-Pressure Experimentation: A Tribute to Francis R. (Joe) Boyd*, edited by Y. Fei, C. M. Berkta, and B. O. Mysen, *Spec. Publ. Geochem. Soc.*, 6, 13–45.
- Griffin, W., O'Reilly, S., Afonso, J., & Begg, G. (2009). The composition and evolution of lithospheric mantle: A re-evaluation and its tectonic implications. *Journal of Petrology*, 50 (7), 1185-1204.
- Grose, C., & Afonso, J. (2013). Comprehensive plate models for the thermal evolution of oceanic lithosphere. *Geochemistry, Geophysics, Geosystems*, 14 (9), 3751-3778.
- Gueguen, E., Doglioni, C., & Fernandez, M., (1998). On the post-25 Ma geodynamic evolution of the western Mediterranean. *Tectonophysics* 298, 259–269.
- Guerrera, F., & Martín-Martín, M. (2014). Geodynamic events reconstructed in the Betic, Maghrebien, and Apennine chains (central-western Tethys). *Bulletin de la Société géologique de France*, 185(5), 329-341.
- Hamai, L., Petit, C., Le Pourhiet, L., Yelles-Chaouche, A., Déverchère, J., Beslier, M. O., & Abtout, A. (2018). Towards subduction inception along the inverted North African margin of Algeria? Insights from thermo-mechanical models. *Earth and Planetary Science Letters*, 501, 13-23.
- Hatzfeld, D., & Molnar, P. (2010). Comparisons of the kinematics and deep structures of the Zagros and Himalaya and of the Iranian and Tibetan plateaus and geodynamic implications. *Reviews of Geophysics*, 48(2).
- Hatzfeld, D., & the Working Group for Deep Seismic Sounding, (1978). Crustal seismic profiles in the Alboran Sea — preliminary results. *Pure and Applied Geophysics* 116, 167–180.
- Heiskanen, W.A. & Moritz, H., (1967). *Physical Geodesy*, San Francisco, 364 pp.
- Herrmann, R. (2013). Computer Programs in Seismology: An Evolving Tool for Instruction and Research. *Seismological Research Letters*, 84 (6), 1081-1088.
- Hill, R. (1952). The elastic behaviour of a crystalline aggregate. *Proceedings of the Physical Society. Section A* .
- Hinz, K., (1972). Results of seismic refraction investigations (Project Anna) in Western Mediterranean, south and north of the island of Mallorca. *Bulletin Centre De Recherches Pau-SNPA* 6 (2), 405–426.
- Hoggard, M., Czarnota, K., Richards, F., Huston, D. L., Jaques, A. L. & Ghelichkhan, S. (2020). Gigayear stability of cratonic edges controls global distribution of sediment-hosted metals. <https://doi.org/10.31223/osf.io/2kjvc>.
- Hofmeister, A. M. (2005), Dependence of diffusive radiative transfer on grain-size, temperature, and Fe-content: Implications for mantle processes, *J. Geodyn.*, 40, 51–72.
- Holland, T., & Powell, R. (1998). An internally consistent thermodynamic data set for phases of petrological interest. *Journal of Metamorphic Geology*, 16 (3), 309-343.

- Hunter, J. (2007). Matplotlib: A 2D graphics environment. *Computing In Science & Engineering*, 9 (3), 90-95.
- Ince, E. S., Barthelmes, F., Reißland, S., Elger, K., Förste, C., Flechtner, F., & Schuh, H. (2019). ICGEM-15 years of successful collection and distribution of global gravitational models, associated services and future plans. *Earth System Science Data*, 11, 647–674. <http://doi.org/10.5194/essd-11-647-2019>
- Irfune, T. & Isshiki, M., 1998. Iron partitioning in a pyrolite mantle and the nature of the 410-km seismic discontinuity. *Nature*, 392(6677), pp.702-705.
- Ito, E., & T. Katsura (1989), A temperature profile of the mantle transition zone, *Geophys. Res. Lett.*, 16, 425–428.
- Jackson, I., & Faul, U. (2010). Grainsize-sensitive viscoelastic relaxation in olivine: Towards a robust laboratory-based model for seismological application. *Physics of the Earth and Planetary Interiors*, 183, 151-163.
- Jolivet, L., Faccenna, C., & Piromallo, C. (2009), From mantle to crust: Stretching the Mediterranean, *Earth Planet. Sci. Lett.*, 285, 198–209, doi:10.1016/j.epsl.2009.06.017.
- Jiménez-Munt, I., Torne, M., Fernández, M., Vergés, J., Kumar, A., Carballo, A., & García-Castellanos, D., (2019). Deep Seated Density Anomalies Across the Iberia-Africa Plate Boundary and Its Topographic Response. *J. Geophys. Res. Solid Earth* 124, 13310–13332. doi:10.1029/2019JB018445
- Jiménez-Munt, I., Fernandez, M., Vergés, J., Garcia-Castellanos, D., Fullea, J., Pérez-Gussinyé, M., & Afonso, J. C. (2011). Decoupled crust-mantle accommodation of Africa-Eurasia convergence in the NW Moroccan margin. *Journal of Geophysical Research: Solid Earth*, 116(B8).
- Julià, J., Ammon, C., Herrmann, R., & Correig, A. (2000). Joint inversion of receiver function and surface wave dispersion observations. *Geophysical Journal International*, 143 (1), 99-112.
- Kaban, M. K., Chen, B., Tesauero, M., Petrunin, A. G., El Khrepy, S., & Al-Arifi, N. (2018). Reconsidering effective elastic thickness estimates by incorporating the effect of sediments: A case study for Europe. *Geophysical Research Letters*, 45, 9523–9532, doi:10.1029/2018GL079732
- Katsura, T., Yamada, H., Nishikawa, O., Song, M., Kubo, A., Shinmei, T., Yokoshi, S., Aizawa, Y., Yoshino, T., Walter, M.J. & Ito, E. (2004). Olivine-wadsleyite transition in the system (Mg, Fe)₂SiO₄. *Journal of Geophysical Research: Solid Earth*, 109(B2).
- Katz, R. F., M. Spiegelman, & C. H. Langmuir, A new parameterization of hydrous mantle melting, *Geochem. Geophys. Geosyst.*, 4(9), 1073, doi:10.1029/2002GC000433, 2003.
- Kennett, B. (2006). On seismological reference models and the perceived nature of heterogeneity. *Physics of the Earth and Planetary Interiors*, 159 (3-4), 129-139.
- Kennett, B., Engdahl, E., & Buland, R. (1995). Constraints on seismic velocities in the Earth from traveltimes. *Geophysical Journal International* (122), 108-124.
- Khoms, S., Roure, F., Khelil, M., Mezni, R., & Echihi, O., 2019. A review of the crustal architecture and related pre-salt oil/gas objectives of the eastern Maghreb Atlas and Tell: Need for deep seismic reflection profiling. *Tectonophysics* 766, 232–248. doi:10.1016/j.tecto.2019.06.009
- Klein, E., & Langmuir, C. (1987). Global correlations of ocean ridge basalt chemistry with axial depth: A new perspective. *Journal of Geophysical Research*, 92 (B8), 8089-8115.

- Koulakov, I., Burov, E., Cloetingh, S., El Khrepy, S., Al-Arifi, N., & Bushenkova, N. (2016). Evidence for anomalous mantle upwelling beneath the Arabian Platform from traveltimes tomography inversion. *Tectonophysics*, 667, 176–188.
- Kumar, A., Fernández, M., Jimenez-Munt, I., Torne, M., Vergés, J., & Afonso, J. C. (2020). LitMod2D_2. 0: An improved integrated geophysical-petrological modeling tool for the physical interpretation of upper mantle anomalies. *Geochemistry, Geophysics, Geosystems*, e2019GC008777, doi: 10.1029/2019GC008777
- Kumar, A., Fernandez, M., Peral, M., Funiciello, F., Zlotnik, S., Faccenna, C., & Vergés, J. (2018). Effects of kinematic boundary conditions on trench curvature in a retreating subduction zone: insights from analog modelling. American Geophysical Union, Fall Meeting 2018, abstract #DI51B-0012, 2018AGUFMDI51B0012K.
- Kushiro, I. (2001). Partial melting experiments on peridotite and origin of mid-ocean ridge basalt, *Annu. Rev. Earth Plan. Sci.*, 29, 71–107.
- Lachenbruch, A. H., & P. Morgan (1990), Continental extension, magmatism, and elevation: Formal relations and rules of thumb. *Tectonophysics*, 174, 39–62.
- Langmuir, C. H., Klein, E. M., & Plank, T. (1992), Petrological systematics of mid-ocean ridge basalts: Constraints on melt generation beneath ocean ridges, in *Mantle Flow and Melt Generation at Mid-Ocean Ridges*, *Geophys. Monogr. Ser.*, vol. 71, edited by J. Phipps Morgan, D. K. Blackman, and J. M. Sinton, pp. 183–280, AGU, Washington, D. C.
- Langston, C. (1979). Structure under Mount Rainier, Washington, inferred from teleseismic body waves. *Journal of Geophysical Research*, 84 (B9), 4749–4762.
- Laouar, R., Boyce, A.J., Arafa, M., Ouabadi, A., & Fallick, A.E. (2005). Petrological, geochemical, and stable isotope constraints on the genesis of the Miocene igneous rocks of Chetaibi and Cap de Fer (NE Algeria). *J. Afr. Earth Sci.* 41, 445–465.
- Lau, H.C.P., & Faul, U.H. (2019). Anelasticity from Seismic to Tidal Timescales: Theory and Observations. *Earth and Planetary Science Letters*, 508, 18–29.
- Lee, C. A. (2003), Compositional variation of density and seismic velocities in natural peridotites at STP conditions: Implications for seismic imaging of compositional heterogeneities in the upper mantle, *J. Geophys. Res.*, 108(B9), 2441, doi:10.1029/2003JB002413.
- Lee, C. T. A., Luffi, P., & Chin, E. J. (2011). Building and destroying continental mantle. *Annual Review of Earth and Planetary Sciences*, 39, 59–90.
- Le Roux, V., Bodinier, J.-L., Tommasi, A., Alard, O., Dautria, J.-M., Vauchez, A., & Riches, A.J.V. (2007). The Lherz spinel lherzolite: refertilised rather than pristine mantle. *Earth and Planetary Science Letters* 259, 599–612.
- Leprêtre, R., de Lamotte, D. F., Combier, V., Gimeno-Vives, O., Mohn, G., & Eschard, R. (2018). The Tell-Rif orogenic system (Morocco, Algeria, Tunisia) and the structural heritage of the southern Tethys margin.
- Ligorria, J. P., & Ammon, C. J. (1999). Iterative deconvolution and receiver-function estimation. *Bulletin of the seismological Society of America*, 89(5), 1395–1400.
- López Sánchez-Vizcaíno, V., Rubatto, D., Gómez-Pugnaire, M.T., Trommsdorff, V., & Müntener, O. (2001). Middle Miocene high-pressure metamorphism and fast exhumation of the Nevado-Filábride Complex, SE Spain. *Terra Nova* 13, 327–332.
- Lustrino, M., Duggen, S., & Rosenberg, C. L. (2011). The Central-Western Mediterranean: anomalous igneous activity in an anomalous collisional tectonic setting. *Earth-Science Reviews*, 104(1–3), 1–40.

- Lustrino, M., & Wilson, M. (2007). The circum-Mediterranean anorogenic Cenozoic igneous province. *Earth-Science Reviews*, 81(1-2), 1-65.
- Macchiavelli, C., Vergés, J., Schettino, A., Fernández, M., Turco, E., Casciello, E., Tone, M., Pietrantonio, P.P., & Tunini, L. (2017). A new southern North Atlantic isochron map: Insights into the drift of the Iberian plate since the Late Cretaceous. *Journal of Geophysical Research: Solid Earth*, 122(12), 9603-9626.
- Mahdjoub, Y., Choukroune, P., & Kienast, J. R. (1997). Kinematics of a complex Alpine segment; superimposed tectonic and metamorphic events in the Petite Kabylie Massif (northern Algeria). *Bulletin de la Société Géologique de France*, 168(5), 649-661.
- Magni, V. (2019). The effects of back-arc spreading on arc magmatism. *Earth and Planetary Science Letters*, 519, 141-151.
- Mancilla, F.d.L., Booth-Rea, G., Stich, D., Pérez-Peña, J. V., Morales, J., Azañón, J. M., Martín, R., & Giaconia, F. (2015). Slab rupture and delamination under the Betics and Rif constrained from receiver functions. *Tectonophysics*, 663, 225-237.
- Mancilla, F. d. L., Heit, B., Morales, J., Yuan, X., Stich, D., Molina-Aguilera, A., Azañón, J. M., & Martín, R. (2018). A STEP fault in Central Betics, associated with lateral lithospheric tearing at the northern edge of the Gibraltar arc subduction system. *Earth and Planetary Science Letters*, 486, 32-40.
- Martí, J., Mitjavila, J., Roca, E. and Aparicio, C., (1992). Cenozoic magmatism of the Valencia trough (western Mediterranean): relationship between structural evolution and volcanism. *Tectonophysics*, 203, 145-165.
- Massonne, H. J., Willner, A. P., & Gerya, T. (2007). Densities of metapelitic rocks at high to ultrahigh pressure conditions: What are the geodynamic consequences?. *Earth and Planetary Science Letters*, 256(1-2), 12-27.
- Maury, R.C., Fourcade, S., Coulon, C., El Azzouzi, M., Bellon, H., Coutelle, A., Ouabadi, A., Semroud, B., Megartsi, M., Cotton, J., Belanteur, O., Louni-Hacini, A., Piqué, A., Capdevila, R., Hernandez, J., & Réhault, J.-P. (2000). Post-collisional Neogene magmatism of the Mediterranean Maghreb margin: a consequence of slab breakoff. *CR Acad. Sci. Paris* 331, 159–173.
- Marzán Blas, I., 2000. Régimen térmico en la Península Ibérica. Estructura litosférica a través del Macizo Ibérico y el Margen Sur-Portugués. Tesis Doctoral Universidad de Barcelona (192 pp.).
- McDonough, W., & Sun, S. S. (1995). The composition of the Earth'. *Chemical Geology* 120 (120), 223-253.
- McClusky, S., Reilinger, R., Mahmoud, S., Ben Sari, D., & Tealeb, A. (2003). GPS constraints on Africa (Nubia) and Arabia plate motions. *Geophys. J. Int.* 155:126–38
- McKenzie, D., & Bickle, M. J. (1988), The volume and composition of melt generated by extension of the lithosphere, *J. Petrol.*, 29, 625–679.
- Melchiorre, M., Vergés, J., Fernández, M., Coltorti, M., Torne, M., & Casciello, E. (2017). Evidence for mantle heterogeneities in the westernmost Mediterranean from a statistical approach to volcanic petrology. *Lithos*, 276, 62–74. <https://doi.org/10.1016/j.lithos.2016.11.018>
- Michard, A., Negro, F., Saddiqi, O., Bouybaouene, M. L., Chalouan, A., Montigny, R., & Goffé, B. (2006). Pressure–temperature–time constraints on the Maghrebide mountain building: evidence from the Rif–Betic transect (Morocco, Spain), Algerian correlations, and geodynamic implications. *Comptes Rendus Geoscience*, 338(1-2), 92-114.

- Michard, A., Chalouan, A., Feinberg, H., Goffé, B., & Montingny, R. (2002). How does the Alpine belt end between Spain and Morocco. *Bulletin de la Société Géologique de France* 173, 3–15.
- Miller, M. S., O'Driscoll, L. J., Butcher, A. J., & Thomas, C. (2015). Imaging Canary Island hotspot material beneath the lithosphere of Morocco and southern Spain. *Earth and Planetary Science Letters*, 431, 186-194.
- Miller, M. S., Allam, A. A., Becker, T. W., Di Leo, J. F., & Wookey, J. (2013). Constraints on the tectonic evolution of the westernmost Mediterranean and northwestern Africa from shear wave splitting analysis. *Earth and Planetary Science Letters*, 375, 234-243.
- Morgan, P., & Fernandez, M. (1992). Neogene vertical movements and constraints on extension in the Catalan Coastal Ranges, Iberian Peninsula, and the Valencia trough (western Mediterranean). *Tectonophysics*, 203(1-4), 185-201.
- Morris, S.J.S., & Jackson, I. 2009. Diffusionally-assisted grain-boundary sliding and viscoelasticity of polycrystals. *J. Mech. Phys. Solids* 57:744–61
- Moudnib, L. E., Villaseñor, A., Harnafi, M., Gallart, J., Pazos, A., Serrano, I., Córdoba, D., Pulgar, J. A., Ibarra, P., Himmi, M. N., & Chourak, M. (2015). Crustal structure of the Betic–Rif system, western Mediterranean, from local earthquake tomography. *Tectonophysics*, 643, 94-105.
- Nirrengarten, M., Manatschal, G., Tugend, J., Kuszniir, N., & Sauter, D., (2018), Kinematic Evolution of the Southern North Atlantic: Implications for the Formation of Hyperextended Rift Systems. *Tectonics*, 37, 89–118.
- Niu, Y. (1997). Mantle melting and melt extraction processes beneath ocean ridges: Evidence from abyssal peridotites. *Journal of Petrology*, 38 (8), 1047-1074.
- Negredo, A. M., Mancilla, F. D. L., Clemente, C., Morales, J., & Fullera, J. (2020). Geodynamic modelling of edge-delamination driven by STEP faults: the westernmost Mediterranean margin (central Betic orogen) case study. *Frontiers in Earth Science*, 8, 435.
- Palme, H., & O'Neill, H. (2013). *Cosmochemical Estimates of Mantle Composition* (2 ed., Vol. 3). Elsevier Ltd.
- Palomeras, I., Villaseñor, A., Thurner, S., Levander, A., Gallart, J., & Harnafi, M. (2017). Lithospheric structure of Iberia and Morocco using finite-frequency Rayleigh wave tomography from earthquakes and seismic ambient noise. *Geochemistry, Geophysics, Geosystems*, 18, 1824–1840. <https://doi.org/10.1002/2016GC006657>
- Palomeras, I., Thurner, S., Levander, A., Liu, K., Villaseñor, A., Carbonell, R., & Harnafi, M. (2014). Finite-frequency Rayleigh wave tomography of the western Mediterranean: Mapping its lithospheric structure. *Geochemistry, Geophysics, Geosystems*, 15(1), 140-160.
- Pascal, G.P., Mauffret, A., & Patriat, P. (1993). The ocean-continent boundary in the Gulf of Lion from analysis of expanding spread profiles and gravity modelling. *Geophys. J. Int.* 113 (3), 701–726
- Pascal, G., Torne, M., Buhl, P., Watts, A.B., & Mauffret, A. (1992). Crustal and velocity structure of the Valencia Trough (Western Mediterranean). Part II: Detailed interpretation of 5 Expanding Spread Profiles. *Tectonophysics*. 203, 21-36, DOI: 10.1016/0040-1951(92)90213-P, 1992. Q1; F1: 3.325 - 2.866.
- Pedreira, D., Afonso, J., Pulgar, J., Gallastegui, J., Carballo, A., Fernández, M., D. Garcia-Castellanos, I. Jiménez-Munt, J. Semprich, & O. García-Moreno (2015). Geophysical-petrological modeling of the lithosphere beneath the Cantabrian Mountains and the North-Iberian margin: Geodynamic implications. *Lithos*, 230, 46-68.

- Pedreira, A., Ruiz-Constán, A., García-Senz, J., Azor, A., Marín-Lechado, C., Ayala, C., de Neira, J.A.D. & Rodríguez-Fernández, L.R., 2020. Evolution of the South-Iberian paleomargin: From hyperextension to continental subduction. *Journal of Structural Geology*, 138, p.104122.
- Peral, M., Király, Á., Zlotnik, S., Funicello, F., Fernández, M., Faccenna, C., & Vergés, J. (2018). Opposite subduction polarity in adjacent plate segments. *Tectonics*, 37. <https://doi.org/10.1029/2017TC004896>.
- Peral, M., Zlotnik, S., Fernández, M., Vergés, J., Kumar, A., & Ruh, J. (2019). A numerical model of the Western Mediterranean. *Geophys. Res. Abstr.* 2019, 21, EGU2019-9312.
- Peral, M., Ruh, J., Zlotnik, S., Funicello, F., Fernández, M., Vergés, J., & Gerya, T. (2020a). Analog and numerical experiments of double subduction systems with opposite polarity in adjacent segments. *Geochemistry, Geophysics, Geosystems*, e2020GC009035.
- Peral, L., 2020b, Dynamics of subduction systems with opposite polarity in adjacent segments: application to the Westernmost Mediterranean PhD thesis, University of Barcelona, Barcelona.
- Pérez-Gussinyé, M., Metois, M., Fernández, M., Vergés, J., Fullea, J., & Lowry, A. R. (2009), Effective elastic thickness of Africa and its relationship to other proxies for lithospheric structure and surface tectonics, *Earth Planet. Sci. Lett.*, 287(1-2), 152-167. doi:10.1016/j.epsl.2009.08.004
- Phipps Morgan, J. (2001), Thermodynamics of pressure release melting of a veined plum pudding mantle, *Geochem. Geophys. Geosyst.*, 2(4), doi:10.1029/2000GC000049.
- Piomallo, C., & Morelli, A. (2003). P wave tomography of the mantle under the Alpine-Mediterranean area. *Journal of Geophysical Research: Solid Earth*, 108(B2).
- Platt, J.P., Allerton, S., Kirker, A., Mandeville, C., Mayfield, A., Platzman, E.S., & Rimi, A. (2003). The ultimate arc: differential displacement, oroclinal bending, and vertical axis rotation in the External Betic-Rif arc. *Tectonics* 22 (3), 1017. <http://dx.doi.org/10.1029/2001TC001321>.
- Polyak, B.G., Fernández, M., Khutorskoy, M.D., Soto, J.I., Basov, I.A., Comas, M.C., Khain, V.Y., Alonso, B., Agapova, G.V., Mazurova, I.S. & Negredo, A., 1996. Heat flow in the Alboran Sea, western Mediterranean. *Tectonophysics*, 263(1-4), pp.191-218.
- Poort, J., Lucazeau, F., Le Gal, V., Dal Cin, M., Leroux, E., Bouzid, A., ... & Ferrante, G. M. (2020). Heat flow in the Western Mediterranean: Thermal anomalies on the margins, the seafloor and the transfer zones. *Marine Geology*, 419, 106064.
- Presnall, D. C., Gudfinnsson, H. H., & Walter, M. J. (2002), Generation of mid-ocean ridge basalts at pressures from 1 to 7 GPa, *Geochim. Cosmochim. Acta*, 66, 2073–2090.
- Priestley, K., & McKenzie, D. (2006). The thermal structure of the lithosphere from shear wave velocities. *Earth and Planetary Science Letters*, 244 (1-2), 285-301.
- Priestley, K., & McKenzie, D. (2013). The relationship between shear wave velocity, temperature, attenuation and viscosity in the shallow part of the mantle. *Earth and Planetary Science Letters*, 381, 78-91.
- Puga, E., Nieto, J.M., & Díaz De Federico, A. (2000). Contrasting P–T Paths in eclogites of the Betic Ophiolitic Association, Mulhacen Complex, Southeastern Spain. *The Canadian Mineralogist* 38, 1137–1161.
- Raj R. (1975). Transient behaviour of diffusion-induced creep and creep rupture. *Metall. Trans. A* 6A:1499–509

- Revenaugh, J., & Jordan, T. (2008). Mantle layering from ScS reverberations: 3. The upper mantle. *Journal of Geophysical Research: Solid Earth*, 96 (B12), 19781-19810.
- Rimi, A., Fernandez, M., Manar, A., Matsushima, J., Okubo, Y., & Morel, J.L. (2005). Geothermal anomalies and analysis of gravity, fracturing and magnetic features in Morocco. World Geothermal Congress Antalya, Turkey, vol. 2, pp. 4–290.
- Ringwood, A. (1977). Composition for of the core of the and implications origin earth. *Geochemical Journal*, 11, 111-135.
- Ringwood, A. E. (1974). The petrological evolution of island arc systems: Twenty-seventh William Smith Lecture. *Journal of the Geological Society*, 130(3), 183-204.
- Ritzwoller, M. H., N. M. Shapiro, & S. J. Zhong (2004), Cooling history of the Pacific lithosphere. *Earth Planet. Sci. Lett.*, 226, 69–84.
- Royden, L., & Faccenna, C. (2018). Subduction orogeny and the late cenozoic evolution of the Mediterranean Arcs. *Annual Review of Earth and Planetary Sciences*, 46, 261-289.
- Roca, E. (2001). The Northwest-Mediterranean basin (Valencia Trough, Gulf of Lions and Liguro-Provençal basins): structure and geodynamic evolution. In: Ziegler, P.A., Cavazza, W., Robertson, A.F.H. and Crasquin- Soleau, S. (eds.), *Peri Tethyan Rift/Wrench Basins and Passive margins*. Mémoires du Muséum National d'Histoire Naturelle, 186, 671-706
- Roca, E. (1996). La evolución geodinámica de la Cuenca Catalano-Balear y áreas adyacentes desde el Mesozoico hasta la actualidad. *Acta Geológica Hispánica*, 29,3-25
- Roca, E., Frizon de Lamotte, D., Mauffret, A., Bracène, R., Vergés, J., Benaouali, N., Fernandez, M., Muñoz, J.A., & Zeyen, H. (2004). TRANSMED transect II. In: Cavazza, W., Roure, F., Spakman, W., Stampfli, G.M., Ziegler, P. (Eds.), *The TRANSMED Atlas—the Mediterranean Region from Crust to Mantle*. Springer, Berlin Heidelberg.
- Rossetti, F., Theye, T., Lucci, F., Bouybaouene, M. L., Dini, A., Gerdes, A., ... & Cozzupoli, D. (2010). Timing and modes of granite magmatism in the core of the Alboran Domain, Rif chain, northern Morocco: implications for the Alpine evolution of the western Mediterranean. *Tectonics*, 29(2).
- Rossum, G. (1995). Python tutorial, Technical Report CS-R9526, Centrum voor Wiskunde en Informatica (CWI), Amsterdam.
- Rudnick, R. L., & Gao, S. (2003). Composition of the continental crust. *Treatise on Geochemistry*, 3, 659. <https://doi.org/10.1016/B0-08-043751-6/03016-4>
- Roure, F., Casero, P., & Addoum, B. (2012). Alpine inversion of the North African margin and delamination of its continental lithosphere. *Tectonics*, 31(3).
- Ruiz-Constan, A., Pedrera, A., Galindo-Zaldívar, J., Pous, J., Arzate, J., Roldán-García, F.J., Marin-Lechado, C., & Anahnah, F. (2012). Constraints on the frontal crustal structure of a continental collision from an integrated geophysical research: the central-western Betic Cordillera (SW Spain). *Geochem.Geophys.Geosyst.* 13 (8) (art. no. Q08012).
- Sàbat, F., Roca, E., Muñoz, J.A., Vergés, J., Santanach, P., Masana, E., Sans, M., Estévez, A., & Santisteban, C. (1997). Role of extension and compression in the evolution of the eastern margin of Iberia: the ESCI-València trough seismic profile. *Revista de la Sociedad Geológica de España* 8, 431–448.
- Sandwell, D. T., & Smith, W. H. F. (1997). Marine gravity from Geosat and ERS 1 satellite altimetry. *Journal of Geophysical Research*, 102, 10,039–10,054. <https://doi.org/10.1029/96jb03223>

- Schilling, J., Zajac, M., Evans, R., Johnston, T., White, W., Devine, J., & Kingsley, R. (1983). Petrologic and geochemical variations along the Mid-Atlantic Ridge from 29 degrees N to 73 degrees N. *Am J Sci* 283:510–586
- Schettino, A., & Turco, E. (2011) Tectonic history of the western Tethys since the Late Triassic. *Geol. Soc. Am. Bull.*, 123, 89–105.
- Schubert, G., Turcotte, D.L. & Olson, P. (2001). *Mantle convection in the Earth and planets*. Cambridge Univ. Press. UK, pp 956.
- Shorttle, O., & MacLennan, J. (2011), Compositional trends of Icelandic basalts: Implications for short-length scale lithological heterogeneity in mantle plumes, *Geochem. Geophys. Geosyst.*, 12, Q11008, doi:10.1029/2011GC003748.
- Soto, J.I., & Platt, J.P. (1999) Petrological and structural evolution of high-grade metamorphic rocks from the floor of the Alboran Sea basin, western Mediterranean. *Journal of Petrology* 40, 21–60.
- Sobolev, S., Zeyen, H., Stoll, G., Werling, F., Altherr, R., & Fuchs, K. (1996). Upper mantle temperatures from teleseismic tomography of French Massif Central including effects of composition, mineral reactions, anharmonicity, anelasticity and partial melt. *Earth and Planetary Science Letters*, 139 (1-2), 147–163.
- Spandler, C., & Pirard, C. (2013). Element recycling from subducting slabs to arc crust: A review. *Lithos*, 170, 208–223.
- Spakman, W., & Wortel, M. J. R. (2004). A tomographic view on western Mediterranean geodynamics. In W. Cavazza, F. Roure, W. Spakman, G. M. Stampfli, & P. Ziegler (Eds.), *The TRANSMED Atlas—The Mediterranean region from crust to mantle*, (pp. 31–52). Berlin Heidelberg: Springer.
- Stampfli, G., & Borel, G.D. (2002), A plate tectonic model for the Paleozoic and Mesozoic constrained by dynamic plate boundaries and restored synthetic oceanic isochrones. *Earth Planet. Sci. Lett.*, 196, 17–33.
- Stixrude, L., & Lithgow-Bertelloni, C. (2005). Mineralogy and elasticity of the oceanic upper mantle: Origin of the low-velocity zone. *Journal of Geophysical Research: Solid Earth*, 110 (3), 1–16.
- Strang van Hees, G. L. (2000). Some elementary relations between mass distributions inside the Earth and the geoid and gravity field. *Journal of Geodynamics*, 29: 111–123.
- Talwani, M., Worzel, J., & Landisman, L. (1959), Rapid computations for two-dimensional bodies with application to the Mendocino submarine fracture zone, *J. Geophys. Res.*, 64, 49–59.
- Takei, Y (2017). Effects of Partial Melting on Seismic Velocity and Attenuation: A New Insight from Experiments. *Annual Review of Earth and Planetary Sciences* 2017. 45:447–70.
- Teixell, A., Ayarza, P., Zeyen, H., Fernandez, M., & Arboleya, M. L. (2005). Effects of mantle upwelling in a compressional setting: the Atlas Mountains of Morocco. *Terra Nova*, 17(5), 456–461.
- Torné, M., Banda, E., & Fernandez, M. (1996). The Valencia Trough: geological and geophysical constraints on basin formation models. *Mémoires du Muséum national d'histoire naturelle* (1993), 170, 103–128.
- Torne, M., Fernández, M., Vergés, J., Ayala, C., Salas, M. C., Jimenez-Munt, I., Buffett G.G., & Díaz, J. (2015). Crust and mantle lithospheric structure of the Iberian Peninsula deduced from potential field modeling and thermal analysis. *Tectonophysics*, 663, 419–433.

- Torne, M., Fernandez, M., Comas, M. C., & Soto, J. I. (2000). Lithospheric structure beneath the Alboran Basin: results from 3D gravity modeling and tectonic relevance. *Journal of Geophysical Research: Solid Earth*, 105(B2), 3209-3228.
- Torne, M., Pascal, G., Buhl, P., Watts, A.B., & Mauffret, A. (1992). Crustal structure of the Valencia Trough (Western Mediterranean). Part 1. A combined refraction/wide angle reflection and near-vertical reflection study. *Tectonophysics* 203, 1–20.
- Tunini, L. (2015). The Central Asia collision zone: numerical modelling of the lithospheric structure and the present-day kinematics PhD thesis, University of Barcelona, Barcelona.
- Tunini, L., Fernandez, M., Afonso, J., Villaseñor, A., Jiménez-Munt, I., & Melchiorre, M. (2016). Geophysical-petrological model of the crust and upper mantle in the India-Eurasia collision zone. *Tectonics*, 35 (7), 1642-1669.
- Tunini, L., Jiménez-Munt, I., Fernandez, M., Vergés, J., & Villaseñor, A. (2015). Lithospheric mantle heterogeneities beneath the Zagros Mountains and the Iranian Plateau: A petrological-geophysical study. *Geophysical Journal International*, 200 (1), 596-614.
- Turcotte, D., & Morgan, J. (2013). The Physics of Magma Migration and Mantle Flow Beneath a Mid-Ocean Ridge. *0225*, 155-182.
- Turcotte, D.L., & Schubert, G. (1982). *Geodynamics. Application of continuum physics to geological problems*. John Wiley & Sons, New York, 450 pp.
- Van Hinsbergen, D., Vissers, R., & Spakman, W. (2014). Origin and consequences of western Mediterranean subduction, rollback, and slab segmentation. *Tectonics*, 33, 393–419.
- Van Hinsbergen, D. J., Torsvik, T. H., Schmid, S. M., Mañenco, L. C., Maffione, M., Vissers, R. L., Gürer, D., & Spakman, W. (2020). Orogenic architecture of the Mediterranean region and kinematic reconstruction of its tectonic evolution since the Triassic. *Gondwana Research*, 81, 79-229.
- Van Keken, P., Hauri, E., & Ballentine, C. (2002). Mantle Mixing: The Generation, Preservation, and Destruction of Chemical Heterogeneity. *Annual Review of Earth and Planetary Sciences*, 30 (1), 493-525.
- Vergés, J., & Fernández, M. (2012) Tethys–Atlantic interaction along the Iberia–Africa plate boundary: The Betic–Rif orogenic system. *Tectonophysics*, 579, 144–172.
- Vergés, J., & Fernández, M. (2006), Ranges and basins in the Iberian Peninsula: Their contribution to the present topography. *Geol. Soc. Mem.*, 32, 223–234.
- Vergés, J., & Sàbat, F. (1999). Constraints on the western Mediterranean kinematic evolution along a 1,000-km transect from Iberia to Africa. In: Durand, B., Jolivet, L., Horváth, F., Séranne, M. (Eds.), *On the Mediterranean Basins: Tertiary Extension within Alpine orogen*. Geological Society London Special Publications, 134, pp. 63–80.
- Vidal, N., Gallart, J., & Danobeitia, J.J. (1998). A deep seismic transect from the NE Iberian Peninsula to the Western Mediterranean. *Journal of Geophysical Research* 103, 12381–12396.
- Vilà, M., Fernández, M., & Jiménez-Munt, I. (2010). Radiogenic heat production variability of some common lithological groups and its significance to lithospheric thermal modeling. *Tectonophysics*, 490, 152–164. <https://doi.org/10.1016/j.tecto.2010.05.003>
- Villaseñor, A., Chevrot, S., Harnafi, M., Gallart, J., Pazos, A., Serrano, I., et al. (2015). Subduction and volcanism in the Iberia-North Africa collision zone from tomographic images of the upper mantle. *Tectonophysics*, 663, 238–249. <https://doi.org/10.1016/j.tecto.2015.08.042>

- Villaseca, C., Ancochea, E., Orejana, D., & Jeffries, T. (2010). Composition and evolution of the lithospheric mantle in central Spain: Inferences from peridotite xenoliths from the Calatrava volcanic field. *Geological Society of London, Special Publication*, 337, 125–152. <https://doi.org/10.1144/sp337.7>
- Vinnik, L. (1977). Detection of waves converted from p to sv in the mantle. *Physics of the Earth and Planetary Interiors*, 15 (October 1976), 39-45.
- Watanabe, T. (1993). Effects of water and melt on seismic velocities and their application to characterization of seismic reflectors. *Geophysical Research Letters*, 20 (24), 2933-2936.
- Wilson, M., & Bianchini, G. (1999). Tertiary–Quaternary magmatism within the Mediterranean and surrounding regions. In: Durand, B., Jolivet, L., Horvath, F., Seranne, M. (Eds.), *The Mediterranean Basins: Tertiary Extension within the Alpine Orogen*. Geol. Soc., London Spec. Publ., vol. 156, pp. 141–168.
- Winter, J. D. (2010), *An Introduction to Igneous and Metamorphic Petrology*, Prentice Hall, New York.
- Workman, R., & Hart, S. (2005). Major and trace element composition of the depleted MORB mantle (DMM). *Earth and Planetary Science Letters*, 231 (1-2), 53-72.
- Xu, W., Lithgow-Bertelloni, C., Stixrude, L., & Ritsema, J. (2008). The effect of bulk composition and temperature on mantle seismic structure. *Earth and Planetary Science Letters*, 275 (1-2), 70-79.
- Zeyen, H., Ayarza, P., Fernández, M., & Rimi, A. (2005), Lithospheric structure under the western African-European plate boundary: A transect across the Atlas Mountains and the Gulf of Cadiz. *Tectonics*, 24, TC2001, [doi:10.1029/2004TC001639](https://doi.org/10.1029/2004TC001639).
- Zeyen, H., & Fernández, M. (1994). Integrated lithospheric modeling combining thermal, gravity, 99, 18,089-18,102.
- Zhu, L., & Kanamori, H. (2000). Moho depth variation in southern California from teleseismic receiver functions. *Journal of Geophysical Research: Solid Earth*, 105(B2), 2969-2980.
- Zienkiewicz, O. C. (1977), *The Finite Element Method*, McGraw-Hill, New York.

Appendix

Appendix A: LitMod2D_2.0 User Manual

A1. Introductions

LitMod2D 2.0 is a finite element code which combines potential field, geochemical and seismological data to work out thermo-chemical structure of the lithosphere. This document is a manual for a python based GUI to build the model where the user draws geometry of the bodies in the cross-section and associate physical properties to those bodies.

A2. Installation

User can download or clone the package from https://github.com/ajay6763/LitMod2D_2.0_package_dist_users.git. You will have following directory structure:

```
./LitMod2D_2.0_package_dist_users
  ./Generator_Linux: to generate material file
    ./GUI: includes the GUI in python
  ./Manual: Manual for GUI use
  ./Post_processing: packages for post-processing
    ./flexure_tao
    ./Phase_diagrams
    ./RF
    ./Surface_wave_dispersion
    ./Synthetic_Seismic_tomography
```

To setup Generator, follow the instructions in REAME.md file in the Generator Linux directory. Now we need to setup the GUI which essentially means we need to install python libraries. Generally, Linux comes with installed python2.7 but in Windows you might have to install python2.7 (<https://www.python.org/getit/>). This GUI uses packages from python which do not come pre-installed with stand-alone python installation. This GUI is python2.7 compatible. All packages used here can be installed using "pip" a python package manager which can be easily installed in Windows or Linux distributions (<https://pip.pypa.io/en/stable/installing/>).

Once you have the python and pip setup go into the GUI directory and run the following command:

```
pip install -r requirements.txt
```

This should have you almost everything needed for the GUI. In addition to this you might have to install “Tkinter” and “PyQt4”, and can installed using following commands:

```
sudo apt-get update
```

```
sudo apt-get python-tk
```

```
sudo apt-get PyQt4
```

If python-tk does not install than try installing using Synaptic package manager. Open it and search for Tkiner and install python-tk from there. Once you have everything installed you need to add the LitMod2D to you your path. To do this simply open `/.bashsrc` and add following lines:

```
export LitModHOME= "absolute path of LitMod2D 2.0"
```

where “absolute path of LitMod2D 2.0” is the path to LitMod2D 2.0 dist users in your system.

A3. How to make and work with models?

To start the LitMod2D 2.0 go into GUI folder and run `main.py` (in Linux type “python `main.py`” in Windows you can double click on the `main.py` file), running which Figure 1 will appear. Here you have three options. Build model option is to build a model from scratch. Load Model is to load a previously build model and the last option is about help.

*Note: In dialog boxes, put your mouse in a field and additional information will appear.

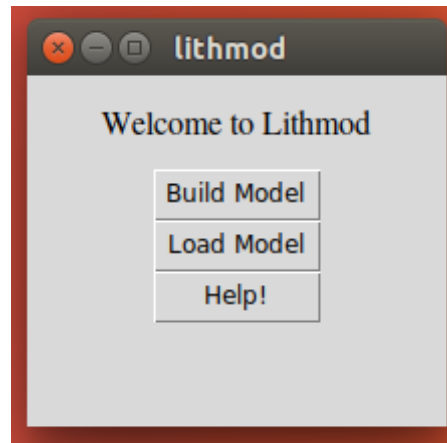


Figure A1 Welcome Page

A3.1. Build Model

Before building a model user should have a clear idea and sketch of the model user wants to build. User should know nodes along which different bodies will be connected. A model is build from top-to-bottom and left to right and every time user wants to exit and wants to save the model, user should close the model by clicking the close Model button on top right. After clicking close model click

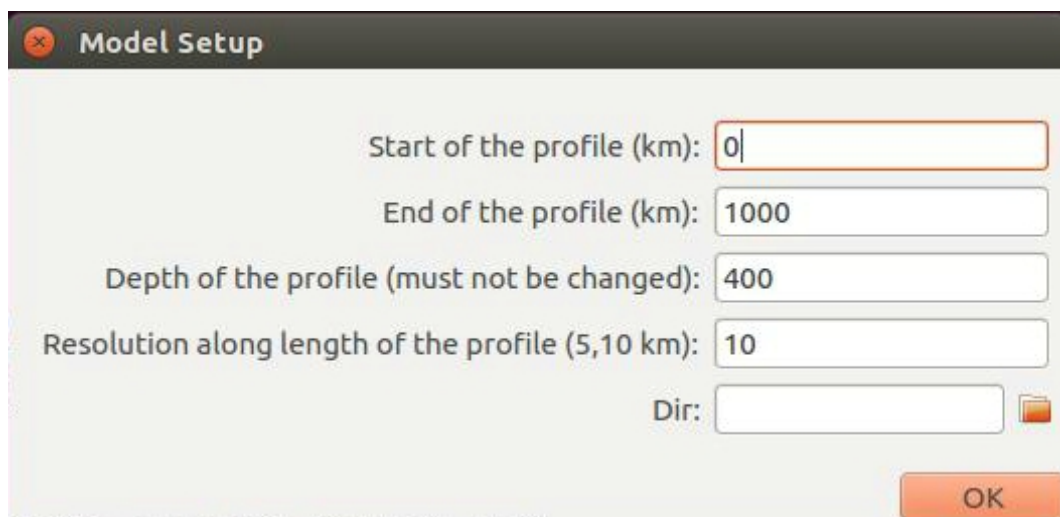


Figure A2 Model setup on dialog box about model size and location some info about the model.

After user hits Build Model option a dialogue box appears (Figure A2) asking for information about the model and another dialogue box asking for digitized file where you already have nodes of the bodies (e.g., digitized sketch, Moho and LAB

depths; two column, X (distance along profile, km) Y(depth, km)). This digitized file will be plotted in background and you can click on the plotted points.

****Note:** Bodies are added from left to right

Start of the profile (km): This is the left most starting point of profile (it can be negative too. In that case all the observable files should have same limits).

End of the profile (km): This the right most end point of profile.

Depth of the profile: This is the depth of the profile in km. It must be 400km, so it must not be changed.

Resolution along the profile: resolution of the profile

Folder: Here user selects the folder in which observable files are put and it becomes the working folder for LitMod2D 2.0. All the outputs files are stored in this folder.

Tip: For each of your model you can make folder where you put all observables files, material files from Generator. Later you can load the model by browsing into this folder.

After the user hits OK button build model window will appear (Figure A3). Here the user has different option.

Add Body

Bodies are added from top to bottom, each body is drawn left to the right. To add a body press the add button on the window (Figure A3), which will open a dialog box asking for information about the body (Figure A4)

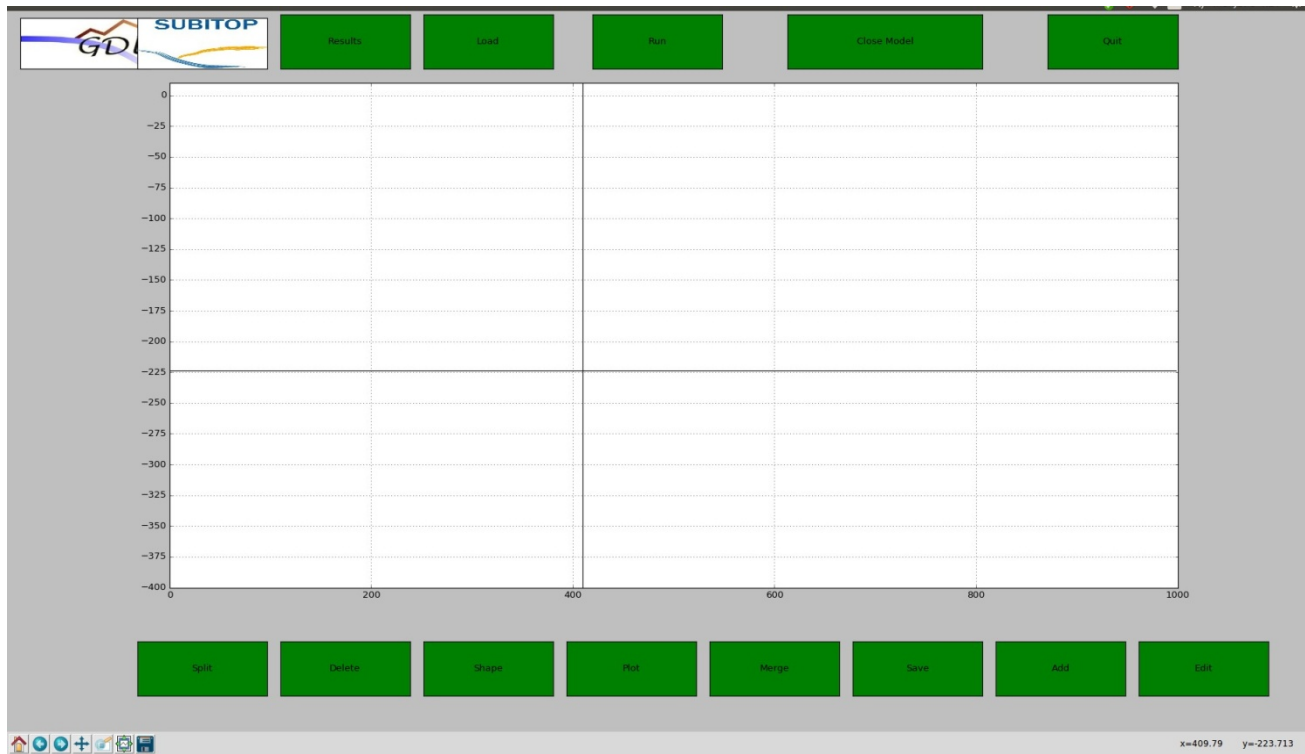


Figure A3 Build Model Window.

*Please note that format in which default values appear should be maintained.

Fields description:

Name: Name of the body. Just for your reference

Body number: Index of the body starting from the top.

Material: Type of material of the body

Body type: if you are adding a body which is new, this option should be normal. If you are splitting a body change this option to split. If you are adding an anomaly, change this option to type of anomaly you are adding (thermal or seismic or from a file).

Once the user is done with adding properties user should hit OK and control will be back to the plotting area.

To add point: Middle mouse click (Scroller)

To delete current point: double left click.

To close body: right click

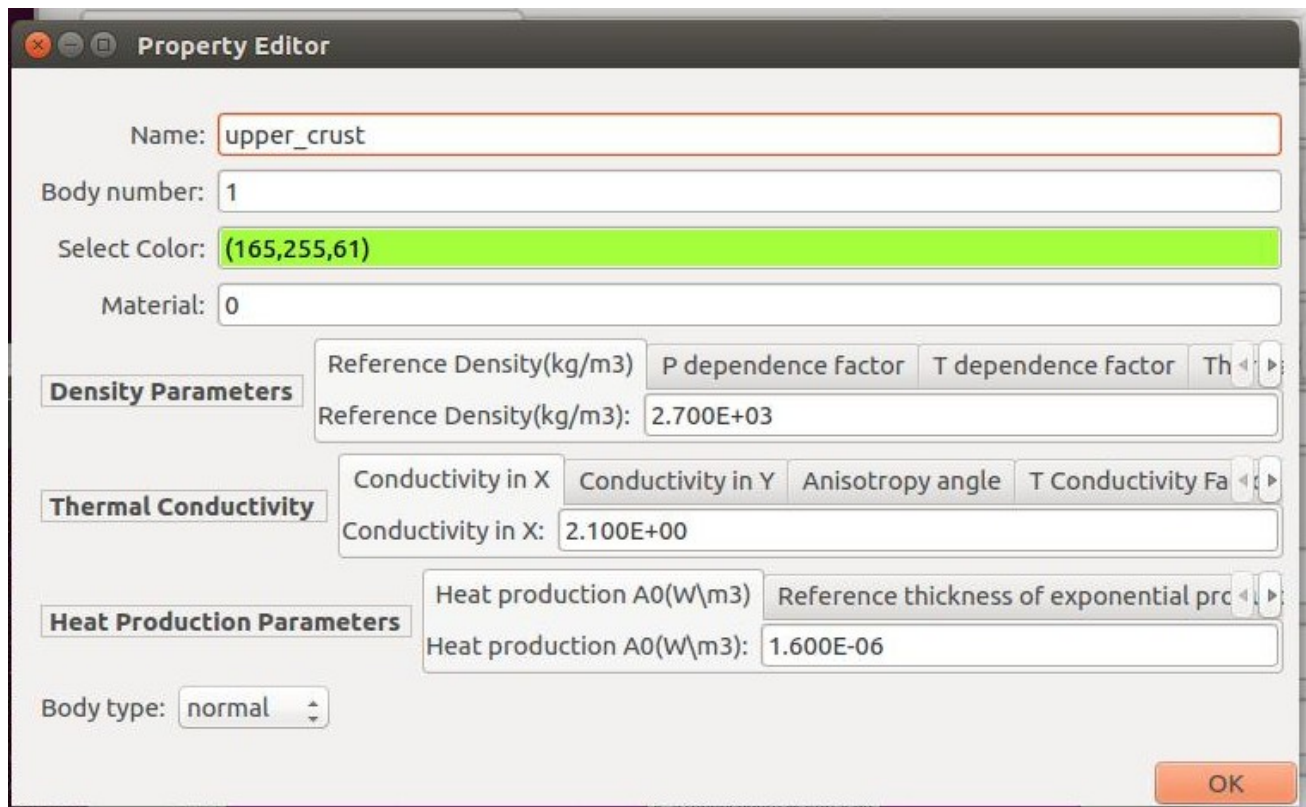


Figure A4 Body property editor.

Delete body

The user can delete the last body entered by clicking on the delete button. Let us say a user has drawn three bodies. To delete second body first user has to delete the third body. So essentially you can only delete the last entered body. If you want to delete a body in between, then you can use the merge function (see following sections).

Change shape of the bodies

To move, delete or add node points of the drawn body's user can click on shape button. After clicking this button a separate plot will appear where all bodies will be drawn as points (In case you have anomalies in the model other than from a external file then second window also appears where you can edit anomalous bodies too). Now user can move these point by left click drag, to delete a point move the

cursor on the point and then press 'd' key on the keyboard (sometimes there are more than one points so keep pressing 'd' until the point is gone). To insert a node go to the node and press 'i' key on the keyboard. After you are done changes can be saved with right click while the cursor is on the edit plot window. Once you have saved changes close the window and come back to the main window and hit plot button which will update the changes. This function will only work after you have closed your model.

*Note: when you see the plot of the bodies (for anomalies) in separate window, you might see some lines connecting different bodies, just ignore them. To have clear idea keep main window where you added bodies in front of you along with this separate window

Edit properties

To edit properties of a body already drawn click on edit button and a dialog box will appear asking for the index of the body you want to edit.

Split body

This function allows the user to split a body into two (does not work for anomalous bodies). This function should be used with a lot of care. The user should know exactly where to start split. Tip to use this option is that when you enter a body it is added in counter-clockwise direction, but when body is save it is save in clock-wise direction. Now the start point of the axis along which you have to split the body should be first in clock-wise direction than the last point. Once you have split a body save the model and then again load it.

*Note: If for some reasons split does not work then you can load model again and try to split it again.

Anomalies in the sublithospheric mantle

In this GUI anomalies (Composition, thermal, seismic) are added on top of the completely closed profile. You can edit the shape of these anomalies and properties (type and amount of anomaly) with shape and edit function respectively. These types of anomalies can be drawn in the profile. There is another way to enter anomalies where you enter them in a file and you choose the file (For more information about this file refers to the *LitMod2D_usage.pdf*, supplied in this folder. Only seismic anomalies can be added in this way.

* Note that if you have selected anomalies in form of a file then all other anomalies (drawn on the profile) are not considered even if you have added them.

Save Model

When you are done with the profile and you have closed it by clicking on the Close model button, it can be saved by clicking on save button. After you click on the save button a window will appear asking for some more information. You can choose observable file, where you should have three columns with distance, data value, and error. Total length and sampling of these observables should be exactly same as that in your profile. One important thing is to have starting and end point of these observables data as that of start and end you choose to make your profile. After browsing the file try to keep only the name of the input file try to delete the absolute path. Here making a folder for each of your model, which can be at any location in your computer, helps keeping things in track.

Every time you save a model, a back-up of three files, and 1) *litmod.inp*, 2) *bodies_GUI.dat*, 3) *bodies_GUI_envelops.out*, with a date and time added. You can later rename these set of files and load them again.

A3.2. Run model

To run a model first you have to save the model by clicking on the save button, but before that, your model should be closed. You should also put the observables file (topography, Bouguer, geoid, free air, heat flux) and composition files (e.g., 80, 81, 88, 99 etc.) which you have associated with the bodies in your model, in the same folder.

Note: To run a model you should have LitMod2D 2.0 program executable for Windows or Linux based on your system. Executable for Linux is provided with the distribution. Name of these executables should be LitMod2D 2.0_V4_Windows for windows and should be in LitMod2D 2.0 package folder and for Linux it should be in same folder with name LitMod2D_2.0_V4_Linux.

A 3.4. Load Model

This option lets the user load previously build models. To load models user need three files, 1) *litmod.inp*, an input file to the LitMod2D 2.0, 2) *bodies_GUI.out*, this file contains nodes point of the bodies in the model and colour of the body and 3) *bodies_GUI_envelops.out*. Units of nodes points in bodies GUI.dat are in kilometres. This option also allows you to restore changes while you are working. For instance if something goes wrong (e.g., split body, merge body) you can load last saved session

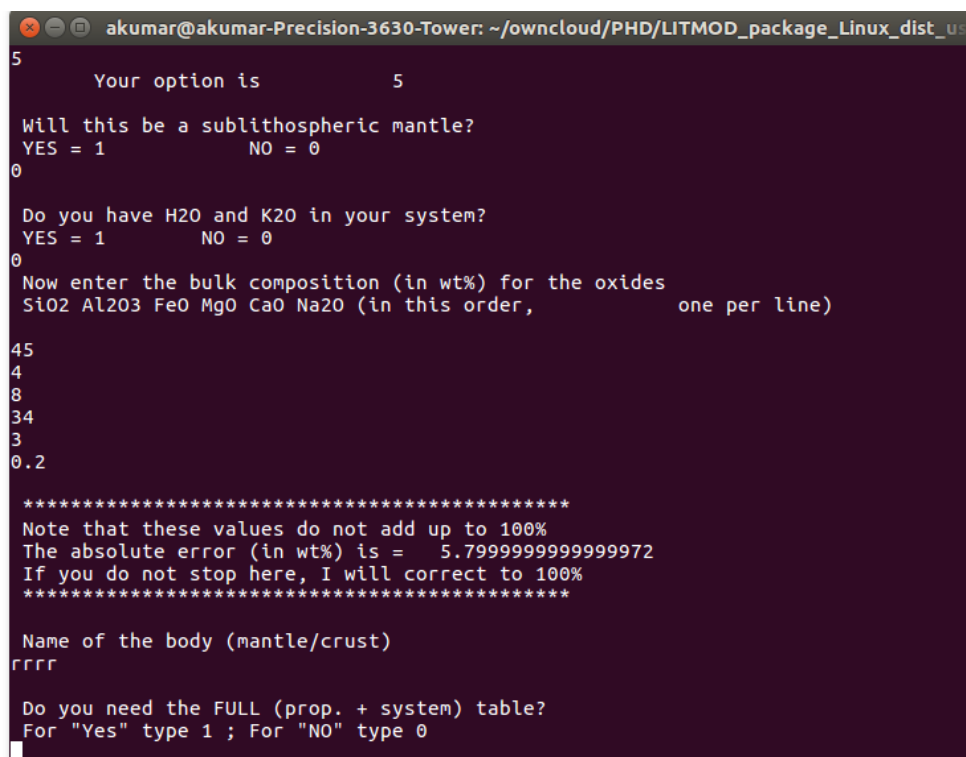
and start from there again. You can also track this three files saved in same folder at any time you have saved them, rename them and can load them again.

A4. Post-processing toolbox

Post-processing toolbox contains a set of codes/scripts linking with outputs from LitMod2D 2.0 with other softwares. At this point is it coupled with “*Computer programs in Seismology (CPS)*” tool (Herrmann, 2013) and “*tao-geo*” (Garcia-Castellanos et al., 2002) software. It also includes scripts to produce stable phase and mineral assemblages in the profile. Installations of coupled softwares are explained below.

A4.1. Passive Seismological data

Forward prediction of surface wave dispersion curves and receiver functions can be calculated from the seismic velocities distribution with depth at each node along the profile. This is done by feeding in seismic velocities to CPS. CPS can be easily downloaded and install from <http://www.eas.slu.edu/eqc/eqccps.html> and needs to in your path.



```

akumar@akumar-Precision-3630-Tower: ~/owncloud/PHD/LITMOD_package_Linux_dist_us
5
    Your option is          5

Will this be a sublithospheric mantle?
YES = 1          NO = 0

0

Do you have H2O and K2O in your system?
YES = 1          NO = 0

0

Now enter the bulk composition (in wt%) for the oxides
SiO2 Al2O3 FeO MgO CaO Na2O (in this order,          one per line)
45
4
8
34
3
0.2

*****
Note that these values do not add up to 100%
The absolute error (in wt%) is = 5.799999999999972
If you do not stop here, I will correct to 100%
*****

Name of the body (mantle/crust)
rrrr

Do you need the FULL (prop. + system) table?
For "Yes" type 1 ; For "NO" type 0

```

Figure A5 Generator console showing option to generate full property table.

A4.2. Flexural Isostasy

Flexural isostasy is incorporated via “tao-geo” and can be downloaded and installed from <https://github.com/danigeos/tao-geo> and should be added in your path.

A4.3. Stable phase and mineral assemblages

To do this user should have full property tables from the GENERATOR module. Opting for option “1” shown in 5 produces both full property material file along with simple material file with physical properties only. Full property material file contains information on stable phase and mineral assemblages (weight percentage, volume percentage) along with the physical properties (density, seismic velocities). Simple material files, with material code ‘90, 99...’ are read in the LitMod2D 2.0 whereas full property material files named as ‘99_FULL etc.’ are used to produce stable phase and mineral assemblages. Full property material files should be in the model directory. First user should run “*make_mineral_wise_files_full.sh*”. This produces mineral wise properties along the profile. User can plot a property (e.g., weight%) of stable mineral at a distance point along the profile running ‘*phase_diagram 1D.py*’ 6 or depth distribution of individual minerals along the profile using ‘*phase_diagram 2D.py*’

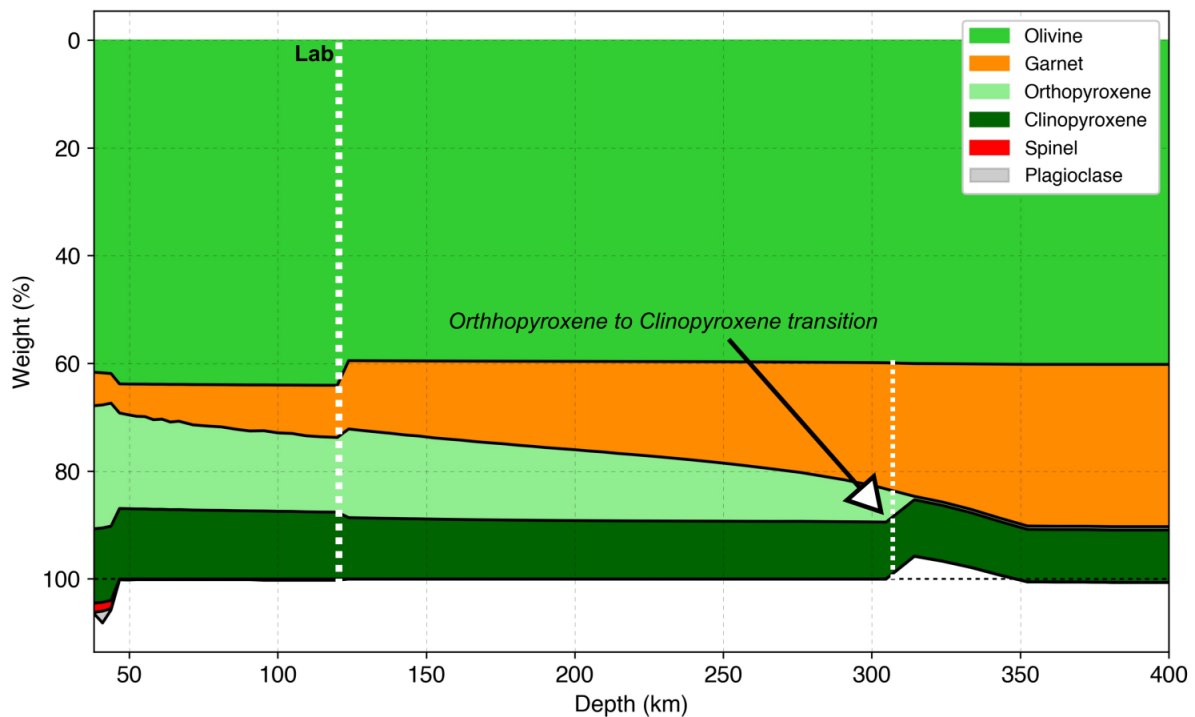


Figure A6 Example of stable mineral wt% distribution at a distance point.

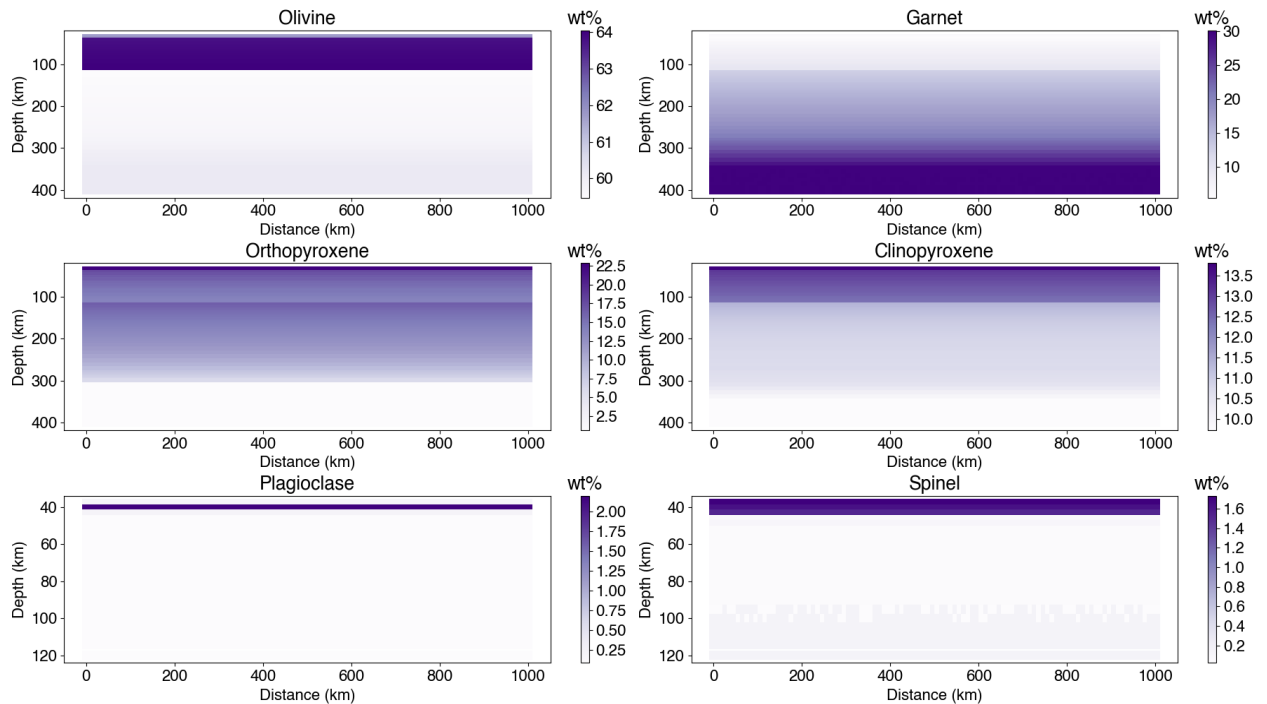


Figure A7 Example of stable mineral wt% distribution along a profile.

A5. Miscellaneous

User can also use other functionality. They are listed below:

Values of coordinates are shown at the bottom right corner of the plot. It is useful to add points at specific positions.

You can zoom in at any area of the profile by clicking at the functions in the left bottom of the window. You can also go to the zoom mode by pressing “o” on the keyboard. Then you can select area to zoom in with mouse and navigate back and forth with arrow keys on the keyboard. It is useful for small area bodies.

To go back out of zoom mode you should press “o” again.

You can drag the profile and to go to this mode you can press “p” on the keyboard.

If you want to go straight to the initial level after zooming at different levels just press “h” key on the keyboard.

Departament de Dinàmica de la Terra i de l'Oceà
Facultat de Ciències de la Terra
Universitat de Barcelona

THERMAL AND CHEMICAL IMAGING OF THE UPPER MANTLE ANOMALIES: APPLICATION TO WESTERN MEDITERRANEAN

Tesi doctoral presentada per Ajay Kumar en el Departament de Dinàmica de la Terra i de l'Oceà de la Universitat de Barcelona per optar al grau de Doctor en Ciències de la Terra

Group of Dynamics of the Lithosphere (GDL)
Geosciences Barcelona (GEO3BCN)
Consejo Superior de Investigaciones Científicas (CSIC)

Directors

Prof. Dr. Manel Fernàndez Ortiga

Prof. Dr. Jaume Vergés Masip

Tutor

Prof. Dr. Juan José Ledo Fernández

Barcelona, Octubre 2020



To my parents and brother

Acknowledgements

It is my pleasure to be indebted to various people, who directly or indirectly contributed in the development of this thesis and who influenced my thinking, behaviour and acts during the course of this thesis.

First and foremost are my thesis supervisors Prof. Dr. Manel Fernàndez Ortega and Prof. Dr. Jaume Vergés Masip at ICTJA-CSIC (now Geo3Bcn), Barcelona. Manel has been an absolute source of motivation, support and fine tuned supervision. I still remember the first day I met him in his office in 2016 and till date the temperament of the meetings stayed same. Manel allowed me to explore things at my own pace and in case of dead end always brought me back on track. I am immensely thankful and grateful to him for tolerating my mistakes along the way and devoting time during the last stages of this thesis even after his retirement. Jaume has been another absolute source of motivation, support and supervision especially in the geological aspects of the complex Western Mediterranean and its implications for regional geodynamics. Greeting every day in the mornings complimented with a hand shake added an element of care to my day-to-day life at ICTJA. I am also grateful to Jaume for his good eye for aesthetics and presentation of the scientific data and making it much more appealing. I have tried to dig out every bit of an artist in me (though I am really bad in art) during this thesis. Huge thanks to Jaume. I am also thankful to both, Manel and Jaume, for the open-discussions in our meetings and laughs we shared. I also would like to thank Dr. Montserrat Torné Escasany, Dr. Ivone Jiménez Munt, and Dr. Daniel García-Castellanos for support and supervision on various research projects I have been involved at Geo3Bcn.

I also thank Prof. Dr. Juan José Ledo Fernández for accepting the tutoring of this thesis and the commission of doctorate from the UB (University of Barcelona) for the progress follow-up carried out during these years.

I also would like to thank friends, I made at ICTJA Geo3Bcn and Barcelona, Mireia, Encarni, Lavinia, Jonas, Angel, Max, Jordi, Luis, Pili, Mari, Marc, Ana, Milton, Hanneke, Erik, Enric, Cris, for their support and my Spanish name “Pepe”. Big thanks to Kittiphon (KB) for being an excellent friend, officemate, and shared interest in FOOD! A big hug and thanks to SUBITOP friends with whom I shared wonderful 3 years of my life. I am also thankful to Ranjana for being there and supporting me at long-distances (inter-state and trans-continental) for 10 years now.

I also thank the administrative and computing staff at Geo3Bcn (Chelo, Leonor, Montse, Nuria, Xavi, Esmeralda, Oscar, and Marc) for handling my affairs and “a curious case of an Indian without a surname”.

Lastly, I would like to thank my parents for their unconditionally support (whenever, wherever) and my brother for staying with them and handling the family matters for all these years for which I was too busy to care.

Funding

This thesis is funded by the EU Marie Curie Initial Training Network ‘SUBITOP’ (674899-SUBITOP-H2020-MSCA-ITN-2015) and partly by SUBTETIS (PIE-CSIC-201830E039, CSIC), GeoCAM (PGC2018-095154-B-I00, Spanish Government), and Equinor R&T Fornebu (Norway) projects. This thesis has been developed using the facilities of the Laboratory of Geodynamic Modelling from Geo3Bcn-CSIC.

Table of Contents

Table of Contents.....	vii
Summary.....	1
Chapter 1	9
Introduction	9
1.1. Objectives	18
1.2. Thesis outline	19
Chapter 2	25
Fundamentals	25
2.1. Lithosphere	25
2.2. Sublithospheric mantle.....	27
2.3. Gravitational field	28
2.3.1. Gravity anomaly	29
2.3.2. Geoid anomaly.....	30
2.4. Temperature field.....	32
2.5. Mineral physics	34
2.6. Physical properties.....	38
2.6.1. Density	38
2.6.2. Thermal conductivity	38
2.6.3. Mantle seismic velocities	39
2.7. Isostasy and elevation	41
2.8. Mantle melting and volcanism.....	42
Chapter 3	47
Integrated geophysical-petrological modelling of the upper mantle anomalies.....	47
3.1. General modelling workflow	48
3.2. Anelasticity	50
3.3. Sublithospheric mantle composition	55
3.4. Recalibration of elevation.....	57
3.5. Reference model for synthetic seismic tomography	58
3.6. Sublithospheric mantle anomalies	60
3.6.1. Thermal anomalies	61

3.6.2. Chemical composition anomalies	62
3.6.3. Seismic velocity anomalies.....	64
3.7. Open source graphic user interface (GUI) and input/output data	66
3.8. Application to a synthetic subduction zone.....	67
3.8.1. Input data, model geometry, and physical properties.....	67
3.9. Post-processing toolbox	70
3.9.1. Seismic velocities post-processing example	71
3.9.2. Depth distribution of stable mineral-assemblages.....	74
Chapter 4.....	77
Present-day crust and upper mantle structure of the Alboran and Algerian basins and their margins.....	77
4.1. Data	78
4.1.1. Regional geophysical data	78
4.1.2. Crustal data	81
4.1.3. Mantle structure and chemical composition	83
4.2. Alboran Basin geo-transect: structure, temperature, and density	85
4.2.1. Crustal and upper mantle structure	85
4.2.2. Temperature and density distribution	92
4.3. Algerian Basin geo-transect: structure, temperature, and density.....	94
4.3.1. Crustal and upper mantle structure	94
4.3.2. Temperature and density distribution	98
4.4. Mantle seismic velocities and comparison with passive seismological data	100
4.4.1. Alboran Basin geo-transect	100
4.4.2. Algerian Basin geo-transect	106
Chapter 5.....	113
Discussion	113
5.1. LitMod2D_2.0	114
5.2. Present-day crust and upper mantle structure of the Alboran and Algerian basins and their margins.....	115
5.2.1. Crustal and lithospheric structure	115
5.2.2. Mantle composition.....	118
5.2.3. Subducted Ligurian-Tethys slabs	128

5.2.4. Geodynamic implications	129
Chapter 6	139
Conclusions	139
6.1. LitMod2D_2.0: An improved tool for the integrated geophysical-petrological interpretation of upper mantle anomalies.....	140
6.2. Present-day crust and upper mantle structure in the Alboran and Algerian basins and their margins	142
List of Figures and Tables.....	145
References.....	154
Appendix	171

Summary

Summary

The closure of the Ligurian-Tethys Ocean, opened during Jurassic and consisting of highly segmented margins in between Africa and Iberia, has produced the Alboran and Algerian basins in the Western Mediterranean through subduction and slab roll-back processes during the Cenozoic. Towards the end of the slab roll back, collision with the continental margins led to the formation of the Betic-Rif orogen in south Iberia and the Tell-Kabylies in north Algeria. Both, the Betics-Rif and Tell-Kabylies, shows the high-pressure and low-temperature (HP-LT) rocks exhumed from the subduction channel but with opposite tectonic vergence, to the NW in Betics and to the SE in Kabylies. While the Cenozoic evolution of the back-arc basins in the Central and Eastern Mediterranean (i.e., Liguro-Provenca, Tyrrhenian and Aegean) are well understood, the evolution of the Alboran and Algerian basins in the Western Mediterranean is under debate, leading to the proposal of different geodynamic evolution models. All the models agree on that the subduction and subsequent slab-rollback was operating but argues for the direction of subduction trench and slab-rollback. At present, positive seismic velocity anomalies in the upper mantle are observed in the tomography models around the Alboran Basin and beneath the North-Algeria margin. These high velocity anomalies are qualitatively interpreted to be cold, hence, remnant of the subducted Ligurian-Tethys lithosphere in order to explain geodynamic evolution of the Alboran and Algerian basins.

Subduction processes must have left its imprint on the crust and upper mantle structure, temperature and chemical composition, which dictate the present-day physical state. Physical state inside the Earth controls the physical properties (i.e., density, seismic velocities, and thermal conductivity) which in turn control the geophysical observables at the surface (i.e., elevation, gravity anomaly, geoid height, and surface heat flow). Integrated geophysical-petrological modelling of these surface observables allows exploring and reconciling observations from different datasets and methods. However, thermal and/or chemical nature of the imaged seismic velocity anomalies (e.g., subducted Ligurian-Tethys) needs to be incorporated in such models. In general, seismic tomography models reports relative positive or negative velocities with respect to a reference model which are further inferred qualitatively as cold or hot regions in the upper mantle, respectively. Quantitative interpretation of the seismic velocity anomalies in terms of temperature and/or chemical composition is challenging and is at the forefronts of the modern day geophysics.

Hence, the objectives of this thesis is twofold: 1) to develop a methodological framework to incorporate the sublithospheric anomalies observed in seismic tomography in the integrated geophysical-petrological modelling of the geophysical surface observables, and 2) its application to the Alboran and Algerian basins and their margins to model the present-day crust and upper mantle thermo-chemical structure yielding temperature, density (i.e., chemical composition) and seismic velocities to put constraints on their geodynamic evolution.

In the first part, an already existing tool, LitMod2D_1.0, is improved into a new LitMod2D_2.0 version which allows to model the sublithospheric anomalies and to be available for the scientific community. Various synthetic tests of the upper mantle anomalies have been performed to understand the sensitivity of temperature and chemical composition to the density and seismic velocities. Results show nonlinearity between the sign of thermal and seismic velocity anomalies, and that S-wave velocities are more sensitive to temperature whereas P-wave velocities are to composition. A synthetic example of subduction is made to understand the sensitivity of sublithospheric mantle anomalies associated with the slab and the corner flow, on surface observables (elevation, geoid height, and gravity anomalies). A new open-source graphic user interface is incorporated in the new version for ease of application. The output of the code is simplified by writing only the relevant physical parameters (temperature, pressure, material type, density, and seismic velocities) to allow the user to utilize predefined post-processing codes from a toolbox (flexure, mineral assemblages, synthetic passive seismological data, and tomography) or designing new ones. A post-processing example is demonstrated by calculating synthetic seismic tomography, Rayleigh-surface-wave dispersion curves, P-wave receiver functions and stable minerals distribution from the output file of LitMod2D_2.0.

In the second part of this thesis, I apply improved LitMod2D_2.0 to define the present day crustal and lithospheric structure along two 2D geo-transects beneath the Betics-Alboran and Greater Kabylies-Tell-Algerian orogenic systems to discuss the highly debated and contrasting existing models. Results show a thick crust (37 km and 30 km) and a relative deep LAB (130 km and 150 km) underneath the HP-LT metamorphic units of the Internal Betics and Greater Kabylies that contrast with the ~16 km thick magmatic crust of the Alboran Basin and the ~10 km thick oceanic crust of the Algerian Basin, respectively. This sharp change in crustal thickness, from the orogenic wedge to the back-arc basins, contrasts with the gentler crustal thickening towards the respective opposed margins. Despite the similar LAB depth (~60 km) in both basins, the chemical composition of the lithospheric mantle beneath the Alboran

Basin is slightly more fertile than beneath the Algerian Basin. At sublithospheric levels, results show that both the Alboran slab beneath the Betics and Algerian slab beneath the Kabylies, are about -400 °C colder than the ambient mantle but have different chemical composition. Alboran slab is slightly fertile compared to the typical oceanic lithospheric of the Algerian slab. Both slabs are detached from the respective continental lithospheric mantle of Iberia and Africa, since their weight is not transmitted isostatically to the surface. Results show that the uplift related to the slab break-off is ~700–1000 m in the Betics and is ~600–1200 m in north Algeria.

The Ligurian-Tethys slab beneath the SE Iberia shows an apparent dip to the SSE whereas the slab below Algeria dips to the NNW, matching the NW- and SE-tectonic transport direction of the fold and thrust belts of the Betics and Greater Kabylies-Tell-Atlas subduction-related orogens, respectively. The large-scale configuration of present-day SE Iberia and Algerian margins as well as their mantle compositions in the Alboran and Algerian geo-transects is consistent with opposite dipping subduction of two segments of the Jurassic Ligurian-Tethys domain. Their present configurations agree with Neogene slab roll-back process triggering mantle delamination followed by slab break-off in both opposite subductions.

CHAPTER 1

Introduction

“Necessity is the mother of invention”

-Unknown

Chapter 1

Introduction

The closure of the Tethys Ocean, located along the northern margin of the paleo-continent Gondwana, associated with the northward displacement of India, Arabia, and Africa lead to the subduction of its different segments and has produced the ~12000 km long Alpine-Himalayan collision zone (Figure 1.1). The convergence velocity with respect to Eurasia was decreasing from east to west, such that India was moving ~120 mm/yr to NNE, Arabia was moving ~32 mm/yr to NNE-N, and Africa was moving 4 mm/yr -10 mm/yr to N-NNW (e.g., Hatzfeld and Molnar, 2010). To the east, after the consumption of the Tethys lithosphere, which at present is sitting in the underlying mantle, the Indian (at ~50 Ma) and Arabian (at ~35 Ma) continental lithosphere collided with Eurasia and has generated the Tibetan Plateau and the Zagros Mountains (e.g., Hatzfeld and Molnar, 2010). In the Mediterranean region, collision between Eurasia and Africa is not achieved yet and represents an early stage of continent-continent collision where a mixture of oceanic and transitional lithosphere is still present (Royden and Faccenna, 2018). The subduction of the different segments of the Tethys and subsequent slab rollback, in an overall slow convergent setting with Africa, generated different back-arc basins (e.g., Aegean Basin, Tyrrhenian Basin, Alboran Basin, Algerian Basin) in overriding plates leading to the formation of highly extended continental crust or new ocean floor, and several narrow arcuate orogens (e.g., Hellenic Arc, Calabrian Arc, Betic-Rif Arc) which are characteristic of the Alpine-Mediterranean system (e.g., Faccenna et al., 2014; Royden and Faccenna, 2018; van Hinsbergen et al., 2020).

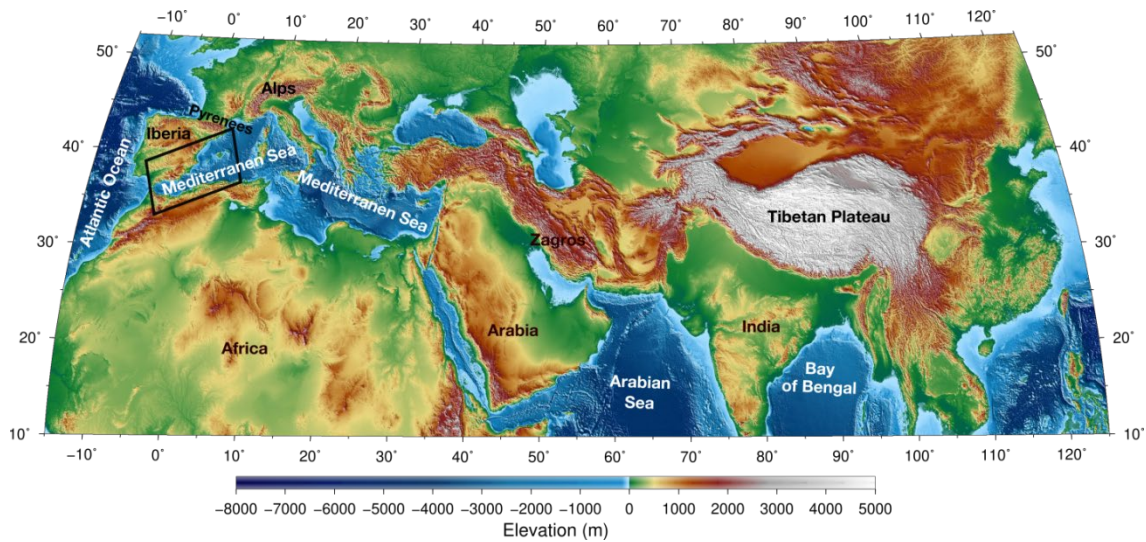


Figure 1.1 Topography map of the Alpine-Himalayan collision zone. The area inside the black box is the focus of this thesis.

The North Balearic Transform Zone is recognized as a major transform fault separating the Liguro-Provençal and the Tyrrhenian realm from the Alboran-Algerian realm (Figure 1.2). The Alboran and Algerian basins lie in the western end of the Alpine-Himalayan collision zone and constitute the Western Mediterranean in between Iberia and Africa (Figure 1.2). The origin of these basins, like other Mediterranean basins, has been attributed to the roll-back of the subducted Ligurian-Tethys lithosphere at the western end of the Tethys Ocean (Faccenna et al., 2004). The Ligurian-Tethys was generated by the propagation of the Central Atlantic ridge during the Early Jurassic in between Africa, Iberia and Adria, and was composed of several transtensive and highly extended continental segments transitioning to oceanic lithosphere to the east (Schettino and Turco, 2011; Stampfli and Borel, 2002). Trans-tension ceased in the Early Cretaceous as the mid-Atlantic ridge propagated northwards along the Newfoundland-Iberia margin and triggered the eastward motion of the Iberia plate together with the African plate (Nirrengarten et al., 2018). The protracted N-NNW displacement of Africa relative to Eurasia, varying from several millimetres per year across the Western Mediterranean to approximately 10 mm/yr across the eastern Mediterranean (e.g., Dewey et al. 1989, McClusky et al. 2003), since the Late Cretaceous is accommodated by the consumption of the highly segmented Ligurian-Tethys, a significant intra-plate deformation in the Iberian plate and the formation of the Pyrenees in the northern Iberian margin (Vergés and Fernández 2006; Macchiavelli et al., 2017). Subduction of the highly segmented Ligurian-Tethys and subsequent extension from the slab roll-back in an overall slow

convergence setting produced the Alboran and Algerian basins, and the consequent collision with the passive margins producing the Betic-Rif orogen in south Iberia and the Tell-Kabylies orogen in north Algeria (Figure 1.2).

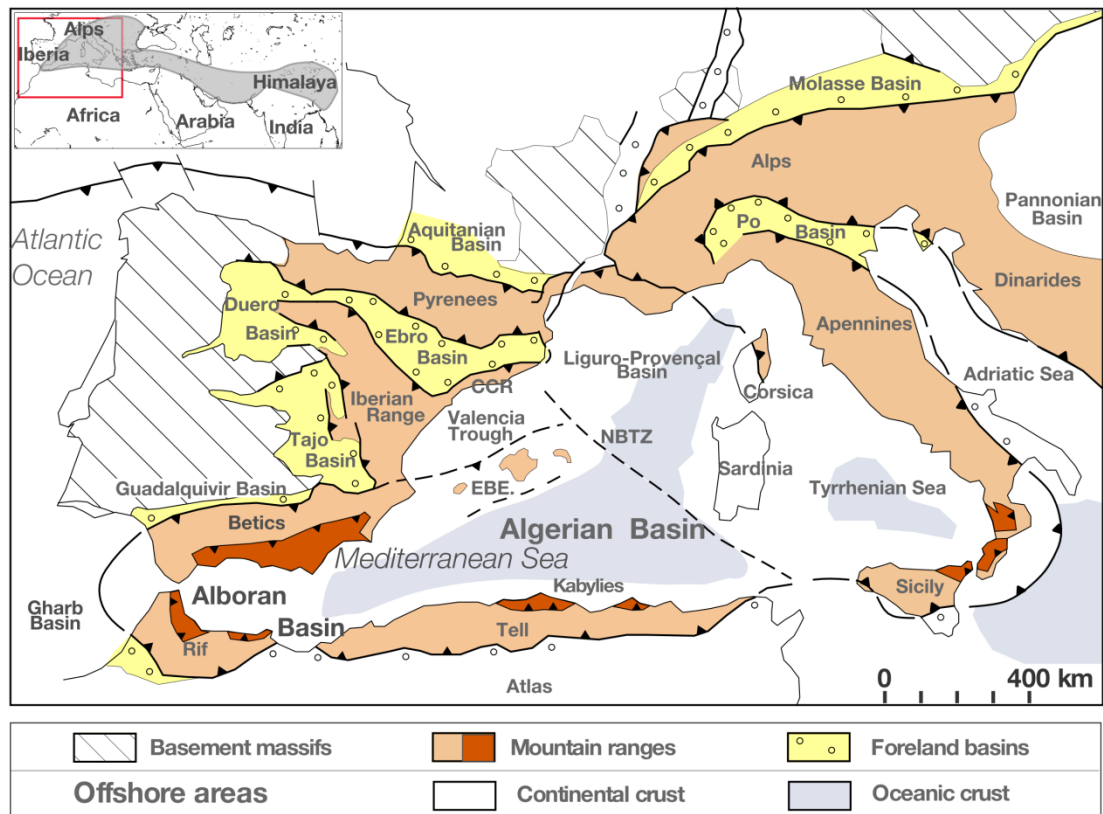


Figure 1.2 Geological map of the Western Mediterranean showing the main orogenic belts and basins (Modified from Vergés and Sàbat, 1999). NBTZ, North Balearic Transform Zone; EB, Emile-Baudot Escarpment.

Exhumation of high-pressure and low-temperature (HP/LT) metamorphic rocks is a typical process of roll-back subduction systems (e.g., Agard et al., 2018). Such metamorphic rocks, referred to as Internal Units in the literature, are found in the Betics-Rif orogen in the southern margin of Iberia and along the northern margin of Africa in Algeria (Figure 1.3). The Betic-Rif orogenic system consists of a typical subduction-related fold and thrust belt, which from the External to Internal Units is formed by the Guadalquivir and Rharb flexural foreland basins, the External Betics, the Flysch units, the Internal Betics, and the extensional back-arc Alboran Basin (see the structural style of these units in Michard et al., 2002; Vergés and Fernández, 2012). The HP/LT metamorphic rocks of the Betics Internal Units from bottom to top are the Nevado-Filabride, the Alpujarride and the Malaguide (Figure 1.3). The Rif fold and

thrust belt shows a similar tectonic architecture except for its N-S direction and for the lack of the equivalent Nevado-Filabride unit. The northern margin of Algeria shows similar characteristics but opposite spatial association compared to the Betic-Rif orogen (Figure 1.3). The main tectonic units, from the Internal to External units, are the extensional back-arc Algerian Basin, the HP/LT rocks in the Kabylies in the Internal Units followed by the thrusting of the Flysch Units over the External Units, and farther to the SSE, the fold and thrust belt in the Tell-Atlas Mountains (see the structural style in Khomsi et al., 2019).

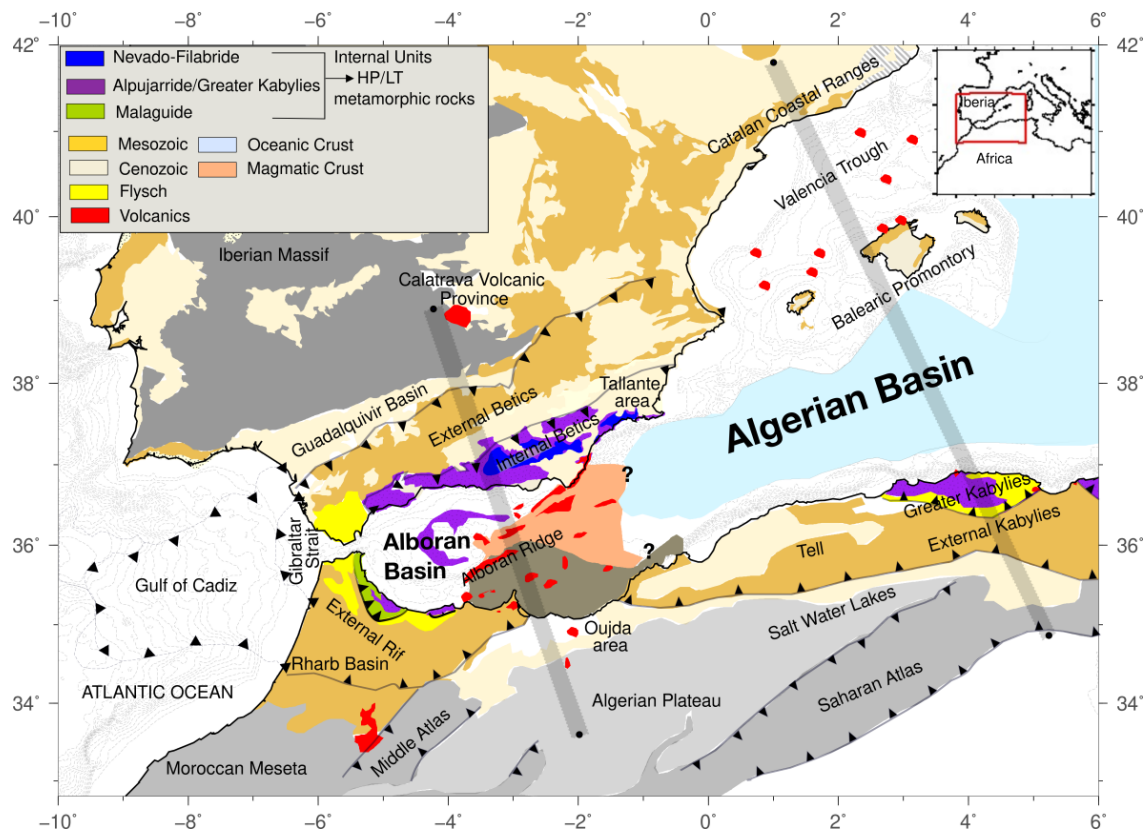


Figure 1.3 Detailed geological map of the Western Mediterranean showing main geologic units in the Alboran and Algerian basins, and the Betics-Rif and Kabylies-Tell-Atlas Mountains. Locations of the two geo-transects modelled in this thesis are shown by grey shadowed strips.

The basement in the Alboran Basin changes from the west to the east (Figure 1.3). The Western Alboran basin is floored by thin continental crust, including the HP Alpujarride metamorphic basement units (Soto and Platt, 1999), and numerous volcanic intrusions (Gómez de la Peña et al., 2018), whereas the Eastern Alboran basin is mostly floored by magmatic crust (Booth-Rea et al., 2007). South of the Alboran Ridge, situated in the middle of the Alboran Basin, the basin is floored by an

African continental crust with magmatic intrusions (Gómez de la Peña et al., 2018). The magmatic crustal domain of the Eastern Alboran basin transitions eastward to the oceanic crust of the Algerian Basin (Booth-Rea et al., 2007; Pascal et al., 1993). The Valencia Trough, situated NW of the Algerian Basin, in between the Catalan Coastal Ranges and the Balearic Promontory, has a very thin continental basement (Torné et al., 1992; Pascal et al., 1992), which experienced a huge extension during Mesozoic (Roca, 2001; Etheve et al., 2018). The trough underwent compression in late Paleogene during the convergence between Africa and Iberia, and renewed extension from Late Oligocene to Langhian period (Morgan and Fernández, 1992; Fernández et al., 1995; Roca, 1996; Torné et al., 1996; Sàbat et al., 1997; Gaspar-Escribano et al., 2004). The basement of the Balearic Promontory is continental, similar to the Iberian basement beneath the Catalan Coastal Ranges (Torné et al., 1992; Pascal et al., 1992; Vidal et al. 1998).

Volcanism in the Western Mediterranean has been a focus of numerous studies (Melchiorre et al., 2017; Lustrino et al., 2011; Lustrino and Wilson, 2007; Duggen et al., 2005, 2008; Martí et al., 1992). In the Alboran Basin volcanism is mainly orogenic with wide geochemical variation (Lustrino et al., 2011) showing tholeiitic Miocene affinity in the centre surrounded by calc-alkaline volcanism (Duggen et al., 2008). The southern Iberian (e.g., Tallante area) and north-western African (e.g., Oujda area) continental margins show Lower Pliocene to Upper Miocene Si-K-rich (i.e., orogenic) and Upper Miocene to Pleistocene Si-poor (i.e., anorogenic or intra-plate volcanism) magmatism (Duggen et al., 2005). The northern coast of Algeria, along the Algerian basin, experienced K-rich (and minor medium-K) calc-alkaline volcanic activity (i.e., orogenic) along a ~450 km long E-W trending zone during Miocene (17 to 11 Ma) (Maury et al., 2000; Fourcade et al., 2001; Laouar et al., 2005). The younger anorogenic volcanism (alkaline) is observed in the eastern and western end of the Tell Mountains (Coulon et al. 2002; Maury et al., 2000; Wilson and Bianchini, 1999). The Valencia Trough experienced calc-alkaline volcanism (i.e., orogenic) in the Early-Middle Miocene and alkaline volcanic activity (i.e., anorogenic) from Middle Miocene to Recent (Martí et al., 1992).

The upper mantle structure in the Western Mediterranean has been studied by various global, regional and local seismic tomography studies. A high-velocity anomaly around the Alboran Basin (Figure 1.4a) has been reported in global to local seismic tomography models (Palomeras et al., 2017; Villaseñor et al., 2015; Bezada et al., 2013; Spakman and Wortel, 2004). This anomaly shows an arcuate shape and lies in the mantle roughly beneath the Betics-Rif Mountains and is interpreted as a subducted

slab from the Ligurian-Tethys (i.e., Alboran slab). Imaging the mantle in the northern margin of Africa is limited by the absence of passive seismic data and hence, by intermediate to poor resolution in the standard travel-time seismic tomography models. Recently, Fichtner and Villaseñor (2015), using state of the art full-waveform inversion seismic tomography reported high-velocity anomalies beneath the North-Africa margin (Figure 1.4b). Full waveform tomography leverages the station coverage by using earthquake source and recording station in pairs and utilizing the complete recorded waveform instead of a part of the seismic waveform. These high-velocity anomalies are also interpreted as the subducted slabs from the Ligurian-Tethys and are detached from the African lithosphere.

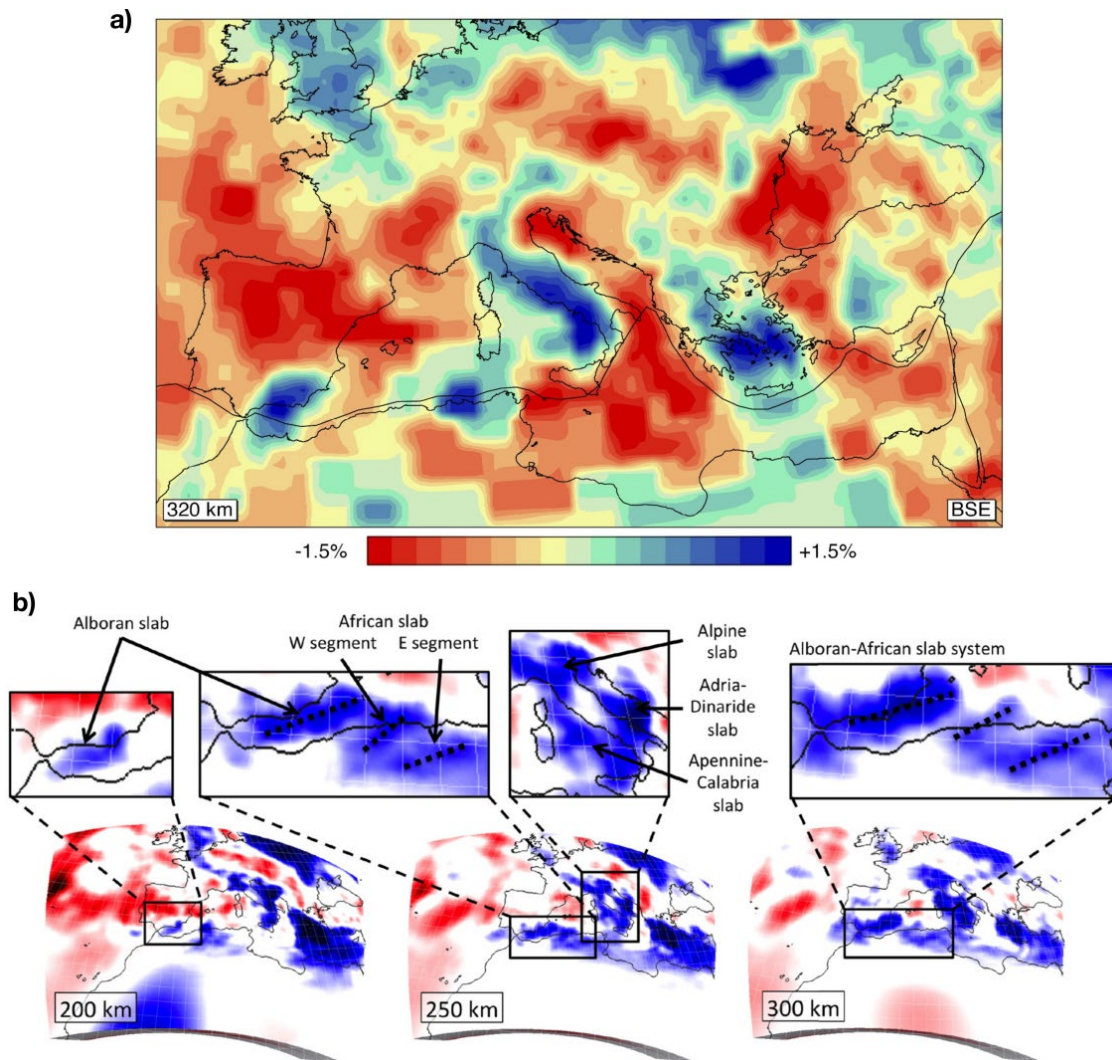


Figure 1.4 Upper mantle seismic tomography models in the Alboran and Algerian basins.(a) P-wave travel time tomography model slice at 320 km depth (Villaseñor et al.,2013) and (b) Full-waveform inversion seismic tomography model at different depths (Fichtner and Villaseñor, 2015).

While the Cenozoic evolution of the Liguro-Provençal, Tyrrhenian, and Aegean back-arc basins are well understood (Faccenna et al., 2004), the evolution of the Alboran and Algerian basins in the Western Mediterranean is still debated (Casciello et al., 2015; Faccenna et al., 2004; Jolivet et al., 2009; Spakman and Wortel, 2004; van Hinsbergen et al., 2014; Vergés and Fernández 2012). The opening of both basins for the last 35 My, is being explained by three different geodynamic scenarios, each based on slab roll-back as the driving mechanism (Figure 1.5). There is consensus that the Algerian Basin is an oceanic basin opened in the upper plate during the NW-dipping Tethys slab retreat, in agreement with the SSE-polarity of the Kabylies-Tell-Atlas orogenic system; however no agreement has been reached so far on the origin and evolution of the Alboran Basin and related Betic-Rif orogenic system. Main disagreements are on the original disposition of the tectono-sedimentary domains involved in the Betic-Rif subduction-related orogenic system and on the geodynamic interpretation used to build-up this orogenic system. The pros and cons of the three scenarios are discussed in detail by Chertova et al. (2014) using numerical modelling and concluding that both Scenario 1 and Scenario 3 are plausible despite the authors favour Scenario 1.

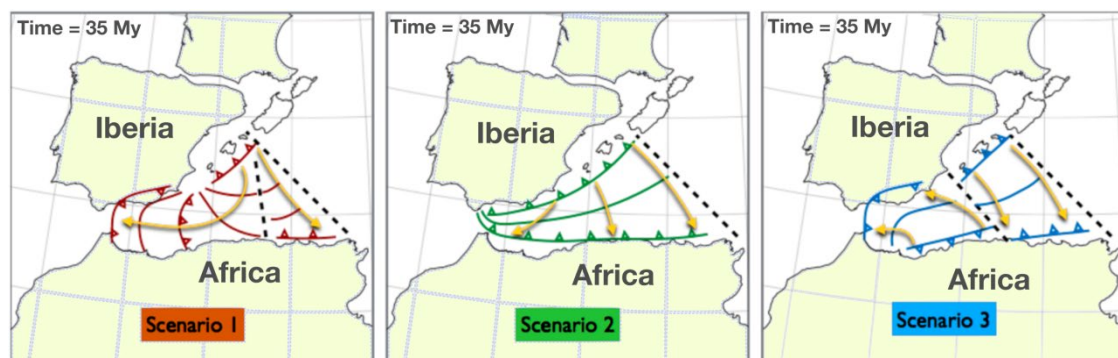


Figure 1.5 Models purposed for the geodynamic evolution of the Western Mediterranean. Scenario 1 after Van Hinsbergen et al. (2014) involves a single short subduction zone initially dipping to NW starting near the Balearic Promontory and then retreats to the SE before it separates into two different segment. One of the segments continue retreating to SE before it collides with North Africa and other continue retreating to the west and collides with Iberia resulting in 180° clock-wise rotation. Scenario 2 involves a long initial subduction dipping to the N-NW along the entire Gibraltar-Balearic Promontory margin (e.g., Gueguen et al., 1998; Faccenna et al., 2004; Jolivet et al., 2009). Scenario 3 after Vergés and Fernández (2012) involves two separate subduction segments with opposite subduction direction for the Alboran (subduction dipping to the SE and retreating to the NW) and Algerian (subduction dipping to the NW and retreating to the SE) basins. Direction of rollback is shown by the yellow arrows. Black dashed lines represent the proposed transform faults separating the different subduction segments (Figure modified after Chertova et al., 2014).

Presence of subduction in the Western Mediterranean during the Cenozoic is evident from the geological and geophysical observations (previous paragraphs). Although purposed models differ in the paleo-geographic setting of subduction, they all have subduction processes common to them (e.g., slab rollback, back-arc extension, slab tear). Irrespective of the model applicable to the Western Mediterranean, the subduction process must have left imprints on the present-day crust and mantle structure. A typical subduction system involves compression and the orogenic volcanism near the arc. In settings dominated by slab rollback, the upper plate undergoes extension and thins, producing anorogenic volcanism by mantle decompression. Sufficient decompressional melting can produce a new oceanic lithosphere as is observed in the Western Mediterranean basins (e.g., Algerian and Tyrrhenian basins). During the final stages of slab roll-back subduction system, collision with the continental lithosphere leads to the stacking and exhumation of the metamorphic slices of the subducted thinned continental crust of the former extended margins (Brun and Faccenna, 2008). Involvement of the passive margin also introduces mechanical weakness and the dense slabs can break-off/tear/detach (Fernández-García et al., 2019). Hence, the compression near the subduction front and extension in the back-arc must have affected the present-day lithospheric thickness. Further, the chemical composition of the lithospheric mantle must also be affected. Therefore, precise knowledge of the present-day lithospheric structure and chemical composition of the upper mantle are crucial constraints to decipher the geodynamic evolution of the Western Mediterranean.

The characterization of the present-day physical state (pressure, temperature, density, i.e. chemical composition, and seismic velocities) of the lithosphere and sublithospheric upper mantle and its architecture are fundamental for understanding their evolution through geological time scale and is a primary goal of modern geophysics (Afonso et al., 2016a; Hoggard et al., 2020). In this context a great deal of information comes from modelling, standalone or in pairs, of surface observables sensitive to temperature (surface heat flow), density (gravity, geoid, elevation), seismic velocities (passive and active seismic data), and chemical composition derived from mantle xenocrysts and xenoliths (e.g., Lachenbruch and Morgan, 1990; Griffin et al., 1999; Deen et al., 2006; Goes et al., 2000; Ritzwoller et al., 2004; Zeyen et al., 2005; Priestley and McKenzie, 2006; Fullea et al., 2007). However, significant discrepancies in the predictions from these methods are rather common in the literature (Afonso et al., 2008 and references therein)

Integrated geophysical-petrological modelling of these observables (i.e., elevation, gravity anomalies, geoid height, surface heat-flow, seismic velocities, mantle xenoliths and xenocrysts data) is a particular approach that allows exploring and reconciling observations from different datasets and methods. In particular, LitMod2D_1.0 (Afonso et al., 2008) is a tool developed to study the thermal, compositional, density, and seismological structure of the crust and the lithospheric and sublithospheric mantle by combining information from petrology, mineral physics, and geophysical observables within a self-consistent thermodynamic framework. As such, this approach is well suited to i) handle the intrinsic non-uniqueness problem associated with the modelling of single observables and ii) distinguish thermal from compositional effects in geophysical signatures.

LitMod2D_1.0 has been successfully applied in various tectonic settings including continental margins (e.g., Fernández et al., 2010; Pedreira et al., 2015) and continental collision regions (e.g., Carballo et al., 2015a; Tunini et al., 2015). It allows considering different chemical compositional domains within the lithospheric mantle, but assumes a homogeneous sublithospheric mantle with a theoretically determined primitive upper mantle (PUM) chemical composition (McDonough and Sun, 1995). The latter assumption limits the use of LitMod2D_1.0 to regions affected by mantle upwelling, subduction, and/or delamination (e.g., Western Mediterranean). These regions are often characterized by changes in temperature and/or chemical composition in the sublithospheric mantle, as suggested by tomography models and are imaged in terms of seismic velocities variation (e.g., Koulakov et al., 2016; Cammarano et al., 2009). Seismic tomography models usually report positive and negative velocity anomalies with respect to global average reference seismic velocity models (e.g., ak135) in the mantle and are qualitatively interpreted. Positive seismic velocity anomalies are commonly interpreted, as in the case of the Western Mediterranean, as colder than average subducted slabs. The prompt question one could ask is: how much cold are these slabs with respect to the ambient mantle? And further to be comprehensive: what is the chemical composition of these slabs? For such a quantitative interpretation, one needs to decouple the temperature and chemical composition signal from the observed seismic velocities, which is not a straightforward task (Cammarano et al., 2009). Challenges in doing so come from the highly non-linear nature of the problem, computation of the temperature field in regions with subducted slabs, and temperature-pressure dependent anelastic attenuation correction of mineral physics derived anharmonic seismic velocities in the mantle.

1.1. Objectives

The generic objective of this thesis is twofold:

- To develop a methodology to decipher temperature and chemical composition of upper mantle anomalies observed in seismic tomography models.
- Using the developed methodology to model the present-day crust to upper mantle (~400 km) structure across the Alboran and Algerian basins in the Western Mediterranean and to interpret the results in terms of the geodynamic evolution of the region.

Hence, this thesis is divided into two main parts (Figure 1.6). In the first part, the LitMod2D_1.0 software package (Afonso et al., 2008) has been improved to incorporate sublithospheric mantle anomalies in the modelling along with other improvements into a new LitMod2D_2.0 version. The specific objectives of this part are:

- Use of a depleted chemical composition of the sublithospheric mantle determined from geochemical data as opposed to the theoretical primitive upper mantle (PUM; McDonough and Sun, 1995) used in LitMod2D_1.0.
- Incorporation of anelasticity calculations in the GENERATOR module to allow the conversion of seismic velocities to temperature anomalies and vice versa using the latest experimentally determined anelastic attenuation parameters on the anharmonic seismic velocities calculated from stable mineral assemblages.
- Defining a reference chemical compositional model of the upper mantle to compare the seismic velocity anomalies obtained in LitMod2D_2.0 with seismic tomography models.
- Development of a new open-source graphic user interface (GUI) with improved functionalities to facilitate its updating and cross-platform use.
- To simplify the input and output data in the LitMod2D_2.0 to facilitate the use of a central post-processing tool-box. The post-processing tool-box will help the users to use provided codes/scripts according to specific modelling needs.

In the second part of the thesis, the new LitMod2D_2.0 package is employed to model the present-day crust to upper mantle (~400 km) scale temperature, density and seismic velocity structure along two NNW-SSE oriented cross-sections (from now on

referred as geo-transects) across the Alboran and Algerian basins and the respective Iberian and African margins (Figure 1.3). Orientation and location of the geo-transects are chosen based on: i) the regional vergence of the major tectonic units (Figure 1.3), ii) available recent geophysical data (e.g., seismic tomography, active seismic lines and geological cross-sections), and iii) the different tectonic style, crustal nature, and lithospheric geometry of both basins. These two geo-transects are also chosen to see the possible opposite symmetry in the crust and upper mantle structure related to the opposite subduction polarity proposed for the geodynamic evolution of the Alboran and Algerian basins (Scenario 3, Figure 1.5; Vergés and Fernández, 2012). The specific objectives of this part are:

- To develop a detailed crustal cross-section along the geo-transects incorporating surface geology, geological data, seismic tomography and active seismic lines.
- To identify different lithospheric mantle domains along the geo-transects based on surface geology and mantle xenoliths. In regions dominated by extensive magmatism the mantle chemical composition must be compatible with melting models.
- To determine the composition and temperature of the subducted slabs inferred from the seismic tomography models, and their control on the elevation.
- Finally, to compare the obtained results along the geo-transects and to discuss their tectonic significance in terms of the geodynamic evolution of the Western Mediterranean.

1.2. Thesis outline

This thesis is divided into six chapters which are organised as follows:

Chapter 2 focuses on basic concepts. The general definition of the lithosphere and sublithosphere are described. Mathematical formulation of the physical properties (i.e., density, seismic velocities and thermal conductivity) and how they are sensitive to the surface observables (e.g., the gravitational field of the Earth, surface heat-flow, and elevation) are described.

Chapter 3 is dedicated to methodological improvements to the previous LitMod2D_1.0 version incorporated into a new LitMod2D_2.0 version. In this chapter, I present the numerical implementation of the new improvements, which are directed to provide a modelling tool for the scientific community to be used in regions affected by

geodynamic processes that can affect temperature and chemical composition in the sublithospheric mantle. The dependence of relevant physical properties of the upper mantle (i.e., seismic velocities and density) on the temperature and chemical composition is analyzed through synthetic models. The new graphic user interface (GUI) is used to perform synthetic model of a subduction zone to demonstrate full capability of LitMod2D_2.0. Post-processing tool-box is used to calculate synthetic receiver functions and surface-wave dispersion curves using the seismic velocities from the synthetic subduction zone model, and the stable minerals in the mantle.

The results presented in Chapter 3 are published in the scientific journal *Geochemistry, Geophysics, Geosystems* (American Geophysical Union):

Kumar, A., Fernández, M., Jiménez-Munt, I., Torne, M., Vergés, J., & Afonso, J. C. (2020). *LitMod2D_2.0: An improved integrated geophysical-petrological modelling tool for the physical interpretation of upper mantle anomalies*. *Geochemistry, Geophysics, Geosystems*, 21, <https://doi.org/10.1029/2019GC008777>.

A version of the LitMod2D_2.0 has been used in a collaborative study along a geo-transect running from South Iberia to North Africa crossing the western Gibraltar Arc and published in the scientific journal:

Jiménez-Munt, I., Torne, M., Fernández, M., Vergés, J., Kumar, A., Carballo, A., & García-Castellanos, D. (2019). *Deep seated density anomalies across the Iberia-Africa plate boundary and its topographic response*. *Journal of Geophysical Research: Solid Earth*, 124, <https://doi.org/10.1029/2019JB018445>.

Chapter 4 presents the results of the present-day structure along two selected geo-transects in the Alboran and Algerian basins. Previously published geological cross-sections, active seismic lines, Moho depths active and passive seismic data and surface geology along the geo-transects are used to constrain crustal-scale cross-sections. The lithospheric mantle is incorporated to the model based on published LAB depths, and chemical compositional domains are added based on available mantle xenoliths and surface geology data. Predictions of the surface observables from the lithospheric scale models are compared with the observed data, and finally, sublithospheric mantle anomalies observed in seismic tomography are added to the model. A range of possible chemical compositions of the subducted slabs are tested in order to fit the surface observables. Computed seismic velocities are also compared with the available passive seismological data.

A manuscript showing the results presented in Chapter 4 is in preparation to be submitted in a scientific journal.

Chapter 5 presents the general discussion on the new LitMod2D_2.0 software package and its application to model the present-day crust to upper mantle structure in the Western Mediterranean. The discussion on LitMod2D_2.0 is focused on the assumptions made and the potential future developments. The obtained results along the two modelled geo-transects are compared and discussed in terms of their tectonic significance.

Finally, Chapter 6 presents the final conclusions of this thesis.

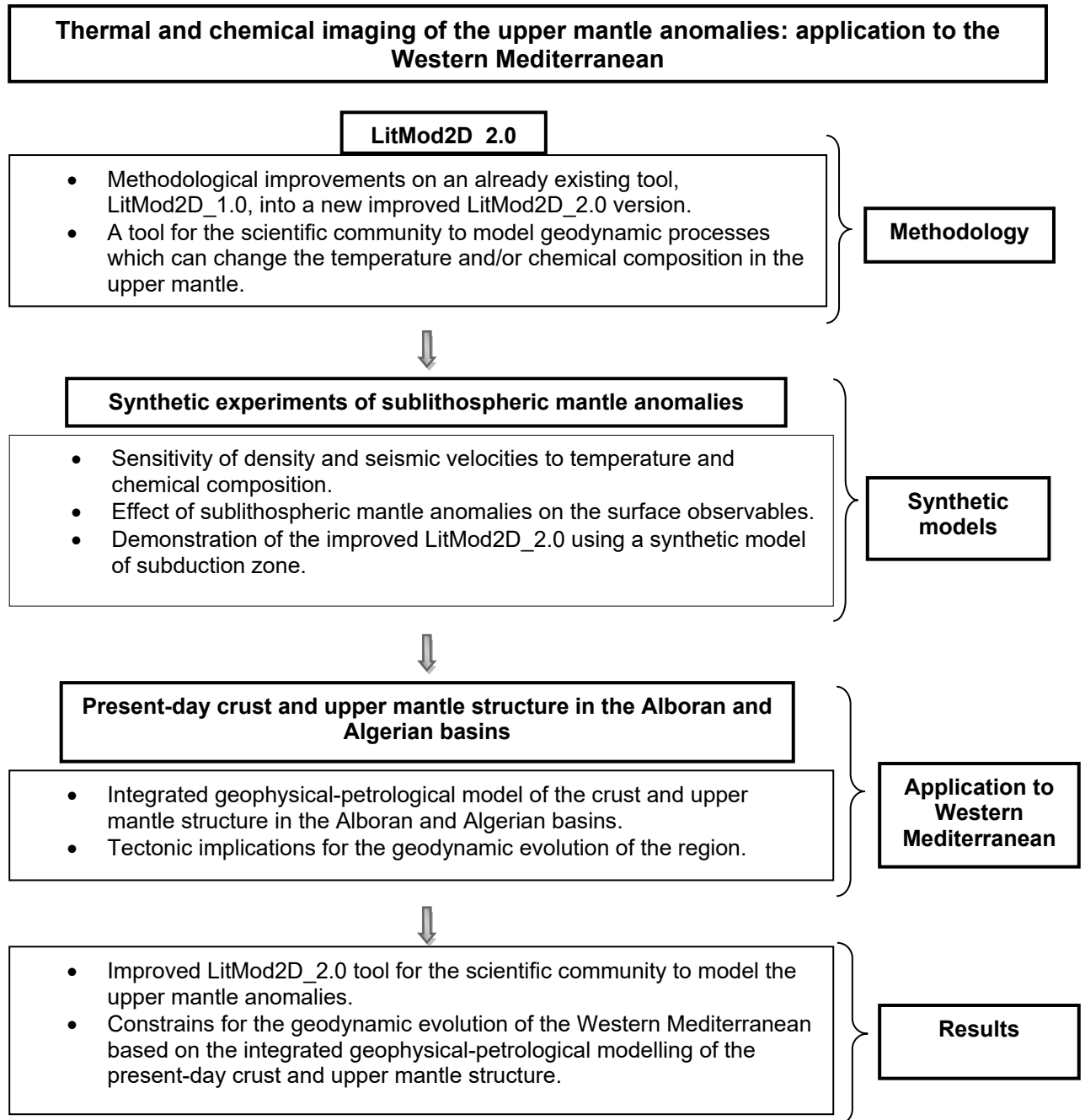


Figure 1.6 Flow chart showing the work-flow and the steps followed to achieve the objectives of this thesis.

CHAPTER 2

Fundamentals

“If you want to find the secrets of the universe, think in terms of energy, frequency and vibration”

-Nikola Tesla

Chapter 2

Fundamentals

This thesis is based on integrating the surface observables (i.e., gravity anomaly, geoid height, and surface heat flow, elevation, and mantle xenoliths and xenocrysts) and the physical properties sensitive to them (i.e., temperature, density, and seismic velocities) in a self-consistent thermodynamic manner to model the thermal, chemical and physical architecture of the lithosphere and upper mantle. Hence, it is necessary to state the basic principles and definitions adopted and the physical laws used in this thesis. In this chapter, I describe the basic definitions of the lithosphere, sublithosphere, surface observables (i.e., data) and their dependence on the physical properties.

2.1. Lithosphere

The lithosphere is the long-term rigid outer shell of the Earth and it is subdivided into tectonic plates, fundamental units of plate tectonics. However, depending on the timescale of applied stresses and the amount of strain rate, rocks in the Earth can show distinct behaviour (elastic, viscous, plastic). The lithosphere is a chemical, mechanical, and thermal boundary layer that overtops a hotter and rheological weak material. Chemically, the lithosphere is divided into the crust (usually silica rich) and the uppermost mantle (lithospheric mantle) where the conductive mode of heat transfer prevails.

The crust is the outermost layer of the Earth consisting mainly of sediments, granite, gneisses, granodiorite, gabbro, amphibolite, granulite and volcanic material for the continental crust, and of sediments, basalts, gabbros and some serpentinites for the oceanic crust. From a chemical point of view five oxides: SiO_2 , Al_2O_3 , FeO , MgO , CaO , and Na_2O dominate in the crust (Table 2.1). The continental crust contains higher silica and aluminium than the basaltic oceanic crust, hence is less dense than basalt. The Mohorovičić discontinuity (Moho) separates the crust from the relatively ductile mantle and represents a major chemical discontinuity from felsic crust to mafic upper mantle resulting in a major seismic velocity and density contrast. This major velocity contrast is imaged using earthquake waveforms or active seismic sources to map the depth of this discontinuity. The continental crust is usually divided

into three layers: an upper crust with densities between 2650 kg/m³ and 2710 kg/m³, a middle crust with densities from 2710 kg/m³ to 2860 kg/m³, and a lower crust ranging from 2860 kg/m³ to 2960 kg/m³ (Christensen and Mooney, 1995). The oceanic crust is composed by a gabbroic layer, overlain by basaltic pillow lavas and sheeted dykes. A low velocity and density sedimentary layer is usually present in the crust regardless of continental or oceanic showing a wide variety of density values (2000-2650 kg/m³).

Table 2.1 Major oxide compositions (weight %) of the crust.

Name	SiO ₂	Al ₂ O ₃	FeO	MgO	CaO	Na ₂ O
Continental upper crust ^a	66.60	15.40	5.00	2.50	3.59	3.27
Continental middle crust ^a	63.50	15.00	6.02	3.60	5.25	3.39
Continental lower crust ^a	53.40	16.90	8.57	7.20	9.59	2.65
Oceanic upper crust ^b	48.99	14.89	9.86	7.56	11.26	2.70
Oceanic lower crust ^c	52.58	13.83	6.74	12.48	10.52	1.20

^a Rudnick and Gao (2003); ^b Schilling et al. (1983); ^c Behn and Kelemen (2003)

The lithospheric mantle is a chemically distinct layer spanning from the Moho to the top of the asthenosphere. The base of the lithospheric mantle is also denoted as the lithosphere-asthenosphere boundary (LAB) whose depth and physical characteristics depend on the way it is observed. The seismological lithosphere is defined as the high velocity lid that overlies the upper mantle Low Velocity Zone (LVZ), although this definition is more appropriate for oceanic rather than for continental lithospheres (Anderson, 1989; Carlson et al., 2005). Thermally, the lithosphere is defined as the thermal boundary layer in which the heat transfer by conduction predominates over convective processes. The base of the lithospheric mantle or LAB is commonly defined as a particular isotherm (usually 1200 °C - 1350 °C) determined by the intersection between a conductive geotherm and a mantle adiabat (Schubert et al., 2001). From a geochemical point of view the LAB would be the maximum depth from which low-Y (< 10 ppm) garnets, characteristic of depleted lithosphere, are derived (Griffin et al., 1999). This definition matches pretty well with the thermal definition of the LAB being at the 1200 °C - 1300 °C isotherm. The mechanical lithosphere can be defined as a layer not affected by the convection beneath it, at geological time scales. The boundary between mechanical lithosphere and convective mantle is typically around 800 °C - 900 °C, based on the deformation of the olivine-rich rocks (Schubert et al., 2001). Hence, the thermal lithosphere includes the mechanical lithosphere. Accordingly, there is an upper layer that takes no active part in

convection, underlain by the lower part of the thermal boundary layer which, under some circumstances, can become unstable and convect. Hence, depending on the considered physical property in observing or modelling the lithosphere its definition can change. In this thesis, LAB is referred to as a thermal and a chemical boundary unless specified otherwise.

2.2. Sublithospheric mantle

The Earth's mantle beneath the LAB spans until the core-mantle boundary, which is roughly at ~2900 km. The mantle is further divided into upper and lower mantle separated by the mantle transition zone (MTZ). The MTZ starts at 410 km, which is marked by the exothermic phase transition of olivine to its high-pressure polymorph, wadsleyite. The bottom of the MTZ lies at 660 km depth involving the endothermic phase transition of wadsleyite to its high-pressure polymorph called ringwoodite. The thickness and depth of the mantle transition zone can vary locally since it is defined by endothermic and exothermic phase transition (e.g., if a cold subducting slab penetrates the MTZ its thickness increases whereas if a hot plume rises through MTZ its thickness decreases). In this thesis, I only focus up to the upper mantle (400 km depth) and refer to it as sublithospheric mantle (i.e., asthenosphere). Hence, the base of the sublithospheric mantle is fixed at 400 km depth, and the temperature at this depth is taken to be 1520 °C (Afonso et al., 2008) which is consistent with the experiments at high-pressure and high-temperature on phase equilibria of olivine-wadsleyite (Ito and Katsura, 1989; Katsura et al., 2004) giving a temperature of $1487 \pm 45^\circ\text{C}$ at the 410km discontinuity.

The sublithospheric mantle is the hotter layer beneath the LAB in which convection prevails, implying a more ductile behaviour than the lithosphere at geologic time scale. Heat transport in the sublithospheric mantle is carried out by convection and is parameterized with an adiabatic thermal gradient.

Chemically, the sublithospheric mantle is homogenous but distinct than the lithospheric mantle. One basis on which composition in the mantle is compared is the fertility, which simply means enrichment in compatible elements concentration and depletion in incompatible elements. The compatible/incompatible nature of elements depends on the bulk distribution coefficient during solid to liquid phase transition called chemical differentiation. The bulk distribution coefficient is the ratio of the element concentration in the solid phase over the liquid phase. In Figure 2.1, it can be seen that MgO is highly compatible and Al_2O_3 , CaO, and Na_2O are incompatible whereas

FeO and SiO₂ are slightly incompatible. The sublithospheric mantle is a chemical reservoir source to Mid-Oceanic-Ridge-Basalts (MORB) since the onset of plate-tectonics and is depleted in incompatible elements (i.e., Ca, Al, Fe) and enriched in compatible elements (Mg) and hence, is more fertile than the lithospheric mantle.

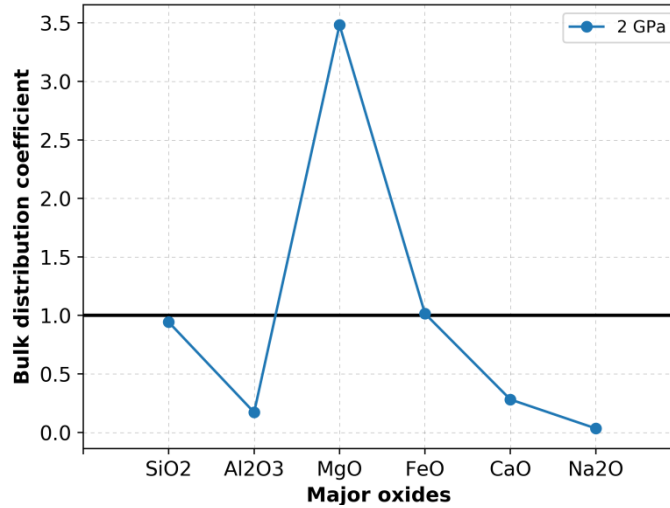


Figure 2.1 Bulk distribution coefficients of major oxides during melting at the mid-oceanic-ridge calculated using empirical relations from Niu (1997). A black horizontal line with bulk distribution coefficient of 1 separates compatible elements above it from the incompatible elements below it.

2.3. Gravitational field

The Earth's gravitational field is a direct manifestation of the density distribution in the Earth's interior and hence, complements other geophysical observables (i.e., elevation and passive and active seismic data). The real equipotential surface of the Earth, called geoid, follows the mean sea level in the oceanic areas and referenced sea level surface over the continents. As a good approximation, the geoid can be described by an equipotential revolution ellipsoid and is called the normal or theoretical field, or the reference geoid.

Mathematically, the gravity potential of the Earth can be adequately described using a global geopotential model, i.e., a spherical harmonic expansion, to degree and order N , plus a centrifugal term:

$$W(r, \phi, \lambda) = \frac{GM_T}{r} \left(\sum_{n=2}^N \left(\frac{a}{r} \right)^n \sum_{m=0}^n [\overline{C_{nm}} \cos(m\lambda) + \overline{S_{nm}} \sin(m\lambda)] \overline{P_{nm}}(\sin \phi) \right) + \frac{1}{2} \omega^2 (x^2 + y^2) \quad (2.1)$$

where G is the universal gravitational constant ($6.674 \times 10^{-11} \text{ m}^3/\text{kg.s}^2$), M_T the total mass of the Earth, r , ϕ , λ , x and y the geocentric coordinates of the observation point, $\overline{C_{nm}}$, $\overline{S_{nm}}$ a set of fully normalized coefficients, $\overline{P_{nm}}$ the fully normalized associated Legendre functions, and ω is the angular rotation velocity of the Earth.

The actual gravity potential of the Earth, W , can be written as sum of the potential from the reference ellipsoid, U , and the difference between W and U called anomalous potential:

$$W = U + T \quad (2.2)$$

Such partition of the Earth's gravity field simplifies the mathematical formulation of the normal potential (U) as the ellipsoidal field and its deviation with respect to the real field. Both, the gravity (free air and Bouguer) and the geoid anomalies, are referred to the normal field produced by the reference ellipsoid.

2.3.1. Gravity anomaly

The gravity anomaly (Δg) is the difference between the measured gravity over or reduced to the geoid, g , and the normal (theoretical) gravity at a point projected along a normal to the reference ellipsoid from the measurement point, λ . Both, the measured and the normal gravity, can be derived from the Earth and ellipsoidal potentials:

$$g = \nabla W \quad (2.3)$$

$$\lambda = \nabla U \quad (2.4)$$

Since gravity anomaly follows the inverse square law, it is mainly sensitive to lateral density variations at crustal depths. Measured gravity data contain the effects of latitude, Earth tides, instrumental drift, distance from the reference ellipsoid and masses between the actual topography and the reference ellipsoid. Hence, in order to obtain anomalies comparable over large areas, corrections must be applied for the above mentioned effects. Corrections for Earth tides, instrumental drift, latitude, and free air to the measured gravity gives us the free air gravity anomaly (Δg_{FA}), which at short wavelengths correlates strongly with topography. The free air correction takes into account whether the measuring point is above or below the reference ellipsoid, considering the vertical gravity gradient. Once the correction for the topography masses are applied to the free-air gravity anomaly, called terrain correction, the Bouguer anomaly (Δg_B) is obtained. The primary objective of the complete Bouguer

correction is to remove all non-geological components of the gravity anomalies enhancing subsurface mass variations by correcting for the gravitational attraction of topography to the free-air anomaly. Hence, Bouguer anomaly correlates mainly with lateral variations of the density and thickness of the crust.

2.3.2. Geoid anomaly

The geoid is the equipotential surface of the Earth and coincides with the average sea level and contains, ideally, all the mass of the Earth. However, this is not a rigorous definition, since the average sea level is not completely equipotential (dynamic ocean processes) and, in addition, onshore topographical masses can lie above the geoid. The geoid anomaly is then the distance between the geoid surface and the reference ellipsoid model. The geoid anomaly, N , and the anomalous potential, T , in equation 2.2, are related by the Brun's formula:

$$N = \frac{T}{\gamma} \quad (2.5)$$

where γ is the normal gravity field. In equation 2.5 it is assumed that the potential of the geoid and the reference ellipsoid are equal. In addition, the geoid anomaly, the gravity anomaly and the anomalous potential are related by the fundamental equation of the physical geodesy (Heiskanen and Moritz, 1967):

$$\nabla g = -\frac{\partial T}{\partial E} + N \frac{\partial \gamma}{\partial E} \quad (2.6)$$

where E is the elevation or orthometric height along the plumb line (positive upwards, negative towards the Earth's interior). Although equation 2.6 has the form of a partial differential equation, it must be considered as a boundary condition, as the gravity anomaly, g , is only known over a surface (the geoid). If we assume that the mass distribution outside the geoid is null, T becomes a harmonic function and:

$$\nabla^2 T = 0 \quad (2.7)$$

Equation 2.7, in conjunction with the boundary condition expressed by equation 2.6, is a genuine partial differential equation. The knowledge of the anomalous potential using gravity measurements (Equations 2.6 and 2.7) allows us to determine the geoid anomaly through equation 2.5. The spherical approximation considers the reference ellipsoid as a sphere and it is interesting for practical purposes. In the spherical approximation, equation 2.6 has the following form:

$$\nabla g + \frac{\partial T}{\partial r} + 2 \frac{T}{R_T} = 0 \quad (2.8)$$

where r is the radial distance and R_T is the radius of the Earth. Offshore, geoid variations can be determined straightforward via satellite altimetry. Onshore, the geoid anomaly must be determined by indirect methods. The Stokes formula gives us the geoid anomaly as a function of the gravity anomalies in the spherical approximation:

$$N = \frac{R_T}{4\pi g_0} \iint \nabla g S(\psi) d\sigma \quad (2.9)$$

where ψ is the spherical distance between the calculation point and the mass distribution, g_0 is an average value of the gravity attraction over the surface of the Earth, $d\sigma$ is the differential element of surface, and $S(\psi)$ is the Stokes function, defined as:

$$S(\psi) = \frac{1}{\sin\left(\frac{\psi}{2}\right)} - 6 \sin\left(\frac{\psi}{2}\right) + 1 - 5 \cos(\psi) - 3 \cos(\psi) L \left[\sin\left(\frac{\psi}{2}\right) + \sin^2\left(\frac{\psi}{2}\right) \right] \quad (2.10)$$

The surface integral of equation 2.9 spans the whole surface of the Earth, and assumes the following assumptions:

- The mass within the reference ellipsoid is equal to the mass of the Earth.
- The potential of the geoid and the reference ellipsoid are equal.
- The centre of the reference ellipsoid is coincident with the centre of the Earth.
- There are no masses outside the geoid (equation 2.7).
- Spherical approximation.

The assumption that no masses lie outside the geoid is not valid over the continents, since the geoid surface is located beneath the topography. In such cases, topography outside the geoid must be removed by some procedure (e.g., Helmert condensation) taking into account the indirect effect that such procedure introduces in the geoid determination.

Since the geoid anomaly is the difference between two potential surfaces, it depends on the inverse of the distance to density anomalies and is affected by lateral density variations located in a wide range of depths ranging from the core-mantle boundary up to crustal levels. As a general rule of thumb, an excess of mass produces positive geoid anomalies and vice versa. Unfortunately, it is not possible to determine univocally the depth of the density anomaly, i.e., to decompose the potential field of

the Earth into its causative sources (Bowin, 2000). However, global studies show that the geoid anomalies with wavelengths greater than 4000 km are produced by density variations at sublithospheric depths (Bowin, 1983). As consequence, to study the upper mantle structure, we must retain only geoid signal with wavelengths smaller than 4000 km. The relation between the degree, n , and the associated wavelength of the spherical harmonics, λ , is (Strang van Hees, 2000):

$$\lambda = \frac{4\sqrt{\pi}R_T}{n+1} \quad (2.11)$$

According to equation 2.11, for the degree 10 harmonic, the associated wavelength is about 4106 km. Therefore, degrees $n \leq 10$ must be removed in order to keep the more likely “upper mantle” contribution to the geoid anomaly. For a punctual mass, m_p , we can obtain an equation that relates the gravity anomaly and the geoid anomaly in spherical coordinates. The anomalous potential produced by a punctual mass anomaly at a depth z is:

$$T = G \frac{m_p}{z} \quad (2.12)$$

The gravity anomaly produced by the same punctual mass anomaly reads:

$$\Delta g = G \frac{m_p}{z^2} \quad (2.13)$$

Combining equations 2.12 and 2.13 with equation 2.5, the following expression is obtained for the depth at which the punctual mass anomaly is located:

$$z = \frac{N\gamma}{\Delta g} \quad (2.14)$$

According to equation 2.14, a punctual mass anomaly that produces a gravity anomaly of 50 mGal, and a geoid anomaly of 1 m, would be located at a depth of about 20 km.

2.4. Temperature field

Dynamics of the Earth is essentially related with dissipation of the primordial heat (i.e., the heat generated during formation of the Earth) and the heat generated from the decay of radioactive elements. Inside the Earth heat can be transferred in four different ways: advection, convection, conduction, and radiation. The advection heat transfer occurs due to forced motion of mass and, in geological processes, via

erosion/sedimentation, isostatic uplift, magmatic ascent, and tectonic deformation. Convection is a special form of advection in which the motion is related to the grain level boundaries of the material, and is important in fluids and gases. Conduction of heat implies the transmission of the kinetic energy between adjacent atoms in the crystalline lattice or between neighbourhood molecules. Radiation involves the direct transfer of heat by electromagnetic radiation.

Although convection is not applicable to the rigid solids, over geological times the mantle behaves as a very high viscosity fluid and, therefore, slow convection is possible in the mantle. The lithosphere acts as a thermal boundary layer where the primary mode of heat transfer is conductive.

The heat transport inside the Earth can be expressed by the general equation (e.g., Schubert et al., 2001):

$$\rho C_p \frac{dT}{dt} = \nabla \cdot (k \nabla T) + H - \rho C_p \vec{u} \cdot \nabla T \quad (2.17)$$

where, T is the temperature, t is the time, k is the thermal conductivity (W/K.m), ρ is the density (kg/m³), C_p is the specific heat at constant pressure (J/K.kg), u is the vector of velocity (m/s), and H is the radiogenic heat production per unit volume (μ .W/m³). The first term of the right-hand side of equation 2.17 corresponds to diffusion of heat by conduction, the second one reflects the presence of heat sources, and the third one is the advective/convective transfer of heat.

Under steady-state conditions and in the absence of advection, equation 2.17 can be written as:

$$\nabla \cdot (k \nabla T) = -H \quad (2.18)$$

In absence of advection/convection, the main contribution to the heat source term, H , comes from the radiogenic heat production from the radioactive decay of isotopes U²³⁸, Th²³² and K⁴⁰. On average, uranium and thorium contribute more to the heat production than potassium. In general, granite has a more important internal heat generation ($2 - 4 \mu$.W/m³) than mafic igneous rocks ($0.2 - 0.4 \mu$.W/m³) (e.g., Vilà et al., 2010). The undepleted mantle contribution to the heat source term is very low ($0.01 - 0.02 \mu$.W/m³).

Numerically computed temperature field yields forward prediction of the surface heat flow (SHF), which is a measure of the energy released from the Earth per unit area and per unit time, and can be compared with measurements at the surface.

However, SHF measurements are expensive (particularly for continental areas) and, therefore, are sparse. Further, SHF data are submitted to various perturbation processes like water circulation, faults, paleoclimate variations or data acquisition. In continents (including arcs and continental margins), the average SHF (64.7 m.W/m²) is low compared to the average value for the oceans (95.9 m.W /m²; Davis, 2013). In the absence of advection due to tectonic activity, SHF is mainly controlled by the radiogenic heat production in the crust and the heat flow from the underlying mantle. SHF values tend to be higher in the areas with recent tectonic activity.

2.5. Mineral physics

For any given thermodynamic system (e.g., a mineral) with its chemical composition and components, the equilibrium state in terms of state variables (i.e. pressure and temperature) can be calculated by minimizing the Gibb's free energy. This equilibrium state consists of thermodynamically stable components at a given pressure and temperature and allows calculating the physical properties. Recalling the first law of thermodynamics, the total energy of a system is conserved or, in other words, the internal energy, U of a mineral structure, considered as a thermodynamic system, is constant. The internal energy is the sum of the potential energy stored in the interatomic chemical bonds and the kinetic energy related to atomic vibrations. If any heat is supplied to the system, the kinetic energy through the vibrations of chemical bonds will increase, leading to an increase in the temperature and, ultimately, in the internal energy. If any work is done on a mineral structure or if it is allowed to expand, it will do some work on the surrounding and its internal energy will change. The change in the internal energy can be expressed as

$$dU = dQ - PdV \quad (2.19)$$

where dQ is the exchanged heat, and PdV is the work done during expansion, P being the pressure and dV the change in volume (V) due to the expansion. Since temperature is a state variable, any property changing it, is a fundamental property of a material and hence, heat capacity C is defined as the amount of heat dQ required to raise the temperature of a mole of material by dT . Expressing dQ in the equation 2.19 in terms of C gives the following expression:

$$C = \frac{dU}{dT} + \frac{PdV}{dT} \quad (2.20)$$

If the volume is constant then C in equation 2.20 becomes the heat capacity at constant volume that is C_v , which then becomes the direct measure of change in the internal energy. In experiments involving solids, it is easier to maintain constant pressure than constant volume, so we need to define another energy function called enthalpy, H as

$$H = U + PV \quad (2.21)$$

Since we are interested in changes of these energy functions, let us differentiate it

$$dH = dU + PdV + VdP \quad (2.22)$$

Substituting for dU from equation 2.19 and for heat capacity and rearranging we get

$$C = \frac{dH}{dT} + \frac{VdP}{dT} \quad (2.23)$$

Now if pressure is constant, the above equation becomes the heat capacity at constant pressure, C_p , which is the heat change, dQ , required to change the temperature by dT at constant pressure and is equal to the enthalpy change and can be easily measured in the laboratory experiments. Hence, enthalpy becomes analogous to internal energy. The difference between C_p and C_v is expressed as

$$C_p - C_v = TV \frac{\alpha^2}{\beta} \quad (2.24)$$

where α is the thermal expansion coefficient and β is the compressibility which are again properties of a system. α and β can be experimentally measured for individual minerals, hence C_v can be calculated using equation 2.24 and the change in the internal energy can be calculated.

During the change in internal energy of a mineral, heat is exchanged with the surrounding and the state of order, a measure of entropy (S), changes. Now, recalling the second law of thermodynamics, for any reaction in nature entropy always increases and the entropy change is defined as

$$dS > \frac{dQ}{T} \quad (2.25)$$

Since the exchange of heat is related to enthalpy, the final criteria for feasibility of reactions become

$$dH - TdS < 0 \quad (2.26)$$

The left-hand side of equation 2.26 is defined as the Gibb's free energy (Equation 2.27) of the reaction, and its change should be negative for a reaction to proceed or, in other words, the components assemblages that have the minimum Gibb's free energy change will be stable for a given temperature and pressure.

$$G = H - TS \quad (2.27)$$

Hence, to determine thermodynamically stable minerals assemblages inside the Earth, a thermodynamic database is needed which consists of V , α , β , H , S , $C_p(T, P)$ values for the possible mantle minerals to determine the Gibb's free energy for a give geotherm.

The chemical composition of the mantle can be described by the bulk rock major element oxides (in weight %), within the $\text{Na}_2\text{O}-\text{CaO}-\text{FeO}-\text{MgO}-\text{Al}_2\text{O}_3-\text{SiO}_2$ (NCFMAS) system since they account for the ~99% of the Earth's mantle (Palme and O'Neill, 2013). Since observational data (i.e., gravity field, SHF, seismograms, elevation) depends on bulk rock physical properties (density, bulk and shear modulus, and thermal conductivity), the major oxides chemical composition needs to be converted to pressure-temperature dependent stable phases called P-T phase diagrams for the mantle (Figure 2.2). Phases include the stable mineral assemblages found in the mantle, which allows calculating their physical properties. Minerals in the mantle exist in the form of solid solutions (Table 2.2) and have thermodynamically stable equilibrium assemblages as a function of pressure-temperature and composition. The upper mantle down to 400 km depth is mainly composed of olivine, garnet, orthopyroxene, and clinopyroxene (Figure 2.2). In the lithospheric mantle, at shallower depths, two other Al bearing minerals, plagioclase and spinel, are present depending on the depth (plagioclase is stable at shallow depths which converts to spinel at relatively higher depths and ultimately to garnet at greater depths).

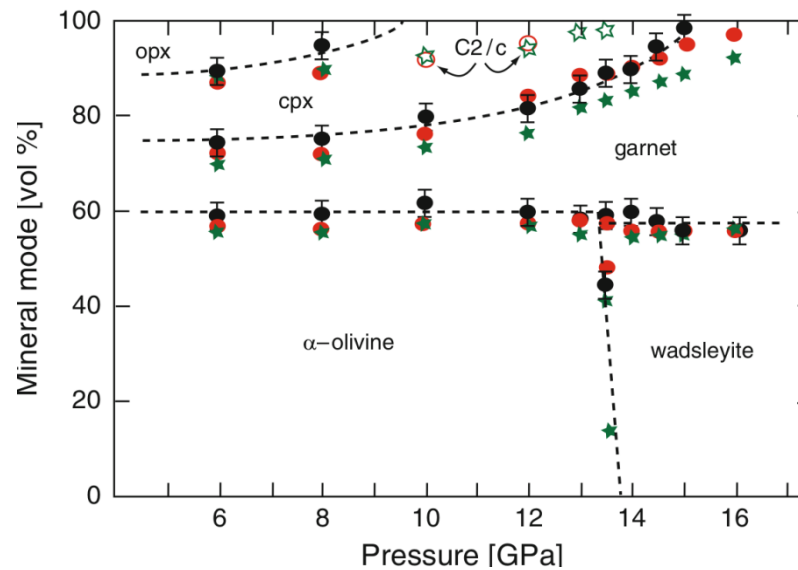


Figure 2.2 Mineral proportions for a pyrolitic composition as function of pressure and temperature range in the mantle. Black circles with error bars shows the experimentally determined phase proportions in dry pyrolite from Irifune and Isshiki (1998) based on high-T-P experiments. Red circles are predictions from Afonso and Zlotnik (2011) thermodynamic database and stars are predictions from the dataset of Xu et al. (2008). Figure is taken from Afonso and Zlotnik (2011).

Stable phase and mineral assemblages can be computed numerically using a Gibbs free-energy minimization algorithm (e.g., Connolly, 2005, 2009), which requires a thermodynamic database as explained above. A thermodynamic database contains experimentally determined thermodynamic parameters of end-member minerals contribution to the phase solution and their pressure-temperature dependent physical properties (e.g., density, bulk and shear modulus, thermal conductivity).

Table 2.2 Mineral solid solution notation and formulae.

Symbol	Solution	Chemical formula
Ol	Olivine	$[\text{Mg}_x\text{Fe}_{1-x}]_2\text{SiO}_4$
Gt	Garnet	$\text{Fe}_{3x}\text{Ca}_{3y}\text{Mg}_{3(1-x+y+z/3)}\text{Al}_{2-2z}\text{Si}_{3+z}\text{O}_{12}$; $x+y+4z/3 \leq 1$
Opx	Orthopyroxene	$[\text{Mg}_x\text{Fe}_{1-x}]_{2-y}\text{Al}_y\text{Si}_{2-y}\text{O}_6$
Cpx	Clinopyroxene	$\text{Ca}_{1-y}[\text{Mg}_x\text{Fe}_{1-x}]_{1+y}\text{Si}_2\text{O}_6$
C2/c	Pyroxene	$[\text{Mg}_x\text{Fe}_{1-x}]_4\text{Si}_4\text{O}_{12}$
Sp	Spinel	$\text{Mg}_x\text{Fe}_{1-x}\text{Al}_2\text{O}_4$
Pl	Plagioclase	$\text{Na}_x\text{Ca}_{1-x}\text{Al}_{2-x}\text{Si}_{2+x}\text{O}_8$
Wad	Wadsleyite	$[\text{Mg}_x\text{Fe}_{1-x}]_2\text{SiO}_4$

2.6. Physical properties

The equilibrium compositions of the phases using Gibb's free energy minimization allow estimating the amount of end-member minerals present in each phase. The relative amount of end-member minerals present in each phase allows calculating the bulk rock physical properties using rules of mixtures.

2.6.1. Density

In general, the mineral equilibria within the crust are not solved due to the large variety of mineral phases and then, the density can be calculated using

$$\rho(T, P) = \rho_0 - \rho_0 \alpha (T - T_0) + \rho_0 \beta (P - P_0) \quad (2.28)$$

where ρ_0 is the reference density at temperature (T_0) and pressure (P_0), α is the thermal expansion coefficient and β is the compressibility.

In the mantle, the fourth-order Birch-Murnaghan equation of state (EoS) allows to calculate the density of end-member minerals. Density of phases is computed using experimental models (e.g., Brey et al., 1999; Lee, 2003) where densities of each end-member are weighted by their mole fraction in each stable phase. Finally, the bulk rock density as a function of temperature and pressure for a given composition, including phase changes as well, can be calculated using a rule of mixture as:

$$\rho = \sum_{i=1}^{i=n} \rho_i v_i \quad (2.29)$$

where n is the number of stable phases, ρ_i and v_i are the density and volumetric fraction of the i th phase, respectively.

2.6.2. Thermal conductivity

Thermal conductivity, which controls the heat transport, depends on pressure, temperature and chemical composition. Conductive heat transport occurs by two processes: 1) lattice vibrations and 2) diffusive radiation. Lattice vibrations mainly involve vibration of the chemical bonds upon transfer of heat from neighboring molecules and dissipating it. Diffusive radiation involves electromagnetic radiation from the molecules upon receiving the heat from neighbouring molecules and, in turn, affecting them. Since these processes occur simultaneously, the total thermal conductivity is the sum of the lattice vibrations and the radiative transfer.

Thermal conductivity, k , is related to the thermal diffusivity, D , by:

$$D = \frac{k}{\rho C_p} \quad (2.30)$$

where ρ is the density and C_p is the heat capacity at constant pressure. Equation 2.30 suggests strong dependence of thermal conductivity on the chemical composition since density and heat capacity are specific for each mineral.

Thermal diffusivity for each mineral can be expressed as (Grose and Afonso, 2013):

$$D(T) = a + b \cdot \exp^{-cT} + d \cdot \exp^{-eT} \quad (2.31)$$

where T is temperature and a, b, c, d, e are the coefficients corresponding to each mineral derived from laboratory measurements.

The radiative contribution to the thermal conductivity is calculated as a function of the temperature, composition, grain size, and optical properties of crystals (Hofmeister, 2005), using:

$$k_{rad}(T, d) = A \exp\left(\frac{(T - T_A)^2}{2x_A^2}\right) + B \left(\frac{(T - T_B)^2}{2x_B^2}\right) \quad (2.32)$$

where A, B, T_A, T_B, x_A, x_B are all a function of grain size d (further details in Grose and Afonso, 2013; Tunini, 2015).

Then thermal conductivity for each mineral is calculated using equation 2.30 including thermal diffusivity (Equation 2.31), and radiative contribution is added using equation 2.32.

2.6.3. Mantle seismic velocities

Mantle seismic velocities depend on composition, pressure and temperature. The calculation requires knowledge of the elastic moduli (K : bulk modulus and G : shear modulus) of each end-member mineral and the bulk rock density at the pressures and temperatures of interest. In this manner, isotropic anharmonic seismic compressional (V_p) and shear (V_s) wave velocities can be calculated using the following equations:

$$V_p^2 \rho = K + \frac{4}{3} G \quad (2.33)$$

$$V_s^2 \rho = G \quad (2.34)$$

where ρ is the temperature-, pressure- and composition-dependent bulk rock density, K is the bulk modulus, and G is the shear modulus of each end-member mineral determined experimentally and are included in the thermodynamic database. Bulk rock density is calculated as mentioned in section 2.6.1.

To calculate the bulk rock elastic moduli used in equations 2.33 and 2.34, first the elastic moduli of each phase is calculated using the molar proportions weighted arithmetic mean of the elastic moduli of each end-member mineral. These elastic moduli are pressure and temperature dependent, and are calculated when constructing the thermodynamic database (e.g., Connolly and Kerrick, 2002). Then, bulk rock elastic moduli are computed from volumetrically weighted elastic moduli of each phase using a Voigt-Reuss-Hill (VRH) averaging scheme (Hill, 1952) as:

$$M_B = \left[\left(\sum_{i=1}^{i=n} \frac{w_i}{M_i} \right)^{-1} + \sum_{i=1}^{i=n} w_i M_i \right] \quad (2.35)$$

where n is the total number of phases, M_i and w_i are the moduli of the phases calculated in the first step and their volumetric fractions, respectively.

Seismic velocities calculated from elastic moduli of stable mineral and phase assemblages represent the unrelaxed oscillation of the chemical bonds in response to the elastic stresses produced by the propagation of high-frequency waves. In nature, rocks are not perfect solids or simple oscillators and the presence of defects in the crystalline structure, melt, and viscous nature at high temperatures can lead to dissipation of the energy imparted by elastic stresses, leading to relaxation of chemical bonds. This dissipation, called anelastic attenuation, results in loss of energy or relaxation of the elastic modulus leading to dispersion and change in the seismic velocities. Hence, in order to be able to compare calculated seismic velocities with the modelled seismic velocities using passive seismological data, anelastic effects must be accounted in the calculated seismic velocities (Chapter 3).

2.7. Isostasy and elevation

Under the assumption of isostatic equilibrium, local isostasy implies that a series of rigid vertical columns (the lithosphere) float freely on an inviscid liquid (the sublithospheric mantle) such that the pressure does not vary laterally below a certain compensation level. Alternatively, this implies that the lithosphere does not support vertical shear stresses. Local isostasy is an alternative statement of Archimedes' principle of hydrostatic equilibrium. Local isostasy has been proven to be an apt approximation in the absence of short-wavelength, elastically supported, features such as topographic and/or buried loads (Turcotte and Schubert, 1982). The principle of isostasy implies that all regions of the Earth with the same elevation must have the same buoyancy when referenced to a common compensation level. For the lithosphere and sublithosphere mantle, it can be assumed that the compensation level is located at 400 km depth (Afonso et al., 2008). The choice of a global compensation level at this depth has two advantages: (1) it covers the whole range of estimated lithospheric thicknesses, and (2) there is no need to change the calibration constants for different regions.

To calculate the absolute elevation, a calibration with respect to a reference column is needed. This reference column can be taken at a mid-oceanic ridge (MOR), where the mean elevation and the density-depth distribution are assumed to be known (Afonso et al., 2008). The absolute elevation is calculated using the following equations:

$$E_a = \int_{L_{top}}^{L_{bottom}} \frac{\rho_b - \rho_l(z)}{\rho_b} dz - \Pi_o \quad (2.36)$$

$$E_b = E_a \frac{\rho_b}{\rho_b - \rho_w} \quad (2.37)$$

where E_a and E_b are the elevations above and below the sea level, respectively. L_{top} is top of the column and L_{bottom} is the bottom of the column, ρ_b is the density of the mantle at 400 km depth and ρ_l is the depth-dependent density of the column, and ρ_w is the density of seawater. Π_o is a calibration constant which depends on the average density, structure, and the elevation of the reference column (see Afonso et al., 2008).

Due to the long-term rigid nature of the lithosphere, it flexes under vertical loading and can be considered as an elastic plate with an effective elastic thickness, T_e , resting on an inviscid or on a viscous fluid. Local isostasy ignores the short-

wavelength loads, and such loads can partly be supported elastically resulting in lithospheric deflection. The flexural response of a thin elastic plate is (e.g., Turcotte and Schubert, 1982):

$$q(x) = D \frac{d^4 w(x)}{dx^4} + N \frac{d^2 w(x)}{dx^2} + q_d(x) \quad (2.38)$$

$$D = \frac{E_y T_e^3}{12(1 - \nu^2)} \quad (2.39)$$

where D is the flexural rigidity, q the vertical load, q_d the restoring force, w is the deflection, N is the horizontal force per unit length, E_y is the Young's modulus, ν is the Poisson's ratio, and T_e is the elastic thickness of the plate. Solving for the surface deflections using equation 2.38 allows integrating the elastic nature of the lithosphere along with its thermal and chemical nature in order to reconcile the short wavelength variations of elevation.

2.8. Mantle melting and volcanism

Melting of rocks inside the Earth requires either its temperature to increase, such that it surpasses the solidus, or changes in the composition (e.g., the addition of volatiles), which lowers the solidus temperature. One other process which leads to melting at the Mid-Oceanic-Ridge is the adiabatic decompression. In thermodynamics, adiabatic processes occur without transfer of heat to the surroundings, hence when decompression occurs and the mantle is brought up with an almost constant temperature that surpasses the solidus temperature, melting occurs.

Volatiles (e.g., water in sediments) brought into the subduction channel leads to melting along the fore-arc in the subduction zones. The volcanic rocks produced in these settings inherit a crustal geo-chemical imprint and the associated volcanism is called orogenic volcanism. In contrast, melting in the intra-plate regions that does not have this crustal imprint is called anorogenic volcanism. However, the interaction of the ascending melts with the crust can change the geochemical signature of the emplaced volcanic rocks. Likewise, sediments brought into the mantle by subduction can change the mantle composition locally and influence the composition of volcanic rocks upon its melting.

Partial melting experiments on natural mantle peridotites have put important constraints on the total amount of partial melting (Kushiro, 2001). Combining information from laboratory melting experiments with the formal thermodynamic relations, we can calculate the total amount of partial melting necessary to generate a “standard” oceanic crust ~6–7 km thick (e.g., Klein and Langmuir, 1987; McKenzie and Bickle, 1988; Asimow et al., 2001, 2004; Kushiro, 2001; Presnall et al., 2002). Klein and Langmuir (1987) first proposed such formalism for the relationship between fraction melting, F , and the thickness of oceanic crust, h_c , at the ridge. The total amount of F can be calculated from a path integral of pressure from the pressure at which melting starts, P_0 , to the pressure at which melting stops, P_f , as follows:

$$F = \int_{P_0}^{P_f} F(P) dP \quad (2.40)$$

The mean fractional melting, \bar{F} can be calculated as

$$\bar{F} = \frac{\int_{P_0}^{P_f} F(P) dP}{(P_0 - P_f)} \quad (2.41)$$

The function $F(P)$ is a complex function of P (depth); however, it can be approximated within a finite pressure interval, n , by a constant slope, γ_n called the productivity function as (Langmuir et al., 1992; Phipps Morgan, 2001)

$$\gamma_n = \left(\frac{dF}{dP} \right)_s = \frac{\frac{\alpha T}{\rho c_p} - \left(\frac{dT_s}{dP} \right)_F}{\frac{H_m}{c_p} + \left(\frac{dT_s}{dF} \right)_P} \quad (2.42)$$

where T_s is the solidus temperature, α the coefficient of thermal expansion (CET), c_p the heat capacity, and H_m the latent heat of melting. For commonly accepted values of these variables, average γ values range between 10%- 20% per GPa of pressure release (e.g., Langmuir et al., 1992). The amount of melt present at any pressure P_x is given by the sum of $\gamma_n(P_{n-1} - P_n)$ for all relevant n (i.e., pressure intervals), where P_n becomes P_f in the last pressure interval and P_{n-1} is P_0 in the first pressure interval. Thus, equation 2.42 becomes

$$\rho_c g h_c = \bar{F}(P_0 - P_f) \quad (2.43)$$

Rearranging equation 2.43 and taking pressure in GPa, densities in kg/m³, and \bar{F} in % crustal thickness, h_c , can be approximated as

$$h_c = \bar{F}(P_0 - P_f) \frac{10^4}{\rho_c g} \quad (2.44)$$

For example, for typical values of $\bar{F} = \sim 7.2\%$, $P_0 = 2.75$ GPa, $P_f = 0.2$ GPa, and $\rho_c = 2880$ kg/m³, gives $h_c = 6.5$ km (Asimow et al., 2001).

Once melt is produced and segregated from the source, the chemical composition of the residue changes. The composition of the residue can be calculated from mass-balance using the initial concentration of element or component in the system (e.g., major oxides), the bulk distribution coefficient D , and the fraction of liquid F . As a first-order approximation the composition of the solid residue can be estimated as (Langmuir et al., 1992)

$$x_i^s = \frac{x_i^o}{\frac{F}{D_i} (1 - F)} \quad (2.45)$$

where x_i^o and x_i^s is the concentration of the i^{th} oxide in the original source and in the residue, respectively. D_i is the bulk distribution coefficient of the i^{th} oxide. The bulk distribution coefficients are function of pressure and amount of the melting (Niu, 1997). Therefore if the mean fractional melting, F , is known then equation 2.45 allows calculating the amount of each oxide in the solid residue after melting.

CHAPTER 3

Integrated geophysical-petrological modelling of the upper mantle anomalies

Chapter 3

Integrated geophysical-petrological modelling of the upper mantle anomalies

Integrated geophysical-petrological modelling of surface observables (i.e., gravity anomalies, geoid height, SHF, seismic velocities, xenolith data, and elevation) is a comprehensive approach and allows reconciling observations made by different datasets and methods. Each one of these observables is sensitive to the thermophysical properties of the materials under study, which in turn depend on temperature, pressure, and composition (Chapter 2). Therefore, a simultaneous fit to the surface observables reduces the uncertainties associated with the modelling of each of them alone or in pairs, as commonly found in the literature. Moreover, since these observables have a distinctive sensitivity to shallow/deep, thermal/compositional density anomalies (Chapter 2), this approach allows having improved control of thermal and density (i.e., composition) variations at different depths.

In this chapter, I present the new LitMod2D_2.0 software package, an updated version of the original 2D software by Afonso et al. (2008). In order to make physical inferences on seismic velocities, results on anelastic attenuation from recent laboratory-based measurements are incorporated in the anharmonic seismic velocities obtained from stable mineral assemblages that were considered externally in the previous version, LitMod2D_1.0. I test different available depleted chemical compositions in the sublithospheric mantle in order to be consistent with geochemical data. The numerical implementation of sublithospheric mantle anomalies is illustrated with the help of synthetic models. The nature of these anomalies can be i) chemical composition, ii) thermal, iii) seismic velocities (relative or absolute), and a combination of chemical composition with the latter two. LitMod2D_2.0 works under a forward modelling scheme and needs interactive input based on the assessment of the fit to the geophysical observables within uncertainty bounds. A new open-source graphic user interface (GUI) has been developed under Python programming language (Hunter 2007; Rossum, 1995), with improved functionalities, ease of use, and cross-platform dependence. Further, I make a synthetic model of a subduction zone setting to illustrate the sensitivity of sublithospheric mantle anomalies to the surface

observables. Finally, I discuss the post-processing capabilities of the LitMod2D_2.0 outputs to incorporate additional datasets in the modelling. As an example of post-processing, I compute Rayleigh-surface-wave dispersion curves, synthetic P-wave receiver-functions, and stable minerals distribution with depth in the mantle. Dispersion curves and receiver functions are calculated to demonstrate the possibility of comparing the resultant seismic velocities from LitMod2D_2.0 with passive seismological data.

3.1. General modelling workflow

LitMod2D is a software package based on the finite-element forward modelling approach of the CAGES code (Zeyen and Fernández 1994). LitMod2D_1.0 incorporated an external GENERATOR module based on Perple_X subroutines (Connolly, 2005), later upgraded (Connolly, 2009), to calculate the mineral assemblages and their physical properties as functions of the bulk composition of mantle domains. It also incorporates a MATLAB-based GUI. For a detailed description of LitMod2D_1.0 the reader is referred to Afonso et al. (2008). Here, I provide a brief summary of the critical aspects of the method and focus on the implementation of the new features/improvements in LitMod2D_2.0.

The general work-flow (Figure 3.1) in both versions is similar, except for the simplified input/output files, new improvements, and the new post-processing toolbox module. The numerical domain extends from the surface to 400 km depth and comprises different crustal and mantle bodies characterized by their individual thermo-physical properties and chemical composition. Crustal bodies are characterized by user-defined thermo-physical properties (e.g., thermal conductivity, volumetric heat production rate, coefficient of thermal expansion, and compressibility), with an option of depth and/or temperature dependence. The composition of upper mantle bodies is assigned within the $\text{Na}_2\text{O-CaO-FeO-MgO-Al}_2\text{O}_3\text{-SiO}_2$ (NCFMAS). Stable mineral assemblages are calculated by the external module GENERATOR using a Gibbs free-energy minimization algorithm (Connolly, 2005; 2009; Chapter 2 section 2.5) for pressure and temperature ranges in the upper mantle (Chapter 2, Table 2.2). Here, I use an augmented-modified version of Holland and Powell (1998) thermodynamic database (Afonso and Zlotnik, 2011). Relevant physical properties (density, thermal conductivity, and bulk and shear modulus) are calculated for each mineral and averaged according to Voigt-Reuss-Hill procedure (Hill, 1952) producing look-up tables as function of P and T (Chapter 2, section 2.6). In this way, the user can produce its own library of look-up tables for different mantle compositions beforehand.

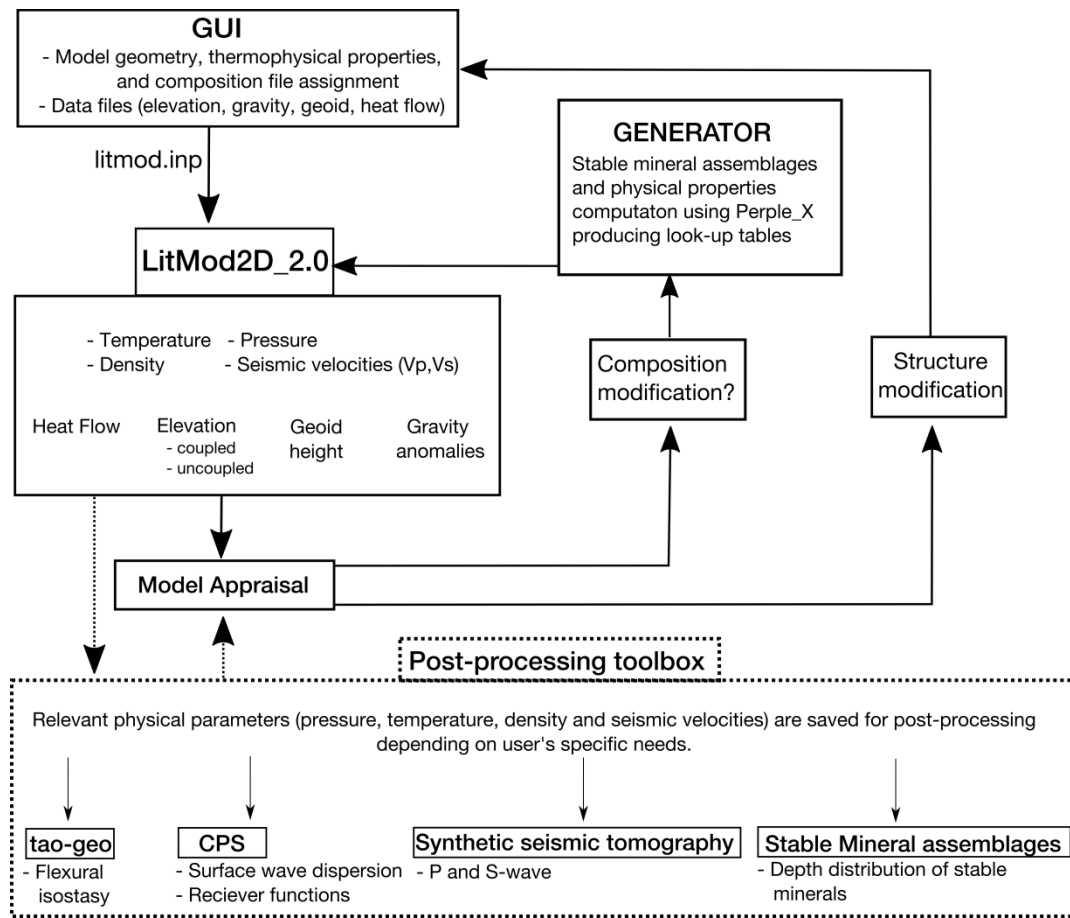


Figure 3.1 Flow chart diagram showing the workflow of LitMod2D_2.0. The new LitMod2D version may account for sublithospheric mantle anomalies in which case coupled elevation is calculated. It also has an option for post-processing of relevant physical properties (temperature, pressure, density and seismic velocities) to compare with additional datasets. Flexural isostasy is included by coupling ‘tao-geo’ software (Garcia-Castellanos et al., 2002). “Computer Programs in Seismology” (CPS, Herrmann, 2013) is also coupled to work with passive seismological datasets. Stable mineral-assemblages are extracted from the material files produced by the GENERATOR subprogram.

The heat transport equation 2.18, Chapter 2, is solved with finite elements using Galerkin’s ponderation method (Zienkiewicz, 1977) under steady-state, subjected to prescribed boundary conditions at the surface (e.g., 0 °C), at the LAB (e.g., 1320 °C) , and no heat flow across the lateral boundaries of the model. Thermal conductivities for crustal bodies are taken from literature, whereas for the lithospheric mantle are calculated by GENERATOR (Chapter 2, section 2.6.2), and are temperature, pressure, and composition dependent and read from the look-up tables. Below the LAB, the algorithm considers a 40 km thick thermal buffer with a temperature of 1400 °C at its base to avoid unrealistic discontinuities between a conductive thermal gradient within the lithospheric mantle and an adiabatic thermal

gradient within the sublithospheric mantle. The temperature gradient below the thermal buffer layer is restricted to $0.35 \leq dT/dz \leq 0.50$ °C/km.

The density distribution is obtained with an iterative scheme to include the effect of pressure, temperature and composition. Pressure is calculated at every node as a function of the overburden lithostatic pressure and it is then used to obtain the P-T-composition dependent density at the node. In case of bodies with assigned composition (e.g., in the mantle), density is read from the look-up tables produced by GENERATOR. This density then is used in the next iteration to update the overburden pressure and to solve for an updated density.

Once the final density distribution is obtained, the gravity potential field is calculated. Gravity anomalies are calculated by applying the Talwani's algorithm for polygonal bodies (Talwani et al., 1959) to the elements of the mesh, therefore considering both horizontal and vertical density variations. The gravity effect of all the elements is finally added and calculated either at the top of the model or at the sea level, depending on if the elevation is above or below sea level, respectively. .

Geoid height is calculated converting the adjacent elements of the numerical mesh into rectangular prisms, then solving the integral of the gravity potential and substituting the result into the Brun's formula (Equation 2.5) and is expressed as:

$$N = \frac{G \rho}{g_0} \iiint_{x_1, y_1, z_1}^{x_2, y_2, z_2} \frac{1}{\sqrt{x^2 + y^2 + z^2}} dx dy dz \quad (3.1)$$

where G is the universal gravitational constant, g_0 the normal gravity acceleration, ρ the rectangular prism density, and x, y, z the prism boundary coordinates. LitMod2D uses the method by Zeyen et al. (2005), based on an analytical solution of equation 3.1, to obtain 2.5-D geoid heights along the model. In calculating both gravity and geoid anomalies, the models are extended horizontally 1×10^5 km beyond the profile limits to avoid boundary effects.

3.2. Anelasticity

A physical interpretation of seismic velocities in terms of temperature and/or chemical composition requires anelastic effects to be incorporated in the anharmonic seismic velocities from stable mineral assemblages (Lau and Faul, 2019; Takei, 2017; Abers et al., 2014; Afonso et al., 2008; Cammarano et al., 2008; Goes et al., 2000;

Sobolev et al., 1996). Understanding of anelasticity mainly comes from two approaches: 1) attenuation tomography using passive seismological data, and 2) laboratory experiments on materials representative of the mantle (e.g., olivine). Attenuation tomography using passive seismological data is often low resolution and has large uncertainties. Controlled laboratory experiments on the polycrystalline olivine help understanding the fundamental physical processes involved and then extrapolation of observations to the physical conditions (mainly for grain size and pressure) inside the Earth.

Experiments at mantle temperatures and seismic wave frequencies show that grain boundary sliding is the main process of energy dissipation (attenuation). Grain boundaries have a finite width and viscosity and, under the application of shear stress, result in relative motion on either side. Motion is resisted by the viscosity of the grain boundary resulting in dissipation of energy, which is termed as elastically accommodated grain boundary sliding. In case the shear stresses are continued to high temperatures, the normal stresses concentrated at the grain corners resulting from the grain boundary sliding drive diffusion (Raj, 1975), and these normal stresses act as a restoring force upon removal of shear stresses. Redistribution of the stresses from diffusion results in transient creep, termed as diffusion assisted grain boundary sliding (Morris and Hackson, 2009) resulting in continuously increasing dissipation with increasing timescale and causing the high-temperature background or absorption band (Anderson and Minster 1979; Gribb and Cooper 1998). This transient phase ends when the stress distribution matches the steady-state diffusion creep stress distribution. This type of diffusion occurs on the scale of the grain size because of a constant grain boundary normal stress, and the resulting strain is not recoverable. The transition from diffusion assisted grain boundary sliding to steady-state diffusion creep is a function of timescale as it is evident that at earthquake time scale mantle behaves as elastic solid, but at geological time scales it behaves as a fluid.

A consistent and robust feature of the experimental studies on melt-free polycrystalline aggregates is an absorption band with mild frequency dependence between 900 °C - 1100 °C temperature range prevalent in the lithospheric mantle (Jackson and Faul, 2010; Faul and Jackson, 2015). Jackson and Faul (2010) showed that the experimental data on dissipation for this absorption band are consistent with power-law variation of dissipation, however, they propose more complex models (e.g., extended Burgers model) mainly to explain the dissipation peak at temperatures < 900 °C representing elastically accommodated grain boundary sliding. This peak occurs at the experimental resolution limit and is less constrained (Faul and Jackson, 2015);

therefore I use the power-law attenuation model to correct for anelastic attenuation (Jackson and Faul, 2010). Further, the power law formulation reproduces the seismological determined global average attenuation (Figure 3.2).

In the previous LitMod2D_1.0 version, the anelastic attenuation correction was incorporated a posteriori using an external code. The new LitMod2D_2.0 package incorporates the anelastic effects according to stable mineral assemblages at the corresponding P-T conditions in the look-up tables produced by the GENERATOR module, using equations 3.2 to 3.4 and the empirical parameters proposed by Jackson and Faul (2010).

$$V_P = V_{Po}(T, P) \left[1 - \frac{2}{9} \cot\left(\pi \frac{\alpha}{2}\right) Q_S^{-1} \right] \quad (3.2)$$

$$V_S = V_{So}(T, P) \left[1 - \frac{1}{2} \cot\left(\pi \frac{\alpha}{2}\right) Q_S^{-1} \right] \quad (3.3)$$

$$Q_S^{-1} = A \left[T_o d^{-1} \exp\left(\frac{(-E + VP)}{RT}\right) \right]^\alpha \quad (3.4)$$

where $Q_P = (9/4)Q_S$ is assumed. $V_{Po}(T, P)$ and $V_{So}(T, P)$ are the anharmonic seismic velocities at a given temperature and pressure for a given chemical composition, and $A = 816 \text{ s}^{-\alpha} \mu\text{m}^{-\alpha}$, $\alpha = 0.36$ is the frequency dependence factor, $E = 293 \text{ kJ/mol}$ is the activation energy, $V = 1.2 \times 10^{-5} \text{ m}^3/\text{mol}$ is the activation volume, and R the universal gas constant. Here, I use a grain size of $d = 10 \text{ mm}$ in the mantle and an oscillation period of $T_o = 75 \text{ s}$, since this combination produces Q_P and Q_S values in the range of global average attenuation models, particularly close to the LAB where anelastic attenuation is believed to be high (Figure 3.2). Both grain size and oscillation period are input parameters that can be modified. Moreover, the user can incorporate her/his preferred attenuation model into the GENERATOR module by changing the provided source code. Hereinafter, I use seismic velocities corrected for anelastic attenuation unless specified otherwise.

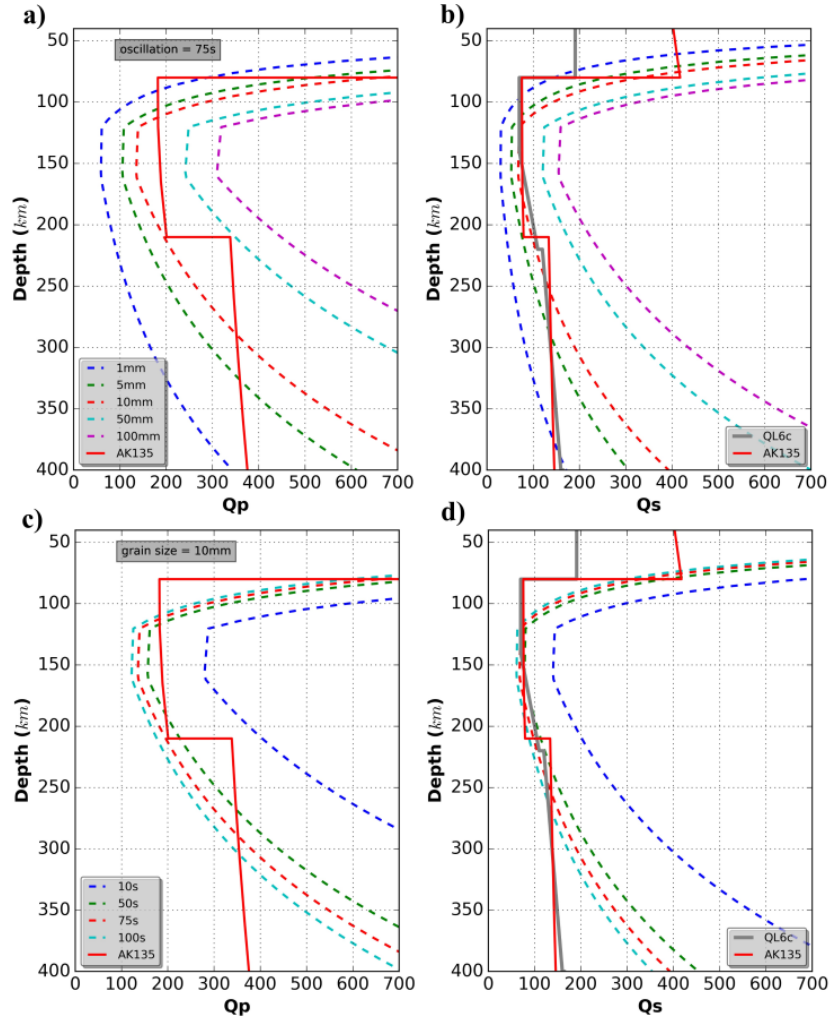


Figure 3.2 Depth distribution of anelastic attenuation parameter (Q , quality factor) for a range of grain sizes (1-100 mm) and oscillation periods (10-100s) compared with global average Q_P and Q_S models. (a) and (b) shows the depth distribution of Q_P and Q_S for varied grain size and constant oscillation period of $T_0 = 75$ s, respectively. (c) and (d) shows depth distribution of Q_P and Q_S for varied oscillation period (10-100 s) and constant grain size of $d = 10$ mm, respectively. Q_P and Q_S from ak135 global average model (continuous red solid line, Kennett et al., 1995), and Q_S from QL6c (continuous grey line, Durek and Ekström, 1996), are also plotted for comparison.

Anelastic attenuation parameters derived from laboratory measurements on dry polycrystalline olivine often need to be extrapolated to conditions pertaining to the upper mantle, as explained above, thus introducing unquantifiable uncertainties (Priestley and McKenzie, 2013; Faul and Jackson, 2015). While it is hard to put quantifiable uncertainty values on these parameters, here I assume 10 % error and explore how these errors propagate to the calculated seismic velocities. Uncertainties in computed seismic velocities (V_P and V_S) are calculated using:

$$\delta V_{P/S} = \sqrt{\left(\frac{\partial V_{P/S}}{\partial \alpha} \delta \alpha\right)^2 + \left(\frac{\partial V_{P/S}}{\partial E} \delta E\right)^2 + \left(\frac{\partial V_{P/S}}{\partial V} \delta V\right)^2} \quad (3.5)$$

where $\frac{\partial V_{P/S}}{\partial \alpha}$ is the partial derivative of the P- or S-wave velocities (Equations 3.2 and 3.3) with respect to α , and $\delta \alpha$ is the assumed error in α ; similar terms apply for E and V .

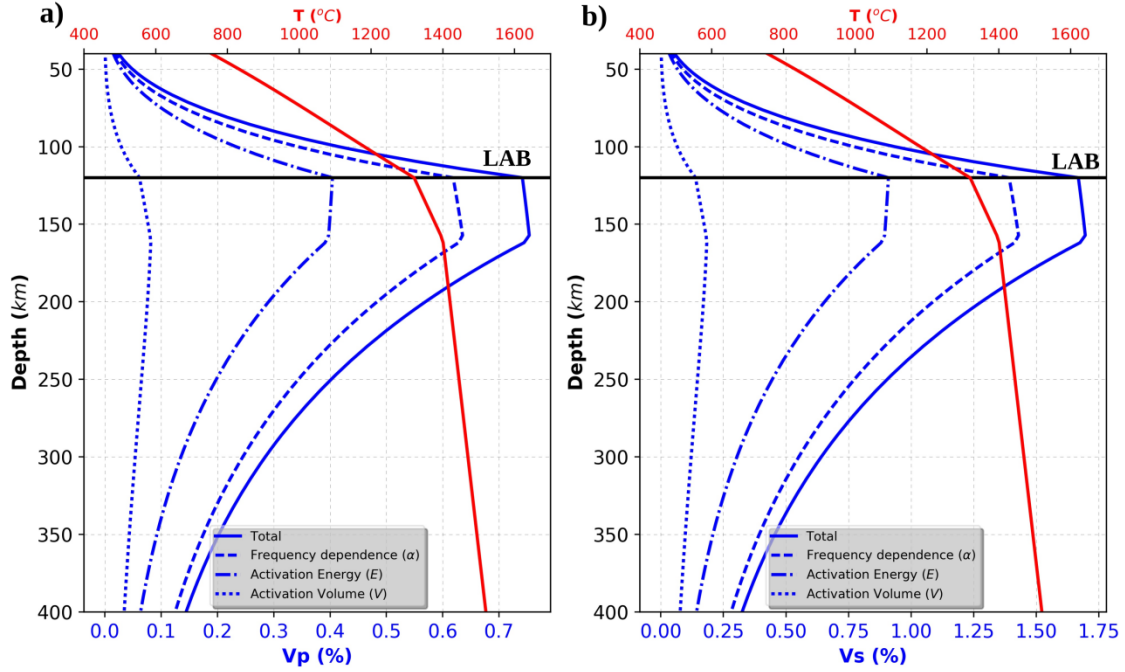


Figure 3.3 Percentage error introduced in the (a) P-wave velocities and (b) S-wave velocities considering 10% error in α (dashed blue line), E (dotted-dashed blue line), and V (dotted blue line). The total error is plotted in solid blue line and temperature distribution is plotted in solid-red line.

Figure 3.3 shows the resulting errors in V_P and V_S . These errors have the largest effect on seismic velocities around the LAB, being the frequency, α , the dominant source of uncertainty affects the seismic velocities the most and V , the activation volume, the least influential. Note that the error in velocity (Equation 3.5) is directly proportional to the error in anelastic parameters and therefore increasing uncertainty in any individual parameter will scale the uncertainty in the velocity in a quasi-linear fashion. The effects of melt or water content on seismic velocities are not included here. If melt is present, an additional correction needs to be applied to the computed seismic velocities (e.g., Afonso et al., 2016b) which can easily be included into the GENERATOR module by changing the provided codes.

3.3. Sublithospheric mantle composition

The chemical composition of the lithospheric mantle may be estimated from available mantle xenoliths and xenocrysts and/or exposed massifs in mobile belts. Although sublithospheric mantle rocks are less represented in these suites, compositional estimates can sometimes be obtained by analyzing the chemistry of primitive basaltic melts when available (e.g., Shorttle and MacLennan, 2011; Brown et al., 2020). As mentioned in the Chapter 1, LitMod2D_1.0 uses a fixed chemical composition for the sublithospheric mantle, corresponding to the primitive upper mantle (PUM) of McDonough and Sun (1995). The upper mantle however, has been a source for oceanic and continental crust since the onset of plate tectonics and should be less fertile than PUM (Van Keken et al., 2002). Here, I test the most common sublithospheric mantle compositions proposed so far (Table 3.1), and compare their relevant physical properties with that of PUM. The depleted MORB mantle (DMM) is a source reservoir to mid-ocean-ridge basalts (MORBs) and has been computed using a robust geochemical dataset (trace elements) on abyssal peridotites (Workman and Hart, 2005). Other commonly used sublithospheric mantle compositions are PUM-3%_N_MORB (Workman and Hart, 2005) and pyrolite (Ringwood, 1977). PUM-3%_N_MORB is computed by extracting 3% of normal MORB from PUM composition, whereas pyrolite is calculated by mixing appropriate fractions of basalts (partial melts from the mantle) and peridotites (the presumed residues from partial melting).

Table 3.1 Major oxide compositions (weight %) in the mantle.

Name	SiO ₂	Al ₂ O ₃	FeO	MgO	CaO	Na ₂ O	Mg# ^a
Lithospheric mantle							
Average Garnet Tecton ^b	44.50	3.50	8.00	39.80	3.10	0.240	89.8
Oceanic lithosphere	44.43	2.97	8.23	40.78	2.70	0.045	89.7
Sublithospheric mantle							
PUM	45.00	4.50	8.10	37.80	3.60	0.360	89.3
DMM ^c	44.70	3.98	8.18	38.73	3.17	0.130	89.4
PUM - 3% N_MORB	44.90	4.07	8.05	38.68	3.27	0.300	89.5
Pyrolite	45.10	4.60	7.60	38.10	3.10	0.400	89.9

^aMg# = 100xMgO/[MgO + FeO], ^bAfter (Griffin et al., 2009), ^cWater 100 ppm (Workman and Hart, 2005), PUM- Primitive upper mantle (McDonough and Sun, 1995), DMM- depleted mid-oceanic ridge basalt mantle (Workman and Hart, 2005), PUM-3% N_MORB- Primitive upper mantle after 3% extraction of normal mid-oceanic ridge basalt (Workman and Hart, 2005).

All tested compositions are less dense than PUM at sublithospheric mantle depths (Fig 3.4a), which is consistent with their higher Mg# ($100 \times \text{MgO} / [\text{MgO} + \text{FeO}]$) and depleted reservoirs. DMM shows a small density change of -0.18% relative to PUM between 120 km and 340 km depth and an increase of $\sim 0.1\%$ below ~ 340 km, whereas pyrolite shows a maximum change of $\sim -0.6\%$. PUM-3%_NMORB exhibits variations in between those associated with DMM and pyrolite. In terms of anharmonic P- and S-wave velocities (Figures 3.4b and 3.4c), pyrolite is the slowest, DMM is slightly faster in comparison to PUM, and PUM-3%_NMORB is intermediate. A water content of 100 ppm (70-160 ppm; Workman and Hart, 2005) in DMM slightly decreases the density compared to its dry counterpart and produces a decrease in P-waves velocities higher than in S-wave velocities because of its lower bulk modulus (Watanabe, 1993).

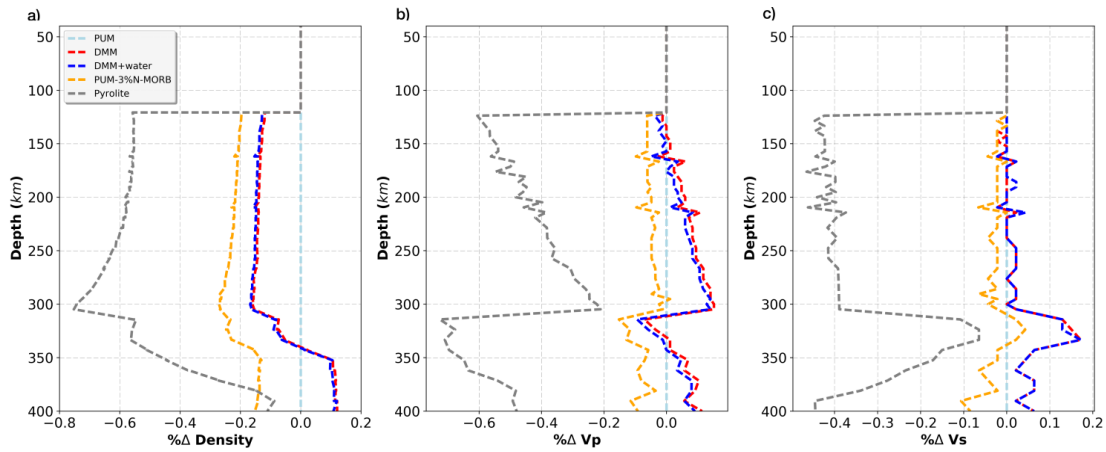


Figure 3.4 Comparison of different compositions tested in the sublithospheric mantle (Table 3.1). Resulting density (a), P-wave velocities (b) and S-wave velocities (c) are compared with that to PUM.

Although PUM-3%_NMORB and pyrolite attest to be depleted with respect to PUM, they still are theoretically computed. Furthermore, the pyrolite composition has been reported not to satisfy trace elements or isotopic data on basalts, violating the chondritic abundances (Anderson, 1989). DMM composition is consistent with trace elements data and with $\sim 6\%$ aggregated fractional melting to produce an average 6 km thick oceanic crust at the mid-oceanic-ridge (Workman and Hart, 2005; Klein and Langmuir, 1987). In addition, DMM has also been shown to be balanced by continental crust, ocean-island-basalt (OIB) source, and oceanic crust, which are the products of mantle melting (Workman and Hart, 2005). Although the differences in physical

properties are small, in the new LitMod2D_2.0 version I fix the sublithospheric mantle chemical composition corresponding to DMM for geochemical consistency.

3.4. Recalibration of elevation

Changing the chemical composition of the sublithospheric mantle requires a recalibration of the calculated absolute elevations since the total load of the sublithospheric mantle will vary according to the adopted composition. In contrast to LitMod2D_1.0, that considers a reference column at mid-oceanic-ridge (MOR) down to 400 km depth, in LitMod2D_2.0I consider a reference column corresponding to a thermally stable oceanic lithosphere and the underlying sublithospheric mantle. A thermally stable oceanic lithosphere is chosen because the depth-dependent T-P-composition is arguably less complicated than at actively spreading MOR, where melt content and short-lived buoyancy sources can complicate its characterization. Four compositional layers have been considered in the lithosphere and their bulk composition is calculated according to the depth-dependent melt fraction for a standard MOR model (Turcotte and Morgan, 2013; Niu, 1997) as used in Fernández et al. (2010) (Table 3.2). Calibration is done using the formulation described in Afonso et al. (2008) and Fullea et al. (2009), where I solve for a calibration parameter Π_0 , the thermal and lithostatic equations on a given reference column (Equations 2.36 and 2.37; Chapter 2). This reference column, corresponding to a stable oceanic lithosphere, consists of a 5.37 km water layer with a density of 1030 kg/m³, 6.8 km crustal thickness including sediments, with an average density of 2858 kg/m³, and a LAB depth of ~122 km with an average density resulting from the mineral compositions and assemblages mentioned previously (Table 3.2).

Table 3.2 Physical properties and major oxides composition in the mantle of a column at an old oceanic lithosphere used to compute calibration parameters for elevation.

Layer	Thickness (km)	Density (kg/m³)					
Crust							
Water	5.37	1030					
Sediments	0.80	2200					
Oceanic crust	6.140	2930					
Lithospheric Mantle							
Mantle layer	Thickness (km)	SiO ₂	Al ₂ O ₃	FeO	MgO	CaO	Na ₂ O
Layer 1	17.4	44.00	1.50	8.23	43.40	1.90	0.010
Layer 2	20.0	44.60	2.77	8.14	40.70	2.75	0.035
Layer 3	25.0	44.90	3.60	8.08	39.20	3.30	0.170
Layer 4	48.0	44.95	4.00	8.06	38.50	3.48	0.235
Sublithospheric Mantle (DMM)	278.0	44.70	3.98	8.18	38.73	3.17	0.130

3.5. Reference model for synthetic seismic tomography

The calculated seismic velocities in the sublithospheric mantle also depend on chemical composition. Seismic tomography models are usually reported as deviations from global reference velocity models, ak135 being one of the most widely used reference models (Kennett et al., 1995). To compare the seismic velocities obtained from LitMod2D_2.0 with those from ak135, I consider a model with i) a 35-km thick continental crust, and ii) a 85-km thick lithospheric mantle, similar to ak135 model, with Average Garnet Tecton composition (Tc_1 in Griffin et al., 2009), resulting in a LAB depth of 120 km. The composition of the sublithospheric mantle corresponds to DMM. The thermo-physical parameters used in the crust and the composition used in the lithospheric mantle are listed in Table 3.3 and Table 3.1, respectively.

The ak135 model was designed to predict arrival times for seismic phases in observational seismology by inverting smoothed empirical travel times (Kennett et al., 1995; Kennett, 2006). P-wave velocities are better constrained than S-wave velocities since P-waves are first arrivals, whereas S-waves have low frequency and can be interfered by the CODA of P-waves. Considering this and the inherent uncertainties in earthquake hypocentres, I assign uncertainties of 0.5% and 1% to P- and S-wave velocities, respectively.

Table 3.3 Thermophysical parameters used in the crust to compare calculated seismic velocities with those from ak135 model.

Body name	Density (kg/m ³)	Heat Production (μ W/m ³)	Thermal conductivity (W/K.m)
Continental crust	2800	1.00	2.5
Oceanic crust	2950	0.30	2.2

Different thermodynamic databases produce noticeably different seismic velocities, particularly in the sublithospheric mantle (Figure 3.5), resulting in a dispersion of ~1%. Formal errors resulting from each thermodynamic database can be calculated from the uncertainties in the elastic moduli of individual minerals. Both Stixrude and Lithgow-Bertelloni (2005) and Holland and Powell (1998) modified by Afonso and Zlotnik (2011) databases reasonably reproduce the ak135 model for depths between 35 km and 250 km, whereas Xu et al. (2008) database results in very slow P-wave velocities (Figure 3.5a). Below 250 km depth, only Stixrude and Lithgow-Bertelloni (2005) database shows good agreements with ak135 model, both in P- and S-velocities, whereas Holland and Powell (1998) modified by Afonso and Zlotnik (2011) and Xu et al. (2008) databases are significantly slower (~1–2%). Slow velocities below 250 km depth are also observed in Cammarano et al. (2005). Fitting the ak135 velocities below 250 km with these thermodynamic databases would require either a lower temperature than that predicted by the assumed adiabatic thermal gradient, or a change in the chemical composition at these depths (Cammarano et al., 2009). Another possible contribution to the discrepancies between predicted and reference velocities could be that the temperature and pressure derivatives of elastic moduli in Afonso and Zlotnik (2011) need to be updated. In contrast to the other two databases/formalisms, that of Afonso and Zlotnik (2011) supplements equilibrium phase diagrams with an independent database of velocity derivatives. Small corrections to these derivatives can produce changes in the velocities of the same order as the discrepancies in Figure 3.5. Despite this, the phase equilibria predictions show excellent agreement with experimental data (Figure 2.2, Chapter 2; Afonso and Zlotnik, 2011).

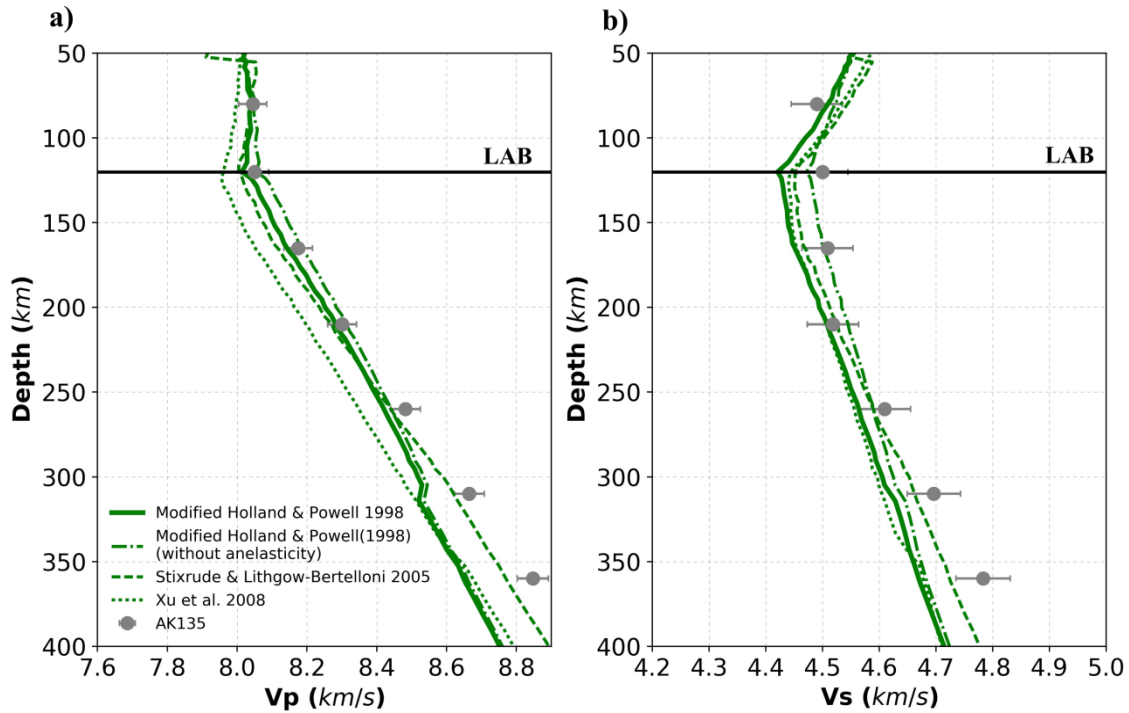


Figure 3.5 Depth distributions of seismic velocities, (a) P-wave and (b) S-wave assuming an Average Garnet Tecton composition in the lithosphere mantle and a DMM composition in the sublithospheric mantle. Seismic velocities are calculated using Afonso and Zlotnik (2011) (solid, modified Holland and Powell, 1998), Stixrude and Lithgow-Bertelloni (2005) (thick dashed) and Xu et al. (2008) (thin dashed) thermodynamic databases. Resulting seismic velocities are corrected for anelastic attenuation using a constant grain size of 10 mm and oscillation period of 75 s. Global average seismic velocities from ak135 (Kennett et al., 1995), in solid grey circles, with an error of 0.5% in P-wave velocities and 1% in S-wave velocities are plotted for comparison.

Here, I choose the Holland and Powell (1998) modified by Afonso and Zlotnik (2011) database in LitMod2D_2.0 to calculate the physical properties in the upper mantle given its performance in reproducing experimental data, but I note that a future reassessment of the elastic moduli derivatives is necessary. Since deviations with respect to the ak135 model are always negative below ~250 km (in the absence of thermal or compositional perturbations at these depths), I use the aforementioned reference model (35 km thick crust and 120 km LAB depth; Figure 3.5) to avoid this systematic misfit when calculating synthetic tomography from LitMod2D_2.0.

3.6. Sublithospheric mantle anomalies

A major contribution of LitMod2D_2.0 is the possibility to incorporate sublithospheric mantle anomalies into the modelling workflow, thus opening up the possibility of modelling complex geodynamic processes, such as mantle upwelling,

subduction, delamination, and metasomatism (i.e., processes that can easily modify the temperature and/or the chemical composition beneath the LAB). Since seismic tomography has the potential to detect such perturbations in terms of fast/slow velocities, I added in LitMod2D_2.0 a functionality to incorporate i) thermal anomalies, ii) compositional anomalies, and iii) seismic velocity (V_P, V_S) anomalies, in the sublithospheric mantle.

In this section I discuss the numerical implementation of sublithospheric mantle anomalies and its applicability to various geological settings considering the reference model defined in the previous section to calculate synthetic tomography. I consider an anomalous region in the depth range of 200–325 km and change systematically its nature to i) thermal, ii) chemical composition, and iii) seismic velocities (V_P and V_S).

3.6.1. Thermal anomalies

Mantle flow can change the temperature in the sublithospheric mantle producing colder and hotter domains, which can be represented as thermal anomalies in LitMod2D_2.0. To account for these thermal perturbations, I modify the constant adiabatic thermal gradient such that the imposed temperature perturbation (ΔT) is added to the steady state temperature distribution. Then, LitMod2D_2.0 recalculates the relevant physical properties (density, seismic velocities, phase changes, and thermal conductivity) at $T+\Delta T$ and P conditions, where T and P , are pressure and temperature at a given depth below the LAB.

To illustrate the effect of hot and cold thermal anomalies on the sublithospheric mantle with a DMM composition, I consider a thermal anomaly ranging from $-400\text{ }^{\circ}\text{C}$ to $+400\text{ }^{\circ}\text{C}$ in steps of $100\text{ }^{\circ}\text{C}$ (Figure 3.6). As expected, cold thermal anomalies increase density, P - and S -wave velocities, while hot anomalies have the opposite effect. The amplitude of the resulting anomalies varies such that density has the least relative change, whereas S -waves have the highest change due to the high sensitivity of S -wave velocities to temperature. To first order, the absolute density change depends linearly on the sign of the thermal anomaly, thus similar perturbations (in magnitude) can be seen at both sides of the 0% anomaly in Figure 3.6b. In contrast, seismic velocities show higher relative changes for positive temperature perturbations than for the equivalent negative ones (Figures 3.6c and 3.6d). This is because of the enhanced anelastic attenuation at higher temperatures. Moreover, the amplitude of seismic velocity anomalies decreases with depth due to the decreasing attenuation of seismic waves (low Q factor, Figure 3.2) at lithosphere-sublithosphere transition depths. This

non-linear dependence of seismic velocities on temperature has strong implications for qualitative interpretation of seismic tomography models (Cammarano et al., 2003). A second order variation in density and seismic velocities occurs around 310 km depth (Figure 3.6, inset) coinciding with the orthopyroxene-clinopyroxene (Figure 3.12) phase transition and could be the reason for the X-discontinuity imaged in seismic data (Revenaugh et al., 2008).

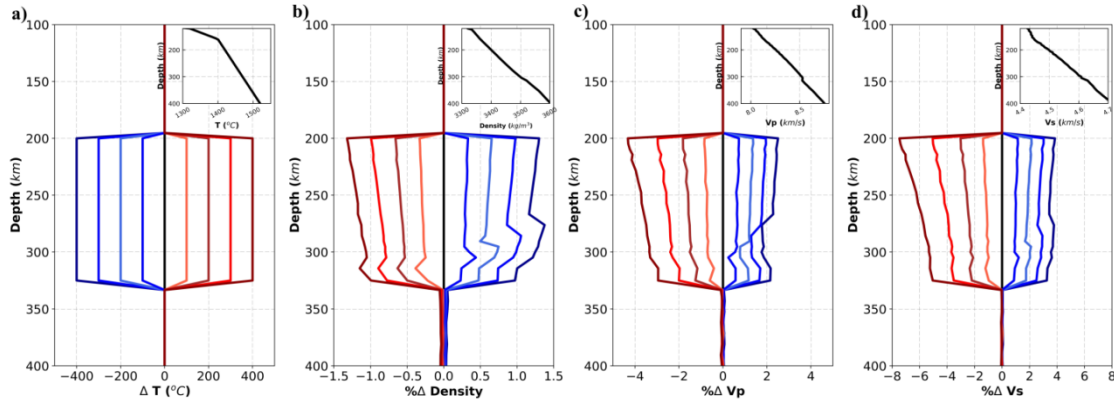


Figure 3.6 Synthetic examples of thermal anomalies in the sublithospheric mantle. Input thermal anomalies are plotted in (a). Resultant change in (b) density, (c) P-wave velocities, and (d) S-wave velocities are plotted with same colour code as input. All anomalies are referred to a reference model, shown as inset in the upper right corner.

3.6.2. Chemical composition anomalies

Understanding of chemical heterogeneity in the upper mantle is crucial for the geochemical evolution of the Earth governed by lithosphere recycling, mineral phase changes and mantle mixing models (Van Keken et al., 2002). Chemical heterogeneity in the upper mantle can be a result of metasomatic processes changing the chemical composition in the sublithospheric mantle by enrichment or depletion of the major elements. In turn, delamination, slab break-off, and slab tear processes can induce the sinking of pieces of cold lithosphere, with different chemical composition, into the sublithospheric mantle. LitMod2D_2.0 allows considering such types of anomalies of chemical origin, or a combination of chemical composition and temperature. For the case of chemical compositional anomalies, LitMod2D_2.0 recalculates the relevant physical parameters at the corresponding P-T conditions according to the prescribed composition in a given region beneath the LAB. For the case of combined thermal and compositional anomalies, the relevant parameters are recalculated at $T+\Delta T$ and P conditions from the prescribed chemical composition.

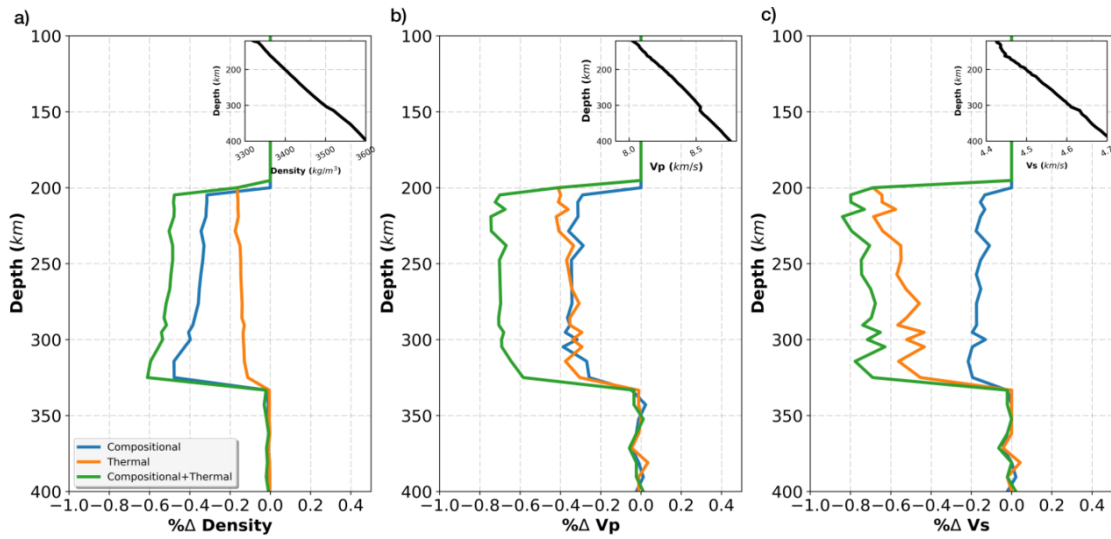


Figure 3.7 Synthetic example illustrating the contribution of compositional (Average Garnet Tecton, blue), thermal (+50 °C, orange), and combination of both (green) anomalies to (a) density, (b) P-wave velocities, and (c) S-wave velocities, with respect to the reference model shown as inset in the upper right corner.

Figure 3.7 shows a synthetic example of a compositional and a combination of thermal and compositional anomalies, where the separate effect of temperature is also shown. In the case of compositional anomaly, I have considered an Average Garnet Tecton chemical composition, which is depleted with respect to DMM (Table 3.1). Results show that density reduces by ~0.4% (Figure 3.7a), which is almost equal to the average change in P-wave velocities (~0.4%, Figure 3.7b) and higher than the change in S-wave velocities (~0.2%, Figure 3.7c). A combination of compositional and thermal anomalies ($\Delta T = +50$ °C) results in a maximum decrease in density and seismic velocities (Figure 3.7) because increasing temperature also tends to decrease density and seismic velocities. Indeed, P-wave velocities are more sensitive to composition than S-wave velocities. By studying the effect of melt removal from a fertile composition (i.e., range of Mg#) on S-wave velocities, Priestley and McKenzie (2006) have also reported low sensitivity of S-waves to composition. Note that depending on the chemical composition of the anomaly (degree of depletion) and the temperature perturbation, the sublithospheric anomalies can have competing effects on density and seismic velocities.

3.6.3. Seismic velocity anomalies

LitMod2D_2.0 allows for implementing seismic velocity anomalies by providing the absolute velocity values or the velocity variation, in percentage, relative to a reference model. The anomalies are incorporated in two ways: 1) giving the average absolute or relative value of the anomaly over a predefined region beneath the LAB; and 2) varying the absolute or relative magnitude of the anomaly along up to five depth levels beneath the LAB. In the first case, a chemical compositional anomaly can also be assigned to the anomalous region. In the second case, a separate input file including horizontal distances and depth levels together with the anomalous values must be specified. Seismic velocities are non-linear function of temperature because of the non-linear dependence of the anelastic attenuation on temperature (Eqns. 3.2-3.4) and stability of stable mineral phase-assemblages (Chapter 3, Section 2.5). Hence, in order to convert input seismic velocity anomaly (relative or absolute) to temperature, LitMod2D_2.0 looks up for the temperature at the prevailing pressure and adjusted seismic velocities for the input anomaly from the assigned chemical composition material file for the anomalous region. Once seismic velocity anomalies are converted to temperature, they are treated as thermal anomalies (section 3.6.1) and, in case of assigned chemical composition, as a combination of thermal and compositional anomalies (section 3.6.2).

Figure 3.8 shows an example of seismic velocities anomalies at different depth levels below LAB along the profile using a separate input file. This is applicable in regions where seismic tomography depth slices are available. Figure 3.8a show an input file with a relative P-wave seismic velocity anomaly with varying magnitude along the profile at five depths levels, namely 160 km, 250 km, 300km, 350 km and 400 km. In every input file, the level at 400 km, base of the model, must be specified. Lines below the specified depth of each level indicate the anomaly magnitude at each node (distance) along the profile. This allows the user to define a varying magnitude of anomaly along the profile as well in depth by specifying different depth levels. Figure 3.8b shows the resultant variation in temperature, density and absolute seismic velocities (P- and S-wave).

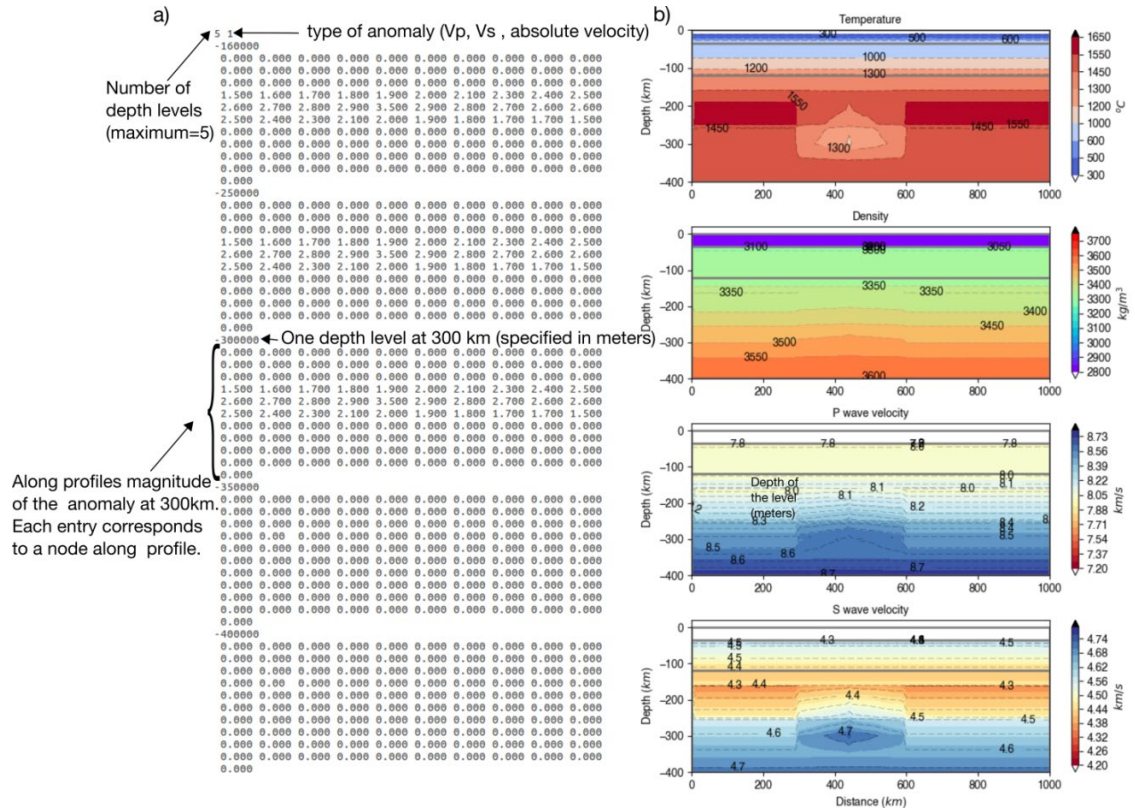


Figure 3.8 Example of a varying magnitude (along the profile) relative P-wave seismic velocity anomaly. (a) Screenshot of the input file used in this synthetic example. (b) Resultant temperature, density and seismic velocities.

Here, I focus on anomalous seismic velocities (V_P and V_S) assigned to a predefined region beneath the LAB and their translation into temperature and densities. I consider relative anomalies of $\pm 1.5\%$ in P- and S-wave velocities below the LAB and discuss the equivalent thermal and density recovery (Figure 3.9). Results show that for a given magnitude of seismic anomaly, 1.5% in the presented example, P-wave translates into a higher temperature anomaly of $\sim 250^\circ\text{C}$ than that from S-wave ($\sim 150^\circ\text{C}$) (Figure 3.9a) which is consistent with the higher sensitivity of S-waves to temperature. In other words, a given temperature change requires a higher percentage variation in the S-wave velocities than in the P-wave velocities as shown in Figure 3.6. Subsequently, density change (Figure 3.9b) is higher ($\sim 0.75\%$) in case of P-wave velocity input than S-wave input ($\sim 0.45\%$). Note that density and temperature changes are not symmetric for positive and negative velocity anomalies. Changes in density depend on the P-T conditions, which control stable phase and mineral assemblages.

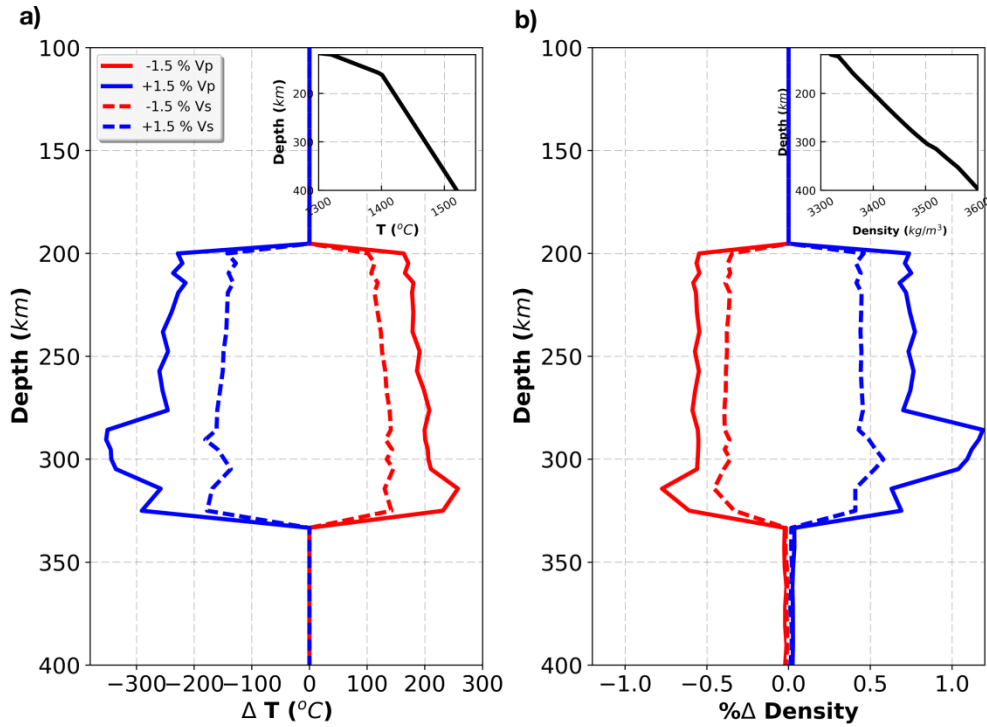


Figure 3.9 Synthetic examples of input P- and S-wave anomalies of $\pm 1.5\%$ in the sublithospheric mantle. Recovered temperature (a) and density (b) from the input seismic velocity anomalies are plotted with respect to the reference model shown in the upper right corner.

3.7. Open source graphic user interface (GUI) and input/output data

To make LitMod2D_2.0 more accessible to users, I have developed an open source GUI in Python, which is not platform depending and can be easily updated/modified by the user. A detailed manual (Appendix A) is provided with the new LitMod2D_2.0 version distributed through online GitHub repository (https://github.com/ajay6763/LitMod2D_2.0_package_dist_users). Here, I briefly discuss the main features. The new GUI allows the organization of different projects in separate folders containing the relevant surface geophysical observables (e.g., elevation, Bouguer and free-air gravity anomaly, geoid height, and SHF) and the material files with thermo-physical properties for each project. Mantle material files are lookup tables of all relevant physical properties (density, thermal conductivities and seismic velocities) as functions of pressure, temperature, and chemical composition. These are computed by the GENERATOR module (Section 3.1) using components of the software Perple_X (Connolly, 2005; 2009). An option to plot previously digitized data on the background (e.g., Moho depths, LAB depths, interpretation from active seismic lines) is also provided.

The GUI main window allows defining the geometry of the model made up of different bodies, each one with its physical properties. Different buttons are provided in the top and bottom of the main window to add and delete bodies, edit properties and shape of bodies, and to run the model (Figure 3.10a). After the run finishes, a window shows up with the geometry of the model and the fit between surface observables and the calculated values (Figure 3.10b, left panel), and the calculated temperature, density, and seismic velocities distributions (Figure 3.10b, right panel). Results are plotted in an interactive Matplotlib environment and can be modified for publication purposes. All the surface observables (elevation, Bouguer and free-air gravity anomalies, geoid height, and surface heat-flow) are saved, and can be used for customized visualization and further processing of the model output. Likewise, a master output file containing the Cartesian coordinates of the grid nodes and the corresponding temperature, pressure, seismic velocities, density, and material file code are saved to be used in the post-processing toolbox according to the particular needs of the user (Section 3.9).

3.8. Application to a synthetic subduction zone

To illustrate the applicability of the new LitMod2D_2.0 package, I performed a synthetic model representing a simplified active margin with a subducting slab and the associated mantle wedge. The objective of this section is to show the functionalities and practicalities of LitMod2D_2.0, as well as the possibilities of the post-processing tool-box rather than studying specific aspects of a real subduction setting.

3.8.1. Input data, model geometry, and physical properties

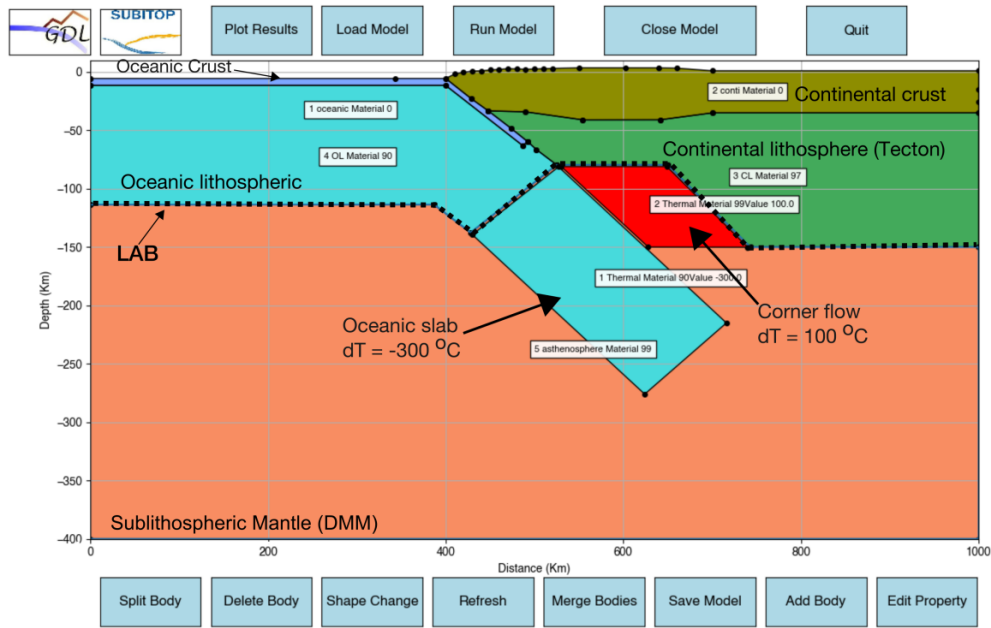
The synthetic model is 1000 km long, and comprises three regions: the oceanic domain, the active subduction zone, and the continental domain (Fig 3.10a). The oceanic domain is characterized by a bathymetry of 5.5 km, and a 6 km thick crust without sediments, and a 100 km thick lithospheric mantle with a composition calculated by 7% fractional melting considering DMM as source. Active subduction zones are characterized by inverted isotherms such that the 1300 °C can be found at three different depths for the same horizontal position, resulting in a triple LAB. This boundary condition cannot be solved by the 2D heat transport equation under steady-state incorporated in the LitMod2D_2.0 code and hence, the subducted oceanic lithosphere is modelled as a sublithospheric thermo-compositional anomaly, with $\Delta T =$

-300 °C and with an oceanic lithosphere chemical composition. Similarly, the mantle wedge is modelled as a sublithospheric thermal anomaly with $\Delta T = +100$ °C. This simple treatment of the active subduction zone allows calculating the average physical properties of the anomalous bodies and their effects on elevation, seismic velocities, and gravity potential field. The stable continental domain consists of a 35 km thick crust and a 115 km thick lithospheric mantle with Average Garnet Tecton composition. Near the subduction zone the crust thickens up to 40 km whereas the lithospheric mantle thins to minimum values of 78 km. For simplicity, I have considered a single crustal layer but the user can add as many layers and bodies as needed through the GUI. Thermo-physical parameters in the crust and chemical composition in the lithosphere mantle are incorporated via GUI and correspond to those listed in Table 3.3 and Table 3.1, respectively.

Figure 3.10b shows a screenshot of the main results window, which includes the calculated and measured surface observables together with the model geometry and the calculated temperature, density and P- and S-wave velocities distribution. The anomalous sublithospheric bodies have a clear signature on the temperature distribution, as they have been defined as thermal anomalies, but also on the calculated density and seismic velocities. In the case of the subducting slab, the combined thermal and compositional anomalies increase density and P- and S-wave seismic velocities, whereas along the mantle wedge, the temperature increase of 100 °C results in a decrease of the three observables.

As the modelled profile is a synthetic model, I have considered that the observed elevation, gravity, geoid and heat flow coincide exactly with the calculated values and an additional run of the model is made without sublithospheric anomalies, all the other parameters unmodified. In this way, I highlight the effect of the sublithospheric anomalies on the surface observables (Figure 3.10b).

a) GUI input window



b) GUI output windows

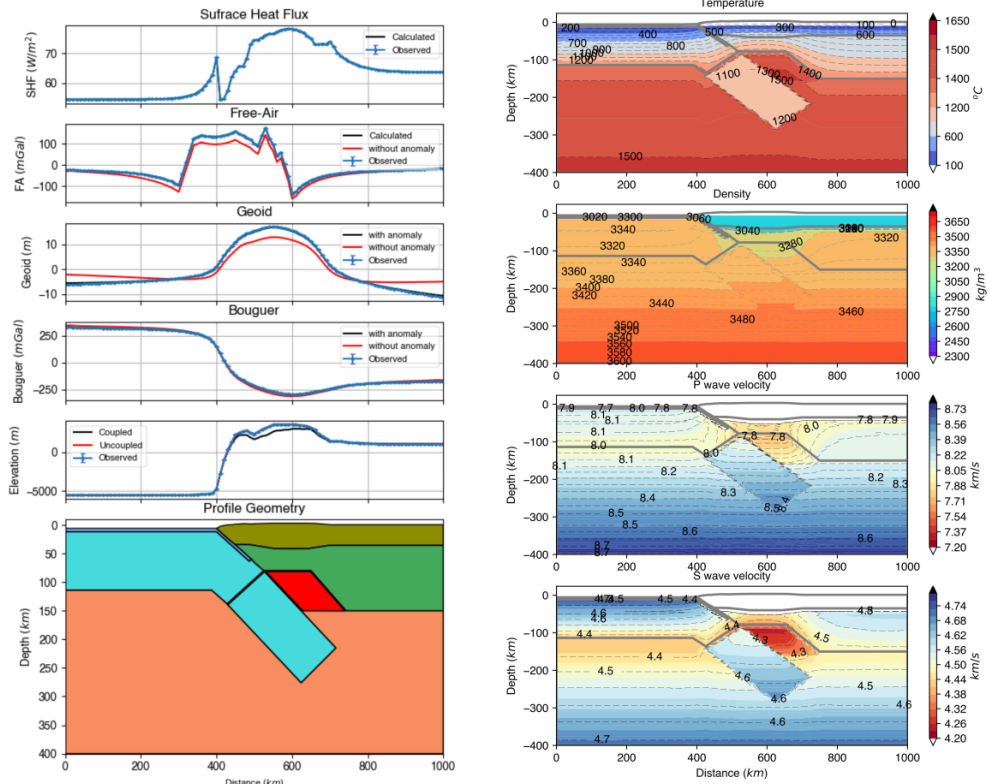


Figure 3.10 Screen shots from the new open-source GUI, provided with LitMod2D_2.0, (a) Graphic user interface input window showing the geometry of the modelled profile and various functions to interact and work with the model. (b) Screenshots of model outputs from the model, in the left panel forward prediction of surface observables, observed (blue) and calculated (red and black) and the model geometry at the bottom. Surface observables without the sublithospheric mantle anomalies are plotted in red to highlight their effect. Right panel in (b) shows the temperature, density and seismic velocity distribution (P-wave and S-wave) from the model.

LitMod2D_2.0 calculates the absolute elevation from the final density distribution, under the assumption of local isostatic equilibrium with a compensation depth at the base of the model (400 km). Lateral density variations beneath the LAB will tend to generate dynamic Stokes flow in the underlying less viscous mantle which can be enhanced by sublithospheric mantle anomalies. Vertical stresses associated with this dynamic flow can be transmitted to the surface topography depending on the viscosity distribution with depth. By default, LitMod2D_2.0 estimates the influence of sublithospheric mantle anomalies on the calculated elevation by considering two end member conditions representing the upper and lower bounds of the dynamic topography contribution (Carballo et al., 2015b; Tunini et al., 2016; Jiménez-Munt et al., 2019): 1) coupled elevation, when the vertical stresses induced by the buoyancy of sublithospheric mantle anomalies are completely transmitted to the surface; and 2) uncoupled elevation, when sublithospheric mantle anomalies have no effect on topography. In the synthetic model presented here, the net effect of the sublithospheric anomalies on elevation is of ≤ 1000 m (Fig 3.10b). In the case of coupled anomalies, the cold slab near the subduction zone pushes down the elevation because of its higher density. The relatively lower density of the mantle wedge does not suffice to cancel the negative slab buoyancy. Density perturbations from the cold subducted slab and the hot corner flow primarily affect the geoid height and free-air gravity anomaly across the model whereas Bouguer anomaly is slightly affected. This is because geoid is sensitive to the density moment which in the modelled synthetic profile is mainly related to the topography and the sublithospheric anomalies. Free-air is very sensitive to topography and in a less extent to sublithospheric anomalies due to the inverse square law dependence; whereas Bouguer anomaly is also depending on the inverse square law but corrected for topography effects and then, is essentially sensitive to lateral crustal density variations.

3.9. Post-processing toolbox

The main idea of the post-processing toolbox is that from the obtained parameters characterizing the physical state of the crust and upper mantle (pressure, temperature, density, P- and S-wave seismic velocities, and material type) at each node, the user can further process these data to do a variety of additional calculations, such as strength envelopes, flexural effects on elevation, Stokes flow, distribution of stable mineral-assemblages, synthetic passive seismological data, etc. The post-processing toolbox is a set of independent scripts/codes linking the LitMod2D_2.0 master output with other software (Figure 3.1). The user can use, adapt or create new

scripts or codes according to her/his own interest and needs and can add them to the GitHub (https://github.com/ajay6763/LitMod2D_2.0_package_dist_users) for the community to use.

3.9.1. Seismic velocities post-processing example

The following example illustrates the potential of the post-processing toolbox focused, in this case, on the calculation of synthetic seismic tomography and synthetic passive seismological data. Post-processing of seismic velocities is done in the light of non-uniqueness and variability in the tomography models, as discussed in Foulger et al. (2013).

I provide shell scripts to compute synthetic tomography from the LitMod2D_2.0 seismic velocities, using the reference model defined in section 3.5. For the presented synthetic example, maximum positive anomalies are observed along the oceanic lithosphere, whereas the thinned continental lithosphere above the subducted slab results in negative velocity anomaly (Figure 3.11a). Thick continental lithosphere results in positive velocity anomaly but with smaller magnitude relative to the oceanic lithosphere. In the sublithospheric mantle, the subducted slab and corner flow regions result in positive and negative velocity anomalies, respectively, and the rest of the sublithospheric mantle show no deviation from the reference model.

Joint inversion of receiver-functions and surface-wave dispersion has been widely used to image major velocities discontinuities and absolute seismic velocity distributions with depth (e.g., Julià et al., 2000; Langston, 1979; Vinnik, 1977). P-wave receiver functions are sensitive to the S-wave velocity discontinuities where P-to-S converted waves sample the subsurface discontinuities, whereas surface-waves are sensitive to the average S-wave velocities distribution.

LitMod2D_2.0 gives the depth distribution of absolute P- and S-wave velocities from a structural (e.g., Moho and LAB geometries), thermal and chemical composition model. Hence, comparing observed surface-wave dispersions and P-wave receiver functions with those inferred from LitMod2_2.0 can further constrain the obtained models. This is done by coupling the calculated P- and S-wave seismic velocities from LitMod2D_2.0 with the ‘Computer Programs in Seismology’ tool by Herrmann (2013) through Shell and Python scripts to calculate synthetic Rayleigh-surface-wave dispersion curves and P-wave receiver functions. Within the crust, P-wave velocities are calculated using empirical V_P -density relationships from Brocher (2005), whereas S-wave velocities are calculated assuming a constant input of $V_P/V_S = 1.73$ (Fig 3.11b).

Indeed, an option including crustal material files is kept for future or if user have a thermodynamic database for the crustal chemical composition (e.g., Diaferia and Cammarano, 2017). Below 400 km depth (base of the model), velocities from ak135 model are used.

The depth distributions of the resulting S-wave velocity at three locations along the synthetic profile are shown in Figure 3.11b corresponding to: a) ocean (300 km), b) subduction zone (500 km), and c) continent (950 km). Synthetic P-wave receiver functions (Figure 3.11c) show a clear positive converted phase (P_s , black) at Moho discontinuity, which arrives earlier for oceanic domain because of the lower crustal thickness, and is delayed for thick continental crust. Each of the converted phase at Moho (P_s) has a positive phase (P_{pps}) and a negative phase (P_{pss}) multiples which are helpful in determining whether the P_s phase corresponds to a velocity discontinuity. Rayleigh group and phase velocities (Figure 3.11d) are faster for the oceanic domain than for the continental domain because of the high S-wave velocities of the oceanic lithosphere at lithospheric depths (Figures 3.11b and 3.10b). At short periods, velocities are lower than at higher periods because shallow structures (slow velocities) are more sensitive to surface waves at short time periods. Group velocities show an absolute maximum, whereas phase velocities show relative maxima increasing for higher periods. This behaviour is because of the differential depth sensitivity of group and phase velocities. For the oceanic domain the maxima of group velocities is at ~ 25 s, whereas for the subduction zone and the continental domains maxima is reached at ~ 75 s. Phase velocities show a local maxima which is shifted towards lower periods relative to the maximum of group velocities. The effect of lithosphere thickness is observed in the continental domain showing higher velocities (both group and phase) in regions with thick lithosphere than in the thin lithosphere near the subduction zone. The effect of the cold subducted slab is clearly visible in both group and phase velocities (black dashed line), where maxima for group velocities (local maxima in case of phase velocities) has been shifted towards high periods and velocities are increased in comparison to dispersion curves without slab.

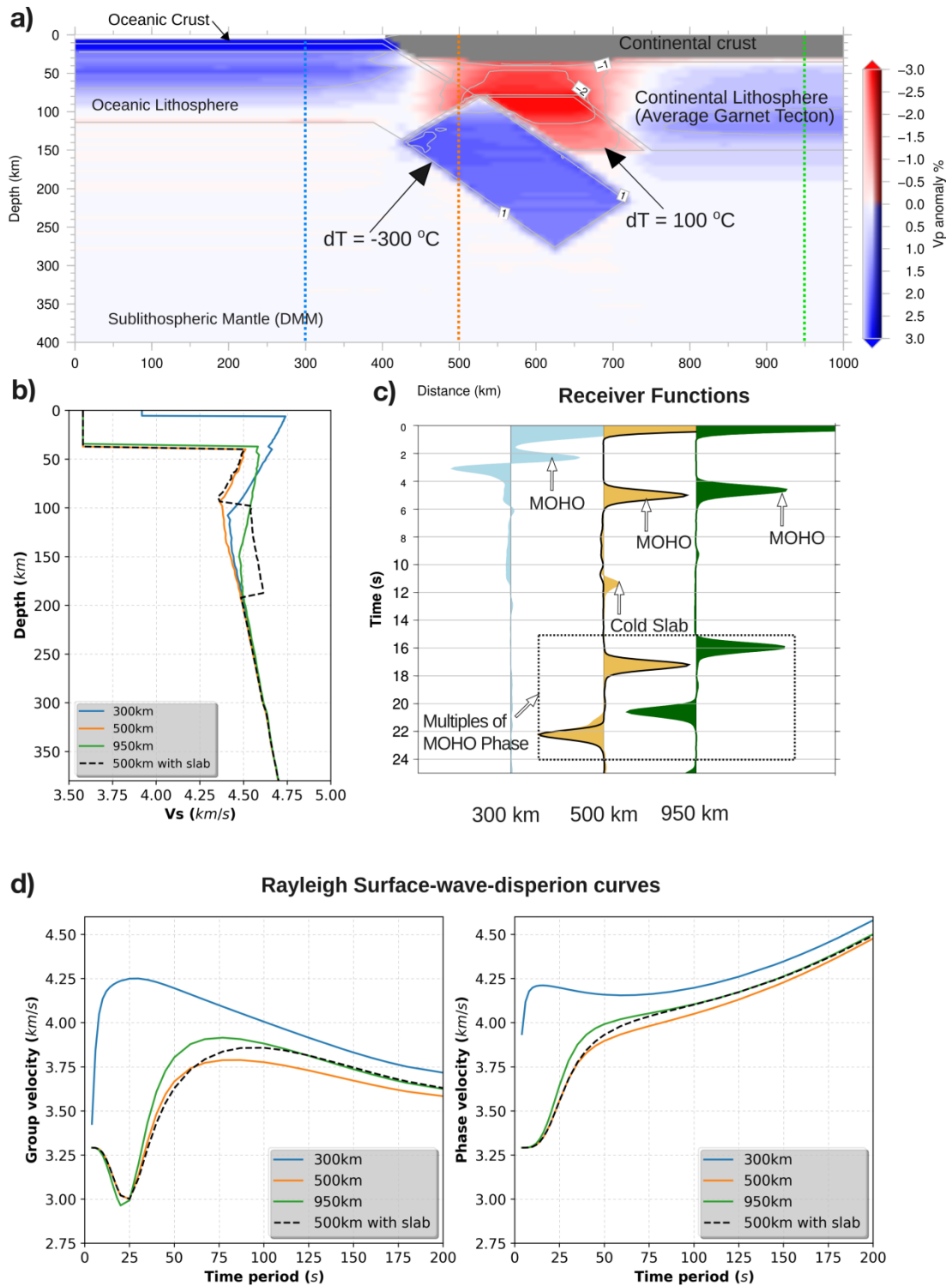


Figure 3.11 Example of seismic velocities post-processing. (a) Synthetic P-wave tomography along the modelled synthetic profile. (b) Depth distribution of S-wave velocities at three locations along the profile with colour coded and marked in (a). (c) Synthetic P-wave receiver functions at the three locations marked in (a). At the subduction zone two receiver functions with (filled orange) and without (black line) the subducted slab, are plotted for comparison. (d) Synthetic Rayleigh-surface-wave group (left) and phase (right) velocities. At the subduction zone orange dispersion curves corresponds to the model without the slab and dashed-black line to the model with the slab.

3.9.2. Depth distribution of stable mineral-assemblages

I provide a collection of Python and bash-shell scripts to plot the depth distribution of volume fraction, weight%, density, and seismic velocities of stable mineral-assemblage in LitMod2D_2.0. These scripts look for the stable mineral assemblages, at the pressure and temperature conditions along the profile, in the extended material files. Extended material files are produced by opting for the full property and system option in the GENERATOR module (Appendix A). Options for depth distribution of all minerals at a distance point (Figure 3.12), or depth distribution of individual mineral along the profile (Figure 3.13), are provided. Figure 3.12 shows an example of stable mineral distribution with depth for the reference model defined in section 3.5. Major discontinuities in the upper mantle (Moho and LAB) are manifested by changes in stable mineral weight percentages. Plagioclase and spinel are stable in the shallow part of the lithosphere and constitute few weight percentage of the total. Olivine constitutes most of the upper mantle, about ~60 weight%. The weight% increases with depth for garnet, whereas it decreases for orthopyroxene which almost disappears at around 310 km. Clinopyroxene weight% varies from around 13–10% in the upper mantle.

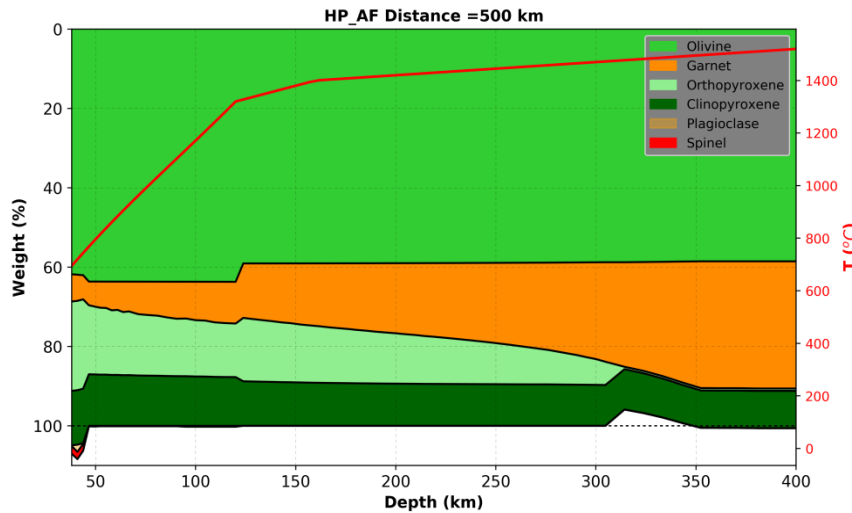


Figure 3.12 Weight% of different stable minerals with depth for the reference model defined in LitMod2D_2.0 (section 3.5). Note that total weight% does not add to 100% in the shallow lithosphere (< 50 km) and around 300 km; this could be because of the failed numerical energy minimizations during the computation of stable mineral assemblage, although difference is only about <5%.

CHAPTER 4

Present-day crust and upper mantle structure of the Alboran and Algerian basins and their margins

Chapter 4

Present-day crust and upper mantle structure of the Alboran and Algerian basins and their margins

In this chapter, I present the modelling results of the present-day crust to upper mantle (~400 km depth) structure along two NNW-SSE oriented geo-transects in the Alboran and Algerian basins (Figure 4.1a). Improved LitMod2D_2.0 presented in Chapter 3 (Kumar et al., 2020) is used to model the temperature, density (i.e., chemical composition) and seismic velocity distribution by combining surface geology, elevation, Bouguer anomaly, geoid height, SHF and mantle xenoliths data in a self-consistent thermodynamic framework.

The Alboran Basin geo-transect is presented for the first time while the Algerian Basin geo-transect follows the TRANSMED-II profile, that was modelled using a thermal approach (Roca et al., 2004), and later refined in Carballo et al. (2015a) using integrated geophysical-petrological modelling. Although the regional structure of the lithosphere across the region has already been studied by Carballo et al. (2015a,b) and Fullea et al. (2010), I focus here on more detailed structure of the Betics and Greater Kabylies belts and offshore regions (i.e. Alboran and Algerian basins) using the new LitMod2D_2.0 version. LitMod2D_2.0 allows to model thermal/seismic/compositional sublithospheric mantle anomalies (Chapter 3), thus allowing to incorporate the well imaged positive seismic velocity anomalies in the high resolution tomography, beneath the Betics (Figure 4.1b; Palomeras et al., 2017; Villaseñor et al., 2015; Bezada et al., 2013; Spakman and Wortel, 2004), and the Kabylies (Figure 4.1; Fichtner and Villaseñor, 2015). The models presented here also integrate the latest geophysical results along the Algerian margin of NW Africa, mainly new active seismic data (e.g., SPIRAL, Aïdi et al., 2018), and the Moroccan margin (Gómez de la Peña et al., 2018).

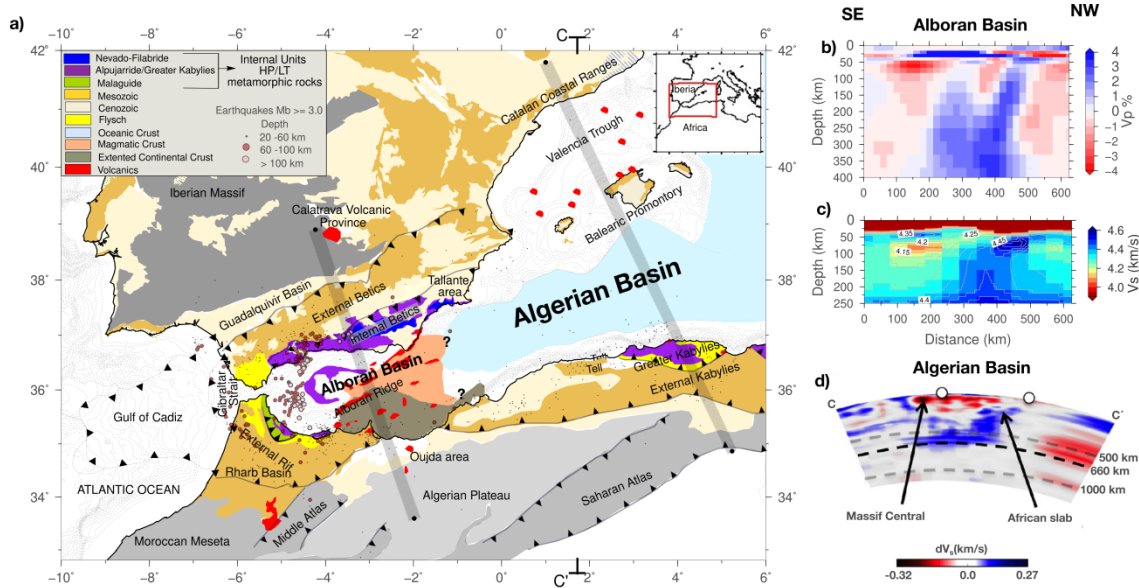


Figure 4.1 (a) Simplified geological map of the study region showing the location of the Alboran and Algerian basin geo-transects in shaded grey line. Earthquakes location colour coded for depth from 1964-2016 taken from International Seismological Centre (ISC, <https://doi.org/10.31905/D808B830>) catalogue are also plotted. (b) P-wave travel-time tomography along the Alboran Basin geo-transect from Bezada et al. (2013). (c) Absolute S-wave velocity model from Rayleigh surface-wave dispersion tomography (Palomeras et al. 2014) along the Alboran Basin geo-transect. (d) S-wave tomography using full-waveform inversion (modified after Figure 8 of Fichtner and Villaseñor, 2015) along the direction of cross-section C-C' marked in (a).

4.1. Data

4.1.1. Regional geophysical data

Elevation data from ETOPO1 (Amante and Eakins, 2009), a global elevation model of the Earth surface with 1x1-min arc resolution available on the NOAA website (National Oceanic and Atmospheric Administration, <http://www.ngdc.noaa.gov/mgg/global/global.html>) is used (Figure 4.2a). The Bouguer gravity anomaly data comes from a recent compilation of gravity data in Iberia (Ayala, et al., 2016) (Figure 4.2b). For the rest of Africa and offshore regions, it is calculated by applying the complete Bouguer correction to free air satellite data (Sandwell and Smith, 1997), updated 2007) using the software FA2BOUG (Fullea et al., 2008) with a density reduction of 2670 kg/m³. Geoid height data come from ICGEM (Ince et al., 2019; <http://icgem.gfz-potsdam.de>) where GECO model (Gilardoni et al., 2016) is used (Figure 4.2c). Geoid data is filtered up to degree and order 10, to retain geoid anomalies coming from lateral density variations within the crust and upper mantle to ~400 km depth (Chapter 2, Section 2.3.2). SHF measurements have been compiled

from Poort et al. (2020) in the Algerian Basin, Rimi et al. (2005) in Morocco, Marzán (2000) and Fernández et al. (1998a) in Iberia, Polyak et al. (1996) in the Alboran Basin, Foucher et al. (1992) in the Valencia Trough, and the International Heat Flow Commission global data set for Algeria (<http://www.heatflow.und.edu/index2.html>) (Figure 4.2a).

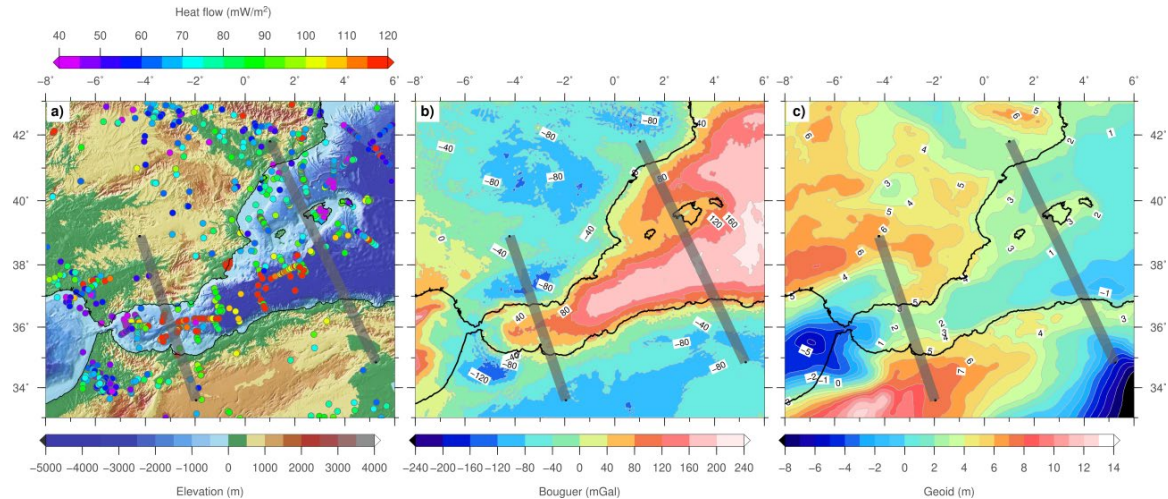


Figure 4.2 Geophysical observables in the region. (a) Shaded elevation and surface heat flow (dots), (b) Bouguer anomaly, (c) geoid filtered up to degree and order 10. Grey thick lines show the locations of the modelled NNW-SSE oriented geo-transects.

Alboran Basin geo-transect

In onshore Iberia, elevation increases from 500 m in the Iberia Massif to as much as ~2500 m in the eastern Internal Betics, coinciding with a decrease of the Bouguer anomaly to values of -120 mGal. Geoid height also decreases from 6–7 m in the SW Iberian Massif to 3–0 m in the western Betics and the Guadalquivir Basin, respectively. A local geoid high of 6 m is observed in the eastern Internal Betics where elevation attains its maximum values (Figure 4.2). The Alboran Basin shows positive Bouguer anomalies, except in its westernmost end where large accumulations (up to 8–9 km) of Oligocene to Recent sediments are recorded. An ENE-WSW relative high delineates the central region of the basin, attaining values of up to 160 mGal in its easternmost end, in the transition to the oceanic crust of the Algerian Basin. Along the geo-transect, Bouguer anomalies decrease asymmetrically from the axis of the basin to the onshore regions. While to the Iberian margin there is a rapid decrease of the anomalies, towards the African margin there is a gentler decrease towards the Algerian Plateau where values of -90 mGal are achieved (Figure 4.2b). The Alboran

Basin shows a geoid high (~ 3 m) in its central region that asymmetrically decreases to the east and west, increasing in an N-S direction, with values of 5–6 m in onshore Iberia and >7 m in the Algerian Plateau (Figure 4.2c). The N-S geoid high delineates the magmatic arc region and the North African continental margin block and separates the prominent geoid low associated with the Gulf of Cadiz accretionary wedge and the fore-arc West Alboran Basin from the Algerian oceanic back-arc basin. Interestingly along the geo-transect, geoid height and elevation follow a similar regional trend, characterized by a rapid increase from the centre of the basin to the Internal Betics with local highs of 6 m and >2000 m, respectively, and a smoother increase towards the Algerian Plateau, where geoid and elevation attain values of up to 8 m and 1000 m, respectively. On the contrary, the Bouguer anomaly does not record a similar local high and instead there is a rapid decrease from the gravity high of central Alboran Basin to the gravity low of the Internal Betics. SHF data, though sparse, shows relatively higher values in the Alboran Basin increasing from west to east into the Algerian Basin (Figure 4.2a). Onshore Iberia shows lower SHF (~ 48 mW/m²) than the onshore north Africa (~ 100 mW/m²).

Algerian Basin geo-transect

In the interior regions of the Tell Mountains and Salt Waters Lakes, elevation ranges from 500 m to 1000 m, with a local low located at the SSE end of the geo-transect, whereas Bouguer anomalies are in the range of -40 mGal to -80 mGal decreasing towards the Saharan Atlas. Geoid shows values of ~ 3 –4 m in the Tell Mountains that rapidly decrease to the SE where a prominent regional geoid low is located (Figure 4.2c). Along the geo-transect, local highs of elevation and Bouguer anomaly are observed in the Greater Kabylies and Tell Mountains, which coincide with a geoid regional high. The Bouguer anomaly increases abruptly from 60–80 mGal close to the shoreline, to above 160 mGal in the central regions of the Algerian Basin indicating the pronounced crustal thinning along the continental slope and slope break, and the oceanic nature of the crust in the central Algerian Basin. Elevation and geoid abruptly decrease to reach values of < -3000 m and 0–1 m, respectively, in the slope break, values that characterize the central regions of the basin.

A very abrupt increase of elevation is observed along the Emile-Baudot escarpment that marks the southeast side of the Balearic Promontory, a ~ 350 km long and 105–155 km wide topographic feature with an average elevation of 500 m that separates the Valencia Trough to the northwest, from the Algerian Basin to the southeast. The Promontory is characterized by a smooth decrease of the Bouguer

anomaly and an increase of geoid heights (Figure 4.2b and c). Elevation and geoid decrease towards the central region of the Valencia Trough coinciding with an increase of the gravity anomalies indicating the presence of a thinned continental crust. SHF data exhibit a wide scatter around a mean value of 65 mW/m² onshore eastern Iberia, increasing to 70–90 mW/m² in the Valencia Trough, and decreasing again to the Balearic Promontory, where measurements are strongly affected by shallow groundwater circulation (Fernández and Cabal, 1992). SHF data show a very poor coverage in the Algerian Basin and onshore Africa along the geo-transect. Nevertheless, seafloor heat flow measurements carried out in the western Algeria Basin show values ranging from 90–120 mW/m² (Marzán Blas, 2000) (Figure 4.2a). In summary both basins show a rather similar regional pattern of the surface observables, the main difference being their amplitude that reflects the different stages of their evolution. While back-arc extension in the Algerian Basin progressed to the onset of new oceanic crust, in the Valencia Trough extension resulted in noticeable crustal thinning that progresses in a SW-NE direction towards the Ligurian-Provencal Basin.

4.1.2. Crustal data

Thermo-physical properties in the crust are taken from the previous studies and are listed in Table 4.1. The initial crustal geometry along the geo-transects is based on geological maps and cross-sections, and active and passive seismology experiments. Along the Alboran Basin geo-transect, the crustal structure in the Iberian Massif is mainly based on the ALCUDIA2 Wide-Angle Seismic Reflection Transect (Ehsan et al., 2015). In the Guadalquivir Basin and Betics (Internal and External), seismic data come from different experiments (e.g., Banda et al., 1993; Carbonell et al., 1997; Comas et al., 1995; Gallart et al., 1995) and geological cross-sections (e.g., Ruiz-Constan et al., 2012; Frizon de Lamotte et al., 2004; Platt et al., 2003; Michard et al., 2002; Berástegui et al., 1998; Banks and Warburton, 1991). Crustal data in the Alboran Basin and the North Africa margin come from active seismic lines processed and interpreted in Gómez de la Peña et al. (2018). In addition to these data, the Moho depth along the geo-transect is also constrained by the active and passive seismic data compilation (Diaz et al., 2016), joint inversion of elevation and gravity (Globig et al., 2016; Torne et al., 2015), surface wave dispersion tomography (Palomeras et al., 2017) and previous integrated geophysical-petrological modelling (Carballo et al., 2015a, b; Fullea et al., 2010) (Figure 4.3a).

Table 4.1 Thermo-physical properties of the different tectonic units in the crust along the geo-transects.

Tectonic units		Density (kg/m ³)	Thermal Conductivity (W/K·m)	Radiogenic Heat Production (μW/m ³)
Sediments	Neogene	2400	2.2	1.00
	Neogene/Mesozoic	2600	2.4	1.00
	Mesozoic sediments	2650	2.5	1.00
Betics	Nevado-Filabride	2900	2.5	1.00
	Alpujarride	2850*	2.5	1.00
	External Units	2600*	2.5	1.20
Greater Kabylies	Internal Units	2900*	2.5	1.00
	External Units	2600*	2.5	1.20
Continental crust	Upper crust	2750	2.4	1.65
	Middle crust	2850	2.1	0.50
	Lower crust	2950	2.0	0.20
Volcanic crust		2820	2.1	0.20
Oceanic crust		2950	2.5	0.30

*Calculated as a function of depth to incorporate pressure dependence. Densities are assigned according to previous studies (e.g., Carballo et al., 2015a, b) and using velocity-density envelopes defined in Brocher (2005). The densities of the HP/LT units result from modelling (Figure 4.4). Thermal conductivities are taken from previous studies (e.g., Carballo et al., 2015a,b; Torne et al., 2000, 2015; Teixell et al., 2005; Zeyen et al., 2005), and radiogenic heat production comes from direct measurements in the Iberian Massif and Betics (Fernández et al., 1998b) and a global compilation of relevant crustal rocks (Vilà et al., 2010).

The crustal geometry along the Algerian Basin geo-transect, except for the onshore northern Africa margin, is well known from the numerous deep seismic reflection and wide-angle/refraction geo-transects collected during the last decades (Figure 4.3b). Moho depths for the Valencia Trough and Balearic Promontory are taken from Torne et al. (1992) and Pascal et al. (1992), while the crustal structure is summarized in TRANSMED-II transect (Roca et al., 2004) and Carballo et al. (2015a). For the sake of completeness, original seismic data come from VALSIS-II (Torne et al., 1992), ESCI-Valencia (Vidal et al., 1998), Hinz (1972), and ALE-4 (an industry transect) in the Algerian Basin. In the North Africa margin, crustal structure is taken from the SPIRAL active seismic experiment (Aïdi et al., 2018) and further south from the geological cross-section by Frizon de Lamotte et al. (2011). Onshore, in the

Catalan Coastal Ranges, receiver function and deep seismic sounding Moho depths are taken from Diaz et al. (2016).

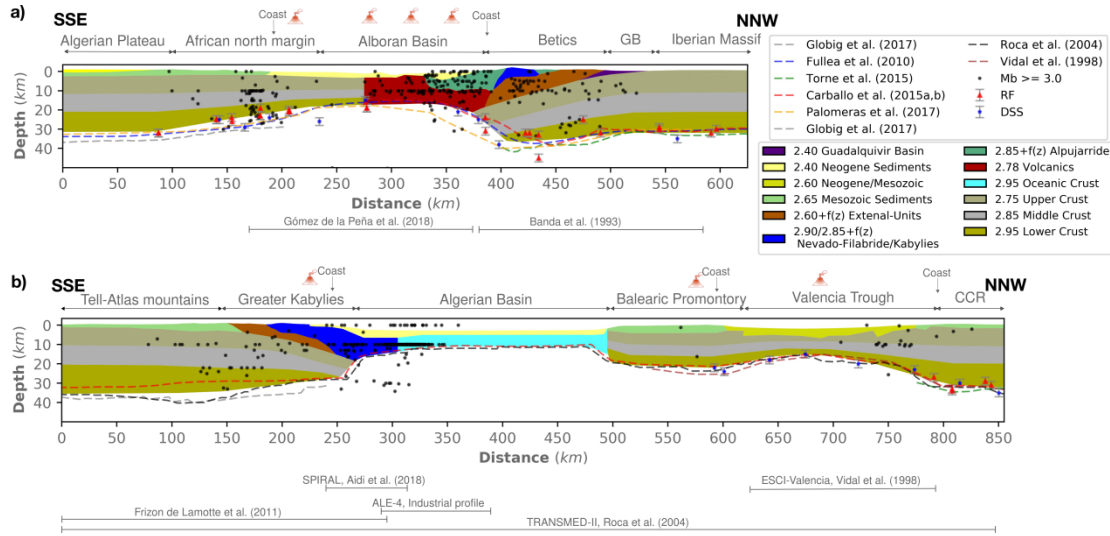


Figure 4.3 Crustal structure corresponding to the best fitting model for the (a) Alboran Basin and (b) Algerian Basin geo-transects. Densities used in each body are colour-coded (see the legend). Moho depths from previous studies (including active seismic, receiver functions, surface wave dispersion and joint modelling of gravity and elevation) are also plotted for comparison. Earthquakes ($M_b \geq 3.0$; 1964-2016, ISC catalogue) projected 50 km across the geo-transects are plotted with black circles. Note that the y-axis is exaggerated by two times the x-axis for better visualization. GB, Guadalquivir Basin; CCR, Catalan Coastal Ranges; RF, Receiver functions; DSS, Deep seismic sounding.

4.1.3. Mantle structure and chemical composition

The depth to the base of the lithosphere (LAB), the chemical composition of the defined lithospheric domains, and the sublithospheric mantle anomalies are constrained by available tomography studies, geochemical analyses from mantle xenoliths and exhumed rocks, and previous modelling results. Initial LAB depths along the geo-transects come from previous 2D and 3D lithospheric models using elevation, gravity and geoid height, based on pure thermal and geophysical-petrological approaches (e.g., Carballo et al., 2015a, b; Fulla et al., 2010; Globig et al., 2016; Torne et al., 2015) and, in the case of the Alboran Basin geo-transect, also from the regional seismic tomography model by Palomeras et al. (2017).

Table 4.2 Major elements composition (weight %) in the NCFMAS system for the lithospheric mantle and sublithospheric domains used in the modelling and corresponding relevant physical properties at lithosphere and sublithospheric mantle pressure and temperature.

Name	SiO ₂	Al ₂ O ₃	FeO	MgO	CaO	Na ₂ O	#Mg	ρ (kg/m ³)		V _P & V _S (km/s)	
								P=3GPa (~100km) T=1300 °C	P=6GPa (~200km)T =1400°C	P=3GPa (~100km)T =1300 °C	P=6GPa (~200km) T=1400°C
PUM	45.00	4.50	8.10	37.80	3.60	0.360	89.3	3310	3396	7.986 4.441	8.254 4.523
DMM	44.70	3.98	8.18	38.73	3.17	0.130	89.4	3307	3391	7.950 4.396	8.232 4.491
DMM - 3%*	44.59	3.51	8.21	39.63	3.02	0.007	89.6	3300	3385	7.936 4.390	8.222 4.488
DMM - 6%*	44.47	3.08	8.23	40.54	2.78	0.051	89.7	3294	3378	7.929 4.388	8.211 4.484
DMM - 7%*	44.43	2.97	8.23	40.78	2.70	0.045	89.8	3293	3376	7.927 4.388	8.209 4.484
Tc_1	44.50	3.50	8.00	39.79	3.10	0.240	89.8	3296	3381	7.934 4.391	8.213 4.488
Pr_6	45.40	3.70	8.30	39.90	3.20	0.260	90.6	3299	3385	7.931 4.388	8.213 4.486
CVP	44.51	3.76	8.75	37.89	3.28	0.360	91.0	3309	3395	7.909 4.374	8.194 4.473

*Calculated using melting model described in Chapter 2, Section 2.8. PUM, Primitive Upper mantle (McDonough and Sun, 1995); DMM, Depleted mid-oceanic-ridge-basalt Mantle (Workman and Hart, 2005); Tc_1, Average Garnet Tecton (Griffin et al., 2009); Pr_6, Average Proton Lherzolite (Griffin et al., 2009; Le Roux et al., 2007); CVP, Calatrava Volcanic Province (Villasaca et al., 2010)

In the onshore regions (Iberia and north Africa) lithospheric mantle compositional domains are taken from the previous studies in the same zone, which are based on mantle xenoliths, exhumed mantle rocks or tectono-thermal age of the crust (e.g., Jiménez-Munt et al., 2019; Carballo et al., 2015a,b; Fullea et al., 2010; Griffin et al., 2009). In the Algerian and Alboran basins, the Valencia Trough, and the Kabylies and Betics, mantle chemical composition is calculated from the major oxides partition as a function of aggregate melting using the empirical formulation of Niu (1997), as discussed in Chapter 2.

4.2. Alboran Basin geo-transect: structure, temperature, and density

4.2.1. Crustal and upper mantle structure

The crust of the Iberian and African mainland and their margins has been modelled using a three-layer crustal model; upper, middle and lower crust (Table 4.1 and Figure 4.3a). In the Iberian Massif the crust is ~32 km thick which is consistent with previous studies and thickens up to ~37 km below the Internal Betics over a distance of 100 km. The Guadalquivir foreland basin, reaches a maximum depth of 4 km close to the Betic fold belt front. The structure of the External Betics is constrained by low seismic velocity anomalies at crustal levels as observed in tomography models (Moudnib et al., 2015; Carbonell et al., 1998), while the structure of the Nevado-Filabride and Alpujarride Internal Units are mainly defined from geological observations (Figure 4.3a). These two tectonically stacked HP/LT Betics Internal Units are defined as high density tectonic nappes according to P-T conditions of their metamorphic facies and densities of their basement and cover protoliths after metamorphic peaks (e.g., Gómez-Pugnaire et al., 2019) (Figure 4.4). The Nevado-Filabride, at the base of the thrust sheet pile, forms an open and elongated dome that is overlaid to the N by the Alpujarride thrusts. To the SSE, the Alpujarride Unit is slightly dipping towards the Alboran Basin and thus forming the basement of the Neogene sedimentary infill in the proximal Iberian margin. The crust of the Alboran Basin is modelled as a highly intruded volcanic domain cropping out near the Alboran Ridge (Gómez de la Peña et al., 2018). The thinnest crust along the whole geo-transect is found in the Alboran Basin with Moho depths of 16–17 km being consistent with previous estimates (Figure 4.3a). Southeast of the Alboran Ridge, the crust is interpreted as African continental crust of about 18 km thickness, with thinning localized mainly at mid- and lower-crustal levels (Gómez de la Peña et al., 2018). Moho depth increases gradually southwards from 17 km to 31 km across the North Africa margin (Figure 4.3a).

Present-day crust and upper mantle structure of the Alboran and Algerian basins

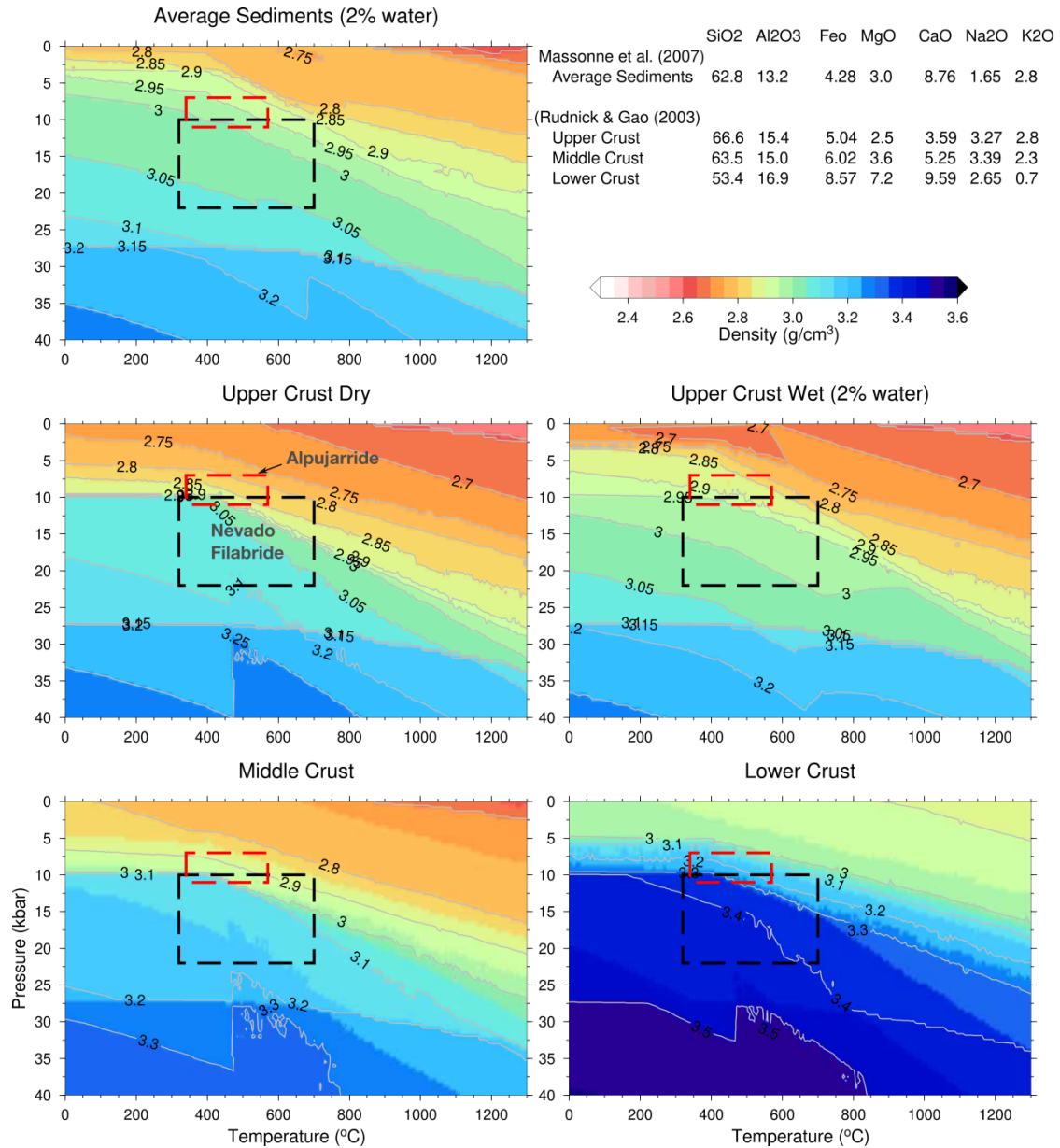


Figure 4.4 Pressure and temperature dependent density distribution for average sediments, upper crust, middle crust and lower crust compositions (see legend), computed from stable phases and mineral assemblages using the Gibbs free-energy minimization algorithm (Connolly, 2005, 2009). Red and black dashed line boxes mark the range of high pressure metamorphic peaks for Alpujarride and Nevado-Filabride HP/LT metamorphic units, respectively, determined from thermo-barometry (Augier et al., 2005; López Sánchez- Vizcaíno et al., 2001; Puga et al., 2000; Azañón and Crespo-Blanc, 2000).

Three different chemical composition domains are deemed within the lithospheric mantle along the Alboran Basin geo-transect (Table 4.2 and Figure 4.5). For the Iberian lithosphere, a depleted composition is considered which is taken from mantle xenoliths sampled in the Calatrava Volcanic Province (CVP, Villaseca et al., 2010) as in Jiménez-Munt et al. (2019). In the Alboran Basin, the lithospheric mantle

composition corresponds to the residual of 6% aggregate decompressional melting of DMM based on the pervasive magmatic intrusion related to the retreat of the Alboran slab. This chemical domain extends also beneath the Betics as a result of the NNW directed slab roll-back and associated mantle delamination (Figure 4.5). In the North African margin and the Algerian Plateau, the composition of the lithospheric mantle corresponds to Average-Garnet-Tecton, an average Phanerozoic mantle composition (Tc_1; Griffin et al., 2009), in agreement with previous models on the region (e.g., Carballo et al., 2015a; Fullea et al., 2010). The LAB depth is ~110 km beneath the stable Iberian Massif increasing to ~130 km beneath the Betics and decreasing abruptly to ~64 km towards the Alboran Basin from where the LAB deepens gently beneath the North African margin down to ~112 km below the Algerian Plateau (Figure 4.5e).

Seismic tomography models show a positive velocity anomaly beneath the Betics that amounts ~2–3 % in P-wave relative to the ak135 global velocity model (e.g., Garcia-Castellanos and Villaseñor, 2011; Bezada et al., 2013; Villaseñor et al., 2015) and an excess of 0.15-0.3 km/s in S-wave (e.g., Palomeras et al., 2014,2017; Civiero et al., 2018). This anomaly extends down to 670 km depth and has been interpreted as the Tethyan subducted lithosphere that is detached from the Iberian lithosphere along a lateral tear affecting the region crossed by the geo-transect (e.g., Spakman and Wortel, 2004; Garcia-Castellanos and Villaseñor, 2011; Bezada et al., 2013; Palomeras et al., 2017) (Figures 1.4, 4.1b and 4.1c). Consequently, I have considered a sublithospheric mantle anomaly situated below 140 km depth simulating the detached Alboran slab characterized by a P-wave velocity anomaly of $\Delta V_P = +2\%$ and using the residual composition after 3% aggregate melting from DMM (DMM-3%; Figure 4.5). I have tested different possible chemical compositions for the Alboran slab ranging from pure oceanic lithosphere to CVP (Table 4.3 and Figure 4.6), DMM-3% being the one with the best-fitting

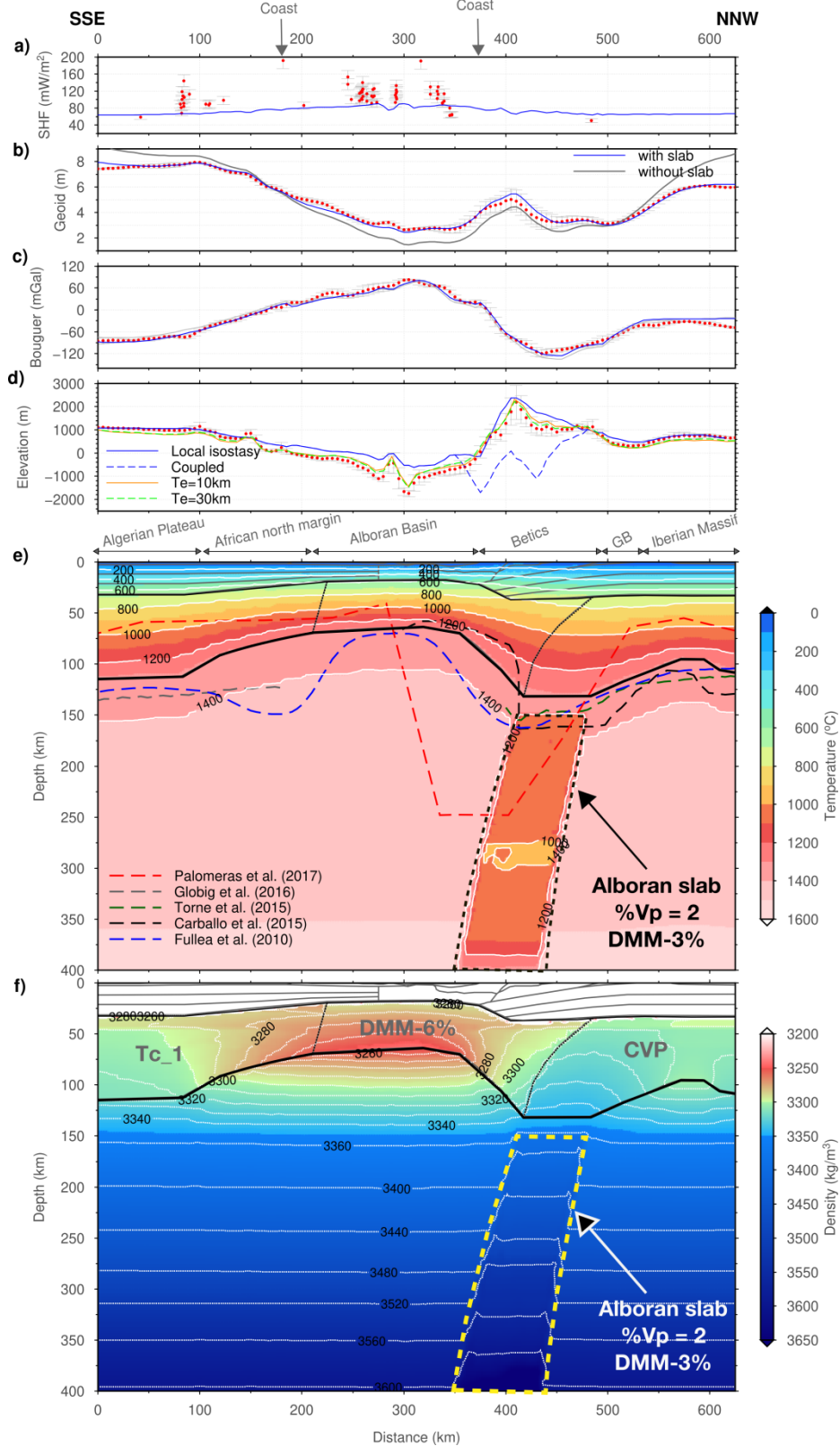


Figure 4.5 Best fitting model along the Alboran Basin geo-transect. (a) Surface heat flow. (b) Geoid height. (c) Bouguer anomaly. (d) Elevation. Blue line represents the calculated values from the model. Red dots denote measured data, and vertical bars denote the standard deviation calculated across a strip of 25 km half width. In (b) geoid height with no slab anomaly is plotted in grey for comparison. In (d) isostatic elevation is plotted in solid blue while the effect of slab on elevation (coupled elevation) is plotted

in dashed blue line. Elevation assuming flexural isostasy for elastic thickness of 10 km and 30 km are plotted in orange and light-green, respectively. (e) Temperature distribution along the geo-transect. Continuous black lines highlight the Moho and LAB depth from our model. LAB depths from previous studies (dashed colour lines) are overlay plotted for comparison. (f) Density distribution in the mantle. The different composition domains in the lithospheric mantle are separated by thin black lines. The bold text in grey colour denotes chemical composition used in the different lithospheric mantle domains listed in Table 4.2.

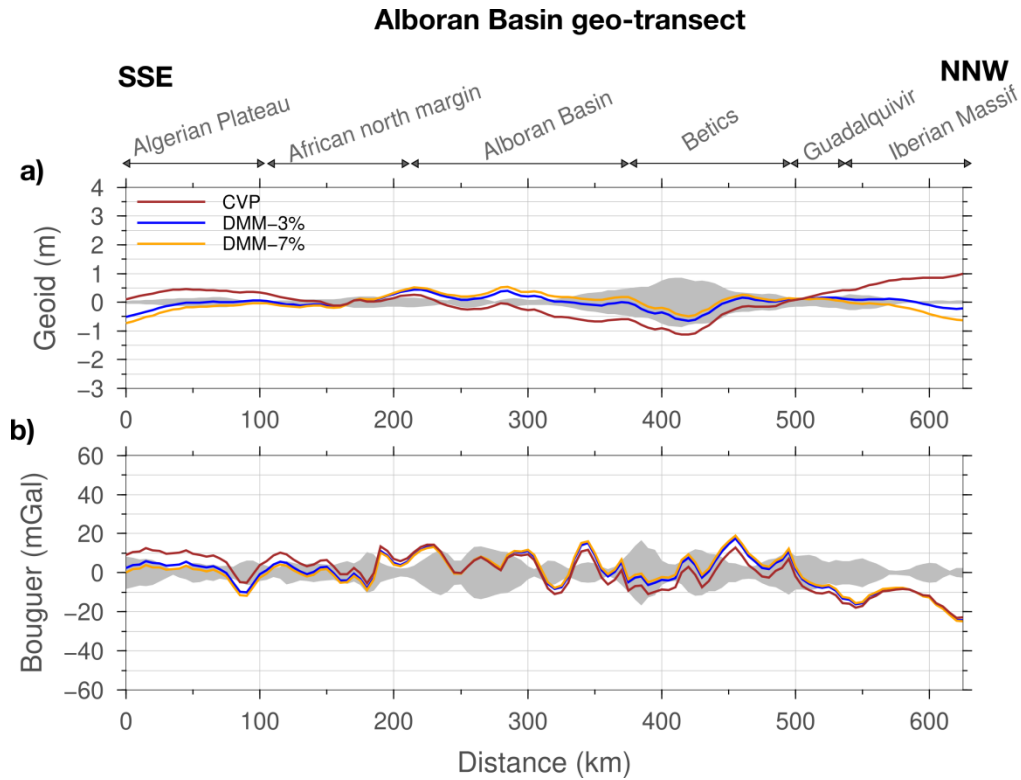


Figure 4.6 Alboran slab chemical composition sensitivity to the (a) geoid height and (b) Bouguer anomaly. Chemical composition has minuscule effect on the Bouguer anomaly and has noticeable effect on the geoid height. Variation in the Alboran slab composition, situated at depths >140 km, changes the mass distribution in the slab region and consequently affects the geoid at longer wavelengths along the geo-transect. DMM-3% chemical composition fits the geoid better along the Alboran Basin geo-transect.

The geophysical observables and the calculated values obtained with the proposed model are shown in the upper panels of Figure 4.5. The calculated SHF falls within the available measurements though these are sparse and uncorrected for surface perturbations and transient effects (Figure 4.5a). Deep groundwater circulation in the Tell Mountains can result in anomalously high heat flow in the Algerian Plateau. Similarly, recent mantle upwelling and volcanism can be responsible for the high heat flow measured in the Alboran Basin. The calculated geoid height and the Bouguer gravity anomaly match satisfactorily the observations (Figures 4.5b and 4.5c), whereas

local isostatic elevation shows remarkable misfits of ~ 100 m in the Guadalquivir Basin, and ~ 500 m in the Betics and the Alboran Basin (Figure 4.5d). However, when flexural rigidity of the lithosphere is considered and vertical loads associated with the topography misfits are applied, the calculated elevation fits well with the observations (Figure 4.5d). An effective elastic thickness (T_e) of 10 km is enough to fit the elevation over most of the geo-transect. This value agrees with the elastic thickness obtained in the same region from other methodologies (e.g. Kaban et al., 2018). It is worth noting that elevation is well reproduced when considering that the sublithospheric anomaly related to the detached slab does not transfer any traction stress on the overlying lithosphere. In the case that the slab would transfer all the gravitational potential to the surface, i.e. when the sublithospheric anomaly is fully coupled to the lithosphere, the resulting isostatic elevation would decrease by ~ 1000 – 2000 m in the Betic region and increase by few 100 m in the Alboran Basin depending on the considered equivalent elastic thickness (dashed lines in Figure 4.7a).

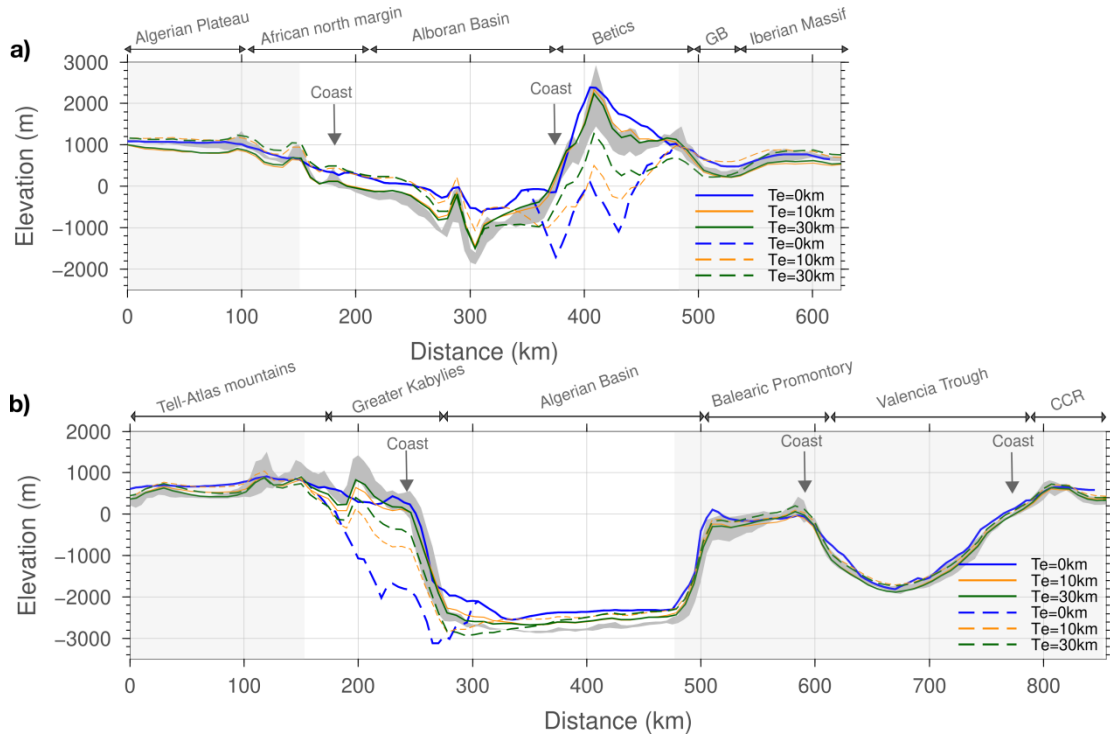


Figure 4.7 Observed and modelled elevation across (a) Alboran Basin geo-transect and (b) Algerian basin geo-transect. Region highlighted in white shows extend along the geo-transect to which the slabs would affect the elevation. Dark-grey shaded strip shows the observed elevation across 50 km wide swath along the geo-transects. Solid coloured lines represent elevation with no slab anomaly (uncoupled), while dashed colour lines show calculated elevation considering the slab (coupled elevation). Blue lines shows isostatic elevation (i.e. $T_e = 0$ km). Orange and green lines show elevation considering flexural isostasy, $T_e = 10$ km, and 30 km, respectively.

Table 4.3 Root mean square error (RMSE) associated with the tested models. RMSE is calculated by considering the lateral variability of the observables through the assigned error bars (see text for explanation).

Geo-transect	Model	Model fit (RMSE)				
		Geoid (m)	Bouguer anomaly (mGal)	Topography (m)		
				Te=0 km	Te=10 km	Te=30 km
Alboran Basin	homogenous lithospheric mantle composition (Tc_1)	0.96	12.41	332	96	73
	without the slab	0.85	7.41	256	62	42
	Alboran slab with CVP composition	0.31	5.55	256	500	339
	Alboran slab with DMM-7% Composition	0.20	5.42	256	197	113
	Alboran slab with DMM-3% composition (Figure 4.5)	0.10	5.26	256	266	164
Algerian Basin	homogenous lithospheric mantle composition (Tc_1)	0.78	15.17	226	48	31
	without the slab	0.56	14.80	202	52	30
	Algerian slab with DMM-7% composition (Figure 4.9)	0.25	13.14	202	212	153

Table 4.3 displays the root mean square error (RMSE) associated with different tested models including no slab with homogenous and non-homogeneous lithosphere, detached slab of different compositions (CVP, DMM-3% and DMM-7%; Table 4.2), and different elastic thickness ($T_e = 0$ km, 10 km and 30 km). To calculate the RMSE related to geoid, gravity and elevation, I have considered the absolute difference between the calculated and observed values and its associated standard deviation. Therefore, $RSME = 0$, for $|calc - obs| \leq std$, and $RMSE = |calc - obs| - std$, for $|calc - obs| > std$; where *calc*, *obs*, and *std* are the calculated and observed values, and the standard deviation, respectively. Variations in the composition of the detached slab decrease noticeably the RMSE of the geoid height and in a lesser extent the RSME of the Bouguer gravity anomaly. If the sublithospheric anomaly is ignored the RMSE related to the geoid height is eight times higher than the best fitting model and then is unacceptable as shown in Figure 4.5b. Note that the RMSE of elevation for $T_e = 0$ km

does not vary with the composition of the slab because in all the cases I am considering that it acts as an uncoupled sublithospheric anomaly and then it is irrelevant for the calculated elevation. Whereas, for $T_e = 10$ km and $T_e = 30$ km, RMSE for elevation varies because of density variations associated with slab composition and resulting pressure variations related to topography loads at the base of the model.

4.2.2. Temperature and density distribution

The temperature distribution along the entire geo-transect is shown in Figure 4.5e. The Iberian Massif is characterized by flat isotherms in the crust with a Moho temperature of ~ 650 °C, and a slight upward deflection at deep lithospheric mantle levels related to the thinning of the lithosphere beneath the Calatrava Volcanic Province. In the Betics, the slab break-off produces the deepening of the LAB and the consequent downward deflection of the isotherms. The maximum Moho temperature along the geo-transect is reached in the Betics (800 °C) as a combined effect of crustal thickening and the sharp lithospheric thinning towards the adjacent Alboran Basin, where Moho temperatures are around 550 °C. Towards the stable Algerian Plateau the isotherms become roughly horizontal with a Moho temperature similar to the Iberian Massif (~ 650 °C). The temperature distribution within the sublithospheric mantle results from the combined effect of lithospheric thickness variations and the imposed adiabatic thermal gradient except within the detached lithospheric slab where the P-wave velocity anomaly of $\Delta V_P = +2\%$ translates into a depth average temperature anomaly of $\Delta T \approx -430$ °C. Note that the temperature variation with depth within the slab is not constant because of the non-linear relationship between temperature and seismic velocities. The calculated density variations in the lithospheric mantle are due to the different chemical compositions and the P-T conditions resulting from laterally varying the lithospheric thickness (Figure 4.5f). In the Iberian Massif density is almost constant in the Calatrava Volcanic Province (3300–3310 kg/m³) increasing rapidly towards the Betics where density increases with depth from 3300 kg/m³ beneath the Moho to ~ 3350 kg/m³ near the LAB. This lateral change in the density distribution is mainly related to the variations in the LAB depth and its effect on pressure and temperature distribution. The pronounced lithospheric thinning affecting the Alboran Basin results in high temperature and low pressure conditions that decrease the density in the lithospheric mantle. This effect adds to the density decrease associated with the compositional change between the Iberian lithospheric mantle (CVP) to the oceanic-like lithospheric mantle of the Alboran Basin (DMM-6%), which may amount

10 - 15 kg/m³ (Table 4.2). As a result, the lithospheric mantle density in the central part of the Alboran Basin shows the lowest values along the geo-transect with a depth-dependent decrease from 3290 kg/m³ beneath the Moho to 3250 kg/m³ near the LAB. Towards the Iberian and African margins density increases laterally and keeps almost constant with depth due to strong variations in the LAB depth indicating that in these regions pressure and temperature effects tend to counterbalance each other. Beneath the stable Algerian Plateau density in the lithospheric mantle increases with depth from 3270 kg/m³ beneath the Moho to 3320 kg/m³ near the LAB.

At shallow sublithospheric mantle levels, the lateral density variations are related to the changes in the lithospheric thickness such that the thinner the lithosphere the lower the density, with values ranging from 3345 kg/m³ beneath the Betics to 3260 kg/m³ beneath the Alboran Basin. At deeper sublithospheric mantle depths (>150 km) density increases with depth almost linearly and lateral variations are negligible, except for the cold and detached Alboran slab region, where the associated depth averaged density anomaly amounts ~50 kg/m³ (Figure 4.8) and increases as much as ~125 kg/m³ at the base of the model (400 km) due to the depth decrease of the olivine-wadsleyite phase transition resulting from the colder temperatures within the slab.

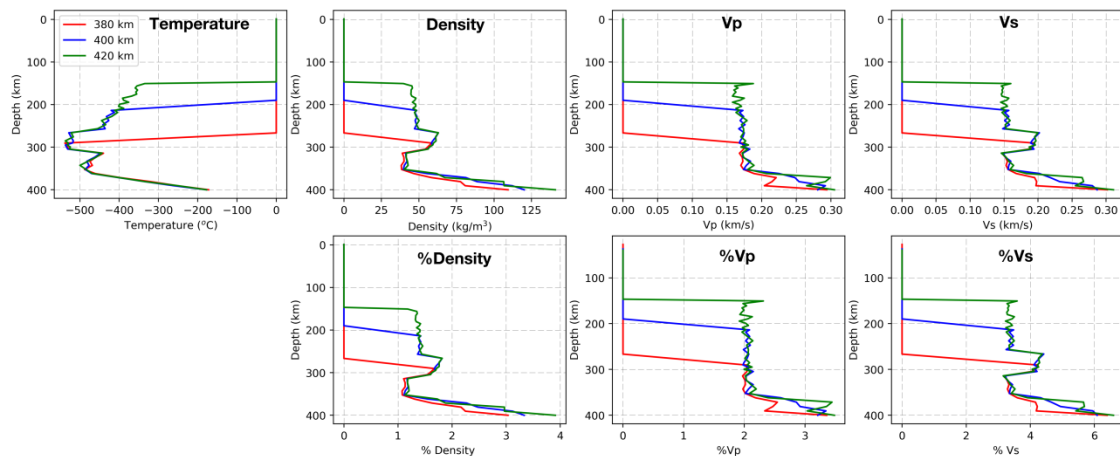


Figure 4.8 Temperature, density, and P- and S-wave velocity depth distribution in the Alboran slab at three locations spanning the slab region along the Alboran Basin geo-transect (see the legend). Upper panel shows the absolute deviation with respect to the LitMod reference column (Chapter 3) and lower panel shows the percentage change.

4.3. Algerian Basin geo-transect: structure, temperature, and density

4.3.1. Crustal and upper mantle structure

The crustal structure roughly coincides with that proposed by Carballo et al. (2015a) except for the three-layered continental crust and the internal structure of the Greater Kabylies (Figure 4.3b). The crust is ~36 km thick beneath the Tell-Atlas Mountains gently thinning towards the margin up to ~30 km with the basement deepening smoothly beneath the Greater Kabylies. The Greater Kabylies are characterized by high density metamorphic slices (Internal Units) thrusting onto the folded non-metamorphic Mesozoic External Units overlying the African crust showing an architecture similar to the Betics (Figure 4.3a). Further to the NNW, the crust thins abruptly towards the Algerian Basin where the Moho is found at 10–12 km depth. The crust of the Algerian Basin is composed of a ~6 km thick oceanic layer overlaid by a ~3 km thick Neogene sedimentary layer. The Balearic Promontory, the Valencia Trough and the Catalan Coastal Ranges are characterized by a thinned continental crust and a Mesozoic to Neogene sedimentary cover of variable thickness. Our results are consistent with previous findings derived from active seismic experiments (e.g., Torne et al., 1992; Vidal et al., 1996), which proposed a clear crustal asymmetry between the Catalan Coastal Ranges, with a thickness of ~32 km, and the thinner crust (~22 km) below the Balearic Promontory. In the axis of the Valencia Trough, the Moho is found at ~18 km along the modelled transect, in agreement with the aforementioned works (Figure 4.3b).

In the mantle along the Algerian Basin geo-transect, I have considered five lithospheric mantle domains (Figure 4.9 and Table 4.2) following the structure from Carballo et al. (2015a) and the different tectonic domains. In the Catalan Coastal Ranges and the Balearic Promontory I use an Average Proton Lherzolite (Pr_6; Griffin et al., 2009; Le Roux et al., 2007) as in Carballo et al. (2015a), except for the Balearic Promontory where they used a primitive upper mantle composition. In the Valencia Trough I use a residual composition corresponding to DMM-6% based on the inferred high degree of decompression melting driven by lithospheric extension and mantle upwelling (Martí et al., 1992). Since the Algerian Basin is a back-arc oceanic basin with a ~6 km thick oceanic magmatic layer (Booth-Rea et al., 2007), I have increased the amount of melting to ~7% (Klein and Langmuir, 1987), while beneath the Greater Kabylies this percentage is reduced to 3% to account for the melting of the depleted asthenosphere (DMM) following delamination and slab detachment (Chazot et al.,

2017). In the North Africa margin, beneath the Tell-Atlas Mountains, I have considered a lithospheric mantle with a Phanerozoic Tc_1 composition according to Carballo et al. (2015a), which is similar to the North Africa margin mantle to the west along the Alboran Basin geo-transect. The LAB depth varies from ~135 km over a flat region beneath the Tell-Atlas Mountains to ~150 km below the Greater Kabylies and decreases rapidly to ~60 km in the Algerian Basin. Towards the Balearic Promontory the LAB deepens abruptly to ~84 km shallowing slightly towards the centre of the Valencia Trough (~80 km) and increases gradually to ~120 km onshore Iberia.

The positive seismic velocity anomaly beneath the North Africa margin (Figures 1.4b and 4.1d; after Fichtner and Villaseñor, 2015) is modelled as a sublithospheric mantle body situated below 200 km depth with an anomalous S-wave velocity of $\Delta V_s = +3.5\%$ and a chemical composition similar to that of the current Algerian Basin lithospheric mantle (DMM-7%). This composition fits better the geoid height than the African lithospheric mantle composition (i.e., Tc_1) and the more enriched DMM-3% considered for the delaminated mantle beneath the Greater Kabylies (Table 4.3 and Figure 4.10).

Present-day crust and upper mantle structure of the Alboran and Algerian basins

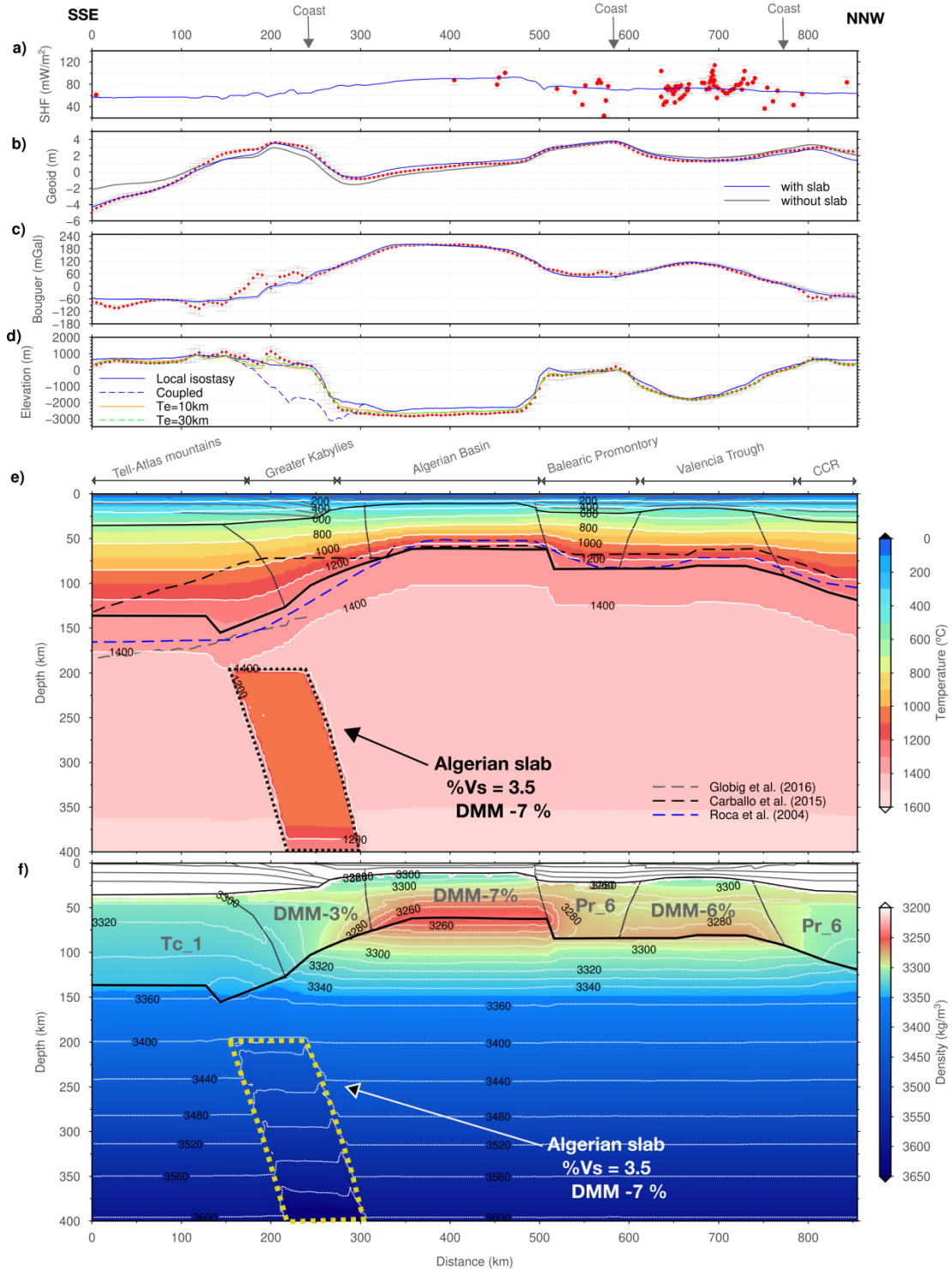


Figure 4.9 Best fitting model along the Algerian Basin geo-transect, rest of the caption as in Figure 4.5.

Figure 4.9 shows the fitting of the geophysical observables from the proposed model. The calculated SHF falls within the range of measured values though these are unevenly distributed and show a high scatter (Figure 4.9a). The calculated geoid height shows a very good fit with observations all along the geo-transect (Figure 4.9b),

with minor misfits ($< 1\text{ m}$) in the Greater Kabylies. The calculated Bouguer anomaly matches the regional trend (Figure 4.9c) with significant misfits all along the Greater Kabylies, where the calculated values are clearly underestimated though the low quality of available gravity data in the region does not allow for firm conclusions. This model shows the minimum RMSE values for geoid height and Bouguer anomaly, 0.25 m and 13.14 mGal, respectively when compared to a no slab model or to model with DMM-3% and Tc_1 slab composition (Table 4.3 and Figure 4.10).

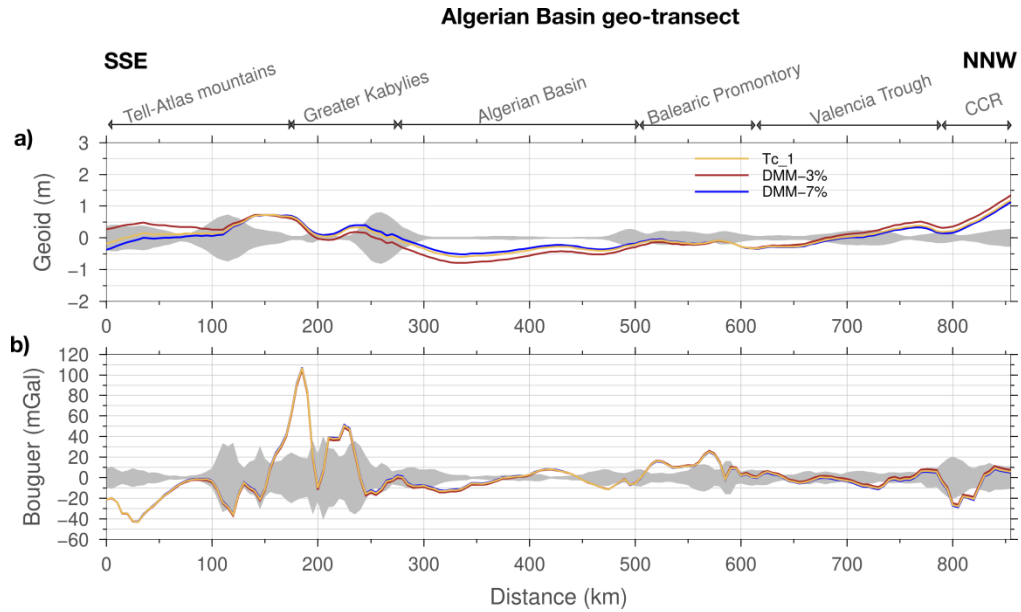


Figure 4.10 Algerian slab chemical composition sensitivity to the (a) geoid height and (b) Bouguer anomaly. DMM-7% chemical composition, resulting from 7%melting of DMM, fits better the geoid height along the Algerian Basin geo-transect.

The calculated isostatic elevation also matches the regional trend but shows a long wavelength misfit of $\sim 400\text{ m}$ in the Algerian Basin and $\sim 250\text{ m}$ in the Tell-Atlas Mountains, with local misfits of $\sim 700\text{ m}$ in the Greater Kabylies (Figure 4.9d). However, when I consider the flexural rigidity of the lithosphere, the fit between calculated and observed elevation is largely improved (Figure 4.7b). Along most of the profile, an effective elastic thickness of $T_e = 10\text{ km}$ reduces the RMSE from 202 m to 52 m (Table 3), although a higher elastic thickness ($T_e = 30\text{ km}$) is required for the Africa mainland resulting in $\text{RMSE} = 30\text{ m}$ (Figure 4.7b and Table 4.3). These elastic thickness values are in agreement with those predicted by coherence analysis of topography and gravity (e.g. Pérez-Gussinyé et al., 2009; Kaban et al, 2018). The estimated coupled elevation, which includes the isostatic effect of the cold and denser slab, would decrease the elevation by 500–2000 m in the Greater Kabylies. Near the

coast, elevation decreases because of the fore-deep and increases in the Algerian Basin because of the fore-bulge associated with the assumed Algerian slab attached to the lithosphere (Figure 4.7b). These variations in elevation amount few hundred meters depending on the considered elastic thickness.

4.3.2. Temperature and density distribution

The temperature distribution along the Algerian Basin geo-transect is shown in Figure 4.9e. At deep lithospheric levels, isotherms mimic the depth variations of the LAB showing a step-like shape. In the Tell-Atlas Mountains region isotherms are roughly flat showing an upward deflection beneath the Great Kabylies and the Africa margin, and become flat again in the Algerian Basin. Further to the NNW, isotherms deepen slightly below the Balearic Promontory flattening beneath the Valencia Trough and deepening gently towards the Catalan Coastal Ranges. The calculated temperature at the Moho varies from ~630 °C in the Tell-Atlas Mountains, decreasing rapidly beneath the Greater Kabylies (600–400 °C) and reaching the minimum value of ~250 °C in the Algerian Basin. Towards the Iberia Margin, the Moho temperature shows noticeable variations reaching ~600 °C in the Balearic Promontory, ~400 °C in the Valencia Trough and ~700 °C in the Catalan Coastal Ranges. At sublithospheric mantle levels, below 200 km depth, the temperature distribution responds to the imposed adiabatic thermal gradient except within the detached slab where the seismic anomaly of $\Delta V_s = 3.5\%$ translates into a depth average temperature anomaly of $\Delta T \approx -400$ °C (Figure 4.11).

The calculated density distribution along the Algerian Basin geo-transect is shown in Figure 4.9f, reflecting the different chemical compositions and P-T conditions in the upper mantle. The lithospheric mantle in the Tell-Atlas Mountains, with the same composition than in the Algerian Plateau (i.e., Tc_1, Table 4.2) shows a density increase with depth from ~3280 kg/m³ at the Moho to ~3340 kg/m³ at the LAB being slightly higher than in the Algerian Plateau lithosphere of the parallel Alboran Basin geo-transect (3270kg/m³-3320 kg/m³, Figure 4.5f) due to the higher lithospheric thickness. Density decreases laterally across the margin, beneath the Greater Kabylies, and towards the Algerian Basin from 3320 kg/m³ to less than 3290 kg/m³ being almost constant with depth. These density changes are the combined effect of varying the chemical composition from Tc_1 to DMM-3% (Table 4.2) and the lithospheric thinning which counterbalance the depth-dependent pressure and temperature effects. The oceanic lithospheric mantle in the Algerian Basin, with a DMM-7% composition (Table 4.2), shows a density exceeding 3300 kg/m³ at the

uppermost mantle levels until a depth of ~ 20 km related to the plagioclase-spinel phase transition. Below this depth, density decreases with depth to 3250 kg/m^3 at the LAB, which is the lowest mantle density along the geo-transect. To the NNW, the transition to a Proterozoic composition (Pr-6, Table 4.2) beneath the Balearic Promontory together with the lithosphere thickening, results in a lateral increase of densities to an average value of $\sim 3285 \text{ kg/m}^3$ which keeps almost constant with depth. The lithospheric mantle beneath the Valencia Trough, with DMM-6% composition, shows a density of $\sim 3300 \text{ kg/m}^3$ at the Moho depth decreasing to 3280 kg/m^3 at the LAB demonstrating some oscillations in the pressure gradient related to the plagioclase-spinel (25–35 km depth) and spinel-garnet (60–90 km depth) phase transitions. Density increases again laterally towards the Catalan Coastal Ranges as a combined effect of composition and P-T conditions.

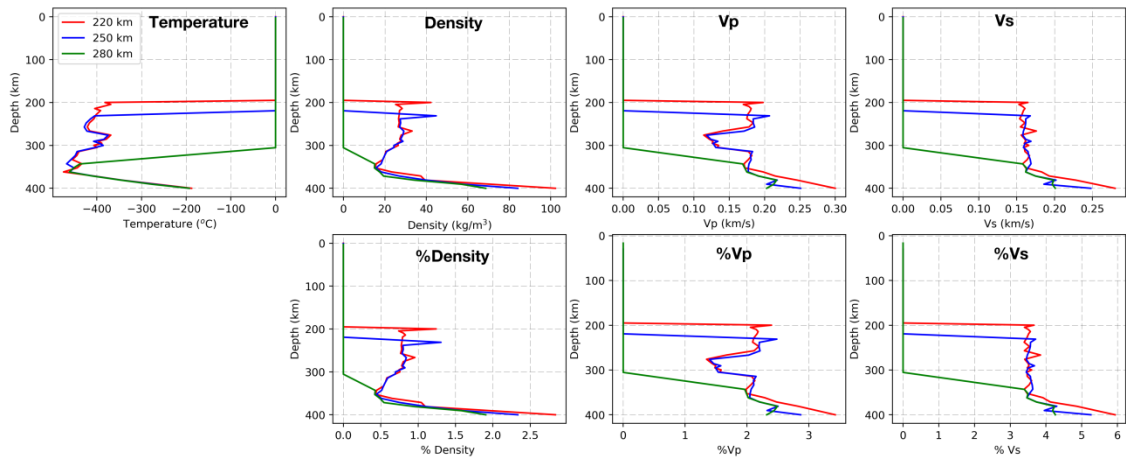


Figure 4.11 Temperature, density, P-wave velocity and S-wave velocity depth distribution in the Algerian slab at three locations (see the legend) spanning the slab region along the Algerian Basin geo-transect. Rest of the caption is same as in Figure 4.8.

Similar to the Alboran Basin geo-transect, at shallow sublithospheric mantle levels, density variations are related to LAB depth variations affecting especially the Algerian Basin, the Balearic Promontory and the Valencia Trough regions. At deeper sublithospheric mantle levels (> 150 km), lateral variations are negligible, except for the detached Algerian slab region where above 300 km depth, density increases by $\sim 30 \text{ kg/m}^3$ and decreases to $< 20 \text{ kg/m}^3$ at 350 km depth, as composition effects competes with those of the temperature (Figure 4.11). Close to the base of the model, density increases by as much as $\sim 100 \text{ kg/m}^3$ in the slab region due to the olivine-wadsleyite phase transition alike to the Alboran slab at these depths (Figures 4.8 and

4.11). It is interesting to note that the density change in case of the Alboran slab at 400 km is higher than that for the Algerian slab. The temperature change at these depths is similar for both slabs at these depths; hence, the difference in the density change can be attributed to the composition which is relatively more fertile in the Alboran slab (DMM-3%, Table 4.2) than in the Algerian slab (DMM-7%, Table 4.1).

4.4. Mantle seismic velocities and comparison with passive seismological data

In this section, I show the calculated seismic velocities in the upper mantle according to the mineral aggregates resulting from the ascribed chemical composition, and the prevailing pressure and temperature conditions. The results are compared with the available seismic data and tomography models.

As discussed in Chapter 3, absolute seismic velocities obtained in LitMod2D_2.0 can be used to compute passive seismological data (e.g., receiver functions and surface wave dispersion curves). Forward prediction of P-wave receiver functions and dispersion curves of Rayleigh surface-wave phase velocities dispersion curves are computed using the post-processing toolbox in LitMod2D_2.0 and are also compared with the available observed data.

4.4.1. Alboran Basin geo-transect

Figure 4.12a shows the P-wave velocity distribution along the Alboran Basin geo-transect. As shown in Table 4.2, seismic velocities depend to a larger extent on temperature and pressure than on composition. The lower V_P values within the lithospheric mantle are found close to the LAB in regions affected by lithospheric thinning, as the Calatrava Volcanic Province in the Iberian Massif ($V_P < 8.0$ km/s), and the Alboran Basin and its margins ($V_P < 7.85$ km/s). In these regions, V_P decreases with depth indicating that the temperature effect prevails on the pressure effect. In contrast, P-wave velocities beneath the Betics, in the thicker lithosphere region, increase from ~ 8.05 km/s in the uppermost mantle, consistent with the observed P_n velocities of 8.0 km/s - 8.2 km/s (Diaz et al., 2008, 2013), to 8.1 km/s at LAB depths. Beneath the Algerian Plateau, P-wave velocities keep almost constant with depth ($V_P \approx 8.0$ km/s) showing a lateral decrease towards the Africa margin.

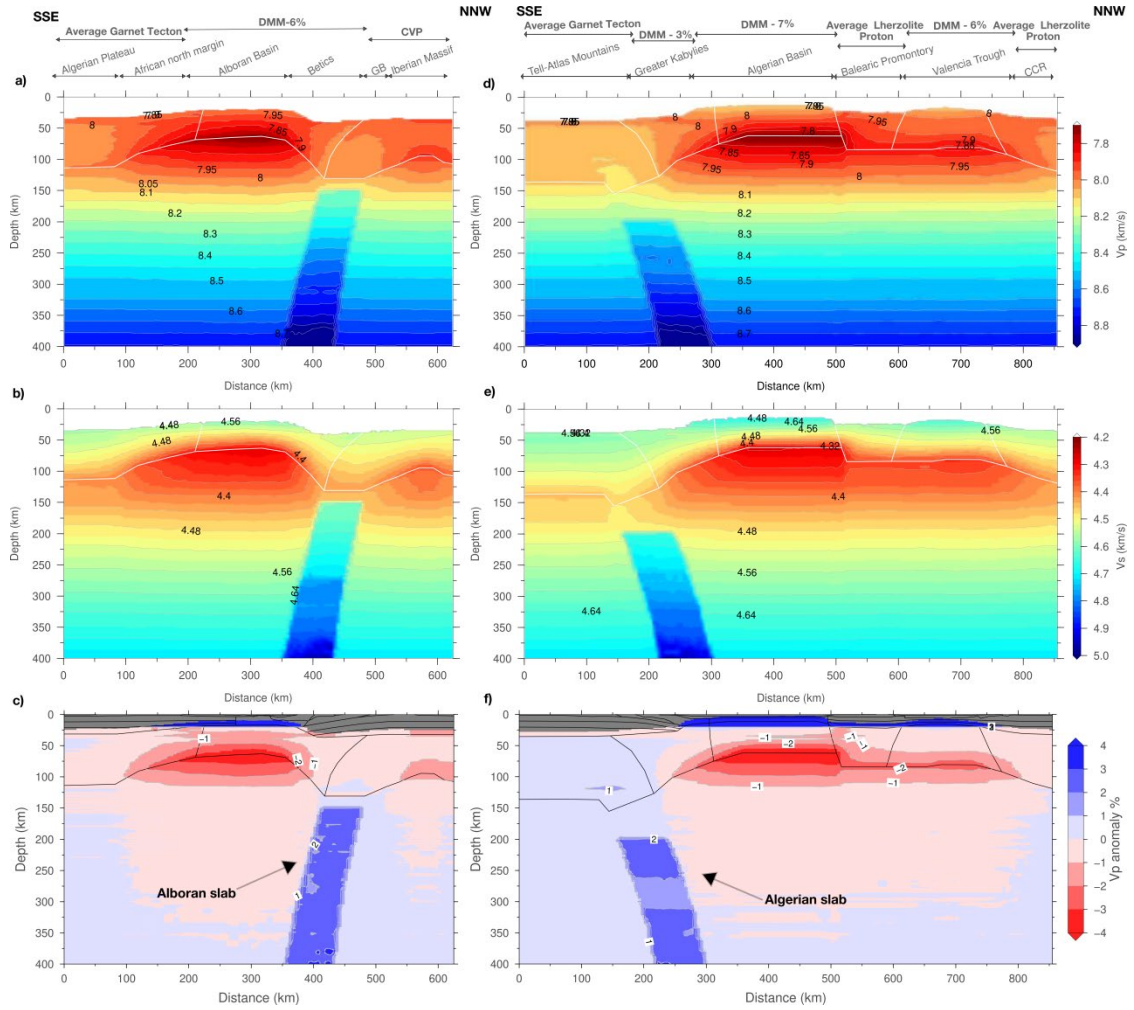


Figure 4.12 Seismic velocities and synthetic seismic tomography along the geo-transects. (a) and (b) shows the absolute P-wave and S-wave velocities, respectively and (c) synthetic P-wave anomalies for the Alboran Basin geo-transect. Similarly (d) and (e) shows the absolute P- and S-wave velocities, respectively, and (f) synthetic P-wave anomalies along the Algerian Basin geo-transect.

The relatively fertile (DMM-6%) composition of the central segment of the geo-transect, close to primitive upper mantle (PUM; McDonough and Sun, 1995), produces shallow mantle P-wave velocities of 7.97 km/s in the Alboran Basin as found by Fulla et al. (2010). These low P-wave velocities can be further reduced by the presence of partial melts, as the geotherm intersects the dry peridotite solidus (Figure 4.13a), and anisotropy (not considered here) becoming close to the observed low Pn velocities (7.5–8.1 km/s, Hatzfeld et al., 1978; Calvert et al., 2000b). At sublithospheric mantle depths down to 150 km, lateral variations of seismic velocities result solely from the P-T conditions imposed by the lateral lithospheric thickness variations since the entire sublithospheric mantle has the same composition, except in the slab region. Below 150 km, P-wave velocities increase almost linearly with depth up to >8.7 km/s at 400

km depth. In the region of the detached Alboran slab, P-wave velocities increase by ~ 0.18 km/s as imposed from tomography models ($\Delta V_P = 2\%$) with a highest increase of ~ 0.3 km/s just above 400 km depth related to the olivine-wadsleyite phase transition (Figure 4.8).

Calculated S-wave velocities (Figure 4.12b) show a similar pattern than P-wave velocities but with a lesser influence of pressure such that, V_S decreases with depth from Moho to LAB all along the geo-transect. Likewise, changes in the composition domain show smaller effects on V_S than on V_P due to the lesser sensitivity of S-wave to composition (e.g., Kumar et al., 2020; Priestley and McKenzie, 2006). Below the LAB, V_S increases with depth delineating a low-velocity zone down to 200–250 km which is enhanced in magnitude in those regions affected by lithospheric thinning.

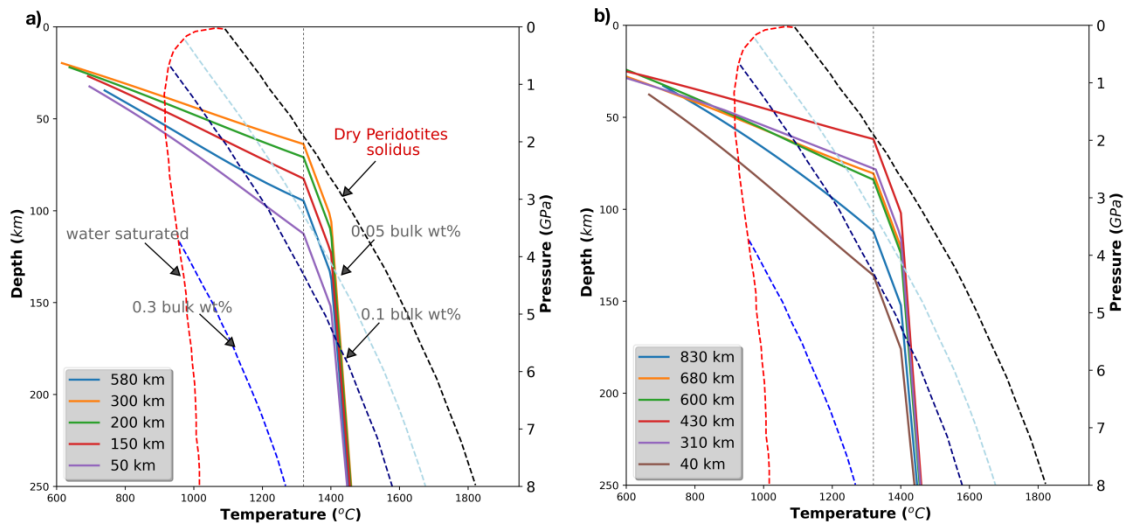


Figure 4.13 Geotherms (solid lines) at selected locations along the (a) Alboran Basin and (b) Algerian Basin geo-transects. Dry and wet peridotites solidus for different amount of bulk water from Katz and Spiegelman (2003) are also plotted. Presence of water in the mantle brings down the solidus resulting in presence of partial melts.

The Alboran slab shows an S-wave velocity increase of ~ 0.15 km/s (+3.5%) up to ~ 270 km resulting from the prescribed 2% P-wave anomaly. The resulting variation in the S-wave velocities below ~ 270 km is related to the implied temperature in the slab and increases to a maximum value ~ 0.30 km/s (+7%) at 400 km depth which is related to the olivine-wadsleyite phase transition (Figure 4.8). The calculated S-wave velocity pattern compares well with the regional S-wave tomography model projected onto the transect (Figure 4.1c) obtained by Palomeras et al. (2017) from Rayleigh surface-wave dispersion tomography.

In order to compare the computed mantle velocities with the P-wave travel-time tomography models, the lateral variations of P-wave in % (Figure 4.12c) are calculated relative to the reference column defined in LitMod2D_2.0 (Chapter 3; Kumar et al., 2020). The computed synthetic tomography reproduces the main pattern of slow and fast velocity regions observed in the global/regional P-wave tomography models (Bezada et al., 2013, Figure 4.1b) with minor discrepancies in the amplitudes. Note that the colour scale of the calculated tomography saturates in the regions of Moho depth < 35 km because of the used reference model, which consists of a 35 km crust (Kumar et al., 2020) and, highlights the crustal thinning as observed in the tomography model of Bezada et al. (2013) (Figure 4.1b).

Comparison with the passive seismological data

Broadband teleseismic earthquake waveform data recorded at stations shown in Figure 4.14 are downloaded from the IRIS-DMC (<https://ds.iris.edu/ds/nodes/dmc/>). Earthquakes in the epicentral distance range of 30° to 90° are used for P-wave receiver function calculations.

I use the following processing steps to calculate P-receiver functions:

- The three-component broadband earthquake waveform data are pre-processed by rotating the horizontal (north-south and east-west) components into radial and tangential directions to separate P-SV energy.
- Waveforms are cut 20s before and 60 s after the hand-picked arrival of P-wave on the vertical component.
- Waveforms are filtered using a low-pass Gaussian filter of width 2.5 with a corner frequency of ~ 1.2 Hz.
- Iterative time-domain deconvolution algorithm (Ligorria and Ammon, 1999) is applied to construct a spike train by cross-correlating the radial waveforms with the vertical waveforms. The spike train is then convolved with the observed vertical component waveform to produce synthetic radial component and is compared with the observed radial component in a least square manner. This step is repeated until a threshold least square fit is reached (chosen 0.001) or the maximum numbers of iterations are reached (200).
- The final P-wave receiver functions are assessed for quality by % fit of the calculated radian component to the observed radial component. I use waveforms with fit $> 80\%$ for further analysis.

This procedure is repeated for all stations along the Alboran Basin geo-transect (Figure 4.14). Then, I calculate the piercing point for all the calculated P-wave receiver functions at 35 km depth by back-projecting the traces using the ak135 velocity model and obtain a latitude and longitude for each receiver function at 35 km depth. Then, I stack all the receiver functions along the geo-transect within a 10 km distance bin along the profile and 25 km half-width window across the profile.

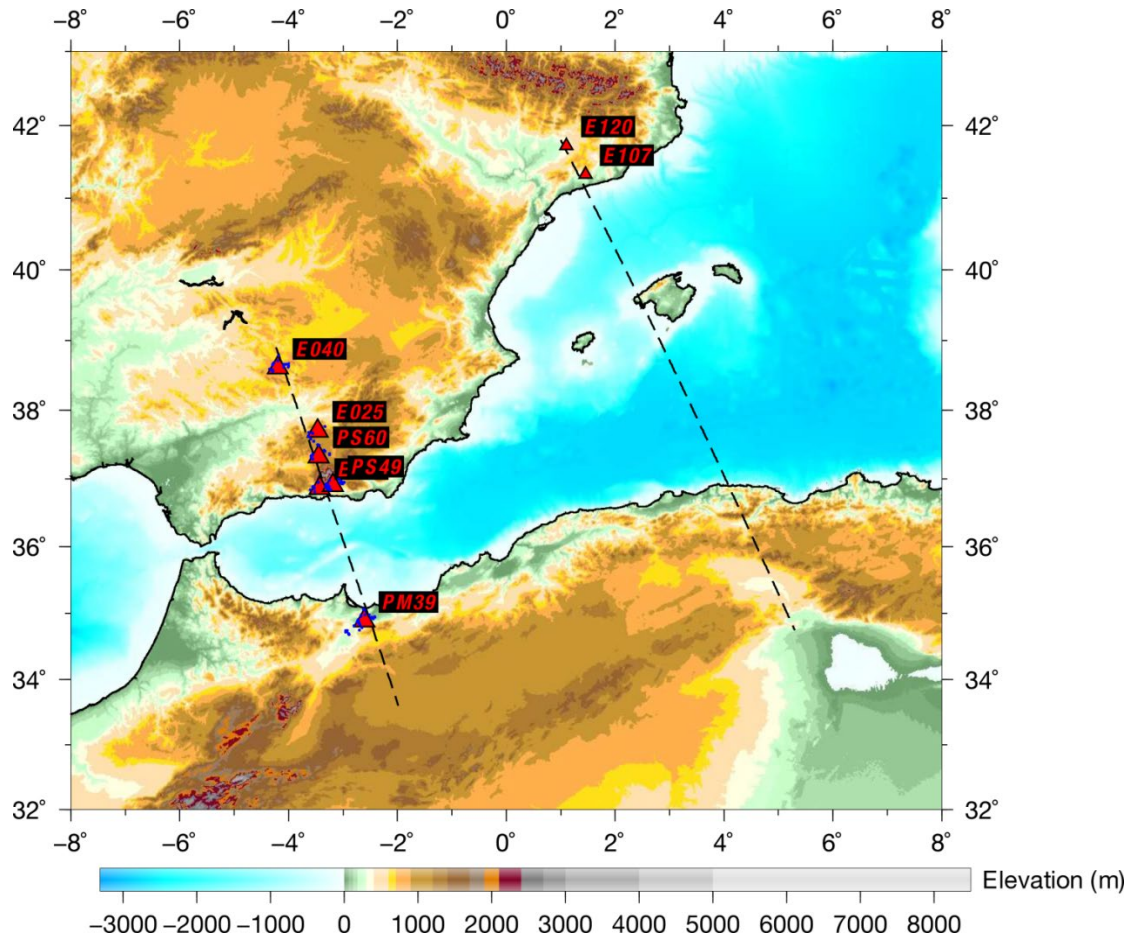


Figure 4.14 Location of the seismic stations along the geo-transects used to calculate P-wave receiver functions. Blue points show the location of piercing point at a depth 35 km along the Alboran Basin geo-transect.

Fundamental mode Rayleigh-surface-wave phase velocity tomography model from Palomeras et al. (2017) is used to extract dispersion curves along the Alboran Basin geo-transect. This tomography model uses data from 368 broadband seismic stations of permanent and temporary arrays in Morocco, Spain, Portugal, IberArray (2007-2013, Spain), and PICASSO (2009-2012) experiments. The model includes Ambient Noise Tomography between 4 s - 50 s periods to enhance the shallow depth structure

together with natural earthquake data in 20–167 s periods for deep structure until ~200 km. Note that the North Africa margin along the Alboran Basin geo-transect falls outside the good-ray-coverage/less-resolved region of Palomeras et al. (2017) (see their Figure 2)

Post-processing tool-box in the LitMod2D_2.0 (Chapter 3) is used to calculate synthetic the P-receiver functions and fundamental mode Rayleigh-surface-wave phase velocities from the S-wave velocity along the Alboran Basin geo-transect (Figure 4.12b). As I do not solve for phase equilibrium in the crust, the P-and S-wave velocities are calculated using empirical V_P -density relationships from Brocher (2005), and S-wave velocities in the crust are calculated assuming a constant $V_P/V_S = 1.73$ ratio (Figure 4.15a). In the lithospheric and sublithospheric mantle, seismic velocities from LitMod2D_2.0 are used (Figure 4.12b). Below 400 km depth (base of the model), velocities from the ak135 model are used.

Forward calculated P-wave receiver functions (Figure 4.15b, green) matches reasonably well with the observed P-wave receiver functions (wherever available, Figure 4.15b, grey). Some misfit can be seen, delay or advance of phases which can be attributed to the assumption of constant V_P/V_S ratio used here. V_P/V_S ratio should vary with depth at least in the Alboran Basin and Betics because of the HP/LT metamorphic and volcanic rocks (Figure 4.3a).

In case of Rayleigh-surface-wave phase velocity dispersion, forward predictions fit very well at long-periods (> 30 s), which are sensitive to the mantle velocity structure, for the Alboran Basin, Betics, and Iberian Massif regions (Figure 4.15c). For the North Africa margin (distance along profile < 225 km) synthetic phase velocities are consistently higher than observed ones (period 30–100 s) which can be attributed to less resolution for this region in the observed phase velocities, as mentioned before. Hence, S-wave velocities for the Alboran Basin geo-transect model are consistent with the available surface wave dispersion data in the upper mantle. Predicted higher phase velocities at the short-period (< 30 s) could be again explained by using a constant V_P/V_S ratio.

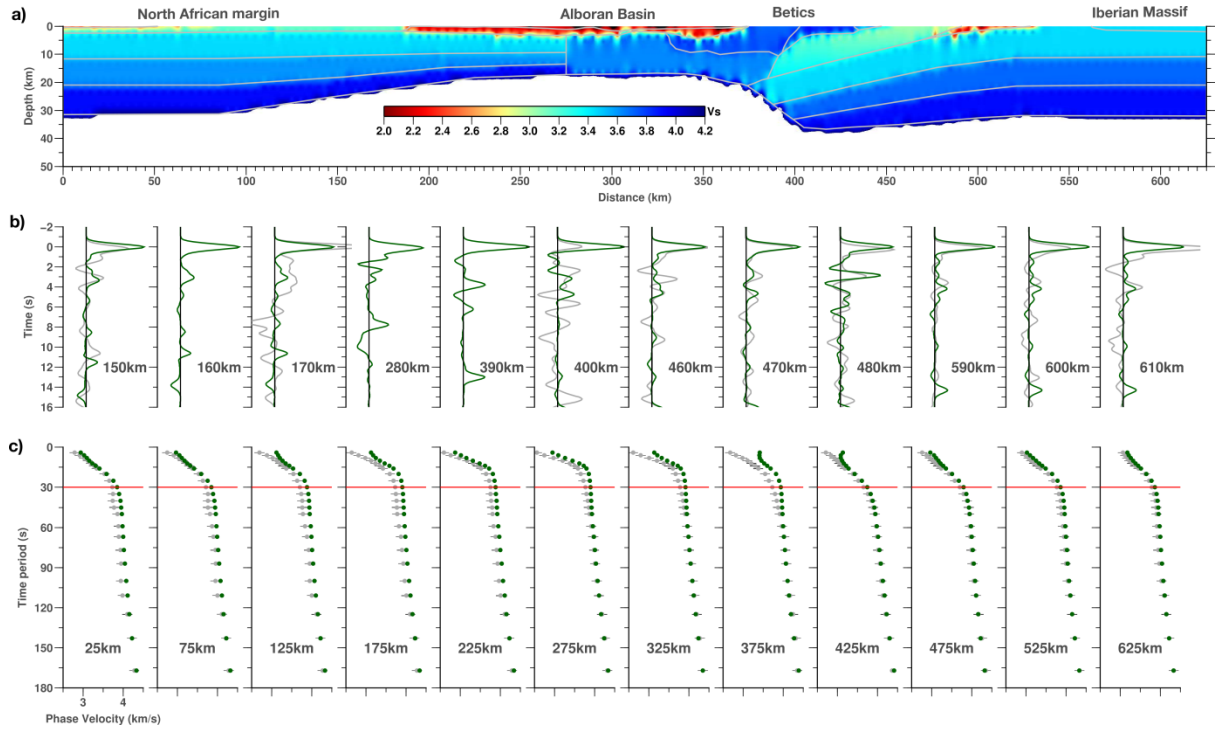


Figure 4.15 Plot showing the forward calculation of passive seismological data from the velocities obtained along Alboran Basin geo-transect. (a) Crustal S-wave velocities calculated using empirical relations (see text for details). (b) P-wave receiver function at distance, labelled in each plot, along the geo-transect. Solid green represent forward calculation and grey is observed P-wave receiver function (where available). (c) Rayleigh surface-wave fundamental mode phase velocity dispersion curves along the Alboran Basin geo-transect at distance along the geo-transect labelled in each plot. Grey circles represent the observed phase velocities and bars represent corresponding error. Green circles represent the forward calculation from the seismic velocity model obtained from LitMod2D_2.0.

Receiver functions are sensitive to depths of impedance contrasts (i.e., seismic velocity discontinuities), while surface wave dispersion curves are sensitive to the vertical averages of shear wave velocity. Joint inversion of the two data sets complements each other and provides better constrained S-wave velocity structure of the crust. S-wave velocities from integrated geophysical-petrological modelling can serve as the starting model, and joint inversion will allow better imaging of the crustal S-wave velocity structure. I note it to be one of the future directions to perform such joint inversion.

4.4.2. Algerian Basin geo-transect

Figure 4.12d shows the calculated P-wave mantle velocities along the Algerian Basin geo-transect. As in the Alboran Basin geo-transect, the lower velocities are found at LAB levels in regions affected by lithospheric thinning including the Algerian

Basin, the Balearic Promontory and the Valencia Trough. In these regions, V_P decreases from 7.90–7.95 km/s beneath the Moho to < 7.9 km/s at LAB depths with the lowest value along the whole geo-transect (< 7.8 km/s) being at the Algerian Basin. The calculated uppermost mantle velocities are slightly higher than the reported P_n velocities in the Valencia Trough and the Algerian Basin, ranging from 7.7 km/s to 7.95 km/s (Torne et al., 1992; Dañobeitia et al., 1992; Vidal et al., 1998). Note that I do not include the effects of melt; hence, calculated velocity will further decrease as the geotherm in Algerian Basin is intersecting the mantle solidus (Figure 4.13b). Towards the Iberian and African margins (Catalan Coastal Ranges and Greater Kabylies, respectively), P-wave velocities increase laterally showing almost constant values with depth. Beneath the thicker lithosphere of the Tell-Atlas Mountains, P-wave velocities increase with depth from 7.9 km/s at the Moho to 8.1 km/s at the LAB, being slightly higher than in the Algerian Plateau lithosphere (Figure 4.12a). Down to ~ 150 km depth, the effect of lithosphere thickness is reflected in P-wave velocities where the thin lithosphere of the Algerian Basin results in a low velocity zone, similar to that in the Alboran Basin, extending towards the Balearic Promontory and the Valencia Trough. Below this depth, P-wave velocities are essentially depending on pressure increasing mostly linearly with depth up to > 8.7 km/s at 400 km depth. In the region of the detached Algerian slab, P-wave velocities are increased by ~ 0.18 km/s ($\sim 2\%$) and near the base of the slab (400 km) increase to as high as 0.30 km/s ($> \sim 3\%$) because of the olivine-wadsleyite phase transition (Figure 4.14).

S-wave velocities also show a low velocity zone extending from mid-lithospheric mantle levels to 200–250 km depth being more pronounced beneath the Algerian Basin, the Balearic Promontory and the Valencia Trough due to the prevalence of temperature effects on pressure effects in these regions (Figure 4.9e). Minimum values of S-wave velocities (≤ 4.35 km/s) are obtained at the base of the lithosphere along the thinned lithosphere regions, whereas beneath the Africa and Iberia mainland, minimum S-wave velocities exceed 4.45 km/s. The region corresponding to the detached Algerian slab, is characterized by an average increase of S-wave velocity of ~ 0.16 km/s in agreement with the prescribed anomaly of $\Delta V_S = 3.5\%$. The computed synthetic P-wave tomography (Figure 4.12f) shows negative V_P anomalies of less than -2% beneath the Algerian Basin and the Valencia Trough, in agreement to regional and global P-wave tomography models (e.g., Amaru, 2007; Piromallo and Morelli, 2003; Spakman and Wortel, 2004). The detached Algerian slab is characterized by a positive V_P anomaly of $\sim 2\%$ resulting from the prescribed V_S anomaly ($\Delta V_S = 3.5\%$; Fichtner and Villaseñor, 2015).

Comparison with the passive seismological data

There is a lack of passive seismic data along most of the Algerian Basin geo-transect (Figure 4.14); hence in this section, I compare the synthetic receiver functions and Rayleigh surface-wave dispersion curves in the Algerian and Alboran basins, and in the regions of subducted slabs (Figure 4.16).

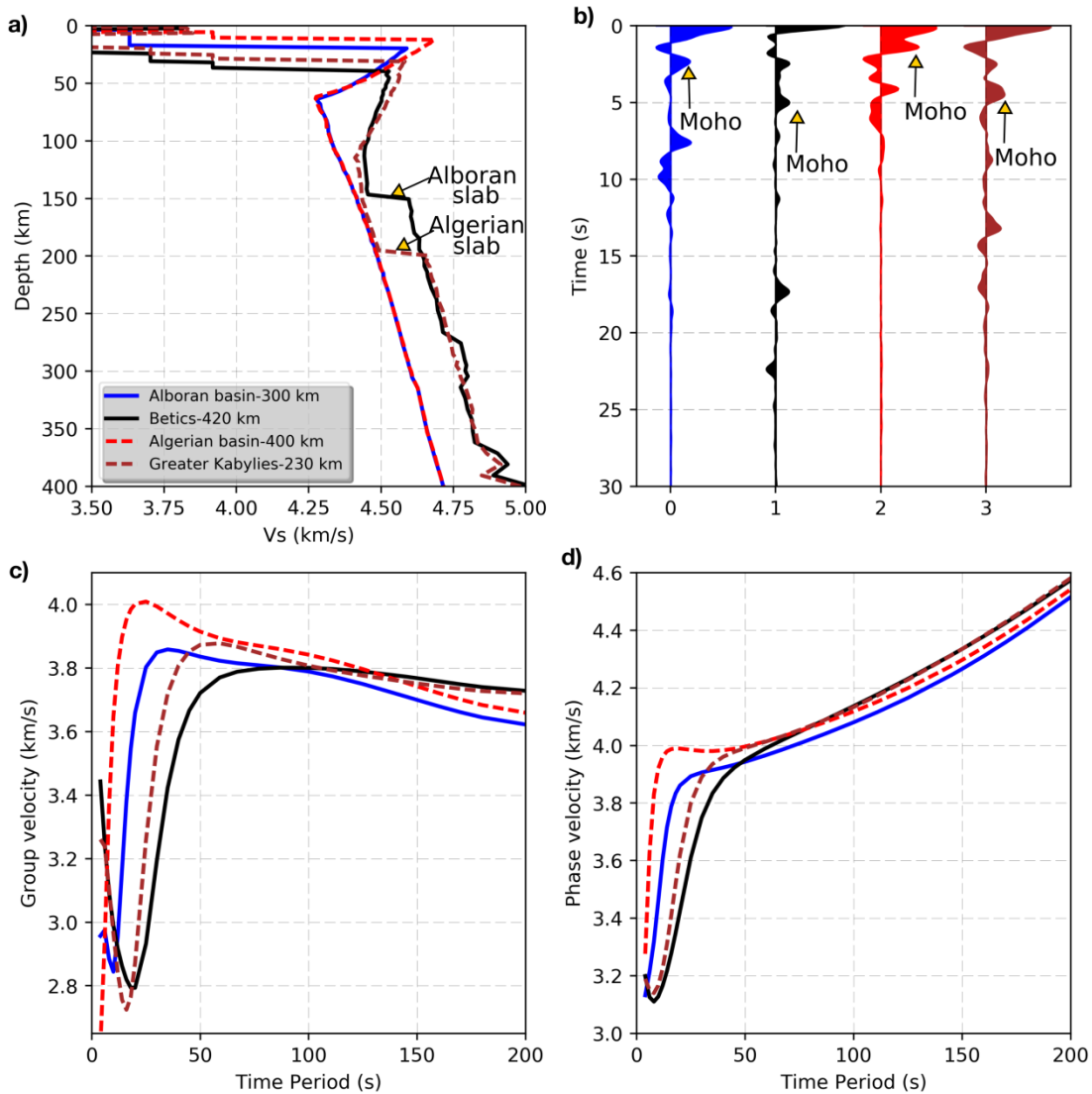


Figure 4.16 Plot showing the comparison between forward prediction of receiver functions and Rayleigh surface-wave dispersion curves at selected locations. (a) Shows the depth distribution of S-wave velocities colour coded for location (see the legend). (b) P-wave receiver function, (c) group velocities, and (d) phase velocities colour coded for location (see legend in a).

Both the P-wave receiver functions and Rayleigh surface-wave dispersion curves show distinctive features at the selected locations (Figure 4.16). The effect of

thin crust and higher seismic velocities in the Algerian Basin is clearly reflected by the early arrival of Moho converted phase (P_s) compared to the delayed arrival in the thicker Alboran Basin (Figure 4.16b). The P-wave receiver functions for the Betics and Greater Kabylies show much delayed Moho converted phase in comparison to the Algerian and the Alboran basins, though that of the Betics is slightly more delayed than that of the Greater Kabylies because of the thicker crust in the Betics. Phases before the Moho phase reflect the three-layered continental crust considered beneath the Betics and the Greater Kabylies. Rayleigh surface-wave dispersion curves at low periods (< 50 s) show a distinct pattern, being highest in the Algerian Basin and lowest in the Betics reflecting the highest and lowest S-wave velocities pattern at crustal depths, respectively (Figure 4.16a). Both, the group and phase velocities, shows higher values at longer periods (> 100 s) reflecting the increased S-wave velocities in the sublithospheric mantle because of the Alboran and Algerian slabs.

CHAPTER 5

Discussion

Chapter 5

Discussion

The observed sublithospheric mantle positive seismic velocity anomalies beneath the Betics-Rif and the north-Algeria margin in the Western Mediterranean motivated this thesis. These anomalies are qualitatively interpreted as the subducted Ligurian-Tethys lithosphere, which is one of the constraining basis for the geodynamic evolution models of the Western Mediterranean. In general, such anomalies are understood qualitatively as colder than average mantle in case of positive seismic velocity anomalies, or as hotter in case of negative seismic velocity anomalies. A quantitative physical interpretation (thermal and/or compositional) of sublithospheric mantle anomalies is challenging and is required to understand the geodynamic and geological processes. In the first part of this thesis, I improved an already existing tool, LitMod2D_1.0, to LitMod2D_2.0 to model such seismic velocity anomalies to quantitatively infer them in terms of temperature and/or composition using thermodynamically self-consistent integrated geophysical-petrological modelling approach. In the second part of the thesis, I applied the improved LitMod2D_2.0 to model the present-day crust and upper mantle (up to 400 km depth) structure of the Betics-Rif and Kabylies-Tell-Atlas orogenic systems along two geo-transects crossing the Alboran and Algerian back-arc basins and their opposed margins of North Africa and Iberia, respectively.

In this chapter, I first present the discussion on the methodological developments in the improved LitMod2D_2.0. Then, I compare and discuss the results of present-day crust and upper mantle structure derived using improved LitMod2D_2.0 in the Alboran and Algerian Basin geo-transects. The results are discussed in terms of the geodynamic implications for the closure of the Jurassic Ligurian-Tethys Ocean and the opening of the new oceanic and thinned continental domains of the Algerian and Alboran back-arc basins in an overall convergence regime that has lasted for the past 85 My involving the African and European plates.

5.1. LitMod2D_2.0

The improved LitMod2D_2.0 software has been presented in Chapter 3, which allows studying the temperature, density (i.e., chemical composition), and seismic velocities of the crust and upper mantle, including thermal, chemical, and seismic-velocities anomalies in the sublithospheric mantle. The discussion related to each improvement is already included in Chapter 3. In the following paragraphs, I will mainly discuss the assumptions made in LitMod2D_2.0 and how they can be relaxed in future.

The integrated geophysical-petrological modelling in LitMod2D_2.0 assumes thermal steady-state regime without advection. Although this assumption is valid for old tectono-thermal regions (>100 Ma) it is less valid in regions with recent tectonic deformation (e.g., in Western Mediterranean where tectonic deformation is Cenozoic). Despite this, the modelling results are constrained by the simultaneous fitting of a set of “instantaneous” density-dependent observables such as gravity, geoid and elevation. Hence, the results must be considered as a snapshot of the present-day density distribution related to active tectonic processes. In regions affected by thermal relaxation after lithospheric thinning, the actual temperature at Moho depth levels is higher than the calculated assuming thermal steady-state because the mass deficit associated with the transient thermal perturbation must be compensated by a larger lithospheric thickness to keep elevation. Therefore, steady-state modelling tends to underestimate the Moho temperature and overestimate the actual lithospheric thickness in regions of lithospheric thinning, showing the opposite effects where the lithosphere is thickened (Fullea et al., 2007). Temperature and density distribution could be improved using a transient thermal model but this requires a more sophisticated numerical approach (i.e., solving the diffusion and advection terms in heat flow equation with time) and, more importantly, an in-depth knowledge of the past and ongoing geodynamic processes and particularly their evolution through time.

LitMod2D_2.0 integrates data across disciplines to put integrated constraints on the present-day structure but makes it challenging to put uncertainties introduced from the errors in the used parameters (e.g., thermodynamic database, Moho depths, and LAB depths). A formal solution to put uncertainties on the final results, noted to be one of the future directions, would be to formulate the modelling in an inversion scheme as recently done in the 3D versions of LitMod (LitMod_4INV; Afonso et al., 2013a, b and 2016b) at the cost of computation resources. Although, inversion algorithms allow an exhaustive sampling of the parameter space, they still need an

initial model and appraisal of the inversion results, requiring additional information (e.g., geology of the study area). However, an ad-hoc procedure can be applied by iteratively changing the parameters of interest to study their sensitivity as done in composition of subducted slabs and lithospheric mantle in Chapter 4.

Surface topography has contributions from three fundamental processes: isostasy, flexure and dynamic flow in the mantle. Decoupling the individual contribution of these three processes to the surface topography is fundamental to understand landscape evolution and facilitates linking deep Earth processes to surface processes. LitMod2D_2.0 does model the isostatic and flexural component of the topography but does not model the dynamic component (also known as dynamic topography) explicitly, which is most likely to be present in tectonically active areas (e.g., subduction zones). In cases where upper mantle anomalies are detached from the overlying lithosphere, LitMod2D_2.0 calculates coupled elevation by accounting for the density variations from anomalous regions, which together with the uncoupled elevation (i.e., isostatic elevation) can serve as lower and upper bound for the dynamic topography, respectively. A more complete treatment of the problem would require using the density and viscosity distribution, calculated as a function of pressure, temperature and composition from LitMod2D_2.0 to solve the Stokes flow equation for the whole modelling domain. The resulting normal stresses at the surface or at the base of the lithosphere will allow calculating a more realistic dynamic topography contribution (e.g., Afonso et al., 2016b). Integrating a Stokes flow solver in the post-processing LitMod2D_2.0 tool-box is one of the future directions.

5.2. Present-day crust and upper mantle structure of the Alboran and Algerian basins and their margins

5.2.1. Crustal and lithospheric structure

The multiple seismic surveys carried out in the study region allowed me to have a good constraint on the Moho depth along most of the sections of both the Alboran and Algerian basins geo-transects (Figure 4.3). The sections that are less constrained are the Algerian Plateau, the Tell-Atlas Mountains and the Greater Kabylies where deep seismic data are not available.

To overcome the uncertainties associated with seismic data and its uneven coverage, I have considered that the crust of the Iberia and Africa mainland consists of three layers, namely upper, middle and lower crust, plus a sedimentary cover. The geometry of these crustal layers responds to the density variations required to fit the observables (Bouguer anomaly, geoid, and elevation) and to tectonic criteria. The structure of the Betics and Greater Kabylies is more complex and differs noticeably from previous lithospheric cross-sections (e.g., Frizon de Lamotte et al., 2004; Roca et al., 2004; Carballo et al., 2015a, b). In these regions, I have included exhumed high-density metamorphic rocks of the Internal Units overthrusting the folded External Units that belonged to the former passive margins (see latter in Geodynamic implications section). Across the Alboran Basin, main differences with previous sections are due to the incorporation of recent interpretations of seismic data (Gómez de la Peña et al., 2018) that led me to consider a thin and highly intruded continental crust in the north Alboran margin transitioning to a magmatic crust in the central part of the Alboran Basin. Seismic data suggest a sharp transition in the centre of the basin (Alboran Ridge), separating the magmatic crust domain from the thinned north-Africa continental crust domain, which continues towards the Africa mainland.

After incorporating these changes, the Moho depth obtained from the models is generally within the uncertainty bounds of seismic data and follows similar trends of previous studies with some localized differences in the margins of the Alboran and Algerian basins and the Valencia Trough (Figure 4.3). Moho depth is a major physical and chemical discontinuity which is imaged by modelling the data sensitive to physical properties, i.e., seismic velocities and density. P-wave receiver functions are routinely used to determine the depth of this contrast using standard H-k stacking method (Zhu and Kanamori, 2000). In H-k stacking, depth of the Moho (H) is determined by assuming an average $V_P/V_S(k)$ for the crust and fitting the arrival time of the Moho converted phase and associated reverberations valid for the isotropic velocity structure. Note that P-wave receiver functions are also sensitive to the intra-crustal structure (e.g., dipping layers) and anisotropy which is not considered in H-k stacking method. Indeed, noticeable discrepancies on Moho depths derived from receiver functions (Diaz et al., 2016) are observed beneath the Betics, which can be attributed to the presence of intra-crustal dipping layers with varying V_P/V_S ratio with depth, and to a heterogeneous crustal structure (Figure 4.3).

Figures 4.5e and 4.9e compare the calculated LAB depths to that reported from other modelling approaches and techniques showing that although there is coincidence with the main trends of lithospheric thickness variations, there are also

pronounced discrepancies in the LAB depth values. Along the Alboran Basin geo-transect, the LAB depth beneath the Iberian Massif, the Betics Mountains and the north Alboran margin is consistent with previous models based on potential field modelling and thermal analysis (Torne et al., 2015) and 2D geophysical-petrological modelling (Carballo et al., 2015b), though our LAB depth values are consistently shallower. These discrepancies in LAB depth ($< 15\%$) are related to the different modelling approach and the simplified crustal structure used in Torne et al. (2015), and differences in the geometry of intra crustal bodies beneath the Betics and the chemical composition of the upper mantle used in Carballo et al. (2015b).

Discrepancies with the LAB depth derived from the 3D geophysical-petrological model by Fullea et al. (2010) are noticeably larger (Figure 4.5e). The LAB proposed by Fullea et al. (2010) beneath the Betics and the north-African margin is much deeper in comparison, with a similar lithospheric thinning below the Alboran Basin affecting a narrower region. These discrepancies may be related to the simpler crustal structure considered by these authors, differences in crustal thickness and chemical compositional domains in the Alboran Basin lithosphere (PUM instead of DMM-6%) and sublithospheric mantle (PUM instead of DMM), and lack of the radiative contribution in calculating the mantle thermal conductivities. The LAB depth beneath the north African margin derived from combined elevation and geoid modelling by Globig et al. (2016) is also noticeably higher (Figure 4.5e) due to the different approach used by these authors, yielding a > 5 km thicker crust in this region (Figure 4.3a).

The LAB depth proposed by Palomeras et al. (2017) from surface wave tomography shows a similar lateral trend with consistently shallower depths that roughly follows the 1000 ± 50 °C isotherm, except beneath the Betics where the LAB is deeper coinciding with the high velocity anomaly related to the Alboran slab (Figure 4.5e). Seismically, the LAB is defined as a low-velocity layer and in Palomeras et al. (2017) it is derived from the depth of the negative S-wave velocity gradient and, therefore, is a proxy of the base of the high-velocity mantle lid. A major misfit occurs at the central part of the Alboran Basin, where the seismically derived LAB is at 250 km depth. Although the precise determination of the LAB depth depends on how it is measured (Eaton et al., 2009), the different definitions should show a similar trend as they all are imaging the rheological strong outer layer of the Earth.

Along the Algerian Basin geo-transect, the only previous works extending along the whole profile are from Roca et al. (2004), based on a pure-thermal

integrated geophysical approach with a temperature-dependent lithospheric mantle density; and Carballo et al. (2015a), based on an integrated geophysical-petrological methodology. Both works show similar results from the Catalan Coastal Ranges to the southern margin of the Algerian Basin, which are also roughly coincident with the model presented in this thesis, despite the methodological differences (Figure 4.8e). It is worth noting that beneath the Algerian margin and the Greater Kabylies region none of the previous works, including Globig et al. (2016) for Africa mainland, considered the presence of a detached Ligurian-Tethys slab segment (i.e., Algerian slab, Figure 4.1d). Despite of that, main discrepancies are found regarding to the work by Carballo et al. (2015a), who proposed a LAB depth up to 60 km shallower than that proposed in this thesis beneath the Greater Kabylies, whereas discrepancies with Roca et al. (2004) and Globig et al. (2016) amount less than 20–25 km. The method used in Carballo et al. (2015a) is similar to the approach used in this thesis; however, calculation of mantle thermal conductivity including the radiative contribution was still not included. Therefore, differences in the LAB-depth can be mainly attributed to small differences in the calculated mantle thermal conductivity, but also to the crustal structure differences (Figure 4.3b) and to the positive seismic velocity anomaly beneath north Algeria (Figure 4.1d) resulting in a deeper LAB in this part of the geo-transect.

5.2.2. Mantle composition

Identifying bulk mantle composition based on density and seismic velocities is not straightforward because of the highly non-linear nature of the problem and the lack of uniqueness. Based on a non-linear 3D multi-observable probabilistic (Bayesian) inversion, Afonso et al. (2013a, b) showed that a wide range of compositions can, equally well, explain multiple geophysical data. In consequence, the considered mantle chemical compositions compatible with the geophysical observables needs further appraisal based on the geological history of the study region.

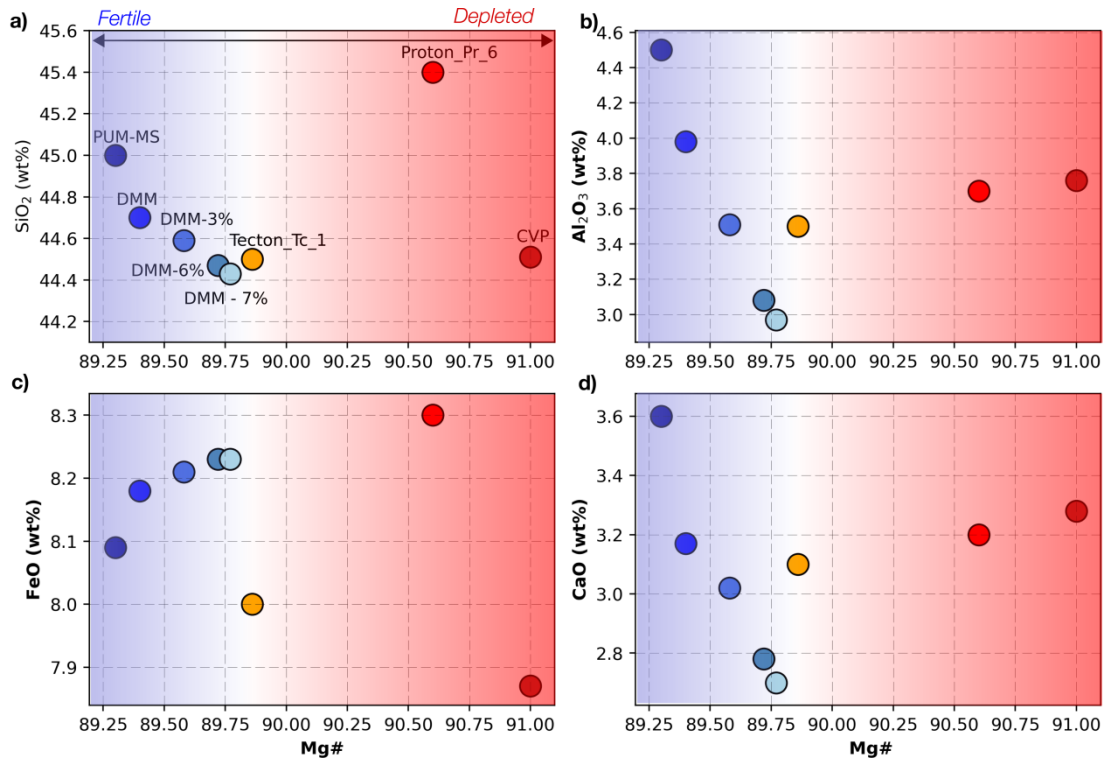


Figure 5.1 Major element oxide weight% of the upper mantle compositions (Table 4.2) are plotted as function of Mg#, a measure of the fertility of the mantle. PUM-MS is also plotted for comparison. Blue shaded region represents the oceanic lithospheres and red shaded area the continental lithospheres.

DMM composition and its derivatives (Table 4.2) show correlation between #Mg and major oxides as a function of the percentage of melting indicating progressive depletion (Figure 5.1). The mantle compositions used in the onshore lithospheres (i.e., continental lithospheres), though have higher #Mg, does not follow the depletion trend as the derivatives of DMM, suggesting that these compositions might have experienced refertilization through metasomatism events, as they are geologically much older than the oceanic lithosphere. CVP composition has been reported to be refertilized indicating mixing between asthenospheric mantle and deeply recycled enriched mantle from oceanic subduction (e.g., Bianchini et al., 2010; Villaseca et al., 2010). High CaO and Al₂O₃ content in the Average Proton Lherzolite (Pr_6) has been reported to be representative of Phanerozoic reworking of Proterozoic to Archean crust (Griffin et al., 2009). Interestingly Average Garnet Tecton (Tc_1) lies near the transition between DMM derivative compositions to continental composition suggesting its juvenile nature because of the moderate depletion from the primitive upper mantle (Griffin et al., 2009).

Although lithospheric mantle compositions in Table 4.2 show small variations in major oxides and #Mg space (Figure 5.1), the computed stable minerals in the models show noticeable differences in the mantle (Figures 5.2 and 5.3). Variation in weight% of each mineral is a function of pressure-temperature and elements these minerals can accommodate in their lattice structure, hence, the bulk mantle composition (Table 2.2).

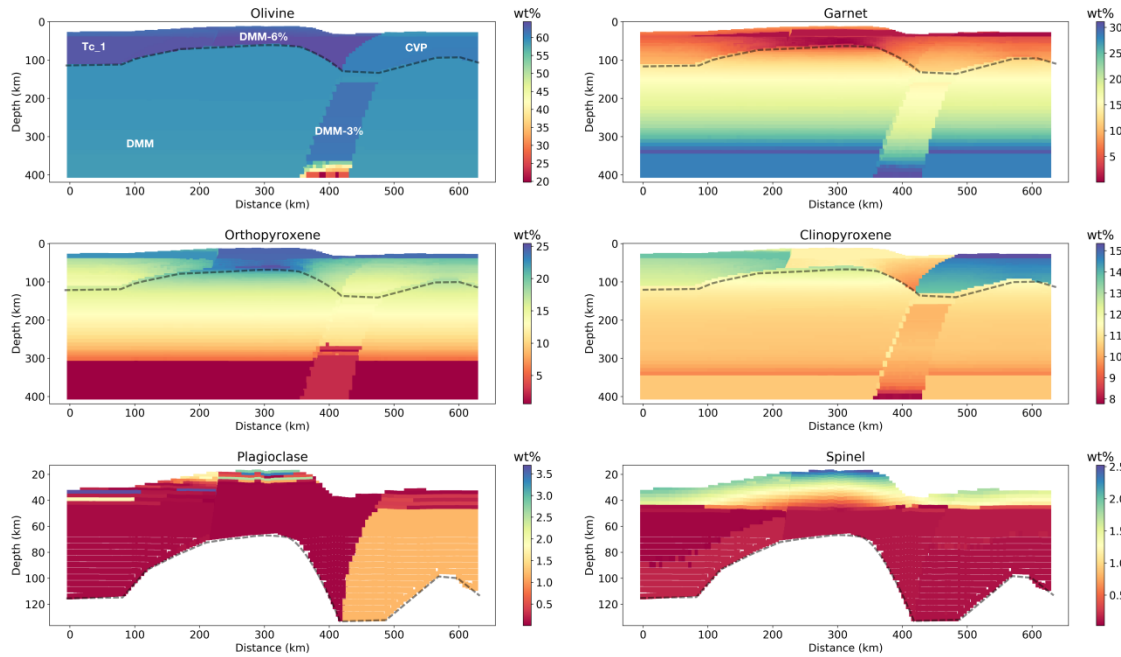


Figure 5.2 Depth distribution of weight% of the stable minerals (see the title of each subplot) along the Alboran Basin geo-transect computed from the Gibbs-free energy minimization. Dashed light black line indicates the LAB and text in white colour indicates the chemical composition listed in the Table 4.2.

In the lithospheric mantle, different compositional domains show variation in weight% of the minerals (Figures 5.2 and 5.3). Plagioclase and spinel are stable at shallow mantle depths and accommodates Al, Ca and Na, hence, there is low weight% of garnet at shallow depths. The regions with thin lithosphere (i.e., Alboran and Algerian basins, Valencia Trough, Balearic Promontory) shows higher weight% of plagioclase and spinel whereas regions corresponding to thick lithosphere (i.e., onshore Iberia and Africa) shows relatively higher weight% of garnet because of the resultant pressure-temperature conditions. Olivine, orthopyroxene, and clinopyroxene also show variations laterally, as well as, with depth. Lateral variations in the mineral weight% occur because of the different compositional domains defined in the lithospheric mantle. Depth-wise variations in the mineral weight% are stronger in the

regions of thin lithosphere in the Western Mediterranean in comparison to the thick lithosphere in the onshore regions.

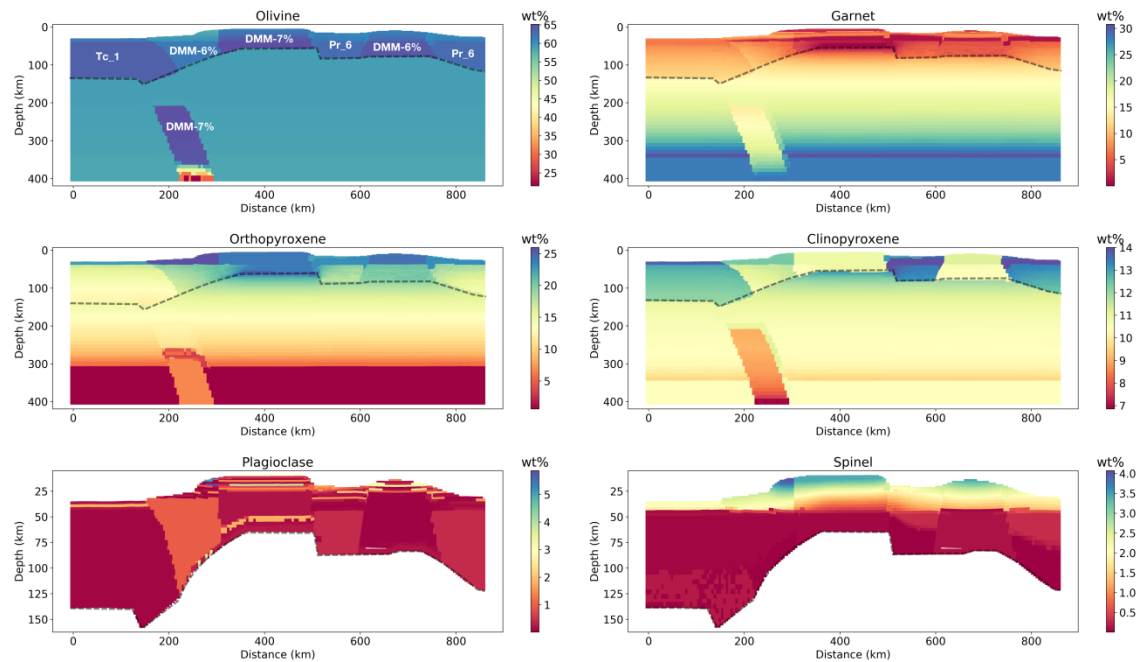


Figure 5.3 Depth distribution of weight% of the stable minerals (see the title of each subplot) along the Algerian Basin geo-transect computed from the Gibbs-free energy minimization chemical compositions used in the mantle. Rest of the caption as in Figure 5.2.

Sublithospheric mantle shows, except in the slab regions, a rather constant distribution of olivine and a varying distribution with depth of garnet, orthopyroxene, and clinopyroxene. A major change in the weight% of these minerals occurs at ~310 km depth, where garnet weight% increases while that of orthopyroxene decreases. This is because both the garnet and orthopyroxene can accommodate Al and increasing the stability of one of them results in decreasing the other (Table 2.2). The variation of minerals weight% in the slab regions is mainly related to the colder temperature and different chemical composition relative to that of the ambient sublithospheric mantle. A clear example of such variation is the decrease in the olivine weight% at ~400 km, indicating transformation to its denser polymorph, wadsleyite (Figure 2.2).

Al_2O_3 , FeO , and SiO_2 are three main oxides primarily controlling the physical properties (i.e., density, P-wave velocity, S-wave velocity) of the mantle. The amount of Al_2O_3 controls the amount of the high-density-velocity Al phases (i.e., spinel - shallow mantle, garnet - deep mantle), which in turn exerts a first-order control on the

physical properties of the bulk mantle. FeO controls the bulk physical properties of all dominant phases, olivine and pyroxene and their relative proportions are controlled by the SiO₂ content. Hence, the variations in weight% of individual minerals will affect the relevant bulk rock physical properties as they are calculated by taking in account the individual mineral abundance (Equations 2.29 and 2.35) and the physical properties are different for each mineral (Figure 5.4). Garnet shows highest density as well as both the P-and S-wave velocities in the upper mantle. Orthopyroxene shows the least density and increases progressively for: clinopyroxene, and olivine. For the seismic velocities, both the P-and S-wave, this trend breaks and clinopyroxene shows the least values and increases for olivine and orthopyroxene. Variation in the individual minerals weight% in the slab regions (Figures 5.2 and 5.3) causes the second order variations of density and P-and S-wave velocities (Figures 4.8 and 4.11). As pointed out in Chapter 4, Section 4.3.2, at 400 km depth the Alboran slab shows a higher density change than the Algerian slab, which is due to the higher amount of garnet in the case of the Alboran slab (Figures 5.2 and 5.3) as DMM-3% composition has higher amount of Al₂O₃ than DMM-7% (Figure 5.1).

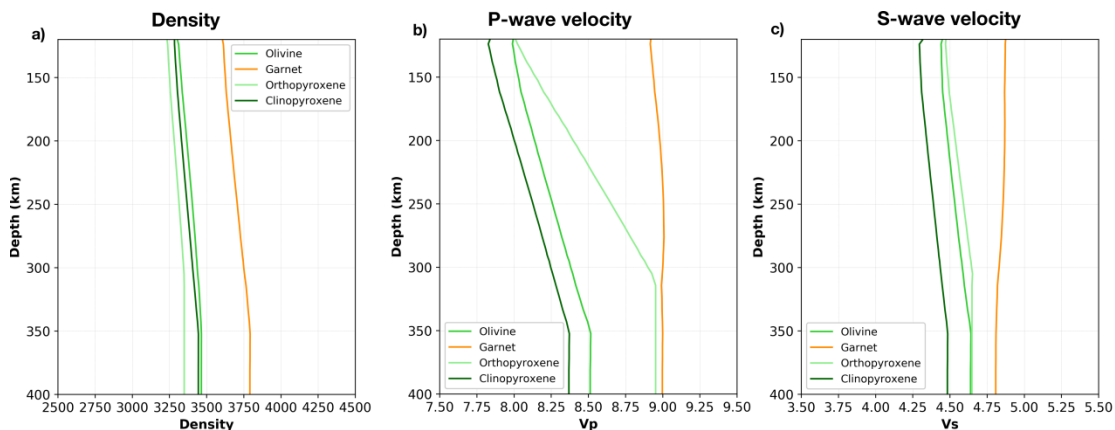


Figure 5.4 Plots showing depth variation of (a) density, (b) P-wave velocity, and (c) S-wave velocity for different minerals present in the mantle.

The bulk density of DMM derivative compositions (e.g., DMM-3%, DMM-6%, DMM-7%) decreases with depletion or in other words with increasing #Mg; however, this trend breaks for the continental lithospheric mantle compositions (Figure 5.5a). Interestingly, Al₂O₃ shows a positive correlation with density for all the compositions used here, since it controls the abundance of the high-density mineral garnet (Figure 5.4), serving as a metric for mantle fertility (Afonso et al., 2013a) (Figure 5.5b). Seismic velocities show a decreasing trend with increasing #Mg, though the

magnitude of its variation among the compositions used is within <0.1 km/s for the P-wave velocities and < 0.04 km/s for the S-wave velocities (Figures 5.5c and d), which is contrary to the positive correlation between #Mg and seismic velocities (Griffin et al., 2009). Note that the mantle compositions I used here are skewed to the lower #Mg values, so the dichotomy in density versus #Mg and decreasing seismic velocities with Mg# for DMM derivatives and continental compositions might not be representative of the mantle composition variability. Afonso et al. (2010), using global database of garnet and spinel peridotite xenoliths (#Mg range ~88 to 95), have shown negative correlation between density and #Mg whereas positive correlation between seismic velocities and #Mg.

Although there is no univocal relationship between mantle chemical composition and its density and elastic properties, the considered lithospheric mantle compositions can be related to major geodynamic processes operating in the Western Mediterranean, which are dominated by subduction of the Ligurian-Tethys Ocean. Subduction processes can modify the mantle chemical composition by incorporating fluids and sediments carried by the subducting slab resulting in chemical enrichment by metasomatism (Ringwood, 1974; Spandler and Pirard, 2013). At the same time, mantle flow generated during subduction can produce melting by adiabatic decompression which will deplete the sublithospheric mantle (Magni, 2019). Generally, volcanic rocks produced from mantle melting show the geochemical signatures similar to the environment in which they are produced. However, interactions of magmas with crustal rocks during ascent and emplacement can influence their geochemical signature. Melchiorre et al. (2017) using Principal Component Analysis (PCA) applied to the Western Mediterranean volcanism concluded that the subduction-related (i.e., orogenic) volcanism shows a greater compositional variability than the intraplate (i.e., anorogenic) volcanism. Compositional variation in orogenic volcanism is associated with the extensive recycling of geochemically different lithologies producing large heterogeneities in the lithospheric mantle (Melchiorre et al., 2017). The large variability of volcanic chemical composition in the Mediterranean region impedes to assign a unique genetic origin to the volcanism and it has been interpreted as the interaction of multiple processes as mentioned by many authors (e.g., Lustrino et al., 2011; Duggen et al., 2008; Melchiorre et al., 2017).

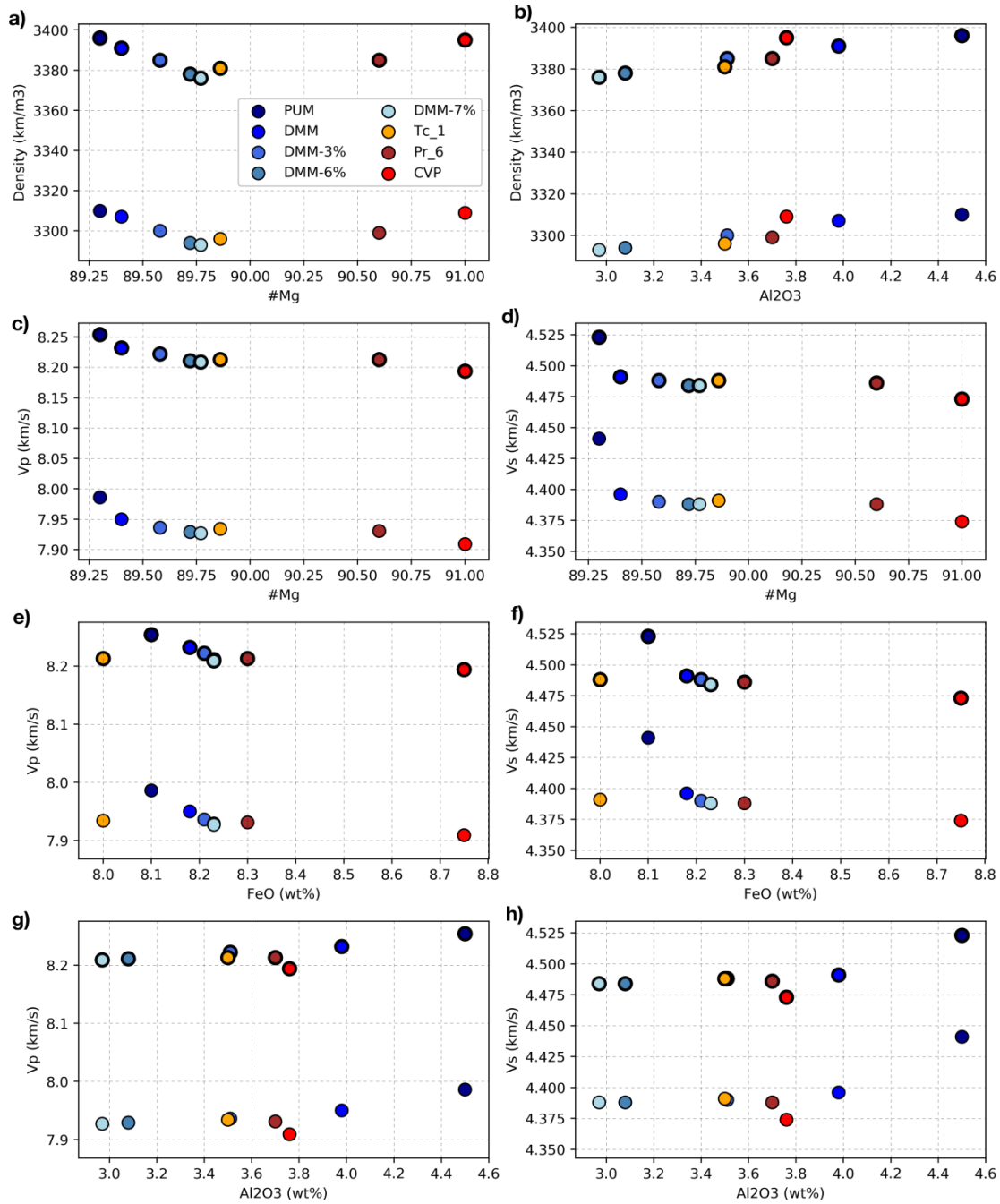


Figure 5.5 Plots showing variation of relevant physical properties with #Mg and major oxide weight percentages for the composition in Table 4.2, colour coded in (a). (a) Shows variation of density with #Mg and (b) with Al₂O₃. (c) - (h) show variation of P-wave and S-wave velocity with #Mg, FeO, Al₂O₃. Circles with thin-black outline corresponds to $P = 3$ GPa (~ 100 km) and $T = 1300$ °C, and circles with thick black outline corresponds to at $P = 6$ GPa (~ 200 km) and $T = 1400$ °C (listed in Table 4.2).

The lithospheric mantle composition of the offshore segments is related to their back-arc origin and the degree of partial melting expected from the nature and volume of magmatic events. During slab roll-back the space opened between the trench and the upper plate is replaced by fertile sublithospheric mantle with DMM composition that

will undergo partial melting by adiabatic decompression. The Algerian Basin shows a typical oceanic crust of 6 km thickness (Booth-Rea et al., 2007) which corresponds to a ~7% of sublithospheric mantle melting and hence to the DMM-7% composition (Klein and Langmuir, 1987; Workman and Hart, 2005). However, in the Valencia Trough and the Alboran Basin melting was less extensive producing large magmatic intrusions and volcanism, hence a DMM-6% composition is more likely. These subtle differences in the chemical composition of the lithospheric mantle respond to geodynamic criteria that require a depleted DMM composition and allow fitting the geophysical observables. Moreover, compositions in the offshore lithospheric mantle also reproduce the seismic velocities derived from seismic data (see Chapter 4, section 4.4).

In the models presented in this thesis, the lithospheric mantle beneath the Betics and Greater Kabylies is fertile compared to the Iberian and North African lithospheric mantle (Figures 4.5 and 4.9). This suggests that continental basement beneath the South Iberia and North Algeria is not attached to the continental lithospheric mantle and indicates the delamination of the continental lithospheric mantle during collision of the retreating slabs with the passive margins. The Alboran Basin geo-transect runs across the zone where the Iberian lithosphere has been interpreted to be delaminated, and the Alboran slab has broken off, whereas to the west delamination has not been achieved, and slab-tear is in progress (Mancilla et al., 2015), as is manifested by the lack of lithospheric mantle level earthquakes in the eastern Betics (depth 60–100 km) (Figures 4.1). A similar situation occurs in the Algerian Basin geo-transect beneath the Greater Kabylies.

In order to test the implied delamination and replacement by the relatively fertile sublithospheric mantle (DMM) beneath the Betics and Greater Kabylies, I run models where composition of the mantle beneath the Betics and Greater Kabylies is changed to as that of the continental lithosphere and LAB depths varies smoothly towards the back-arc basins (Figures 5.6 and 5.7). These models results in a noticeable misfit in geoid height in the Betics and Greater Kabylies.

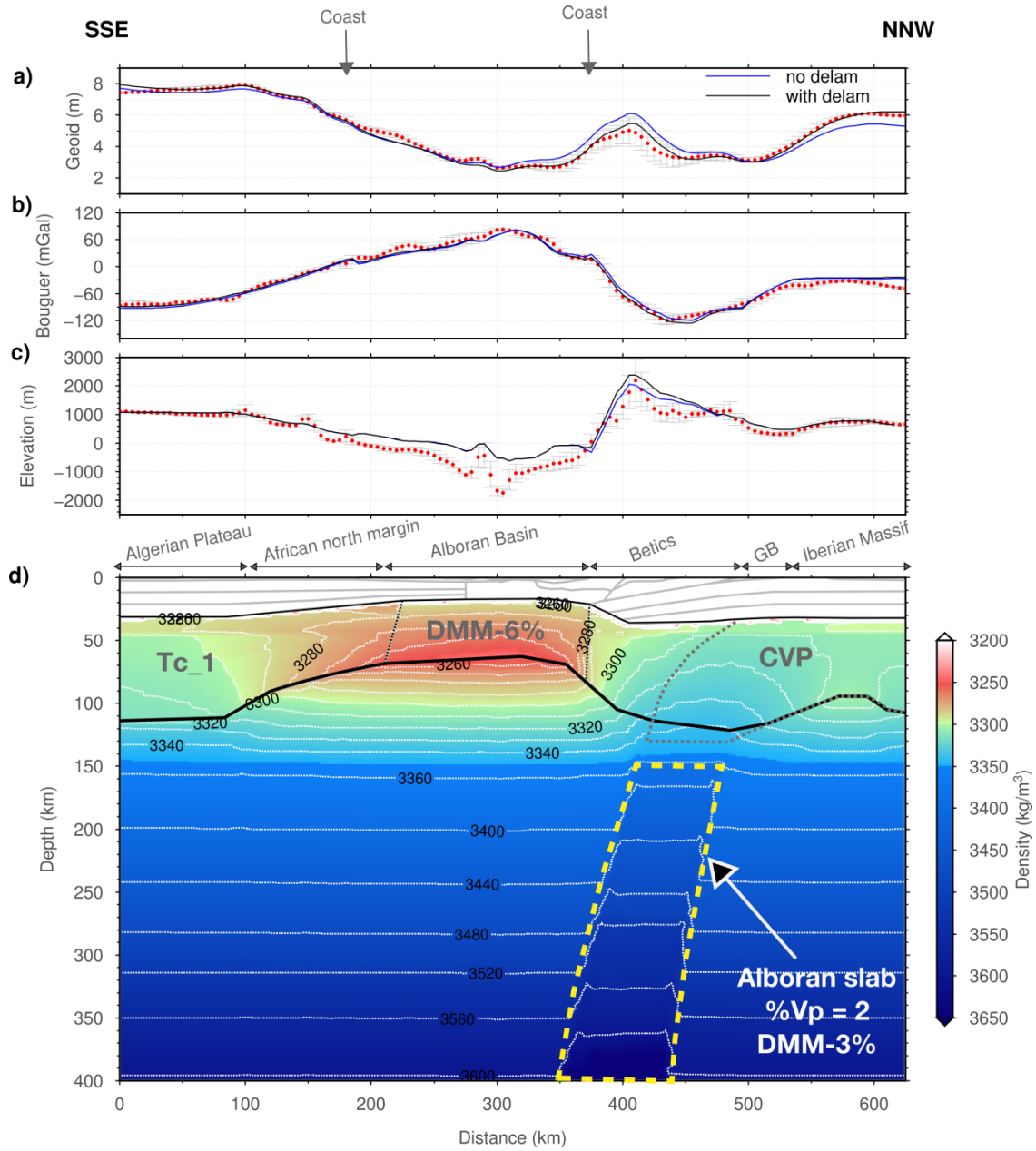


Figure 5.6 Model showing the effect of the delaminated Iberian lithospheric mantle on (a) geoid, (b) Bouguer anomaly, and (c) elevation. In (d) resulting density distribution in the mantle is plotted. Blue line represents the calculated values from the model. Red dots denote measured data, and vertical bars denote the standard deviation calculated across a strip of 25 km half width. Continuous black lines highlight the Moho and LAB depth. The different composition domains in the lithospheric mantle are separated by thin black lines. The bold grey text denotes different chemical composition listed in Table 4.2. Note the continuation of the Iberian lithospheric mantle (CVP) beneath the Betics to simulate no delamination and geometry of the delaminated lithosphere corresponding to the best fitting model is shown with thick dashed grey line.

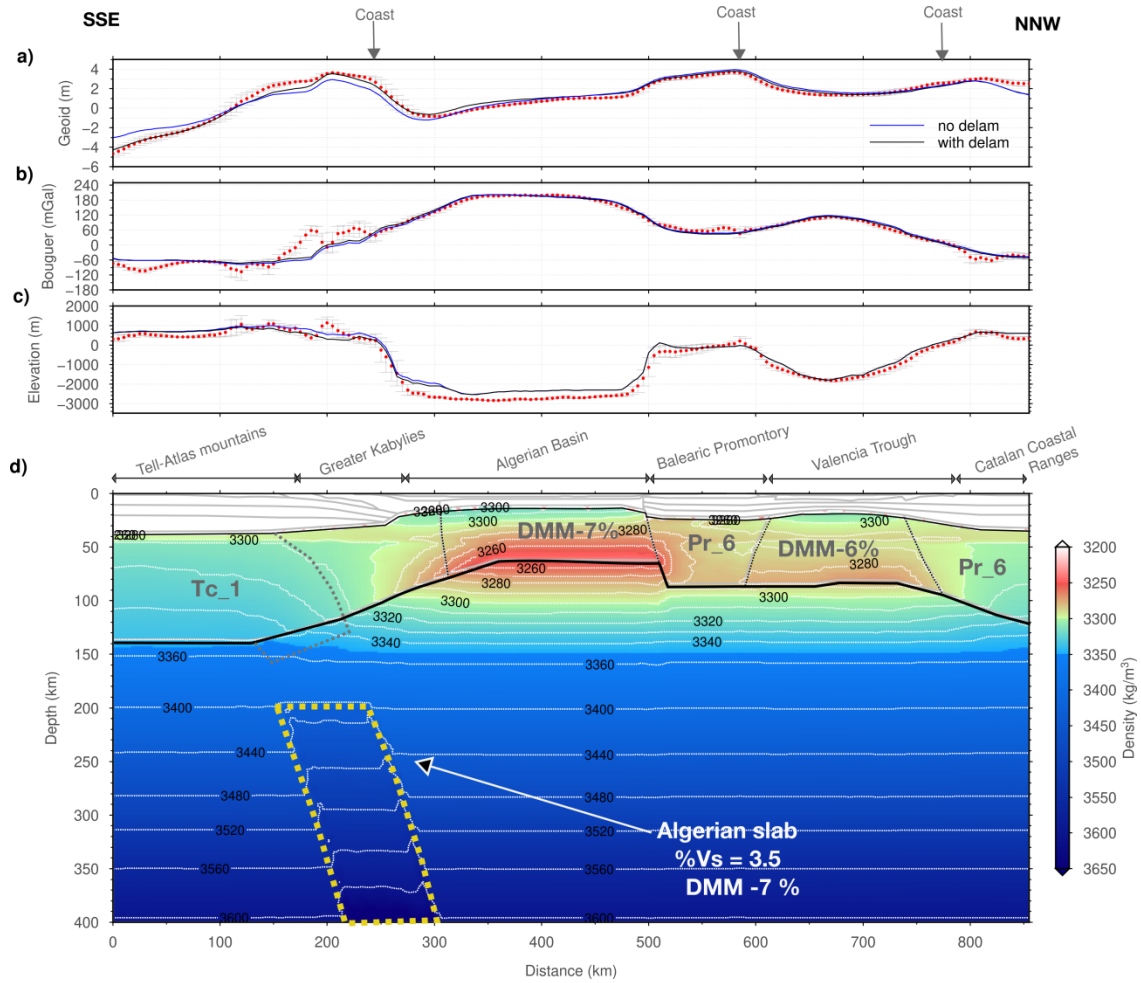


Figure 5.7 Model showing the effect of the delaminated African lithospheric mantle on (a) geoid, (b) Bouguer anomaly, and (c) elevation. In (d) resulting density distribution in the mantle is plotted. Note the continuation of the African lithospheric mantle (Tc_1) beneath the Greater Kabylies to simulate no delamination. Rest of the caption is same as in Figure 5.6.

As mentioned before, different compositional domains in the lithosphere are required in order to fit the geophysical data (Table 4.3) and have consistency with the geological and geodynamic constrains. Having said that, it does not mean that these compositional domains are homogeneous with depth and depth dependent variation in composition is plausible. For example, the oceanic lithosphere is known to have pressure dependent (i.e., depth dependent) degree of fraction melting and hence, depth varying composition (Chapter 2, Section 2.8). Also in the case of the continental lithosphere, mantle xenoliths from Slave, Siberian, and Kaapval cratons show depth dependent fertility where at depths >150 km, composition is more fertile (Lee et al., 2011). Hence, the composition considered in the different lithospheric mantle domains should be conceived as a depth averaged composition.

5.2.3. Subducted Ligurian-Tethys slabs

During subduction, the slab exchanges heat with the hotter ambient sublithospheric mantle and the temperature of the slab increases while the amplitude of the positive seismic velocity anomaly decreases through time (e.g., Boonma et al., 2019). The precise quantification of these transient effects needs additional data regarding the angle and velocity of subduction and other parameters that are poorly constrained (e.g., thermal diffusivity, mantle viscosity, volatile content etc.). The Cenozoic evolution of the Alboran and Algerian basins is related to the subduction of the Ligurian-Tethys Ocean which, according to paleo-geographic reconstructions, was composed of several transtensive and highly extended continental segments transitioning to oceanic lithosphere to the east (Fernández et al., 2019; Schettino and Turco, 2011; Stampfli and Borel, 2002).

Both the Alboran and Algerian slabs have been modelled as ~80 km thick bodies centred on the highest positive velocity anomaly and converted to temperature anomalies according to their chemical composition and P-T conditions, resulting in $\Delta T \approx -400$ °C in both cases (Figures 4.5 and 4.9). It is of interest to highlight the consistency of the seismic velocity anomalies depicted by two independent tomography models based on P-wave travel-time (Alboran slab) and S-wave full-waveform inversion (Algerian slab), which result in very similar temperature anomalies as corresponds to slabs of comparable ages. Further, DMM-3% composition in the Alboran slab is consistent with the paleo-geographic reconstructions purposing highly extended segments in west as compared to the fully developed oceanic lithosphere in the east (i.e. DMM-7% composition of the Algerian slab).

The weight of the cold and dense slabs is not transmitted isostatically to the surface because they have torn/broken off (Figure 4.7). If the slabs were attached, it would decrease the elevation in the Betics by 700–1000 m, and in the Greater Kabylies by 600–1200 m, and increase it by few 100 m in both the Alboran and Algerian basins for an effective elastic thickness of 30 km (Figure 4.7). The subsidence produced by the attached Alboran slab in the Betics compares well with the residual topography model of Civiero et al. (2020) indicating the magnitude of the isostatic rebound after slab tear which can be related to the closure of the connection between the Atlantic Ocean and the Mediterranean Sea through the Betics corridor before the Messinian salinity crisis (García-Castellanos and Villaseñor, 2011). The modelled unhooked slab below the Betics agrees with the reported slab tearing from tomography images (e.g. García-Castellanos and Villaseñor, 2011; Civiero et al.,

2020). Increased elevation in the Alboran and Algerian basins also hints towards the fact that slabs are not attached to the lithosphere, hence, does not contribute to the flexural isostasy. Further, the best fitting modelled elevation (i.e., isostasy + flexure for the uncoupled case) falls at the upper bound of the observed elevation in the Betics and the lower bound in the Greater Kabylies. This suggests that the potential dynamic pull associated with the dense slabs in the less viscous mantle, not modelled here, is higher in the Betics because the torn Alboran slab lies at shallow depths (Figure 4.5). The exact magnitude of the contribution of the dynamic slab pull to elevation will depend on the coupling in between the slabs and the ambient mantle, and requires computation of the induced mantle flow.

5.2.4. Geodynamic implications

The present-day structure of the crust and lithospheric mantle in the Western Mediterranean is the result of a long-lived tectonic evolution since the Jurassic stretching and ocean spreading of the Ligurian Tethys Ocean to the present-day configuration of Western Mediterranean. The analyzed geo-transects show the present-day crust mostly formed during the pervasive Cenozoic northern Africa convergence triggering the building of the Betics-Rif and Kabylies-Tell-Atlas subduction-related orogenic systems. On the contrary, the upper mantle structure shows its current state that is mostly post-tectonic, since it is the result of the lithosphere-asthenosphere interaction governed by the subduction of Ligurian-Tethys lithosphere.

The Alboran Basin has experienced different and partially coeval geodynamic processes. These are the subduction of the Ligurian-Tethys due to the convergence of Africa-Iberia and further roll-back, delamination and slab break-off processes related to the subducting slab. The high density Internal Betics, mostly characterized by Paleozoic and pre-Upper Triassic HP/LT metamorphic rocks, are interpreted to represent the highly extended Iberian distal margin (Vergés and Fernández, 2012; Figure 4.3a). This SE Iberian margin of the Ligurian-Tethys Ocean underwent partial subduction during Africa-Iberia convergence as evidenced from P-T-t paths and ages of HP/LT metamorphic peaks (summary in Gómez-Pugnaire et al., 2019). These HP/LT metamorphic units were later exhumed along the subduction interface forming a roughly NW-directed stack of relatively thin tectonic nappes, each nappe recording specific metamorphic histories. The low-density External Units in the Betics is constituted by a thick sedimentary sequence starting in the Upper Triassic evaporites

that constitute the main detachment level of the Betics orogenic system at the scale of the whole orogenic system as discussed in Vergés and Fernández (2012).

I also test the alternative scenario where the Internal Units are thicker and overlie the Iberian basement as proposed by Mancilla et al. (2015) from receiver function data (Figure 5.8). Increasing the thickness of the Internal Units significantly increases the geoid and the Bouguer anomaly because of the higher volume of the denser Nevado-Filabride units (2900 kg/m^3 ; Table 4.1). It can be argued that the density of the HP/LT units could be $< 2900 \text{ kg/m}^3$ improving the fit to the gravity data, however, as shown in Figure 4.4, the high density of Internal Units are highly plausible.

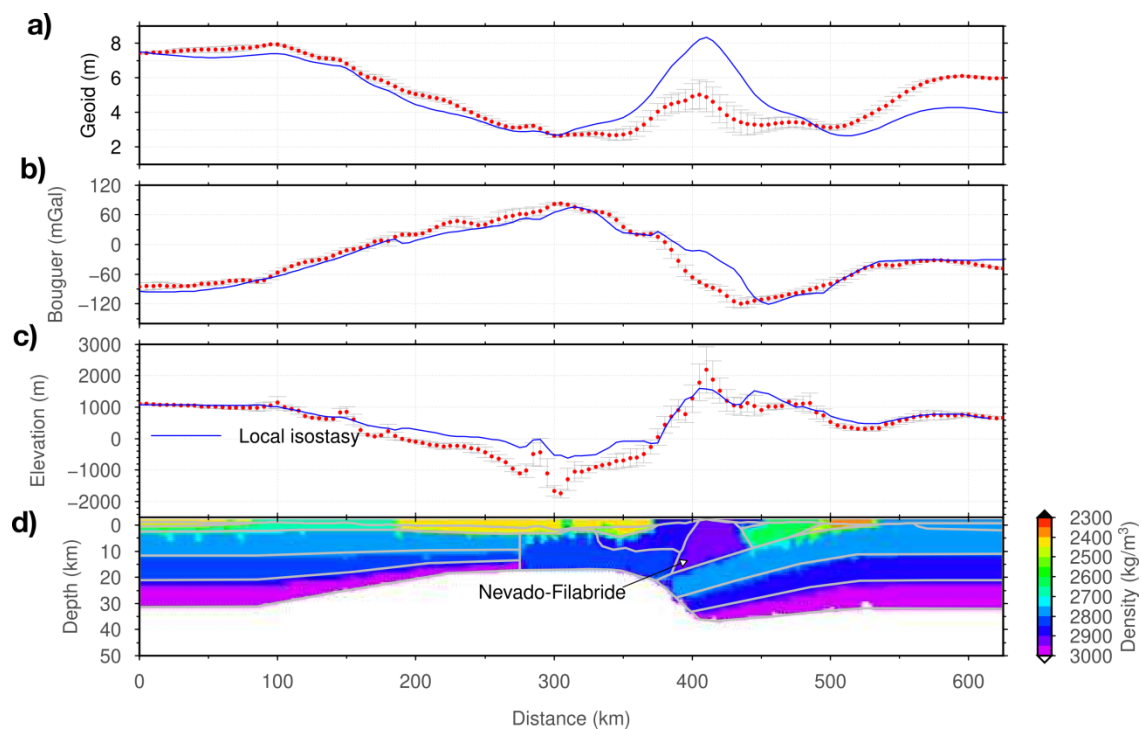


Figure 5.8 Model showing the effect of the thick Nevado-Filabride HP/LT Internal Units on (a) geoid, (b) Bouguer anomaly, and (c) elevation. In (d) resulting density distribution in the crust is plotted. Blue line represents the calculated values from the model. Red dots denote measured data, and vertical bars denote the standard deviation calculated across a strip of 25 km half width. Note that below the crust, the model is the same as that of the best fitting model in Figure 4.5.

The External Betics represents the Upper Triassic and post-Upper Triassic non-metamorphic sedimentary rocks. The External Units attain a similar density at mid-crustal depths as that of the upper crust because of the higher pressure and cannot be distinguished solely based on the gravity field, allowing for an alternative interpretation (Figure 5.9). However, underthrusting of the cover is conceptually

consistent with the NW retreat of the Alboran slab. Additionally, clustering of the seismicity in the External Betics, beneath the Internal Units, points to activated weaknesses (i.e., faults) developed during accretion of the cover. The Betic orogenic system is therefore formed by a system of thrusts that tectonically emplace the large Jurassic Ligurian-Tethys extensional domains that configured the SE Iberian margin on top of each other from the most distal margin (Internal Betics) in the hinterland to the proximal margin (External Betics) in the foreland (e.g., Vergés and Fernández, 2012; Pedrera et al., 2020).

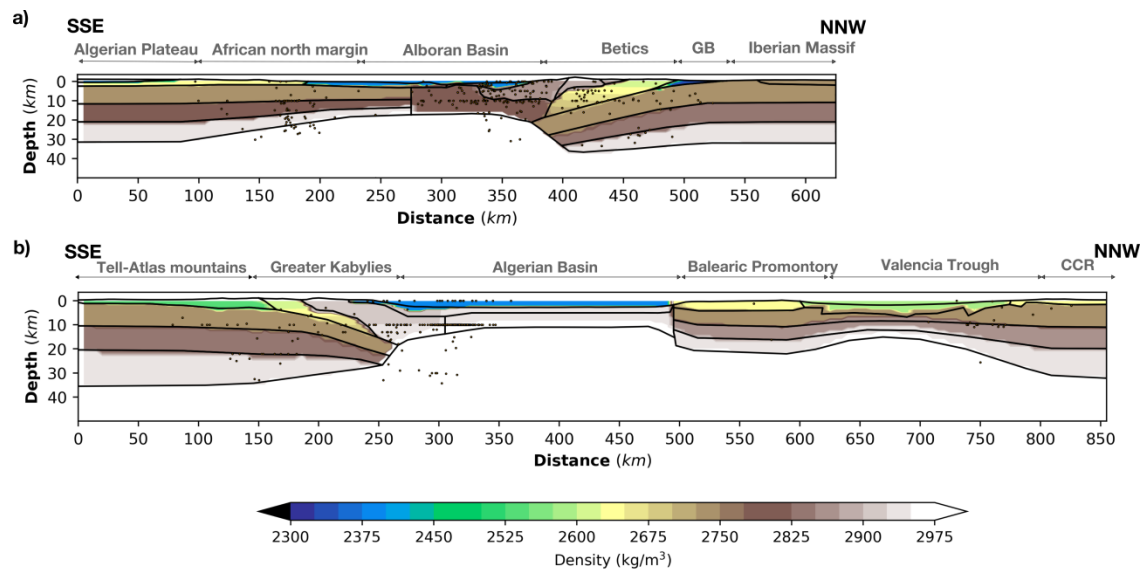


Figure 5.9 Crustal density distribution along the (a) Alboran Basin and (b) Algerian Basin geo-transects. Seismicity similar to the Figure 4.3 is also plotted. Note the increasing density with depth in the External units reaching values close to the upper crust.

The evolution of the Algerian Basin is triggered by the NW-dipping subduction of the Ligurian-Tethys oceanic segments existing between the Balearic Promontory and the Algerian domain of the NW Africa margin (Alvarez et al., 1974), and is widely accepted by most models (e.g., Frizon de Lamotte et al., 2000; Roure et al., 2012; Verges and Sabat, 1999; van Hinsbergen et al., 2014; Casciello et al., 2015; among others). The Kabylies form the HP/LT Internal Units with a relatively high density (Bruguier et al., 2017; Caby et al., 2014; Fernandez et al., 2016; Mahdjoub et al., 1997; Michard et al., 2006; Platt et al., 2013; Rossetti et al., 2010); the Flysch units represent the detached cover above the Ligurian-Tethys sea floor from Jurassic to Late Miocene (e.g., Guerrera and Martín-Martín, 2014, among others), while the Tell and the Atlas form the External Units corresponding to the Algerian margin of the

Ligurian-Tethys Ocean (Leprêtre et al., 2018; Roure et al., 2012). For the modelling purposes the Flysch and External Units are combined since they represent the sedimentary cover (Figure 4.3b). Similar to the Betics, the Internal Units of the Greater Kabylies Massif are thrusting on the Flysch units which are further thrust over the Tellian External Units. Seismicity beneath the Greater Kabylies is distributed in the African basement and the External and Internal Units, although it does not show clear clustering probably due to the lack of local seismic recording stations. Earthquakes below Moho near the present-day passive margin of Algeria could represent the proposed initiation of a new subduction zone (e.g., Déverchère et al., 2005; Hamai et al., 2018).

In a slab roll-back subduction system the crust thickens in the arc region and thins/stretches in the back-arc. Sufficient stretching in the back-arc can lead to the decompressional melting of the fertile mantle producing new oceanic lithosphere. In the models for the Alboran and Algerian basin geo-transects, Crust is thicker in the regions of HP/LT exhumed metamorphic rocks and thins drastically over short distance to the oceanic/magmatic crust of the back-arc regions in comparison to the gradual thickening in the opposed margins (Figure 5.10). Along the Alboran Basin geo-transect, ~37 km thick crust beneath the Betics thins drastically to ~16 km magmatic and volcanism intruded crust of the East Alboran Basin before it transitions to the thinned continental crust south of the Alboran Ridge and thickens gradually further to the SSE in the NW African margin (e.g., Booth-Rea et al., 2007; Gómez de la Peña et al., 2020). Along the Algerian basin geo-transect a relatively thick crust of ~30 km beneath northern Algeria (Greater Kabylies) transitions abruptly to ~10 km thick oceanic crust of the Algerian Basin to the NNW (Figure 5.10). Similarly, thicker lithospheres beneath the Betics and northern Algeria transitions abruptly to only ~60 km thick and fertile lithosphere (i.e., oceanic lithosphere) of both the Alboran and Algerian back-arc basins (Figure 5.10).

The lithospheric structures beneath Algeria and SE Iberia margins, though comparable, are different in width and thickness. The Algerian margin is ~200 km wide while that of Alboran is only 80 km wide. The maximum lithospheric thickness is ~150 km below Algeria and ~130 km below Iberia, although the regional lithospheric thickness of Africa is thicker than in Iberia (Figure 5.10). The existence of quasi-vertical detached Ligurian-Tethys lithospheric slabs under the north Algeria and SE Iberian margins is another feature of resemblance although with opposite apparent dip, to the SSE under Iberia and to the NNW beneath Algeria (Figure 5.10). The two lithospheric slabs are located ~80 km inland from the current shoreline because of the

post slab roll-back mantle delamination and subsequent slab tear, detachment or break-off, of subduction and collision with the margins Iberia and Algeria. Mantle delamination could have promoted the inflow of the fertile sublithospheric mantle beneath the Iberian and Algerian crusts underlying the allochthonous HP/LT metamorphic nappes of the Internal Betics and Greater Kabylies explaining their relatively fertile lithospheric mantle compared to the depleted continental lithospheres of foreland regions in Iberia and Saharan Atlas (Figure 5.10).

Interestingly, the crustal and upper mantle structures in the Betics and the Kabylies-Tell-Atlas are roughly similar, but with opposite tectonic vergence, which could be conceived as having been moulded by similar lithospheric and sublithospheric processes (Figure 5.10). According to our models, the South Iberia margin acted as active margin where the HP/LT slices are stacked leaving the NW Africa margin, in between Rif and Tell-Atlas, as a passive margin influenced by the extension during the slab retreat. An opposite situation occurs in the Algerian Basin where north Algeria acted as an active margin and the Balearic Promontory and Valencia Trough acted as passive margins experiencing extension from the slab retreat (Figure 5.10).

The present-day lithospheric scale thickening beneath the Greater Kabylies and extensional back-arc oceanic Algerian Basin is consistent with SSE retreating subduction kinematics, hence can be explained by all the three geodynamic scenarios proposed for the Western Mediterranean evolution (Figures 1.5 and 5.10). However, each of these models imply different lithospheric structure along the Alboran Basin geo-transect. The geodynamic model with a single long subduction, scenario 2, covering both the Alboran and Algerian basins, retreating to the south cannot explain the NW vergence of the Internal and External Units of the Betics nor their age of tectonic emplacement, the lithospheric structure, and the position of the Alboran slab beneath the Betics (Figure 1.5, scenario 2). Whereas the other two models, scenario 1 and scenario 3 are consistent with the structure beneath the Betics but implying contrary lithospheric structure along the NW Africa margin. According to the scenario 1 model (Figure 1.5, van Hinsbergen et al., 2014), the Alboran slab segment retreated to the west, before colliding with the Iberian margin and rotating by $\sim 180^\circ$, along the purposed North Africa transform fault (i.e. Subduction-Transform Edge Propagator, or STEP fault; Govers and Wortel, 2005) and should produce a significant step in the lithospheric structure of NW Africa, in between Rif and Tell-Atlas Mountains, which is contrary to the observed gradual lithospheric thinning in our lithospheric structure model (Figure 5.10).

The opposite direction of slab retreat in the adjacent segments according to the scenario 3 (Figure 1.5, Vergés and Fernández, 2012) implies opposite symmetry in the crust and upper mantle structure as observed in our models (Figure 5.10). This scenario 3 is based on the pre-convergence geometry of the Iberia-Africa Ligurian Tethys segmented margin configuration (Frizon de Lamotte et al., 2011; Schettino & Turco, 2011; Vergés & Fernández, 2012; Fernández et al., 2019; Fernandez, 2019; Ramos et al., 2020; Martín-Chivelet et al., 2019) that exerted a strong control on further evolution during Africa northern convergence since the Late Cretaceous (e.g., Macchiavelli et al., 2017). The dynamics of such subduction system has been studied using analogue and numerical experiments by Peral et al. (2018) and Peral et al. (2020a and b). The observed lithospheric scale thickening beneath the HP/LT metamorphic rocks of the Betics followed by extension driven thinning and abundant volcanism in the Alboran Basin is consistent with a NW retreating subduction. It must be noted that, to the west of NW Africa margin, in the Rif mountains, lithosphere is thick, which is related to NW-W retreat of the Alboran slab and the trench curvature produced by the higher resistance to slab retreat in the western end of the segment and the further tightening due to the protracted Iberia–Africa convergence (Fernández et al., 2019; Kumar et al., 2018; Peral et al., 2020a, b).

The amount of isostatic rebound in both margins after slab tearing/detachment could reach 500 m - 1200 m when considering T_e values between 10 and 30 km or up to 1500m - 2000 m in the absence of flexural rigidity, as calculated indirectly in the region of Gibraltar (Jiménez-Munt et al., 2019). The slab is still attached under the western Betics (e.g., Civiero et al., 2020; Mancilla et al., 2015). Slab break-off, that along strike, is defined as slab tear with a large gap in the east decreasing towards the west where the slab is continuous at depth below the Gibraltar arc (Mancilla et al., 2018; Negredo et al., 2020).

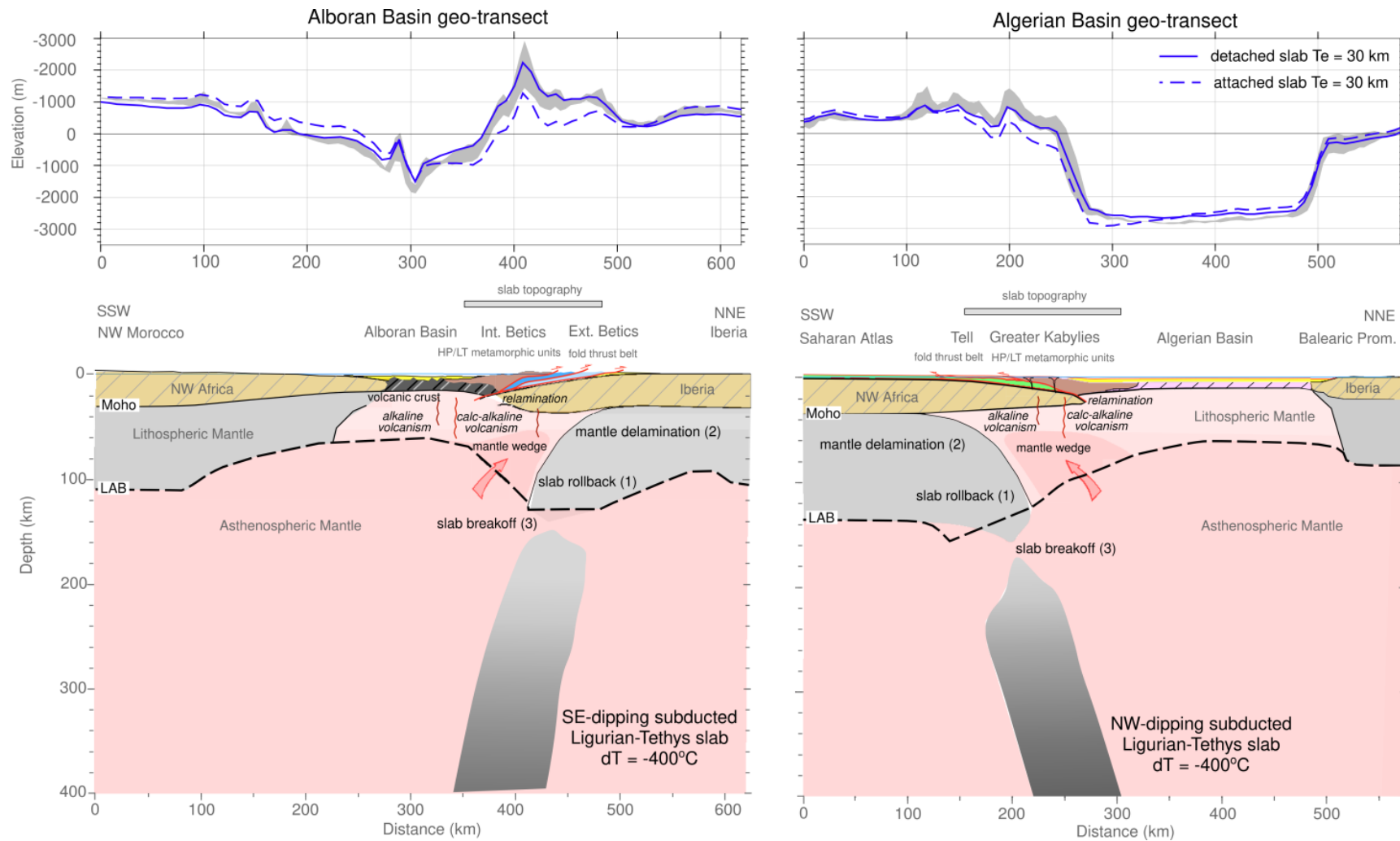


Figure 5.10 Crustal and lithospheric cross-sections at scale along modelled Algerian Basin-Kabylies-Tell-Atlas and Alboran Basin-Internal Betics-External Betics-foreland geo-transects. The structure of both the margins is similar and comparable implying that the underlying geodynamic processes are same for both the margins.

CHAPTER 6

Conclusions

Chapter 6

Conclusions

In this thesis, I have presented an improved LitMod2D_2.0 software package, which allows studying the thermal, density (i.e., composition), and seismic velocity structure of the non-homogeneous lithosphere and sublithospheric mantle by integrating geophysical and geochemical datasets in a self-consistent thermodynamic way. The most exciting improvement in LitMod2D_2.0 is to infer the thermal and/or chemical nature of the sublithospheric mantle anomalies observed in seismic tomography models and their effect on the elevation. The main motivation for this improvement came from the Western Mediterranean, which has experienced subduction during Cenozoic, resulting in subducted slabs in the sublithospheric mantle. Hence, it became the first part of the thesis. In general, this improvement allows the application of LitMod2D_2.0 to regions affected by complex geodynamic processes, such as mantle upwelling, subduction, delamination, and metasomatism (i.e., processes that can easily modify the temperature and/or chemical composition beneath the LAB). In the second part of the thesis, the improved LitMod2D_2.0 is applied to study the present-day thermal, density and seismic velocity structure along two geo-transects in the Alboran and the Algerian basins and their corresponding margins in Iberian and North Africa. The main novelty relative to previous studies is the incorporation of the positive seismic velocity anomalies observed in the seismic tomography models as subducted slabs of the Liguria-Tethys lithosphere. Knowledge of the present-day deep structure and composition of the lithosphere and uppermost sublithospheric mantle may help to discriminate among the proposed models and therefore in constraining the geodynamic evolution of the region. In the following, I report the conclusion from the two parts separately.

6.1. LitMod2D_2.0: An improved tool for the integrated geophysical-petrological interpretation of upper mantle anomalies

In Chapter 3, I have presented an improved version of the LitMod2D_2.0. The new improvements have been demonstrated with the help of synthetic examples. Based on the synthetic experiment, I draw the following conclusions and list the main improvements included in the new LitMod2D_2.0 software package:

- All the purposed depleted chemical compositions for the sublithospheric mantle shows $< 1\%$ of variations in physical properties (i.e., density and seismic velocities) with respect to the Primitive Upper Mantle composition (PUM).
- DMM (depleted MORB mantle) instead of PUM (primitive upper mantle) chemical composition is used in the sublithospheric mantle for geochemical consistency. Nevertheless, the relative differences with respect to PUM in the calculated density and P- and S-wave seismic velocities are less than 0.2% .
- Anelasticity is now calculated in the GENERATOR thermodynamic module using updated parameters in the power-law attenuation model allowing for the physical (temperature, composition) characterization of sublithospheric mantle anomalies. Both oscillation period and grain size remain as input parameters. Assuming the same errors in anelastic attenuation parameters, the frequency dependence of anelastic attenuation and activation energy contributes more to the errors in the final seismic velocities than the activation volume.
- Sublithospheric mantle anomalies may have a thermal, seismic or compositional origin, or a combination of them, allowing for estimating the response of geodynamic processes such as mantle upwelling, subduction, delamination, and metasomatism on the surface observables (elevation, gravity, and geoid).
- Synthetic experiments on thermal anomalies in the sublithospheric mantle show a non-linear dependence between the sign of the thermal anomaly and the resulting magnitude of seismic velocities. Depending on the sign (decreasing/increasing), thermal anomalies produce different magnitude of seismic velocity anomalies. This non-linearity has an important implication for the qualitative interpretation of seismic velocity anomalies observed in tomography models.
- Synthetic experiments show that shear wave velocities are more sensitive to temperature, whereas P-wave velocities are to composition. Hence, modelling

both P-and S-wave velocities together with geoid height, which is sensitive to deep mantle level density variations, holds a potential to infer the thermal and/or chemical heterogeneity in the mantle.

- To compute synthetic V_P and V_S tomography models, an upper mantle model is made, which consists of Average Garnet Tecton composition in the lithospheric mantle, with $Z_{\text{Moho}} = 35$ km and $Z_{\text{LAB}} = 120$ km, and a DMM composition in the sublithospheric mantle down to 400 km depth. This model reproduces the P-wave seismic velocities of the global average reference model ak135 in the depth range of 35 – 250 km and avoids the unsolved mismatch between the thermodynamically calculated seismic velocities and those from ak135 model below 250 km depth.
- A new open-source graphic user interface is developed under Python programming language simplifying the input/output data files to obtain across platforms versatility, to gain ease of use, and allow future user developments.
- A post-processing toolbox is incorporated allowing the user to apply predefined/customized codes and scripts linking with the LitMod2D_2.0 output file to calculate additional observables according to specific needs (synthetic tomography, regional isostasy, stable mineral assemblages, surface wave dispersion curves and receiver functions, etc.). The user can customize the provided codes/scripts or develop new ones to be shared with the scientific community.

6.2. Present-day crust and upper mantle structure in the Alboran and Algerian basins and their margins

In the second part of the thesis, Chapter 4, I presented an integrated geophysical-petrological models of the crust and upper mantle structure of the Western Mediterranean along two geo-transects crossing the Alboran and Algerian basins, and the active/orogenic margins of the Betics and Kabylies-Tell-Atlas Mountains, and the passive/conjugate margins of NW Africa and Eastern Iberia (i.e., Balearic Promontory and Valencia Trough), respectively. At the crust level models presented in this thesis differ from previous crustal-scale models highlighting the use of relatively thin Internal Units above sediments of the External Units in the Betics and Greater Kabylies. The resulting models are constrained by geological and geophysical data and are consistent with the surface observables (elevation, gravity, geoid and surface heat flow) and seismic tomography models. Different lithospheric mantle compositional domains in accordance with geological domains are required to fit the surface observables. Modelling results show an active interaction between the lithosphere and the underlying sublithospheric mantle which was governed by the Alpine subduction dynamics in addition to the NW-SE Africa-Eurasia convergence acting since Late Cretaceous. From the results presented in Chapter 4, I draw following conclusions:

- The thick crust beneath the Betics (~37 km) thins abruptly to 16 km below the Eastern Alboran Basin, which is modelled as a mostly magmatic crust largely intruded by volcanic rocks, and thickens gradually to ~31 km further to the SE in NW Morocco. The thick crust beneath the Greater Kabylies (~30 km) is thinning more abruptly to the northwest reaching ~10 km below the Algerian Basin, modelled as oceanic crust.
- The lithospheres beneath the Internal Betics and the Greater Kabylies are thick and structures are comparable but showing an opposite symmetry, though the lithospheric thickness is larger below the Greater Kabylies. In SE Iberia, the lithosphere beneath the Betics is ~130 km thick thinning sharply to the SSE to ~60 km under the Alboran Basin and thickens again, but gradually, towards NW Africa to ~112 km. The lithosphere beneath the Greater Kabylies is of ~150 km thickness and thins to the NNW to ~60 km thick oceanic lithosphere of the Algerian Basin.

- The present-day lithospheric mantle composition of the Alboran and Algerian basins are modelled as depleted residue from 6–7% aggregate decompressional melting of the relatively fertile sublithospheric mantle composition. This is consistent with the back-arc setting of both the Alboran and Algeria basins related to the retreating of the Ligurian-Tethys lithosphere. Slab retreat triggered the melting of the underlying fertile sublithospheric mantle generating oceanic crust in the Algerian Basin and extensive magmatic and volcanic crust in the Alboran Basin.
- The modelled lithospheric mantle composition beneath the Internal Betics and Greater Kabylies HP/LT metamorphic domains is fertile compared to the corresponding continental lithosphere of the External Betics and Saharan Atlas, respectively. This fertile composition beneath the internal domains of the orogenic systems is related to mantle delamination and inland displacement of the slabs during the later stages of subduction and collision, which promoted the inflow of the fertile sublithospheric mantle material.
- Two detached sub-vertical Ligurian-Tethys lithospheric slabs, with an anomalous temperature of about -400 °C, constrained using the seismic tomography models, about 80 km onshore from the present-day coastlines and restricted to beneath SE Iberia and Algeria. Their most suitable composition is relatively fertile (alike to an oceanic lithosphere), than those below the continental lithospheres of Iberia and North Africa.
- The Ligurian-Tethys slab beneath the SE Iberia shows an apparent dip to the SE whereas the slab below Algeria dips to the NNW, matching the NW- and SE-tectonic transport direction of the fold and thrust belts of the Betics and Greater Kabylies-Tell-Atlas subduction-related orogens, respectively.
- The large-scale configuration of present-day SE Iberia and Algerian margins as well as their mantle compositions in the Alboran and Algerian geo-transects is consistent with opposite dipping subduction of two segments of the Jurassic Ligurian-Tethys domain. Their present configurations agree with Neogene slab roll-back process triggering mantle delamination followed by slab break-off in both opposite subduction segments.
- Uplift related to the slab break-off, considering local and regional isostasy, is ~700–1000 m in SE Iberia and ~600–1200 m in Algeria. These detached Ligurian-Tethys slabs might exert a vertical pull down related to the induced dynamic mantle flow.

List of Figures and Tables

Figure 1.1 Topography map of the Alpine-Himalayan collision zone. The area inside the black box is the focus of this thesis.....	10
Figure 1.2 Geological map of the Western Mediterranean showing the main orogenic belts and basins (Modified from Vergés and Sàbat, 1999). NBTZ, North Balearic Transform Zone; EB, Emile-Baudot Escarpment.	11
Figure 1.3 Detailed geological map of the Western Mediterranean showing main geologic units in the Alboran and Algerian basins, and the Betics-Rif and Kabylies-Tell-Atlas Mountains. Locations of the two geo-transects modelled in this thesis are shown by grey shadowed strips.	12
Figure 1.4 Upper mantle seismic tomography models in the Alboran and Algerian basins.(a) P-wave travel time tomography model slice at 320 km depth (Villaseñor et al.,2013) and (b) Full-waveform inversion seismic tomography model at different depths (Fichtner and Villaseñor, 2015).	14
Figure 1.5 Models purposed for the geodynamic evolution of the Western Mediterranean. Scenario 1 after Van Hinsbergen et al. (2014) involves a single short subduction zone initially dipping to NW starting near the Balearic Promontory and then retreats to the SE before it separates into two different segment. One of the segments continue retreating to SE before it collides with North Africa and other continue retreating to the west and collides with Iberia resulting in 180° clock-wise rotation.Scenario 2 involves a long initial subduction dipping to the N-NW along the entire Gibraltar-Balearic Promontory margin (e.g., Gueguen et al., 1998; Faccenna et al., 2004; Jolivet et al.,2009). Scenario 3 after Vergés and Fernàndez (2012) involves two separate subduction segments with opposite subduction direction for the Alboran (subduction dipping to the SE and retreating to the NW) and Algerian (subduction dipping to the NW and retreating to the SE) basins. Direction of rollback is shown by the yellow arrows. Black dashed lines represent the proposed transform faults separating the different subduction segments (Figure modified after Chertova et al., 2014).....	15
Figure 1.6 Flow chart showing the work-flow and the steps followed to achieve the objectives of this thesis.	22

Figure 2.1 Bulk distribution coefficients of major oxides during melting at the mid-oceanic-ridge calculated using empirical relations from Niu (1997). A black horizontal

line with bulk distribution coefficient of 1 separates compatible elements above it from the incompatible elements below it.....	28
Figure 2.2 Mineral proportions for a pyrolitic composition as function of pressure and temperature range in the mantle. Black circles with error bars shows the experimentally determined phase proportions in dry pyrolite from Irifune and Isshiki (1998) based on high-T-P experiments. Red circles are predictions from Afonso and Zlotnik (2011) thermodynamic database and stars are predictions from the dataset of Xu et al. (2008). Figure is taken from Afonso and Zlotnik (2011).	37
Figure 3.1 Flow chart diagram showing the workflow of LitMod2D_2.0. The new LitMod2D version may account for sublithospheric mantle anomalies in which case coupled elevation is calculated. It also has an option for post-processing of relevant physical properties (temperature, pressure, density and seismic velocities) to compare with additional datasets. Flexural isostasy is included by coupling 'tao-geo' software (Garcia-Castellanos et al., 2002). "Computer Programs in Seismology" (CPS, Herrmann, 2013) is also coupled to work with passive seismological datasets. Stable mineral-assemblages are extracted from the material files produced by the GENERATOR subprogram.....	49
Figure 3.2 Depth distribution of anelastic attenuation parameter (Q , quality factor) for a range of grain sizes (1-100 mm) and oscillation periods (10-100s) compared with global average Q_P and Q_S models. (a) and (b) shows the depth distribution of Q_P and Q_S for varied grain size and constant oscillation period of $T_0 = 75$ s, respectively. (c) and (d) shows depth distribution of Q_P and Q_S for varied oscillation period (10-100 s) and constant grain size of $d = 10$ mm, respectively. Q_P and Q_S from ak135 global average model (continuous red solid line, Kennett et al., 1995), and Q_S from QL6c (continuous grey line, Durek and Ekström, 1996), are also plotted for comparison.	53
Figure 3.3 Percentage error introduced in the (a) P-wave velocities and (b) S-wave velocities considering 10% error in α (dashed blue line), E (dotted-dashed blue line), and V (dotted blue line). The total error is plotted in solid blue line and temperature distribution is plotted in solid-red line.....	54
Figure 3.4 Comparison of different compositions tested in the sublithospheric mantle (Table 3.1). Resulting density (a), P-wave velocities (b) and S-wave velocities (c) are compared with that to PUM.	56

Figure 3.5 Depth distributions of seismic velocities, (a) P-wave and (b) S-wave assuming an Average Garnet Tecton composition in the lithosphere mantle and a DMM composition in the sublithospheric mantle. Seismic velocities are calculated using Afonso and Zlotnik (2011) (solid, modified Holland and Powell, 1998), Stixrude and Lithgow-Bertelloni (2005) (thick dashed) and Xu et al. (2008) (thin dashed) thermodynamic databases. Resulting seismic velocities are corrected for anelastic attenuation using a constant grain size of 10 mm and oscillation period of 75 s. Global average seismic velocities from ak135 (Kennett et al., 1995), in solid grey circles, with an error of 0.5% in P-wave velocities and 1% in S-wave velocities are plotted for comparison.	60
Figure 3.6 Synthetic examples of thermal anomalies in the sublithospheric mantle. Input thermal anomalies are plotted in (a). Resultant change in (b) density, (c) P-wave velocities, and (d) S-wave velocities are plotted with same colour code as input. All anomalies are referred to a reference model, shown as inset in the upper right corner.	62
Figure 3.7 Synthetic example illustrating the contribution of compositional (Average Garnet Tecton, blue), thermal (+50 °C, orange), and combination of both (green) anomalies to (a) density, (b) P-wave velocities, and (c) S-wave velocities, with respect to the reference model shown as inset in the upper right corner.	63
Figure 3.8 Example of a varying magnitude (along the profile) relative P-wave seismic velocity anomaly. (a) Screenshot of the input file used in this synthetic example. (b) Resultant temperature, density and seismic velocities.	65
Figure 3.9 Synthetic examples of input P- and S-wave anomalies of $\pm 1.5\%$ in the sublithospheric mantle. Recovered temperature (a) and density (b) from the input seismic velocity anomalies are plotted with respect to the reference model shown in the upper right corner.	66
Figure 3.10 Screen shots from the new open-source GUI, provided with LitMod2D_2.0, (a) Graphic user interface input window showing the geometry of the modelled profile and various functions to interact and work with the model. (b) Screenshots of model outputs from the model, in the left panel forward prediction of surface observables, observed (blue) and calculated (red and black) and the model geometry at the bottom. Surface observables without the sublithospheric mantle anomalies are plotted in red to highlight their effect. Right panel in (b) shows the temperature, density and seismic velocity distribution (P-wave and S-wave) from the model.	69
Figure 3.11 Example of seismic velocities post-processing. (a) Synthetic P-wave tomography along the modelled synthetic profile. (b) Depth distribution of S-wave	

velocities at three locations along the profile with colour coded and marked in (a). (c) Synthetic P-wave receiver functions at the three locations marked in (a). At the subduction zone two receiver functions with (filled orange) and without (black line) the subducted slab, are plotted for comparison. (d) Synthetic Rayleigh-surface-wave group (left) and phase (right) velocities. At the subduction zone orange dispersion curves corresponds to the model without the slab and dashed-black line to the model with the slab. 73

Figure 3.12 Weight% of different stable minerals with depth for the reference model defined in LitMod2D_2.0 (section 3.5). Note that total weight% does not add to 100% in the shallow lithosphere (< 50 km) and around 300 km; this could be because of the failed numerical energy minimizations during the computation of stable mineral assemblage, although difference is only about <5%. 74

Figure 4.1 (a) Simplified geological map of the study region showing the location of the Alboran and Algerian basin geo-transects in shaded grey line. Earthquakes location colour coded for depth from 1964-2016 taken from International Seismological Centre (ISC, <https://doi.org/10.31905/D808B830>) catalogue are also plotted. (b) P-wave travel-time tomography along the Alboran Basin geo-transect from Bezada et al. (2013). (c) Absolute S-wave velocity model from Rayleigh surface-wave dispersion tomography (Palomeras et al. 2014) along the Alboran Basin geo-transect. (d) S-wave tomography using full-waveform inversion (modified after Figure 8 of Fichtner and Villaseñor, 2015) along the direction of cross-section C-C' marked in (a). 78

Figure 4.2 Geophysical observables in the region. (a) Shaded elevation and surface heat flow (dots), (b) Bouguer anomaly, (c) geoid filtered up to degree and order 10. Grey thick lines show the locations of the modelled NNW-SSE oriented geo-transects. 79

Figure 4.3 Crustal structure corresponding to the best fitting model for the (a) Alboran Basin and (b) Algerian Basin geo-transects. Densities used in each body are colour-coded (see the legend). Moho depths from previous studies (including active seismic, receiver functions, surface wave dispersion and joint modelling of gravity and elevation) are also plotted for comparison. Earthquakes ($M_b \geq 3.0$; 1964-2016, ISC catalogue) projected 50 km across the geo-transects are plotted with black circles. Note that the y-axis is exaggerated by two times the x-axis for better visualization. GB,

Guadalquivir Basin; CCR, Catalan Coastal Ranges; RF, Receiver functions; DSS, Deep seismic sounding.....	83
--	----

Figure 4.4 Pressure and temperature dependent density distribution for average sediments, upper crust, middle crust and lower crust compositions (see legend), computed from stable phases and mineral assemblages using the Gibbs free-energy minimization algorithm (Connolly, 2005, 2009). Red and black dashed line boxes mark the range of high pressure metamorphic peaks for Alpujarride and Nevado-Filabride HP/LT metamorphic units, respectively, determined from thermo-barometry (Augier et al., 2005; López Sánchez- Vizcaíno et al., 2001; Puga et al., 2000; Azañón and Crespo-Blanc, 2000).....	86
--	----

Figure 4.5 Best fitting model along the Alboran Basin geo-transect. (a) Surface heat flow. (b) Geoid height. (c) Bouguer anomaly. (d) Elevation. Blue line represents the calculated values from the model. Red dots denote measured data, and vertical bars denote the standard deviation calculated across a strip of 25 km half width. In (b) geoid height with no slab anomaly is plotted in grey for comparison. In (d) isostatic elevation is plotted in solid blue while the effect of slab on elevation (coupled elevation) is plotted in dashed blue line. Elevation assuming flexural isostasy for elastic thickness of 10 km and 30 km are plotted in orange and light-green, respectively. (e) Temperature distribution along the geo-transect. Continuous black lines highlight the Moho and LAB depth from our model. LAB depths from previous studies (dashed colour lines) are overlay plotted for comparison. (f) Density distribution in the mantle. The different composition domains in the lithospheric mantle are separated by thin black lines. The bold text in grey colour denotes chemical composition used in the different lithospheric mantle domains listed in Table 4.2.....	88
--	----

Figure 4.6 Alboran slab chemical composition sensitivity to the (a) geoid height and (b) Bouguer anomaly. Chemical composition has minuscule effect on the Bouguer anomaly and has noticeable effect on the geoid height. Variation in the Alboran slab composition, situated at depths >140 km, changes the mass distribution in the slab region and consequently affects the geoid at longer wavelengths along the geo-transect. DMM-3% chemical composition fits the geoid better along the Alboran Basin geo-transect.	89
--	----

Figure 4.7 Observed and modelled elevation across (a) Alboran Basin geo-transect and (b) Algerian basin geo-transect. Region highlighted in white shows extend along the geo-transect to which the slabs would affect the elevation. Dark-grey shaded strip shows the observed elevation across 50 km wide swath along the geo-transects. Solid coloured lines represent elevation with no slab anomaly (uncoupled), while dashed colour lines show calculated elevation considering the slab (coupled elevation). Blue	
--	--

lines shows isostatic elevation (i.e. $T_e = 0$ km). Orange and green lines show elevation considering flexural isostasy, $T_e = 10$ km, and 30 km, respectively.....	90
Figure 4.8 Temperature, density, and P- and S-wave velocity depth distribution in the Alboran slab at three locations spanning the slab region along the Alboran Basin geo-transect (see the legend). Upper panel shows the absolute deviation with respect to the LitMod reference column (Chapter 3) and lower panel shows the percentage change.....	93
Figure 4.9 Best fitting model along the Algerian Basin geo-transect, rest of the caption as in Figure 4.5.....	96
Figure 4.10 Algerian slab chemical composition sensitivity to the (a) geoid height and (b) Bouguer anomaly. DMM-7% chemical composition, resulting from 7%melting of DMM, fits better the geoid height along the Algerian Basin geo-transect.....	97
Figure 4.11 Temperature, density, P-wave velocity and S-wave velocity depth distribution in the Algerian slab at three locations (see the legend) spanning the slab region along the Algerian Basin geo-transect. Rest of the caption is same as in Figure 4.8.	99
Figure 4.12 Seismic velocities and synthetic seismic tomography along the geo-transects. (a) and (b) shows the absolute P-wave and S-wave velocities, respectively and (c) synthetic P-wave anomalies for the Alboran Basin geo-transect. Similarly (d) and (e) shows the absolute P- and S-wave velocities, respectively, and (f) synthetic P-wave anomalies along the Algerian Basin geo-transect.....	101
Figure 4.13 Geotherms (solid lines) at selected locations along the (a) Alboran Basin and (b) Algerian Basin geo-transects. Dry and wet peridotites solidus for different amount of bulk water from Katz and Spiegelman (2003) are also plotted. Presence of water in the mantle brings down the solidus resulting in presence of partial melts...	102
Figure 4.14 Location of the seismic stations along the geo-transects used to calculate P-wave receiver functions. Blue points show the location of piercing point at a depth 35 km along the Alboran Basin geo-transect.....	104
Figure 4.15 Plot showing the forward calculation of passive seismological data from the velocities obtained along Alboran Basin geo-transect. (a) Crustal S-wave velocities calculated using empirical relations (see text for details). (b) P-wave receiver function at distance, labelled in each plot, along the geo-transect. Solid green represent forward calculation and grey is observed P-wave receiver function (where available). (c) Rayleigh surface-wave fundamental mode phase velocity dispersion curves along	

the Alboran Basin geo-transect at distance along the geo-transect labelled in each plot. Grey circles represent the observed phase velocities and bars represent corresponding error. Green circles represent the forward calculation from the seismic velocity model obtained from LitMod2D_2.0. 106

Figure 4.16 Plot showing the comparison between forward prediction of receiver functions and Rayleigh surface-wave dispersion curves at selected locations. (a) Shows the depth distribution of S-wave velocities colour coded for location (see the legend). (b) P-wave receiver function, (c) group velocities, and (d) phase velocities colour coded for location (see legend in a). 108

Figure 5.1 Major element oxide weight% of the upper mantle compositions (Table 4.2) are plotted as function of Mg#, a measure of the fertility of the mantle. PUM-MS is also plotted for comparison. Blue shaded region represents the oceanic lithospheres and red shaded area the continental lithospheres. 119

Figure 5.2 Depth distribution of weight% of the stable minerals (see the title of each subplot) along the Alboran Basin geo-transect computed from the Gibbs-free energy minimization. Dashed light black line indicates the LAB and text in white colour indicates the chemical composition listed in the Table 4.2. 120

Figure 5.3 Depth distribution of weight% of the stable minerals (see the title of each subplot) along the Algerian Basin geo-transect computed from the Gibbs-free energy minimization chemical compositions used in the mantle. Rest of the caption as in Figure 5.2. 121

Figure 5.4 Plots showing depth variation of (a) density, (b) P-wave velocity, and (c) S-wave velocity for different minerals present in the mantle. 122

Figure 5.5 Plots showing variation of relevant physical properties with #Mg and major oxide weight percentages for the composition in Table 4.2, colour coded in (a). (a) Shows variation of density with #Mg and (b) with Al_2O_3 . (c) - (h) show variation of P-wave and S-wave velocity with #Mg, FeO, Al_2O_3 . Circles with thin-black outline corresponds to $P = 3 \text{ GPa}$ ($\sim 100 \text{ km}$) and $T = 1300 \text{ }^\circ\text{C}$, and circles with thick black outline corresponds to at $P = 6 \text{ GPa}$ ($\sim 200 \text{ km}$) and $T = 1400 \text{ }^\circ\text{C}$ (listed in Table 4.2). 124

Figure 5.6 Model showing the effect of the delaminated Iberian lithospheric mantle on (a) geoid, (b) Bouguer anomaly, and (c) elevation. In (d) resulting density distribution in the mantle is plotted. Blue line represents the calculated values from the model. Red dots denote measured data, and vertical bars denote the standard deviation calculated across a strip of 25 km half width. Continuous black lines highlight the Moho and LAB

depth. The different composition domains in the lithospheric mantle are separated by thin black lines. The bold grey text denotes different chemical composition listed in Table 4.2. Note the continuation of the Iberian lithospheric mantle (CVP) beneath the Betics to simulate no delamination and geometry of the delaminated lithosphere corresponding to the best fitting model is shown with thick dashed grey line. 126

Figure 5.7 Model showing the effect of the delaminated African lithospheric mantle on (a) geoid, (b) Bouguer anomaly, and (c) elevation. In (d) resulting density distribution in the mantle is plotted. Note the continuation of the African lithospheric mantle (Tc_1) beneath the Greater Kabylies to simulate no delamination. Rest of the caption is same as in Figure 5.6..... 127

Figure 5.8 Model showing the effect of the thick Nevado-Filabride HP/LT Internal Units on (a) geoid, (b) Bouguer anomaly, and (c) elevation. In (d) resulting density distribution in the crust is plotted. Blue line represents the calculated values from the model. Red dots denote measured data, and vertical bars denote the standard deviation calculated across a strip of 25 km half width. Note that below the crust, the model is the same as that of the best fitting model in Figure 4.5. 130

Figure 5.9 Crustal density distribution along the (a) Alboran Basin and (b) Algerian Basin geo-transects. Seismicity similar to the Figure 4.3 is also plotted. Note the increasing density with depth in the External units reaching values close to the upper crust..... 131

Figure 5.10 Crustal and lithospheric cross-sections at scale along modelled Algerian Basin-Kabylies-Tell-Atlas and Alboran Basin-Internal Betics-External Betics-foreland geo-transects. The structure of both the margins is similar and comparable implying that the underlying geodynamic processes are same for both the margins. 135

Table 2.1 Major oxide compositions (weight %) of the crust..... 26

Table 2.2 Mineral solid solution notation and formulae..... 37

Table 3.1 Major oxide compositions (weight %) in the mantle. 55

Table 3.2 Physical properties and major oxides composition in the mantle of a column at an old oceanic lithosphere used to compute calibration parameters for elevation. . 58

Table 3.3 Thermophysical parameters used in the crust to compare calculated seismic velocities with those from ak135 model..... 59

Table 4.1 Thermo-physical properties of the different tectonic units in the crust along the geo-transects.	82
Table 4.2 Major elements composition (weight %) in the NCFMAS system for the lithospheric mantle and sublithospheric domains used in the modelling and corresponding relevant physical properties at lithosphere and sublithospheric mantle pressure and temperature.....	84
Table 4.3 Root mean square error (RMSE) associated with the tested models. RMSE is calculated by considering the lateral variability of the observables through the assigned error bars (see text for explanation).	91

References

- Abers, G. A., K. M. Fischer, G. Hirth, D. A. Wiens, T. Plank, B. K. Holtzman, C. McCarthy, & E. Gazel (2014). Reconciling mantle attenuation-temperature relationships from seismology, petrology, and laboratory measurements, *Geochem. Geophys. Geosyst.*, 15, 3521–3542, doi:10.1002/2014GC005444.
- Afonso, J., Moorkamp, M., Fullea, J. (2016a). Imaging the lithosphere and upper mantle. *Geophysical Monograph Series*, pp. 191–218.
- Afonso, J. C., Fernández, M., Ranalli, G., Griffin, W. L., & Connolly, J. A. D. (2008). Integrated geophysical-petrological modeling of the lithosphere and sublithospheric upper mantle: Methodology and applications. *Geochemistry, Geophysics, Geosystems*, 9, Q05008.
- Afonso, J. C., Fullea, J., Griffin, W. L., Yang, Y., Jones, A. G., Connolly, J. A. D., & O'Reilly, S. Y. (2013a). 3-D multiobservable probabilistic inversion for the compositional and thermal structure of the lithosphere and upper mantle. I: A priori petrological information and geophysical observables. *Journal of Geophysical Research: Solid Earth*, 118, 2586–2617. <https://doi.org/10.1002/jgrb.50124>
- Afonso, J. C., Fullea, J., Yang, Y., Connolly, J. A. D., & Jones, A. G. (2013b). 3-D multi-observable probabilistic inversion for the compositional and thermal structure of the lithosphere and upper mantle. II: General methodology and resolution analysis. *Journal of Geophysical Research: Solid Earth*, 118, 1650–1676.
- Afonso, J.C., Ranalli, G., Fernández, M., Griffin, W.L., O'Reilly, S.Y. & Faul, U. (2010). On the Vp/Vs–Mg# correlation in mantle peridotites: Implications for the identification of thermal and compositional anomalies in the upper mantle. *Earth and Planetary Science Letters*, 289(3–4), pp.606–618.
- Afonso, J. C., Rawlinson, N., Yang, Y., Schutt, D., Jones, A. G., Fullea, J., & Griffin, W. L. (2016b). 3-D multiobservable probabilistic inversion for the compositional and thermal structure of the lithosphere and upper mantle: III. Thermochemical tomography in the Western-Central U.S. *Journal of Geophysical Research: Solid Earth*, 121, 7337–7370. <https://doi.org/10.1002/2016JB013049>
- Afonso, J. C., & Zlotnik, S. (2011). The subductability of the continental lithosphere: The before and after story. In D. Brown & P. D. Ryan (Eds.), *Arc-Continent Collision* (pp. 53–86). Berlin: *Frontiers in Earth Sciences*, Springer.
- Agard, P., Plunder, A., Angiboust, S., Bonnet, G., & Ruh, J. (2018). The subduction plate interface: rock record and mechanical coupling (from long to short timescales). *Lithos*, 320–321, 537–566.
- Aïdi, C., Beslier, M. O., Yelles-Chaouche, A. K., Klingelhoefer, F., Bracene, R., Galve, A., Bounif, A., Schenini, L., Hamai, L., Schnurle, P., Djellit, H., Sage, F., Charbis, P., & Déverchère, J., (2018). Deep structure of the continental margin and basin off Greater Kabylia, Algeria—New insights from wide-angle seismic data modeling and multichannel seismic interpretation. *Tectonophysics*, 728, 1–22.
- Alvarez, W., Coccozza, T., & Wezel, F. C. (1974). Fragmentation of the Alpine orogenic belt by microplate dispersal. *Nature*, 248(5446), 309–314.
- Amante, C., & Eakins, B. W. (2009). ETOPO1 1 Arc-minute global relief model: Procedures, data sources and analysis. NOAA Technical Memorandum NESDIS NGDC-24, <http://www.ngdc.noaa.gov/mgg/global/global.html>

- Amaru, M. L. (2007). Global travel time tomography with 3-D reference models (Vol. 274). Utrecht University.
- Anderson, D.L. & Minster, J.B. (1979). The frequency dependence of Q in the Earth and implications for mantle rheology and Chandler wobble. *Geophys. J. R. Astron. Soc.* 58:431–40
- Anderson, D. (1989). Appendix "Theory of the Earth". *Theory of the Earth*, 52 (1354), 569–569.
- Asimow, P.D., Hirschmann, M.M. & Stolper, E.M. (2001). Calculation of peridotite partial melting from thermodynamic models of minerals and melts, IV. Adiabatic decompression and the composition and mean properties of mid-ocean ridge basalts. *Journal of Petrology*, 42(5), pp.963–998.
- Asimow, P. D., M. M. Hirschmann, & L. M. Stolper (2001), Calculation of peridotite partial melting from thermodynamic model of minerals and melts, IV. Adiabatic decompression and the composition and mean properties of mid-ocean basalts, *J. Petrol.*, 42, 963–998.
- Asimow, P. D., Dixon, J. E. & Langmuir, C. H. (2004), A hydrous melting and fractionation model for mid-ocean ridge basalts: Application to the Mid-Atlantic Ridge near the Azores, *Geochem. Geophys. Geosyst.*, 5, Q01E16, doi:10.1029/2003GC000568.
- Augier, R., Agard, P., Monié, P., Jolivet, L., Robin, C., Booth-Rea, G., (2005). Exhumation, doming and slab retreat in the Betic Cordillera (SE Spain): in situ $^{40}\text{Ar}/^{39}\text{Ar}$ ages and P–T–d–t paths for the Nevado-Filabride complex. *Journal of Metamorphic Geology* 23, 357–381.
- Ayala, C., Bohoyo, F., Maestro, A. Reguera, M. I., Rubio, F. M., Torne, M., et al. (2016). Updated Bouguer anomaly map of the Iberian Peninsula: A new perspective to interpret the regional geology. *Journal of Maps*. <https://doi.org/10.1080/17445647.2015.1126538>
- Azañón, J.M., Crespo-Blanc, A. (2000). Exhumation during a continental collision inferred from the tectonometamorphic evolution of the Alpujarride Complex in the central Betics (Alboran Domain, SE Spain). *Tectonics* 19, 549–565.
- Banda, E., Gallart, J., Garcia-Duenas, V., Danobeitia, J.J., Makris, J. (1993). Lateral variation of the crust in the Iberian Peninsula. New evidence from the Betic Cordillera. *Tectonophysics* 221, 53–66
- Banks, C.J., Warburton, J. (1991). Mid-crustal detachment in the Betic system of southeast Spain. *Tectonophysics* 191, 275–289.
- Behn, M., & Kelemen, P. (2003). The relationship between seismic P-wave velocity and the composition of anhydrous igneous and meta-igneous rocks. *Geochem Geophys Geosyst* 4:1041. doi:10.1029/2002GC000393
- Berástegui, X., Banks, C.J., Puig, C., Taberner, C., Waltham, D., Fernandez, M. (1998). Lateral diapiric emplacement of Triassic evaporites at the southern margin of the Guadalquivir Basin, Spain. In: Mascle, A., Puigdefabregas, C., Luterbacher, H., Fernandez, M. (Eds.), *Cenozoic Foreland Basins of Western Europe*. Geological Society Special Publications 134, pp. 49–68.
- Bezada, M. J., Humphreys, E. D., Toomey, D. R., Harnafi, M., Dávila, J. M., & Gallart, J. (2013). Evidence for slab rollback in westernmost Mediterranean from improved mantle imaging. *Earth and Planetary Science Letters*, 368, 51–60. <https://doi.org/10.1016/j.epsl.2013.02.024>
- Boonma, K., Kumar, A., García-Castellanos, D., Jiménez-Munt, I., & Fernández, M. (2019). Lithospheric mantle buoyancy: the role of tectonic convergence and mantle composition. *Scientific reports*, 9(1), 1–8.

- Booth-Rea, G., Ranero, C. R., Martínez-Martínez, J. M., & Grevemeyer, I. (2007). Crustal types and Tertiary tectonic evolution of the Alborán sea, western Mediterranean. *Geochemistry, Geophysics, Geosystems*, 8(10).
- Bianchini, G., Beccaluva, L., Bonadiman, C., Nowell, G. M., Pearso, D. G., Siena, F., & Wilson, M. (2010). Mantle metasomatism by melts of HIMU piclogite components: New insights from Fe-Iherzolite xenoliths (Calatrava Volcanic District, central Spain). In M. Coltorti, H. Downes, M. Gregoire, & S. O'Renly (Eds.), *Petrological evolution of the European lithospheric mantle*, Special Publications (Vol. 337, pp. 107–124). London: Geological Society.
- Bowin, C., (1983). Depth of principal mass anomalies contributing to the Earth's Geoidal Undulations and gravity anomalies. *Marine Geodesy*, 7: 61-100.
- Bowin, C., (2000). Mass anomalies and the structure of the Earth. *Physics and Chemistry of the Earth*, 25 (4): 343-353.
- Brey, G. P., Doroshev, A. M., Giris, A. V. & Turkin, A. I. (1999), Garnet-spinel-olivine-orthopyroxene equilibria in the FeO-MgO-Al₂O₃-SiO₂-Cr₂O₃ system: I. Composition and molar volumes of minerals, *Eur. J. Mineral.*, 11, 599–617.
- Brocher, T. (2005). Empirical relations between elastic wavespeeds and density in the Earth's crust. *Bulletin of the Seismological Society of America*, 95 (6), 2081-2092.
- Brown, E. L., Petersen, K. D., & Leshner, C. E. (2020). Markov chain Monte Carlo inversion of mantle temperature and source composition, with application to Reykjanes Peninsula, Iceland. *Earth and Planetary Science Letters*. 2020. 532. <https://doi.org/10.1016/j.epsl.2019.116007>.
- Bruguier, O., Bosch, D., Caby, R., Vitale-Brovarone, A., Fernandez, L., Hammor, D., Laouar, R., Ouabadi, A., Abdallah, N., & Mechat, M. (2017). Age of UHP metamorphism in the Western Mediterranean: insight from rutile and minute zircon inclusions in a diamond-bearing garnet megacryst (Edough Massif, NE Algeria). *Earth and Planetary Science Letters*, 474, 215-225.
- Brun, J. P., & Faccenna, C. (2008). Exhumation of high-pressure rocks driven by slab rollback. *Earth and Planetary Science Letters*, 272(1-2), 1-7.
- Caby, R., Bruguier, O., Fernandez, L., Hammor, D., Bosch, D., Mechat, M., Laouar, R., Ouabadi, A., Abdallah, N., & Douchet, C. (2014). Metamorphic diamonds in a garnet megacryst from the Edough Massif (northeastern Algeria). *Recognition and geodynamic consequences*. *Tectonophysics*, 637, 341-353.
- Calvert, A., Sandvol, E., Seber, D., Barazangi, M., Roecker, S., Mourabit, T., Vidal, F., Alguacil, G., Jabour, N., (2000). Propagation of regional seismic phases (Lg and Sn) and Pn velocity structure along the Africa–Iberia plate boundary zone. *Geophysical Journal International* 142, 384–408.
- Cammarano, F., & Romanowicz, B. (2008). Radial profiles of seismic attenuation in the upper mantle based on physical models. *Geophysical Journal International*, 175 (1), 116-134.
- Cammarano, F., Deuss, A., Goes, S., & Giardini, D. (2005). One-dimensional physical reference models for the upper mantle and transition zone: Combining seismic and mineral physics constraints. *Journal of Geophysical Research: Solid Earth*, 110 (1), 1-17.
- Cammarano, F., Goes, S., Vacher, P., & Giardini, D. (2003). Inferring upper-mantle temperatures from seismic velocities. *Physics of the Earth and Planetary Interiors*, 138 (3-4), 197-222.
- Cammarano, F., Romanowicz, B., Stixrude, L., Lithgow-Bertelloni, C., & Xu, W. (2009). Inferring the thermochemical structure of the upper mantle from seismic data. *Geophysical Journal International*, 179 (2), 1169-1185.

- Carlson, R.W., Pearson, D.G. & James, D.E. (2005). Physical, chemical, and chronological characteristics of continental mantle. *Reviews of Geophysics*, 43:RG1001.
- Casciello, E., Fernández, M., Vergés, J., Cessarano, M., & Torne, M. (2015). The Alboran Domain in the Western Mediterranean evolution: The birth of a concept. *Bull. Soc. Géol.*, 186, 23–34.
- Carballo, A., Fernandez, M., Torne, M., Jiménez-Munt, I., & Villaseñor, A. (2015a). Thermal and petrophysical characterization of the lithospheric mantle along the northeastern Iberia geo-transect. *Gondwana Research*, 27, 1430-1445.
- Carballo, A., Fernandez, M., Jiménez-Munt, I., Torne, M., Vergés, J., Melchiorre, M., et al. (2015b). From the North-Iberian Margin to the Alboran Basin: A lithosphere geo-transect across the Iberian Plate. *Tectonophysics*, 399-418.
- Carbonell, R., Torne, M., García-Dueñas, V., Moya, R., & Banda, E., (1997). The ESCI-Béticas: a seismic reflection image of the Betics orogen. *Rev. Soc. Geol. Esp.* 8, 503–512.
- Carbonell, R., Sallarès, V., Pous, J., Dan, J. J., Queralt, P., Ledo, J. J., & Duen, V. G. (1998). A multidisciplinary geophysical study in the Betic chain (southern Iberia Peninsula). *Tectonophysics*, 288(1-4), 137-152.
- Chazot, G., Abbassene, F., Maury, R. C., Déverchère, J., Bellon, H., Ouabadi, A., & Bosch, D. (2017). An overview on the origin of post-collisional Miocene magmatism in the Kabylies (northern Algeria): evidence for crustal stacking, delamination and slab detachment. *Journal of African Earth Sciences*, 125, 27-41.
- Chertova, M.V.; Spakman, W.; Geenen, T.; van den Berg, A.P.; & van Hinsbergen, D.J.J. (2014). Underpinning tectonic reconstructions of the western Mediterranean region with dynamic slab evolution from 3-D numerical modeling. *J. Geophys. Res.: Solid Earth*, 119, 5876–5902.
- Christensen, N., Mooney, W. (1995). Seismic velocity structure and composition of the continental crust: a global view. *J. Geophys. Res.* 100 (B6), 9761–9788. <http://dx.doi.org/10.1029/95JB00259>
- Civiero, C., Strak, V., Custódio, S., Silveira, G., Rawlinson, N., Arroucau, P., & Corela, C. (2018). A common deep source for upper-mantle upwellings below the Ibero-western Maghreb region from teleseismic P-wave travel-time tomography. *Earth and Planetary Science Letters*, 499, 157-172.
- Civiero, C., Custódio, S., Duarte, J. C., Mendes, V. B., & Faccenna, C. (2020). Dynamics of the Gibraltar Arc System: A Complex Interaction Between Plate Convergence, Slab Pull, and Mantle Flow. *Journal of Geophysical Research: Solid Earth*, 125(7), e2019JB018873.
- Comas, M.C., Dañobeitia, J.J., Alvarez-Marrón, J., Soto, J.I., (1995). Crustal reflections and structure in the Alboran Basin: Preliminary Results of the SCI-Alboran Survey. In: Santanach, P. (Ed.) *Revista de la Sociedad Geológica de España* 8, pp. 75–88
- Connolly, J. (2005). Computation of phase equilibria by linear programming: A tool for geodynamic modeling and its application to subduction zone decarbonation. *Earth and Planetary Science Letters*, 236 (1-2), 524-541.
- Connolly, J. A. D. (2009). The geodynamic equation of state: What and how, *Geochem. Geophys. Geosyst.*, 10, Q10014, doi:10.1029/2009GC002540.
- Connolly, J. A. D., & Kerrick, D. M. (2002), Metamorphic controls on seismic velocity of subducted oceanic crust at 100–250 km depth, *Earth Planet. Sci. Lett.*, 204, 61–74.
- Coulon, C., Megartsi, M., Fourcade, S., Maury, R.C., Bellon, H., Louni-Hacini, A., Cotten, J., Coutelle, A., & Hermitte, D., (2002). Post-collisional transition from calc-alkaline to alkaline

- volcanism during the Neogene in Oranie (Algeria): magmatic expression of a slab breakoff. *Lithos* 62, 87–110.
- Dañobeitia, J.J., Arguedas, M., Gallart, F., Banda, E., & Makris, J., (1992). Deep crustal configuration of the Valencia trough and its Iberian and Balearic borders from extensive refraction and wide-angle reflection profiling. *Tectonophysics* 203, 37–55.
- Davies, J. H. (2013). Global map of solid Earth surface heat flow. *Geochemistry, Geophysics, Geosystems*, 14(10), 4608–4622.
- Deen, T. J., W. L. Griffin, G. Begg, S. Y. O'Reilly, L. M. Natapov, & J. Hronsky (2006), Thermal and compositional structure of the subcontinental lithospheric mantle: Derivation from shear wave seismic tomography. *Geochem. Geophys. Geosyst.*, 7, Q07003, doi:10.1029/2005GC001120.
- Déverchère, J., Yelles, K., Domzig, A., Mercier de Lépinay, B., Bouillin, J.P., Gaullier, V., Bracène, R., Calais, E., Savoye, B., Kherroubi, A. & Le Roy, P., 2005. Active thrust faulting offshore Boumerdes, Algeria, and its relations to the 2003 Mw 6.9 earthquake. *Geophysical research letters*, 32(4).
- Dewey, J.F., Helman, M.L., Turco, E., Hutton, D.H.W., Knott, S.D. (1989). Kinematics of the western Mediterranean. In *Alpine Tectonics*, ed. M.P. Coward, D. Dietrich, R.G. Park, pp. 265–83. *Geol. Soc. Spec. Publ.* 45. London: Geol. Soc. Lond.
- Diaferia, G., & Cammarano, F. (2017). Seismic Signature of the Continental Crust: What Thermodynamics Says. An Example From the Italian Peninsula. *Tectonics*, 36 (12), 3192–3208.
- Díaz, J., Gallart, J., & Carbonell, R. (2016). Moho topography beneath the Iberian-Western Mediterranean region mapped from controlled- source and natural seismicity surveys. *Tectonophysics*, 692, 74–85. <https://doi.org/10.1016/j.tecto.2016.08.023>
- Díaz, J., Gallart, J. (2009). Crustal structure beneath the Iberian Peninsula and surrounding waters: a new compilation of deep seismic sounding results. *Phys. Earth Planet. Sci. Lett.* 173, 181–190. <http://dx.doi.org/10.1016/j.pepi.2008.11.008>.
- Díaz, J., Gil, A., Gallart, J. (2013). Uppermost mantle seismic velocity and anisotropy in the Euro-Mediterranean region from Pn and Sn tomography. *Geophys. J. Int.* <http://dx.doi.org/10.1093/gji/ggs016>.
- Duggen, S., Hoernle, K., van den Bogaard, P., & Garbe-Schönberg, D. (2005). Post-collisional transition from subduction- to intraplate-type magmatism in the westernmost Mediterranean: Evidence for continental-edge delamination of subcontinental lithosphere. *Journal of Petrology*, 46, 1155–1201. <https://doi.org/10.1093/petrology/egi013>
- Duggen, S., Hoernle, K. A., Klugel, A., Geldmacher, J., Thirlwall, M. F., Hauff, F., et al. (2008). Geochemical zonation of the Miocene Alborán Basin volcanism (westernmost Mediterranean): Geodynamic implications. *Contributions to Mineralogy and Petrology*, 156, 577–593. <https://doi.org/10.1007/s00410-008-0302-4>
- Durek, J., & Ekström, G. (1996). A radial model of anelasticity consistent with long-period surface-wave attenuation. *Bulletin of the Seismological Society of America*, 86 (1 SUPPL. A), 144–158.
- Eaton, D. W., Darbyshire, F., Evans, R. L., Grütter, H., Jones, A., & Yuan, X. (2009). The elusive lithosphere-asthenosphere boundary (LAB) beneath cratons. *Lithos*, 109, 1–22. <https://doi.org/10.1016/j.lithos.2008.05.009>
- Ehsan, S. A., Carbonell, R., Ayarza, P., Martí, D., Jesús Martínez-Poyatos, D., Simancas, J., et al. (2015). Lithospheric velocity model across the Southern Central Iberian Zone (Variscan Iberian Massif): The ALCUDIA wide-angle seismic reflection transect. *Tectonics*, 34, 535–554. <https://doi.org/10.1002/2014TC003661>

- Etheve, N., Mohn, G., Frizon de Lamotte, D., Roca, E., Tugend, J., & Gómez-Romeu, J. (2018). Extreme Mesozoic crustal thinning in the eastern Iberia margin: the example of the Columbrets Basin (Valencia Trough). *Tectonics*, 37(2), 636-662.
- Faccenna, C., Becker, T. W., Auer, L., Billi, A., Boschi, L., Brun, J. P., & Piromallo, C. (2014). Mantle dynamics in the Mediterranean. *Reviews of Geophysics*, 52(3), 283-332.
- Faccenna, C., Piromallo, C., Crespo-Blanc, A., Jolivet, L., & Rossetti, F. (2004). Lateral slab deformation and the origin of the western Mediterranean arcs. *Tectonics*, 23(1).
- Faul, U. & Jackson, I. (2015). Transient Creep and Strain Energy Dissipation: An Experimental Perspective. *Annual Review of Earth and Planetary Sciences* 2015 43:1, 541-569.
- Fernandez, L., Bosch, D., Bruguier, O., Hammor, D., Caby, R., Monié, P., et al. (2016). Permo-carboniferous and early miocene geological evolution of the internal zones of the Maghrebides-new insights on the western Mediterranean evolution. *Journal of Geodynamics* 96: 146–173.
- Fernández-García, C., Guillaume, B., & Brun, J. P. (2019). 3D slab breakoff in laboratory experiments. *Tectonophysics*, 773, 228223.
- Fernàndez, M., & Cabal, J. (1992). Heat-flow data and shallow thermal regime on Mallorca and Menorca (western Mediterranean). *Tectonophysics*, 203(1-4), 133-143.
- Fernàndez, M., Afonso, J., & Ranalli, G. (2010). The deep lithospheric structure of the Namibian volcanic margin. *Tectonophysics*, 481 (1-4), 68-81.
- Fernàndez, M., Marzan, I., Correia, A., Ramalho, E., (1998a). Heat flow, heat production, and lithospheric thermal regime in the Iberian Peninsula. *Tectonophysics* 291, 29–53. [http://dx.doi.org/10.1016/S0040-1951\(98\)00029-8](http://dx.doi.org/10.1016/S0040-1951(98)00029-8).
- Fernàndez, M., Berástegui, X., Puig, C., García-Castellanos, D., Jurado, M.J., Torné, M., Banks, C., (1998b). Geophysical and geological constraints on the evolution of the Guadalquivir foreland basin, Spain. In: Mascle, A., Puigdefàbregas, C., Luterbacher, H.P., Fernàndez, M. (Eds.), *Cenozoic Foreland Basins of Western Europe: Geological Society Special Publications*, 134, pp. 29–48.
- Fernàndez, M., Foucher, J.P., & Jurado, M.J. (1995). Evidence for the multi-stage formation of the south- western Valencia Trough. *Marine and Petroleum Geology*, 12, 101-109.
- Fernàndez, M., Torne, M., Vergés, J., Casciello, E., & Macchiavelli, C. (2019). Evidence of Segmentation in the Iberia–Africa Plate Boundary: A Jurassic Heritage?. *Geosciences*, 9(8), 343.
- Fichtner, A., Villaseñor, A., (2015). Crust and upper mantle of the western Mediterranean - constraints from full-waveform inversion. *Earth Planet. Sci. Lett.* 428, 52–62.
- Foucher, J.E., Mauffret, A., Steckler, M., Brunet, M.E., Maillard, A., Rehanlt, J.E., Alonso, B., Desegaulx, E., Murillas, J., & Ouillon, G., (1992). Heat flow in the Valencia trough: geodynamic implications. *Tectonophysics* 203, 77–97.
- Foulger, G.R., Panza, G.F., Artemieva, I.M., Bastow, I.D., Cammarano, F., Evans, J.R., Hamilton, W.B., Julian, B.R., Lustrino, M., Thybo, H. & Yanovskaya, T.B., (2013). Caveats on tomographic images. *Terra Nova*, 25 (4), 259-281.
- Fourcade, S., Capdevila, R., Ouabadi, A., & Martineau, F. (2001). The origin and geodynamic significance of the Alpine cordierite-bearing granitoids of northern Algeria. A combined petrological, mineralogical, geochemical and isotopic (O, H, Sr, Nd) study. *Lithos*, 57(2-3), 187-216.
- Fullea, J., Fernàndez, M., Zeyen, H., & Vergés, J. (2007). A rapid method to map the crustal and lithospheric thickness using elevation, geoid anomaly and thermal analysis: Application

- to the Gibraltar Arc System, Atlas Mountains and adjacent zones. *Tectonophysics*, 430, 97–117.
- Fullea, J., Fernàndez, M., Afonso, J. C., Vergés, J., & Zeyen, H. (2010). The structure and evolution of the lithosphere–asthenosphere boundary beneath the Atlantic–Mediterranean Transition Region. *Lithos*, 120(1-2), 74-95.
- Fullea, J., Afonso, J., Connolly, J., Fernàndez, M., García-Castellanos, D., & Zeyen, H. (2009). LitMod3D: An interactive 3-D software to model the thermal, compositional, density, seismological, and rheological structure of the lithosphere and sublithospheric upper mantle. *Geochemistry, Geophysics, Geosystems*, 10 (8), 1-21.
- Fullea, J., Fernàndez, M., & Zeyen, H. (2008). FA2BOUG—A FORTRAN 90 code to compute Bouguer gravity anomalies from gridded free air anomalies: Application to the Atlantic–Mediterranean transition zone. *Computers & Geosciences*, 34, 1665–1681. <https://doi.org/10.1016/j.cageo.2008.02.018>
- Frizon de Lamotte, D., Crespo-Blanc, A., Saint-Bezar, B., Comas, M., Fernandez, M., Zeyen, H., Ayarza, P., Robert-Charreau, C., Chalouan, A., Zizi, M., Teixel, A., Arboleya, M.L., Alvarez-Lobato, F., Julivert, M., Michard, A., (2004). TRASNSMED-transect I (Betics, Alboran Sea, Rif, Moroccan Meseta, High Atlas, Jbel Saghro, Tindouf basin). In: Cavazza, W., Roure, F., Spakman, W., Stampfli, G.M., Ziegler, P.M. (Eds.), *The TRANSMED Atlas- the Mediterranean region from Crust to Mantle*. Springer, Berlin Heidelberg.
- Frizon de Lamotte, D., Saint Bezar, B., Bracène, R., & Mercier, E. (2000). The two main steps of the Atlas building and geodynamics of the western Mediterranean. *Tectonics*, 19(4), 740-761.
- Frizon de Lamotte, D., Raulin, C., Mouchot, N., Wrobel-Daveau, J.-C., Blanpied, C., Ringenbach, J.C., (2011). The southernmost margin of the Tethys realm during the Mesozoic and Cenozoic: initial geometry and timing of the inversion processes. *Tectonics* 30, TC3002. <http://dx.doi.org/10.1029/2010TC002691>.
- Gallart, J., Vidal, N., Dañobeitia, J.J., (1995). Multichannel seismic image of the crustal thinning at the NE Iberian margin combining normal and wide angle reflection data. *Geophys. Res. Lett.* 22, 489–492.
- Garcia-Castellanos, D., Fernandez, M., & Torne, M. (2002). Modeling the evolution of the Guadalquivir foreland basin (southern Spain). *Tectonics*, 21 (3).
- Garcia-Castellanos, D., & Villasenor, A. (2011). Messinian salinity crisis regulated by competing tectonics and erosion at the Gibraltar arc., *Nature*, 480(7377), 359–363. <https://doi.org/10.1038/nature10651>
- Gaspar-Escribano, J. M., Garcia-Castellanos, D., Roca, E., & Cloetingh, S. A. P. L. (2004). Cenozoic vertical motions of the Catalan Coastal Ranges (NE Spain): The role of tectonics, isostasy, and surface transport. *Tectonics*, 23(1).
- Gilardoni, M., Reguzzoni, M., & Sampietro, D. (2016). GECO: A global gravity model by locally combining GOCE data and EGM2008. *Studia Geophysica et Geodaetica*, 60, 228–247. <https://doi.org/10.1007/s11200-015-1114-4>
- Globig, J., Fernàndez, M., Torne, M., Vergés, J., Robert, A., & Faccenna, C. (2016). New insights into the crust and lithospheric mantle structure of Africa from elevation, geoid, and thermal analysis. *Journal of Geophysical Research - Solid Earth*, 121, 5389–5424. <https://doi.org/10.1002/2016JB012972>
- Goes, S., Govers, R., & Vacher, P. (2000). Shallow mantle temperatures under Europe from P and S wave tomography . *Journal of Geophysical Research: Solid Earth*, 105 (B5), 11153-11169.

- Gómez de la Peña, L., Ranero, C. R., & Gràcia, E. (2018). The crustal domains of the Alboran Basin (western Mediterranean). *Tectonics*, 37, 3352–3377. <https://doi.org/10.1029/2017TC004946>
- Govers, R., Wortel, M., 2005. Lithosphere tearing at STEP faults: response to edges of subduction zones. *Earth Planet. Sci. Lett.* 236, 505–523. doi:10.1016/j.epsl.2005.03.022
- Gribb, T.T. & Cooper, R.F. 1998. Low-frequency shear attenuation in polycrystalline olivine: Grain bound- ary diffusion and physical significance of the Andrade model for viscoelastic rheology. *J. Geophys. Res.* 103:27,267–79
- Griffin, W., O'Reilly, S. Y. & Ryan, C. G. (1999). The composition and origin of sub-continental lithospheric man- tle, in *Mantle Petrology: Field Observations and High-Pressure Experimentation: A Tribute to Francis R. (Joe) Boyd*, edited by Y. Fei, C. M. Berkta, and B. O. Mysen, *Spec. Publ. Geochem. Soc.*, 6, 13–45.
- Griffin, W., O'Reilly, S., Afonso, J., & Begg, G. (2009). The composition and evolution of lithospheric mantle: A re-evaluation and its tectonic implications. *Journal of Petrology*, 50 (7), 1185-1204.
- Grose, C., & Afonso, J. (2013). Comprehensive plate models for the thermal evolution of oceanic lithosphere. *Geochemistry, Geophysics, Geosystems*, 14 (9), 3751-3778.
- Gueguen, E., Doglioni, C., & Fernandez, M., (1998). On the post-25 Ma geodynamic evolution of the western Mediterranean. *Tectonophysics* 298, 259–269.
- Guerrera, F., & Martín-Martín, M. (2014). Geodynamic events reconstructed in the Betic, Maghrebian, and Apennine chains (central-western Tethys). *Bulletin de la Société géologique de France*, 185(5), 329-341.
- Hamai, L., Petit, C., Le Pourhiet, L., Yelles-Chaouche, A., Déverchère, J., Beslier, M. O., & Abtout, A. (2018). Towards subduction inception along the inverted North African margin of Algeria? Insights from thermo-mechanical models. *Earth and Planetary Science Letters*, 501, 13-23.
- Hatzfeld, D., & Molnar, P. (2010). Comparisons of the kinematics and deep structures of the Zagros and Himalaya and of the Iranian and Tibetan plateaus and geodynamic implications. *Reviews of Geophysics*, 48(2).
- Hatzfeld, D., & the Working Group for Deep Seismic Sounding, (1978). Crustal seismic profiles in the Alboran Sea — preliminary results. *Pure and Applied Geophysics* 116, 167–180.
- Heiskanen, W.A. & Moritz, H., (1967). *Physical Geodesy*, San Francisco, 364 pp.
- Herrmann, R. (2013). Computer Programs in Seismology: An Evolving Tool for Instruction and Research. *Seismological Research Letters*, 84 (6), 1081-1088.
- Hill, R. (1952). The elastic behaviour of a crystalline aggregate. *Proceedings of the Physical Society. Section A* .
- Hinz, K., (1972). Results of seismic refraction investigations (Project Anna) in Western Mediterranean, south and north of the island of Mallorca. *Bulletin Centre De Recherches Pau-SNPA* 6 (2), 405–426.
- Hoggard, M., Czarnta, K., Richards, F., Huston, D. L., Jaques, A. L. & Ghelichkhan, S. (2020). Gigayear stability of cratonic edges controls global distribution of sediment-hosted metals. <https://doi.org/10.31223/osf.io/2kjvc>.
- Hofmeister, A. M. (2005), Dependence of diffusive radiative transfer on grain-size, temperature, and Fe-content: Implications for mantle processes, *J. Geodyn.*, 40, 51–72.
- Holland, T., & Powell, R. (1998). An internally consistent thermodynamic data set for phases of petrological interest. *Journal of Metamorphic Geology*, 16 (3), 309-343.

- Hunter, J. (2007). Matplotlib: A 2D graphics environment. *Computing In Science & Engineering*, 9 (3), 90-95.
- Ince, E. S., Barthelmes, F., Reißland, S., Elger, K., Förste, C., Flechtner, F., & Schuh, H. (2019). ICGEM-15 years of successful collection and distribution of global gravitational models, associated services and future plans. *Earth System Science Data*, 11, 647–674. <http://doi.org/10.5194/essd-11-647-2019>
- Irfune, T. & Isshiki, M., 1998. Iron partitioning in a pyrolite mantle and the nature of the 410-km seismic discontinuity. *Nature*, 392(6677), pp.702-705.
- Ito, E., & T. Katsura (1989), A temperature profile of the mantle transition zone, *Geophys. Res. Lett.*, 16, 425–428.
- Jackson, I., & Faul, U. (2010). Grainsize-sensitive viscoelastic relaxation in olivine: Towards a robust laboratory-based model for seismological application. *Physics of the Earth and Planetary Interiors*, 183, 151-163.
- Jolivet, L., Faccenna, C., & Piromallo, C. (2009), From mantle to crust: Stretching the Mediterranean, *Earth Planet. Sci. Lett.*, 285, 198–209, doi:10.1016/j.epsl.2009.06.017.
- Jiménez-Munt, I., Torne, M., Fernández, M., Vergés, J., Kumar, A., Carballo, A., & García-Castellanos, D., (2019). Deep Seated Density Anomalies Across the Iberia-Africa Plate Boundary and Its Topographic Response. *J. Geophys. Res. Solid Earth* 124, 13310–13332. doi:10.1029/2019JB018445
- Jiménez-Munt, I., Fernandez, M., Vergés, J., Garcia-Castellanos, D., Fullea, J., Pérez-Gussinyé, M., & Afonso, J. C. (2011). Decoupled crust-mantle accommodation of Africa-Eurasia convergence in the NW Moroccan margin. *Journal of Geophysical Research: Solid Earth*, 116(B8).
- Julià, J., Ammon, C., Herrmann, R., & Correig, A. (2000). Joint inversion of receiver function and surface wave dispersion observations. *Geophysical Journal International*, 143 (1), 99-112.
- Kaban, M. K., Chen, B., Tesauero, M., Petrunin, A. G., El Khrepy, S., & Al-Arifi, N. (2018). Reconsidering effective elastic thickness estimates by incorporating the effect of sediments: A case study for Europe. *Geophysical Research Letters*, 45, 9523–9532, doi:10.1029/2018GL079732
- Katsura, T., Yamada, H., Nishikawa, O., Song, M., Kubo, A., Shinmei, T., Yokoshi, S., Aizawa, Y., Yoshino, T., Walter, M.J. & Ito, E. (2004). Olivine-wadsleyite transition in the system (Mg, Fe)₂SiO₄. *Journal of Geophysical Research: Solid Earth*, 109(B2).
- Katz, R. F., M. Spiegelman, & C. H. Langmuir, A new parameterization of hydrous mantle melting, *Geochem. Geophys. Geosyst.*, 4(9), 1073, doi:10.1029/2002GC000433, 2003.
- Kennett, B. (2006). On seismological reference models and the perceived nature of heterogeneity. *Physics of the Earth and Planetary Interiors*, 159 (3-4), 129-139.
- Kennett, B., Engdahl, E., & Buland, R. (1995). Constraints on seismic velocities in the Earth from traveltimes. *Geophysical Journal International* (122), 108-124.
- Khamsi, S., Roure, F., Khelil, M., Mezni, R., & Echihi, O., 2019. A review of the crustal architecture and related pre-salt oil/gas objectives of the eastern Maghreb Atlas and Tell: Need for deep seismic reflection profiling. *Tectonophysics* 766, 232–248. doi:10.1016/j.tecto.2019.06.009
- Klein, E., & Langmuir, C. (1987). Global correlations of ocean ridge basalt chemistry with axial depth: A new perspective. *Journal of Geophysical Research*, 92 (B8), 8089-8115.

- Koulakov, I., Burov, E., Cloetingh, S., El Khrepy, S., Al-Arifi, N., & Bushenkova, N. (2016). Evidence for anomalous mantle upwelling beneath the Arabian Platform from traveltimes tomography inversion. *Tectonophysics*, 667, 176–188.
- Kumar, A., Fernández, M., Jimenez-Munt, I., Torne, M., Vergés, J., & Afonso, J. C. (2020). LitMod2D_2. 0: An improved integrated geophysical-petrological modeling tool for the physical interpretation of upper mantle anomalies. *Geochemistry, Geophysics, Geosystems*, e2019GC008777, doi: 10.1029/2019GC008777
- Kumar, A., Fernandez, M., Peral, M., Funiciello, F., Zlotnik, S., Faccenna, C., & Vergés, J. (2018). Effects of kinematic boundary conditions on trench curvature in a retreating subduction zone: insights from analog modelling. American Geophysical Union, Fall Meeting 2018, abstract #DI51B-0012, 2018AGUFMDI51B0012K.
- Kushiro, I. (2001). Partial melting experiments on peridotite and origin of mid-ocean ridge basalt, *Annu. Rev. Earth Plan. Sci.*, 29, 71–107.
- Lachenbruch, A. H., & P. Morgan (1990), Continental extension, magmatism, and elevation: Formal relations and rules of thumb. *Tectonophysics*, 174, 39–62.
- Langmuir, C. H., Klein, E. M., & Plank, T. (1992), Petrological systematics of mid-ocean ridge basalts: Constraints on melt generation beneath ocean ridges, in *Mantle Flow and Melt Generation at Mid-Ocean Ridges*, *Geophys. Monogr. Ser.*, vol. 71, edited by J. Phipps Morgan, D. K. Blackman, and J. M. Sinton, pp. 183–280, AGU, Washington, D. C.
- Langston, C. (1979). Structure under Mount Rainier, Washington, inferred from teleseismic body waves. *Journal of Geophysical Research*, 84 (B9), 4749–4762.
- Laouar, R., Boyce, A.J., Arafa, M., Ouabadi, A., & Fallick, A.E. (2005). Petrological, geochemical, and stable isotope constraints on the genesis of the Miocene igneous rocks of Chetaibi and Cap de Fer (NE Algeria). *J. Afr. Earth Sci.* 41, 445–465.
- Lau, H.C.P., & Faul, U.H. (2019). Anelasticity from Seismic to Tidal Timescales: Theory and Observations. *Earth and Planetary Science Letters*, 508, 18–29.
- Lee, C. A. (2003), Compositional variation of density and seismic velocities in natural peridotites at STP conditions: Implications for seismic imaging of compositional heterogeneities in the upper mantle, *J. Geophys. Res.*, 108(B9), 2441, doi:10.1029/2003JB002413.
- Lee, C. T. A., Luffi, P., & Chin, E. J. (2011). Building and destroying continental mantle. *Annual Review of Earth and Planetary Sciences*, 39, 59–90.
- Le Roux, V., Bodinier, J.-L., Tommasi, A., Alard, O., Dautria, J.-M., Vauchez, A., & Riches, A.J.V. (2007). The Lherz spinel lherzolite: refertilised rather than pristine mantle. *Earth and Planetary Science Letters* 259, 599–612.
- Leprêtre, R., de Lamotte, D. F., Combier, V., Gimeno-Vives, O., Mohn, G., & Eschard, R. (2018). The Tell-Rif orogenic system (Morocco, Algeria, Tunisia) and the structural heritage of the southern Tethys margin.
- Ligorria, J. P., & Ammon, C. J. (1999). Iterative deconvolution and receiver-function estimation. *Bulletin of the seismological Society of America*, 89(5), 1395–1400.
- López Sánchez-Vizcaíno, V., Rubatto, D., Gómez-Pugnaire, M.T., Trommsdorff, V., & Müntener, O. (2001). Middle Miocene high-pressure metamorphism and fast exhumation of the Nevado-Filábride Complex, SE Spain. *Terra Nova* 13, 327–332.
- Lustrino, M., Duggen, S., & Rosenberg, C. L. (2011). The Central-Western Mediterranean: anomalous igneous activity in an anomalous collisional tectonic setting. *Earth-Science Reviews*, 104(1–3), 1–40.

- Lustrino, M., & Wilson, M. (2007). The circum-Mediterranean anorogenic Cenozoic igneous province. *Earth-Science Reviews*, 81(1-2), 1-65.
- Macchiavelli, C., Vergés, J., Schettino, A., Fernández, M., Turco, E., Casciello, E., Tone, M., Pietrantonio, P.P., & Tunini, L. (2017). A new southern North Atlantic isochron map: Insights into the drift of the Iberian plate since the Late Cretaceous. *Journal of Geophysical Research: Solid Earth*, 122(12), 9603-9626.
- Mahdjoub, Y., Choukroune, P., & Kienast, J. R. (1997). Kinematics of a complex Alpine segment; superimposed tectonic and metamorphic events in the Petite Kabylie Massif (northern Algeria). *Bulletin de la Société Géologique de France*, 168(5), 649-661.
- Magni, V. (2019). The effects of back-arc spreading on arc magmatism. *Earth and Planetary Science Letters*, 519, 141-151.
- Mancilla, F.d.L., Booth-Rea, G., Stich, D., Pérez-Peña, J. V., Morales, J., Azañón, J. M., Martín, R., & Giaconia, F. (2015). Slab rupture and delamination under the Betics and Rif constrained from receiver functions. *Tectonophysics*, 663, 225-237.
- Mancilla, F. d. L., Heit, B., Morales, J., Yuan, X., Stich, D., Molina-Aguilera, A., Azañón, J. M., & Martín, R. (2018). A STEP fault in Central Betics, associated with lateral lithospheric tearing at the northern edge of the Gibraltar arc subduction system. *Earth and Planetary Science Letters*, 486, 32-40.
- Martí, J., Mitjavila, J., Roca, E. and Aparicio, C., (1992). Cenozoic magmatism of the Valencia trough (western Mediterranean): relationship between structural evolution and volcanism. *Tectonophysics*, 203, 145-165.
- Massonne, H. J., Willner, A. P., & Gerya, T. (2007). Densities of metapelitic rocks at high to ultrahigh pressure conditions: What are the geodynamic consequences?. *Earth and Planetary Science Letters*, 256(1-2), 12-27.
- Maury, R.C., Fourcade, S., Coulon, C., El Azzouzi, M., Bellon, H., Coutelle, A., Ouabadi, A., Semroud, B., Megartsi, M., Cotton, J., Belanteur, O., Louni-Hacini, A., Piqué, A., Capdevila, R., Hernandez, J., & Réhault, J.-P. (2000). Post-collisional Neogene magmatism of the Mediterranean Maghreb margin: a consequence of slab breakoff. *CR Acad. Sci. Paris* 331, 159–173.
- Marzán Blas, I., 2000. Régimen térmico en la Península Ibérica. Estructura litosférica a través del Macizo Ibérico y el Margen Sur-Portugués. Tesis Doctoral Universidad de Barcelona (192 pp.).
- McDonough, W., & Sun, S. S. (1995). The composition of the Earth'. *Chemical Geology* 120 (120), 223-253.
- McClusky, S., Reilinger, R., Mahmoud, S., Ben Sari, D., & Tealeb, A. (2003). GPS constraints on Africa (Nubia) and Arabia plate motions. *Geophys. J. Int.* 155:126–38
- McKenzie, D., & Bickle, M. J. (1988), The volume and composition of melt generated by extension of the lithosphere, *J. Petrol.*, 29, 625–679.
- Melchiorre, M., Vergés, J., Fernández, M., Coltorti, M., Torne, M., & Casciello, E. (2017). Evidence for mantle heterogeneities in the westernmost Mediterranean from a statistical approach to volcanic petrology. *Lithos*, 276, 62–74. <https://doi.org/10.1016/j.lithos.2016.11.018>
- Michard, A., Negro, F., Saddiqi, O., Bouybaouene, M. L., Chalouan, A., Montigny, R., & Goffé, B. (2006). Pressure–temperature–time constraints on the Maghrebide mountain building: evidence from the Rif–Betic transect (Morocco, Spain), Algerian correlations, and geodynamic implications. *Comptes Rendus Geoscience*, 338(1-2), 92-114.

- Michard, A., Chalouan, A., Feinberg, H., Goffé, B., & Montingny, R. (2002). How does the Alpine belt end between Spain and Morocco. *Bulletin de la Société Géologique de France* 173, 3–15.
- Miller, M. S., O'Driscoll, L. J., Butcher, A. J., & Thomas, C. (2015). Imaging Canary Island hotspot material beneath the lithosphere of Morocco and southern Spain. *Earth and Planetary Science Letters*, 431, 186-194.
- Miller, M. S., Allam, A. A., Becker, T. W., Di Leo, J. F., & Wookey, J. (2013). Constraints on the tectonic evolution of the westernmost Mediterranean and northwestern Africa from shear wave splitting analysis. *Earth and Planetary Science Letters*, 375, 234-243.
- Morgan, P., & Fernandez, M. (1992). Neogene vertical movements and constraints on extension in the Catalan Coastal Ranges, Iberian Peninsula, and the Valencia trough (western Mediterranean). *Tectonophysics*, 203(1-4), 185-201.
- Morris, S.J.S., & Jackson, I. 2009. Diffusionally-assisted grain-boundary sliding and viscoelasticity of polycrystals. *J. Mech. Phys. Solids* 57:744–61
- Moudnib, L. E., Villaseñor, A., Harnafi, M., Gallart, J., Pazos, A., Serrano, I., Córdoba, D., Pulgar, J. A., Ibarra, P., Himmi, M. N., & Chourak, M. (2015). Crustal structure of the Betic–Rif system, western Mediterranean, from local earthquake tomography. *Tectonophysics*, 643, 94-105.
- Nirrengarten, M., Manatschal, G., Tugend, J., Kuszniir, N., & Sauter, D., (2018), Kinematic Evolution of the Southern North Atlantic: Implications for the Formation of Hyperextended Rift Systems. *Tectonics*, 37, 89–118.
- Niu, Y. (1997). Mantle melting and melt extraction processes beneath ocean ridges: Evidence from abyssal peridotites. *Journal of Petrology*, 38 (8), 1047-1074.
- Negredo, A. M., Mancilla, F. D. L., Clemente, C., Morales, J., & Fulla, J. (2020). Geodynamic modelling of edge-delamination driven by STEP faults: the westernmost Mediterranean margin (central Betic orogen) case study. *Frontiers in Earth Science*, 8, 435.
- Palme, H., & O'Neill, H. (2013). *Cosmochemical Estimates of Mantle Composition* (2 ed., Vol. 3). Elsevier Ltd.
- Palomeras, I., Villaseñor, A., Thurner, S., Levander, A., Gallart, J., & Harnafi, M. (2017). Lithospheric structure of Iberia and Morocco using finite-frequency Rayleigh wave tomography from earthquakes and seismic ambient noise. *Geochemistry, Geophysics, Geosystems*, 18, 1824–1840. <https://doi.org/10.1002/2016GC006657>
- Palomeras, I., Thurner, S., Levander, A., Liu, K., Villaseñor, A., Carbonell, R., & Harnafi, M. (2014). Finite-frequency Rayleigh wave tomography of the western Mediterranean: Mapping its lithospheric structure. *Geochemistry, Geophysics, Geosystems*, 15(1), 140-160.
- Pascal, G.P., Mauffret, A., & Patriat, P. (1993). The ocean-continent boundary in the Gulf of Lion from analysis of expanding spread profiles and gravity modelling. *Geophys. J. Int.* 113 (3), 701–726
- Pascal, G., Torne, M., Buhl, P., Watts, A.B., & Mauffret, A. (1992). Crustal and velocity structure of the Valencia Trough (Western Mediterranean). Part II: Detailed interpretation of 5 Expanding Spread Profiles. *Tectonophysics*. 203, 21-36, DOI: 10.1016/0040-1951(92)90213-P, 1992. Q1; F1: 3.325 - 2.866.
- Pedreira, D., Afonso, J., Pulgar, J., Gallastegui, J., Carballo, A., Fernández, M., D. García-Castellanos, I. Jiménez-Munt, J. Semprich, & O. García-Moreno (2015). Geophysical-petrological modeling of the lithosphere beneath the Cantabrian Mountains and the North-Iberian margin: Geodynamic implications. *Lithos*, 230, 46-68.

- Pedreira, A., Ruiz-Constán, A., García-Senz, J., Azor, A., Marín-Lechado, C., Ayala, C., de Neira, J.A.D. & Rodríguez-Fernández, L.R., 2020. Evolution of the South-Iberian paleomargin: From hyperextension to continental subduction. *Journal of Structural Geology*, 138, p.104122.
- Peral, M., Király, Á., Zlotnik, S., Funicello, F., Fernández, M., Faccenna, C., & Vergés, J. (2018). Opposite subduction polarity in adjacent plate segments. *Tectonics*, 37. <https://doi.org/10.1029/2017TC004896>.
- Peral, M., Zlotnik, S., Fernández, M., Vergés, J., Kumar, A., & Ruh, J. (2019). A numerical model of the Western Mediterranean. *Geophys. Res. Abstr.* 2019, 21, EGU2019-9312.
- Peral, M., Ruh, J., Zlotnik, S., Funicello, F., Fernández, M., Vergés, J., & Gerya, T. (2020a). Analog and numerical experiments of double subduction systems with opposite polarity in adjacent segments. *Geochemistry, Geophysics, Geosystems*, e2020GC009035.
- Peral, L., 2020b, Dynamics of subduction systems with opposite polarity in adjacent segments: application to the Westernmost Mediterranean PhD thesis, University of Barcelona, Barcelona.
- Pérez-Gussinyé, M., Metois, M., Fernández, M., Vergés, J., Fullea, J., & Lowry, A. R. (2009), Effective elastic thickness of Africa and its relationship to other proxies for lithospheric structure and surface tectonics, *Earth Planet. Sci. Lett.*, 287(1-2), 152-167. doi:10.1016/j.epsl.2009.08.004
- Phipps Morgan, J. (2001), Thermodynamics of pressure release melting of a veined plum pudding mantle, *Geochem. Geophys. Geosyst.*, 2(4), doi:10.1029/2000GC000049.
- Piomallo, C., & Morelli, A. (2003). P wave tomography of the mantle under the Alpine-Mediterranean area. *Journal of Geophysical Research: Solid Earth*, 108(B2).
- Platt, J.P., Allerton, S., Kirker, A., Mandeville, C., Mayfield, A., Platzman, E.S., & Rimi, A. (2003). The ultimate arc: differential displacement, oroclinal bending, and vertical axis rotation in the External Betic-Rif arc. *Tectonics* 22 (3), 1017. <http://dx.doi.org/10.1029/2001TC001321>.
- Polyak, B.G., Fernández, M., Khutorskoy, M.D., Soto, J.I., Basov, I.A., Comas, M.C., Khain, V.Y., Alonso, B., Agapova, G.V., Mazurova, I.S. & Negredo, A., 1996. Heat flow in the Alboran Sea, western Mediterranean. *Tectonophysics*, 263(1-4), pp.191-218.
- Poort, J., Lucazeau, F., Le Gal, V., Dal Cin, M., Leroux, E., Bouzid, A., ... & Ferrante, G. M. (2020). Heat flow in the Western Mediterranean: Thermal anomalies on the margins, the seafloor and the transfer zones. *Marine Geology*, 419, 106064.
- Presnall, D. C., Gudfinnsson, H. H., & Walter, M. J. (2002), Generation of mid-ocean ridge basalts at pressures from 1 to 7 GPa, *Geochim. Cosmochim. Acta*, 66, 2073–2090.
- Priestley, K., & McKenzie, D. (2006). The thermal structure of the lithosphere from shear wave velocities. *Earth and Planetary Science Letters*, 244 (1-2), 285-301.
- Priestley, K., & McKenzie, D. (2013). The relationship between shear wave velocity, temperature, attenuation and viscosity in the shallow part of the mantle. *Earth and Planetary Science Letters*, 381, 78-91.
- Puga, E., Nieto, J.M., & Díaz De Federico, A. (2000). Contrasting P–T Paths in eclogites of the Betic Ophiolitic Association, Mulhacen Complex, Southeastern Spain. *The Canadian Mineralogist* 38, 1137–1161.
- Raj R. (1975). Transient behaviour of diffusion-induced creep and creep rupture. *Metall. Trans. A* 6A:1499–509

- Revenaugh, J., & Jordan, T. (2008). Mantle layering from ScS reverberations: 3. The upper mantle. *Journal of Geophysical Research: Solid Earth*, 96 (B12), 19781-19810.
- Rimi, A., Fernandez, M., Manar, A., Matsushima, J., Okubo, Y., & Morel, J.L. (2005). Geothermal anomalies and analysis of gravity, fracturing and magnetic features in Morocco. World Geothermal Congress Antalya, Turkey, vol. 2, pp. 4–290.
- Ringwood, A. (1977). Composition for of the core of the and implications origin earth. *Geochemical Journal*, 11, 111-135.
- Ringwood, A. E. (1974). The petrological evolution of island arc systems: Twenty-seventh William Smith Lecture. *Journal of the Geological Society*, 130(3), 183-204.
- Ritzwoller, M. H., N. M. Shapiro, & S. J. Zhong (2004), Cooling history of the Pacific lithosphere. *Earth Planet. Sci. Lett.*, 226, 69–84.
- Royden, L., & Faccenna, C. (2018). Subduction orogeny and the late cenozoic evolution of the Mediterranean Arcs. *Annual Review of Earth and Planetary Sciences*, 46, 261-289.
- Roca, E. (2001). The Northwest-Mediterranean basin (Valencia Trough, Gulf of Lions and Liguro-Provençal basins): structure and geodynamic evolution. In: Ziegler, P.A., Cavazza, W., Robertson, A.F.H. and Crasquin- Soleau, S. (eds.), Peri Tethyan Rift/Wrench Basins and Passive margins. Mémoires du Muséum National d'Histoire Naturelle, 186, 671-706
- Roca, E. (1996). La evolución geodinámica de la Cuenca Catalano-Balear y áreas adyacentes desde el Mesozoico hasta la actualidad. *Acta Geológica Hispánica*, 29,3-25
- Roca, E., Frizon de Lamotte, D., Mauffret, A., Bracène, R., Vergés, J., Benaouali, N., Fernandez, M., Muñoz, J.A., & Zeyen, H. (2004). TRANSMED transect II. In: Cavazza, W., Roure, F., Spakman, W., Stampfli, G.M., Ziegler, P. (Eds.), The TRANSMED Atlas—the Mediterranean Region from Crust to Mantle. Springer, Berlin Heidelberg.
- Rossetti, F., Theye, T., Lucci, F., Bouybaouene, M. L., Dini, A., Gerdes, A., ... & Cozzupoli, D. (2010). Timing and modes of granite magmatism in the core of the Alboran Domain, Rif chain, northern Morocco: implications for the Alpine evolution of the western Mediterranean. *Tectonics*, 29(2).
- Rossum, G. (1995). Python tutorial, Technical Report CS-R9526, Centrum voor Wiskunde en Informatica (CWI), Amsterdam.
- Rudnick, R. L., & Gao, S. (2003). Composition of the continental crust. *Treatise on Geochemistry*, 3, 659. <https://doi.org/10.1016/B0-08-043751-6/03016-4>
- Roure, F., Casero, P., & Addoum, B. (2012). Alpine inversion of the North African margin and delamination of its continental lithosphere. *Tectonics*, 31(3).
- Ruiz-Constan, A., Pedrera, A., Galindo-Zaldívar, J., Pous, J., Arzate, J., Roldán-García, F.J., Marin-Lechado, C., & Anahnah, F. (2012). Constraints on the frontal crustal structure of a continental collision from an integrated geophysical research: the central-western Betic Cordillera (SW Spain). *Geochem.Geophys.Geosyst.* 13 (8) (art. no. Q08012).
- Sàbat, F., Roca, E., Muñoz, J.A., Vergés, J., Santanach, P., Masana, E., Sans, M., Estévez, A., & Santisteban, C. (1997). Role of extension and compression in the evolution of the eastern margin of Iberia: the ESCI-València trough seismic profile. *Revista de la Sociedad Geológica de España* 8, 431–448.
- Sandwell, D. T., & Smith, W. H. F. (1997). Marine gravity from Geosat and ERS 1 satellite altimetry. *Journal of Geophysical Research*, 102, 10,039–10,054. <https://doi.org/10.1029/96jb03223>

- Schilling, J., Zajac, M., Evans, R., Johnston, T., White, W., Devine, J., & Kingsley, R. (1983). Petrologic and geochemical variations along the Mid-Atlantic Ridge from 29 degrees N to 73 degrees N. *Am J Sci* 283:510–586
- Schettino, A., & Turco, E. (2011) Tectonic history of the western Tethys since the Late Triassic. *Geol. Soc. Am. Bull.*, 123, 89–105.
- Schubert, G., Turcotte, D.L. & Olson, P. (2001). Mantle convection in the Earth and planets. Cambridge Univ. Press. UK, pp 956.
- Shorttle, O., & MacLennan, J. (2011), Compositional trends of Icelandic basalts: Implications for short-length scale lithological heterogeneity in mantle plumes, *Geochem. Geophys. Geosyst.*, 12, Q11008, doi:10.1029/2011GC003748.
- Soto, J.I., & Platt, J.P. (1999) Petrological and structural evolution of high-grade metamorphic rocks from the floor of the Alboran Sea basin, western Mediterranean. *Journal of Petrology* 40, 21–60.
- Sobolev, S., Zeyen, H., Stoll, G., Werling, F., Altherr, R., & Fuchs, K. (1996). Upper mantle temperatures from teleseismic tomography of French Massif Central including effects of composition, mineral reactions, anharmonicity, anelasticity and partial melt. *Earth and Planetary Science Letters*, 139 (1-2), 147–163.
- Spandler, C., & Pirard, C. (2013). Element recycling from subducting slabs to arc crust: A review. *Lithos*, 170, 208–223.
- Spakman, W., & Wortel, M. J. R. (2004). A tomographic view on western Mediterranean geodynamics. In W. Cavazza, F. Roure, W. Spakman, G. M. Stampfli, & P. Ziegler (Eds.), *The TRANSMED Atlas—The Mediterranean region from crust to mantle*, (pp. 31–52). Berlin Heidelberg: Springer.
- Stampfli, G., & Borel, G.D. (2002), A plate tectonic model for the Paleozoic and Mesozoic constrained by dynamic plate boundaries and restored synthetic oceanic isochrones. *Earth Planet. Sci. Lett.*, 196, 17–33.
- Stixrude, L., & Lithgow-Bertelloni, C. (2005). Mineralogy and elasticity of the oceanic upper mantle: Origin of the low-velocity zone. *Journal of Geophysical Research: Solid Earth*, 110 (3), 1–16.
- Strang van Hees, G. L. (2000). Some elementary relations between mass distributions inside the Earth and the geoid and gravity field. *Journal of Geodynamics*, 29: 111–123.
- Talwani, M., Worzel, J., & Landisman, L. (1959), Rapid computations for two-dimensional bodies with application to the Mendocino submarine fracture zone, *J. Geophys. Res.*, 64, 49–59.
- Takei, Y (2017). Effects of Partial Melting on Seismic Velocity and Attenuation: A New Insight from Experiments. *Annual Review of Earth and Planetary Sciences* 2017. 45:447–70.
- Teixell, A., Ayarza, P., Zeyen, H., Fernandez, M., & Arboleya, M. L. (2005). Effects of mantle upwelling in a compressional setting: the Atlas Mountains of Morocco. *Terra Nova*, 17(5), 456–461.
- Torné, M., Banda, E., & Fernandez, M. (1996). The Valencia Trough: geological and geophysical constraints on basin formation models. *Mémoires du Muséum national d'histoire naturelle* (1993), 170, 103–128.
- Torne, M., Fernández, M., Vergés, J., Ayala, C., Salas, M. C., Jimenez-Munt, I., Buffett G.G., & Díaz, J. (2015). Crust and mantle lithospheric structure of the Iberian Peninsula deduced from potential field modeling and thermal analysis. *Tectonophysics*, 663, 419–433.

- Torne, M., Fernandez, M., Comas, M. C., & Soto, J. I. (2000). Lithospheric structure beneath the Alboran Basin: results from 3D gravity modeling and tectonic relevance. *Journal of Geophysical Research: Solid Earth*, 105(B2), 3209-3228.
- Torne, M., Pascal, G., Buhl, P., Watts, A.B., & Mauffret, A. (1992). Crustal structure of the Valencia Trough (Western Mediterranean). Part 1. A combined refraction/wide angle reflection and near-vertical reflection study. *Tectonophysics* 203, 1–20.
- Tunini, L. (2015). The Central Asia collision zone: numerical modelling of the lithospheric structure and the present-day kinematics PhD thesis, University of Barcelona, Barcelona.
- Tunini, L., Fernandez, M., Afonso, J., Villaseñor, A., Jiménez-Munt, I., & Melchiorre, M. (2016). Geophysical-petrological model of the crust and upper mantle in the India-Eurasia collision zone. *Tectonics*, 35 (7), 1642-1669.
- Tunini, L., Jiménez-Munt, I., Fernandez, M., Vergés, J., & Villaseñor, A. (2015). Lithospheric mantle heterogeneities beneath the Zagros Mountains and the Iranian Plateau: A petrological-geophysical study. *Geophysical Journal International*, 200 (1), 596-614.
- Turcotte, D., & Morgan, J. (2013). The Physics of Magma Migration and Mantle Flow Beneath a Mid-Ocean Ridge. *0225*, 155-182.
- Turcotte, D.L., & Schubert, G. (1982). *Geodynamics. Application of continuum physics to geological problems*. John Wiley & Sons, New York, 450 pp.
- Van Hinsbergen, D., Vissers, R., & Spakman, W. (2014). Origin and consequences of western Mediterranean subduction, rollback, and slab segmentation. *Tectonics*, 33, 393–419.
- Van Hinsbergen, D. J., Torsvik, T. H., Schmid, S. M., Mañenco, L. C., Maffione, M., Vissers, R. L., Gürer, D., & Spakman, W. (2020). Orogenic architecture of the Mediterranean region and kinematic reconstruction of its tectonic evolution since the Triassic. *Gondwana Research*, 81, 79-229.
- Van Keken, P., Hauri, E., & Ballentine, C. (2002). Mantle Mixing: The Generation, Preservation, and Destruction of Chemical Heterogeneity. *Annual Review of Earth and Planetary Sciences*, 30 (1), 493-525.
- Vergés, J., & Fernández, M. (2012) Tethys–Atlantic interaction along the Iberia–Africa plate boundary: The Betic–Rif orogenic system. *Tectonophysics*, 579, 144–172.
- Vergés, J., & Fernández, M. (2006), Ranges and basins in the Iberian Peninsula: Their contribution to the present topography. *Geol. Soc. Mem.*, 32, 223–234.
- Vergés, J., & Sàbat, F. (1999). Constraints on the western Mediterranean kinematic evolution along a 1,000-km transect from Iberia to Africa. In: Durand, B., Jolivet, L., Horváth, F., Séranne, M. (Eds.), *On the Mediterranean Basins: Tertiary Extension within Alpine orogen*. Geological Society London Special Publications, 134, pp. 63–80.
- Vidal, N., Gallart, J., & Danobeitia, J.J. (1998). A deep seismic transect from the NE Iberian Peninsula to the Western Mediterranean. *Journal of Geophysical Research* 103, 12381–12396.
- Vilà, M., Fernández, M., & Jiménez-Munt, I. (2010). Radiogenic heat production variability of some common lithological groups and its significance to lithospheric thermal modeling. *Tectonophysics*, 490, 152–164. <https://doi.org/10.1016/j.tecto.2010.05.003>
- Villaseñor, A., Chevrot, S., Harnafi, M., Gallart, J., Pazos, A., Serrano, I., et al. (2015). Subduction and volcanism in the Iberia-North Africa collision zone from tomographic images of the upper mantle. *Tectonophysics*, 663, 238–249. <https://doi.org/10.1016/j.tecto.2015.08.042>

- Villaseca, C., Ancochea, E., Orejana, D., & Jeffries, T. (2010). Composition and evolution of the lithospheric mantle in central Spain: Inferences from peridotite xenoliths from the Calatrava volcanic field. *Geological Society of London, Special Publication*, 337, 125–152. <https://doi.org/10.1144/sp337.7>
- Vinnik, L. (1977). Detection of waves converted from p to sv in the mantle. *Physics of the Earth and Planetary Interiors*, 15 (October 1976), 39-45.
- Watanabe, T. (1993). Effects of water and melt on seismic velocities and their application to characterization of seismic reflectors. *Geophysical Research Letters*, 20 (24), 2933-2936.
- Wilson, M., & Bianchini, G. (1999). Tertiary–Quaternary magmatism within the Mediterranean and surrounding regions. In: Durand, B., Jolivet, L., Horvath, F., Seranne, M. (Eds.), *The Mediterranean Basins: Tertiary Extension within the Alpine Orogen*. Geol. Soc., London Spec. Publ., vol. 156, pp. 141–168.
- Winter, J. D. (2010), *An Introduction to Igneous and Metamorphic Petrology*, Prentice Hall, New York.
- Workman, R., & Hart, S. (2005). Major and trace element composition of the depleted MORB mantle (DMM). *Earth and Planetary Science Letters*, 231 (1-2), 53-72.
- Xu, W., Lithgow-Bertelloni, C., Stixrude, L., & Ritsema, J. (2008). The effect of bulk composition and temperature on mantle seismic structure. *Earth and Planetary Science Letters*, 275 (1-2), 70-79.
- Zeyen, H., Ayarza, P., Fernández, M., & Rimi, A. (2005), Lithospheric structure under the western African-European plate boundary: A transect across the Atlas Mountains and the Gulf of Cadiz. *Tectonics*, 24, TC2001, [doi:10.1029/2004TC001639](https://doi.org/10.1029/2004TC001639).
- Zeyen, H., & Fernández, M. (1994). Integrated lithospheric modeling combining thermal, gravity, 99, 18,089-18,102.
- Zhu, L., & Kanamori, H. (2000). Moho depth variation in southern California from teleseismic receiver functions. *Journal of Geophysical Research: Solid Earth*, 105(B2), 2969-2980.
- Zienkiewicz, O. C. (1977), *The Finite Element Method*, McGraw-Hill, New York.

Appendix

Appendix A: LitMod2D_2.0 User Manual

A1. Introductions

LitMod2D 2.0 is a finite element code which combines potential field, geochemical and seismological data to work out thermo-chemical structure of the lithosphere. This document is a manual for a python based GUI to build the model where the user draws geometry of the bodies in the cross-section and associate physical properties to those bodies.

A2. Installation

User can download or clone the package from https://github.com/ajay6763/LitMod2D_2.0_package_dist_users.git. You will have following directory structure:

```
./LitMod2D_2.0_package_dist_users
    ./Generator_Linux: to generate material file
        ./GUI: includes the GUI in python
    ./Manual: Manual for GUI use
    ./Post_processing: packages for post-processing
        ./flexure_tao
        ./Phase_diagrams
        ./RF
        ./Surface_wave_dispersion
        ./Synthetic_Seismic_tomography
```

To setup Generator, follow the instructions in REAME.md file in the Generator Linux directory. Now we need to setup the GUI which essentially means we need to install python libraries. Generally, Linux comes with installed python2.7 but in Windows you might have to install python2.7 (<https://www.python.org/getit/>). This GUI uses packages from python which do not come pre-installed with stand-alone python installation. This GUI is python2.7 compatible. All packages used here can be installed using "pip" a python package manager which can be easily installed in Windows or Linux distributions (<https://pip.pypa.io/en/stable/installing/>).

Once you have the python and pip setup go into the GUI directory and run the following command:

```
pip install -r requirements.txt
```

This should have you almost everything needed for the GUI. In addition to this you might have to install “Tkinter” and “PyQt4”, and can installed using following commands:

```
sudo apt-get update
```

```
sudo apt-get python-tk
```

```
sudo apt-get PyQt4
```

If python-tk does not install than try installing using Synaptic package manager. Open it and search for Tkiner and install python-tk from there. Once you have everything installed you need to add the LitMod2D to you your path. To do this simply open `/.bashsrc` and add following lines:

```
export LitModHOME= "absolute path of LitMod2D 2.0"
```

where “absolute path of LitMod2D 2.0” is the path to LitMod2D 2.0 dist users in your system.

A3. How to make and work with models?

To start the LitMod2D 2.0 go into GUI folder and run `main.py` (in Linux type “python `main.py`” in Windows you can double click on the `main.py` file), running which Figure 1 will appear. Here you have three options. Build model option is to build a model from scratch. Load Model is to load a previously build model and the last option is about help.

*Note: In dialog boxes, put your mouse in a field and additional information will appear.

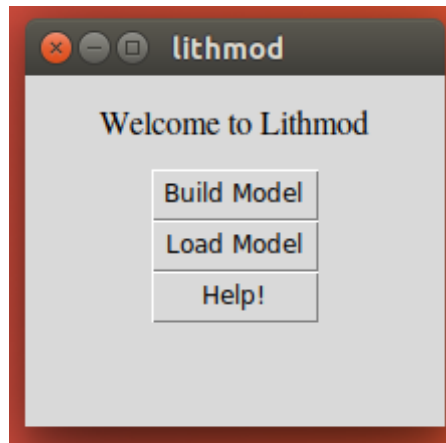


Figure A1 Welcome Page

A3.1. Build Model

Before building a model user should have a clear idea and sketch of the model user wants to build. User should know nodes along which different bodies will be connected. A model is build from top-to-bottom and left to right and every time user wants to exit and wants to save the model, user should close the model by clicking the close Model button on top right. After clicking close model click

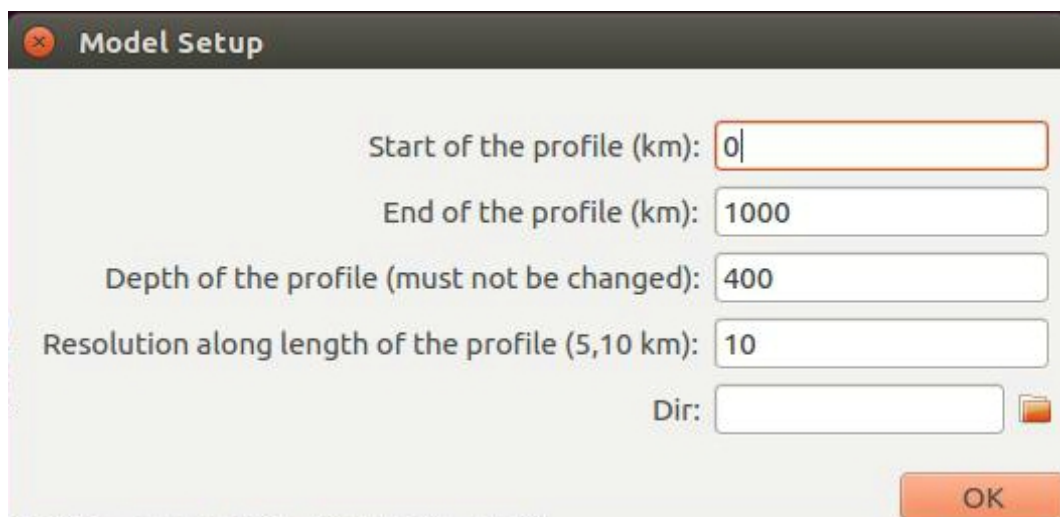


Figure A2 Model setup on dialog box about model size and location some info about the model.

After user hits Build Model option a dialogue box appears (Figure A2) asking for information about the model and another dialogue box asking for digitized file where you already have nodes of the bodies (e.g., digitized sketch, Moho and LAB

depths; two column, X (distance along profile, km) Y(depth, km)). This digitized file will be plotted in background and you can click on the plotted points.

****Note:** Bodies are added from left to right

Start of the profile (km): This is the left most starting point of profile (it can be negative too. In that case all the observable files should have same limits).

End of the profile (km): This the right most end point of profile.

Depth of the profile: This is the depth of the profile in km. It must be 400km, so it must not be changed.

Resolution along the profile: resolution of the profile

Folder: Here user selects the folder in which observable files are put and it becomes the working folder for LitMod2D 2.0. All the outputs files are stored in this folder.

Tip: For each of your model you can make folder where you put all observables files, material files from Generator. Later you can load the model by browsing into this folder.

After the user hits OK button build model window will appear (Figure A3). Here the user has different option.

Add Body

Bodies are added from top to bottom, each body is drawn left to the right. To add a body press the add button on the window (Figure A3), which will open a dialog box asking for information about the body (Figure A4)

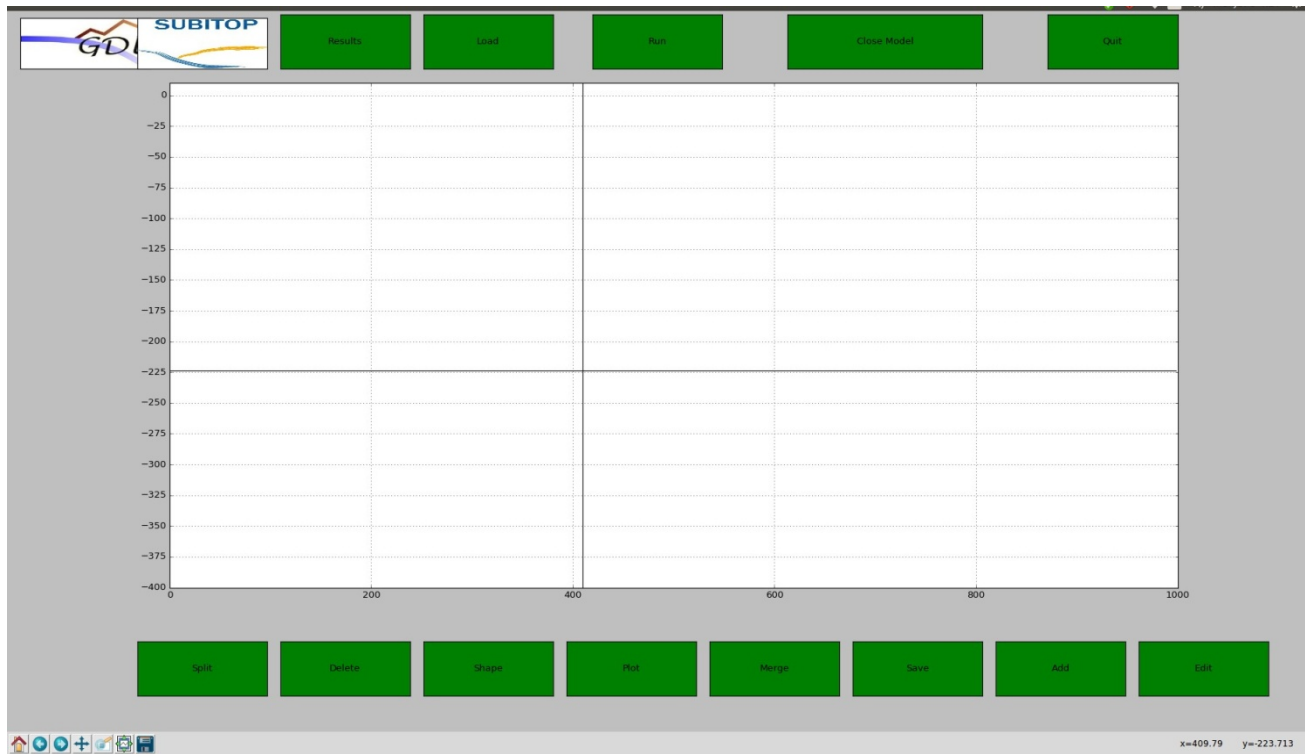


Figure A3 Build Model Window.

*Please note that format in which default values appear should be maintained.

Fields description:

Name: Name of the body. Just for your reference

Body number: Index of the body starting from the top.

Material: Type of material of the body

Body type: if you are adding a body which is new, this option should be normal. If you are splitting a body change this option to split. If you are adding an anomaly, change this option to type of anomaly you are adding (thermal or seismic or from a file).

Once the user is done with adding properties user should hit OK and control will be back to the plotting area.

To add point: Middle mouse click (Scroller)

To delete current point: double left click.

To close body: right click

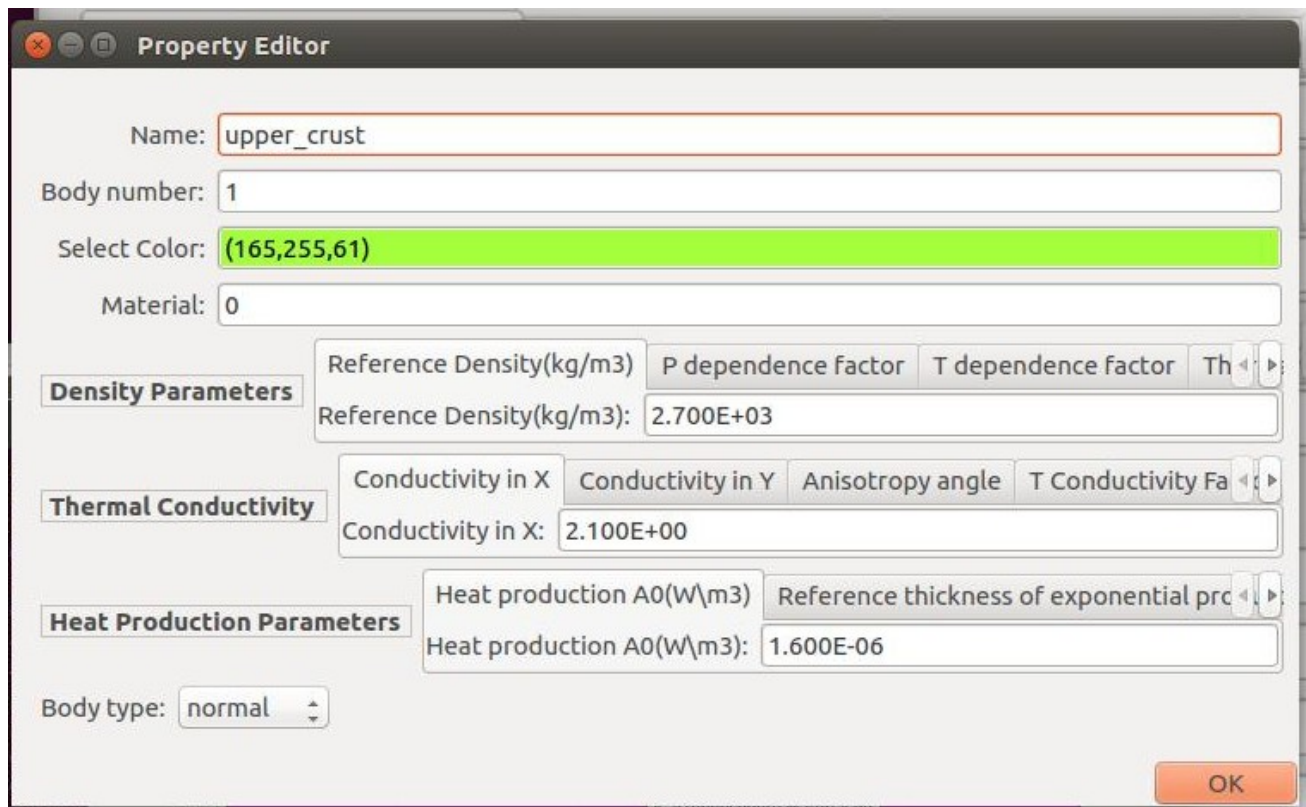


Figure A4 Body property editor.

Delete body

The user can delete the last body entered by clicking on the delete button. Let us say a user has drawn three bodies. To delete second body first user has to delete the third body. So essentially you can only delete the last entered body. If you want to delete a body in between, then you can use the merge function (see following sections).

Change shape of the bodies

To move, delete or add node points of the drawn body's user can click on shape button. After clicking this button a separate plot will appear where all bodies will be drawn as points (In case you have anomalies in the model other than from a external file then second window also appears where you can edit anomalous bodies too). Now user can move these point by left click drag, to delete a point move the

cursor on the point and then press 'd' key on the keyboard (sometimes there are more than one points so keep pressing 'd' until the point is gone). To insert a node go to the node and press 'i' key on the keyboard. After you are done changes can be saved with right click while the cursor is on the edit plot window. Once you have saved changes close the window and come back to the main window and hit plot button which will update the changes. This function will only work after you have closed your model.

*Note: when you see the plot of the bodies (for anomalies) in separate window, you might see some lines connecting different bodies, just ignore them. To have clear idea keep main window where you added bodies in front of you along with this separate window

Edit properties

To edit properties of a body already drawn click on edit button and a dialog box will appear asking for the index of the body you want to edit.

Split body

This function allows the user to split a body into two (does not work for anomalous bodies). This function should be used with a lot of care. The user should know exactly where to start split. Tip to use this option is that when you enter a body it is added in counter-clockwise direction, but when body is save it is save in clock-wise direction. Now the start point of the axis along which you have to split the body should be first in clock-wise direction than the last point. Once you have split a body save the model and then again load it.

*Note: If for some reasons split does not work then you can load model again and try to split it again.

Anomalies in the sublithospheric mantle

In this GUI anomalies (Composition, thermal, seismic) are added on top of the completely closed profile. You can edit the shape of these anomalies and properties (type and amount of anomaly) with shape and edit function respectively. These types of anomalies can be drawn in the profile. There is another way to enter anomalies where you enter them in a file and you choose the file (For more information about this file refers to the *LitMod2D_usage.pdf*, supplied in this folder. Only seismic anomalies can be added in this way.

* Note that if you have selected anomalies in form of a file then all other anomalies (drawn on the profile) are not considered even if you have added them.

Save Model

When you are done with the profile and you have closed it by clicking on the Close model button, it can be saved by clicking on save button. After you click on the save button a window will appear asking for some more information. You can choose observable file, where you should have three columns with distance, data value, and error. Total length and sampling of these observables should be exactly same as that in your profile. One important thing is to have starting and end point of these observables data as that of start and end you choose to make your profile. After browsing the file try to keep only the name of the input file try to delete the absolute path. Here making a folder for each of your model, which can be at any location in your computer, helps keeping things in track.

Every time you save a model, a back-up of three files, and 1) *litmod.inp*, 2) *bodies_GUI.dat*, 3) *bodies_GUI_envelops.out*, with a date and time added. You can later rename these set of files and load them again.

A3.2. Run model

To run a model first you have to save the model by clicking on the save button, but before that, your model should be closed. You should also put the observables file (topography, Bouguer, geoid, free air, heat flux) and composition files (e.g., 80, 81, 88, 99 etc.) which you have associated with the bodies in your model, in the same folder.

Note: To run a model you should have LitMod2D 2.0 program executable for Windows or Linux based on your system. Executable for Linux is provided with the distribution. Name of these executables should be LitMod2D 2.0_V4_Windows for windows and should be in LitMod2D 2.0 package folder and for Linux it should be in same folder with name LitMod2D_2.0_V4_Linux.

A 3.4. Load Model

This option lets the user load previously build models. To load models user need three files, 1) *litmod.inp*, an input file to the LitMod2D 2.0, 2) *bodies_GUI.out*, this file contains nodes point of the bodies in the model and colour of the body and 3) *bodies_GUI_envelops.out*. Units of nodes points in bodies GUI.dat are in kilometres. This option also allows you to restore changes while you are working. For instance if something goes wrong (e.g., split body, merge body) you can load last saved session

and start from there again. You can also track this three files saved in same folder at any time you have saved them, rename them and can load them again.

A4. Post-processing toolbox

Post-processing toolbox contains a set of codes/scripts linking with outputs from LitMod2D 2.0 with other softwares. At this point is it coupled with “*Computer programs in Seismology (CPS)*” tool (Herrmann, 2013) and “*tao-geo*” (Garcia-Castellanos et al., 2002) software. It also includes scripts to produce stable phase and mineral assemblages in the profile. Installations of coupled softwares are explained below.

A4.1. Passive Seismological data

Forward prediction of surface wave dispersion curves and receiver functions can be calculated from the seismic velocities distribution with depth at each node along the profile. This is done by feeding in seismic velocities to CPS. CPS can be easily downloaded and install from <http://www.eas.slu.edu/eqc/eqccps.html> and needs to in your path.

```

akumar@akumar-Precision-3630-Tower: ~/owncloud/PHD/LITMOD_package_Linux_dist_us
5
    Your option is          5

Will this be a sublithospheric mantle?
YES = 1          NO = 0
0

Do you have H2O and K2O in your system?
YES = 1          NO = 0
0

Now enter the bulk composition (in wt%) for the oxides
SiO2 Al2O3 FeO MgO CaO Na2O (in this order,          one per line)
45
4
8
34
3
0.2

*****
Note that these values do not add up to 100%
The absolute error (in wt%) is = 5.799999999999972
If you do not stop here, I will correct to 100%
*****

Name of the body (mantle/crust)
rrrr

Do you need the FULL (prop. + system) table?
For "Yes" type 1 ; For "NO" type 0

```

Figure A5 Generator console showing option to generate full property table.

A4.2. Flexural Isostasy

Flexural isostasy is incorporated via “tao-geo” and can be downloaded and installed from <https://github.com/danigeos/tao-geo> and should be added in your path.

A4.3. Stable phase and mineral assemblages

To do this user should have full property tables from the GENERATOR module. Opting for option “1” shown in 5 produces both full property material file along with simple material file with physical properties only. Full property material file contains information on stable phase and mineral assemblages (weight percentage, volume percentage) along with the physical properties (density, seismic velocities). Simple material files, with material code ‘90, 99...’ are read in the LitMod2D 2.0 whereas full property material files named as ‘99_FULL etc.’ are used to produce stable phase and mineral assemblages. Full property material files should be in the model directory. First user should run “*make_mineral_wise_files_full.sh*”. This produces mineral wise properties along the profile. User can plot a property (e.g., weight%) of stable mineral at a distance point along the profile running ‘*phase_diagram 1D.py*’ 6 or depth distribution of individual minerals along the profile using ‘*phase_diagram 2D.py*’

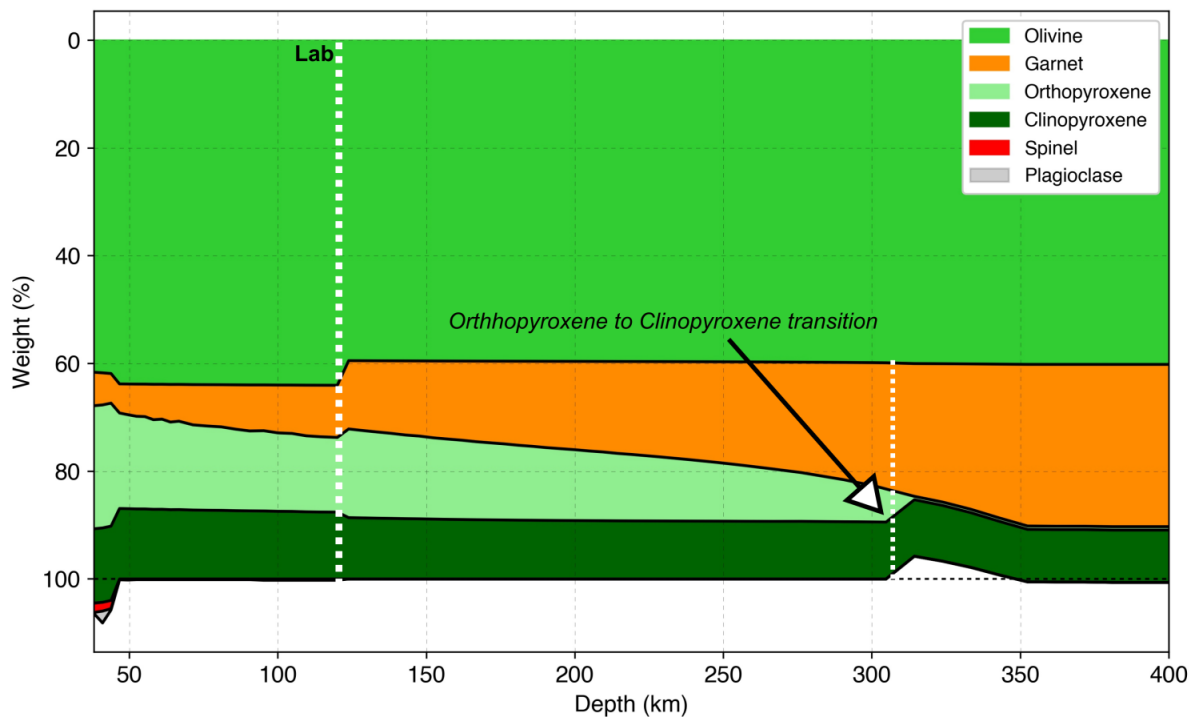


Figure A6 Example of stable mineral wt% distribution at a distance point.

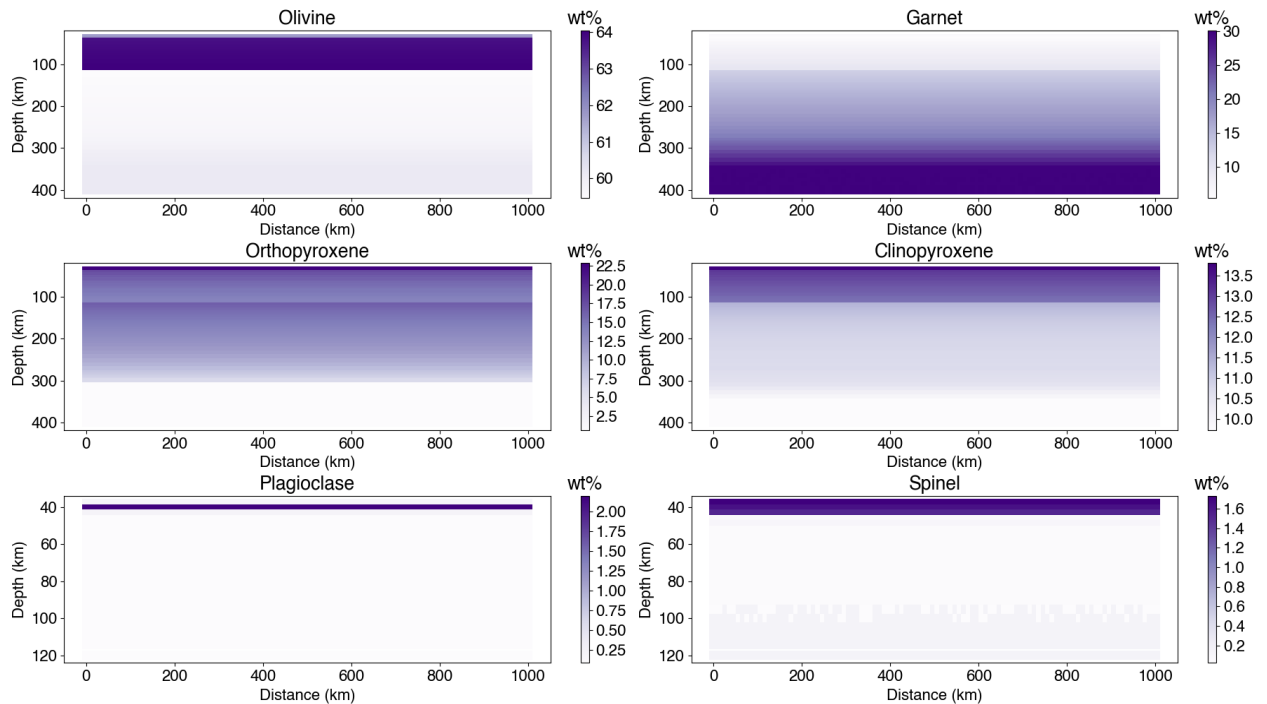


Figure A7 Example of stable mineral wt% distribution along a profile.

A5. Miscellaneous

User can also use other functionality. They are listed below:

Values of coordinates are shown at the bottom right corner of the plot. It is useful to add points at specific positions.

You can zoom in at any area of the profile by clicking at the functions in the left bottom of the window. You can also go to the zoom mode by pressing “o” on the keyboard. Then you can select area to zoom in with mouse and navigate back and forth with arrow keys on the keyboard. It is useful for small area bodies.

To go back out of zoom mode you should press “o” again.

You can drag the profile and to go to this mode you can press “p” on the keyboard.

If you want to go straight to the initial level after zooming at different levels just press “h” key on the keyboard.